Role of Viscoelasticity and Non-Linear Rheology in Flows of Complex Fluids at High Deformation Rates

by

Thomas Joseph Ober

B.S., Chemical Engineering, 2008, Cornell University (Ithaca, NY)
S.M., Mechanical Engineering, 2010, Massachusetts Institute of Technology (Cambridge, MA)

Submitted to the Department of Mechanical Engineering
in partial fulfillment of the requirements for the degree of

Doctor of Philosophy in Mechanical Engineering

at the

MASSACHUSETTS INSTITUTE OF TECHNOLOGY

September 2013

Author .....
Department of Mechanical Engineering
August 12, 2013

Certified by .....
Gareth H. McKinley
Professor, Mechanical Engineering
Thesis Supervisor

Accepted by .....
David E. Hardt
Graduate Officer, Department Committee on Graduate Students

Role of Viscoelasticity and Non-Linear Rheology in Flows of Complex Fluids at High Deformation Rates

by

Thomas Joseph Ober

Submitted to the Department of Mechanical Engineering
on August 12, 2013, in partial fulfillment of the
requirements for the degree of
Doctor of Philosophy in Mechanical Engineering

Abstract

We combine pressure, velocimetry and birefringence measurements to study three phenomena for which the fluid rheology plays a dominant role: 1) shear banding in micellar fluids, 2) extension-dominated flows in microfluidic devices, and 3) flow-induced particle migration in microchannels.

Firstly, worm-like micellar solutions are model non-Newtonian fluids having a single relaxation time λ. At shear rates larger than $\dot{\gamma} \gtrsim \lambda^{-1}$, however, these systems exhibit shear banding and non-linear rheological behavior, whose importance is characterized by the Weissenberg number $Wi \equiv \lambda\dot{\gamma}$. We develop a stability criterion for the onset of a purely viscoelastic instability for shear-banding fluids, to establish the limitations of conventional rheometric techniques for studying these fluids.

A second challenge for conventional rheometers is inertially-driven secondary flows. The onset of these flows is governed by the Reynolds number $Re \equiv \mathcal{U}D/\nu$, where $\mathcal{U}$ is the velocity, D is the flow geometry length and ν is the fluid kinematic viscosity. We develop microfluidic devices to impose shear and extensional deformation rates up to $\mathcal{O}(10^5)$ s^{-1} at low Re. These experiments combine pressure measurements, micro-particle image velocimetry (μ-PIV) and birefringence measurements. We develop a microfluidic chip that enables applied rheologists to quantitatively differentiate between fluid formulations intended for applications at high deformation rates.

Finally, we study the interplay between fluid inertia and elasticity on particle migration. The inertially-dominated case is governed by the channel Reynolds number Re_c and particle Reynolds number $Re_p \equiv Re_c(a/D)^2$, where a is the particle diameter. In a microfluidic device, the particle and channel size are on the same order, and hence migration occurs at $Re_p \sim 1$, in the so-called 'inertial focusing' regime which may have applications in clinical medicine. However, most physiological fluids are viscoelastic and therefore particle migration in these fluids occurs at high Reynolds and Weissenberg numbers, which is a mostly unstudied regime. We combine pressure measurements, streak imaging, μ-PIV and particle trajectory analysis (PTA) to study the migration of polystyrene beads. Inertia drives particles toward the channel walls, whereas elasticity drives particles toward the channel centerline even at $Re_c \sim 2000$.

Thesis Supervisor: Gareth H. McKinley
Title: Professor, Mechanical Engineering

Acknowledgments

I wish to dedicate this work principally to my parents, grandparents and extended family.

I am greatly indebted to my research collaborators with whom I have been privileged to work, namely Chris Dimitriou, Simon Haward, Bavand Keshavarz, Eugene Lim, Vivek Sharma and Johannes Soulages (MIT), Michael Cromer and Pam Cook (University of Delaware), Marc-Antoine Fardin (MIT/Paris Diderot 7) and Sandra Lerouge (Paris Diderot 7), Laura Casanellas (MIT/Universitat de Barcelona), Mónica Oliveira (University of Strathclyde), Jon Edd (Vanderbilt University), Douglas Neal (LaVision) and many others.

I also acknowledge financial support from the National Science Foundation Graduate Research Fellowship for providing me the freedom to pursue research topics of interest to me.

Finally, I am grateful for the mentoring of my advisor.

Contents

Chapter 1

Introduction

1.1 Motivation

Water-based polymeric and surfactant solutions are encountered across a broad range of industries and applications, from rheological modifiers in foodstuffs (*e.g.* xanthan and guar gum) and consumer products (*e.g.* sodium laureth sulfate), to inks and paints (*e.g.* cellullose derivatives), to additives for drag reduction in turbulent pipe flows (*e.g.* polyethylene oxide and polyacrylamide) and hydraulic fracturing fluids for enhanced oil recovery (Kefi *et al.*, 2005). Furthermore, polymer solutions are found in a large number of physiological fluids in the human body. For example, hyaluronic acid is found in synovial fluid (Kogan *et al.*, 2007), mucin is a major component of saliva (Haward *et al.*, 2011), and the addition of drag reducing polymers to blood has been suggested as a means of preventing death from hemorrhagic shock (Kameneva, 2012).

The addition of a polymer to a Newtonian solvent, even at dilute concentrations, introduces viscoelasticity to the resultant liquid, which can dramatically alter its rheological behavior and suitability for a particular application. A viscoelastic material is one that exhibits both a fluid-like (*i.e.* viscous) and a solid-like (*i.e.* elastic) behavior in response to an imposed deformation or stress (Bird *et al.*, 1987). There are generally two dimensionless groups that are used to quantify the relative importance of viscoelasticity in a flow (Dealy, 2010). The first is the Deborah number De which is a measure of the importance of elasticity in a transient flow. This number is defined as

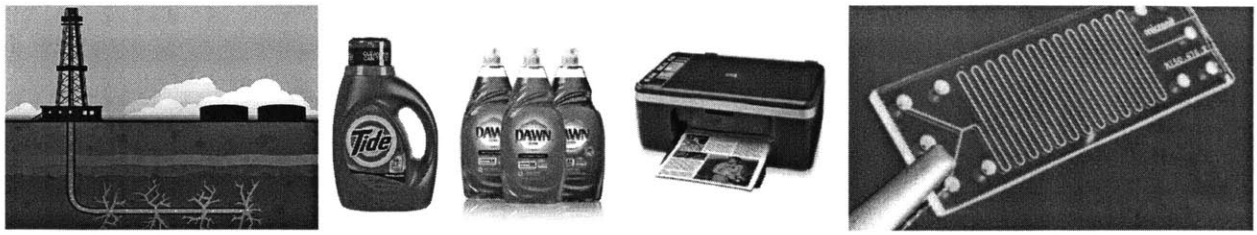

(a) Enhanced oil recovery (b) House-hold products (c) Inkjet printing (d) Lab-on-a-chip experiments

Figure 1.1.1: Common applications of micellar and surfactant solutions.

the ratio of the relaxation time of the material λ to the timescale of observation t_{obs}, hence $De \equiv \lambda/t_{obs}$. The second group is the Weissenberg number $Wi \equiv \lambda\dot{\gamma}$, defined as the product of the material relaxation time and the imposed deformation rate. It is a measure of the strength of the non-linearity in a fully developed flow.

The primary viscoelastic materials considered in this study are the aforementioned surfactant systems (Larson, 1998). Surfactants are amphiphilic, rheological modifiers, that are composed of both hydrophobic and hydrophilic groups and can associate or *self-assemble* into large molecular aggregates, known as micelles. Micellar solutions are found in consumer products and inks, and they are used for turbulent drag reduction (Rothstein, 2008) and enhanced oil recovery (Kefi *et al.*, 2005) as depicted in Figure 1.1.1. Depending on temperature, salinity and concentration (Israelachvili, 2007), the aggregates take on a variety of shapes and sizes (*e.g.* spherical, bilayer, cylindrical), which significantly influence the rheological properties of the material. Here the focus is on worm-like micelles (WLM), which take the form of flexible cylinders and are often called *living polymers*, due to their ability to associate reversibly and dynamically and their entangled structure that is topologically similar to that of many entangled polymeric solutions. WLM solutions mimic the generic rheological behavior of many other entangled polymeric systems and they are commonly considered to be model rheological fluids, because in the limit of small deformations and deformation rates their linear viscoelastic behavior can be described by the single-mode Maxwell model (Cates, 1990; Rehage & Hoffmann, 1991; Cates & Fielding, 2006). Unlike typical polymeric systems which irreversibly degrade at large stresses, WLM can reversibly self-assemble after undergoing stresses significant enough to break the aggregates, and hence they are suitable also for the study of non-linear rheological behavior.

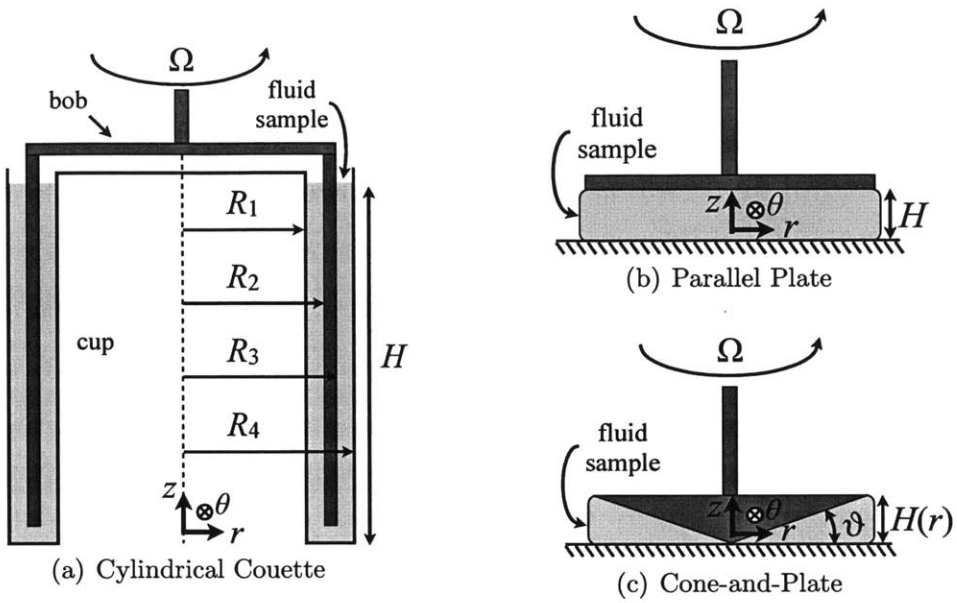

Figure 1.1.2: Commonly used fixtures for use with rotational rheometers.

The rheological characterization of these surfactant systems and other complex fluids is therefore of paramount importance in evaluating their performance for a particular application. *Rheometry* is the practical science of measuring the material properties of a viscoelastic material under flow (Macosko, 1994). Accordingly, a *rheometer* is a scientific instrument used to measure quantities such as viscosity, normal stress coefficients and other rheological material functions. One of the most commonly used rheometers is the torque-based rotational rheometer, which imposes a stress or a deformation rate on a material sample and measures the corresponding deformation rate or stress, respectively. Generally, the material sample is contained in the gap between two coaxial solid surfaces, which rotate relative to each other, in configurations such as those depicted in Figure 1.1.2. Most conventional macroscale rheometers can be used to measure the material functions of a test fluid at shear rates up to at most $\dot{\gamma} \lesssim \mathcal{O}(10^3)\ \mathrm{s}^{-1}$, depending on the test fixture dimensions and the rheological properties of the particular test fluid. At higher shear rates, inertially or elastically-driven instabilities give rise to secondary flows including turbulent flows, which prevent accurate measurement of viscometric material functions.

The dimensionless control parameter for inertial instabilities is the Reynolds number $Re \equiv \mathcal{U}\ell/\nu$, where $\mathcal{U}$ is a characteristic velocity of the flow, ℓ is the characteristic length

scale of the flow geometry and ν is the kinematic viscosity of the fluid. Conversely, the control parameter for an elastically-driven instability is typically proportional to the aforementioned Weissenberg number Wi. Generally, if either of these numbers is larger than some critical value that depends on the flow geometry, the base flow becomes unstable. Many of the flow instabilities that are relevant to rheometry have been reviewed by Larson (1992), and they include the inertial and elastic Taylor-Couette instabilities in the cylindrical Couette geometry (Taylor, 1923; Larson *et al.*, 1990), as well as edge fracture in the free surface of the parallel plate and cone-and-plate geometries (Tanner & Keentok, 1983; Lee *et al.*, 1992). These instabilities place an upper bound on the deformation rates at which conventional rotational rheometers can be used to measure material functions.

In all cases, however, the characterization of a complex fluid must be completed over a range of deformation rates relevant to its intended industrial process, many of which occur at significantly higher shear rates than those that can be achieved with conventional rheometers. For example, high rate deformations can be achieved even for moderate velocities when the characteristic length scale of the flow is small such as in flow through porous media, the chewing of foodstuffs, coating flows and flows through small orifices. For the flow of ink through the nozzle of an inkjet printer, where the length ℓ of the smallest printable feature may be on the order of tens of microns and ejection velocities $\mathcal{U}$ are on the order of meters per second, characteristic deformation rates are easily on the order of $\dot{\gamma} \sim \mathcal{U}/\ell \sim \mathcal{O}(10^5)$ s^{-1}. An alternative measurement technique is therefore necessary for accurate rheological characterization at these large deformation rates.

1.2 Flows of Complex Fluids in Microfluidic Devices

1.2.1 Microfluidic Rheometry

A microfluidic device is composed of a channel or a set of channels that have been etched or molded into a material such as glass or a silicon elastomer, for which the smallest length scale of the channels is on the order of tens or hundreds of micrometers.

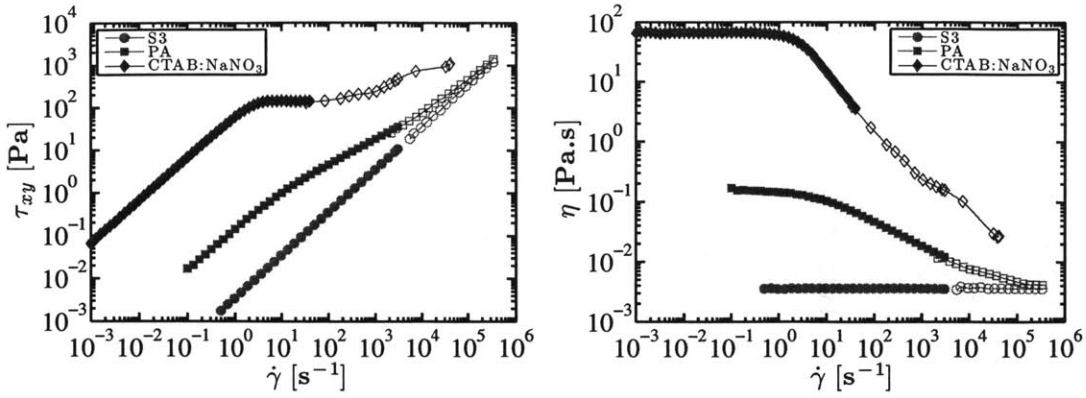

(a) (b)

Figure 1.2.1: Measured flow curves. Solid symbols correspond to data measured on a rotational rheometer. Hollow symbols correspond to data measured using a microfluidic slit rheometer. The fluids are a Newtonian S3 calibration oil, 1 wt% 6 MDa polyacrylamide solution and 300:405 mM cetyltrimethylammonium bromide:sodium nitrate solution.

The ability to manipulate small volumes of fluids with these devices has enabled their widespread adoption in research areas from biomedicine to microelectronics (Whitesides, 2006). The relatively low cost and ease of fabrication associated with microfluidic devices have also resulted in their growing use amongst applied rheologists over the last decade, (Pipe & McKinley, 2009; Galindo-Rosales *et al.*, 2013). The key insight behind the use of microfluidic devices for rheometry is that by shrinking the characteristic length scale of the geometry and holding the characteristic velocity constant, the Reynolds number is reduced while the characteristic deformation rate is simultaneously increased. Therefore, *microfluidic rheometry* is a rheometric technique that exploits the small length scales of a microchannel to characterize the rheological properties of a complex fluid at deformation rates generally on the order $10^3 \leq \dot{\gamma} \leq 10^6$ s^{-1}.

To illustrate the value of using microfluidic devices, the flow curves of a Newtonian calibration oil, a polyacrylamide solution and surfactant solution are shown in Figure 1.2.1. The measurements at low shear rates plotted with the solid symbols were obtained using a conventional macroscale rotational rheometer. As discussed above, inertial or elastic instabilities limit the upper bound of accessible shear rates with this rheometer. To extend the measurements to shear rates as large as $\dot{\gamma} \sim 3.3 \times 10^5$ s^{-1}, a microfluidic slit rheometer fabricated with internal pressure sensors was used. The com-

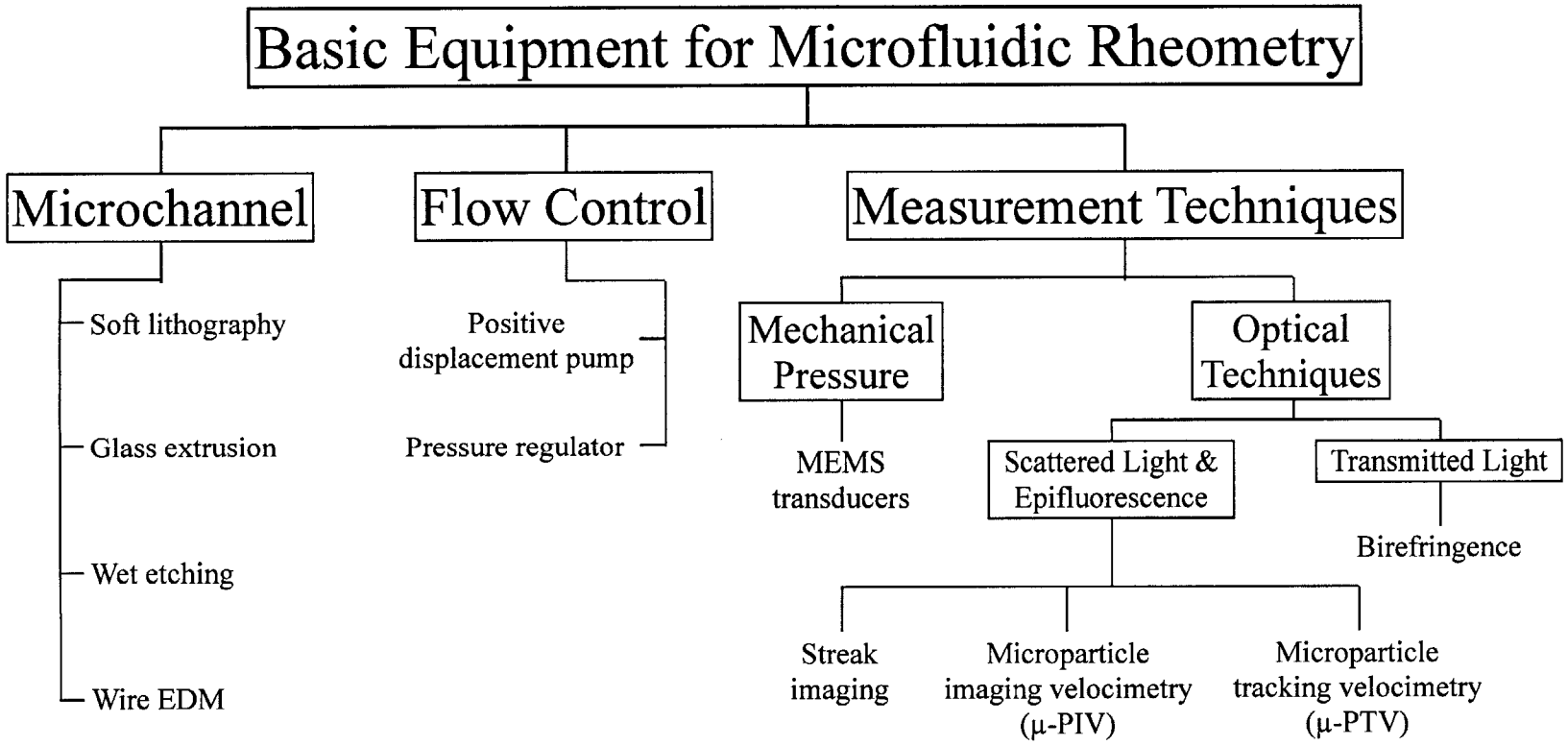

Figure 1.2.2: Equipment for microfluidic rheometry.

bination these two rheometric techniques enables viscosity measurements for a single fluid over as much as eight orders of magnitude of shear rates.

The basic array of equipment that is necessary for microfluidic rheometry is given in the schematic flow diagram in Figure 1.2.2. Clearly, a microfluidic device on its own is not sufficient for the quantitative determination of a material function such as the shear viscosity. Instead, it must be complemented with an instrument such as a syringe pump to the control flow rate through the channel, and with equipment to measure mechanical pressure, flow kinematics and other quantities such as flow-induced birefringence.

Flow Control and Pressure Measurements

Whereas on a rotational rheometer a torque or angular displacement is applied to the fixture and thereby imposed on the test sample, for a microfluidic device the analogous control parameters are the pressure drop across the device and the volumetric flow rate through it, respectively. Typically, the volumetric flow rate though a microchannel is controlled by a positive displacement syringe pump and the pressure drop across the channel is recorded using differential pressure transducers or sensors based on micro-electromechanical systems (MEMS) that are embedded in the channel. In certain cases, however, it is more convenient to impose a pressure drop across the channel and measure the corresponding volumetric flow rate through the channel.

For a rheometric instrument, the mathematical relationships between these quantities and the stress and deformation rate imposed on the test material are functions that are specific to the configuration and dimensions of the test geometry. While there are many geometries for a rotational rheometer for which exact mathematical relationships are available (Macosko, 1994), there are comparatively few configurations for a microfluidic device for which similar relationships can be rigorously derived from first principles. It is therefore often the case when using a microfluidic device for rheometry, that the imposed flow kinematics cannot be known precisely *a priori*, and thus it is necessary to incorporate velocimetry measurements to accurately determine the experimentally realized deformation field.

Particle-based Flow Visualization Techniques

The ability to obtain spatially-resolved measurements of the a flow field is one of the most powerful tools for an experimental rheologist to study the roles of viscoelasticity and inertia in the behavior of a test fluid in a complex flow. Among the many flow visualization techniques (Smits & Lim, 2012), particle-based imaging has been widely adopted to study the flow in microfluidic devices. According to this method, small tracer particles are seeded in the fluid and their trajectories are recorded under the assumption that the particles faithfully follow the local flow field. The exact size, buoyancy, seeding density and optical properties of the tracer particles must be tailored to the particular application, but typically for visualization measurements in microfluidic devices particles are approximately neutrally buoyant and one micrometer in diameter.

One of the simplest particle-based flow visualization techniques is streakline imaging, whereby particle streaks are recorded by increasing the exposure time of the imaging system to allow the tracer particles to travel through a large fraction or all of the field of view in a single image. This imaging technique has been used prolifically to study flows in complex geometries at the macroscale (Van Dyke, 1982) and the microscale (Groisman & Quake, 2004; Rodd *et al.*, 2005). Streakline imaging enables the experimentalist to gain qualitative information about a complex flow, but it cannot be used to extract quantitative information about the velocity field.

Alternative imaging methods such as particle tracking velocimetry (PTV) (Malik *et al.*, 1993) and particle image velocimetry (PIV) (Raffel *et al.*, 1998) can instead be used to determine velocity magnitudes in a microchannel. Both methods require short exposure times to capture the instantaneous position of all particles in the field of view. The respective particle positions in a sequence of images that are captured at regular time intervals are then compared to reconstruct the local velocity field. In PTV, generally the particle seeding is sufficiently low that the trajectories of individual particles can be identified, whereas PIV is a correlative technique that tracks the local average trajectory of a collection of particles in an interrogation region in the field of view. A further distinction must be made between the illumination methods used for experiments in macroscale and microscale geometries. For PTV/PIV, typically a laser is used

to form a thin focused light sheet to illuminate a particular cross-section of the flow for visualization. In a microfluidic device, however, optical access may be restricted or the effective thickness of the light sheet may be on the order of the dimensions of the geometry (Meinhart *et al.*, 2000). So instead, the alternative approach for experiments in microchannels is known as volume illumination, whereby the entire volume of a region of flow is illuminated and the spatial resolution of all measurements is controlled by selecting the appropriate combination of optical components (*e.g.* objective, light wavelength, camera resolution etc.). This illumination technique is what differentiates conventional PTV/PIV from μ-PTV/μ-PIV.

Flow-Induced Birefringence

The microstructure of many optically transparent complex fluids, such as the polymer solutions studied in this work, is isotropic under quiescent equilibrium conditions. When a complex fluid is subject to an imposed stress, however, its microstructure becomes preferentially oriented, and this structural anisotropy gives rise to optical anisotropy, also called flow-induced birefringence (FIB), which can be quantified using appropriate imaging techniques. Accordingly, optical rheometry is the measurement of the interaction of light with an optically anisotropic material in order to determine its state of structure (Fuller, 1990). In certain cases, FIB measurements can also be related to the stress in the material with the semi-empirical *stress-optical rule* (Fuller, 1995). Simply put, this rule states that the difference between the principal indices of refraction Δn in the imaging plane is linearly proportional to the principal stress difference in the fluid $\Delta\sigma$. The coefficient of proportionality is the stress-optical coefficient C, which is normally an empirically determined constant for a given fluid. Hence $\Delta n = C\Delta\sigma$. According to this rule, it is therefore possible to obtain optically non-invasive measurements of the state of stress in a flowing complex fluid.

For experiments in macroscale geometries, birefringence measurements are commonly completed with a columnated light source, such as a laser, whose spot size is on the order of one millimeter. For flows through a microfluidic device, the spatial variations in birefringent quantities occur on much smaller length scales, so accurate measurements

require a birefringence microscopy system with optical resolution on the order of micrometers. The ABRIO^{TM} imaging system (CRi, Inc.) is a commercially available instrument designed to obtain such highly spatially-resolved measurements with an optical microscope, and it has been used for all optical rheometry experiments in microfluidic devices studied in this thesis.

The combination of flow visualization methods, and pressure and flow-induced birefringence measurements forms a versatile tool kit for the applied rheologist to study the rheological behavior of a wide range of viscoelastic materials undergoing large deformation rates in microfluidic devices. In this thesis, the measurement techniques have been used for the rheometric characterization of WLM and other polymeric solutions in both shear and extension-dominated flows at low Reynolds number.

1.2.2 Inertial Effects in Microfluidic Devices

As mentioned above, a major benefit of using microfluidic devices is their small characteristic length scales, which generally minimize the role of inertial effects in the flow through the device. Yet, over the last decade there have been a number of emerging applications that rely on high-speed flows through microfluidic devices. For instance, many important biomedical processes require the isolation of micron-sized particles or cells from a background fluid. The performance of many of the current microfluidic technologies used for such biomedical separation processes, however, greatly diminishes with increasing flow rate (Gossett *et al.*, 2010). Therefore it is a major challenge to carry out this task at biomedically-high processing rates (flow rates $Q > 1$ mL.min^{-1}), and few experimental techniques are capable of precisely localizing particles in a flow field.

One possible revolutionary technology in this area is called "inertial focusing" (Di Carlo, 2009a), a label-free, high flow rate technology in which particles of a given size, transported by a flow through a channel, preferentially migrate to well-defined positions in the channel cross-section. In this phenomenon, the channel Reynolds number, defined in terms of the hydraulic diameter of the channel d_h, is actually quite large

($10 \leq Re_c \leq 2000$). Furthermore, because the hydraulic diameter of a microchannel is usually on the same order as the particle diameter a, inertial effects even in the immediate vicinity of a particle are also significant. These effects are characterized by the particle Reynolds number $Re_p \equiv Re_c(a/d_h)^2$, which is often greater than unity in a microfluidic device, and is the reason particles are driven or *focused* to a few very specific locations in the channel cross-section in this regime.

The physical phenomenon of particle migration in channel flows of Newtonian fluids is commonly called the Segré-Silberberg effect and was discovered over fifty years ago in large-scale systems (Segré & Silberberg, 1961). It originates from a competition between a *wall effect* lift pushing the particle away from the wall and a *particle shear* lift pushing it towards the wall. Yet at the time, there were few proposed applications for large-scale devices. With the current growth in the use of microfluidic devices, however, particle migration was rediscovered at the microscale (Di Carlo *et al.*, 2007), where it offers great promise for impactful biomedical applications, including disease diagnostics and treatment. In particular, this technology has been proposed as a compact and inexpensive alternative to current high-speed flow cytometers and for applications in point-of-care diagnostics (Yager *et al.*, 2008; Chin *et al.*, 2012). It has also been identified as a potential breakthrough technique for high-throughput cell manipulation and the sorting of diseased cells from the bloodstream.

Despite the robustness of particle focusing in Newtonian fluids, its practical implementation for real-world applications has been limited, in part, due to a rudimentary fundamental understanding of the phenomenon and due to the lack of available engineering design guidelines. Furthermore, in most studies with whole blood and other clinically relevant physiological fluids, it has been necessary to dilute the samples, partly because the undiluted fluids are complex, non-Newtonian suspensions displaying nonlinear rheological properties whose role in particle focusing at high-flow rates has not yet been addressed. This dilution step also increases the complexity of any such particle-focusing procedure, thereby mitigating the viability of this otherwise simple, reliable, and inexpensive biomedical technology.

Therefore, the migration behavior of polystyrene beads, white blood cells and other

cells in water, physiological saline, dilute and semidilute polymer solutions and blood is studied. The use of viscoelastic carrier fluids introduces the channel Weissenberg number Wi_c as an additional control parameter for this phenomenon, allowing for the study of particle migration in the Re_c–Wi_c phase space. Special attention is given to particle migration at simultaneously high Reynolds and Weissenberg numbers, which is a regime that has not been thoroughly studied previously. This study utilizes many of the techniques that have been used for microfluidic rheometry, such as pressure measurements, long exposure fluorescence (streak) imaging, and μ-PTV and μ-PIV. Additionally, particle trajectory analysis (PTA) is an imaging technique that is developed to determine the distribution of the particles in the channel cross-section by scanning for optically in-focus particles at a sequence of vertical positions in the microchannel. Whereas, streak imaging and μ-PTV/μ-PIV provide information about the distribution of particles in one dimension of the channel, PTA is capable of determining the two-dimensional particle distribution function in the channel cross-section. The results gathered by this experimental study of flow-induced particle localization in complex fluids are valuable for the eventual exploitation of this migration phenomenon for real-world particle sorting and separation processes.

1.3 Goals of this Thesis

This thesis is partitioned into nine chapters, including this introductory section, Chapter 1. There are three primary areas of focus in studying the role of viscoelasticity in flows of complex fluids at high deformation rates. These topics are 1) the effects of shear rate localization in flow of worm-like micellar fluids, 2) the rheological characterization of shear banding and other complex fluids in microfluidic devices in shear and extension-dominated flows, and 3) the effects of viscoelasticity on the migration behavior of micron-sized particles and cells in high Reynolds number flows in microchannels. The interrelations between each of these topics is shown in Figure 1.3.1. Literature reviews of previous studies in areas of relevance for all three of these topics are given in Chapter 2. The results of experiments and analysis on each of these research topics form the basis

of the subsequent chapters.

In Chapter 3, a detailed rheological characterization of the worm-like micellar test fluids used in this study in shear flows is presented. The characterizations include measurements of steady shear viscosity $\eta(\dot{\gamma})$, first and second normal stress coefficients $\Psi_1(\dot{\gamma})$ and $\Psi_2(\dot{\gamma})$, relaxation modulus $G(t, \gamma_0)$, step strain stress relaxation measurements, and the rheological behavior in small amplitude oscillatory shear (SAOS) using conventional cone-and-plate rheometry (Bird *et al.*, 1987) and particle image velocimetry (Raffel *et al.*, 1998). In the following Chapter 4, the diffusive Johnson-Segalman model (Radulescu *et al.*, 1999) is studied for rectilinear, steady shear flows and used to develop a stability criterion for the onset of a purely elastically-driven secondary flow in shear-banding fluids. The basic framework for the criterion comes from the already established understanding of the onset of secondary flows driven by inertia or elasticity in flows with curved streamlines shown schematically in the $Wi - Re$ plane in Figure 1.3.1. The instability criterion proposed in Chapter 4 is aimed to extend to a regime of high Weissenberg number and finite lengthscale ratio parameter ξ, since the thickness of the shear-banding interface is a finite fraction of the characteristic width of the flow geometry.

The development and use of microfluidic devices for the low Reynolds number rheological characterization of complex fluids at high deformation rates are discussed in Chapters 5 and 6. In particular, the calibration of a birefringence microscopy system (ABRIO^{TM} System; CRi, Inc.) is presented, in order to demonstrate the suitability of the device for optical, microfluidic rheometry in a rectilinear shear flow. This imaging technology is then combined with kinematics and pressure measurements to study the rheological behavior of the micellar solutions and other complex fluids in an extension-dominated flow.

In Chapter 7, the use of microfluidic devices is extended to high Reynolds number in order to study inertially-driven particle migration of polystyrene beads and blood cells. The same flow velocimetry techniques utilized in the microfluidic rheometry experiments discussed in the preceding chapters are refined to experimentally determine the equilibrium distribution of particles in the microchannel cross-section. Essentially all previous studies of the particle migration phenomenon in microchannels have been in either the

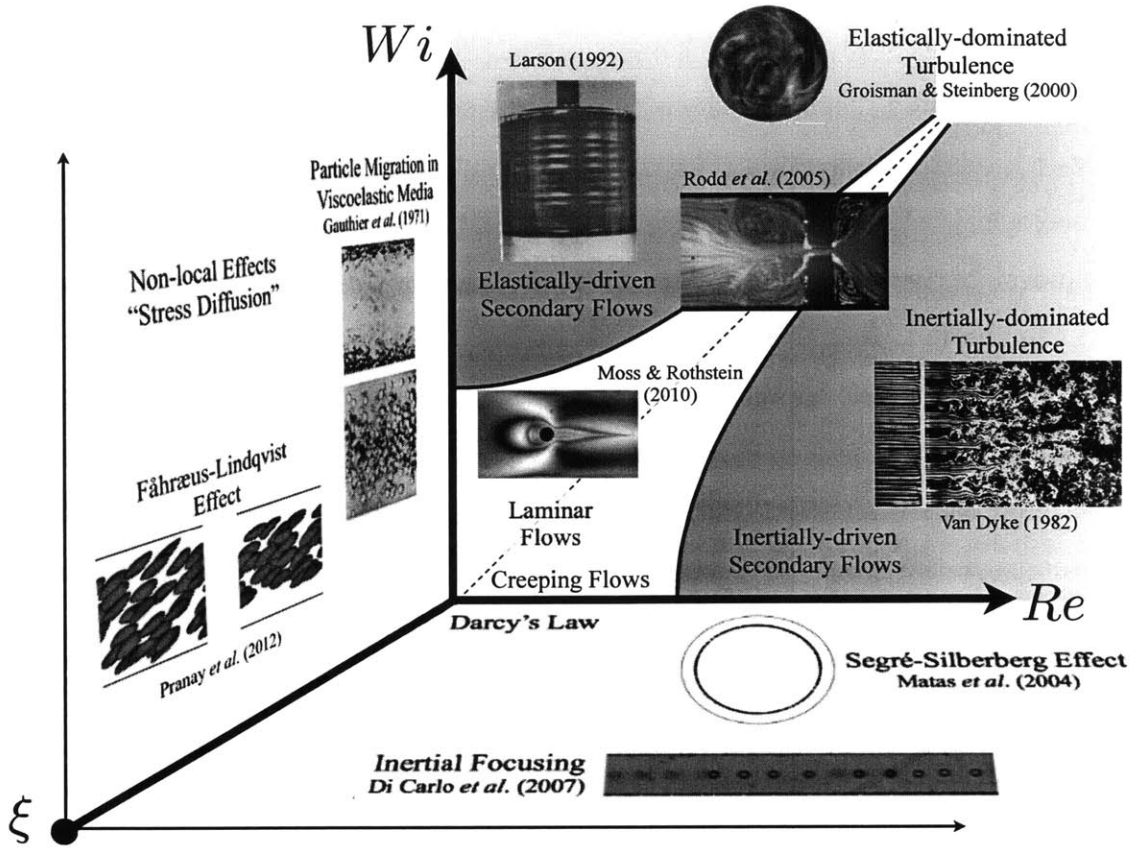

Figure 1.3.1: Operating diagram for flows of complex fluids as a function of Reynolds number Re, Weissenberg number Wi a lengthscale ratio ratio $0 \leq \xi \leq 1$. Here the lengthscale ratio is loosely defined to be some ratio of a characteristic length scale of the fluid or suspended medium to the characteristic length scale of the flow geometry. The gray shaded regions indicate regimes in which secondary flows occur. Di Carlo *et al.* (2007): Ordered particle trains flowing in a microchannel at $Re_c = 120$. Gauthier *et al.* (1971): Images illustrating radial migration of rigid spheres in non-Newtonian liquids. (Upper) Particles migrate to the walls in a shear-thinning liquid. (Lower) Particles migrate to centerline in a liquid with significant normal stresses. Groisman & Steinberg (2000): Flow patterns in an elastically turbulent flow of polyacrylamide in a viscous syrup at $Wi = 13$. Larson (1992): Elastically-driven secondary flow patterns in the Taylor-Couette flow of a viscoelastic Boger fluid. Matas *et al.* (2004b): Moss & Rothstein (2010): Birefringent patterns of a worm-like micellar fluid flowing past a cylinder. Pranay *et al.* (2012): Snapshots of simulations of flexible capsule migration at the inlet of a channel (left) and downstream (right). The formation of a depletion layer is analogous to the the Fåhræus-Lindqvist effect in blood. Rodd *et al.* (2005): Streakline image of the flow of a polyethylene oxide solution through and abrupt contraction-expansion at $Re = 56$ and $Wi = 212$. Van Dyke (1982): Generation of turbulence by a grid.

inertially-dominated regime (*i.e.* $Re_c \gg 1,\ Wi_c \simeq 0$) or the elastically-dominated regime (*i.e.* $Re_c \simeq 0,\ Wi_c \gg 1$) at a finite particle diameter to channel size ratio $\xi \sim \mathcal{O}(0.1)$. Therefore in Chapter 8, small amounts of polymers, such as polyethylene oxide or hyaluronic acid are added to the fluid in order to study the role of viscoelasticity in a relatively unexplored regime indicated in the three-dimensional operating diagram in Figure 1.3.1 of finite lengthscale ratio ξ and simultaneously high Reynolds number and Weissenberg number.

In the last section, Chapter 9, concluding remarks on these high deformation rate rheometry measurements are made and perspectives for future work are considered. At the conclusion of this thesis are the appendices that contain mathematical derivations of many of the results used in this work along with other useful reference material.

Chapter 2

Background & Literature Review

The research topics considered in this thesis fall broadly into three different categories. Firstly, a worm-like micellar (WLM) fluid is characterized using a range of conventional rheometric flows in order to study the effect of shear banding and other flow inhomogeneities at low to moderate Weissenberg numbers. The study is then extended to large Weissenberg numbers using microfluidic devices. Finally, the role of inertia and viscoelasticity on flow-induced particle migration in microchannels is studied using dilute and semidilute polymer solutions. A short introduction and motivation for studying these topics was discussed in Chapter 1, but in this Chapter a more extensive review of all three research areas is presented to provide the context for the work in this thesis. For each of these topics, the prevailing focus is the role of the non-linear rheological behavior of the test fluids on the observed flow kinematics and stress.

The research overview presented here is divided into separate Sections for each topic. The purpose of partitioning the literature survey in this way is to allow the reader to consider each topic individually, yet within the overriding framework of applying flow diagnostic measurements to develop microfluidic devices for rheometry.

2.1 Rheology & Rheometry

Rheology is the study of the flow and deformation of matter. *Rheometry* is the branch of rheology that is concerned with the practical science of measuring *rheological ma-*

terial functions of a test specimen undergoing a deformation. A material function is a parameter that is used to quantitatively characterize the behavior of a material under flow. These parameters can depend on the deformation rate, frequency, duration or some other feature of the flow, and they include quantities such as shear viscosity, normal stress coefficients, relaxation modulus and so forth. They are also commonly used as inputs to rheological constitutive models. A list of some of the most commonly measured material functions is given by Bird *et al.* (1987).

Each material function is measured by forcing the material to undergo a particular flow type. A subset of these rheometric flows is briefly described below to introduce the reader to the material functions that can be measured with each flow type. A more comprehensive description of flows used in rheometry is given by Macosko (1994).

2.1.1 Small Amplitude Oscillatory Shear (SAOS)

A small amplitude oscillatory shear (SAOS)[1] measurement is one of the simplest tests to determine the linear viscoelastic properties of a material. In this test, an oscillating shear strain or stress is imposed on a material, such that the shear strain of the material follows the relation $\gamma(t) = \gamma_0 \sin(\omega t)$, where γ_0 is the shear strain amplitude, ω is the frequency of oscillation and t is time as shown schematically in Figure 2.1.1 (a). Since this test is performed in the limit of small strains, it is a probe of the near-equilibrium rheological properties of the material, which are independent of the magnitude of the applied strain. It follows that the corresponding shear stress also varies sinusoidally in time and its amplitude depends linearly on the applied strain according to the relation $\tau(t) = G'(\omega)\gamma_0 \sin(\omega t) + G''(\omega)\gamma_0 \cos(\omega t)$. In this way, the stress has been decomposed into an elastic contribution in phase with the applied strain and characterized by the storage modulus G' and into a viscous contribution in phase with the strain rate and characterized by the loss modulus G''. Both of these parameters can depend on the frequency of the applied deformation.

[1]The use of the phrase *small amplitude* is in contrast to *large amplitude*, for which the strain amplitude γ_0 is sufficiently large that it can no longer be assumed that the amplitude of the measured stress wave depends linearly on strain nor that the stress is composed of only a single harmonic. For an introduction to non-linear viscoelasticity see Dealy & Wissbrun (1990) and an overview of large amplitude oscillatory shear (LAOS) see Ewoldt *et al.* (2008).

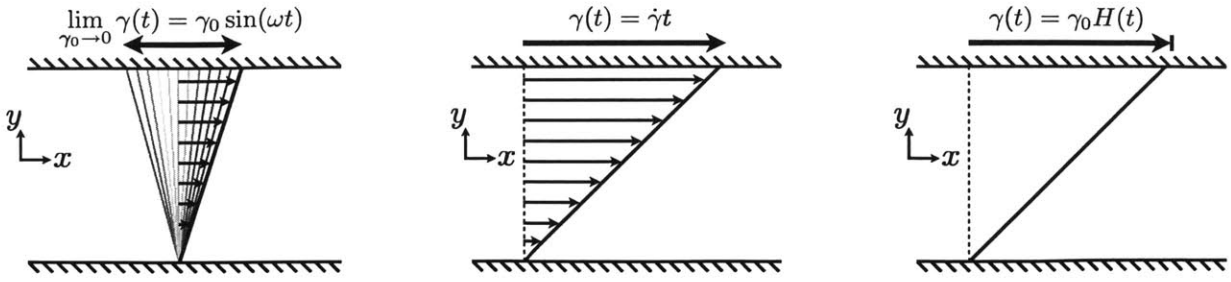

(a) SAOS (b) Steady shear (c) Step strain

Figure 2.1.1: Rheometric flows for measuring rheological material functions. (a) Small amplitude oscillatory shear (SAOS). (b) Steady shear flow. (c) Step strain stress relaxation. $H(t)$ is the Heaviside function.

The simplest model for linear viscoelastic behavior is the single-mode Maxwell model (see Appendix A). The mechanical analogue of this model consists of a linear spring with modulus G_0, and a linear dashpot with damping coefficient $\eta_0 = G_0\lambda$, where λ is the relaxation time of the material. The value of this parameter is the characteristic timescale over which a stress grows or decays in the material. The storage and loss moduli for the Maxwell model are

$$G'(\omega) = G_0\left(\frac{(\lambda\omega)^2}{1+(\lambda\omega)^2}\right) \quad \& \quad G''(\omega) = G_0\left(\frac{\lambda\omega}{1+(\lambda\omega)^2}\right) \tag{2.1.1}$$

When $\lambda\omega = 1$, the moduli are equal $G' = G''$. At this frequency the elastic and viscous properties of the material are of equal relative importance. Accordingly, the relaxation time of a material that exhibits Maxwellian behavior can be readily identified from SAOS measurements since it is equal to the inverse of the angular frequency at which the storage and loss moduli cross over.

2.1.2 Viscometric Steady Shear

A *rheologically steady shear flow* or *viscometric flow* is a unidirectional shear flow for which the shear rate $\dot{\gamma}$ is constant in time for a given material element (Bird *et al.*, 1987). There are a variety of flow geometries that can be used with a rotational rheometer to experimentally realize a viscometric flow (Macosko, 1994), but the main objective in performing any such experiment is to measure the shear viscosity as well as the shear-

induced normal stress differences in the test material.

The steady shear viscosity is defined as the ratio of shear stress τ_{xy} to the imposed shear rate $\dot{\gamma}$ at steady state,

$$\eta(\dot{\gamma}) \equiv \frac{\tau_{xy}(\dot{\gamma})}{\dot{\gamma}} \tag{2.1.2}$$

In the limit of small shear rates, most fluids exhibit a constant dynamic viscosity known as the *zero-shear-rate viscosity* η_0. For a Newtonian fluid this quantity is by definition constant for all shear rates in an isothermal flow and is typically denoted by the symbol μ. Conversely, the shear viscosity of a non-Newtonian fluid can depend on shear rate. For such fluids, generally at shear rates that are approximately equal to or greater than the inverse of the longest relaxation time of the fluid (*i.e.* $\lambda\dot{\gamma} \sim \mathcal{O}(1)$) the viscosity deviates from the zero-shear-rate value. Most polymer solutions exhibit a shear-thinning behavior, and thus above a critical shear rate the viscosity decreases with increasing $\dot{\gamma}$. For this reason, the viscosity is usually measured over many orders of magnitude of shear rates, and the resultant plot of the shear stress or viscosity versus shear rate is called a *flow curve.*

In addition to a shear viscosity, most non-Newtonian fluids exhibit a non-zero first normal stress difference, $N_1 \equiv \tau_{xx} - \tau_{yy}$, and possibly a second normal stress difference, $N_2 \equiv \tau_{yy} - \tau_{zz}$. These stress differences result from shear-induced tension in the fluid microstructure as described in Bird *et al.* (1987), and they are characterized by material functions called the first and second normal stress coefficients, Ψ_1 and Ψ_2, respectively.

$$\Psi_1(\dot{\gamma}) \equiv \frac{N_1(\dot{\gamma})}{\dot{\gamma}^2} = \frac{\tau_{xx}(\dot{\gamma}) - \tau_{yy}(\dot{\gamma})}{\dot{\gamma}^2} \tag{2.1.3}$$

$$\Psi_2(\dot{\gamma}) \equiv \frac{N_2(\dot{\gamma})}{\dot{\gamma}^2} = \frac{\tau_{yy}(\dot{\gamma}) - \tau_{zz}(\dot{\gamma})}{\dot{\gamma}^2} \tag{2.1.4}$$

Like the viscosity, both Ψ_1 and Ψ_2 can depend on shear rate. The first normal stress coefficient can be measured using a cone-and-plate fixture with a rheometer equipped with an axial force transducer. Typically, the values of Ψ_1 and Ψ_2 have opposite sign, (*i.e.* $\text{sign}(\Psi_1) = -\text{sign}(\Psi_2)$), and the magnitude of Ψ_1 is larger than that of Ψ_2, (*i.e.* $|\Psi_1| > |\Psi_2|$). Measurement of the second normal stress coefficient is generally more

complicated and is discussed by Macosko (1994) as well as Jackson & Kaye (1966).

2.1.3 Step Strain Stress Relaxation

In a step strain stress relaxation test, a finite shear strain γ_0 is instantaneously applied to the test material and the subsequent evolution of stress is measured. The stress measured in a step strain stress relaxation test is given by $\tau_{xy}(t) = G(t, \gamma_0)\gamma_0$, where $G(t, \gamma_0)$ is the relaxation modulus. As in the case of SAOS measurements, in the limit of small strain amplitudes, the relaxation modulus is independent of the strain amplitude, hence

$$\lim_{\gamma_0 \to 0} G(t, \gamma_0) = G(t) \tag{2.1.5}$$

For a Maxwell fluid the stress relaxation modulus decays exponentially in time following the relation $G(t) = G_0 \exp(-t/\lambda)$, where G_0 is the same parameter as that in Eq. 2.1.1.

For step strain measurements performed with a cone-and-plate geometry it is also possible to measure the evolution of the first normal stress difference in time. It is often found that although the values of the first normal stress difference and the shear stress decay in time, their ratio is constant and given by

$$\frac{N_1(t)}{\tau_{xy}(t)} = \gamma_0 \tag{2.1.6}$$

This observation is commonly called the Lodge-Meissner rule (Bird *et al.*, 1987).

At large strain amplitudes, the relationships given in Eq. 2.1.5 and 2.1.6 do not necessarily hold. For this reason, step strain stress relaxation measurements provide a systematic way of quantitatively characterizing the transition from linear to non-linear behavior with increasing strain amplitude γ_0, which can also be used for the validation and development of constitutive models for viscoelastic liquids (Larson, 1988).

2.2 Rheology of Worm-Like Micellar Fluids

2.2.1 Linear Rheology of Worm-Like Micellar Fluids

A *micelle* is an aggregate of amphiphilic surfactant molecules, which are themselves composed of a hydrophilic head group and a hydrophobic tail group. Some examples of the type of surfactant molecules that have been used to study the rheological behavior of micellar solutions include erucyl bis(2-hydroxyethyl) methyl ammonium chloride (EHAC) studied by Yesilata *et al.* (2006), cetyltrimethylammonium tosylate (CTAT) by Berret *et al.* (2002), cetylpyridinium chloride (CPyCl) by Rehage & Hoffmann (1991) and cetyltrimethylammonium bromide (CTAB) by Shikata *et al.* (1994). The molecular structures of the latter two surfactants are depicted in Figure 2.2.1 (a) and (b). In both of these molecules, the head group is polar or ionic and the long tail group is an organic, covalently bonded, non-polar molecular chain. Depending on the polarity of the surrounding medium (*e.g.* water, oil), one group of the surfactant molecule will be more soluble than the other, such that, for a given temperature, if the surfactants are present above a minimum concentration, called the *critical micelle concentration*, it is energetically favorable for them to aggregate in order to increase exposure of the more soluble group to the surrounding medium while minimizing the contact of the other group (Israelachvili, 2007). For example, in a polar medium such as water, the surfactant molecules will micellize to maximize exposure of the hydrophilic heads to the surrounding water and to isolate the hydrophobic tails from the polar solvent. The morphology and size of the micelles depend on the surfactant concentration, prevailing ionic activity, law of mass action, and the relative size of head and tail groups. It is therefore common to add a salt or counterion, such as sodium salicylate (NaSal) or sodium ($NaNO_3$) shown in Figure 2.2.1 (c) and (d), to alter the charge screening between the surfactant molecules and thereby control the morphology of the micellar structures. Possible morphologies include single molecules, spheres, multilayered spheres, vesicles, bilayers, and rigid or flexible cylindrical chains (Larson, 1998).

Under appropriate conditions of temperature, concentration and salinity, it is energetically favorable for the surfactants to form cylindrical micelles (Israelachvili, 2007;

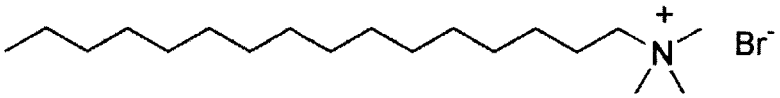

(a) Cetyltrimethylammonium Bromide Molecule ($C_{19}H_{42}BrN$)

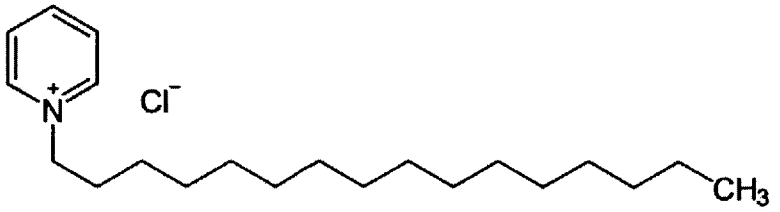

(b) Cetylpyridinium Chloride Molecule ($C_{21}H_{38}ClN$)

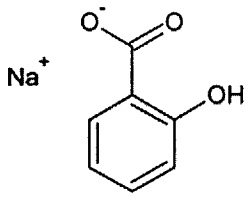

(c) Sodium Salicylate Molecule ($C_7H_5NaO_3$)

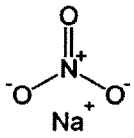

(d) Sodium Nitrate ($NaNO_3$)

Figure 2.2.1: Molecular structures of the surfactant molecules and counterions commonly considered in rheological studies of micellar fluids. In (a) and (b) the positively charged nitrogen, is a constituent of the hydrophilic, polar head group, while the flexible hydrocarbon backbone forms the hydrophobic, non-polar tail group.

Larson, 1998). In this regime, the end-caps of the cylinders have an associated energy penalty due to their necessary deviation from the preferred cylindrical configuration (Cates & Fielding, 2006), which drives the formation of long cylindrical micelles to minimize the number of higher energy end-caps in the system. If the length of the cylindrical micelle is substantially greater than its persistence length[2], a flexible or even entangled network of micelles can be expected. It is this entangled network that gives rise to the viscoelastic behavior of giant, *worm-like micellar* (WLM) solutions.

Micelles taking the form of worm-like, flexible cylinders are often known as *living polymers*, on account of their ability to associate reversibly and dynamically and their entangled structure that is topologically similar to that of many entangled polymeric solutions. WLM fluids have been extensively reviewed in the literature (Rehage &

[2]Persistence lengths are commonly on the order of 10-20 nm, as reported in Cates & Fielding (2006), but may be as large as 40 nm for neutral WLM as reported in Berret (2006).

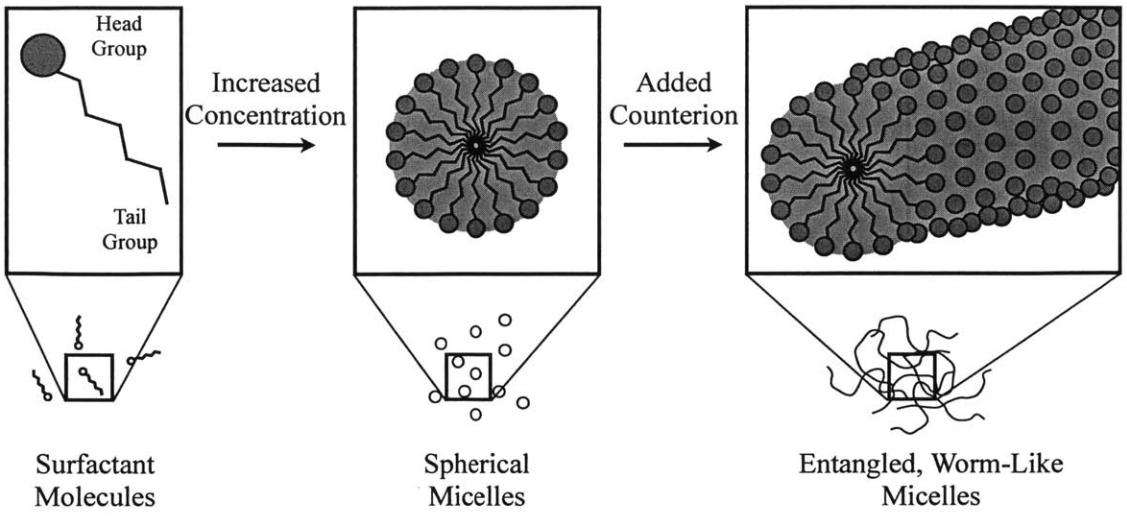

Figure 2.2.2: Schematic diagram of various surfactant aggregate morphologies. Increased concentration and salinity facilitate the formation of entangled, worm-like micelles which are responsible for the viscoelasticity of such systems.

Hoffmann, 1991; Cates & Fielding, 2006; Anderson *et al.*, 2006; Rothstein, 2008) and in textbooks (Israelachvili, 2007; Larson, 1998). Along with being used as rheological modifiers, entangled WLM solutions, depicted in Figure 2.2.2, are considered model rheological systems, because they exhibit ideal linear viscoelastic behavior in the limit of small deformations and deformation rates, which can be described by the Maxwell model with a single relaxation time λ. Furthermore, unlike typical polymeric systems which degrade at high deformation rates, the ability of WLM to dynamically self-assemble after undergoing deformations significant enough to have broken the aggregates makes them suitable also for the study of non-linear rheological behavior (Rehage & Hoffmann, 1991; Cates & Fielding, 2006).

Whereas the relaxation processes of many polymeric systems is only describable by a spectrum of relaxation times, the single relaxation time characteristic of many WLM systems arises from their special ability to break and reform dynamically. This unique timescale, however, results from a combination of stress relaxation mechanisms that can each have a different timescale. These relaxation processes include *reptation* (de Gennes, 1979), *breaking and recombination* (Cates, 1987), as well as *breathing* and *Rouse modes* (Larson, 1998). Each of these processes is schematically depicted in Figure 2.2.3.

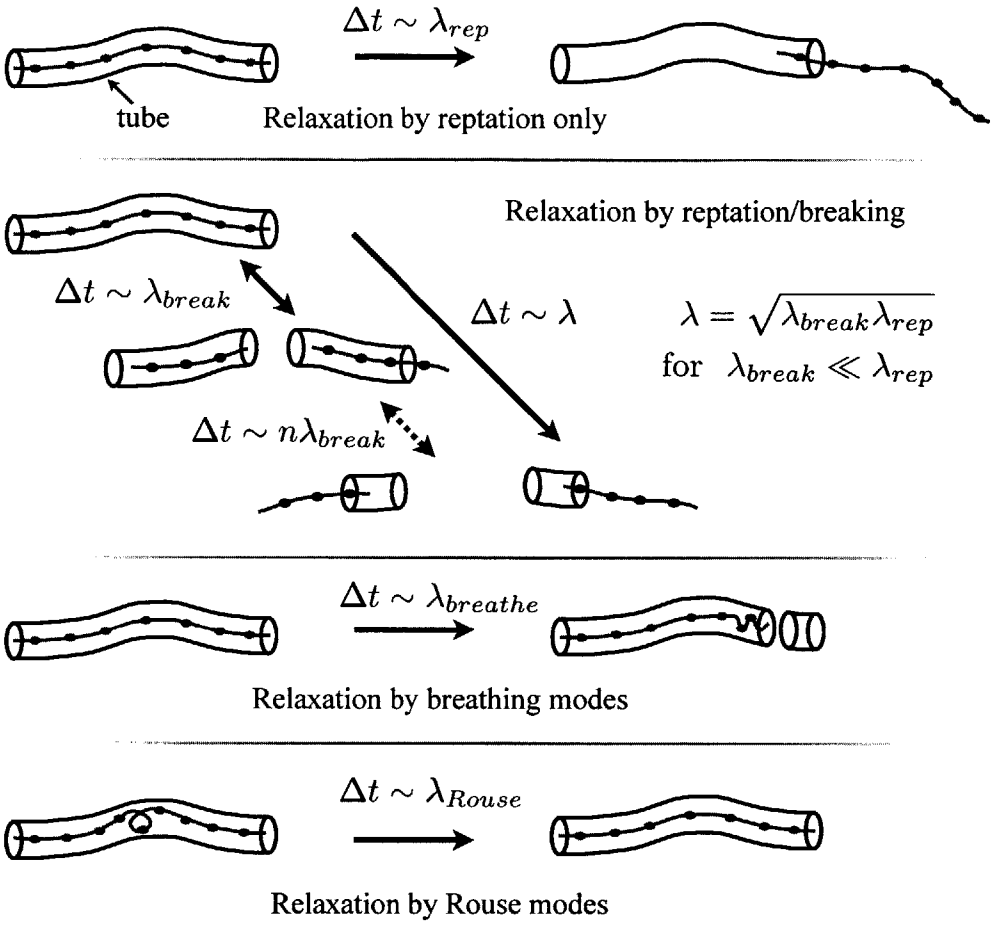

Figure 2.2.3: Schematic depictions of various relaxation processes of a WLM chain confined to a curvilinear tube.

In a reptative process, the path of movement of an unbranched polymer chain in a sufficiently entangled polymeric network is assumed to be constrained by its neighboring polymer chains to an imaginary tube which encompasses the molecule. The timescale on which the equilibrium polymer network responds to an external perturbation is the reptation time λ_{rep}, which is proportional to the time required for the individual, constituent polymer chains to diffuse along the confining tube to a new preferred configuration.

Since surfactant molecules in a micelle are bound together by relatively weak Van der Waals forces, the micelles are capable of breaking and reforming dynamically. The lifespan of a typical micelle is therefore equal to the breakage time λ_{break}, which is the average timescale between consecutive scission and fusion reactions.

Other non-reptative relaxation processes pertinent to micelles are described by Larson (1998). These processes include primitive-path fluctuations or *breathing* modes, which refer to the independent relaxation of individual constituent elements of the WLM. For example, the extremities of the chain can diffuse on a timescale $\lambda_{breathe}$ by retracting into the confining tube causing the length of the tube to fluctuate in time and thereby expedite the collective relaxation process of the micelle. A chain can also relax via *Rouse* modes in which only a particular portion of the chain relaxes on a timescale λ_{Rouse}, by reconfiguring itself within the tube to a more entropically favorable orientation. Both mechanisms typically occur rapidly compared to the macroscopic relaxation time of the network λ (Granek & Cates, 1992), and hence they can only be identified experimentally with high frequency deformations.

Cates (1987) showed that for a polymer network that can both reptate and break and reform, in the limit $\lambda_{break} \to \infty$, the stress relaxation would follow the relation

$$\tau(t) \sim \exp\Big(- (t/\lambda)^{\alpha} \Big) \tag{2.2.1}$$

where $\lambda = \lambda_{rep}$ and $\alpha = 1/4$. In this limit, breaking occurs so infrequently that the micelles relax entirely through a reptative process. This limiting value of α was observed experimentally by Rehage & Hoffmann (1991) for low salt concentrations. For WLM solutions with increased salinity, however, the increased ionic screening expedites breaking and recombination processes, thereby reducing the value of λ_{break}. In the case that $\lambda_{break} \lesssim \lambda_{rep}$, Cates (1987) found that $\alpha \to 1$ and $\lambda = \sqrt{\lambda_{break}\lambda_{rep}}$, leading to a faster overall relaxation process. The monoexponential stress response described in this limit has also been found experimentally by Shikata *et al.* (1987) and Cates & Candau (1990) among others. The shorter net relaxation time comes from the breaking process which causes a more rapid progressive reduction in the length of the confining tube. A more thorough physical and quantitative explanation for this scaling can be found in (Larson, 1998). Since the values of λ_{break} and λ_{rep} are independent, they cannot be determined from the measurement of the Maxwell relation time of the fluid λ alone, but instead using the techniques discussed by Turner & Cates (1991, 1992) and Turner *et al.* (1993).

In viscometric steady shear flows in the limit of sufficiently small shear deformation

rates, $\dot{\gamma} \ll \lambda^{-1}$, WLM solutions exhibit a constant shear viscosity η_0 and deform homogeneously across the gap. Normal stress differences also scale quadratically with shear rate in this regime, as predicted by simple fluid theory (see Appendix A). The relevant dimensionless control parameter for this flow is the Weissenberg number $Wi \equiv \lambda\dot{\gamma}$, which is less than unity in this flow regime. As this parameter is increased above unity, the rheological behavior can deviate strongly from the predictions of simple fluid theory, coinciding with the onset of a strongly non-linear phenomenon known as shear banding that is ubiquitous to semi-dilute and concentrated WLM fluids.

2.2.2 Shear Banding in Worm-Like Micellar Fluids

By *shear banding*, scientists can mean several things. For some non-Hookean solid materials, shear banding refers to the notion of *strain* localization. When a solid material is deformed, the strain can take large values in narrow zones of the sample. Similarly, for some non-Newtonian fluids, shear banding refers to the notion of *strain rate* localization. When a fluid material is sheared, the strain rate can take large values in narrow zones of the sample. In both cases, for solids or liquids, shear banding is linked to a sharp inhomogeneity in the deformation or deformation rate field. Clear domains of different strains or strain rates are identifiable. This phenomenology is associated with complex materials as it is clearly distinct from the simpler homogeneous deformation or deformation rate fields in ideal Hookean solids and Newtonian fluids, or even weakly plastic or weakly shear-thinning materials (Larson, 1998).

Even when restraining the list of examples to only liquids, there are numerous classes of non-Newtonian fluids known to exhibit shear banding (Olmsted, 2008), from telechelic polymers (Manneville *et al.*, 2007; Sprakel *et al.*, 2008), entangled polymer melts (Tapadia *et al.*, 2006; Hu, 2010), emulsions (Coussot *et al.*, 2002; Becu *et al.*, 2006), dispersions (Divoux *et al.*, 2010), granular materials (Losert *et al.*, 2000), various kinds of yield stress fluids (Moller *et al.*, 2008; Divoux *et al.*, 2010) and to foams (Gilbreth *et al.*, 2006). In this thesis, the steady shear-banding phenomenon in micellar solutions is described for the range of concentrations and temperatures in which surfactants form WLM at equilibrium (Britton & Callaghan, 1997; Salmon *et al.*, 2003; Manneville *et al.*, 2004a,b;

Lopez-Gonzalez *et al.*, 2006; Boukany & Wang, 2008; Lettinga & Manneville, 2009).

When a semi-dilute or concentrated WLM system is deformed in a Couette flow, the fluid deforms homogeneously as depicted in Figure 2.2.4 (a), provided the average imposed shear rate is sufficiently small, $\dot{\gamma} = \mathcal{U}/H \ll \lambda^{-1}$, where $\mathcal{U}$ is the imposed wall velocity, and H is the gap height. In this limit, the fluid exhibits a constant zero-shear-rate viscosity η_0, and a first normal stress difference $N_1 \equiv \tau_{xx} - \tau_{yy}$, that is usually small compared to the applied shear stress τ_{xy}. However, for larger shear rates, $\dot{\gamma} \gtrsim \lambda^{-1}$, the fluid begins to shear band as depicted schematically in Figure 2.2.4 (b). This inhomogeneous velocity field typically occurs over a range of average shear rates $\dot{\gamma}_1 < \dot{\gamma} < \dot{\gamma}_2$, often spanning multiple orders of magnitude. In this regime, the first normal stress difference typically exceeds the shear stress and the sample exhibits a particularly remarkable shear-thinning behavior, in that its effective viscosity scales inversely with shear rate such that an essentially constant shear stress can be applied to deform the material over the entire range of shear rates. This *stress plateau* is a striking example of the non-linear rheological behavior of WLM solutions and is discussed in many review articles (Berret, 2006; Cates & Fielding, 2006; Olmsted, 2008; Lerouge & Berret, 2010). It is generally believed to arise from a non-monotonicity in the underlying flow curve of the material, depicted schematically in Figure 2.2.4 (c), resulting in an unstable range of shear rates for which the shear stress associated with homogeneous kinematics decreases with increasing shear rate. In this shear rate regime, it is not possible for a system both to lie simultaneously on a single stable branch of the flow curve and to satisfy the average shear rate $\dot{\gamma}$. Consequently, the system partitions itself into adjacent layers of material, each undergoing different deformation rates, nominally $\dot{\gamma}_1$ and $\dot{\gamma}_2$, yet coexisting at the same applied shear stress τ_c.

In the simplest approximation, the fraction of the gap height occupied by the low shear rate band β_1 and the high shear rate band β_2 may be determined by the lever rule such that the average imposed shear rate $\dot{\gamma}$ is equal to the imposed shear rate, namely

$$\frac{\mathcal{U}_b}{H} = \dot{\gamma} = \beta_1 \dot{\gamma}_1 + \beta_2 \dot{\gamma}_2 \tag{2.2.2}$$

where $\beta_1 + \beta_2 = 1$ (Cates & Fielding, 2006). This lever rule has been observed experimen-

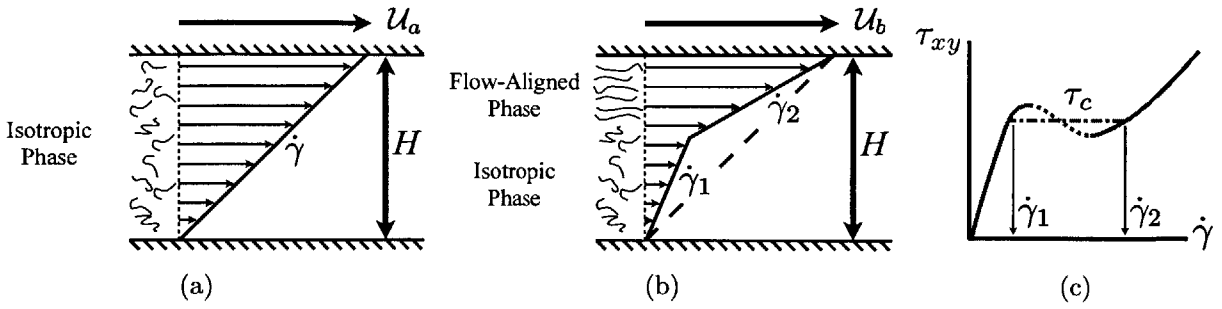

Figure 2.2.4: (a) Homogeneous Couette flow with average shear rate $\dot{\gamma}_a = \mathcal{U}_a/H \ll \dot{\gamma}_1 \approx \lambda^{-1}$, where λ is the fluid relaxation time. (b) Inhomogeneous Couette flow for which $\dot{\gamma}_1 < \dot{\gamma}_b = \mathcal{U}_b/H < \dot{\gamma}_2$. (c) Non-monotonic underlying flow curve.

tally for a CPyCl:NaSal:NaCl system (Salmon *et al.*, 2003), but it was found inadequate for describing the shear-banding behavior of other systems (Lerouge *et al.*, 2008; Feindel & Callaghan, 2010). The coexistence of more than two bands is also possible (Miller & Rothstein, 2007). Evidently, Eq. (2.2.2) should be taken only as a simplistic generalization of the complicated shear-banding phenomenon. Much experimental effort aimed at understanding more fully the complex rheological behavior in the shear-banding regime has focused on complementing the rheometry of the bulk flow, such as the studies of Rehage & Hoffmann (1991); Berret *et al.* (1994); Schmitt *et al.* (1994); Cates & Fielding (2006); Lerouge & Berret (2010), with detailed measurements of the interplay between flow kinematics and microstructure of the fluid (Manneville, 2008). Such measurements can serve as sensitive tests of the predictions of different proposed constitutive models for shear-banding materials.

There are numerous experimental techniques that have been used to study shear banding and other types of spatial heterogeneities in steady shear flow. These include NMR velocimetry (Callaghan, 2008; Moller *et al.*, 2008; Davies *et al.*, 2010), in which velocity fields are extracted from the spin polarization of nuclei that interact with a strong external magnetic field gradient. Another widely used method is ultrasound velocimetry (Manneville *et al.*, 2005; Gibaud *et al.*, 2008), which involves using high frequency ultrasonic pulses to produce ultrasonic speckle patterns from which velocity fields across the gap of a Couette cell can be extracted. Finally, numerous workers have used particle tracking methods (Meeker *et al.*, 2004a,b; Tapadia *et al.*, 2006; Fardin

et al., 2009; Helgeson *et al.*, 2009a; Dimitriou *et al.*, 2011) in order to quantify local velocity and deformation fields.

In much of the recent work that has used particle tracking methods to observe flow in shear-banding fluids, experiments have been carried out in the limit of low seeding density, where individual particles are tracked in order to determine the velocity field within the fluid. This type of tracking method is called particle tracking velocimetry (PTV). When the seeding density in the fluid is higher, the displacement of local groups of particles is determined by spatial correlations rather than tracking individual particles. This method is referred to as particle image velocimetry, or PIV (Adrian, 1991, 2005). Both PTV and PIV are well suited for observing transient responses in fluid flows, due to the good temporal and spatial resolution of these methods (Manneville, 2008), and this has been exploited by some workers to study transient evolution of shear banded flows (Miller & Rothstein, 2007). Both PTV and PIV are therefore a good choices for probing shear banding in oscillatory flows, although recent developments in Rheo-NMR techniques discussed by Callaghan (2008) and Davies *et al.* (2010) have provided spatial and temporal resolutions that rival those of PIV/PTV methods. One advantage of PIV over PTV is that it is a whole field technique, returning velocimetric data on a uniformly-spaced grid (Raffel *et al.*, 1998). Vector fields obtained from PTV tend to be sparser than those obtained from PIV, and the individual vectors are located randomly throughout the imaged domain due to the randomly positioned particles in the flow (Adrian & Westerweel, 2011). This disadvantage in general makes subsequent data analysis, including computation of differential quantities such as shear rate and vorticity, more cumbersome for PTV.

Some of the earliest investigations of shear banding in WLM solutions studied the phenomenon using Rheo-NMR in a cone-and-plate geometry (Britton & Callaghan, 1997, 1999). This approach is reasonable because it is well known that when viscometric approximations hold, spatial variations in the stress in a cone-and-plate geometry are very small (Bird *et al.*, 1987). Subsequent velocimetric studies have focused more often on observing banding in cylindrical Taylor-Couette geometries (Salmon *et al.*, 2003; Manneville *et al.*, 2004b; Miller & Rothstein, 2007). These velocimetry studies have

shown that there is a clear difference between the structure of the shear-banded profiles observed in the two geometries. Typically a two-banded profile develops in the Taylor-Couette case above a critical shear rate (one low and one high shear rate band) shown in Figure 2.2.5 (a) and (b), whereas three-banded profiles appear in the cone-and-plate geometry shown in Figure 2.2.5 (c) and (d) (two low shear rate bands near the upper and lower rigid plates, and a higher shear rate band at midgap). These differences arise presumably because of the curvilinear nature of the flow fields in each device - the theoretical study by Adams *et al.* (2008) has discussed this in detail for a particular case of the Johnson-Segalman model. Some recent studies have also suggested that wall slip plays an important role in the shear banding behavior of WLM solutions (Boukany & Wang, 2008; Lettinga & Manneville, 2009; Feindel & Callaghan, 2010), further highlighting the value of incorporating velocimetry measurements when interpreting bulk rheology measurements.

In addition to studies of banding in Taylor-Couette cells, velocity profiles of WLM in Poiseuille flow in macroscale devices have also been observed using nuclear magnetic resonance measurements (Mair & Callaghan, 1997), particle image velocimetry (Méndez-Sánchez *et al.*, 2003) and particle tracking velocimetry (Yamamoto *et al.*, 2008). Generally, as the flow rate through the pipe is increased, a transition from a Newtonian-like velocity profile to a profile with thin regions of high shear rate near the walls and plug-like flow in the core of the fluid is observed. For the flow rates coinciding with the high shear rate bands, a marginal change in wall shear stress can lead to very large changes in the volumetric flow rate, this phenomenon known in the literature as *spurt* (McLeish & Ball, 1986; Renardy, 1995). There have also been velocimetric studies of the onset of shear banding in these fluids within pressure driven microchannels (Méndez-Sánchez *et al.*, 2003; Marín-Santibáñez *et al.*, 2006; Nghe *et al.*, 2008). Although the stress and kinematics of steady complex fluid flow in a microchannel are spatially inhomogeneous, these experiments have been useful because they can be used to probe the non-linear rheology of the fluids at much higher shear rates than is usually possible and can probe the onset of *non-local effects* (Lu *et al.*, 2000) when the characteristic length scale of the geometry and of the shear band become comparable. Non-locality refers to the notion

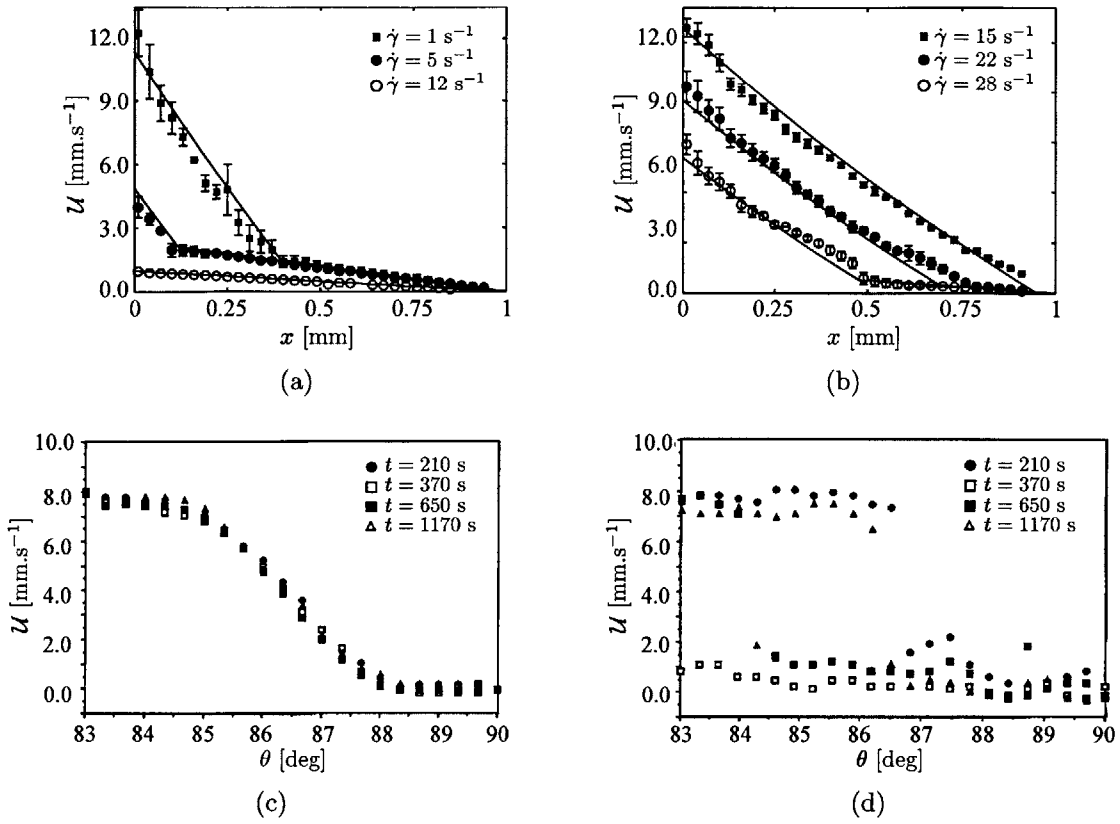

Figure 2.2.5: (a) & (b) Velocity profiles measured in Taylor-Couette flow. A marked two-banded profile is visible at all measured shear rates. Figures and caption adapted from Manneville *et al.* (2004b). (c) & (d) Velocity profiles measured in a cone-and-plate geometry for two WLM fluids. A (c) gradually and (d) abruptly varying three-banded profile that evolves in time is visible at the shear rate measured. Figures and caption adapted from Britton & Callaghan (1999).

that a local physical quantity, such as stress, not only depends on other local quantities, such as the local shear rate, but also on physical quantities at other locations in the entire spatial domain, such as the shear rate some distance away from the point of interest. Thus in flows with large spatial gradients in stress, it has been observed that the measured flow curve of WLM solutions is not necessarily solely dependent on the local shear rate (Masselon *et al.*, 2008, 2010).

2.2.3 Flow-Induced Birefringence

The role of non-local effects are a consequence of spatial inhomogeneities in the microstructure of the fluid which cannot be determined using velocimetric measurements.

Hence, a valuable addition to rheological experiments with WLM systems are microstructural probes such as birefringence measurements (Fuller, 1990, 1995) to measure the molecular anisotropy and its relationship to shear banding and elastic stresses. Flow-induced birefringence (FIB) measurements can be used to observe the degree of molecular alignment and stretching in a material, and provided the deformation of the microstructural network is affine, these measurements may be related to the stress in the material through the *stress-optical rule* (Fuller, 1995; Larson, 1998). According to this rule, the optical anisotropy Δn, in a homogeneous, viscoelastic network of Gaussian chains is linearly proportional to its principal stress difference $\Delta\sigma$, such that $\Delta n = C\Delta\sigma$, where C is the stress-optical coefficient, which is generally an empirically determined value for a particular material. A list of published values of stress-optical coefficients for relevant micellar fluids is given in Table 2.2.1. The magnitudes of C for WLM systems are large (typically 100 times greater than that of polymer systems) making these systems well suited to experimental studies in microfluidic devices. Furthermore, C is found to vary only weakly with temperature, but it does exhibit a slight dependence on concentration.

A number of papers have used FIB measurements to probe the molecular structure of WLM systems and to test the validity of the stress-optical rule for micellar systems (Wunderlich *et al.*, 1987; Rehage & Hoffmann, 1991; Shikata *et al.*, 1994; Decruppe *et al.*, 1997). A comprehensive review is available in (Lerouge & Berret, 2010). Typically, the stress-optical rule holds at shear rates below which the onset of a rate-dependent viscosity occurs. However, it often fails at stresses on the order of the stress plateau for the shear-banding fluids, and for stresses near the onset of shear-thinning for the shear-thinning fluids (Decruppe & Ponton, 2003). In the CTAB:$NaNO_3$ system, deviations between the predictions of the stress-optical rule and experimental results were attributed to a deviation from Gaussian chain statistics for large deformation rates (Lerouge *et al.*, 2000). Complex spatio-temporal flow behavior, discussed in Section 2.2.5, has also been observed in FIB measurements for shear rates coinciding with the stress plateau, including striations in the birefringence across the gap and the existence of three distinct birefringent bands at higher shear rates (Lerouge *et al.*, 2004). Point-wise measurements of birefringence of a shear-banding system across the gap width in a Couette cell geometry

Table 2.2.1: Published values of the stress-optical coefficient for micellar systems.

System	$C \times 10^7$ [Pa^{-1}]	Temperature [°C]	Source
100:60 mM CPyCl:NaSal	-2.3	20	Rehage & Hoffmann (1991)
10-100:50-300 mM CTAB:NaSal	-3.1	25	Shikata *et al.* (1994)
300:100 mM CTAB:KBr	-0.25	30	Humbert & Decruppe (1998)
300:200 mM CTAB:KBr	-0.36	30	Humbert & Decruppe (1998)
300:300 mM CTAB:KBr	$-(0.46 - 0.41)$	30-38	Humbert & Decruppe (1998)
300:400 mM CTAB:KBr	-0.62	30	Humbert & Decruppe (1998)
400-600:100 mM CTAB:KBr	$-(0.42 - 0.96)$	30	Humbert & Decruppe (1998)
300:1790 mM CTAB:$NaNO_3$	-2.78	30	Lerouge *et al.* (2000)
30:230 mM CTAB:NaSal	-2.77	25	Takahashi *et al.* (2002)
100:51-340 mM CTAC:NaSal	$-(2.5 - 6.1)$	25	Decruppe & Ponton (2003)
5.9:1.4 wt% CPyCl:NaSal, 500 mM NaCl	-1.2	23	Hu & Lips (2005)
[CPyCl]:[NaSal]=2, 500 mM NaCl	-1.74	22.1	Raudsepp & Callaghan (2008)

were obtained by (Lee *et al.*, 2005). The authors attributed the observed change in sign of the birefringence between the low and high shear rate bands to the existence of two phases, suggesting that a shear-induced phase separation was an underlying cause of the banding behavior.

In two studies of a concentrated CTAB:D_2O system by Helgeson *et al.* (2009a,b), measurements of velocity profiles, birefringence and small angle neutron scattering (SANS) in a wall-driven flow were combined to develop a more complete pictures of the microstructural features of the shear-banding fluid under flow. The authors found that shear banding in this system was coupled to a flow-induced isotropic-to-nematic transition that could be modeled in terms of an anisotropic drag on the worm-like chains leading to segment-level flow alignment of the micelles. In their study, the nematic phase was found to coincide with the high shear rate band. This result seemed to contradict the earlier findings that the flow-induced nematic phase had a higher viscosity than that of the isotropic phase (Fischer & Callaghan, 2000, 2001). The difference between shear-thinning and shear-banding WLM solutions using 2:1 molar CPyCl:NaSal systems of varying concentrations in 0.5 M NaCl has also been investigated (Hu *et al.*, 2008).

In the first study of birefringence of a WLM solution flowing in a microchannel, measurements of FIB were coupled with velocimetry measurements to test the stress-optical rule for extensional and shear flows in a 100:60 mM CPyCl:NaSal system and a 30:240 mM CTAB:NaSal system (Pathak & Hudson, 2006) in a shallow cross-slot geometry. The authors observed that the stress-optical rule failed in extensional flow for deformation rates at which a sharp birefringence band appeared, indicating high or nearly saturated molecular alignment with the flow. It was also found that the stress-optical rule failed at a lower critical Weissenberg number in extensional flow than in shear flow. More recently, FIB measurements were used to study the onset of a purely elastic instability in a range of WLM fluids with different surfactant concentrations in a cross-slot geometry (Haward *et al.*, 2012a; Haward & McKinley, 2012; Dubash *et al.*, 2012). Shear banding was observed to play a key role in the onset of the flow instability even in this extension-dominated flow.

2.2.4 Constitutive Modeling of Shear-Banding Fluids

Despite considerable experimental effort over the last two decades, a universal explanation for the molecular mechanism behind the shear-banding phenomenon in WLM fluids has not yet been realized (Cates & Fielding, 2006). One of the most persistent ideas in modeling shear banding is the notion of some kind of underlying *flow-structure* coupling. Mechanisms for such coupling include entanglement effects, breakage, liquid-crystalline effects, changes in charge and association, or changes in topology (Olmsted, 2008). Shear banding may even be a generic macroscopic phenomenon, able to spring out of many different underlying mechanisms. For instance, it was thought for some time that shear banding was necessarily associated with non-monotonic constitutive relations (Hunter & Slemrod, 1983; McLeish & Ball, 1986) but it has subsequently been realized that other mechanisms such as stress inhomogeneity inherent to the geometry – in large gap Taylor-Couette geometry for instance – or boundary effects can lead to shear-banding-like flows (Adams & Olmsted, 2009a; Wang, 2009; Adams & Olmsted, 2009b).

Many see a solid understanding of shear banding in micellar fluids as a necessary first step toward a clearer view of the phenomenon in general. In other systems such as dispersions, foams or granular materials, the shear-banding phenomenon is not as well characterized empirically (Divoux *et al.*, 2011), and most models are not tensorial (Coussot & Ovarlez, 2010; Bocquet *et al.*, 2009). In micellar solutions, since the seminal study by Rehage & Hoffmann (1991) much theoretical and experimental effort has been devoted to understand the phenomenon. The most recent review on the subject by Lerouge & Berret (2010) referenced more than three hundred articles. From a theoretical perspective, it is often challenging to understand the connections between the different modeling approaches of shear banding that have been proposed

For WLM, the original idea of an underlying non-monotonic flow curve is most likely to be relevant to almost all experimental situations investigated so far. Theoretically, this idea is justified the reptation-reaction model (Cates & Fielding, 2006). This statistical theory of micelles is an adaptation of the reptation theory of polymers, including micellar breaking and recombination processes (Cates & Fielding, 2006). This theory

can both predict linear rheology with great accuracy and the onset of shear banding, due to an underlying inhomogeneity of the flow curve (Cates & Fielding, 2006). Nonetheless, this model becomes highly intractable in the non-linear flow regime where shear banding occurs, and it has been of little or no help to understand shear banding in more detail. Other researchers have extended the model of Cates to accurately predict many of aspects of the non-linear rheological behavior of WLM solutions (Vasquez *et al.*, 2007; Zhou *et al.*, 2008). However, these models have many fitting parameters and it can be a considerable challenge to use them to derive analytical descriptions of the flow in the non-linear regime. Therefore, simpler quasi-linear constitutive models (Bird *et al.*, 1987) have been used (Larson, 1998; Cates & Fielding, 2006; Fielding, 2007) to obtain more tractable predictions in the non-linear flow regime. These more basic constitutive models, which rely on very general material frame invariance principles, do not usually contain all the information on the microstructural dynamics and deal with coarse-grained quantities defined at the macroscopic scale. They usually at least include a tensorial stress field, and a tensorial velocity gradient field (Larson, 1998).

In the last few years, one particular constitutive model has been used extensively, namely, the diffusive Johnson-Segalman (dJS) equation and its mechanistic interpretation (Cates & Fielding, 2006; Fielding, 2007). It is one of the simplest tensorial models able to predict shear banding. Because it is a quasi-linear model with only few parameters, it is also analytically tractable in many cases. Thus, despite some known shortfalls, especially its violation of the Lodge-Meissner rule, and its troubles in extensional flows and step strains (Larson, 1998), the dJS model has generally been a very useful guide to interpret empirical data and to suggest new experiments.

Like the Maxwell model, the dJS model can be constructed from a handful of mechanical elements (*i.e.* spring, dashpot and slipping element), and therefore when this model was initially developed for modeling the rheology WLM fluids, it was used to support the claim that shear banding arose from a mechanical instability in the material. This view often seemed to be in contrast, however, with the apparent similarities between shear banding and phase transitions, suggesting that it resulted from a thermodynamic instability instead. Thus two seemingly dichotomous approaches to understanding shear

banding emerged, and it often appeared difficult to reconcile the *mechanical* and the *thermodynamical* viewpoints (Berret *et al.*, 1994; Schmitt *et al.*, 1995; Porte *et al.*, 1997). However, more recently it has been shown that it is possible to construct models including ingredients from both perspectives (Fielding & Olmsted, 2003). The so-called dJS-f model includes both mechanical and concentration subspaces, coupled to each other (Fielding & Olmsted, 2003). More broadly, Cates & Fielding (2006) have recently remarked that the distinction between mechanical banding instabilities and shear-induced structural instabilities is likely to be less clear-cut than was initially thought. Later, Olmsted (2008) added that in practice there is little difference between the two. This claim was made even clearer last year by Sato *et al.* (2010). In their paper, they derived a pseudo-thermodynamic potential from the dJS model, though only at the cost of a reduction of the number of degrees of freedom in order to obtain an equation that is not strictly equivalent to the original dJS model.

Overall, the dJS has proven to be a valuable tool for modeling the rheology of WLM solutions. It has been used to predict the onset of shear-banding in various flow geometries (Radulescu *et al.*, 1999; Lu *et al.*, 2000; Radulescu *et al.*, 2000; Fielding, 2007), to understand transient effects (Radulescu *et al.*, 2003) and most importantly, to realize that shear-banding flows could themselves become unstable to elastic instabilities, *i.e.* effects linked to normal stresses differences across bands (Fielding, 2005, 2007, 2010).

2.2.5 Flow Instabilities in Shear-Banding Fluids

It is well known that for flows with curved streamlines, Newtonian fluids can exhibit increasingly unstable flows for large values of the Reynolds number. In a seminal paper by Taylor (1923), the author studied the flow of a Newtonian liquid in a Taylor-Couette geometry with inner and outer radii R_i and R_o shown schematically in Figure 2.2.6 (a), and showed that the purely annular flow eventually becomes unstable as the rotation speed of the cylinder Ω is increased. Above a critical rotation speed Ω_c, a secondary vortex flow sets in, with periodicity $\ell \sim d$ along the vorticity direction, where $d \equiv R_o - R_i$. Later, is was shown by Larson *et al.* (1990) that the Taylor-Couette flow of viscoelastic polymer solutions was also prone to a Taylor-like instability. Although the kinematics

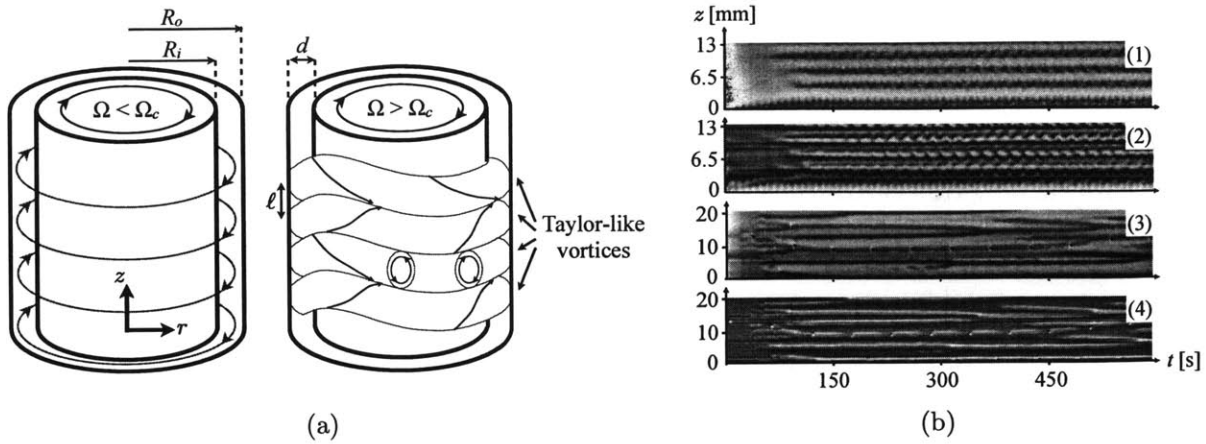

(a) (b)

Figure 2.2.6: (a) Schematic diagrams of flow in the Taylor-Couette geometry with stationary outer cylinder and rotating inner cylinder. At low rotational speeds Ω, the flow is stable and follows curvilinear streamlines. Above a critical speed Ω_c secondary flows emerge. (b) Spatio-temporal diagrams of the evolution in gray scale of (1) & (3) the interface profile and (2) & (4) the reflected intensity distribution in a WLM fluid as a function of time during step shear rate from rest to (1) & (2) $\dot{\gamma} = 35\ ^{-1}$, (3) & (4) $\dot{\gamma} = 75\ ^{-1}$. Figure adapted from Fardin *et al.* (2009).

of the instability in Newtonian and viscoelastic liquids is similar, (*i.e.* after a critical threshold velocity, Taylor-like vortices appear), the destabilizing mechanisms arise from very different non-linearities.

When only the inner cylinder is rotating, the Reynolds number depends on the rotation rate of the inner cylinder Ω, such that $Re = R_i \Omega d/\nu$ where ν is the kinematic viscosity of the fluid (Chandrasekhar, 1981). In a Newtonian fluid, the deviatoric stresses depend linearly on shear rate, so the only non-linearity in the equations of motion that can drive a flow instability comes from the advective term on the velocity $(\vec{v} \cdot \nabla)\vec{v}$. The Reynolds number Re is linked to the relative magnitude of this term with respect to the dissipation terms.

In viscous polymer solutions, and in many non-Newtonian fluids, the primary non-linearity usually comes from the constitutive equation for stress rather than from the momentum balance. The constitutive equation is dynamical, in that it relates to the stress relaxation dynamics and typically includes a convected derivative on the stress $\mathbf{T}$ (Larson, 1998). In this convected derivative, consistency between Eulerian and La-

grangian descriptions requires a convective term, now applied on the stress $(\vec{v} \cdot \nabla)\mathbf{T}$, and material frame invariance requires additional terms of similar dimensionality $\nabla\vec{v} \cdot \mathbf{T}$ (Larson, 1998; Larson *et al.*, 1990). The dimensionless group linked to the magnitude of these non-linear terms is the Weissenberg number $Wi = \lambda\dot{\gamma}$, where $\dot{\gamma} = R_i\Omega/d$ is the typical shear rate in the flow and λ is the stress relaxation time (Dealy, 2010). The analogy between Re and Wi becomes clearer by defining Re as a function of the viscous diffusion time $\lambda_{vd} = d^2/\nu$, $Re = \lambda_{vd}\dot{\gamma}$ (Groisman & Steinberg, 1998). The Reynolds number controls the magnitude of the *inertial* non-linearity, while the Weissenberg number controls the magnitude of the *elastic* non-linearity (Morozov & van Saarloos, 2007). In general, both Re and Wi are non-zero, but in many practical cases for polymer solutions and melts, the elasticity number $El \equiv Wi/Re = \lambda/\lambda_{vd}$ is large, leading to negligible inertial effects.

For the simplest Taylor-Couette flow in the small gap limit, (*i.e.* $d \ll R_i$), with only the inner cylinder is rotating, there exist two analogous dimensionless groups governing the onset of secondary flows. The first is relevant to the purely inertially-driven instability $\Sigma_i = \sqrt{\Lambda}Re$ and was derived and observed by Taylor (1923). The second governs the purely elastically-driven instability $\Sigma_e = \sqrt{\Lambda}Wi$ and was found by Larson *et al.* (1990). Here, $\Lambda \equiv d/R_i$ is the geometrical ratio linked to the streamline curvature, which is necessarily non-zero for the instability to be linear (Taylor, 1923; Morozov & van Saarloos, 2007). In the purely inertial case, the flow becomes unstable for $\Sigma_i > m'$, whereas in the purely elastic case, the flow becomes unstable for $\Sigma_e > m$. Both m' and m are coefficients of order unity, whose precise values depend on the boundary conditions (Chandrasekhar, 1981; Khayat, 1999).

In a series of recent experiments and reviews on Taylor-Couette flows of WLM solutions (Lerouge *et al.*, 2006, 2008; Lerouge & Berret, 2010; Fardin *et al.*, 2009, 2012a,b; Fardin & Lerouge, 2012), it has also been shown that the interface between the bands undulates due to an underlying secondary vortex flow that is mainly localized in the high shear rate band. The observed spatio-temporal fluctuations, shown for example in Figure 2.2.6 (b), appear to be driven by an elastic instability similar to the one observed in polymer solutions. This rationale was reinforced by a recent linear stability

analysis of the diffusive Johnson-Segalman (dJS) model (Fielding, 2010). The onset of a secondary flows as well as elastic turbulence (Fardin *et al.*, 2010) in shear-banding WLM fluids poses a challenge for the accurate rheological characterization of these systems using viscometric measurements, which can be addressed by the development of an appropriate stability criterion for shear-banding fluids.

2.2.6 Present Study

In Chapter 3, a shear-banding WLM fluid composed of 100 mM cetylpyridinium chloride (CPyCl) and 60 mM sodium salicylate (NaSal) and a system of cetyltrimethylammonium bromide (CTAB) with NaSal or sodium nitrate ($NaNO_3$) are characterized in oscillatory shear, steady shear and in step strain stress relaxation measurements. The rheological behavior of the shear-banding CPyCl:NaSal solution in the steady shear is studied with a a cone-and-plate geometry through simultaneous bulk rheometry and localized velocimetric measurements. In addition to the kinematic measurements of shear banding, the methods used to prevent wall slip and edge irregularities are discussed in detail, and these methods are shown to have a measurable effect on the stability boundaries of the shear banded flow.

Subsequently, in Chapter 4, a brief historical account of different interpretations the diffusive Johnson-Segalman (dJS) equation for modeling shear-banding flows is discussed. In the case of anisotropic diffusion, the dJS governing equations for steady flow are analogous to the equations of the dynamics of a particle in a quartic potential, which can be used to derive analytically interesting features about the role of non-local effects on shear banding. These findings are then extended to derive a stability criterion for the onset of a purely elastic instability in the flow of shear-banding liquids.

2.3 Microfluidic Rheometry

Macroscale rheometry alone cannot be used to obtain a complete picture of shear-banding, since it is often confounded by the onset of edge fracture, flow instabilities and air entrainment (Tanner & Keentok, 1983; Wheeler *et al.*, 1998; Fardin *et al.*, 2009),

limiting the maximum observable shear rates to values $\dot{\gamma} \lesssim \dot{\gamma}_2$ (see Figure 2.2.4). Microfluidic devices, however, offer a means of overcoming this limit in observable deformation rates, facilitating investigation of the connection between flow kinematics and microstructual feature of WLM systems in the non-linear regime.

More generally, microfluidic devices are invaluable for many rheometric experiments because they can be easily designed to mimic the micron-sized features of geometries that are found in many industrial applications, (*e.g.* in fiber extrusion spinnerets, the processing of foodstuffs, and as model porous media (Ferer *et al.*, 2011)). Such devices are also inexpensive and easy to fabricate, they require only small sample volumes and allow the rheologist to impose large deformation rates ($10^2 < \dot{\gamma} < 10^6$ s^{-1}) in complex fluids at low Reynolds number and thus without complications from inertial effects (Pipe *et al.*, 2008; Pipe & McKinley, 2009). Large deformation rates may be found in the case of the nozzle of an inkjet printer, for example, where the length ℓ of the smallest printable feature may be on the order of tens of microns and ejection speeds $\mathcal{U}$ are on the order of meters per second, making for characteristic deformation rates of at least $\dot{\gamma}_c \sim \mathcal{U}/\ell \sim \mathcal{O}(10^4)$ s^{-1}. Furthermore, microfluidic devices can be used to generate mixed flows that have shear as well as extensional components, which are more realistic for many real world applications.

2.3.1 Microfluidic Rheometry for Shear Flows

Microfluidic shear rheometry typically focuses on straight, high aspect ratio rectangular ducts of width W, height H and length L, for which $W \ll H \ll L$. For rectilinear flows, the shear stress at any position along the width of the channel is known from direct integration of the equation of motion and the corresponding shear rate can be calculated from the local velocity profile which is often measured with micro-particle image velocimetry (μ-PIV). Knowledge of the local shear rate and shear stress can then be used to directly ascertain the flow curve, as has been shown for aqueous polymer solutions at shear rates up to $\dot{\gamma} \lesssim \mathcal{O}(10^6)$ s^{-1} (Kang *et al.*, 2005, 2006). This process, however, cannot provide information on local elastic stresses, which instead can be measured using rheo-optical probes such as flow-induced birefringence. For shear-thinning

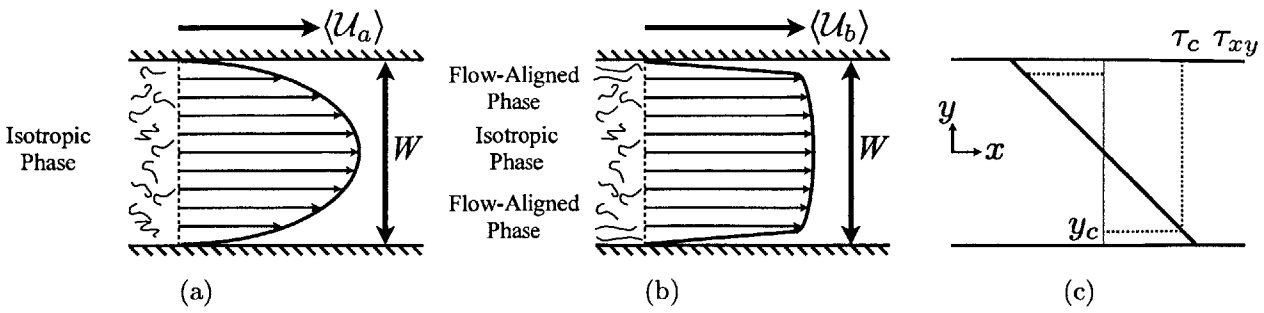

Figure 2.3.1: (a) Homogeneous Poiseuille flow for which the characteristic shear rate $\dot{\gamma}_a = \langle \mathcal{U}_a \rangle / W \ll \dot{\gamma}_1$, where $\langle \mathcal{U} \rangle$ is the average velocity in the channel. (b) Inhomogeneous Poiseuille flow for which $\dot{\gamma}_1 < \dot{\gamma}_b = \langle \mathcal{U}_b \rangle / W < \dot{\gamma}_2$. (c) Shear stress distribution in Poiseuille flow where y_c is the channel position at which $\tau_{xy} = \tau_c$.

or shear-banding micellar solutions in Poiseuille flow, a transition from a Newtonian, parabolic profile at low flow rates depicted in Figure 2.3.1 (a), to a banded profile in Figure 2.3.1 (b), occurs above a critical wall shear stress (Masselon *et al.*, 2008; Nghe *et al.*, 2008), coinciding with Weissenberg number of order unity ($Wi = \lambda \langle \mathcal{U} \rangle / W \approx 1$).

The microfluidic rheometry of shear-thinning polyethylene oxide solutions has been studied in a rectangular, polydimethylsiloxane (PDMS) microchannel (Degre *et al.*, 2006). They found good agreement between their measurements of viscosity from the flow in the microchannel and that measured with a conventional Couette rheometer, but noted that a more rigid geometry was needed to test highly viscous fluids. A silica glass geometry was used to study a worm-like CPyCl:NaSal:NaCl system by (Guillot *et al.*, 2006), who found good agreement between their viscosity measurements in the microchannel and from the rheometer for all shear rates examined.

An important feature noted in microfluidic studies of complex fluids in rectilinear shear flows has been the role of channel size and aspect ratio. This issue was considered in detail using numerical simulation (Nghe *et al.*, 2010; Cromer *et al.*, 2010). In contrast to flows of simple Newtonian fluids, the confining effects of channel walls of a 1 mm $\times$ 200 μm glass channel were found to give rise to non-local (*i.e.* diffusive) effects that influence the numerical value of the stress plateau in CPyCl:NaSal:NaCl and CTAB:$NaNO_3$ systems (Masselon *et al.*, 2008). Experiments with the same CTAB:$NaNO_3$ solution in a 1 mm $\times$ 67 μm glass channel, however, were found not to affect the overall

flow curve (Nghe *et al.*, 2008).

The body of scientific literature regarding flows of micellar solutions at the microscale is considerably smaller than that for corresponding macroscale flows. Additionally, very few microfluidic studies have considered anything beyond the kinematics in shear flows offering little insight into the corresponding state of microstructural stress and orientation of the fluid. Microstructural probes, such as spatially resolved measurements of flow-induced birefringence serve to enhance the present understanding of the complex relationship between stress, flow kinematics and the microstructural state of WLM systems.

2.3.2 Microfluidic Rheometry in Extension-Dominated Flows

The use of microfluidic technology for extensional rheometry has recently been reviewed by Pipe & McKinley (2009) and Galindo-Rosales *et al.* (2013). To generate an internal extensional flow, the test fluid typically travels through a converging region or a contraction such that the mean axial velocity $\mathcal{U}$ of a fluid element changes in the flow direction as the sample travels through the device, (*i.e.* so that $\partial\mathcal{U}/\partial x \neq 0$). Careful consideration must be given to the shape of the contraction in order to realize the desired extensional deformation. Some of the most commonly used geometries are shown schematically in Figure 2.3.2. Many of the earliest studies with converging geometries utilized abrupt or constant-angle, tapered macroscale contractions (Cogswell, 1978; Binding & Walters, 1988). The hyperbolically-shaped contraction is unique in that it can be used to impose a nominally constant extension rate along its centerline for a given volumetric flow rate, as discussed by James (1991). It was first studied in an axisymmetric configuration by Everage & Ballman (1978), but the corresponding planar configuration, was first studied only recently by Oliveira *et al.* (2007). These authors studied the detailed kinematics of planar hyperbolic contraction flows both experimentally and numerically for Newtonian fluids, noting that for creeping flow, the effects of viscous shearing are the dominant contribution to the total pressure drop along the contraction and that it is difficult to isolate purely extensional effects.

For viscoelastic fluids, however, there can be a significant additional elastic contribu-

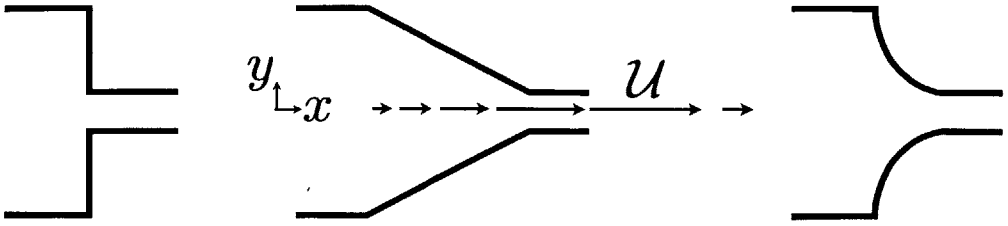

(a) Planar (b) Constant angle (c) Hyperbolic

Figure 2.3.2: Commonly used contraction geometries for extensional rheometry measurements.

tion to the total pressure drop as a result of the transient elongational flow experienced by the fluid elements passing through the contraction. This facilitates the measurement of an effective extensional viscosity using a hyperbolic contraction device. Many studies using a range of model fluids and viscoelastic constitutive models have been performed to assess the suitability of converging dies for measuring extensional viscosity, typically by attempting to decouple the viscous and elastic contributions to the measured pressure drop (James & Saringer, 1982; Rajagopalan, 2000; Feigl *et al.*, 2003; Pandey & Lele, 2007; Oliveira *et al.*, 2008; Wang *et al.*, 2010; Sousa *et al.*, 2011). In the computational study of Rajagopalan (2000), for example, the Phan-Thien-Tanner (PTT) model was used to predict the pressure field in the flow through both abrupt and tapered contractions, from which an extensional viscosity was calculated using different analytical techniques and compared against the predicted extensional viscosity for the PTT model in a homogeneous extensional flow. In general it was found that the analytical procedures for extracting an extensional viscosity from the inhomogeneous flow field gave results that were in agreement with the true extensional viscosity expected in a homogeneous extensional flow, provided the extension rates were sufficiently large. Furthermore, for the range of PTT model parameters considered, Hencky strains of at most $\varepsilon_H = 4.5$ were required to attain steady state, and with decreasing strain rates, the minimum Hencky strain required to attain steady state decreased. Tamaddon-Jahromi *et al.* (2011) performed a parametric study using the PTT and the Bautista–Manero models for simulating the flows of worm-like micellar systems in steady shear and homogeneous extensional flows, as well as flow through an abrupt contraction. In this study,

it was found that the respective predictions of vortex growth and pressure drop values in the contraction flow differed most between the two models for fluids exhibiting increasing levels of strain hardening in homogeneous extensional flow. Nyström *et al.* (2012) used the FENE-CR model to study a range of axisymmetric abrupt, hyperbolic and tapered contractions to determine the optimal geometry for generating a constant extension rate along the centerline of the contraction. The hyperbolic geometry was found to be best for imposing a spatially uniform extension rate and no upstream vortices were observed in this geometry. In the numerical study of Afonso *et al.* (2011), the Oldroyd-B and PTT models were used to simulate flows through axisymmetric and three-dimensional square abrupt contractions at Deborah numbers up to $\mathcal{O}(10^4)$. The formation of upstream vortices was observed as flow rate was increased, along with a transition to unsteady flow at a critical Deborah number and a frequency-doubling behavior with further increases in flow rate ultimately leading to a chaotic regime.

For the experimentalist studying contraction flows, the challenge lies in using kinematic and pressure measurements to extract a quantitative measure of the extensional flow resistance of the test fluid. To illustrate this point, pressure drop measurements for a range of polyethylene oxide (PEO) solutions in the same Newtonian solvent across a planar hyperbolic contraction-expansion at different low Reynolds number flow rates are shown in Figure 2.3.3. For all of the PEO solutions, the pressure drop increases non-linearly with flow rate, and it can be many times larger than the corresponding Newtonian value at a given flow rate. Therefore, it would be valuable to have a method for systematically quantifying the importance of viscoelastic contributions in these total pressure drops in order to quantitatively compare the rheological behavior of different fluids in an extension-dominated mixed flow.

To that end, within the last decade, there have been many experimental studies of extension-dominated mixed flows of non-Newtonian fluids in microfluidic devices. The small length scales of these test geometries facilitate flows at low Reynolds number but large deformation rates, enabling experimentalists to study the importance of viscoelastic effects in high Weissenberg number extensional flows. The viscoelastic flow of polyacrylamide solutions through a series of contraction-expansions has been suggested as a novel

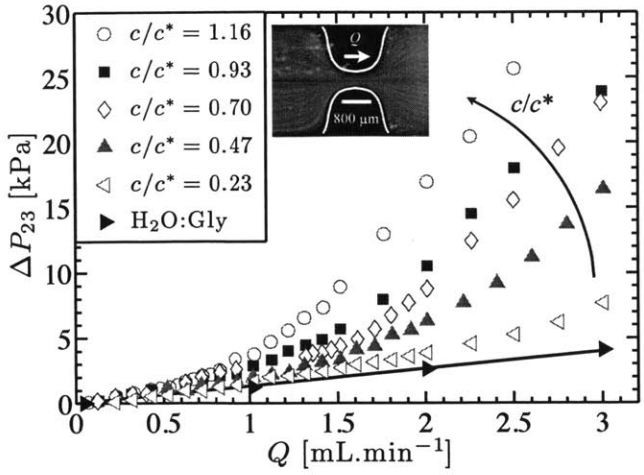

Figure 2.3.3: Measured pressure drop across the planar 7.75:1 hyperbolic contraction-expansion ΔP_{23} as a function of flow rate Q for low viscosity solutions of high molecular weight PEO (2×10^6 g.mol^{-1}, overlap concentration $c^* = 8.58 \times 10^{-4}$ g.mL^{-1}; Sigma-Aldrich) in a water:glycerol solvent ($\mu = 8.2$ mPa.s). The solid black line has been added to guide the eye for the results of the Newtonian solvent. Inset figure is a streakline image of the creeping flow ($Re \ll 1$ and $De \ll 1$) through the contraction (channel thickness $h = 200$ μm, inlet width $w_u = 3100$ μm, throat width $w_c = 400$ μm and contraction length $l_c = 825$ μm).

way to create a microfluidic rectifier (Groisman & Quake, 2004). Recently, Sousa *et al.* (2012) compared the flow of a Newtonian fluid with a high molecular weight PEO solution in a microfluidic rectifier device composed of a series of hyperbolic contractions and different channel depths, finding that diodicity ratios as high as 6.4 could be achieved using the viscoelastic fluid even at very low Reynolds numbers. The competing roles of fluid inertia and viscoelasticity on the kinematics and pressure drop in the flow of PEO solutions through a planar abrupt contraction were studied by Rodd *et al.* (2005, 2007). PEO and hydroxyethyl cellulose solutions were used to study the importance of end effects in the pressure drop across a straight microchannel by Kang *et al.* (2006). They found that for these fluids the dominant contribution to the Bagley correction came from the flow in contraction and expansion regions upstream and downstream of the channel, rather than from the development region in the straight channel itself. Experiments in a T-channel geometry with PEO (Soulages *et al.*, 2009) and xanthan gum (Bandalusena *et al.*, 2009) have also been studied and corresponding computational studies have been preformed by Bandalusena *et al.* (2010). Microfluidic analogues of the four-roll mill have

been studied for imposing mixed extensional and shear flows Hudson *et al.* (2004); Lee *et al.* (2007).

Recently, Wang & James (2011) studied the flow of Newtonian and PEO solutions in a planar microfluidic hyperbolic contraction (19:1 contraction ratio) by using both miscible and immiscible, low viscosity Newtonian lubricating fluids to facilitate a more homogeneous elongational flow in the inner viscoelastic fluid. In calibration experiments with a Newtonian fluid, but no lubricating fluid, very good agreement was found between the velocimetry and pressure measurements and analytical predictions based on the lubrication approximation. In the lubricated experiments with a viscoelastic core fluid, the flow was found to be stable only if the the immiscible fluid was used as the lubricating fluid. However, the location of the fluid-fluid interfaces was dependent on flow rate and thus flow visualization measurements were necessary to complement the pressure measurement for accurate determination of the extensional viscosity.

WLM fluids have also been studied in extension-dominated flows using millifluidic and microfluidic devices (Hashimoto *et al.*, 2006; Stone *et al.*, 2006; Pathak & Hudson, 2006; Marín-Santibáñez *et al.*, 2009; Haward *et al.*, 2012a; Dubash *et al.*, 2012; Haward & McKinley, 2012). The ability of these fluids to shear band enables the formation of effective lubrication layers at the channel walls, facilitating a plug-like flow in the core of the fluid that can be beneficial for obtaining a more homogeneous extensional flow field in a contraction geometry.

From all of these prior studies, it is clear that for extension-dominated flows in microfluidic devices, viscoelasticity plays a crucial role in the resulting kinematic and stress fields making determination of the extensional viscosity challenging. Therefore, a valuable addition to pressure and velocimetry measurements are flow-induced birefringence measurements, which can be used to observe the degree of molecular alignment and stretching in material elements as they flow through the device and in certain cases these measurements can be related to the stress in the material with a stress-optical rule (Fuller, 1990). Such measurements have been used extensively for polymeric and WLM fluids in macroscale geometries, (Fuller, 1990; Lerouge & Berret, 2010), including contraction flows, (Adams *et al.*, 1965; Han & Drexler, 1973a,b; Schuberth & Münstedt,

2008). Recent studies of birefringence in microchannels have focused on WLM fluids (Pathak & Hudson, 2006; Haward *et al.*, 2012a; Dubash *et al.*, 2012; Haward & McKinley, 2012), largely, because WLM systems are typically around one hundred times more birefringent than polymeric systems, so the small optical path lengths associated with microfluidic devices can still provide a strong enough signal for experimental measurements. In these studies, birefringence and velocimetry measurements were used to characterize the flow instabilities and conformational hysteresis of shear banding WLM fluids in extensional flow in microfluidic cross-slot geometries.

2.3.3 Present Study

In Chapter 5, two different entangled WLM fluids, one of which exhibits shear banding and one which shows shear-thinning are compared in a high deformation rate shear flow. The rheological and rheo-optical properties of the fluids are first characterized using conventional macroscale rheometric measurement techniques. Spatially-resolved birefringence measurements of the flow are obtain using a commercial birefringence microscopy system (ABRIO^{TM}; CRi, Inc.). These measurements are compared against corresponding macroscale measurements of the stress-optical rule in a conventional rheometer, to validate the use of this system for microfluidic optical rheometry. Then in Chapter 6, an 'extensional viscometer-rheometer-on-a-chip' (EVROC) is used as a microfluidic extensional viscosity indexer to quantify the rheological behavior of complex fluids in an extension-dominated mixed flow. The combination of pressure, birefringence and velocimetry measurements in this microfluidic contraction-expansion geometry offers the experimental rheologist the ability to obtain spatially resolved measurements of the state of stress as well as the molecular stretching in elastically-dominated flows of complex fluids.

The over arching focus of both Chapters 5 and 6 is on the development and refinement of microfluidic-based rheometric techniques for measuring the rheological behavior of complex fluids undergoing high rate deformations, for which the viscoelasticity of the material plays an important role in the stress generated in response to an imposed deformation. The strain rates associated with the flow of micellar solutions in microscale

geometries are evaluated with micro-particle image velocity (μ-PIV) measurements using standard equipment. The corresponding stresses associated with the flow are measured with pressure transducers and from optically, non-invasive measurements of flow-induced birefringence. The measurements of stress and strain rate may ultimately be coupled to the predictions of select constitutive models to test the performance of those models in predicting the high rate rheology of worm-like micellar solutions. Although these experiments focus on micellar systems, the experimental techniques used are readily transferable to the study of other transparent, complex fluids.

2.4 Particle Migration and 'Inertial Focusing'

It is well known that inertial effects give rise to secondary flows as well as turbulence in flows of Newtonian fluids (Taylor, 1923; Tennekes & Lumley, 1972). The relevant control parameter for such instabilities is the ratio of a characteristic inertial to viscous stresses introduced previously in Section 2.2.5 and is the Reynolds number $Re \equiv \mathcal{U}\ell/\nu$, where $\mathcal{U}$ is the mean channel velocity, ℓ is the characteristic length scale of the flow geometry and ν is the kinematic viscosity of the fluid. Similarly, it is known that even in low-speed flows of viscoelastic liquids, elastic stresses can give rise to laminar secondary flows along with elastic turbulence (Larson, 1992; Groisman & Steinberg, 2000). The corresponding control parameter for these flows is the ratio of elastic to viscous stresses in the flow. This ratio is approximately equivalent to the ratio of the relaxation time of the fluid λ to the intrinsic timescale of the flow, being proportional to an imposed deformation rate $\dot{\gamma} \sim \mathcal{U}/\ell$, given by the Weissenberg number $Wi \equiv \lambda\dot{\gamma}$, which was first introduced in Section 2.2.5. Although both inertia and elasticity are non-linear effects that tend to destabilize a flow, if they are simultaneously important, as for example in the case of Taylor-Couette flows (Larson, 1992; Crumeyrolle *et al.*, 2002) discussed previously, or turbulent polymer drag reduction (Graham, 2004; White & Mungal, 2008), they can act together, in fact, to stabilize it. The relative importance of elastic to inertial stress is given by the elasticity number $El \equiv Wi/Re = \lambda\nu/\ell^2$, which is the ratio of the two control parameters and is, in principle, independent of the dynamics of the flow.

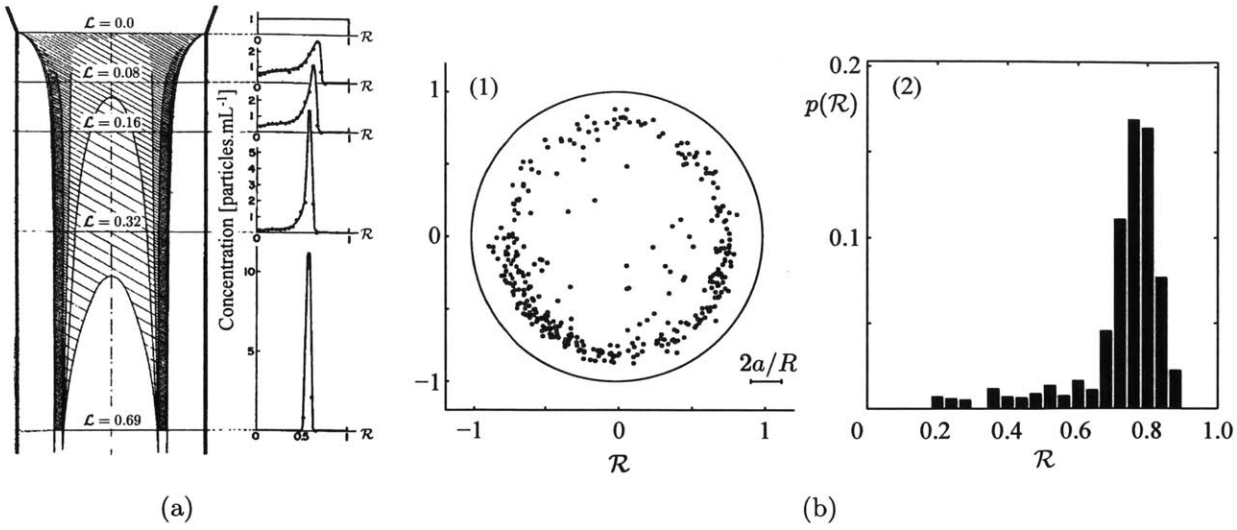

Figure 2.4.1: (a) Particle concentration as a function of radial and longitudinal position in a cylindrical tube. Initial concentration is one particle per milliliter. Particle size is $0.8 \leq 2a \leq 1.6$ mm, pipe radius $R = 5.8$ mm. Dimensionless variables $\mathcal{R} \equiv r/R$ and $\mathcal{L} \equiv Re_p(L/R)$. Figure and caption adapted from Segré & Silberberg (1961). (b) – (1) Particle distribution $p(\mathcal{R})$ over a cross-section and (2) the corresponding histogram showing the probability as a function of the dimensionless radius, for $Re_c = 350$ and $R/a = 9$. Axes are labelled with lengths scaled by the tube radius, and the bar at the lower right-hand side shows the mean particle diameter on the same scale. Figure and caption adapted from Matas *et al.* (2004b).

For an experimentalist, the challenge is to measure the flow kinematics to better understand the governing dynamics of the flow. Some of the most commonly employed experimental techniques for observing the flow field in a channel include particle tracking velocimetry (PTV) and particle image velocimetry (PIV), in which the velocity of small tracer particles that have been seeded in the fluid are measured under the assumption that the particles faithfully follow the local flow field. However, it is not always the case that this assumption is valid. For example, sedimentation effects or particle inertia in a laminar or turbulent flow can prevent a tracer bead from precisely moving with the local fluid velocity (Maxey, 1987; Snyder & Lumley, 1987). In fact, even in Stokes flow the Faxén relations predict that the velocity of neutrally buoyant particles may differ from the local fluid velocity if the flow is nonuniform (Happel & Brenner, 1983; Maxey & Riley, 1983), and only a minute amount of fluid inertia is necessary to cause particles to migrate across streamlines (Ho & Leal, 1974).

Indeed, this inertially-driven particle migration in laminar channel flows of Newtonian fluids at moderate to high Reynolds number is a topic that has received a resurgence in research interest in recent years. The phenomenon, commonly called the Segré-Silberberg effect (Segré & Silberberg, 1961, 1962a,b), was famously observed in Poiseuille flow in macroscale cylindrical pipes, wherein the millimeter-sized particles of diameter a, suspended in a Newtonian carrier fluid moved away from the pipe wall and centerline such that on average they were distributed in an annulus whose radius was some fraction of the pipe radius depending on the channel Reynolds number $Re_c \equiv \mathcal{U} d_h/\nu$, where d_h is the hydraulic diameter of the channel. See Figure 2.4.1. The migration phenomenon is attributed to a balance between a *wall effect lift force* that pushes the particle away from the wall and a *shear gradient force* that drives the particle to regions of higher shear rates (Ho & Leal, 1974; Matas *et al.*, 2004a). Subsequent analytical modeling of particle migration have typically been in the limit of infinitesimal particle Reynolds numbers, $Re_p \equiv Re_c(a/d_h)^2$, which is a measure of the relative importance of inertia at leading order in the vicinity of the particle. The characteristic length scale in this number is taken as the particle diameter a, and the characteristic velocity is based on the relative velocity between the fluid and the particle at a distance a away from the particle based on the characteristic shear rate in the channel $\dot{\gamma}_c \sim \mathcal{U}/d_h$ as illustrated in Figure 2.4.2 (where H and d_h are interchanged). These studies confirmed the existence of preferred particle equilibrium positions in a simplified two-dimensional geometry and predicted the displacement of particles closer to the wall as the channel Reynolds number is increased, up to the transition to inertial turbulence (Schonberg & Hinch, 1989; Hogg, 1994; Asmolov, 1999). These predictions were later substantiated by experimental work (Matas *et al.*, 2004b).

The basic picture of the migration phenomenon in channel flows of Newtonian liquids at low particle Reynolds number $Re_p \ll 1$ is schematically illustrated in Figure 2.4.2. A non-zero drag force arising from the curvature of the velocity profile acts to slow down the particle relative to the local fluid velocity. This drag force is counterbalanced by a Stokes drag that prevents the particle from accelerating upstream. The velocity gradient also causes viscous stresses to exert a torque on the particle causing it to spin with a rate

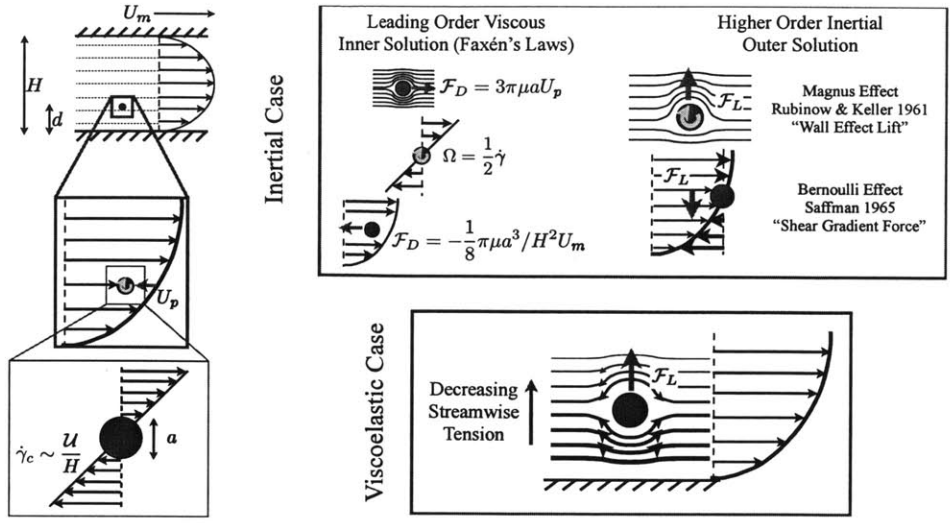

Figure 2.4.2: Schematic illustration of the drag and lift forces acting on a particle in the channel flow at low particle Reynolds number $Re_p \ll 1$ in the inertial case, and gradients in streamwise tension driving particles to regions of low shear rate in the viscoelastic case. Note that U_m is the maximum fluid velocity, whereas $\mathcal{U}$ is the mean fluid velocity.

proportional to the local shear rate. The spin of the particle can be thought to give rise to a Magnus force pushing the particle toward the centerline of the channel. Conversely, the curvature in the velocity profile causes the relative velocity of the fluid on the face of the particle closer to the wall to be larger than that on the other half facing the channel centerline. The larger relative velocity on the wall-side of the particle gives rise to a larger suction pressure due to the Bernoulli effect which thus counteracts the Magnus force and drives the particle toward the wall. The lateral forces therefore arise from non-linear effects associated with the inertia of the fluid. For the migration in complex fluids, however, the non-linearities such as streamwise tension arise from viscoelasticity and hence the equilibrium migration behavior can be different from that in Newtonian liquids.

In truth, the migration phenomenon is more complicated than the description offered here due to other non-linear effects such as the size of the wake behind the particle, especially as the particle Reynolds number becomes large. However the basic picture depicted here can be interpreted as a rudimentary guide to the mechanisms underlying the migration effect.

2.4.1 Particle Migration in Microchannels

Despite the progress made over the last fifty years in understanding and characterizing this inertially-driven particle migration, it was only very recently with the advent of microfluidics based on soft photolithography (McDonald & Whitesides, 2002) that promising applications of the migration phenomenon emerged (Di Carlo *et al.*, 2007). Microfluidic devices are well suited to handling the sample volumes typically encountered for biomedical applications and point of care diagnostics (Chin *et al.*, 2012). Furthermore, due to the fact that the characteristic dimensions of a microchannel are generally on the same order as the size of the particles or a typical blood cell ($6 \leq 2a \leq 10$ μm), particle migration in microfluidic devices occurs in the regime of moderate to large particle Reynolds numbers $Re_p \simeq \mathcal{O}(1)$, for which inertial lift forces are found to scale differently than in macroscale flow (Di Carlo *et al.*, 2009b) and particles are driven or *focused* to a few, very specific locations in the channel cross-section as seen experimentally (Choi *et al.*, 2011; Di Carlo *et al.*, 2009b), and numerically (Chun & Ladd, 2006; Di Carlo *et al.*, 2009b) as shown in Figure 2.4.3. It is widely believed that this robust localization of micron-sized particles in this regime, often called *inertial focusing* (Di Carlo, 2009a), can be exploited for biomedical and clinical applications such as high-speed flow cytometry (Hur *et al.*, 2010; Oakey *et al.*, 2010; Chung *et al.*, 2012) (flow rates $Q > 1$ mL.min^{-1}), particle enrichment (Hur *et al.*, 2011a; Bhagat *et al.*, 2011; Wu *et al.*, 2009; Mao & Alexeev, 2011) and the isolation of rare and diseased cells from the bloodstream.

Particle migration across streamlines on the microscale was observed experimentally (Di Carlo *et al.*, 2007; Choi *et al.*, 2011; Bhagat *et al.*, 2008) and numerically (Chun & Ladd, 2006) in straight square channels, in which randomly distributed particles focus to four positions centered along each face of the channel. As the aspect ratio of the channel increases (*i.e.* a very wide or very tall channel), particle focusing reduces to predominantly two equilibrium positions centered on the long face of the channel (Di Carlo *et al.*, 2009b; Kim & Yoo, 2008). Numerical modeling and direct experiments of varying size particles flowing through straight square channels have yielded scalings of the inertial lift force $\mathcal{F}_L$ (Di Carlo *et al.*, 2009b). The inertial lift force on a particle near

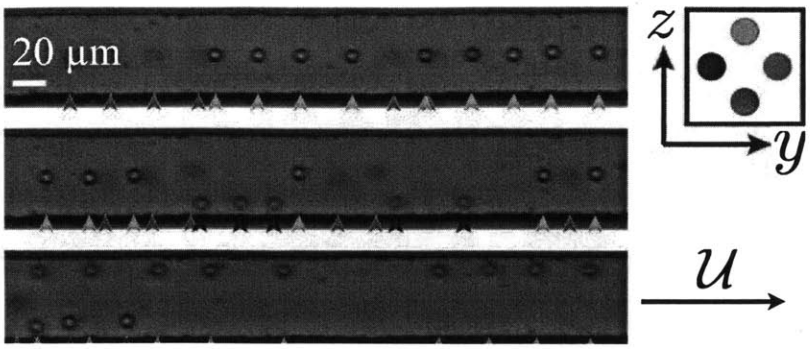

Figure 2.4.3: Three high-speed images (2 μs exposure) are shown, demonstrating ordered spatial distribution of particles at the four equilibrium positions. Particles are 10 μm in diameter and the flow is at $Re_c = 120$. Colored arrows below the images indicate particles at specific positions in the y-z plane that correspond to the legend. Figure and caption adapted from Di Carlo *et al.* (2007).

the channel centerline scales as $\mathcal{F}_L \sim \rho \mathcal{U}^2 a^3 / H$, while $\mathcal{F}_L \sim \rho \mathcal{U}^2 a^6 / H^4$ near the channel wall, where ρ is the fluid density, $\mathcal{U}$ is the mean flow velocity, a is the particle diameter, and H is the channel dimension. Various other microchannel geometries have been used to study the inertial focusing behavior of particles suspended in simple buffer solutions or in highly diluted blood, including spiral channels (Martel & Toner, 2012), channels with multiple turns (Gossett & Di Carlo, 2009; Oakey *et al.*, 2010), arrays of pillars and Weir-type geometries Gossett *et al.* (2010); Chung *et al.* (2012). The introduction of curvature to the flow gives rise to a Dean flow which can produce single stream focusing, but it ultimately destabilizes the particle focusing quality at flow rates that are generally much lower than can be achieved in a straight channel.

2.4.2 Particle Migration in Physiological Fluids

One aspect of inertial focusing that has not been thoroughly studied is how particles suspended in complex fluids such as whole or minimally diluted blood respond to inertial forces in microchannels. Particle focusing in whole or minimally diluted blood has not been studied or utilized due to performance limitations in the imaging techniques (*e.g.* high-speed brightfield imaging and long exposure fluorescence (streak) imaging) commonly used to observe particle migration. In high-speed bright-field imaging, res-

olution speeds exceeding 10^5 frames per second using shutter speeds down to $\mathcal{O}(1)$ μs have been used to measure size, rotation rate, and/or interparticle spacing of individual particles flowing through the channel (Hur *et al.*, 2011a; Di Carlo *et al.*, 2009b; Lee *et al.*, 2010). In long exposure fluorescence imaging, the signal intensity of fluorescently labeled particles accumulated over a time interval on the order of $\mathcal{O}(1)$ s has been used to measure mean equilibrium position, full width at half maximum, and/or separation efficiency of multiple particles flowing through the channel (Oakey *et al.*, 2010; Bhagat *et al.*, 2008; Gossett & Di Carlo, 2009). Both of these imaging techniques have been used to characterize particle focusing in samples consisting of physiological saline or highly diluted blood (Hur *et al.*, 2010, 2011a; Bhagat *et al.*, 2011). The utility of these imaging techniques becomes limited in samples consisting of whole or minimally diluted blood, however. In one milliliter of whole blood, there are approximately 5×10^9 red blood cells (RBCs), 5×10^6 white blood cells (WBCs), and 3×10^8 platelets suspended in plasma. High-speed bright-field imaging is limited by the overwhelming presence of RBCs obscuring vision of individual particles in the channel, while long-exposure fluorescence imaging is limited by attenuation of incident light by hemoglobin absorption and RBC light scattering in the visible region. For both imaging techniques, it is difficult to gather information along the y-axis (*i.e.* along the height dimension of the channel).

In vitro studies of blood flow through capillary tubes have shown that blood behaves as a Newtonian fluid for tube diameters larger than 500 μm, and as a non-Newtonian fluid for tube diameters smaller than 500 μm. This non-Newtonian behavior, known as the Fåhræus-Lindqvist effect, is marked by a decrease in apparent blood viscosity for smaller tube diameters (Fåhræus & Lindqvist, 1931). This is due to the formation of a cell-free layer near the tube wall that has a lower viscosity relative to the RBC-rich tube core (Cokelet & Goldsmith, 1991; Long *et al.*, 2004). Initial studies on the behavior of RBCs in shear flow were primarily limited to dilute blood suspensions due to the lack of imaging techniques capable of obtaining both direct and quantitative measurements of multiple RBC motions in concentrated blood suspensions. Visualization and detection of tracer RBCs at $HCT > 10\%$ was first achieved using ghost cells (*i.e.* ruptured RBCs that were resealed in the absence of hemoglobin) and a traveling microscope for channel

Reynolds numbers $Re_c = U_m d_h/\nu = 0.3$, where U_m is the maximum channel velocity, d_h is the hydraulic diameter, and ν is the kinematic viscosity (Goldsmith & Marlow, 1979). Ghost cells were used as models of RBCs due to attenuation of incident light by hemoglobin absorption and RBC light scattering when measuring high concentrations of normal RBCs.

The development of spinning disk (Nipkow) confocal microscopy combined with laser illumination made it possible to generate a sufficient signal-to-noise ratio for detecting RBC motion for $HCT > 10\%$ (Lima *et al.*, 2008). Recent work utilized fluorescent dye labeling, scanning confocal microscopy, and micro-particle image velocimetry (μ-PIV) to observe near-wall RBC motion at physiological values of hematocrit (*i.e.* $HCT = 48\%$) blood in a rectangular microchannel for $Re_c = 0.03$ (Patrick *et al.*, 2011). The intensity of Nd:YAG (or comparable) laser illumination is such that only brief pulses (10 ns) of light are needed to detect fluorescently labeled particles found in the optical path. Such an imaging technique could be used to identify various properties (*e.g.* three-dimensional position, particle diameter, rotation rate) of individual particles in whole blood flowing through the channel at high Re_p. In order to make quantitative measurements of particle focusing behavior in whole blood. Moreover, an experimental frame of reference can be provided for *in silico* studies of RBC (and other particle) motion in blood that account for both the deformability of an individual RBC and the cell-cell interactions from a large number of RBCs. In particular, it may be possible to provide a physical basis for particle focusing in blood using computational models that quantitatively predict the rheological properties and dynamics of blood flow (Owens, 2006; Fedosov *et al.*, 2011).

2.4.3 Particle Migration in Model non-Newtonian Fluids

At present, however, it has proven challenging to realize any practical implementation of this technology for whole blood or other clinically relevant biofluids, due to the need to pre-process and dilute the samples (Hur *et al.*, 2011a). This is partly because the undiluted fluids are complex, non-Newtonian suspensions displaying non-linear rheological properties whose role in particle focusing at high particle Reynolds numbers in microfluidic devices is currently poorly understood. On the other hand, low Reynolds

number flows of viscoelastic suspensions have elicited research interest in hematology (Fåhræus & Lindqvist, 1931; Goldsmith & Skalak, 1975), as well as for commercial fluids such as drilling fluids (Tehrani, 1996; Boek *et al.*, 1997) and paints (Patton, 1979). In flows of polymeric liquids, two competing effects are known to govern particle migration dynamics. At low Reynolds and low to moderate Weissenberg numbers, normal stress differences have been shown experimentally (Gauthier *et al.*, 1971; D'Avino *et al.*, 2012), and theoretically (Ho & Leal, 1976) to drive particles to regions of low shear rate. Conversely, shear-thinning has been seen to drive particles to regions of high shear rate (Gauthier *et al.*, 1971). The effect of channel aspect ratio, blockage ratio, shear-thinning and viscoelasticity in an inertialess flow have been studied numerically with the Phan-Thien Tanner and Giesekus models recently by Villone *et al.* (2011a,b, 2013). These studies found that viscoelasticity drives a secondary flow in the channel as shown in Figure 2.4.4 (a). The particles then tend to be driven either to the channel centerline or walls depending on their position at the inlet of the channel as shown by the trajectories for the case of cylindrical pipe flow in Figure 2.4.4 (b). The location of the separatrix, and therefore the fraction of the particles that move to the centerline or wall depends on the degree of shear-thinning in the fluid, with stronger shear-thinning driving particles more toward the wall.

Numerical simulations have also investigated the roles of inertia, viscoelasticity and blockage ratio on the equilibrium positions of single particles in Couette and Poiseuille flow (Huang *et al.*, 1997). However, there have been very few studies of particle migration in non-Newtonian fluids in microfluidic devices at concurrently large Reynolds and Weissenberg numbers. For approximately two-dimensional flows of dilute polymer solutions at low Re_c and moderate Wi_c in a microchannel, particles have been observed to migrate to the channel midplane (Leshansky *et al.*, 2007). It is only recently that the effects of inertia and elasticity on particle migration have been considered simultaneously for moderate to large elasticity numbers ($1 \leq El \leq 10$) (Yang *et al.*, 2011), but only at small Re_c and Wi_c. Yet, the high Re_c–Wi_c regime has not been thoroughly studied, likely because of a broadly held notion that high-speed flows of viscoelastic liquids in microfluidic devices are useful for enhancing mixing by generating elastic turbulence

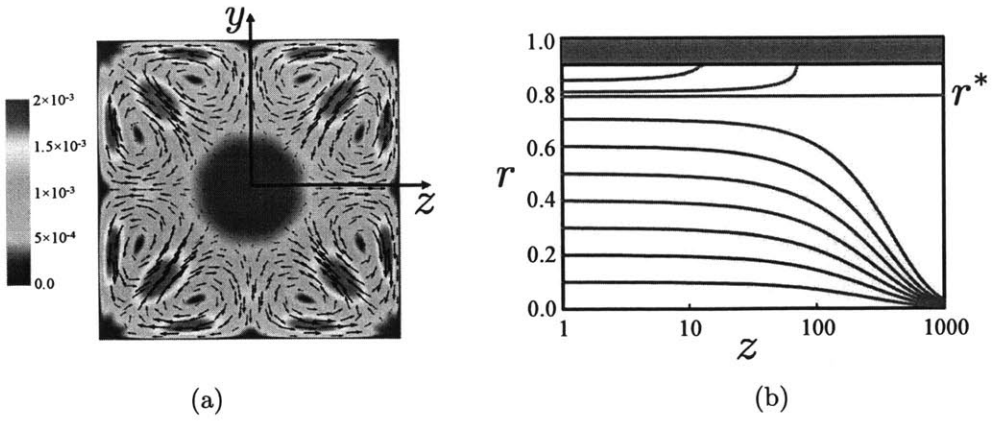

(a) (b)

Figure 2.4.4: (a) Secondary flow field for a Giesekus fluid flowing in a square microchannel in the inertialess limit. Figure and caption adapted from (Villone *et al.*, 2013). (b) Particle trajectories in the inertialess flow of a Giesekus fluid in cylindrical pipe of radius R, particle size is $a/R = 0.1$. The particle position r and its axial position z are made dimensionless with pipe radius R. The cyan line $r = r^*$ is the neutral cylindrical surface. The green area is the unaccessible channel region due to the finite particle size and the excluded volume effect. Figure and caption adapted from (D'Avino *et al.*, 2012).

(Groisman & Steinberg, 2001), precluding the possibility of a laminar flow conducive to high-throughput particle sorting technologies. A further challenge is the inability of conventional siloxane-based microchips to withstand the large pressures associated with high flow rates, requiring more exotic fabrication methods (Ciftlik *et al.*, 2013).

2.4.4 Present Study

In Chapter 7, the effect of RBCs on particle motion in inertia-dominated flow for $Re_p \lesssim \mathcal{O}(1)$ and $Re_c \lesssim \mathcal{O}(100)$ is characterized. Fluorescently labeled particles are suspended in physiological saline, diluted blood, or whole blood prior to being processed in a straight rectangular channel with a 2:1 aspect ratio. Images taken at multiple vertical positions in the channel are used to find optically in-focus particles and determine their particle diameter and two-dimensional spatial coordinates within the channel cross-section using particle tracking analysis (PTA). The inertial focusing behavior of polystyrene beads, WBCs, and PC-3 human prostate cancer cell lines is characterized as a function of flow rate Q and RBC volume fraction f_{RBC}. Rheometer measurements of blood viscosity and shear rate are used to provide insight into PTA measurements of

PC-3 cell focusing behavior in diluted and whole blood.

In Chapter 8, the study of particle migration is extended to channel Reynolds numbers $Re_c \gtrsim 2000$, enabling the experimental investigation of the breakdown in focusing behavior in water and the transition to inertial turbulence in a microchannel. Particle migration in dilute and semi-dilute polymer solutions is also studied at equally high channel Reynolds numbers and at channel Weissenberg numbers $Wi_c \lesssim \mathcal{O}(100)$. The introduction of viscoelasticity into the carrier fluid drives the particles toward the channel centerline even for small channel elasticity numbers $El_c = Wi_c/Re_c < \mathcal{O}(1)$. Furthermore, the centralized particle migration persists to flow rates that are larger than the critical flow rate at which transition to turbulence occurs in the corresponding experiments in a Newtonian carrier fluid. This finding could enable a breakthrough in development of microfludic separation technologies that can process at flow rates up to or above $Q \gtrsim 20$ mL.min^{-1}.

It is eminently clear that non-linear viscoelasticity plays a major role in the observed flow kinematics of a wide range of flows. From shear banding in flows of worm-like micellar fluids to extension-dominated flows in microfluidic devices, and to flow-induced particle migration in microchannels, the rheological behavior of non-Newtonain fluids at high deformation rates give rise to a broad range of exciting and interesting physical phenomena, which must be characterized to optimize a particular complex fluid for a given application.

Chapter 3

Rheological Characterization of the Worm-Like Micellar Solutions

3.1 Introduction

The bulk rheological behavior of a shear-banding solution of cetylpyridinium chloride (CPyCl) with sodium salicylate (NaSal) and a shear-thinning system of cetyltrimethylammonium bromide (CTAB) with NaSal or sodium nitrate ($NaNO_3$) is characterized using a range of standard rheometric flows. The linear rheology of these worm-like micellar (WLM) systems is characterized with small oscillatory measurements, and in steady shear and step strain stress relaxation tests. The results of these measurements indicate that the linear viscoelasticity of these fluids is well described by the Maxwell model with a single relaxation time λ.

The non-linear rheological behavior of these systems is characterized in steady shear and with stress relaxation tests. Non-linearities set in for shear rates $\dot{\gamma} \gtrsim \lambda^{-1}$ in steady shear and strain amplitudes $\gamma_0 \gtrsim 1$ for stress relaxation tests. Measurements of first N_1 and second N_2 normal stress differences are also reported. Highly spatially-resolved velocimetry measurements are then obtained using a Rheo–PIV system developed by Dimitriou *et al.* (2011) to study the shear-banding kinematics of the CPyCl:NaSal system in a cone-and-plate geometry. Some of the experimental issues encountered when carrying out velocimetric measurements on WLM systems are outlined, including a dis-

cussion of the effect of secondary flows on imaging, an experimental method used to delay the onset of wall slip, and the consequences of employing a rigid bounding surface at the edge of the cone-and-plate geometry to improve image quality.

3.2 Materials and Methods

3.2.1 Test Fluid Formulations

Three different worm-like surfactant formulations have been examined in the present experiments. The first solution consists of 100 mM cetylpyridinium chloride (CPyCl) (Alfa Aesar) and 60 mM sodium salicylate (NaSal) (Alfa Aesar) in de-ionized water. This system is studied in Chapters 3–5. A solution with this composition was also discussed at length by (Rehage & Hoffmann, 1991). The second solution consists of 30 mM cetyltrimethylammonium bromide (CTAB) (Sigma Aldrich) and 240 mM NaSal (Alfa Aesar) in de-ionized water. This system is studied in Chapters 3 and 4. Similar CTAB:NaSal solutions were studied by (Shikata *et al.*, 1994). Both of these solutions were also studied by Pathak & Hudson (2006). The third system is composed of 100 mM CTAB and 300 mM sodium nitrate ($NaNO_3$) (Sigma Aldrich) and has been studied by Cappelaere & Cressely (1997). This system is studied only in this Chapter for normal stress measurements. The surfactant and counter ion concentration ratios were selected because it is known that for these ratios the molecules form worm-like micelles (WLM).

The solutions were allowed to equilibrate at room temperature, in a dry and unlighted environment for more than one month from the time of their preparation before any experiments were conducted. All three solutions are strongly shear-thinning, but only the CPyCl:NaSal system exhibits a stress plateau across many decades of shear rates.

It is also well known that the rheological behavior of WLM solutions can be sensitive to the preparation protocol. Hence there can be variations in the quantitative values of the material functions between different batches of each fluid, even if the qualitative behavior between batches is similar. Therefore, in order to avoid apparent ambiguities in any tabulated values of the material functions, a batch number has been specified for each WLM fluid whenever quantitative results are presented.

3.2.2 Strain and Stress-Controlled Rheometry

A rotational, or torsional rheometer is a device that is designed to measure the shear rheology[1] of a material over a range of shear strains γ_0 or shear strain rates $\dot{\gamma}$. The archetypal rotational rheometer consists of a stationary plate and an axially symmetric fixture, illustrated in Figure 3.2.1, separated by some distance H, which can vary with radial position. The test sample is then positioned between the fixture and the plate, and the fixture is rotated at either some angular velocity Ω or with an imposed torque, such that the shear rate at any r and z is $\dot{\gamma}_{z\phi} \equiv \partial v_\phi / \partial z$, and the resultant torque or angular velocity, respectively, is measured, along with any axial loads exerted by the material on the fixture and plate. These measured quantities are then related to the material functions of the test sample through appropriate mathematical relations presented, for example, given by Bird *et al.* (1987) and Macosko (1994).

There are two basic control strategies for the design of a rotational rheometer. The first type is *torque* or *stress-controlled*, in which the torque imposed on the sample is the directly controlled parameter, although using feed-back control it is possible to use this type of rheometer to impose constant strain rates on a sample instead. The second type is *displacement* or *strain-controlled*, for which the imposed strain is the directly controlled parameter. The two main stress-controlled rheometers used in this thesis are the AR-G2 (TA Instruments) and the Discovery Hybrid Rheometer (DHR3, TA Instruments). The strain-controlled rheometer used in this thesis is the Advanced Rheometric Expansion System (ARES) LS-2 strain-controlled rheometer (TA Instruments). Both the DHR3 and ARES are equipped with a force rebalance transducer enabling measurement of axial loads in addition to torque. All rheometers are also equipped with temperature control instrumentation.

Two commonly used fixtures with a rotational rheometer are the cone-and-plate (CP) and the plate-plate (PP) geometries, portrayed in Figure 3.2.1. A CP geometry, depicted in Figure 3.2.1 (a), consists of a flat bottom plate and an upper cone, whose angle with respect to the flat bottom plate is θ. For small θ, the gap height may be

[1]Torsional rheometers can also be adapted for extensional rheometry measurements using an opposed jet device (Fuller *et al.*, 1987) or the Sentmanat extensional rheometer (Sentmanat, 2004).

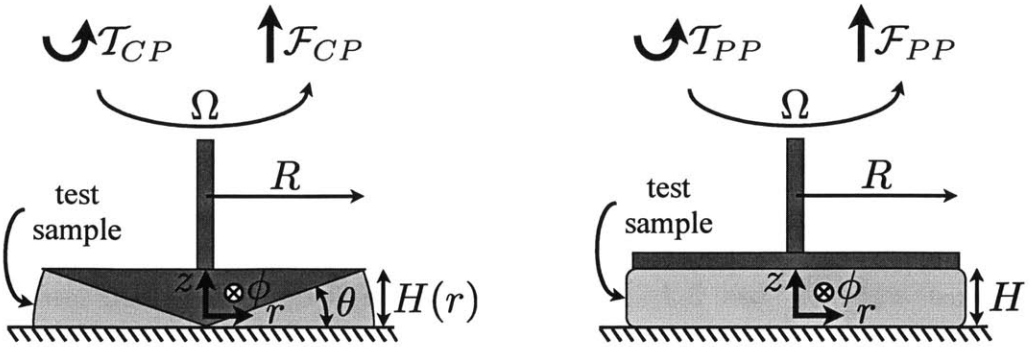

(a) Cone-and-Plate (b) Parallel Plate

Figure 3.2.1: Commonly used fixtures for use with rotational rheometers.

shown to increase linearly with radial position, such that $H(r) = r\tan\theta \approx r\theta$, where H is the gap height at some radial position r. The shear rate imposed by a CP is $\dot{\gamma}_{z\phi} = \Omega/\theta$ and it is therefore invariant to radial position. A PP fixture shown in Figure 3.2.1 (b) consists of two parallel plates separated by some user-selected gap height H, which is constant for all radial positions. The shear rate for a PP fixture is defined $\dot{\gamma}_{z\phi} = r\Omega/H$, and it varies linearly with radial position.

Both geometries rely on kinematically driven *Couette* flow for steady shear measurements. A linear velocity profile in the material is assumed based on the kinematics of the geometry, such that the velocity in the gap follows $v_\theta(r,z) = r\Omega z/H(r)$. In order to determine applied stress $\tau_{z\phi}$, it is necessary to relate the measured torque $\mathcal{T}$, applied on the sample by the rheometer to the applied shear stress $\tau_{z\phi} = \eta(\dot{\gamma}_{z\phi})\dot{\gamma}_{z\phi}$. The measured torque is the integral of the product of the applied force, $2\pi\eta(\dot{\gamma}_{z\phi})\dot{\gamma}_{z\phi}rdr$, and radial position r, from $r = 0$ to $r = R$, where R is the radius of the fixture.

$$\mathcal{T} = 2\pi\int_0^R \eta(\dot{\gamma}_{z\phi})\dot{\gamma}_{z\phi}r^2dr \tag{3.2.1}$$

Since the viscosity $\eta(\dot{\gamma}_{z\phi})$ of a sample is not known *a priori*, evaluation of the integral requires careful consideration. The principal advantage of the CP geometry is that it imposes a spatial homogeneous shear rate, and thus Eq. (3.2.1) can be directly integrated since the viscosity can be assumed constant. It can be shown (Bird *et al.*, 1987), that the torque $\mathcal{T}_{CP}$ acting on the CP geometry is

$$\frac{\mathcal{T}_{CP}}{2\pi R^3} = \frac{1}{3}\eta(\dot{\gamma}_R)\dot{\gamma}_R \tag{3.2.2}$$

where R is the radius of the geometry, η is the shear viscosity and $\dot{\gamma}_R$ is the shear rate at the rim. For the CP, the rim shear rate is $\dot{\gamma}_R = \dot{\gamma}_{z\phi} = \Omega/\theta$.

In certain cases, it is desirable to use the PP geometry, since its gap height is independent of radial position. The shear rate is not independent of position, however, so the relationship between torque $\mathcal{T}_{PP}$ and viscosity in the PP geometry must be derived using the Leibniz rule (Macosko, 1994) and it is

$$\frac{\mathcal{T}_{PP}}{2\pi R^3}\left[3 + \frac{d\ln(\mathcal{T}_{PP}/2\pi R^3)}{d\ln(\dot{\gamma}_R)}\right] = \eta(\dot{\gamma}_R)\dot{\gamma}_R \tag{3.2.3}$$

where the shear rate at the rim is $\dot{\gamma}_R = R\Omega/H$.

The first normal stress coefficient $\Psi_1(\dot{\gamma}_R)$ can also be measured for a CP if the rheometer is equipped with an axial force transducer. The axial force acting $\mathcal{F}_{CP}$ on the CP geometry is

$$\frac{\mathcal{F}_{CP}}{\pi R^2} = \frac{1}{2}\Psi_1(\dot{\gamma}_R)\dot{\gamma}_R^2 \tag{3.2.4}$$

where is the first normal stress coefficient of the test material. The axial force $\mathcal{F}_{PP}$ acting on the PP geometry is

$$\frac{\mathcal{F}_{PP}}{\pi R^2}\left[2 + \frac{d\ln(\mathcal{F}_{PP}/\pi R^2)}{d\ln(\dot{\gamma}_R)}\right] = \Psi_1(\dot{\gamma}_R)\dot{\gamma}_R^2 - \Psi_2(\dot{\gamma}_R)\dot{\gamma}_R^2 \tag{3.2.5}$$

where $\Psi_2(\dot{\gamma}_R)$ is the second normal stress coefficient of the test material.

In principle, the second normal stress coefficient can be measured by performing two steady shear tests with the same material in the CP and PP geometry. The value of $\Psi_1(\dot{\gamma})$ can then be determined over a range of shear rates using Eq. (3.2.4) and then substituting these values into Eq. (3.2.5) to determine $\Psi_2(\dot{\gamma})$. This method of measuring $\Psi_2(\dot{\gamma})$ can be challenging, however, since the need to use two separate material samples can be detrimental to measurement repeatibility.

A possible alternative method of measuring $\Psi_2(\dot{\gamma})$ is with the *offset cone-and-plate* (OCP) geometry of Jackson & Kaye (1966). The OCP geometry is shown schematically in Figure 3.2.2. This fixture uses a CP geometry that is offset by a gap height H that can be varied for a set of tests. This geometry is a hybrid between the CP and PP fixtures. The shear rate in the OCP is given by $\dot{\gamma}(r) = r\Omega/(H + r\theta)$ (Ohl & Gleissle,

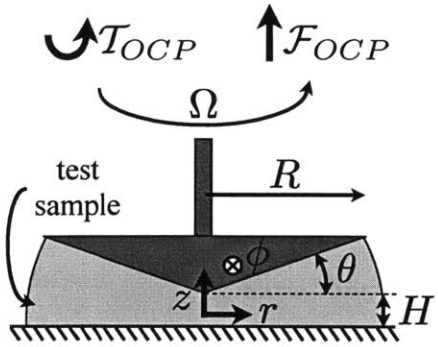

Figure 3.2.2: Offset cone-and-plate geometry.

1992). Therefore the shear rate at the rim is

$$\dot{\gamma}_R = \frac{\Omega}{\theta}\frac{\kappa}{1+\kappa} = \frac{R\Omega}{H}\frac{1}{1+\kappa} \tag{3.2.6}$$

This geometry is a compromise between the CP and PP fixtures based on the ratio $\kappa \equiv R\theta/H$, which is the ratio of the gap height at the rim for the CP geometry to the gap height between the apex of the cone and the lower plate. The equations relating torque $\mathcal{T}_{OCP}$ and axial force $\mathcal{F}_{OCP}$ measured using an OCP to the material functions are derived in Appendix B and they are

$$\frac{\mathcal{T}_{OCP}}{2\pi R^3}\left[3+\frac{1}{1+\kappa}\frac{d\ln\left(\mathcal{T}_{OCP}/2\pi R^3\right)}{d\ln\left(\dot{\gamma}_R\right)}\bigg|_{\frac{\Omega}{\theta}}\right] = \frac{\mathcal{T}_{OCP}}{2\pi R^3}\left[3+\frac{d\ln\left(\mathcal{T}_{OCP}/2\pi R^3\right)}{d\ln\left(\kappa\right)}\bigg|_{\frac{\Omega}{\theta}}\right] = \eta(\dot{\gamma}_R)\dot{\gamma}_R \tag{3.2.7}$$

and

$$\frac{\mathcal{F}_{OCP}}{\pi R^2}\left[2+\frac{1}{1+\kappa}\frac{d\ln\left(\mathcal{F}_{OCP}/\pi R^2\right)}{d\ln\left(\dot{\gamma}_R\right)}\bigg|_{\frac{\Omega}{\theta}}\right] = \frac{\mathcal{F}_{OCP}}{\pi R^2}\left[2+\frac{d\ln\left(\mathcal{F}_{OCP}/\pi R^2\right)}{d\ln\left(\kappa\right)}\bigg|_{\frac{\Omega}{\theta}}\right] = \Psi_1\dot{\gamma}_R^2 - \frac{1}{1+\kappa}\Psi_2\dot{\gamma}_R^2 \tag{3.2.8}$$

The limit $\kappa \to \infty$ corresponds to the CP geometry, whereas in the limit $\kappa \to 0$ the OCP resembles the PP geometry. In these respective limits the equations for torque and axial force given by Eqs. (3.2.2)–(3.2.5) are recovered. The OCP geometry can be used to make a sequence of measurements over a range of rotation rates and gap heights (*i.e.* multiple κ values) in order to evaluate the derivative terms in Eqs. (3.2.7) and (3.2.8) with more data than would otherwise be available from only the two tests that can be obtained with the CP and PP geometries. Furthermore, these measurements can be done with a single material sample, by performing the measurements over a sequence of

decreasing gap heights (*i.e.* increasing κ values).

3.2.3 Rheo–PIV Apparatus

In order to directly observe the local velocity field within the fluid under steady shear, an experimental Rheo–PIV apparatus (Dimitriou *et al.*, 2011) that mounts to the AR-G2 rheometer was designed and fabricated. The apparatus is similar to experimental designs used by other workers that implement particle tracking techniques to observe shear banding and wall slip in rheometers (Meeker *et al.*, 2004a; Tapadia *et al.*, 2006). Two schematic diagrams of the Rheo–PIV system are shown in Figure 3.2.3. This system consists of a laser light sheet which is directed downward into the sample. The sample is loaded into an inverted CP geometry, with the transparent quartz, upper plate ($R = 25$ mm), and a precision machined black anodized aluminum cone ($R = 25$ mm, $\theta = 4°$). A CCD camera (MatrixVision BlueFox) fitted with a macroscopic imaging zoom lens (Edmund Optics Techspec VZM 600i) is positioned such that the imaging plane coincides with the location of the laser light sheet. The light sheet is aligned tangentially to the direction of flow, and approximately 2 mm into the fluid from the edge of the geometry ($R_i = 23$ mm), illuminating seed particles at different positions along the vertical (shear) direction.

The velocity field within the fluid is determined using digital particle image velocimetry (PIV), whereby a cross correlation algorithm is applied to a pair of images separated by a time F^{-1}, (for this system the frame rate is $F = 60$ fps typically). Two consecutively captured images are divided into interrogation windows and the 2D cross correlation function between the two successive frames in each window is computed. The point at which the cross correlation function is a maximum corresponds to the average displacement of fluid elements within the window between the two exposures. The 2D velocity field is formed from the ensemble of these displacements obtained from each interrogation window. Because the lateral width of the laser light sheet ($\Delta x \sim 2$ mm) and its thickness (~ 0.25 mm) are both small compared to the value of R_i, the flow can be assumed to be translationally invariant along the x-direction. This approximation essentially takes a small enough arc segment on the surface of a sphere (and any move-

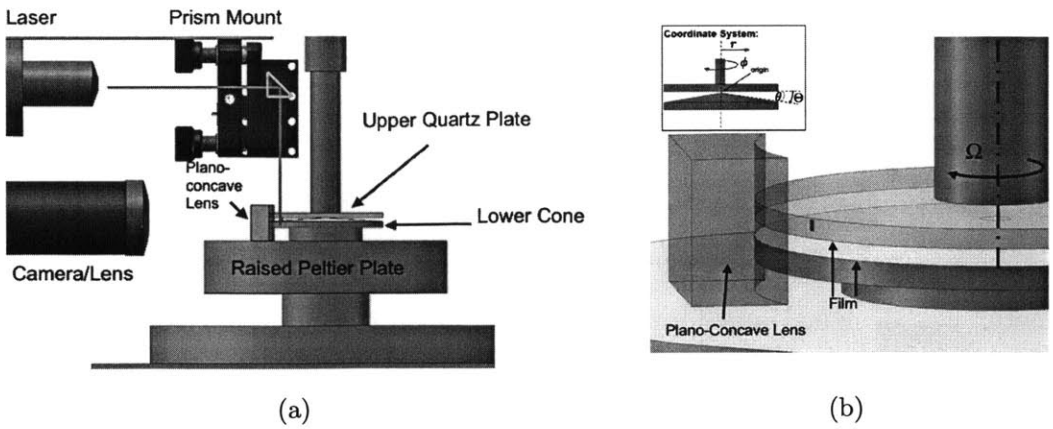

(a) (b)

Figure 3.2.3: Schematic diagram (a) of the Rheo–PIV system. 3D Model (b) showing how a plano concave lens can be placed up against the edge of the cone-and-plate geometry, in addition to how the transparent film is placed on the upper plate and lower cone. The coordinate system used in discussions is annotated in the box.

ment of particles on this surface) and describes it using a rectangular coordinate system (x, y) with $x \simeq R_i\phi$ and $y \simeq R_i\Theta$. The resulting time resolved velocity field is thus a full 2D vector field of the form $\vec{v} = [v_x(x, y), v_y(x, y)]$. Combined with the fact that there is, on average, no flow in the y-direction (discussed in detail in section 3.4.2), this allows for each 2D velocity field to be averaged along the direction of flow to produce a single velocity profile per image pair $v_x(y)$.

In this study, two optional features of the Rheo–PIV system that are used to facilitate the measurement of the local velocity field within the WLM system are considered. The first is a removable plano-concave lens with radius $R = 25$ mm which can be placed up against the edge of the CP geometry, as shown in Figure 3.2.3 (b). A flat front face prevents distortion of the image of the seed particles under flow, because rays reflected from the seed particles towards the CCD camera travel through the air-solid and solid-liquid interface at a direction normal to these interfaces. When the surface is not flat, refraction of the optical rays due to differences in the indices of refraction of the different media result in a distortion of the apparent location of the seed particles making it difficult to determine the true velocity profile. This lens serves to provide a planar outer-facing surface through which the camera can image the field of view containing the illuminated seed particles, and its role on imaging with the viscoelastic test fluid

Table 3.2.1: Comparison of surface roughness and equilibrium contact angle of CPyCl:NaSal test fluid for the aluminum cone and the quartz plate with, and without the transparent adhesive film. The roughness is measured using a Mitutoyo Surftest SJ-210 profilometer and the contact angle is measured with a Ramé Hart Model 590 contact angle goniometer. Surface roughness measures are R_a (arithmetic average of roughness values), R_q (root mean squared roughness) and R_z (maximum roughness).

Material	Aluminum Cone	Quartz Plate	Quartz + Film
Roughness			
R_a (μm)	0.28±0.04	0.014±0.001	0.045±0.007
R_q (μm)	0.35±0.06	0.018±0.001	0.067±0.01
R_z (μm)	1.8±0.5	0.115±0.006	0.5±0.09
Contact Angle	42±3°	27.3±1.4°	43±3°

will be discussed in Section 3.4.

The second feature is a transparent adhesive polymer film (SS-45 screen protector, Vivitar) which can be placed on either (or both) the upper or lower geometry, such that the fluid is in contact with this film instead of the polished quartz upper plate or the machined aluminum lower conical fixture. When affixed to the upper quartz geometry, the film has the effect of increasing the roughness of the upper surface, as well as making the surface slightly more hydrophobic. Table 3.2.1 compares the contact angle of a sessile drop of 100:60 mM CPyCl:NaSal system on the quartz surface with and without the adhesive plastic film, as well as the measured surface roughness. As shown in Section 3.4, a result of this modified surface is that slip effects which are often observed for CPyCl:NaSal solutions at high shear rates (such as those seen by Lettinga & Manneville (2009)) can be suppressed to a substantial degree. The effect of surface roughness and hydrophobicity on inhibition of slip is not surprising, and these effects have been documented in previous studies (Masselon *et al.*, 2010).

Data from calibration experiments are presented in Figure 3.2.4 (a). The velocity profiles obtained by the Rheo–PIV system are linear over a wide range of shear rates spanning those used in this work, for a Newtonian fluid (seeded heavy mineral oil with a viscosity of $\mu = 0.1$ Pa.s and a density of $\rho = 880$ kg/m^3). The velocity profiles $v_x/\mathcal{U}$ are averaged over approximately 450 frames of video (*i.e.* 7.5 seconds of flow) and plotted

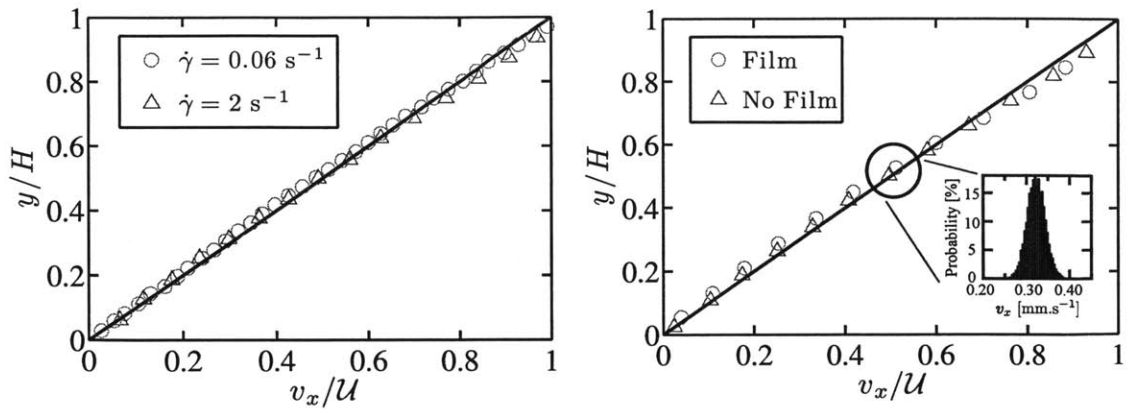

Figure 3.2.4: Scaled velocity profile of a viscous Newtonian fluid undergoing steady shear at two different shear rates in (a), indicating linearity of the profiles. In (b), the velocity profile within the same Newtonian fluid at a fixed shear rate ($\dot{\gamma} = 0.5$ s^{-1}) is compared for when the upper and lower plates are covered with the transparent adhesive film. The inset in (b) shows the probability distribution of the measured velocity values at a height of $y = 0.75$ mm from the lower cone. In each plot, the black line indicates the anticipated homogenous velocity profile.

against y/H, where y is the position across the gap ($y \simeq R_i\Theta$), $H \simeq R_i\Theta$ is the gap height at the position $r = R_i$ ($H = 1.6$ mm) and $\mathcal{U}$ is the velocity of the top surface given by $\mathcal{U} = R_i\Omega = \dot{\gamma}H$. Additionally, a comparison of the velocity profile measured for a Newtonian fluid undergoing a shear rate of $\dot{\gamma} = \Omega/\theta = 0.5$ s^{-1} when the upper and lower geometries are covered with the adhesive film and left uncovered is shown in Figure 3.2.4 (b). As expected, the presence of the film does not alter the velocity profile.

The inset in Figure 3.2.4 (b) gives a Gaussian probability distribution of the measured velocity values at a height of $y = 0.75$ mm from the lower cone. The standard deviation of the velocity measured at that location is 0.02 mm.s^{-1}, which is approximately 5% of the measured velocity (determined from $\sim$ 14000 PIV correlation measurements). The variation arises primarily from small mechanical vibrations in the frame which holds the camera/lens assembly. This results in small random and uncorrelated relative displacements of the camera and rheometer, which are interpreted as small nonzero velocities in the flow by the PIV analysis on the order of the standard deviation. While these vibrations do not have an effect on the time averaged velocity profiles, there is still some small systematic deviations of the time averaged velocity profile from the predicted

linear velocity profile in Figure 3.2.4. These deviations are chiefly a result of the air-fluid interface at the outer sample edge which is not perfectly flat. Despite the fact that the interface is pinned at the upper and lower plates, small variations in sample volume always result in a slightly curved air-fluid interface. While these slight variations in sample volume are impossible to eliminate entirely, inspecting the shape of the interface by eye is typically sufficient to ensure that reliable velocity profiles are obtained by the Rheo–PIV apparatus.

3.3 Bulk Rheology Characterization

3.3.1 Linear Viscoelasticity

The storage and loss moduli $G'(\omega)$ and $G''(\omega)$ of the CPyCl:NaSal and CTAB:NaSal micellar solutions were measured over a range of temperatures with the ARES strain-controlled rheometer using a CP geometry ($R = 25$ mm, $\theta = 2.3°$) and are shown in Figure 3.3.1. The resulting data from the small amplitude oscillatory shear tests have been fitted with the single mode Maxwell model given in Eq. (2.1.1), following the method of Turner & Cates (1991), by which a least squares regression of a single mode Maxwell model was fitted only to the moduli at frequencies equal to or less than the frequency at which G'' reaches its maximum.

$$G'(\omega) = G_0\left(\frac{(\lambda\omega)^2}{1+(\lambda\omega)^2}\right) \quad \& \quad G''(\omega) = G_0\left(\frac{\lambda\omega}{1+(\lambda\omega)^2}\right) \tag{2.1.1}$$

From this fit, values of Maxwellian stress relaxation time λ, zero-shear rate viscosity η_0, and elastic modulus $G_0 \equiv \eta_0/\lambda$, in Table 3.3.1 were determined. Both fluids have Maxwell relaxation times on the order of one second.

In addition to this, the steady shear viscosity exhibits a strong shear-thinning behavior and a clear stress plateau for rates larger than $\dot{\gamma} \simeq 0.3$ s^{-1}. In Figure 3.3.1, the predicted shear stress obtained by using the Cox-Merz rule is also plotted. The Cox-Merz rule is an empirical relation that predicts that the magnitude of the complex viscosity is equal to the shear viscosity at corresponding values of frequency and shear rate (Bird *et al.*, 1987):

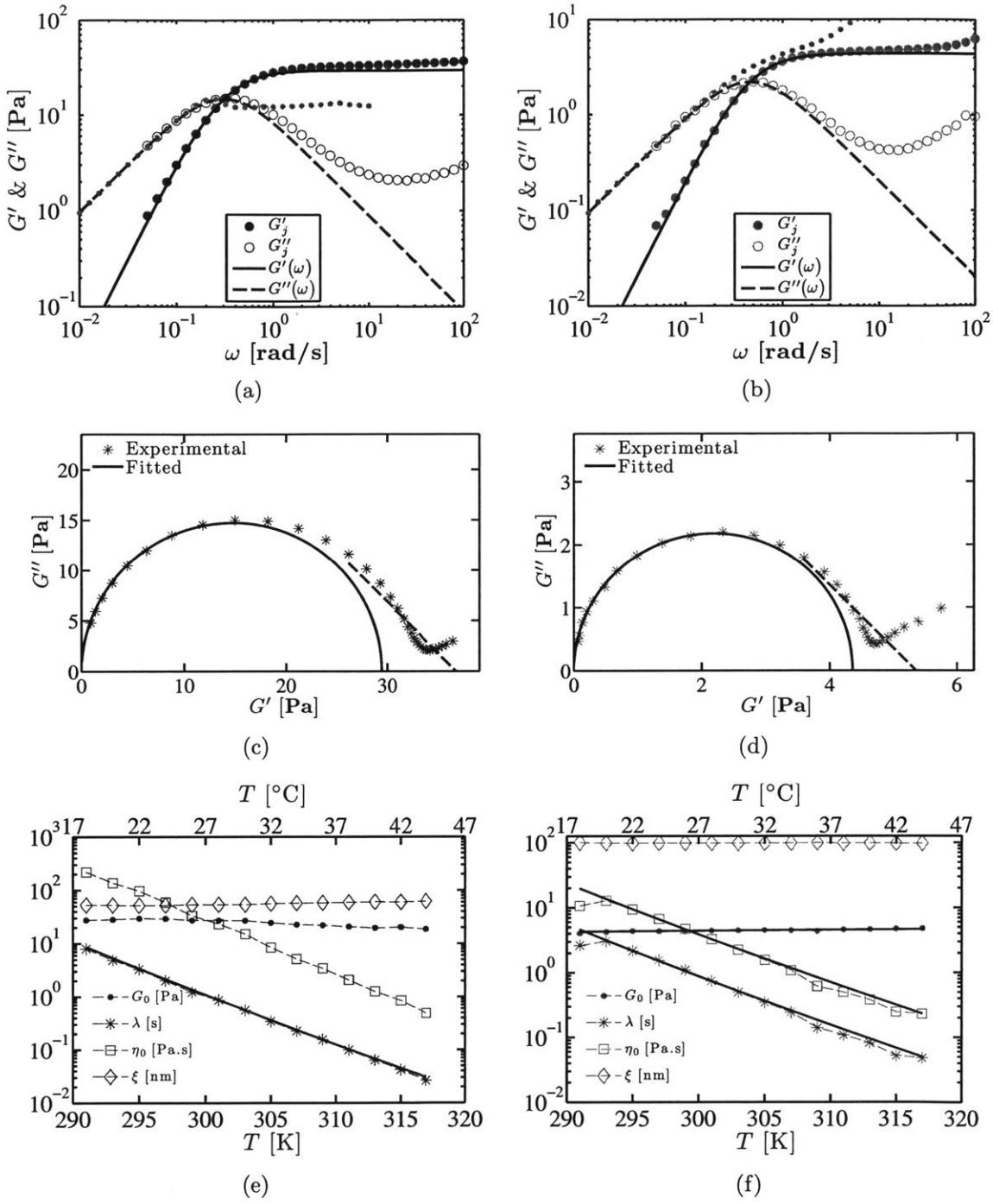

Figure 3.3.1: Storage and loss moduli of (a) 100:60 mM CPyCl:NaSal (Batch 1) and (b) 30:240 mM CTAB:NaSal (Batch 1) solutions in SAOS at 22 °C. The solid and dashed lines are the resultant fit of the low frequency data ($\omega \leq \lambda^{-1}$) of a single mode Maxwell model with relaxation time λ, and modulus G_0 given in Table 3.3.1. The small gray symbols correspond to the shear stress predicted from the dynamic data using the Cox-Merz rule (Bird *et al.*, 1987). Cole-Cole plots of (c) CPyCl:NaSal and (d) CTAB:NaSal. The black semicircle corresponds to ideal Maxwellian behavior and the dashed black line has slope -1 for extracting the value of G_p using the method of Turner & Cates (1991). Temperature dependence of linear viscoelastic material functions for (e) CPyCl:NaSal and (f) CTAB:NaSal.

Table 3.3.1: Rheological and rheo-optical properties of the test solutions at 22 °C. °Persistence length for CPyCl:NaSal has been assumed. *Persistence length for CTAB solution given in Shikata *et al.* (1994) has been assumed. †The stress-optical coefficient was measured at 23±1 °C, but previous studies (Humbert & Decruppe, 1998), indicate a weak temperature dependence of C over a temperature range of ±1 °C.

		100:60 mM CPyCl:NaSal	30:240 mM CTAB:NaSal	Batch
Maxwell Model	λ [s]	3.3	2.1	1
	η_0 [Pa.s]	96.6	9.4	1
	G_0 [Pa]	29.4	4.4	1
	$\Psi_{1,0}$ [Pa.s^2]	637	39.5	1
Ellis Model	η_0 [Pa.s]	83	8.3	2
	α	25	2.8	2
	$\tau_{1/2}$ [Pa]	15	4.1	2
Step Strain ($\gamma_0 \ll 1$)	G^0_∞ [Pa]	30	4.5	3
	λ [s]	3.0	1.3	3
	ξ'	0.71	0.18	3
Additional Parameters	Ψ_1 [Pa.s^2]	3	3	1
	λ_{break} [s]	0.6	1.2	2
	λ_{rep} [s]	2.0	4.1	2
	G_p [Pa]	36.9	5.4	2
	G''_{min} [Pa]	2.01	0.42	2
	ξ [nm]	51.7	97.8	2
	$l_{persist}$ [nm]	20°	26*	
	l_e [nm]	97.4	236	2
	$\langle l \rangle$ [μm]	1.42	2.47	2
	†$C \times 10^7$ [Pa^{-1}]	−1.1	−3.8	1

$$\eta(\dot{\gamma}) = \left|\eta^*(\omega)\right|_{\omega=\dot{\gamma}} \tag{3.3.1}$$

From the Cox-Merz rule and the relationship between complex modulus and complex viscosity ($\eta^* = G^*/i\omega$) a prediction of the shear stress under steady shear can be obtained from oscillatory data. As can be seen in Figure 3.3.1, there is a progressive deviation of this predicted shear stress from the measured value for shear rates larger than $\dot{\gamma} \sim 0.3\,\mathrm{s}^{-1}$ – this is in agreement with the observations made in previous studies (Pipe *et al.*, 2010).

It is also possible to estimate the breaking time λ_{break} for each system, based on the work of Turner & Cates (1991). On the Cole-Cole plots in Figure 3.3.1 (c) and (d), a line of slope −1 was fitted to the storage and loss moduli for which the slope

between adjacent points was -1 ± 0.5. The intersection of this line with the abscissa corresponds to an asymptotic plateau modulus G_p. The storage and loss moduli can be non-dimensionalized by G_p in order to calculate the diameter of the fitted semicircle $DFS \approx G''(\omega = \lambda^{-1})/G_p$, which is then related to the breaking time λ_{break} according to the theory of Turner & Cates (1991). The reptation time λ_{rep} is then obtained from the relation $\lambda_{rep} = \lambda^2 \lambda_{break}^{-1}$. These timescales are listed in Table 3.3.1. At high frequencies $\omega \gg \lambda^{-1}$, both fluids exhibit a minimum in G'', indicating the importance of the breathing and Rouse relaxation modes discussed in Section 2.2.1.

The temperature dependence of the linear viscoelastic material functions of the two WLM solutions are plotted in Figure 3.3.1 (e) and (f). For many entangled polymer solutions, the variation of these quantities with temperature can be captured nicely with a parameter called the *shift factor* (Bird *et al.*, 1987; Larson, 1998) given by

$$a_T = \frac{\eta_0(T) T_0 \rho_0}{\eta_0(T_0) T \rho} \tag{3.3.2}$$

where $\eta_0(T)$ is the zero-shear-rate viscosity at an absolute temperature T, ρ_0 is a reference density at an arbitrary reference absolute temperature T_0 and ρ is the density at T. The shift factor is described by an Arrhenius relation

$$a_T = \exp\left[\frac{\Delta\tilde{H}}{k_B}\left(\frac{1}{T} - \frac{1}{T_0}\right)\right] \tag{3.3.3}$$

where $\Delta\tilde{H}$ is called the activation energy for flow and k_B is the Boltzmann constant[2].

For fluids whose density is relatively constant with temperature, the temperature-dependence of the viscosity can be simplified to $\eta(T) = G_0(T)\lambda(T)$, where $\lambda(t) = \lambda_0 a_T$ with λ_0 being the relaxation time at T_0 and a_T is given by Eq. 3.3.3, and $G_0(T)$ is given by

$$G_0(T) \simeq \frac{k_B T}{\xi^3} \tag{3.3.4}$$

The parameter ξ is the correlation distance, which is the absolute distance between entanglement points in the microstructure of the liquid (Doi & Edwards, 1986), shown schematically in Figure 3.3.2 along with other microstructural length scales described

[2] $k_B = 1.3806503 \times 10^{-23}$ J/K

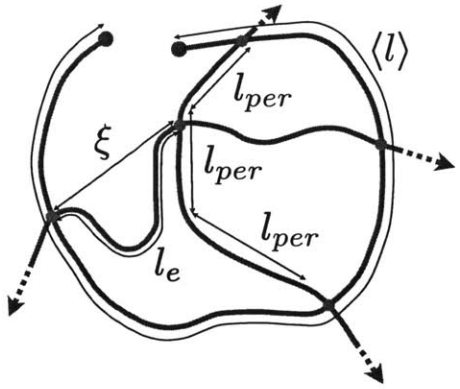

Figure 3.3.2: Schematic depiction of an entangled polymer network.

below. Hence the relaxation time scales exponentially with the inverse of absolute temperature and the plateau modulus scales linearly with temperature provided the quantity ξ is constant.

Fits of the shift factor are shown in Figure 3.3.1 (e) and (f) with $T_0 = 295$ K (22 °C). The value of the activation energy for CPyCl:NaSal is $\Delta\tilde{H} = 2.77 \times 10^{-19}$ J and for CTAB:NaSal is $\Delta\tilde{H} = 2.22 \times 10^{-19}$ J. The plateau modulus of the CTAB:NaSal system in (f) increases approximately linearly with temperature, but in the CPyCl:NaSal system the modulus actually decreases slightly with temperature and hence a fit of the shift factor has only only been plotted for the relaxation time in (e). Values of ξ for the CPyCl:NaSal and CTAB:NaSal micellar systems in this study are listed in Table 3.3.1.

Another microstructural quantity is the entanglement strand length l_e, which is the arc length along the micelle between two adjacent entanglement points may be estimated as

$$l_e \simeq \frac{\xi^{5/3}}{l_{per}^{2/3}} \tag{3.3.5}$$

where l_{per} is the persistence length, which can be interpreted as the length scale on which the micelle acts as a rigid rod. This quantity can be determined from measurements of optical anisotropy in a material as outlined by Shikata *et al.* (1994).

An estimate of the average contour length $\langle l \rangle$, which is the arc length of a fully extended micelle, can be determined according to the work of Granek & Cates (1992). In the case of $\lambda_{break} \gg \lambda_{Rouse}$, where λ_{Rouse} is the Rouse relaxation time of the micelle,

a lower bound for the ratio of length is

$$\frac{l_e}{\langle l \rangle} \simeq \frac{G''_{min}}{G_0} \tag{3.3.6}$$

where G''_{min} is the value of the loss modulus at the local minimum in the Cole-Cole plots at high frequencies ($\omega \gg \lambda^{-1}$). Here, l_e and $\langle l \rangle$ have been determined based on reasonable assumptions for l_{per}, all of which are presented in Table 3.3.1.

3.3.2 Steady Shear Rheology

The steady shear rheology of these systems at 22 °C and at moderate shear rates ($\dot{\gamma} \lesssim 10\lambda^{-1}$) was measured using a 50 mm diameter, 2.3° cone-and-plate geometry on an ARES LS-2 strain-controlled rheometer (TA Instruments). The steady shear data is presented in Figure 3.3.3, and summarized in Table 3.3.1. In the limit of low shear rates ($\dot{\gamma} \ll \lambda^{-1}$), both fluids exhibit Newtonian behavior. For shear rates of the order $\dot{\gamma} \simeq \lambda^{-1}$ or greater, both fluids exhibit shear-thinning, which may be fit empirically with the Ellis model in the form (Bird *et al.*, 1987):

$$\eta = \frac{\eta_0}{1 + \left(\frac{\tau_{xy}}{\tau_{1/2}}\right)^{\alpha-1}} \tag{3.3.7}$$

where η_0 is the zero-shear-rate viscosity, $\tau_{1/2}$ is the value of the shear stress at which the viscosity is equal to half its zero-shear rate value, and α is a fitting coefficient as listed for both fluids in Table 3.3.1. The Ellis model reduces to the simpler Ostwald Power Law model, $\eta = m\dot{\gamma}^{n-1}$ (Bird *et al.*, 1987), in the limit of $\tau_{xy} \gg \tau_{1/2}$, with $\alpha = n^{-1}$. Fits of this model to the flow curve of each fluid are shown in Figure 3.3.3 (b). It is apparent from Figure 3.3.3, that for shear rates $\dot{\gamma} \geq \lambda^{-1} \approx 0.25$ s^{-1}, the CPyCl:NaSal exhibits a pronounced stress plateau $\tau_p \approx 15$ Pa, suggesting a possible shear-banding behavior (Cates & Fielding, 2006; Rothstein, 2008). In this regime, the large value of α indicates that the viscosity of the CPyCl:NaSal system is essentially inversely proportional to shear rate. These results for the CPyCl:NaSal system are very similar to those reported by (Lee *et al.*, 2005). For the shear rates measured with the ARES, the CTAB:NaSal system may be seen to exhibit clear shear-thinning, with $\eta \sim \dot{\gamma}^{-0.6}$, for measured shear

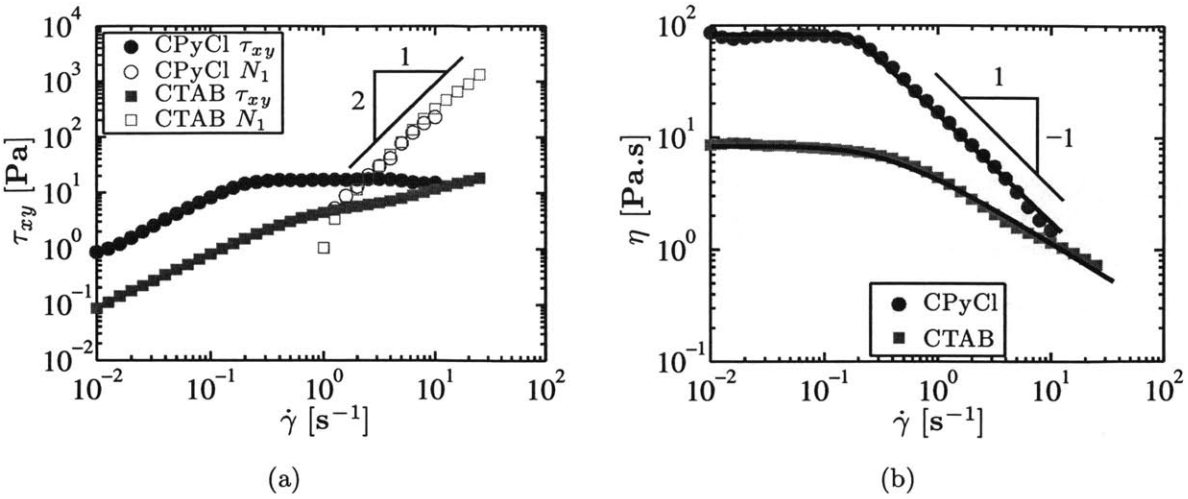

Figure 3.3.3: Steady shear rheology of 100:60 mM CPyCl:NaSal (Batch 2) and 30:240 mM CTAB:NaSal (Batch 2) solutions at 22 °C. (a) Steady shear stress and first normal stress difference. (b) Steady shear viscosity. The fitted curves are those of the Ellis model with parameters from Table 3.3.1. The solid black line of slope −1 indicates an inverse proportionality in viscosity with shear rate.

rates $\dot{\gamma} \geq 0.5$ s^{-1}, but it does not show a constant stress plateau at any point.

For the CPyCl:NaSal system, at $\dot{\gamma} \gtrsim 10$ s^{-1}, and for the CTAB:NaSal system at $\dot{\gamma} \gtrsim 30$ s^{-1}, the meniscus of the test fluid becomes unstable and a large fraction of the sample is ejected from the gap. This instability is not a result of the large centripetal acceleration associated with the rotational motion of the fluid, but rather the large normal stress difference associated with the high deformation rate which overcomes the resisting Laplace pressure of the meniscus (Tanner & Keentok, 1983). This instability renders high shear rate rheometry of these fluids with a rotational rheometer impossible, and provides further motivation for pursuing microfluidic rheometry as discussed in Chapter 5.

Normal Stress Measurements

The first normal stress differences of the CPyCl:NaSal and CTAB:NaSal are measurable at shear rates greater than $\dot{\gamma} \gtrsim \lambda^{-1} \approx 1$ s^{-1}. Both fluids exhibit similar dependence of first normal stress differences N_1 on shear rate in Figure 3.3.3 (a). The first normal stress difference for both fluids increases initially quadratically with shear rate, $N_1 \sim \dot{\gamma}^2$, which

is depicted by the black line in Figure 3.3.3 (a). The quadratic scaling is in agreement with the predictions of the upper convected Maxwell model, see (Bird *et al.*, 1987), for which the first normal stress coefficient is predicted to be $N_1/\dot{\gamma}^2 = \Psi_{1,0} = 2\eta_0\lambda$. This value is, however, a substantial over-estimate of the actual measured first normal stress coefficient, since, for the shear rates at which N_1 was measured, the viscosity of neither fluid is close to the respective zero-shear rate value. In reality, for both systems in the plateau regime, $\Psi_1 \approx 3$ Pa.s^2. The quadratic scaling of N_1 for this shear-banding CPyCl:NaSal fluid in the shear-banding regime differs from the subquadratic or linear scaling with shear rate observed for other shear-banding micellar fluids in the plateau regime, (Helgeson *et al.*, 2009b; Pipe *et al.*, 2010). There is also some variation in the values of N_1 between different batches of the same CPyCl:NaSal WLM system used in this thesis, suggesting that the macroscopically measured values of N_1 in this 100:60 mM CPyCl:NaSal system may be interrelated to the shear-banding dynamics of the particular fluid sample as described further for step strain experiments in Section 3.3.3. As discussed above, at shear rates above $\dot{\gamma} > 10$ s^{-1} for the CPyCl:NaSal system and $\dot{\gamma} > 30$ s^{-1} for the CTAB system, the sample is ejected from the gap, preventing measurements of N_1 at higher shear rates.

Measurements of second normal stress difference N_2 pose the added challenge that multiple tests must be completed as discussed in Section 3.2.2. The magnitudes of N_2 are also typically smaller than those of N_1, making it more difficult to reliably extract N_2 values at the lower end of the dynamic range of the axial force transducer where most of the measurements with the WLM solutions used in this study occur. Furthermore, the limited upper range of accessible shear rates for the CPyCl:NaSal and CTAB:NaSal fluids considered so far is too restrictive to justify using these systems to measure N_2. Therefore, a system of 100 mM CTAB (Sigma Aldrich) and 300 mM $NaNO_3$ (Sigma Aldrich) has been used for these viscometric measurements. This system has been studied previously by Cappelaere & Cressely (1997) and it has been selected to be studied here because it can be tested in a CP geometry at shear rates up to $\dot{\gamma} \lesssim \mathcal{O}(10^3)$ s^{-1} without showing edge instabilities or being ejected from the gap.

Torque and axial force measurements with this WLM system were completed on the

DHR3 with an acrylic PP ($R = 30$ mm) and CP ($R = 30$ mm, $\theta = 1.01°$) geometry in the OCP configuration described in Figure 3.2.2. A range of logarithmically equally-spaced angular velocities were selected ($0.01 \leq \Omega \leq 10$ rad.s^{-1}) and kept constant for all tests with the PP and OCP configurations. It is known that at high enough shear rates, normal stress differences in shear banding liquids can cause edge instabilities in the meniscus of the sample that invalidate the accuracy of the measurements (Skorski & Olmsted, 2011). For this reason, the maximum angular velocity was chosen so that for all gap heights, the shear rates were low enough that no edge fracture occurred in the experiments. Measurements were completed over a sequence of decreasing gap heights starting at $H = \frac{5}{4}R\theta = 0.48$ mm ($\kappa \equiv R\theta/H = 0.8$) and ending at $H = 0$ ($\kappa = \infty$). Each test was performed using a decreasing sweep of shear rates since this order was found to provide the most reliable and repeatable measurements. In order to account for the transient evolution of N_1 and N_2 at each rotation rate, the data were recorded using time-resolved measurements to ensure that each point had attained steady state. After each test, the fixture was lowered to the next gap height and any excess liquid was removed from the edge of the geometry using a razor blade. A solvent trap was used to minimize evaporation of the sample over the duration of the tests.

The measured torque $\mathcal{T}_{OCP}$ and axial force $\mathcal{F}_{OCP}$ values are plotted in Figure 3.3.4 (a) and (b). Measurements completed with a PP geometry ($\kappa = 0$) at two different gap heights $H = R\theta = 532$ μm and $2R\theta = 1064$ μm have also been included. In general, the corresponding values of torque and axial force at a given angular velocity Ω decrease with larger gap heights (*i.e.* smaller κ). This trend is clearly seen in the isocontours of Ω/θ for the torque and axial force measurements plotted in Figure 3.3.4 (c) and (d). Each isocontour was determined from a third order polynomial fit, whose slope is used to evaluate the derivative terms in Eqs. 3.2.7 and 3.2.8, which are repeated here for convenience.

$$\eta(\dot{\gamma}_R)\dot{\gamma}_R = \frac{\mathcal{T}_{OCP}}{2\pi R^3}\left[3 + \frac{1}{1+\kappa}\frac{d\ln\left(\mathcal{T}_{OCP}/2\pi R^3\right)}{d\ln\left(\dot{\gamma}_R\right)}\bigg|_{\frac{\Omega}{\theta}}\right] = \frac{\mathcal{T}_{OCP}}{2\pi R^3}\left[3 + \frac{d\ln\left(\mathcal{T}_{OCP}/2\pi R^3\right)}{d\ln\left(\kappa\right)}\bigg|_{\frac{\Omega}{\theta}}\right] \tag{3.2.7}$$

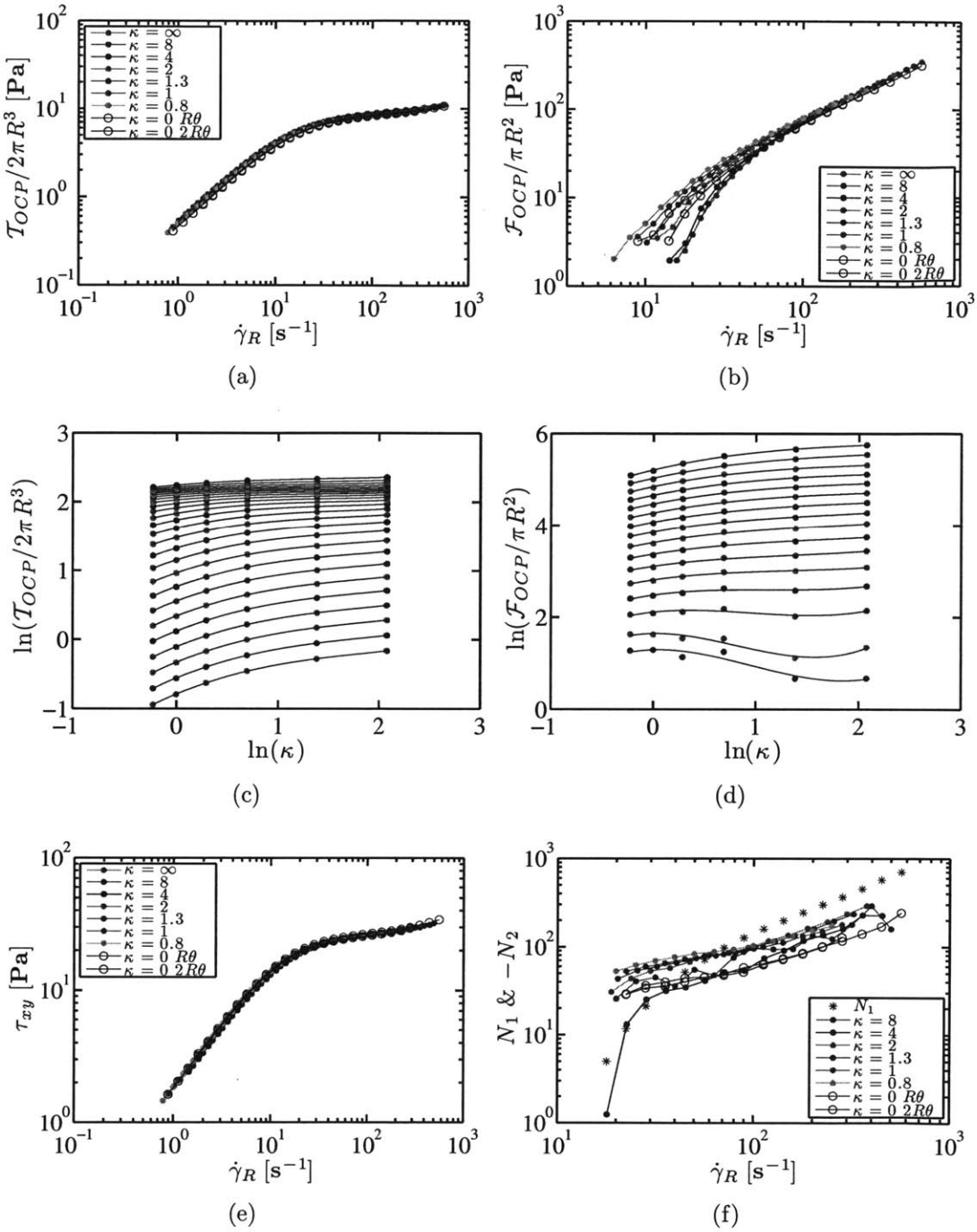

Figure 3.3.4: Measurements of (a) torque $\mathcal{T}_{OCP}$ and (b) axial force $\mathcal{F}_{OCP}$ for the 100:300 mM CTAB:$NaNO_3$ solution ($\lambda = 0.084$ s) at 30 °C using the offset cone-and-plate (OCP). Hollow symbols correspond to data measured using the PP at gap heights $H = R\theta = 532$ μm and $2R\theta = 1064$ μm. Third order polynomial fits of isocontours of Ω/θ to (c) torque and (d) axial force measured over the range of κ values (gap heights). Calculated (e) shear stress using Eq. 3.2.7 and (f) first and second normal stress differences using Eq. 3.2.8.

$$\Psi_2\dot{\gamma}_R^2 = (1+\kappa)\left\{\Psi_1\dot{\gamma}_R^2 - \frac{2\mathcal{F}_{OCP}}{\pi R^2}\right\} + \left.\frac{d\ln\left(\frac{\mathcal{F}_{OCP}}{\pi R^2}\right)}{d\ln\left(\dot{\gamma}_R\right)}\right|_{\frac{\Omega}{\theta}} = (1+\kappa)\left\{\Psi_1\dot{\gamma}_R^2 - \frac{\mathcal{F}_{OCP}}{\pi R^2}\left[2 + \left.\frac{d\ln\left(\frac{\mathcal{F}_{OCP}}{\pi R^2}\right)}{d\ln\left(\kappa\right)}\right|_{\frac{\Omega}{\theta}}\right]\right\} \tag{3.2.8}$$

On the other hand, at a given rim shear rate $\dot{\gamma}_R$, the axial force actually increases with increasing gap heights (*i.e.* smaller κ) as shown in Figure 3.3.4 (b). At first glance, this trend is surprising because it can be shown that for both the upper convected Maxwell (UCM) model (Bird *et al.*, 1987) and a simple viscoelastic liquid with constant normal stress coefficients, provided $|\Psi_2/\Psi_1| < 1$, at constant rim shear rate the axial force measured in the OCP must decrease as the gap height is increased (*i.e.* smaller κ), (see Section B.4.2 in Appendix B). This behavior for a simple viscoelastic liquid can be rationalized by the fact that at larger gap heights in the OCP geometry, for a given rim shear rate $\dot{\gamma}_R$, the shear rate at all $r < R$ is equal to or smaller than that in the CP and so the measured torque and axial force are likewise lower in the OCP than in the CP geometry. However, for a more general viscoelastic liquid with shear-rate-dependent normal stress coefficients, analysis will show that it is possible for the trends in $\mathcal{F}_{OCP}$ with κ at constant $\dot{\gamma}_R$ seen in these OCP measurements to occur (see Section B.4.3 in Appendix B).

It is also straightforward to rule out the relevance of inertial effects on the axial force measurements. At high angular rotation rates, the curvature of the streamlines in the OCP geometry can give rise to strong enough centrifugal acceleration so as to create a measurable suction force on the upper fixture (Macosko, 1994). For a Newtonian fluid, this suction pressure due to inertial acceleration is given by

$$\frac{\mathcal{F}_{in}}{\pi R^2} = -\frac{3}{40}\rho(R\Omega)^2 \tag{3.3.8}$$

where ρ is the density of the fluid. For the range of angular velocities used in the OCP measurements and a characteristic density of the liquid of $\rho \approx 1000$ kg.m^{-3}, the inertial suction pressure ranges from $6.8 \times 10^{-6} \leq -\mathcal{F}_{in}/\pi R^2 \leq 6.8$ Pa. These values are always significantly smaller than the magnitude of the of the axial force measurements shown in Figure 3.3.4 (b), and accordingly inertial effects on the axial force measurements are negligible.

The plots of viscosity and first and second normal stress difference are shown in Figure 3.3.4 (e) and (f). Each curve in (e) and (f) corresponds to a constant value of κ at which the derivative terms in Eqs. 3.2.7 and 3.2.8 were evaluated. Since each test was performed with the same set of angular rotation rates Ω, the corresponding rim shear rate values differ between tests. For the torque measurements, this feature of the OCP tests does not affect the evaluation of shear stress in Eq. 3.2.7. The viscosity data collapse onto the same underlying flow curve, which shows significant shear-thinning but no marked stress plateau suggesting that this fluid does not shear band. For the normal stress measurements, the first normal stress difference can only be determined using the CP geometry (*i.e.* $\kappa \to \infty$), and therefore when evaluating $N_2 = \Psi_2 \dot{\gamma}_R^2$ for a test at a finite κ, it is necessary to determine the precise value of $N_1 = \Psi_1 \dot{\gamma}_R^2$ at a particular value of $\dot{\gamma}_R = \frac{\Omega}{\theta}\frac{\kappa}{1+\kappa}$ from interpolation. Therefore, in order to avoid possible errors due to extrapolation of the N_1 data, N_2 values have been calculated only over the range of rim shear rates measured in the CP.

Both normal stress differences vary monotonically with shear rate. The values of N_1 are positive, whereas all calculated values of N_2 are negative, although there is some variation for each κ value for reasons explained below. The measurements with the PP are also shown by the hollow symbols. The equation for evaluating N_2 from the PP geometry, given below, corresponds to the limit of Eq. 3.2.8 as $\kappa \to 0$ and $\Omega/\theta \to \infty$.

$$\frac{\mathcal{F}_{PP}}{\pi R^2}\left[2 + \frac{d\ln(\mathcal{F}_{PP}/\pi R^2)}{d\ln(\dot{\gamma}_R)}\right] = \Psi_1(\dot{\gamma}_R)\dot{\gamma}_R^2 - \Psi_2(\dot{\gamma}_R)\dot{\gamma}_R^2 \tag{3.2.5}$$

According to this equation, unlike measurements in the OCP, at a given rim shear rate the measurement of N_2 with the PP is independent of the gap height, provided practical issues associated with parallax at small gap heights are not significant (Pipe *et al.*, 2008). The clear agreement between the N_2 values measured at two gap heights with the PP confirms that small gap effects are not important, however they are approximately one half the magnitude of the values measured with the OCP. The source of this discrepancy is unclear, but may be the result of slip on the PP geometry which had a visibly smoother surface than that of the CP geometry. At shear rates below $\dot{\gamma}_R \lesssim 60\ \mathrm{s}^{-1}$ the magnitude of N_2 is actually larger than that of N_1. This result is also found in the measurements

with the PP geometry shown by the hollow symbols.

In order to determine the relative magnitude of N_2 to N_1, the ratio of the average value of Ψ_2 to Ψ_1 is plotted against the rim shear rate $\dot{\gamma}_R$ in Figure 3.3.5. As discussed above, since it is the set of Ω/θ values that is held constant for each test, the set of rim shear rates in fact varies between tests at each κ value, and therefore each rim shear rate at which the Ψ_2 values are averaged corresponds to the closest value of $\dot{\gamma}_R$ from the measurement with the CP configuration (*i.e.* $\kappa \to \infty$). The horizontal error bars in Figure 3.3.5 indicate the range of rim shear rates over which the values of Ψ_2 were averaged and the vertical error bars correspond to the standard deviation in these values. Two curves are shown in the plot to indicate the calculated values of N_2 using either form of the derivative term in Eq. 3.2.8 evaluated with respect to $\ln(\dot{\gamma}_R)$ or $\ln(\kappa)$. These derivatives are mathematically equivalent, but they can show some variation when actually evaluated numerically. This ratio is negative as is expected for most entangled polymeric systems (Larson, 1998), but there is large scatter in this ratio at low shear rates. The measurements of N_2 in a CPyCl:NaSal system of Pipe *et al.* (2010) also show that the ratio $-\Psi_2/\Psi_1$ is positive and less than unity corroborating the findings here at high $\dot{\gamma}_R$ for WLM fluids.

Unlike the shear stress measurements with the OCP, the calculated values of the second normal stress difference N_2 shown in Figure 3.3.4, show some degree of scatter. The discrepancy in the calculated values of $N_2(\dot{\gamma})$ likely arises for a number of reasons. Firstly, the dynamic range of the axial force transducer on the DHR3 is $5 \times 10^{-3} \leq \mathcal{F} \leq 200$ N ($2 \leq \mathcal{F}/\pi R^2 \leq 17680$ Pa for a plate with $R = 30$ mm). Hence many of the axial force measurements at the lower rim shear rates plotted in Figure 3.3.4 (b) coincide with the lower bound of the dynamic range where it can be challenging to obtain reproducible measurements. This fact may explain why the the axial force measurements at the intermediate gap heights ($0.8 \leq \kappa \leq 2$) are actually larger than the respective values in the CP and PP limits at the low rim shear rates $\dot{\gamma}_R \lesssim 50$ s^{-1}. A second difficulty may arise in the numerical evaluation of the derivative terms from the polynomial fits at the extreme values of κ. Since these points lie at the edges of the fitting domain, the local slope of the fitted curve is more liable to be inaccurate due to errors associated with

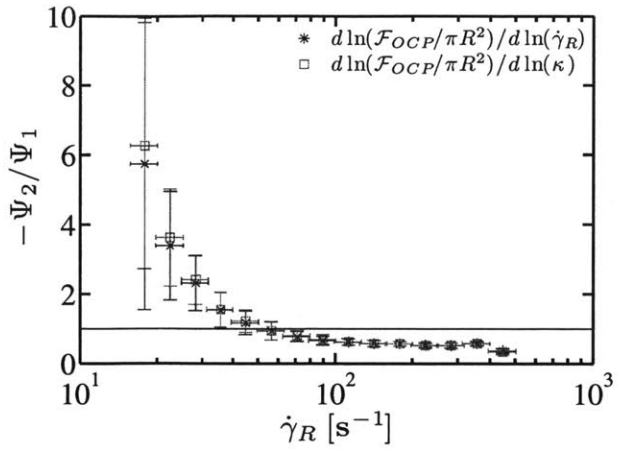

Figure 3.3.5: Ratio of normal stress coefficients in viscometric shear flow of the of 100:300 mM CPyCl:$NaNO_3$ solution at 30 °C measured with the offset cone-and-plate (OCP). Vertical error bars correspond to the standard deviation of the values of Ψ_2 calculated using Eq. 3.2.8 and shown in Figure 3.3.4 (f). Horizontal error bars correspond to the range of rim shear rates over all κ values used to calculate each data point. A black horizontal line is plotted at $-\Psi_2/\Psi_1 = 1$ to guide the eyes.

Runge's phenomenon when extrapolating a high order polynomial beyond the fitting domain.

Accurate measurement of N_2 using the OCP geometry becomes progressively more difficult as the value of κ increases (*i.e.* at lower gap heights), because the geometry approaches the CP configuration and the axial force on the fixture is dominated by contributions from N_1. In this limit $2\mathcal{F}_{OCP}/\pi R^2 \rightarrow \Psi_1\dot{\gamma}_R^2$ (see Eq. 3.2.4) and therefore the difference between these terms in Eq. 3.2.8 becomes small, causing the calculated value of $N_2 = \Psi_2\dot{\gamma}_R^2$ to be very sensitive to any noise in the measurement of the axial force on the OCP. Any small errors are further amplified by the multiplication of $(1+\kappa)$ which becomes increasingly large at small gap heights.

Despite these challenges, careful measurements with the OCP geometry have the advantage over the combination of the CP and PP, because the OCP can enable the rheological characterization of both the first and second normal stress coefficients using the *same* fluid sample. A sequence of tests with the OCP also provides a larger amount of data over which to calculate the values of N_2. WLM solutions are especially suited to measurements with the OCP, since these fluids do not degrade with successive measure-

ments and therefore a single fluid sample can be used to extract reliable measurements of both normal stress coefficients over a range of shear rates.

3.3.3 Step Strain Stress Relaxation

Step strain measurements were performed over a sequence of increasing strains on the ARES using a CP geometry ($R = 25$ mm, $\theta = 2.3°$). The shear stress and normal stress difference were recorded at 100 Hz until the measurements fell below the instrument resolution. The relaxation modulus measured for shear strains $10^{-3} \leq \gamma_0 \leq 10$ for the CPyCl:NaSal system is plotted in Figure 3.3.6 (a) and (b) and for the CTAB:NaSal system in Figure 3.3.7 (a) and (b). For the range of strain amplitudes measured, the relaxation modulus $G(t, \gamma_0) = \tau_{xy}(t, \gamma_0)/\gamma_0$ at long times decays exponentially, following the equation

$$G(t, \gamma_0) = G_\infty(\gamma_0) \exp(-t/\lambda) \tag{3.3.9}$$

where $G_\infty(\gamma_0)$ is the strain-dependent modulus at long times ($t \to \infty$) and λ is the Maxwell relaxation time.

At small strains $\gamma_0 \lesssim 1$, the long time relaxation modulus is independent of strain and approaches a limiting value $G_\infty(\gamma_0 \to 0) = G^0_\infty$. For both WLM systems the value of these parameters at small strains is listed in Table 3.3.1 and they are very similar to their respective values measured in SAOS.

For increasing strains the stress relaxation modulus at long times $t > \lambda$ also decays exponentially in time, but its magnitude and initial behavior for $t \ll \lambda$ is dependent on the strain magnitude. The strain-dependence is made clearer by plotting the modulus normalized by the value of $G_\infty(\gamma_0)$ in Figure 3.3.6 (c) and (d), and Figure 3.3.7 (c) and (d). This non-linear behavior was noted and rationalized for a similar WLM system by Pipe *et al.* (2010). It results because at early times $t \lesssim \lambda_{break} \ll \lambda$, high frequency (short time) relaxation mechanisms such as the Rouse and breathing modes discussed in Section 2.2.1 dominate, facilitating a rapid but short-lived change in the micellar network giving rise to the initial stress relaxation. On the other hand, the relaxation modulus at long times recovers the exponential behavior and Maxwell relaxation time

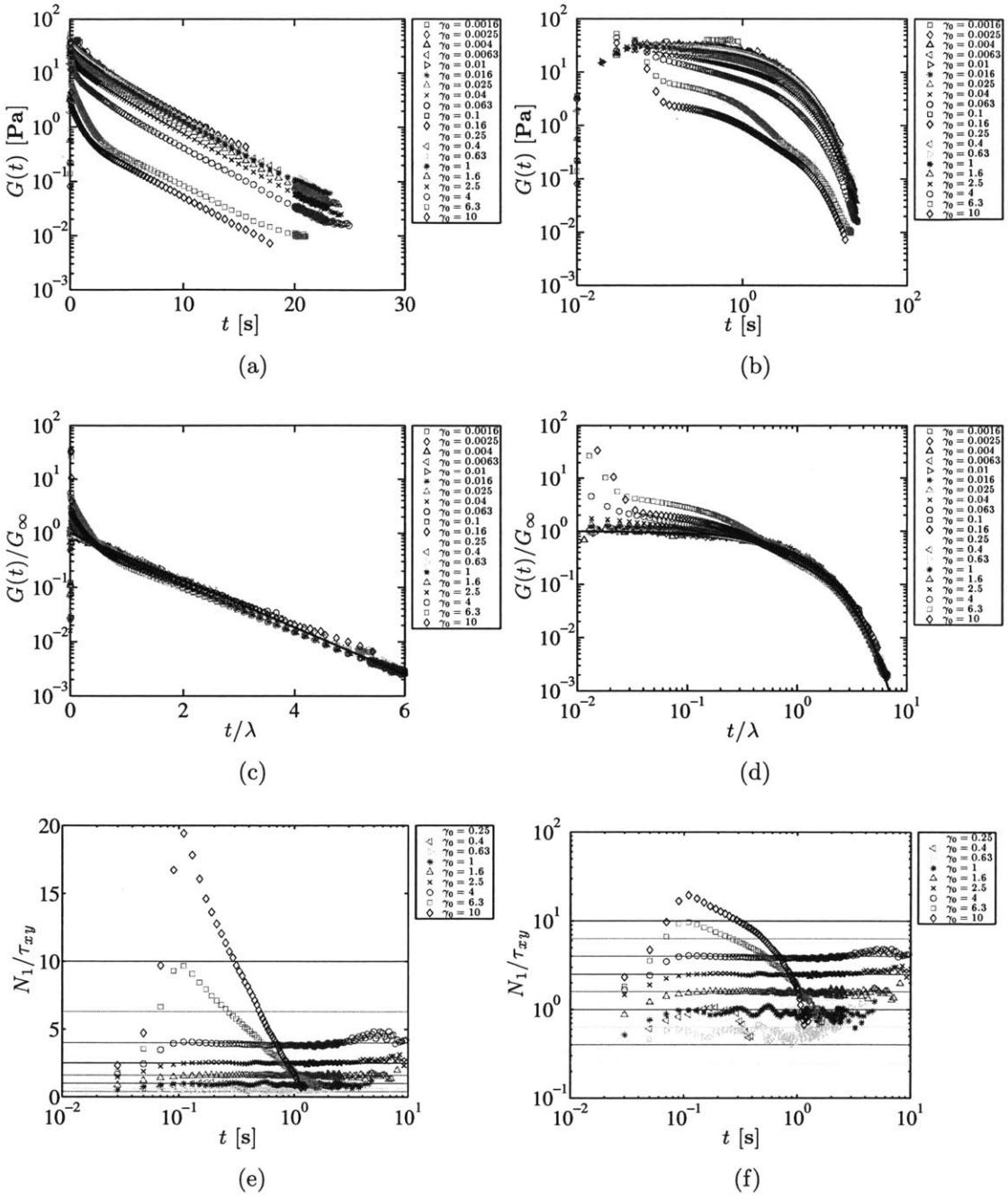

Figure 3.3.6: Step strain stress relaxation measurements for the CPyCl:NaSal system (Batch 3) at 22 °C. (a) & (b) Time evolution of the relaxation modulus at different strains. (c) & (d) Normalized time evolution of the relaxation modulus at different strains. The black curve is the prediction of the Maxwell model. (e) & (f) Time evolution of the ratio of first normal stress difference to shear stress.

observed at small strains because sufficient time has elapsed for multiple chain scission and fusion reactions to occur so that the initial microstructural configuration has been more fully forgotten.

The measured values of $G_\infty(\gamma_0)$ and λ obtained by fitting Eq. (3.3.9) to the stress relaxation data over the range of times at which the stress relaxation was exponential are shown in Figure 3.3.8 (a) and (c). The drop in the relaxation modulus that occurs at large strains is commonly called *strain softening.* It is possible to collapse the relaxation modulus measurements using a shift factor called the damping function $h(\gamma_0)$ based on the approximate form predicted by the single-mode partially-extending convected (PEC) tube model for an infinitely fast step strain (Larson, 1988) given by

$$h(\gamma_0) = \frac{1}{1 + \frac{1}{3}\xi'\gamma_0^2} \tag{3.3.10}$$

where ξ' is the non-linear breakage parameter. The fit of the damping function to the values of $G_\infty(\gamma_0)$ is shown in Figure 3.3.8 (b) and (d), and the value of ξ' is listed in Table 3.3.1. The normalized storage modulus $G'(\omega, \gamma_0)/G'(\omega, \gamma_0 \to 0)$ measured at $\omega = 0.5$ rad.s^{-1} in oscillatory shear is also shown in these plots. In both step and oscillatory shear strains, the onset of non-linear behavior occurs at strains $\gamma_0 \sim 1$. Deviations from linear behavior in step strains at critical strains of this order have also been seen in WLM solutions experimentally (Pipe *et al.*, 2010; Brown *et al.*, 1997) and in numerical simulations with the VCM model (Vasquez *et al.*, 2007; Zhou *et al.*, 2008). In the experiments with a CPyCl:NaSal system (Pipe *et al.*, 2010), the fluid exhibited strain softening due to chain disentanglement resulting in non-affine deformations of the microstructure that are predicted by the PEC model. Conversely, earlier studies with a CTAB:NaSal system (Shikata *et al.*, 1988; Brown *et al.*, 1997) found that the fluid exhibited either strain hardening or softening depending on the concentration of the salicylate ion. It is well known that the addition of salt or a strongly binding counterion such as NaSal to a micellar solution enhances the formation of worm-like micelles and thereby increases the viscoelasticity of the liquid (Berret, 2006). Hence the precise features at the onset on non-linear behavior in WLM fluids are clearly sensitive to the exact features of the microstructure of the network.

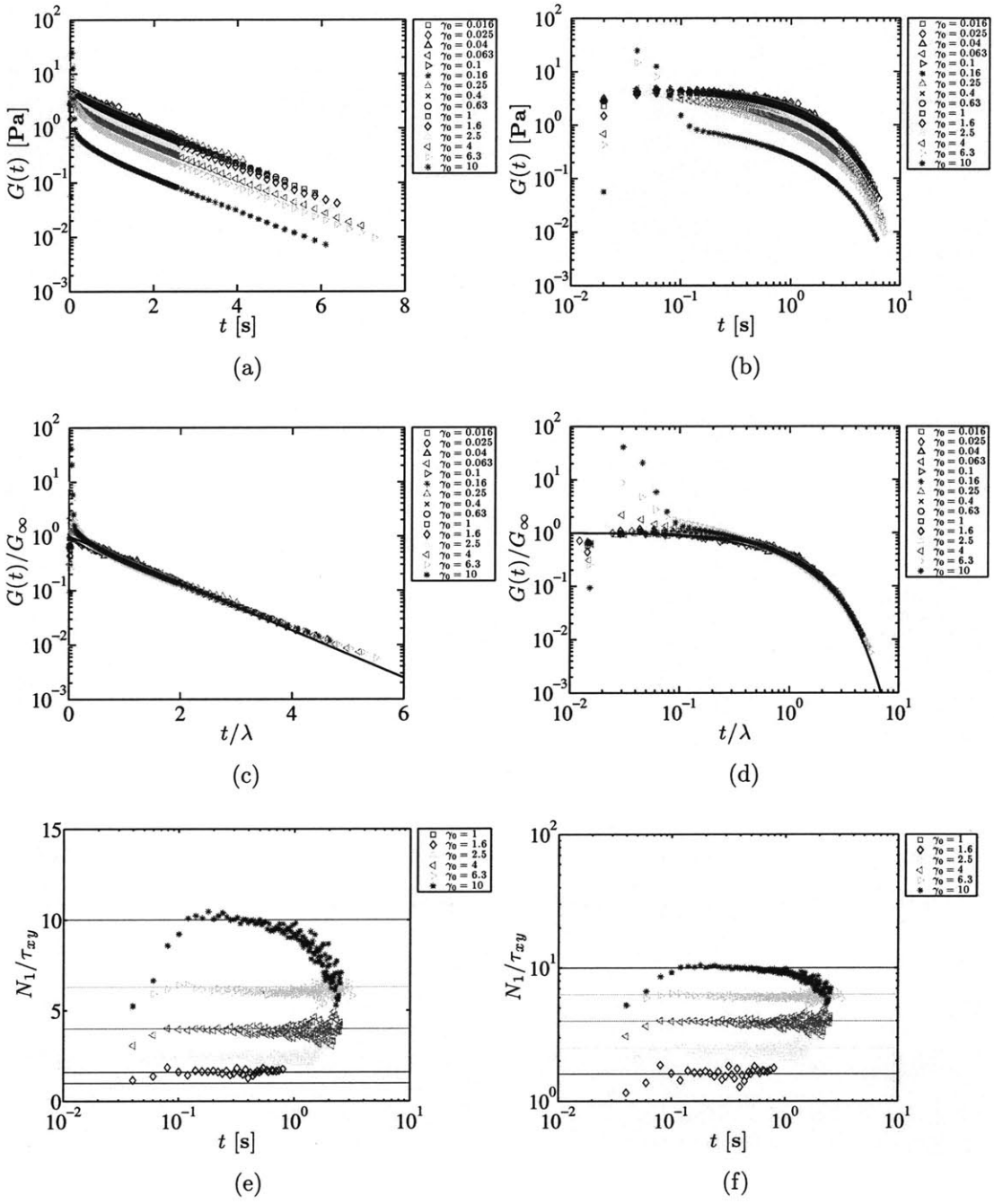

Figure 3.3.7: Step strain stress relaxation measurements for the CTAB:NaSal system (Batch 3) at 22 °C. (a) & (b) Time evolution of the relaxation modulus at different strains. (c) & (d) Normalized time evolution of the relaxation modulus at different strains. The black curve is the prediction of the Maxwell model. (e) & (f) Time evolution of the ratio of first normal stress difference to shear stress.

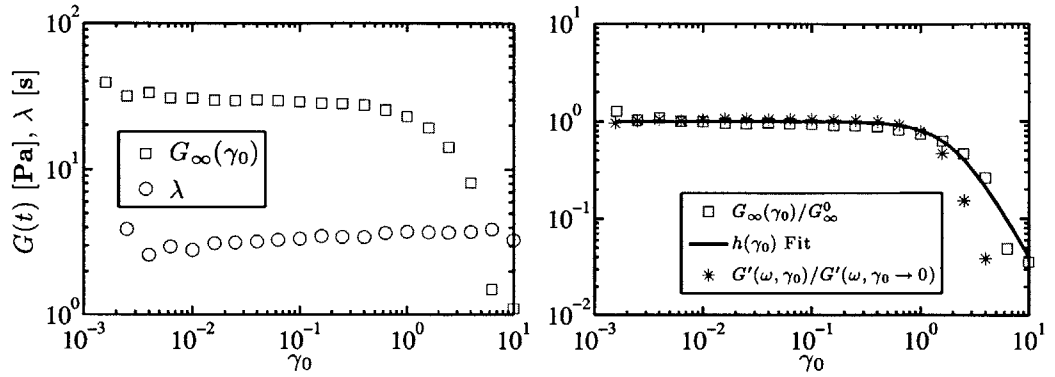

(a) 100:60 mM CPyCl:NaSal

(b) 100:60 mM CPyCl:NaSal

(c) 30:240 mM CTAB:NaSal

(d) 30:240 mM CTAB:NaSal

Figure 3.3.8: Step strain stress relaxation measurements for the (a) & (b) CPyCl:NaSal and (c) & (d) CTAB:NaSal systems at 22 °C. (a) & (c) Modulus and relaxation time at different strain amplitudes. (b) & (d) Normalized modulus in step strain and storage modulus in oscillatory shear and fit from Eq. (3.3.10).

The time evolution of the first normal stress difference was also recorded to evaluate the adherence of the WLM systems to the Lodge-Meissner rule given previously in Eq. 2.1.6. For affine deformations, it follows from this rule that the ratio $N_1(t)/\tau_{xy}(t) = \gamma_0$ is constant throughout the duration of a step strain test. These ratios are shown in Figure 3.3.6 (e) and (f) and Figure 3.3.7 (e) and (f).

For the CPyCl:NaSal system, the Lodge-Meissner rule is followed for strains $\gamma_0 \lesssim 4$, but at higher strains the value of N_1 decays more rapidly than τ_{xy}. In numerical simulations with the VCM model (Vasquez *et al.*, 2007), Zhou *et al.* (2008) find that the Lodge-Meissner rule is uniformly valid for a shear-banding fluid up to $\gamma_0 \lesssim 2.5$, but at higher strains the onset of shear banding introduces non-affine deformations into the network and thus the Lodge-Meissner rule is no longer obeyed. The large overshoots in the stress ratio seen at early times for $\gamma_0 > 4$ was also observed in a shear-banding CTAB:NaSal system by Brown *et al.* (1997), who attributed it to the formation of shear bands. In their case, however, the overshoots were sustained even at long times.

For the CTAB:NaSal system, the Lodge-Meissner rule is obeyed up to the maximum strain measured $\gamma_0 = 10$. In steady shear measurements, the CTAB:NaSal system does not show a stress plateau suggesting that this fluid does not shear band. Therefore, the discrepancy between the apparent affine behavior of the CTAB:NaSal system inferred from the stress ratio measurements and the non-affine behavior observed from the measurements of stress relaxation modulus at large strains strongly suggests that shear banding effects the evolution of normal stresses in the CPyCl:NaSal system. Accordingly, further insight into this peculiar dynamical behavior in the CPyCl:NaSal system can be gained from a more detailed study of the deformation kinematics at the onset of shear banding.

3.4 Velocimetry Measurements

In order to better characterize the shear-banding behavior of the CPyCl:NaSal system, flow visualization experiments were completed using the Rheo–PIV setup discussed in Section 3.2.3. A new fluid sample (Batch 4) of 100:60 mM CPyCl:NaSal was prepared

and seeded with 0.001 wt.% Titanium Dioxide particles (average size 3 μm, density 4200 kg/m^3 from TSI Inc.) for the PIV measurements. The seeding (or number) density of particles was high enough to carry out PIV measurements, but still at low enough volume fraction ($\phi \simeq 2 \times 10^{-5}$) such that the particles did not significantly affect the rheology of the fluid. All rheometry measurements with the Rheo–PIV setup were carried out on a AR-G2 stress-controlled rheometer (TA instruments) equipped with a CP geometry ($R = 25$ mm, $\theta = 4°$ quartz plate and aluminum cone) at 25 °C.

In order to visualize the velocity profile across the gap it is crucial to have a flat interface, through which to image. For the experiments performed with the Rheo–PIV system, the upper and lower geometries have the same diameter, and so for most Newtonian liquids the meniscus is pinned at the top and bottom edges resulting in an almost flat meniscus profile. Therefore, when measuring local velocity fields within a Newtonian fluid, it is typically not necessary to use any optical components such as a plano-concave lens. However, it is well known that viscoelastic fluids that exhibit shear banding are also likely to exhibit edge instabilities, which will result in an irregularly shaped meniscus even when it is pinned at the upper and lower edges (Keentok & Xue, 1999; Inn *et al.*, 2005; Sui & McKenna, 2007). Previous workers used circular bounding films to prevent these edge irregularities (Tapadia *et al.*, 2006). However, the effects of such bounding films can markedly change the local material response (Sui & McKenna, 2007) and should therefore be avoided if possible. The plano-concave lens used in this work serves a similar purpose to a circular bounding film, but it does not surround the entire sample. This has the effect of lowering the incremental frictional torque that is imposed on the rotating fixture by such a surface. Nonetheless, there is still a measurable additional frictional force that is present when this lens is in place, due to the change in boundary conditions at the edge of the geometry and possible secondary flows induced near the rigid wall. This additional frictional force registers as an increase in the shear stress as measured by the rheometer for the CPyCl:NaSal system at a particular shear rate. In Figure 3.4.1 the flow curves for the fluid with and without the lens in place are compared. The decrease in the shear stress for the final data point when the lens is in place is a result of the fluid being ejected from the gap, which is delayed to higher shear

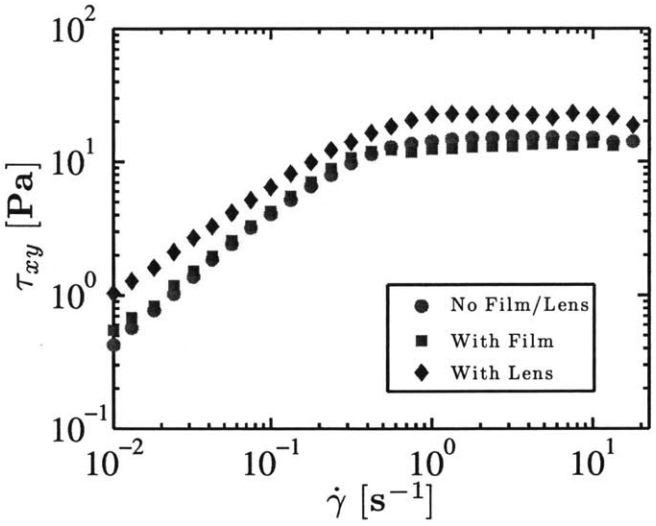

Figure 3.4.1: Comparison of the flowcurve of the CPyCl:NaSal system measured using different configurations. Circle symbols are without the lens or film. Square or diamond symbols are either with the lens, or with the film, but not both. The presence of the lens results in an additional frictional torque being applied to the rotating quartz geometry, which leads to an increase in the apparent shear stress measured by the instrument.

rates when the lens is not in place. A second modification that has been incorporated into these experiments is a film attached to the upper geometry in order to reduce the effects of fluid slip at the wall. Unlike the lens, however, this film does not have a considerable effect on the flow curve shown in Figure 3.4.1.

3.4.1 Steady Shear-Banding Flow

Britton & Callaghan (1997, 1999) showed, using NMR velocimetry, that in a CP geometry a 100:60 mM CPyCl:NaSal system (identical to the one used in this work) exhibited a three-banded velocity profile, in which a high shear rate band is observed in the middle of the gap, connected to two lower shear rate regions near the upper and lower surfaces. Since the WLM system studied in this thesis is identical to that of Britton & Callaghan (1997, 1999) (with similar values of the measured relaxation time and critical shear rate), and a similar flow configuration ($R = 12$ mm and $\theta = 4°$, or $R = 8$ mm and $\theta = 7°$ ceramic cone and plate with an outer containment jacket at the edge), it is reasonable to expect that the velocity profiles observed with the Rheo–PIV system should exhibit a similar three-banded profile.

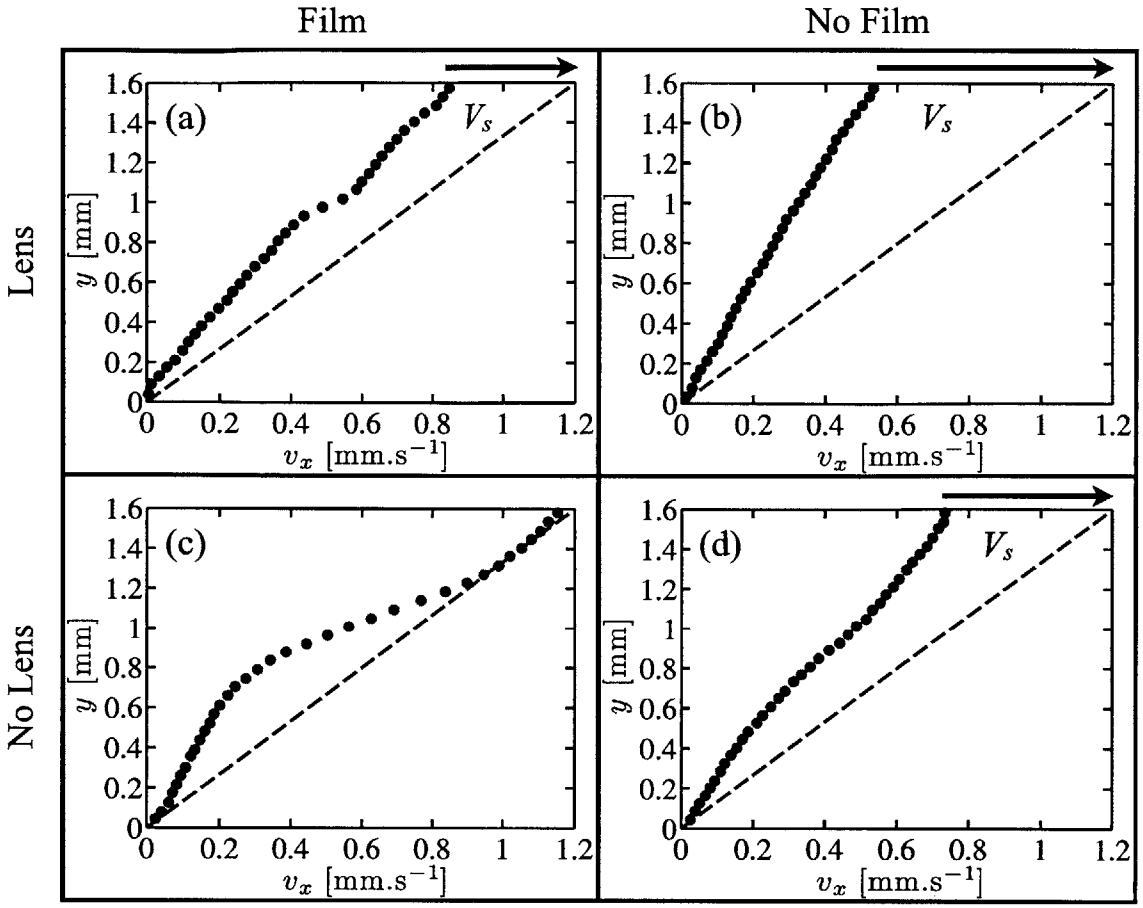

Figure 3.4.2: Steady state velocity profiles measured at $\dot{\gamma} = 0.75$ s^{-1} under different configurations of the Rheo–PIV system. The dashed black line indicates the homogeneous, no-slip velocity profile. The black arrows indicate the magnitude of the slip velocity V_s. When the plano-concave lens is not used, the film clearly eliminates slip at this shear rate. When the lens is used, the film is less effective and the banded behavior exhibited by the fluid is different showing a narrower band appears near the midgap.

In order to understand the the exquisite sensitivity of Rheo–PIV observations to the imposed boundary conditions, the velocity profiles measured with and without the film and lens are shown in Figure 3.4.2. The measured velocity profiles are different in all four cases. The profiles (c) and (d) show that when the lens is not used, the additional presence of the film on the upper plate prevents wall slip from occurring at that surface. The presence of this wall slip in Figure 3.4.2 (d) results in a lower shear rate within the bulk of the fluid, causing the velocity profile to appear homogeneous for shear rates lower than $\dot{\gamma} = 0.75$ s^{-1}. This result suggests that when the plano-concave lens is not used, the transparent film eliminates wall slip and facilitates the formation of the centrally

located high shear rate band. However, when the lens is used, as in Figure 3.4.2 (a) and (b), a rather different behavior is observed. Now, the addition of the transparent film only reduces the degree of slip that is present, and does not completely eliminate it. In addition to this, the appearance of the shear-banded velocity profile for the case when the lens is used (Figure 3.4.2 (a)) is now characterized by a highly localized high shear rate band in the center (only 2 or 3 data points in width) which more closely resembles a discontinuity in the velocity, as opposed to the more gradual variation in the shear rate across the gap that is observed in Figure 3.4.2 (c). In general, these narrow bands, resembling discontinuities in the velocity profile, have only been observed when the plano-concave lens is used as a bounding surface. However, this behavior is mostly erratic and difficult to predict since the bands can be observed in different positions across the gap for the same imposed shear rates, and in other instances a larger degree of wall slip may occur on the upper surface resulting in a less pronounced high shear rate band. Two high shear rate bands have also been observed at some of the larger shear rates. One possible explanation for this irreproducible behavior is that the presence of the lens may result in an earlier onset of secondary flow within the region of the fluid near the lens, due to the altered boundary condition at the bounding surface.

In order to avoid any potential artifacts that may arise from this plano-concave lens, and also in order to avoid artifacts in the bulk rheological data (Figure 3.4.1), the configuration shown in the lower left corner of Figure 3.4.2, *i.e.* an adhesive film attached to both upper and lower fixtures and no lens at the outer edge, was utilized to observe the shear-banding behavior at transitional shear rates at the onset of the stress plateau. This configuration results in reproducible and self consistent behavior as shown in Figure 3.4.3. Furthermore, in Figure 3.4.4 it is clear that at the range of shear rates probed in Figure 3.4.3, no irregularities in the fluid meniscus at the edge of the CP geometry are observed. This shows that a plano-concave lens or any other bounding film is in fact not required in this CPyCl:NaSal fluid for velocimetric measurements at these shear rates.

The velocity field within the CPyCl:NaSal solution observed using the Rheo–PIV system at a number of different imposed shear rates are shown in Figure 3.4.3. Evidently,

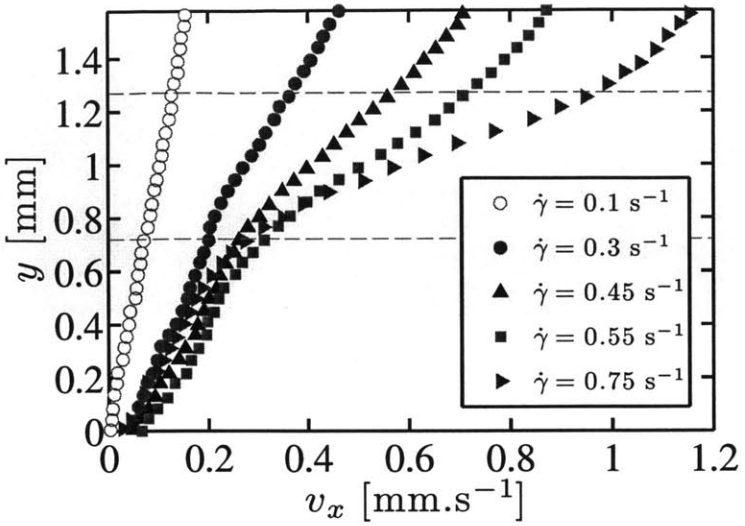

Figure 3.4.3: Series of steady state velocity profiles observed in the CPyCl:NaSal test fluid as the shear rate is incrementally changed from $\dot{\gamma} = 0.1$ s^{-1} to 0.75 s^{-1}. At the lowest shear rate the profile is clearly linear, but develops into a three-banded profile with a region experiencing a higher shear rate near the center of the gap. The dashed grey lines indicate the location of this high shear rate region.

the velocity profiles evolve from a linear response to three-banded profiles as the shear rate is incremented slowly from $\dot{\gamma} = 0.1$ s^{-1} to 0.75 s^{-1} and into the stress plateau region. The three-banded profile in Figure 3.4.3 at a shear rate of $\dot{\gamma} = 0.75$ s^{-1} is characterized by a high shear rate region near the middle of the gap, and lower shear rate regions near the upper and lower surfaces. The behavior at the high shear rates is thus consistent with the three-banded profiles observed by Britton & Callaghan (1997, 1999). However, Britton and Callaghan generally measured their shear banded profiles at even higher shear rates well into the stress plateau region (their use of an outer containment jacket allowed for this by preventing sample from being ejected from the gap). They therefore did not probe the behavior of the fluid in this transitional regime at lower shear rates. During the transition from linear to three-banded profiles (for imposed shear rates of $\dot{\gamma} = 0.3$ s^{-1} and $\dot{\gamma} = 0.45$ s^{-1}) the material exhibits an intermediate behavior in which the flow profile appears to have two developing shear bands instead of three clearly distinct bands. This is in contrast to some shear banding scenarios which have been observed in other geometries (such as those observed by Salmon *et al.* (2003) in Taylor-Couette flow) where the shear rate in the highly sheared band remains constant and the

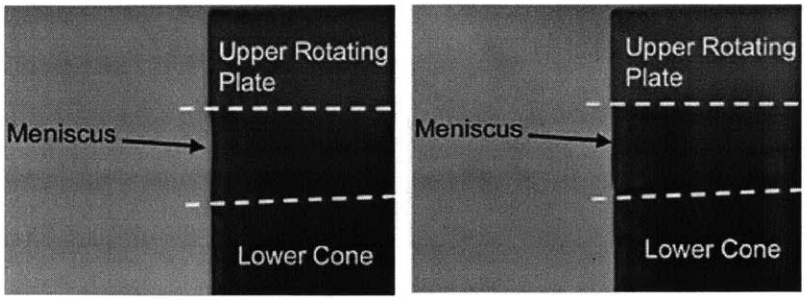

(a) (b)

Figure 3.4.4: Photographic image of fluid meniscus for CPyCl:NaSal undergoing a shear rate of $\dot{\gamma} = 0.1\ s^{-1}$ (a) and $\dot{\gamma} = 0.75\ s^{-1}$ (b). In both cases, the meniscus remains flat and unperturbed.

interface between the low and high shear rate regions moves as the apparent shear rate is increased.

3.4.2 Onset of Secondary Flow

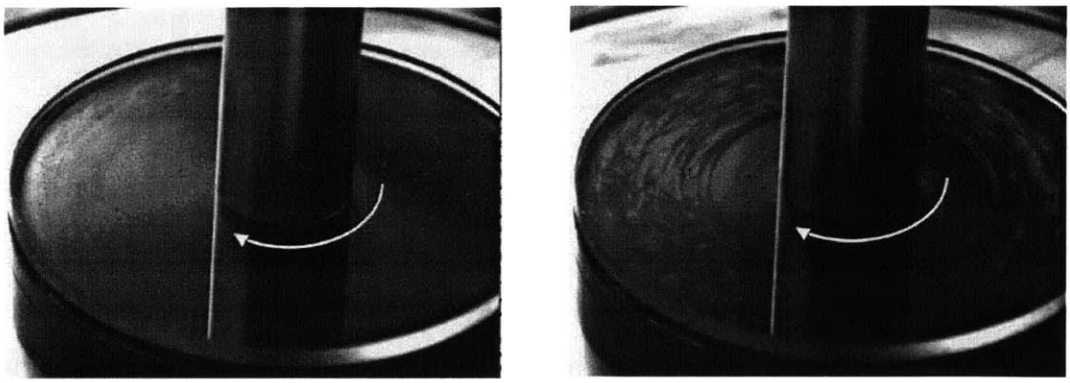

(a) (b)

Figure 3.4.5: Images taken during steady shear at $\dot{\gamma} = 2\ s^{-1}$ (with Reynolds number $Re \equiv \rho\dot{\gamma}R_i^2\Theta_0^2/\eta = 0.001$, and Weissenberg number $Wi = 2.9$) on the left, and $\dot{\gamma} = 5\ s^{-1}$ ($Re = 0.006$, $Wi = 7.3$) on the right. The distortions seen near the outer edge for the higher shear rate case are a result of the onset of secondary flow. The distortions begin appearing near the outer edge at a critical Weissenberg number $Wi \simeq 6$, and grow towards the center over time. The timescale for the distortions to fill the gap is much greater than the relaxation time λ.

The velocimetric data presented in Figures 3.4.2 and 3.4.3 are only given for shear rates as high as $\dot{\gamma} = 0.75\ s^{-1}$. At much larger shear rates, the local shear banded be-

havior of the fluid becomes much more difficult to observe for several reasons. Firstly, the likelihood of a severe edge irregularity in the meniscus arising is much greater. As described in Section 3.2.3, this results in larger errors in the measured velocity values. While the use of the plano-concave lens (or any other type of bounding film) to impose a planar imaging surface may avoid the issue of these edge irregularities, it still affects the bulk measured stress (Figure 3.4.1) as well as the flow kinematics by altering boundary conditions near the edge resulting in the erratic behavior that was discussed in Section 3.4.1. Another difficulty that is faced at very large shear rates (typically exceeding $\dot{\gamma} > 3$ s^{-1}, or Weissenberg numbers $Wi \equiv \lambda\dot{\gamma} \geq 4.4$) is that at the given magnification of the camera/lens, the displacement of seed particles between frames becomes large enough such that the cross-correlation algorithm is unable to resolve the displacement value. This may be avoided by using a lower lens magnification, but at the cost of a concomitant loss of spatial resolution for the velocity profiles. As a result of these difficulties, this study of the CPyCl:NaSal solution is restricted to shear rates generally lower than $\dot{\gamma} < 2$ s^{-1} (or $Wi \leq 2.9$), where secondary flows are less likely to occur and experimental artifacts will not play an important role in the measurements.

To verify that there are not any appreciable secondary flows at these lower shear rates, an alternative imaging method was used to observe flow of the CPyCl:NaSal solution under steady shear in the CP geometry. Specifically, a small amount of Kalliroscope AQ-RF rheoscopic fluid (http://www.kalliroscope.com/) was added to the micellar solution. This rheoscopic fluid contains a high concentration of plate-like mica seed particles. Flow alignment of these seed particles allows for macroscopic flow in the CPyCl:NaSal solution to be visualized and for qualitative changes with increasing shear rate to be observed. These seed particles have been used previously to observe secondary flows in other viscoelastic fluids (McKinley *et al.*, 1995; Fardin *et al.*, 2009). The sample is placed in the CP geometry (with upper transparent quartz plate) and illuminated from above using a white light source. A black anodized lower cone is utilized to enhance contrast of the seed particles and a camera with a telecentric zoom lens is used to observe the evolution of flow induced structures in the fluid. Figure 3.4.5 shows two images obtained from the imaging system during steady shear of the CPyCl:NaSal solution at

two different shear rates. At the low shear rate ($\dot{\gamma} = 2\ s^{-1}$) the fluid appears homogenous with no patterns emerging during the purely tangential flow. However at the higher shear rate ($\dot{\gamma} = 5\ s^{-1}$) radial and tangential striations in the flow field are clearly seen, as evidenced by the regions of varying contrast in the fluid further away from the center. By observing the evolution of these structures during start-up of steady shear at these higher shear rates, it is apparent that the regions of varying contrast begin to form near the rim of the sample, grow in time and propagate radially towards the center. Corresponding measurements of the total torque exerted on the fixture show the growth of temporal fluctuations (Yesilata *et al.*, 2006; Pipe *et al.*, 2010). This suggests that a 3D unsteady secondary flow first develops near the outer edge where the sample meniscus is located, and propagates towards the center. The images in Figure 3.4.5 are not intended to provide quantitative detail about the exact nature of the viscoelastic secondary flow that develops in this micellar fluid (*i.e.* direction, magnitude), however they do show what regions of the fluid are first afflicted, and can be used as a guideline to understand at what shear rates one might expect 2D velocimetric data from Rheo–PIV to begin to show artifacts that arise from significant secondary flow.

3.5 Summary

In this Chapter, the bulk rheological behavior of a selection of WLM fluids has been characterized in oscillatory and steady shear and step strain stress relaxation tests with a cone-and-plate geometry. The values of all measured material functions are listed in Table 3.3.1. The linear viscoelasticity of a 100:60 mM CPyCl:NaSal and a 30:240 mM CTAB:NaSal system is very well described by a single-mode Maxwell model at low to moderate frequencies ($\omega \lesssim \lambda^{-1}$) with modulus G_0, relaxation time λ and viscosity η_0. At high frequencies in oscillatory shear, relaxation mechanisms occurs on short time-scales such as Rouse and breaking modes are detectable, enabling the estimation of the breaking and reptation times, as well as estimates of physical properties of the molecular network.

The step strain stress relaxation tests enabled the rheological characterization of

the onset of non-linear effects in the WLM systems. At small strains ($\gamma_0 \ll 1$), the relaxation modulus decays exponentially with a time constant approximately equal to λ measured in oscillatory shear, and the first normal stress evolves according to the Lodge-Meissner rule. For larger strains, both WLM systems exhibit strain softening. The first normal stress difference follows the Lodge-Meissner rule for strains up to $\gamma_0 = 10$ in the CTAB:NaSal system, but this rule is violated for strains $\gamma_0 \lesssim 4$ in the CPyCl:NaSal system and likely coincides with the onset of the shear banding.

In viscometric steady shear flow, both systems exhibit a constant zero-shear-rate-viscosity η_0 equal to the value measured in oscillatory shear, but they shear-thin at shear rates above $\dot{\gamma} \gtrsim \lambda^{-1}$. In this regime, the viscosity in the CTAB:NaSal system scales with shear rate $\eta \sim \dot{\gamma}^{-0.6}$, whereas the CPyCl:NaSal system shear bands and exhibits a marked stress plateau with $\eta \sim \dot{\gamma}^{-1}$. Measurements of the first normal stress difference in both fluids show an approximately quadratic scaling with shear rate $N_1 \sim \dot{\gamma}^2$, however this scaling in N_1 shows more sensitivity to the particular batch of fluid than the more robust scaling of the shear viscosity with shear rate. The magnitudes of the N_1 are 10 to 100 times larger than the corresponding shear stress τ_{xy} at the highest shear rates before which the sample is ejected from the gap ($\dot{\gamma} \sim \mathcal{O}(10)$ s^{-1}). In order to make measurements of the normal stress coefficients at higher shear rates, a shear-thinning CTAB:$NaNO_3$ system has been tested using the offset cone-and-plate configuration. For all measured shear rates, the ratio $-N_2/N_1 > 0$, but at shear rates below $\dot{\gamma} \simeq 5\lambda^{-1}$ s^{-1} this ratio is anomalously larger than unity. As this shear is increased the ratio approaches approximately 0.5.

The interplay between shear banding and flow kinematics in a 100:60 mM CPyCl:NaSal WLM system has also been studied in a cone-and-plate geometry using particle image velocimetry. The shear banded velocity profiles that are observed in the cone-and-plate device are similar to the three-banded profiles observed by Britton & Callaghan (1997) and they distinctly differ from the two-banded profiles that have been observed for flow of WLM solutions in Taylor-Couette cells. Some consideration has also been given to two different experimental techniques that can be used to mitigate wall slip effects that are endemic to Rheo–PIV experiments with complex fluids, and some of the effects that

edge irregularities in the cone-and-plate rheometer can have on the PIV measurements. Specifically, the use of a plano-concave optical lens placed at the geometry edge to improve image quality was discussed, and it was shown that the change in the boundary condition at the edge due to this rigid no-slip surface can result in a considerable qualitative change in the velocity profile observed within the fluid. Additional flow visualization in the flow-vorticity plane was used to determine the critical shear rates beyond which secondary flows become detectable, and these imaging results were used to select test conditions for which there is minimal secondary flow occurring that might corrupt the PIV measurements. This combination of localized velocimetric measurements and bulk rheological measurements provide detailed insight into the spatio-temporal dynamics of complex fluids under simple viscometric flows.

The onset of a secondary flow driven by elasticity ultimately leads to an edge instability causing the ejection of the fluid sample from the gap. Such elastic instabilities can severely limit the range of shear rates over which conventional macroscale rheometric techniques can be successfully used for the rheological characterization of a material. It is therefore important to understand and to predict the conditions under which elastic instabilities occur in flows of shear-banding WLM fluids, which forms the basis of Chapter 4. It is also advantageous to develop experimental methods of measuring viscometric material functions at much higher shear rates than than be achieved with the rotational-based rheometric instruments used in this Chapter, which is the topic of Chapters 5 and 6.

Chapter 4

Potential Ways of Thinking about the Shear-Banding Phenomenon

4.1 Introduction

Shear banding is a curious but ubiquitous phenomenon occurring in soft matter. The phenomenological similarities between the shear-banding transition and phase transitions has pushed some researchers to adopt a *thermodynamical* approach, as opposed to the more classical *mechanical* approach to understanding these flows. In this Chapter, the diffusive Johnson-Segalman (dJS) model is studied in the context of shear banding to demonstrate why these two approaches are not so dissimilar. The historical development of the dJS model is briefly reviewed along with the analogy between this model and reaction–diffusion equations. In the case of anisotropic diffusion, it can be shown that the dJS governing equations for steady shear flow are analogous to the equations of the dynamics of a particle in a quartic potential. This model is then used to derive a stability criterion for purely elastic Taylor-Couette (TC) instability for shear-banding flows.

4.2 Johnson-Segalman Model and Sketch of Shear Banding

The model originally proposed by Johnson & Segalman (1977) was a modification to the Upper Convected Maxwell model (UCM), the canonical rheological model for viscoelasticity (Larson, 1998; Bird *et al.*, 1987). In order to allow for rate-dependent material properties in steady simple shear, the JS model supposes that network strands in the material can slip with respect to a purely affine deformation. This slipping yields an effective velocity gradient field which is given by

$$\mathbf{L} = \nabla\vec{v} - 2\zeta\mathbf{D} \tag{4.2.1}$$

where ζ is a scalar slip coefficient in the range $0 \leq \zeta \leq 1$, $\nabla\vec{v}$ is the velocity gradient tensor, and $\mathbf{D} = \frac{1}{2}((\nabla\vec{v})^{\dagger} + \nabla\vec{v})$ is the strain rate tensor. The new convected derivative operator is

$$\widehat{(\,)} = \frac{D(\,)}{Dt} - \mathbf{L}^{\dagger}\cdot(\,) - (\,)\cdot\mathbf{L} \tag{4.2.2}$$

where $\frac{D(\,)}{Dt} \equiv \frac{\partial(\,)}{\partial t} + \vec{v}\cdot\nabla(\,)$ is the material derivative. The resulting constitutive equation for the polymeric stress tensor $\mathbf{T}$, is written

$$\mathbf{T} + \lambda\widehat{\mathbf{T}} = 2\eta_p\dot{\gamma} \tag{4.2.3}$$

where λ is the polymer relaxation time and $\eta_p \equiv G_0\lambda$ is the polymer viscosity, defined with respect to the polymer elastic modulus.

In recent publications (Fielding, 2007), Eq. (4.2.3) is usually rewritten in an equivalent form involving a rescaled 'slip parameter $a = 1 - 2\zeta$, where $-1 \leq a \leq 1$:

$$\frac{D\mathbf{T}}{Dt} + \frac{\mathbf{T}}{\lambda} = a(\mathbf{D}\cdot\mathbf{T} + \mathbf{T}\cdot\mathbf{D}) + (\mathbf{\Omega}\cdot\mathbf{T} - \mathbf{T}\cdot\mathbf{\Omega}) + 2G_0\mathbf{D} \tag{4.2.4}$$

where $\mathbf{\Omega} = (\nabla\vec{v})^{\dagger} - \nabla\vec{v}$ is the vorticity tensor. The case of $a = 1$ corresponds to the UCM model, for $a = -1$, the lower convected Maxwell model, and if $a = 0$ the co-rotational Maxwell model (Bird *et al.*, 1987). In a steady simple shear flow, the velocity is $\vec{v} = [u(y), 0, 0]$, and gradients in the flow properties exist only in the y-

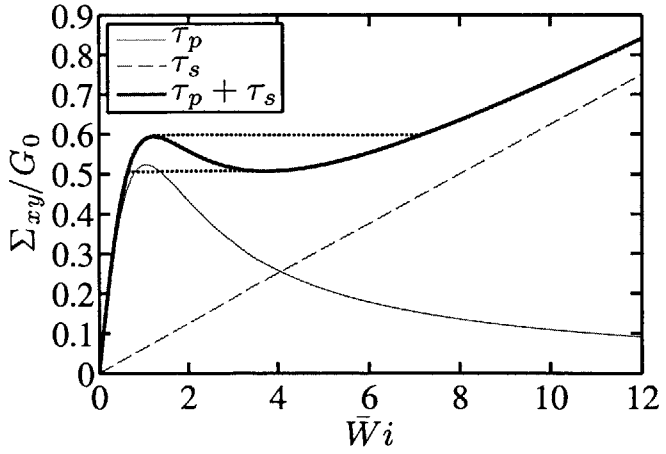

Figure 4.2.1: Non-monotonic homogeneous flow curve for simple steady shear of the JS model, for $a = 0.3$ and $\eta = 1/16$. $\bar{W}i = \lambda\mathcal{U}/H$ is the global Weissenberg number. The fine dashed lines are the polymeric and solvent contributions to the shear stress. The horizontal dashed lines highlight the range of stress in which the flow curve is multivalued. Without any plateau selection rule, the stress can take any value in between the two horizontal dashed lines.

direction, between $y = 0$ and $y = H$. In this reference frame the plate at $y = 0$ is fixed, (*i.e.* $u(0) = 0$), while the plate at $y = H$ is moving with $u(H) = \mathcal{U}$. Then, the characteristic global shear rate as $\bar{\dot{\gamma}} \equiv \mathcal{U}/H$, itself frame independent. The homogeneous solution for this flow is defined as the solution in which the local shear rate is constant $\dot{\gamma}(y) = \bar{\dot{\gamma}}$. Then, if $|a| \neq 1$, the polymeric shear stress, obtained from Eq. (4.2.4) and shown in Figure 4.2.1, is non-monotonic, and drops to zero as $\bar{\dot{\gamma}} \to 0$. To cure this pathology, the common practice is to add a solvent contribution to the stress. Then, the total deviatoric stress of the material is given by the sum of the polymeric stress and the solvent stress $\mathbf{\Sigma} \equiv \mathbf{T} + 2\eta_s\mathbf{D}$, where η_s is the solvent viscosity.

In a simple shear geometry, the momentum balance imposes the value of the local deviatoric shear stress to be constant $\Sigma_{xy}(y) = \bar{\Sigma}_{xy}$, where $\mathbf{\Sigma}_{ij}$ are the components of $\mathbf{\Sigma}$. Then, as pictured in Figure 4.2.1, the global flow curve $\Sigma_{xy}(y) = f(\bar{\dot{\gamma}})$ is known to be non-monotonic if $\eta \equiv \frac{\eta_s}{\eta_p} < \frac{1}{8}$ (Espanol *et al.*, 1996; Cates & Fielding, 2006; Fielding, 2007), which was identified early as being one of the sufficient criteria for triggering shear banding (Hunter & Slemrod, 1983; McLeish & Ball, 1986). Early studies on the JS model (Renardy *et al.*, 1987; Kolkka *et al.*, 1988; Renardy, 1995), empirical observa-

tions (Rehage & Hoffmann, 1991) and a clear analogy with first order phase transitions (Berret *et al.*, 1994) – especially the pressure/specific volume graphs – strongly supported the idea that this non-monotonic flow curve was the signature of an instability of the homogeneous flow. It was commonly observed that in a range of global shear rates $[\bar{\dot{\gamma}}_1, \bar{\dot{\gamma}}_2]$, in the vicinity of the decreasing part of the flow curve, the flow would become inhomogeneous, (*i.e.* $\dot{\gamma}(y) \neq \bar{\dot{\gamma}}$). For global shear rates 'in the shear-banding regime', *i.e.* for $\bar{\dot{\gamma}}_1 < \bar{\dot{\gamma}} < \bar{\dot{\gamma}}_2$, the flow would be split in domains with local shear rates $\bar{\dot{\gamma}}_1$ and $\bar{\dot{\gamma}}_2$, with the proportion of the sample in high (α) or low ($1-\alpha$) shear rates domains defined following a lever rule:

$$\bar{\dot{\gamma}} = \alpha \bar{\dot{\gamma}}_2 + (1-\alpha)\bar{\dot{\gamma}}_1 \tag{4.2.5}$$

From the momentum balance, the total stress must be homogeneous in simple shear. Thus, over the entire shear-banding regime, increasing the global shear rate will not increase the global shear stress, be it will change the relative proportions of the two bands. The additional injected power is used in turning more of the sample into the high shear rate domain, (*i.e.* in increasing α). But contrary to first order phase transitions for which the Maxwell equal area law (Reif, 1965) gives a criterion to select precise values of $[\bar{\dot{\gamma}}_1, \bar{\dot{\gamma}}_2]$ and thus also the *plateau* value of the stress, it was unclear what criterion could be used in the context of the JS model. For some time, it was even believed that such *plateau selection* would not be possible in any mechanical approach such as JS (Porte *et al.*, 1997).

4.2.1 dJS Model and Plateau Selection

After the initial studies of shear banding using the JS model, it was quickly realized that a key ingredient to the model was missing. The degeneracy in the selection of the plateau value was linked to the absence in the JS model of a characteristic length scale that would set the interface thickness between the shear bands, a point raised earlier in consideration of a simpler but similar model (Spenley *et al.*, 1996). Subsequently, many arguments, inspired from dynamical systems (Lu *et al.*, 2000) or from kinetic considerations (Radulescu *et al.*, 2000; Fielding & Olmsted, 2003), were proposed to

rationalize this new length scale as arising from a diffusion or *non-local* term missing in the JS equation. Rheological equations such as JS or UCM can be derived from the kinetic theory of dumbells (Larson, 1998; Bird *et al.*, 1987). And indeed, a careful treatment of the Fokker-Planck equation underlying the kinetic theory leading to the JS models or even the UCM model, brings a diffusion term coming from the finite size of the dumbells (El-Kareh & Leal, 1978). From those considerations, the JS model was modified to account for this diffusion term, leading to the so-called diffusive JS model (dJS). For anisotropic stress diffusion, the diffusion term takes the form $\nabla \cdot \mathcal{D} \cdot \nabla \mathbf{T}$ (Bird *et al.*, 2002). Then, the dJS model is defined as:

$$\frac{D\mathbf{T}}{Dt} + \frac{\mathbf{T}}{\lambda} = a(\mathbf{D}\cdot\mathbf{T} + \mathbf{T}\cdot\mathbf{D}) + (\mathbf{\Omega}\cdot\mathbf{T} - \mathbf{T}\cdot\mathbf{\Omega}) + 2G_0\mathbf{D} + \nabla\cdot\mathcal{D}\cdot\nabla\mathbf{T} \tag{4.2.6}$$

Evidently, the units of the diffusion coefficients $\mathcal{D}_{ij}$ are $[\mathrm{m}^2.\mathrm{s}^{-1}]$. A diffusion length scale $\ell_{ij} \equiv \sqrt{\mathcal{D}_{ij}\lambda}$ can be defined from each diffusion coefficient, which will be involved in the scaling of the typical width of the interface between shear bands.

The additional governing equations for the isothermal and incompressible flow are the continuity equation and the Cauchy momentum equation:

$$\nabla \cdot \vec{v} = 0 \tag{4.2.7}$$

and the Cauchy momentum equation:

$$\rho\left(\frac{\partial}{\partial t} + \vec{v}\cdot\nabla\right)\vec{v} = \nabla\cdot\left(\mathbf{T} + 2\eta_s\mathbf{D} - p\mathbf{I}\right) \tag{4.2.8}$$

p is the isotropic pressure and ρ is the density of the fluid, including the polymeric and the solvent part. $\mathbf{I}$ is the unit tensor.

4.2.2 Simple Shear and Dimensionless Groups

In simple shear flow, the governing equations for the polymer stress take the form given by:

$$\tau_{xx} + \lambda\frac{\partial}{\partial t}\tau_{xx} - (1+a)\lambda\dot{\gamma}\tau_{xy} = \ell_{xx}^2\frac{\partial^2}{\partial y^2}\tau_{xx} \tag{4.2.9}$$

$$\tau_{yy} + \lambda \frac{\partial}{\partial t}\tau_{yy} + (1-a)\lambda\dot{\gamma}\tau_{xy} = \ell_{yy}^2 \frac{\partial^2}{\partial y^2}\tau_{yy} \tag{4.2.10}$$

$$\tau_{zz} + \lambda \frac{\partial}{\partial t}\tau_{zz} = \ell_{zz}^2 \frac{\partial^2}{\partial y^2}\tau_{zz} \tag{4.2.11}$$

$$\tau_{xy} + \lambda \frac{\partial}{\partial t}\tau_{xy} + \frac{1}{2}\lambda\dot{\gamma}\Big[(1-a)\tau_{xx} - (1+a)\tau_{yy}\Big] = \eta_p\dot{\gamma} + \ell_{xy}^2 \frac{\partial^2}{\partial y^2}\tau_{xy} \tag{4.2.12}$$

Finally, the x-component of the momentum equation is Eq. (4.2.8),

$$\rho\frac{\partial u}{\partial t} = \frac{\partial \tau_{xy}}{\partial y} + \eta_s \frac{\partial^2 y}{\partial y^2} \tag{4.2.13}$$

Eqs. (4.2.9)–(4.2.13) are the governing equations of the fluid dynamics in simple shear flow. These equations are still dimensional, and seem to involve many quantities (variables and parameters). Dimensional analysis suggests dimensionless groups that reduce the apparent number of quantities. The different variables and parameters can be recast into six categories, using stress, time, viscosity, length and density as independent units. Then, from there the relevant dimensionless groups can be easily constructed. The stress variables turn into τ_{xx}/G_0, τ_{yy}/G_0, τ_{zz}/G_0, τ_{xy}/G_0. The time variable turns into the inverse of the Deborah number $De^{-1} \equiv t^* \equiv t/\lambda$ and the local Weissenberg number is $Wi \equiv \lambda\dot{\gamma}(y) = \lambda\frac{\partial u}{\partial y}$ (Dealy, 2010). The viscosity ratio is already defined $\eta \equiv \eta_s/\eta_p$. The length variable turns into $y^* = y/H$ and hence the Knudsen numbers for stress diffusion is $\xi_{ij} \equiv \ell_{ij}/H$. A Knudsen number is a ratio of the length akin to the mean free path associated with a diffusive process to a macroscopic length. From the density, one could construct the familiar Reynolds number, but since the main interest is in the creeping flow regime, instead the elasticity number is more relevant $\bar{El} \equiv \frac{\bar{Wi}}{\bar{Re}} = \frac{\lambda^2 G_0}{\rho H^2}$. $\bar{Wi} \equiv \frac{\lambda\mathcal{U}}{H}$ is the global Weissenberg number, and $\bar{Re} \equiv \frac{\rho\mathcal{U}H}{\eta_p}$ is the global Reynolds number. Conventionally, the Reynolds number is constructed from the total viscosity of the fluid $\eta_p + \eta_s$, but it is assumed that $\eta_p \gg \eta_s$ and so this approximation is accepatble. Finally, the slip parameter a (already dimensionless) is another relevant parameter.

4.3 Reaction–Diffusion Interpretation

To simplify even more the form of the governing equations, one can use dimensionless variables introduced previously by Radulescu *et al.* (1999)

$$K \equiv \sqrt{1-a^2}\lambda\frac{\partial u}{\partial y} = \sqrt{1-a^2}\lambda\dot{\gamma} \tag{4.3.1a}$$

$$S \equiv \sqrt{1-a^2}\frac{\tau_{xy}}{G_0} \tag{4.3.1b}$$

$$N \equiv (1-a)\frac{\tau_{xx}}{2G_0} - (1+a)\frac{\tau_{yy}}{2G_0} \tag{4.3.1c}$$

A final quantity is

$$Z \equiv (1-a)\frac{\tau_{xx}}{2G_0} + (1+a)\frac{\tau_{yy}}{2G_0} \tag{4.3.1d}$$

The total dimensionless stress is then $\sigma \equiv S + \eta K$ and is equal to its global value $\bar{\Sigma}$ everywhere in the sample, for a steady simple shear flow. Moreover, Radulescu *et al.* (1999) used a constant Knudsen number ξ_0 for every stress component. Then, after ignoring the z-component, the governing Eqs. (4.2.9)–(4.2.13) can be transformed into their dimensionless counterparts:

$$\frac{\partial}{\partial t^*}N = KS - N + \xi_0^2\frac{\partial^2}{\partial y^{*2}}N \tag{4.3.2}$$

$$\frac{\partial}{\partial t^*}Z = -Z + \xi_0^2\frac{\partial^2}{\partial y^{*2}}Z \tag{4.3.3}$$

$$\frac{\partial}{\partial t^*}S = -KN + K - S - \xi_0^2\frac{\partial^2}{\partial y^{*2}}K \tag{4.3.4}$$

$$\frac{1}{\bar{El}}\frac{\partial}{\partial t^*}K = \frac{\partial^2}{\partial y^{*2}}\Big\{S + \eta K\Big\} \tag{4.3.5}$$

Where the last equation is obtained by differentiating Eq. (4.2.13) with respect to y. The utility of these equations is their independence from the value of the slip parameter a, when $|a| \neq 1$. When the problem was expressed in this form, its connection to the more general class of reaction–diffusion problems was noticed by Radulescu *et al.* (1999). The governing equation for Z being decoupled, its analysis is not usually carried out

(Radulescu *et al.*, 1999, 2000). Moreover, in most experimental situations $\bar{El} \gg 1$. Thus, from Eq. (4.3.5), it is apparent that the dynamics of K happen on a much shorter time scale than the dynamics of S and N. For this reason, the evolution of the kinematics with time is not seen as an independent dynamical variable in the limit $\bar{El} \to \infty$, and the reaction–diffusion problem is written in terms of only two degrees of freedom, a dimensionless shear stress S and a dimensionless normal stress difference N (Radulescu *et al.*, 1999, 2000):

$$\partial_t \begin{pmatrix} S \\ N \end{pmatrix} = \xi_0^2 \partial_{y^*}^2 \begin{pmatrix} S \\ N \end{pmatrix} + \mathcal{C}(S, N; K) \tag{4.3.6}$$

where

$$\mathcal{C}(S, N; K) \equiv \begin{pmatrix} -S + K - KN \\ -N + KS \end{pmatrix} \tag{4.3.7}$$

Within this framework, Radulescu *et al.* (1999, 2000) derived a variety of important properties of shear banding flows. Here those those properties will be reconsidered in a different approach, but repeated connections with their approach will be made.

4.3.1 Steady Simple Shear and the Particle Analogy

Here, only steady flows (*i.e.* $De = 0$) are considered (Dealy, 2010), but transient effects have previously been discussed by Radulescu *et al.* (1999, 2003). For steady flows, Eq. (4.3.6) gives

$$\xi_0^2 \partial_{y^*}^2 \begin{pmatrix} S \\ N \end{pmatrix} = -\mathcal{C}(S, N; K) \tag{4.3.8}$$

Radulescu *et al.* (1999) noted that this equation is analogous to Newton's second law for the movement of a particle. The same analogy had been used previously by Spenley *et al.* (1996) also in the context of shear banding, and more generally by Pomeau (1986). But with two degrees of freedom S and N, the complexity of Eq. (4.3.8) made it difficult to find an analytic solution to the inhomogeneous shear-banding flow.

If the diffusion in the non-linear flow regime becomes anisotropic, a single Knudsen

number ξ_0 cannot describe the flow. If diffusion only concerns the shear component of the stress, then $\xi_{ij} = 0$ for every i and j except $\xi_{xy} = \xi$. In this case, dimensional considerations suggest that the diffusion can be expressed in terms of the shear rate tensor, rather than the stress tensor. In this alternate version of dJS, the diffusion term is of the form $2\eta_p \mathcal{D}_0 \nabla^2 \mathbf{D}$, with $\mathcal{D}_0 \equiv \frac{\xi^2 H^2}{\lambda}$. Note that the sign of this term has to be taken in accordance with the definition of the sign of the shear rate. This type of term was used recently by Sato *et al.* (2010) because it is much more mathematically tractable, as was already apparent in a simpler diffusive model used by Dhont (1999). No clear physical argument for the dominance of diffusion on shear components of the constitutive equation has yet emerged, and the assumption of a diffusion coefficient with no dependence on the shear rate is motivated by its mathematical simplicity.

In order to build on the recent developments by Sato *et al.* (2010), here it is assumed that the diffusion is of the anisotropic kind. More information on how this approach differs from from taking an isotropic stress diffusion coefficient (Radulescu *et al.*, 1999, 2003) is discussed by Sato *et al.* (2010). With diffusion on the shear rate and steady flow ($De = 0$), the system of Eqs. (4.3.2)–(4.3.5) is replaced by

$$N = KS \tag{4.3.9}$$

$$Z = 0 \tag{4.3.10}$$

$$\xi_0^2 \frac{\partial^2}{\partial y^{*2}} K = -KN + K - S \tag{4.3.11}$$

$$\frac{\partial^2}{\partial y^{*2}} \left\{ S + \eta K \right\} = 0 \tag{4.3.12}$$

Eq. (4.3.12) is redundant since the total stress must be spatially uniform. Eq. (4.3.10) is trivial. Eq. (4.3.9) can be used to replace N in Eq. (4.3.11). Then, it is convenient to regard K as the main variable of the problem and by using $\sigma = \bar{\Sigma} = S + \eta K$, S is expressed as a function of K

$$\xi^2 \frac{\partial^2 K}{\partial y^{*2}} = \eta K^3 - \sigma K^2 + (1 + \eta) K - \sigma = 0 \tag{4.3.13}$$

If y^* is reinterpreted as a time variable, then Eq. (4.3.13) is analogous to the equation of the motion of a particle of mass $m \leftrightarrow \xi^2$ and position $q \leftrightarrow K$ under a force deriving from a quartic potential energy function $V(q)$ depending on the parameters $\bar{\Sigma}$ and η. This analogy was stated explicitly in the recent study by Sato *et al.* (2010), building on the idea invoked earlier with Eq. (4.3.8). Using the chain rule, Eq. (4.3.13) is transformed into its energy form:

$$\frac{1}{2}m\dot{q}^2 + V(q) = E \tag{4.3.14}$$

$$V(q) \equiv Fq^4 + Dq^3 + Cq^2 + Bq + A \equiv -\frac{1}{4}\eta q^4 + \frac{1}{3}\sigma q^3 - \frac{1}{2}(1+\eta)q^2 + \sigma q \tag{4.3.15}$$

where E is the total energy of the system, which is conserved. The analogy is $\dot{q} \leftrightarrow \frac{dK}{dy^*}$. To make the analogy explicit, the analogy $t \leftrightarrow y^*$ is made. The double arrow '$\leftrightarrow$' is used here to mean *stands for* when defining the quantities in the particle analogy to differentiate these definitions with regular definitions using '$\equiv$'. In the language of mathematicians, the new variables are used to 'define a new model' for the dJS equation (Hodges, 1997). This is what is meant by 'making an analogy'. In some sense, one could have even used $\leftrightarrow$ in defining the dimensionless variables K, S, N and Z, since they carried the new meaning given in the framework of reaction–diffusion by Radulescu *et al.* (1999).

This new interpretation enables a fuller realization of the syntactic power of the dJS equation, but before the analogy is further exploited, from Eq. (4.3.13), it can be used to obtain the non-monotonic homogeneous flow curve mentioned previously. For a homogeneous flow $K(y) = \bar{K} \equiv (1-a^2)^{1/2}\bar{W}i$. Then $\partial_{y^{*2}}K \equiv 0$ (where $\partial_{y^{*2}}$ stands for $\frac{\partial^2}{\partial y^{*2}}$) for Eq. (4.3.13) reaches

$$\sigma = \frac{\bar{K}}{1+\bar{K}^2} + \eta\bar{K} \tag{4.3.16}$$

Note that this solution can also be obtained by taking $\xi^2 = 0$, (*i.e.* the particle has no mass). This is another way of thinking about why the inhomogeneous flow curve can only be obtained by the addition of a diffusive term in JS.

4.3.2 Properties of the Potential

In the particle analogy, it is important to realize that regions where the shear rate changes abruptly correspond to time intervals where the particle is moving fast, *i.e.* near local minima of the potential $V(q)$ – the inner solution described by Radulescu *et al.* (1999). On the contrary, regions of fairly constant shear rate correspond to time intervals where the particle is moving slowly, near the turning points of the potential $V(q)$ (Landau & Lifshitz, 1976) – the outer solution. The potential $V(q)$ is a quartic potential. The general solution of the motion of a particle in a quartic potential is well known and involves elliptic functions for $q(t)$. A short recent summary of important analytical results can be found by Sanchez *et al.* (1993), who describe the various possible shapes for the quartic potential, depending on relations between the coefficients of the potential (A, B, C, D, F). Evidently, the shape of the potential is critical in determining the solution. To simplify the study of the shape of the potential, three equilibrium points (*i.e* roots of the algebraic equation $dV(q)/dq = 0$) are defined following the ordering $q_l < q_m < q_n$. Those solutions are real if $\eta < 1/8$, *i.e.* when the homogeneous flow curve is non-monotonic. Since $F < 0$, $\lim_{q\to\pm\infty} V(q) = -\infty$, and by continuity, q_l and q_h are unstable equilibrium points whereas q_m is a stable equilibrium, as illustrated on Figure 4.3.1. The particle will move fast near q_m and slowly near q_l and q_h.

To be able to use tabulated coefficient relations of Sanchez *et al.* (1993), it is convenient to rescale the variable q to eliminate the linear term of the potential by using the middle root q_m of the equation $dV(q)/dq = 0$. The idea is to translate the coordinate system such that it is centered on the middle root value, hence $x \equiv q - q_m$. Then, from Sanchez *et al.* (1993) a new potential is found $V^*(x) \equiv A^*x^2 + B^*x^3 + C^*x^4$, such that

$$\frac{1}{2}m\dot{x}^2 + V^*(x) = E^* = E - V(q_m) \tag{4.3.17}$$

With

$$\begin{cases} A^* \equiv C + 3Dq_m + 6Fq_m^2 = -\frac{\eta+1}{2} + \sigma q_m - \frac{3}{2}\eta q_m^2 \\ B^* \equiv D + 4Fq_m = \sigma - \eta q_m \\ C^* \equiv F = -\eta/4 \end{cases} \tag{4.3.18}$$

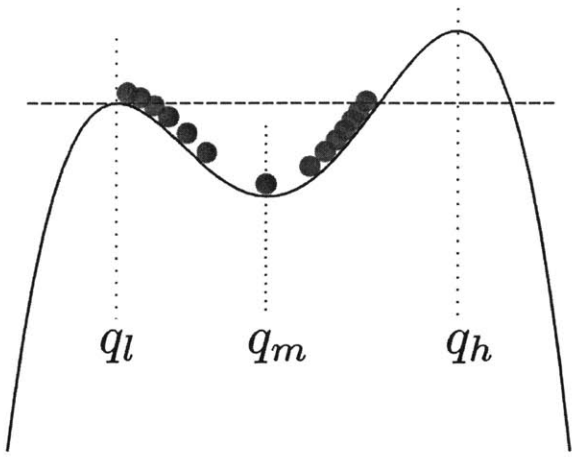

Figure 4.3.1: Sketch of the quartic potential with regions of fast moving and slow moving particle. $q_l < q_m < q_h$ are the equilibrium points. The dashed line is the total energy line above which the motion is unbounded, because the particle may escape the local potential well from the left.

In the rheological framework, the stress must be homogeneous, but the local shear rate can be inhomogeneous. The shear rate associated with a given stress can take a range of values. On the global scale this leads to the so-called stress plateau. For a value of $\bar{\Sigma}$ one can realize several values of $\bar{K}$. This degeneracy means that given a value of stress in the bulk $\bar{\Sigma}$, there is no bulk mechanism capable of selecting a value of $\bar{K}$. This degeneracy means that the solution $q(t)$ contains an arbitrary parameter linked to the arbitrariness of the value of $\bar{K}$. As a particular consequence, the equilibrium points q_l and q_h need to have the same relative stability, *i.e.* as stated by Sato *et al.* (2010) the potential $V(q)$ or $V^*(x)$ needs to be symmetric[1].

For the potential to be symmetric, the coefficients must obey the relation $B^{*2} = 4A^*C^*$. Using Eq. (4.3.18), this equation, together with $\left.\frac{dV}{dq}\right|_{q_m} = 0$ reads

$$B^{*2} = 4A^*C^* \Leftrightarrow \frac{\sigma^2}{9} - \frac{\eta^2 q_m^2}{2} + \frac{\eta\sigma q_m}{3} - \frac{\eta(\eta+1)}{2} = 0 \tag{4.3.19}$$

$$\left.\frac{dV}{dq}\right|_{q_m} = 0 \Leftrightarrow \eta q_m^3 - \sigma q_m^2 + (1+\eta)q_m - \sigma = 0 \tag{4.3.20}$$

Therefore, there are two algebraic equations with unknowns (q_m, $\bar{\Sigma}$). By eliminating

[1]This symmetry is derived mathematically in greater detail in Appendix C.

the variable q_m, one obtains

$$\begin{array}{c} \sigma(9\eta - 18\eta^2 - 2\sigma^2) \\ \sigma = \pm\dfrac{3\sqrt{\eta - 2\eta^2}}{\sqrt{2}} \quad \text{or} \quad \sigma = 0 \end{array} \tag{4.3.21}$$

The negative and positive values correspond to the arbitrariness of the stress sign. Thereafter, $\bar{\Sigma} > 0$ by convention. From Eq. (4.3.21) it is evident that for a given value of the material parameter η, there is a unique value of stress $\bar{\Sigma}$ corresponding to the inhomogeneous solution. For the complete solution to the inhomogeneous flow, one should then replace any instance of the mean stress $\bar{\Sigma}$ by its value depending on η. In particular, now the expression for the three equilibrium points of the potential are:

$$\begin{cases} q_l = \frac{\sqrt{1/\eta-2}-\sqrt{1/\eta-8}}{\sqrt{2}} \\ q_m = \frac{\sqrt{1/\eta-2}}{\sqrt{2}} \\ q_h = \frac{\sqrt{1/\eta-2}+\sqrt{1/\eta-8}}{\sqrt{2}} \end{cases} \tag{4.3.22}$$

Note that since the potential is symmetric, $q_m = \frac{q_l+q_h}{2} = \frac{\bar{\sigma}}{3\eta}$. From Eqs. (4.3.21) and (4.3.22), A^*, B^* and C^* are written as functions of η only

$$\begin{cases} A^* = \frac{1-8\eta}{4} \\ B^* = 0 \\ C^* = -\eta/4 \end{cases} \tag{4.3.23}$$

Figure 4.3.2 draws the original potential $V(q)$ and the rescaled potential $V^*(x)$, for a few values of η. As already mentioned, the potential $V(q)$ has a unique equilibrium point q_m when $\eta \geq 1/8$. At the point $\eta = 1/8$, q_m is a multiple root and $A^* = 0$. This point is the critical point.

The characteristic frequency of the particle near q_m is given by the harmonic approximation of $V(x)$ near $x = 0$, *i.e* by $\omega_0 = \sqrt{\frac{1-8\eta}{4m}}$. $1/\omega_0$ is the time scale of the problem. This is a crucial point, as the time interval [0,1] was indefinite and so it is now clear that the time for the particle to translate from q_l to q_h is in units of the harmonic period near q_m. Note that at the critical point, $\omega_0 = 0$, because the lowest order of thc potential near q_m is quartic, the particle time scale diverges.

Returning to the original rheological framework, the inverse of the harmonic fre-

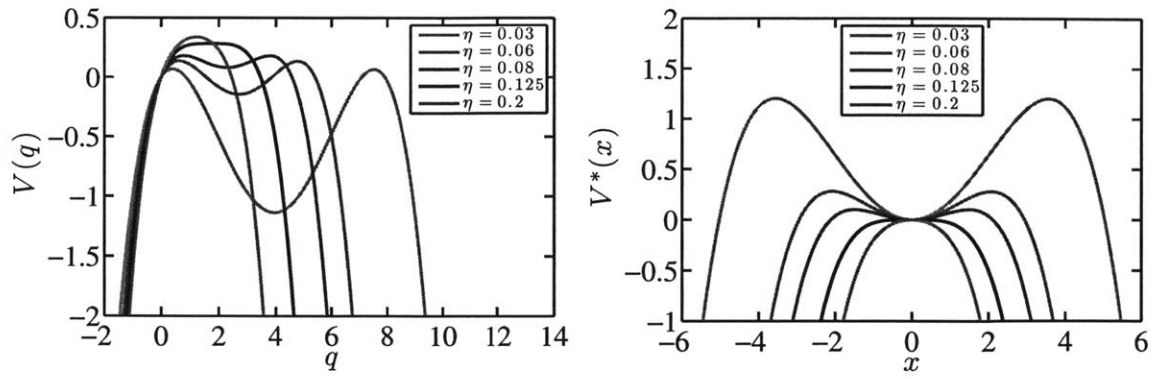

(a) (b)

Figure 4.3.2: Plot of (a) the original quartic potential $V(q)$ and (b) the rescaled potential $V^*(x)$, for $\eta = 0.03, 0.06, 0.08, 1/8, 0.2$.

quency is identifiable with the dimensionless width of the interface between domains of different shear rates $w \leftrightarrow 1/\omega_0$. This corresponds to the inner solution in the reaction–diffusion framework (Radulescu *et al.*, 2000). Thus, the interface width appears to diverge as η approaches the critical point.

4.3.3 Naive Flow Curve and Law of Equal Distances

Returning to the rheological framework, the values $K_l \leftrightarrow q_l$ and $K_h \leftrightarrow q_h$ are the outer solutions. As explained already by Radulescu *et al.* (1999, 2000), in the limit where $\xi \ll 1$, one has to seek matching between the homogeneous solution with the shear-banding solution at K_l and K_h. Then, K_l and K_h are identified as the boundary of the stress plateau with magnitude $\bar{\Sigma}$. Figure 4.3.3 displays the homogeneous and inhomogeneous flow curves for $\eta = 0.04$, highlighting the connection points K_l and K_h between the two solutions. Ultimately, the flow curve that would be measured for a steady simple shear is

$$\sigma(\bar{K}) = \begin{cases} \dfrac{\bar{K}}{1+\bar{K}^2} + \eta K & \text{if } \eta \geq \frac{1}{8} \text{ or } \bar{K} \notin [K_l, K_h] \\ \dfrac{3\sqrt{\eta - 2\eta^2}}{\sqrt{2}} & \text{if } \eta < \frac{1}{8} \text{ or } \bar{K} \in [K_l, K_h] \end{cases} \tag{4.3.24}$$

The plateau intersects the homogeneous flow curve at three locations K_l, K_m and K_h. Then, the symmetry of the potential implies $K_m \frac{K_l + K_h}{2}$. Thus the plateau is such

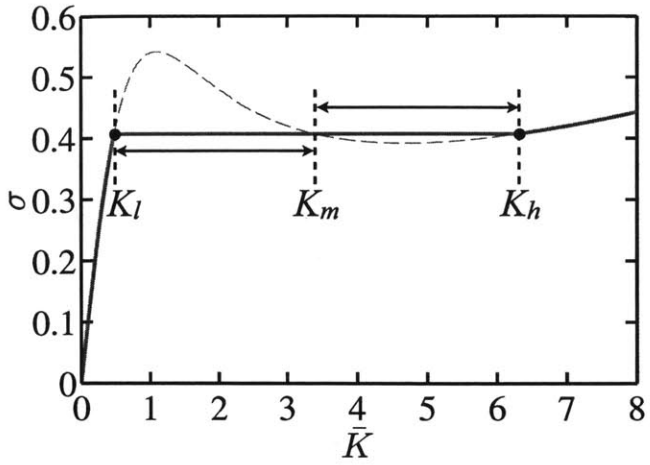

Figure 4.3.3: Dimensionless homogeneous and inhomogeneous flow curve for $\eta = 0.04$. The dashed line is the unstable homogeneous solution. The black circles highlight the connection points K_l and K_h between the inhomogeneous and homogeneous solution. The connection points are related by $K_m - K_l = K_h - K_m$.

that $K_m - K_l = K_h - K_m$. By analogy with the law of equal areas, the constraint can be called the *law of equal distances*. A similar law was found by Dhont (1999) on a scalar model analogue of the dJS model. This result would be an easy criterion, but it does not seem to be recovered by numerical simulations of the dJS model (Fielding, 2005, 2007). The difference arises because a key ingredient has been forgotten in the derivation. This key ingredient was also missing in the derivations of Sato *et al.* (2010).

4.4 Role of Diffusion on the Flow Kinematics

Sato *et al.* (2010) made use of the naive flow curve to obtain a solution for the shear rate profile from Eq. (4.3.13). They considered two boundary conditions for K, $\partial_{y^*} K = 0$ at $y^* = 0$ and 1, assumed to come from $\partial_{y^*} S|_{0,1} = 0$, which is supposed to represent the fact that there is no flux of polymeric components at the wall (Rossi *et al.*, 2006; Sato *et al.*, 2010). In the particle analogy, the boundary conditions translate into the requirement that the particle start with no initial velocity at $t = 0$ and end with no velocity at $t = 1$ (in units of $1/\omega_0$.) If the outer part of the inhomogeneous solutions is required to connect with the homogeneous solutions (Radulescu *et al.*, 1999, 2000), then

it is assumed that $q(0) = q_l$ and $q(1) = q_h$ and $\dot{q}(0) = 0$ and $\dot{q}(1) = 0$, the particle is moving from left to right on the potential. Note that by symmetry one could have chosen $q(0) = q_h$ and $q(1) = q_l$ as well, (*i.e.* the particle moves from right to left). Since the total energy of the particle is conserved, its value is given by the value of the potential at q_l or q_h. Then, in the reduced variable x, the energy of the system is given by,

$$E^* = V^*(q_l - q_m) = \frac{(8\eta - 1)^2}{16\eta} \tag{4.4.1}$$

Returning to Eq. (4.3.17), which reads,

$$\frac{1}{2}m\dot{x}^2 + \left(\frac{1 - 8\eta}{4}\right)x^2 - \frac{\eta}{4}x^4 = \frac{(8\eta - 1)^2}{16\eta} \tag{4.4.2}$$

This equation is separable, $[E^* - V^*(x)]^{-1/2}dx = \sqrt{\frac{2}{m}}dt$. Using the convention that the particle moves from left to right, the solution is found, written with the particle notation $x(t)$, or with the dimensionless rheological notation $K(y^*)$,

$$x(t) = \frac{q_h - q_l}{2}\tanh\Big(\omega_0(t - t_0)\Big) \quad \Leftrightarrow \quad q(t) = \frac{q_h + q_l}{2} + \frac{q_h - q_l}{2}\tanh\Big(\omega_0(t - t_0)\Big)$$

$$K(y^*) = \frac{K_h + K_l}{2} + \frac{K_h - K_l}{2}\tanh\left(\frac{y^* - y_0^*}{w}\right) \quad = \quad K_m + \frac{\Delta K}{2}\tanh\left(\frac{y^* - y_0^*}{w}\right) \tag{4.4.3}$$

where the plateau range is defined $\Delta K \equiv K_h - K_l$ and $w = 2\xi/\sqrt{1 - 8\eta}$. The governing equation for the parameters N and Z are given in Eq. (4.3.9) and (4.3.10), respectively, and hence their values across the gap are given by

$$N(y^*) = (\sigma - \eta K_m)\left[K_m + \frac{\Delta}{2}\tanh\left(\frac{y^* - y_0^*}{w}\right)\right] - \eta\frac{\Delta}{2}\tanh\left(\frac{y^* - y_0^*}{w}\right)\left[K_m + \frac{\Delta}{2}\tanh\left(\frac{y^* - y_0^*}{w}\right)\right] \tag{4.4.4}$$

$$Z(y^*) = 0 \tag{4.4.5}$$

The dimensional shear rate, polymeric shear stress and normal stress differences are given by the equations

$$\dot{\gamma} = \frac{1}{\sqrt{1 - a^2\lambda}}K \tag{4.4.6a}$$

$$\tau_{xy} = \frac{G_0}{\sqrt{1-a^2}} S = \frac{G_0}{\sqrt{1-a^2}} (\sigma - \eta K) = \frac{G_0}{\sqrt{1-a^2}} \left(\frac{3\sqrt{\eta - 2\eta^2}}{\sqrt{2}} - \eta K \right) \tag{4.4.6b}$$

$$N_1 \equiv \tau_{xx} - \tau_{yy} = \frac{2G_0}{1-a^2}(N + aZ) = \frac{2G_0}{1-a^2} N \tag{4.4.6c}$$

$$N_2 \equiv \tau_{yy} - \tau_{zz} = \frac{G_0}{1+a}(Z - N) - \tau_{zz} = -\frac{G_0}{1+a} N \tag{4.4.6d}$$

At this point, y_0^* is an unknown constant which represents the location of the interface between bands in the gap. Following the naive shear-banding scenario described in the introduction, from Eq. (4.2.5) it is expected that $y_0^* = (1-\alpha) = \frac{K_h - \bar{K}}{K_h - K_l}$. Indeed, this is the value of y_0^* set by Sato *et al.* (2010). But as will be shown in Section 4.4.1, this value is not strictly rigorous.

4.4.1 Modification of the Lever Rule by non-Local Effects

The rigorous value of y_0^* needs to be deduced from the requirement that the integral of the shear rate in the sample should be equal to its macroscopic value, or equivalently, that the fluid velocity at $y^* = 1$ is equal to the upper wall velocity. This was indeed noted by Sato *et al.* (2010) and stated in dimensionless form (Eq. (7) of Sato *et al.* (2010)):

$$\int_0^1 K(y^*) dy^* = \bar{K} \tag{4.4.7}$$

where $\bar{K} = \sqrt{1-a^2}\lambda \mathcal{U}/H$. By integrating the profile obtained in Eq. (4.4.3), one obtains the velocity profile in the gap

$$U(y^*) = K_m y^* + \frac{\Delta}{2} w \ln \left[\cosh\left(\frac{y^* - y_0^*}{w} \right) \Big/ \cosh\left(\frac{y_0^*}{w} \right) \right] \tag{4.4.8}$$

where $U \equiv \sqrt{1-a^2}\lambda u/H$, and $u(y)$ is the dimensional local velocity across the gap introduced in Section 4.2. The rigorous expression for y_0^* is determined by satisfying Eq. (4.4.7), and it is actually given by

$$y_0^* = \frac{w}{2} \ln \left[\frac{e^{\frac{1}{w}} - e^{\frac{2\alpha - 1}{w}}}{e^{\frac{2\alpha-1}{w}} - e^{-\frac{1}{w}}} \right] \tag{4.4.9}$$

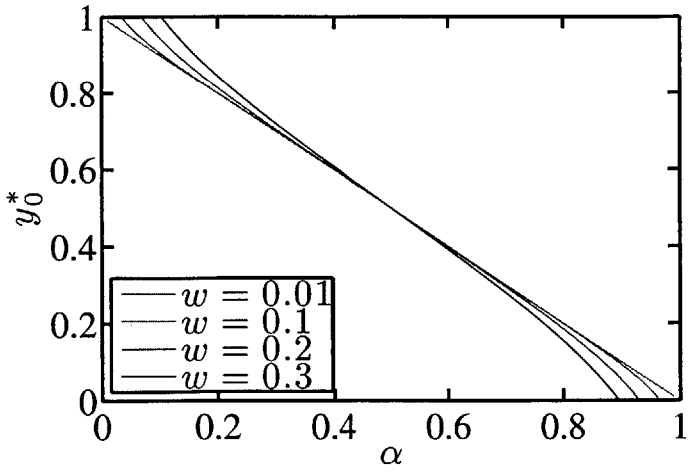

Figure 4.4.1: Modification of the lever rule y_0^*. Value of α for various values of $w = 0.01, 0.1, 0.2, 0.3$. This analytic result has only a heuristic purpose since the precise incorporation of the constraint on the average value of the shear rate would modify the form of this result.

Then, only at the lowest order in $(2\alpha - 1)$ and $1/w$, is $y_0^* = 1 - \alpha$, *i.e.* the interface is located at the position expected from the lever rule. If the interface is too close to the walls, or if the width of the interface w starts to be large, this approximation is invalid. This constraint was explicitly stated in the reaction–diffusion framework by Radulescu *et al.* (1999) in terms of non-asymptotic effects. The case where w becomes large occurs if the Knudsen number ξ is not negligible. It corresponds to the limit in which non-local effects are important (Masselon *et al.*, 2008, 2010). In Figure 4.4.1 the modification of the lever rule $y_0^*(\alpha)$ by non-local effects for various values of w is shown. A key point is that if $w \neq 0$, there are always non-local effects when one of the shear bands – low or high – is small.

In the framework of the energetic potential, the result comes from the inconsistency in the assumptions that the particle starts at a local maximum in the potential at $K_l \leftrightarrow q_l$ or at $K_h \leftrightarrow q_h$ where $dV/dK = dV/dq = 0$ and that it also starts with no initial velocity $dK/dy^* = dq/dt = 0$ due to the condition of no diffusion at the walls. Without any initial velocity and without any local gradient in the potential to provide an accelerative force, the particle must remain stationary and therefore cannot traverse the potential, thereby preventing the shear rate from reaching its asymptotic values K_l and K_h in

the gap interval $y^* \in [0,1]$. As stated in Radulescu *et al.* (1999), matching rigorously happens only if $y^* \in [-\infty, \infty]$. Moreover, the errors made on the boundary conditions are related. For instance, if the interface is close to the wall at $y^* = 0$, then $K(0) = K_l$ and $\partial_{y^*} K(0) = 0$ will be poorly satisfied whereas $K(1) = K_h$ and $\partial_{y^*} K(1) = 0$ will be approximately correct. Physically, this paradox can be interpreted by the fact that for any finite interface width (*i.e.* $\xi > 0$), in the limit of either $\dot{\gamma} \to \dot{\gamma}_1$ or $\dot{\gamma} \to \dot{\gamma}_2$, the interface width cannot vanish as it is squeezed closer to the wall. In either limit then, it is not possible for the interface to lie next to the wall and to satisfy the condition of no flux through the wall, since the gradients in shear rate are necessarily finite in the interface between the bands. This point is elaborated further along with comments on some of the mathematical challenges associated with redressing the problem by Fardin *et al.* (2012b).

In the strictest sense, the solution for the shear rate and velocity profiles given by Eqs. (4.4.3) and (4.4.8), respectively, are only valid in the limiting case of $w \leftrightarrow 0$. In this case the interface becomes vanishing small such that for any value of $0 \leq \alpha \leq 1$, the interface effectively lies infinitely far away from either wall and the effects of non-locality do not propagate to the walls. As the strength of the stress diffusion increases, either at small gaps or for large diffusion coefficients, the accuracy of these solutions will diminish. Nevertheless, experimental measurements of non-local effects in the flow of shear-banding WLM solutions indicate that typical interfacial widths are on the order of $\ell \sim \mathcal{O}(10)$ μm (Masselon *et al.*, 2008; Helgeson *et al.*, 2009a,b), whereas the gaps sizes in most TC flows are on the order of $d \sim \mathcal{O}(1)$ mm. This disparity in length scales suggests that most viscometric experiments with WLM systems using conventional rotational rheometers occur in the limit $\xi \ll 1$ and $w \ll 1$, where the approximations made to obtain Eqs. (4.4.3) and (4.4.8) are most valid. These results can then be utilized further to obtain estimates of the stresses across the gap in the flow of a shear-banding fluids, enabling the development of a theoretical dimensionless stability criterion for the onset of secondary flows in WLM fluids.

4.5 Criterion for Purely Elastic Taylor-Couette Instability in Shear-Banding Flows

In the past twenty years, shear-banding flows have been probed by various techniques, such as rheometry, velocimetry and flow birefringence. In micellar solutions, many of the data collected exhibit unexplained spatio-temporal fluctuations. Recently, it has been suggested that those fluctuations originate from a purely elastic instability of the flow. In cylindrical Couette geometry, the instability is reminiscent of the Taylor-like instability observed in non-shear-banding viscoelastic polymer solutions. The stability criterion has been previously discussed in Section 2.2.5 and in the remainder of this Chapter, this criterion for a purely elastic TC instability is adapted to shear-banding flows. Three categories of shear-banding flows with curved streamlines are also proposed based on this stability criterion.

4.5.1 Rheological and Geometric Scaling of Purely Elastic Flow Instabilities

In Section 2.2.5, the TC instability of the purely Newtonian fluid and the purely elastic fluid was discussed. These are both idealizations that facilitate the analysis, but which capture only the behavior of very specific fluids. In general, however, non-Newtonian fluids can exhibit other attributes such as a Newtonian solvent contribution to the stress, a spectrum of relaxation times instead of a single relaxation time λ, and shear-thinning (Larson, 1998). Experiments with such non-Newtonian fluids have documented the effects of these rheological behaviors on the elastic TC instability (Larson *et al.*, 1994). To rationalize these observations as well as to generalize the elastic instability criterion to different kinds of flows with curved streamlines, McKinley and coworkers established a general criterion for elastic instabilities (Pakdel & McKinley, 1996; McKinley *et al.*, 1996). If $Re = 0$, then the flow of a viscoelastic fluid is unstable if

$$\frac{\mathcal{L}}{\mathcal{R}}\frac{N_1}{\tau_{xy}} > m \tag{4.5.1}$$

where $N_1 \equiv \tau_{xx} - \tau_{yy}$ is the first normal stress difference, τ_{xy} is the shear stress, $\mathcal{L}$ is

the characteristic distance over which perturbations relax along a streamline (Pakdel & McKinley, 1996), and $\mathcal{R}$ is the characteristic radius of curvature of the streamlines. For a purely viscoelastic fluid, $\mathcal{L} \simeq \lambda \mathcal{U} \sim \lambda R_i \Omega_i = Wi_d$, $\mathcal{R} \sim R_i$ and $N_1/\tau_{xy} \sim Wi$ (Pakdel & McKinley, 1996) and one recovers the criterion of Larson *et al.* (1990) for the purely elastic instability: $\sqrt{\Lambda} Wi > m$ (Larson *et al.*, 1990).

In the remainder of this Chapter, a general criterion for the onset of flow instabilities in shear-banding WLM fluids is proposed. The aim is to determine the functional form of the dimensionless ratio $\frac{\mathcal{L}}{\mathcal{R}} \frac{N_1}{\tau_{xy}}$ framed with respect to the general criterion derived by (Pakdel & McKinley, 1996; McKinley *et al.*, 1996). By analogy with polymer solutions, one can expect that this ratio can be expressed in terms of a relevant geometric ratio and an appropriately defined Weissenberg number.

Effective Gap

Roughly speaking, a shear-banding flow is reminiscent of a first-order phase transition as discussed in Section 4.2. Above a lower critical Weissenberg number Wi_l, the shear stress plateaus. Then, up to a second higher critical Weissenberg number Wi_h, the flow is inhomogeneous, split into two bands with local Weissenberg numbers Wi_l and Wi_h. To leading order, for $Wi \in [Wi_l, Wi_h]$, an increase in the value of the macroscopic Weissenberg $\bar{Wi}$ only increases the proportion $\alpha \in [0, 1]$ of the high-Wi band, following a lever rule $Wi \approx \alpha Wi_h + (1 - \alpha) Wi$ presented previously in Eq. (4.2.5). This scenario has been roughly confirmed experimentally with various techniques (*e.g.*, pure viscometry, velocimetry, birefringence, etc.) but many fluctuating behaviors were observed in all the gathered data (Lerouge & Berret, 2010).

The relevant geometric ratio can indeed be inferred from experiments through the notion of an *effective gap*. In recent experiments (Fardin *et al.*, 2009, 2010), it was observed that the vortices were mainly localized in the high-Wi band, and that each interfacial wavelength between the bands corresponded to a pair of counter-rotating vortices (Fardin *et al.*, 2009), as illustrated in Figure 4.5.1 (a). It was also found that the wavelength increases upon the increase of the global shear rate, so one could infer the scaling $l/d \sim Wi$ (Lerouge *et al.*, 2008; Fardin *et al.*, 2009). Then, by combining

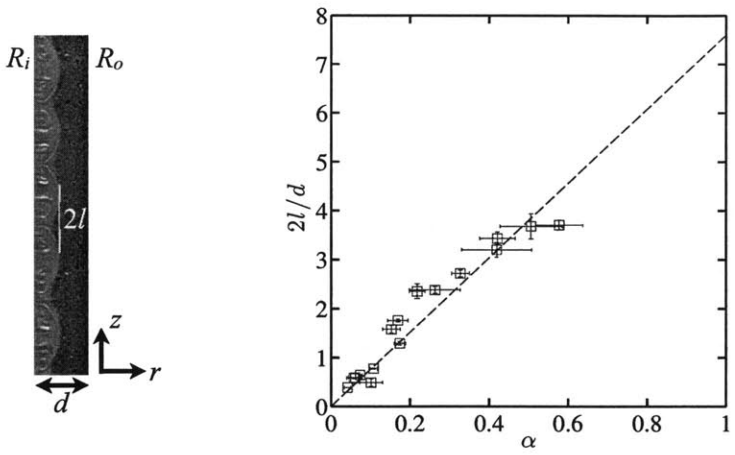

(a) (b)

Figure 4.5.1: Effective gap scaling. (a) Overlay of two visualization techniques showing the secondary vortex flow in the high-Wi band for $\alpha \simeq 0.4$ (Fardin *et al.*, 2009). (b) Wavelength scaling, following $l = n\alpha d$, with $n = 3.8 \pm 0.1$. For $\alpha > 0.6$, the spatio-temporal dynamics of the vortex flow do not allow us to extract a single wavelength (Lerouge *et al.*, 2008; Fardin *et al.*, 2009). For $\alpha < 0.05$, the size of the band is smaller than the spatial resolution.

this scaling and the lever rule it was noted that $l = n\alpha d$ instead of $l = nd$, where n is a number of order unity, whose precise value depends on the boundary conditions. The extent of the high-Wi band acts as the effective gap. Increasing the global Wi increases α and so increases l. The validity of this scaling is shown in Figure 4.5.1 (b) by re-plotting $2l/d$, (*i.e.* twice the wavelength of vortices), against α instead of Wi (Lerouge *et al.*, 2008).

Local Weissenberg Number

As explained in the introduction, in a shear-banding flow, the global value of Wi is not a good measure of the local Weissenberg number in the parts of the flow that are unstable. Instead, the dimensionless group relevant to the flow instability is the local value of Wi_h in the high shear rate band. In the instability criterion, one must replace Wi by Wi_h. Accordingly, the criterion for elastic instabilities in shear-banding flows should involve the term

$$\Sigma^* = \sqrt{\alpha\Lambda} Wi_h \tag{4.5.2}$$

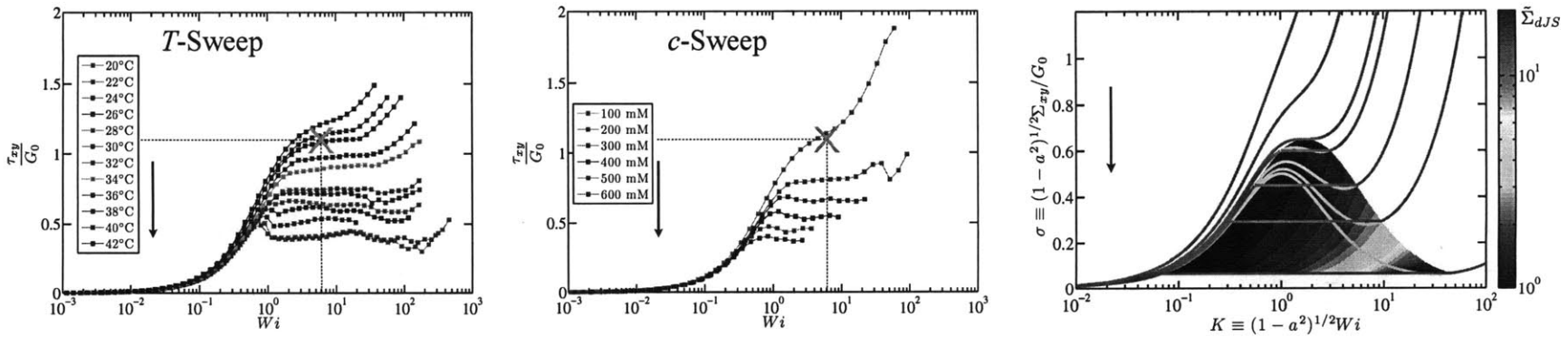

(a) (b) (c)

Figure 4.5.2: Experimental and theoretical 'flow-phase diagrams' (Berret *et al.*, 1997) measured with a cone-and-plate device. (a) Dimensionless flow curves for varying temperatures with a 100:60 mM CPyCl:NaSal system. (b) Dimensionless flow curves for varying concentration in an N:300 mM CTAB:$NaNO_3$ system. The arrow points in the direction of higher c or lower T. The orange X lies at the same Wi-τ_{xy}/G_0 value indicating the approximate location of the *critical point* in the flow curves which is very similar for both systems suggesting they have a similar values for the coefficient a in the framework of the dJS model. For systems with clearly different critical points, refer to Figure 2 (a) in Fardin *et al.* (2011). (c) Analytical dimensionless flow curves obtained for the dJS model in simple shear. The different flow curves are obtained for varying η. The color map gives the value of the scaled dimensionless criterion $\tilde{\Sigma}_{dJS} = \Sigma_{dJS}\sqrt{\frac{1-a^2}{\Lambda}}$. The arrow points in the direction of lower η.

It has been observed in experiments that increasing the concentration c of surfactant, or decreasing the temperature T tends to increase the value of Wi_h. This fact is illustrated in Figure 4.5.2 (a) in the flow curves of two different surfactant systems (Berret *et al.*, 1997; Cappelaere & Cressely, 1997). Note that as c increases, the dimensionless stress plateau decreases and its range of Weissenberg numbers increases. In particular, Wi_h shifts to higher values. For the most concentrated solutions, viscometric measurements had to be stopped because the sample was ejected from the rheometer. This phenomenon is believed to be due to an instability of the free surface of the system, driven by the underlying bulk viscoelastic instability. However, the instability of the free surface could be triggered by second normal stress differences (Skorski & Olmsted, 2011). Furthermore, owing to the larger values of Wi_h solutions of high c or at low T are more likely to be unstable.

4.5.2 A Stability Criterion Based on the dJS Model

So far, a new relevant dimensionless group for elastic instabilities in shear-banding flows has been suggested, without appealing to any particular rheological model. To enhance this argument, the form of the instability criterion will be based on the diffusive Johnson-Segalman (dJS) model discussed above. Recently, it has even been used in numerical simulations confirming the presence of a secondary vortex flow triggered by a bulk viscoelastic instability in the high-Wi band (Fielding, 2010).

An analytic expression for the stress ratio in the high-Wi band is needed to evaluate the ratio in Eq. (4.5.1). In the small gap limit of the TC geometry, one can assume that the stress profile across the gap is homogeneous in order to use the inhomogeneous plane Couette solution recently derived previously in this Chapter. For steady flow in the shear-banding regime, the dimensionless shear stress is

$$\sigma = 3\frac{\sqrt{\eta - \eta^2}}{\sqrt{2}} \tag{4.3.21}$$

and the first normal stress difference is related to the dimensionless quantity N given by

$$N = KS = K(\sigma - \eta K) \tag{4.3.9}$$

where $K(y^*) = \sqrt{1-a^2}Wi(y^*)$ and $S(y^*) \equiv \sqrt{1-a^2}\frac{T^p_{xy}(y^*)}{G_0}$ are, respectively, a dimensionless shear rate and a polymeric shear stress, both functions of the position in the gap. In the shear-banding regime, $K(y^*)$ is given by Eq. (4.4.3), and in the limit of small diffusive effects, (*i.e.* $w \to 0$) the dimensionless shear rates in the low and high shear rate bands are given by

$$K_l = \frac{\sqrt{1/\eta - 2} - \sqrt{1/\eta - 8}}{\sqrt{2}} \tag{4.5.3}$$

$$K_h = \frac{\sqrt{1/\eta - 2} + \sqrt{1/\eta - 8}}{\sqrt{2}} \tag{4.5.4}$$

In the high shear rate band, $K \simeq K_h = \sqrt{1-a^2}Wi_h$. Thus, from Eqs. (4.3.21), (4.3.9) and (4.5.4) one can obtain the following expressions:

$$\left[\frac{N_1}{\tau_{xy}}\right]_h = \left[\frac{N}{\sigma}\right]_h \frac{2}{\sqrt{1-a^2}} = \frac{K_h(\sigma - \eta K_h)}{\sigma}\frac{2}{\sqrt{1-a^2}} = \frac{2}{3}Wi_h\left(2 - \sqrt{\frac{1-8\eta}{1-2\eta}}\right) \tag{4.5.5}$$

Then, if $\mathcal{L} \sim Wi_h \alpha d$ and $R \sim R_i$,

$$\Sigma_{dJS} = \sqrt{\alpha\Lambda}Wi_h f(\eta) = \Sigma^* f(\eta) \tag{4.5.6}$$

Therefore, the result obtained using dJS is slightly more complex than the naive criterion Σ^* since it also depends on the viscosity ratio. A shear-banding fluid requires $\eta < 1/8$, so $0.7 \lesssim f(\eta) \lesssim 1.3$. This result is indeed not surprising, since Σ^* has been obtained in analogy with the purely elastic case derived using the upper convected Maxwell model, where $\eta = 0$ (Larson, 1998). In the homogeneous and non-shear-banding elastic case, adding a Newtonian solvent also modifies the dimensionless group by the addition of a function $f(\eta) \simeq \sqrt{\frac{2}{1+\eta}}$ (Pakdel & McKinley, 1996).

Note that the expression for Σ_{dJS} can also be expressed in terms of the two dimensionless variables K and σ. Indeed, from the lever rule, $\alpha = \frac{K-K_l}{K_h-K_l}$, and from Eqs. (4.5.3) and (4.5.4), K_l and K_h can be expressed in terms of η, which can be subsequently expressed in terms of σ using Eq. (4.3.21). Ultimately, one can reach the following equivalent alternative expression for Σ_{dJS}:

$$\Sigma_{dJS} = \sqrt{\frac{\Lambda}{1-a^2}}\tilde{\Sigma}_{dJS}(K,\sigma) \tag{4.5.7}$$

where $\tilde{\Sigma}_{dJS}(K,\sigma) = (2\sqrt{\frac{K}{3\sigma}} - \sqrt{\frac{\sigma}{3K}}) + O[\sigma^{3/2}]$ is a function of K and σ only, whose precise functional form is a little too cumbersome to be written explicitly. Figure 4.5.2 (b) plots the flow curves computed from Eqs. (4.3.21), (4.5.3) and (4.5.4), together with the magnitude of $\tilde{\Sigma}_{dJS}$. As the shear rate is increased, the proportion of the high-Wi band increases, the magnitude of the scaled criterion $\tilde{\Sigma}_{dJS}$ increases and the flow is increasingly unstabile. By comparing the experimental flow curves in Figure 4.5.2 (a) and the flow curve derived in the case of dJS in Figure 4.5.2 (b) one can see that the effect of decreasing the Newtonian solvent contribution η to the total stress is similar to the effect of increasing the concentration of surfactant, or decreasing the temperature.

4.5.3 Boundary Conditions and Classes of Unstable Shear-Banding Flows

More generally, one can expect the relevant dimensionless group for elastic instability in shear-banding flows to be $\Sigma_{sb} \equiv \Sigma^* f^*(\eta)$, where f^* is a function of the ratio between the zero shear and infinite shear viscosities. The specific form of f^* will depend on the constitutive model used to study shear banding (Cates & Fielding, 2006). Elastic instabilities will generate a secondary vortex flow with wavelength $l = n\alpha d$ for $\Sigma_{sb} > m$. As mentioned already, the precise values of n and m depend on the boundary conditions. Of prime importance are the values of m obtained for *soft* (m_s) or for *hard* (m_h) boundary conditions (Fardin *et al.*, 2010). Essentially, the hard case usually corresponds to a no-slip Dirichlet boundary condition, while the soft case usually corresponds to imposing a Neumann boundary condition on the continuity of the stress. In both the purely inertial case (Chandrasekhar, 1981) and the purely elastic case (Khayat, 1999), it is known that $m_s < m_h$. Khayat (1999) performed stability analysis of the Oldroyd-B fluid for two different sets of boundary conditions. In the first case, one boundary was soft, the other hard, and the threshold was found to be 5.77. In the second case, both boundaries were hard and the threshold was found to be 5.92. For a banded flow with $Wi \in [Wi_l, Wi_h]$, the interface with the low-Wi band should act as a sort of soft boundary for the high-Wi band. But for $Wi \geq Wi_h$, $\alpha = 1$, the flow becomes homogeneous again and the boundary

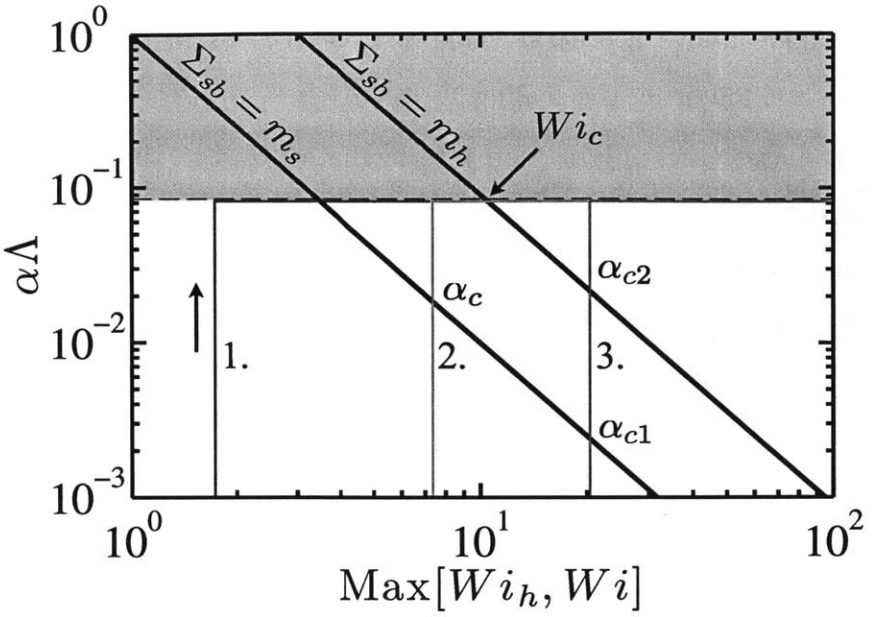

Figure 4.5.3: Schematic instability diagram in the plane (Max[Wi_h, Wi], $\alpha\Lambda$). The black lines represent the stability limits for soft and hard boundaries, $\Sigma_{sb} = m_s \Leftrightarrow \alpha\Lambda = (m_s/Wi_h)^2$ and $\Sigma_{sb} = m_h \Leftrightarrow \alpha\Lambda = (m_h/Wi_h)^2$. To enhance the visibility of the different categories of shear banding $m_s = 1$ and $m_h = 3$. The dashed black line represents the value of $1 \times \Lambda = 1.13/13.33$, the maximum curvature corresponding to recent experiments (Fardin *et al.*, 2010; Fielding, 2007, 2010; Larson *et al.*, 1994). Above this line, the shaded region is inaccessible. The three paths 1., 2. and 3. illustrate the three possible types of shear banding. The direction of the arrows represent the path followed by the state of the flow as the global Weissenberg number Wi is increased. α_c, α_{c1} and α_{c2} are the critical proportions of the high-Wi band at which the flow state crosses a stability limit. Wi_c is the threshold at which the type-1. trajectory becomes unstable for the first time, and at which the type-2. trajectory becomes unstable after a short relaminarization.

switches from soft to hard. The thresholds m_s and m_h, in the case of shear-banding flows would most likely be different than the values computed for the homogeneous flow of the Oldroyd-B fluid. Nonetheless, it is still expected that $m_s < m_h$ and that there may be a larger difference of values $m_h - m_s$.

Therefore, for a given geometry, (*i.e.* a given value of Λ), simple Boolean logic can be used to classify shear-banding flows into three possible categories depending only on the value of Wi_h:

1. For sufficiently low Wi_h – *i.e.* high T and low c – the shear-banding flow is stable for any α, since $\Sigma_{sb} < m_s$ even for $\alpha = 1$. The flow can then become unstable for

Weissenberg numbers above a critical value $Wi_c > Wi_h$ as in the case of a regular viscoelastic fluid, *i.e.* following the scaling $\Sigma_i = \sqrt{\Lambda} Wi$.

2. For intermediate values of Wi_h – *i.e.* intermediate T and c – the shear-banding flow is unstable above a critical value α_c when $\Sigma_{sb} > m_s$ for $\alpha > \alpha_c$. Then as the imposed shear rate is increased and $\alpha \to 1$ the boundary conditions change and the flow is stabilized, because the flow is below the threshold m_h. Eventually for $Wi > Wi_c > Wi_h$ the flow becomes unstable again. This case was observed in recent experiments (Fardin *et al.*, 2010).

3. Finally, if Wi_h is high enough – *i.e.* for low T and high c – there are two critical band widths α_{c1} and α_{c2}. For $\alpha > \alpha_{c1}$, $\Sigma_{sb} > m_s$. And for $\alpha > \alpha_{c2}$, $\Sigma_{sb} > m_h$. In this case, there is no stabilization for $Wi > Wi_h$. The flow remains unstable, although the spatio-temporal characteristics may change.

The three possible shear-banding scenarios can be illustrated on a stability diagram in the plane (Max[Wi_h, Wi], $\alpha\Lambda$), as presented in Figure 4.5.3. When the global Weissenberg number Wi is increased above Wi_l, the flow state is given by a constant abscissa depending on the value of Wi_h (which is a function of the concentration and temperature of the solution). As Wi increases, the thickness of the high shear rate band α increases and so the state of the flow moves vertically to larger ordinates. Once the entire gap is filled, $\alpha\Lambda$ reaches its maximum depending on the geometry of the chosen TC system. Then, since $Wi > Wi_h$, the state of the flow is given by a constant ordinate Λ and moves horizontally as Wi increases. Any flow state with $\alpha\Lambda < \Lambda$ will be stable if below the stability limit $\Sigma_{sb} = m_s$, and unstable if above $\Sigma_{sb} = m_s$ and *a fortiori* if above $\Sigma_{sb} = m_h$. Any flow state with $\alpha\Lambda = \Lambda$ will be stable if on the left of the stability limit $\Sigma_{sb} = m_h$, and unstable otherwise.

Interaction with Interface Modes

So far, only elastic instabilities arising in the bulk of the high-Wi band have been considered. But there exist other elastic instability mechanisms (Larson, 1992). In particular, Fielding has shown that the jump in normal stresses between the bands could generate interfacial modes, even in the plane Couette flow (Fielding (2007). In her

recent study in TC flow, Fielding suggested that the interfacial and bulk elastic modes lie in two separate regions of the space (Λ, $N_1|_h$), *i.e.* of the space (Λ, Wi_h) (Fielding, 2010). The bulk mode prevails at high Wi_h and high curvature Λ. The interfacial mode prevails at low Wi_h and low Λ. Fieldings study would suggest the existence of another unstable region in the lower left corner of the stability diagram sketched in Figure 4.5.3. Nonetheless, only axisymmetric perturbations were considered in Fieldings study, and the stability analysis was performed for a single value of α and η.

Wall Slip and non-Local Effects

The instability criterion that has been derived for shear-banding flows can be a powerful guide to interpret experiments on WLM fluids. Nonetheless, the criterion is fallible since there are at least two additional phenomena that can strongly compromise the validity of the scaling, which have both been shown to be relevant in some experimental situations. In both phenomena the local Weissenberg value in the high shear rate band may not be equal to the upper boundary of the shear-banding regime on the flow curve. The first phenomenon is wall slip, which has been reported recently and may actually be a common feature of many shear-banding flows (Lettinga & Manneville, 2009). The second phenomenon is geometric confinement. The present scaling may be inadequate if non-local effects become dominant (Masselon *et al.*, 2008). Non-local effects are apparent in confined geometries when the size d becomes comparable to the typical interfacial width $\xi \sim \mu$m, linked to the stress diffusion coefficient (Fielding, 2007; Sato *et al.*, 2010). Even in a macroscopic geometry with $d \gg \xi$, non-local effects can be important when the lateral extent of one of the bands is very small, *i.e.* $\alpha = 0$ or $\alpha = 1$.

4.6 Summary

This Chapter has focused on two seemingly different ways of thinking about the shear-banding phenomenon. In both approaches the diffusive Johnson-Segalman model has been used, but it has been possible to go from what can be viewed as a purely mechanical approach, to a more thermodynamic approach based on an energy potential.

The distinction between the two is obviously less clear cut that was once thought. An interesting point can be made by studying the logical implications between the different approaches. The most general formulation of the law governing the motion of mechanical systems is the principle of least action (Landau & Lifshitz, 1976) in that the equations of motion are governed by an explicit dependence on the energy in a system. In this regard, the integral thermodynamic approach seems to be more powerful. Nevertheless, this approach is only possible by the use of an anisotropic diffusion coefficient, so more care should be taken to justify this assumption and future experiments should be conducted to test this hypothesis. An important limitation of the thermodynamic approach comes from the fact that the form of the potential is dependent on the flow geometry. In contrast, the original mechanical approach starts from Eq. (4.2.6), which can be evaluated in any geometry. In this respect, the mechanical approach seems to be more powerful, especially if there is a systematic procedure to generate the correct potential for any geometry. In particular, the spatial inhomogeneity of the stress in a Poiseuille or cylindrical Couette flow translates into a time dependent potential.

Analytical solutions for the shear rate, shear stress, normal stress differences and velocity profile in plane Couette flow based on an energy potential derived from the dJS model have been derived. The inclusion of a non-local term in the governing equation for the polymeric stress ensures the robust selection of a unique value for the stress plateau in the shear-banding regime. These solutions are strictly only valid in the limit of a vanishingly thin interface between the shear rate bands, but experimental findings indicate that most viscometric measurements of WLM solutions in the Taylor-Coutte geometry do in fact occur in this limit.

The analysis of shear banding with the dJS model was then extended to derive a useful dimensionless criterion to rationalize the onset of secondary flows in the base shear-banding flow of worm-like micelles. Recent experiments by Fardin & Lerouge (2012) have undertaken a large study of the stability of shear-banding flows for many different surfactant types, concentrations and temperatures. Ultimately, the criterion could be extended to other flows with curved streamlines, if the localization and number of bands are known.

Chapter 5

Microfluidic Optical-Rheometry: Shear Flow

5.1 Introduction

In this Chapter, micro-particle image velocimetry (μ-PIV) and a commercial birefringence microscopy system for making full-field, quantitative measurements of flow-induced birefringence (FIB) are combined for the purpose of microfluidic optical-rheometry of two worm-like micellar (WLM) solutions. A microfluidic slit rheometer is used to study the properties of a shear-banding solution of cetylpyridinium chloride (CPyCl) with sodium salicylate (NaSal) and a nominally shear-thinning system of cetyltrimethylammonium bromide (CTAB) with NaSal at shear rates up to $\dot{\gamma} \leq \mathcal{O}(10^5)$ s^{-1}. Velocimetry measurements are used to quantify the local kinematics and the birefringence microscopy system is used to obtain high-resolution measurements of the changes in molecular orientation in the worm-like fluids under strong deformations in a microchannel. The FIB measurements reveal that the CPyCl:NaSal system exhibits regions of localized, high optical anisotropy indicative of shear bands near the channel walls, whereas the birefringence in the shear-thinning CTAB:NaSal system varies more smoothly across the width of the channel as the volumetric flow rate is increased. The experimental results are compared to the predictions of a simple constitutive model, and the breakdown in the stress-optical rule is documented as the characteristic rate of deformation is increased.

5.2 High Shear Rate Rheology of WLM Test Fluids

The high shear rate rheology of both solutions was determined with the microfluidic Viscometer/Rheometer-on-a-Chip (VROC, RheoSense Inc.). The VROC device is a high aspect ratio, rectangular microfluidic slit rheometer. It was necessary to use two devices, in order to span the full range of shear rates, from the maximum shear rate attainable with a rotational rheometer (*i.e.* $\dot{\gamma} \sim \mathcal{O}(10)$ s^{-1}) to the maximum shear rates that could be measured with the VROC technology (*i.e.* $\dot{\gamma} = 3.4 \times 10^5$ s^{-1}). Each channel is fitted with four inline, 800×800 μm^2 MEMS-based pressure transducers along the centerline, additional details of this system are described in (Pipe *et al.*, 2008). The first device (ID: 11RB10100212) had dimensions of width, height and length, respectively $W = 99.6$ μm, $H = 3.2$ mm and $L = 8.8$ mm. This device was used with a 2.5 mL syringe (Hamilton Gastight, Reno, NV) at shear rates in the range $10 \lesssim \dot{\gamma} \lesssim 10^4$ s^{-1}. The second device (ID: 12RE05100139) had dimensions $W = 52.7$ μm, $H = 2.08$ mm and $L = 8.8$ mm, and was used with a 10 mL syringe (Hamilton Gastight, Reno, NV) for shear rates $10^3 \lesssim \dot{\gamma} \lesssim 3.4 \times 10^5$ s^{-1}.

The temperature of the test fluids was controlled with a thermal jacket system (Rheosense Inc.), coupled with an F12-ED Refrigerated/Heating Circulator (Julabo Inc.). Temperature within the channel was recorded with an integrated sensor in the VROC device, and varied between 22 and 22.5 °C throughout the duration of the tests. The pressure drop ΔP, along the length of the channel was measured for each imposed flow rate and related to the wall shear stress by $\tau_w = \Delta PW/2L$. The Weissenberg-Rabinowitsch-Mooney correction in Eq. (5.2.1) was applied to account for shear-thinning and to determine the true wall shear rate (Pipe *et al.*, 2008), using:

$$\dot{\gamma}_w = \frac{\dot{\gamma}_N}{3}\left(2 + \frac{d\ln\dot{\gamma}_N}{d\ln\tau_w}\right) \tag{5.2.1}$$

where $\dot{\gamma}_N = 6Q/HW^2$ is the wall shear rate of a Newtonian fluid corresponding to the volumetric flow rate Q, in the rectangular channel. Finally, a third order polynomial was fit to five consecutive data points to determine numerically the local differential correction term in Eq. (5.2.1) for each data point. The resultant flow curves are presented

in Figure 5.2.1.

For the CPyCl:NaSal solution a stress plateau for apparent shear rates $0.2 \leq \dot{\gamma} \leq 500\ \mathrm{s}^{-1}$ can be observed in Figure 5.2.1 (a). There is a very clear reduction in the measured value of the stress plateau from $\tau_{p,ARES} \approx 15$ Pa as measured on the macroscale, ARES rheometer to $\tau_{p,VROC} \approx 12$ Pa as measured with the microfluidic-slit rheometer. This reduction in the value of τ_p may possibly be caused by slip or non-viscometric effects in the entrance and exit regions of the channel, but it is also qualitatively in agreement with the predictions of the VCM model for WLM flowing in rectangular channels, when non-local effects (see Chapter 4) on the flow curve are considered (Cromer *et al.*, 2010). Non-local effects result in the reduction in value of τ_p as the slit width of the channel is decreased due to the increasing importance of diffusive effects and the coupling between stress and microstructure of the micellar system when the length scale of the flow geometry is on the same order as the width of the interface between shear bands (Olmsted, 2008). This interfacial width, $\ell = \sqrt{\mathcal{D}\lambda}$, depends on the relaxation time of the system λ, and the self-diffusion coefficient $\mathcal{D}$. Taking $\mathcal{D} \sim \mathcal{O}(10^{-11} - 10^{-9})$ m^2/s (Helgeson *et al.*, 2009b; Cromer *et al.*, 2010), an estimate for the CPyCl:NaSal system in this study, $5 < \ell < 50$ μm, which is of the same order as W, the channel width of the VROC, confirming that non-local effects can influence the resultant, high shear rate flow curve in Figure 5.2.1 (a). Note, however, that the exact values of and differences between the stress plateaus measured with a cone-and-plate geometry on a rotational rheometer and with the VROC depend on the specific batch of fluid, including the case for which there is practically no difference between the values measured with both rheometer, for example, as seen by Haward *et al.* (2012a).

At shear rates greater than approximately $\dot{\gamma}_2 \gtrsim 500\ \mathrm{s}^{-1}$, the shear stress increases once again with increasing shear rate. In this high shear rate branch of the flow curve, the Reynolds number defined by the rate dependent viscosity, $Re = \rho\langle\mathcal{U}\rangle D_h/\eta(\dot{\gamma}_w)$, ($\rho = 1100$ kg/m^3, hydraulic diameter $D_h = 2HW/(H+W) \approx 2W = 100$ μm) remains less than unity for all shear rates indicating viscous, laminar flow. For this fluid, the viscometric measurements show that the stress increases sublinearly with shear rate ($\tau \sim \dot{\gamma}^{2/3}$) for $\dot{\gamma} \geq \dot{\gamma}_2$, suggesting that the classical assumption of a high shear rate

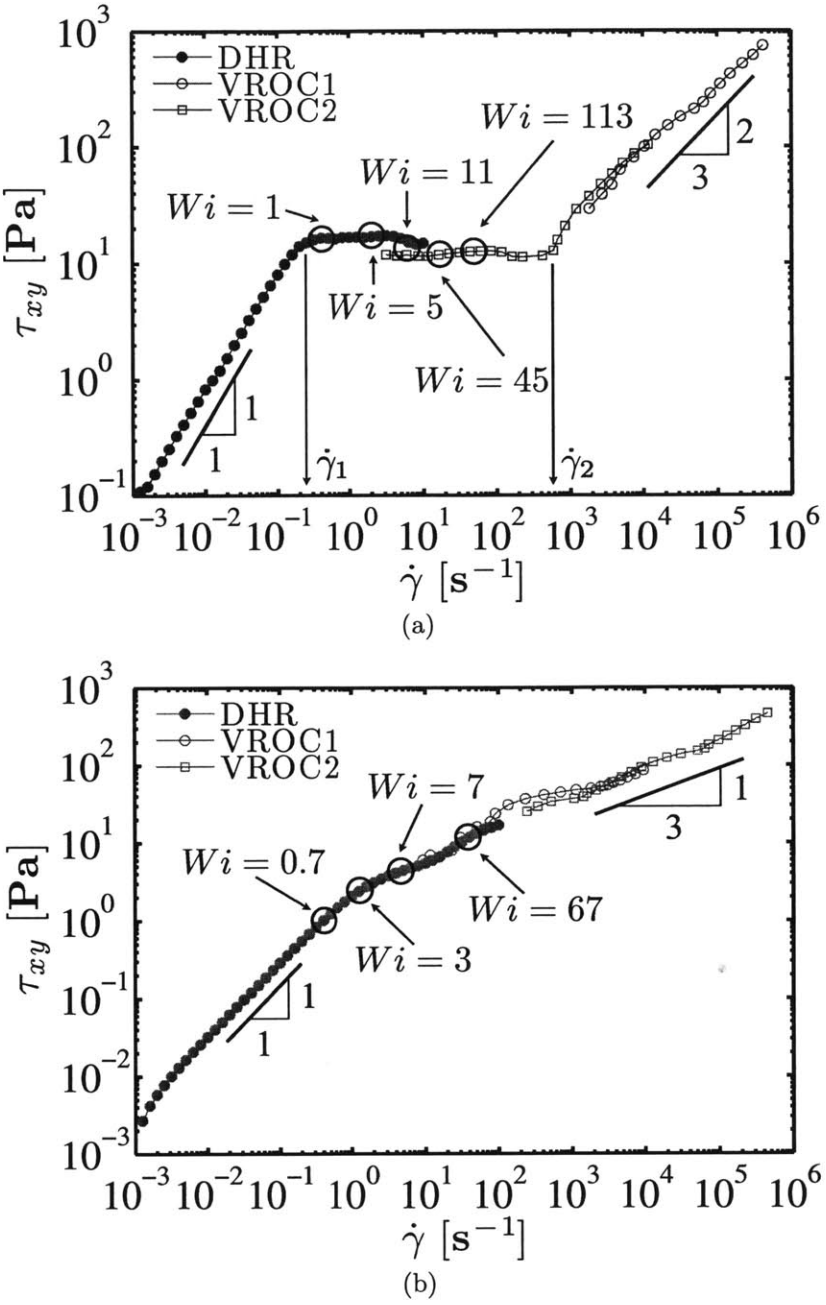

Figure 5.2.1: Steady shear rheology of 100:60 mM CPyCl:NaSal (Batch 5) and 30:240 mM CTAB:NaSal (Batch 5) solutions at 22-22.5 °C obtained with a microfluidic rheometer (VROC). (a) Shear stress of 100:60 mM CPyCl:NaSal. (b) Shear stress of 30:240 mM CTAB:NaSal. The Weissenberg-Rabinowitsch-Mooney Correction in Eq. (5.2.1) is applied to all results measured with VROC. Solid symbols correspond to results measured with a cone-and-plate fixture. Symbols labeled 'VROC1' correspond to data obtained with chip 11RB10100212, and those labeled 'VROC2' with chip 12RE05100139. The large black circles indicate the Weissenberg numbers, $Wi = \lambda\dot{\gamma}_c = \lambda\langle\mathcal{U}\rangle/W$, corresponding to the flow rates in the microchannel experiments. The solid black lines with indicated slope have been added only to guide the eye. (a) Symbols $\dot{\gamma}_1$ and $\dot{\gamma}_2$ indicate the limiting shear rates at the beginning and end of the stress plateau.

branch with constant, Newtonian-like viscosity, as for example in the Johnson-Segalman model (Johnson & Segalman, 1977) is inadequate for describing this fluid. Theoretical descriptions of the rheology of WLM fluids on the high shear rate branch remain relatively unestablished, and further study of this power-law scaling for $\dot{\gamma} > \dot{\gamma}_2$, possibly through molecular dynamics simulations (*e.g.* Anderson *et al.* (2006)) is warranted.

The flow curve of the CTAB:NaSal solution is presented in Figure 5.2.1 (b). At all shear rates measured with VROC, this system exhibits a continually shear-thinning response, but for a small range of shear rates spanning $30 \leq \dot{\gamma} \leq 100$ s^{-1}, for which CTAB:NaSal solution exhibits a local stress plateau indicative of shear-banding. At high shear rates beyond, $\dot{\gamma} > 300$ s^{-1}, the stress increases more weakly with increasing shear rate ($\tau \sim \dot{\gamma}^{1/3}$) than observed for the CPyCl:NaSal fluid. It is also noteworthy that the scaling of stress with shear rate is roughly the same for $0.5 \leq \dot{\gamma} \leq 30$ s^{-1} and $\dot{\gamma} > 300$ s^{-1}.

5.3 Flow-Induced Birefringence Measurements

In the present study, the material stresses and molecular orientation are also determined from measurements of flow-induced birefringence. The stress-optical rule states that the principal stress difference $\Delta\sigma \equiv \sigma_1 - \sigma_2$, is linearly proportional to the difference between the ordinary and extraordinary indices of refraction Δn, with stress-optical coefficient C as the proportionality coefficient. This rule is written

$$\Delta n = C\Delta\sigma \tag{5.3.1}$$

The principal stresses σ_1 and σ_2, are the eigenvalues of the two-dimensional stress tensor which characterizes the deviatoric stresses associated with a material deformation, and may be related to the stresses in the xy-frame by

$$\Delta\sigma = \sqrt{N_1^2 + 4\tau_{xy}^2} \tag{5.3.2}$$

where τ_{xy} is the shear stress and $N_1 \equiv \tau_{xx} - \tau_{yy}$ is the first normal stress difference.

The second quantity of interest is the azimuthal angle χ, and corresponds to the

orientation of the molecules with respect to the x-axis, the direction of flow in the channel. For the systems studied here, the stress-optical coefficient is negative ($C < 0$) and hence the value of χ indicates the orientation of the fast optical axis of the micelles. The azimuthal angle is related to τ_{xy} and $\Delta\sigma$ by

$$\chi = \frac{1}{2}\sin^{-1}\left(\frac{2\tau_{xy}}{\Delta\sigma}\right) \tag{5.3.3}$$

5.3.1 Measurement of the Stress-Optical Coefficient of the Test Fluids

The optical anisotropy cannot be measured directly, but must be inferred from measurements of sample retardance δ. This quantity may be related to the optical anisotropy of a material, if a constant value for the refractive index difference Δn can be assumed along the direction of light propagation. In this case, for a birefringent sample having depth H, along the direction of light propagation, the retardance and optical anisotropy are related by the expression

$$\frac{\delta}{2\pi} = \frac{\Delta n H}{\lambda_l} \tag{5.3.4}$$

where λ_l is the wavelength of the incident light. Provided this relationship is valid, Eq. (5.3.1) and (5.3.4) can be combined and separate measurements of birefringence Δn, and mechanical stress $\Delta\sigma$, can be combined to determine the stress-optical coefficient C.

Measurements of flow-induced birefringence were made at an ambient temperature of 23 ± 1 °C, with a Taylor-Couette (TC) cell ($R_1 = 15$ mm, $R_2 = 17$ mm, gap $d = R_2 - R_1 = 2$ mm, optical path length of $H = 20$ mm) using the optical analyzer module (OAM) on the ARES rheometer and the same forward-backward stepped shear rate procedure described in (Helgeson *et al.*, 2009b). The time-averaged values are shown in Figure 5.3.1. Eq. (5.3.1) and Eq. (5.3.3) may be rearranged to obtain a linear relationship of the stress-optical rule between the quantity $\frac{1}{2}|\Delta n \sin(2\Theta)|$, and the shear stress τ_{xy}. From Figure 5.3.1, it is clear that this relationship holds for low stresses. The onset of a breakdown in the stress-optical rule coincides with $\dot{\gamma} \approx \lambda^{-1}$ for both fluids. On account of the finite spot size of the incident laser ($d_{spot} \approx 1$ mm), measurements at

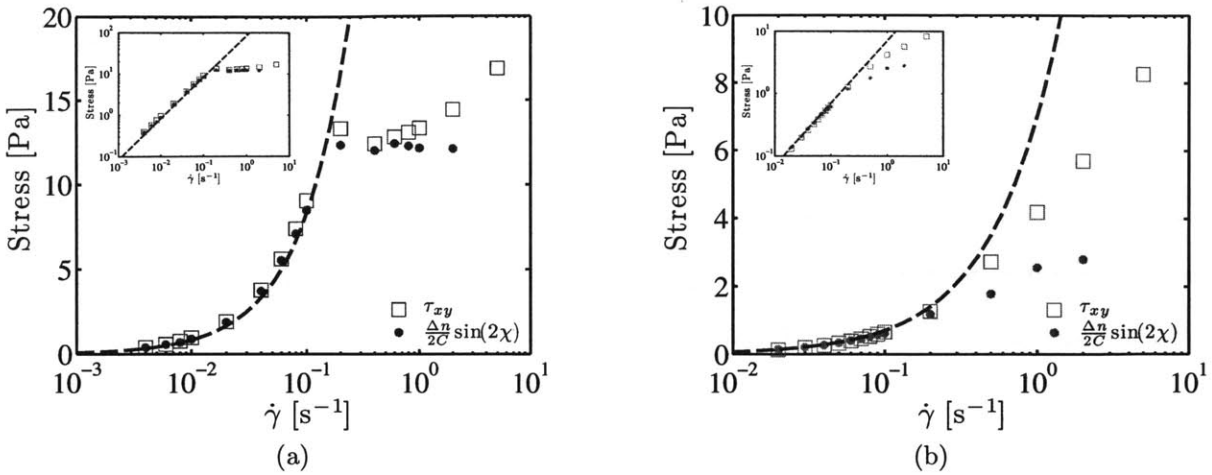

Figure 5.3.1: Flow-induced birefringence and shear stress against shear rate as measured using the optical analyzer module (OAM) on the ARES rheometer at 23±1 °C: (a) 100:60 mM CPyCl:NaSal system, $C = -1.1 \times 10^{-7}$ Pa^{-1}, (b) 30:240 mM CTAB:NaSal system, $C = -3.8 \times 10^{-7}$ Pa^{-1}. The stress-optical coefficient of each system was determined from the linear portion of the data corresponding to shear rates with constant shear viscosity η_0. The data are plotted semi-logarithmically to accommodate the large range of shear rates. Inset plots on log-log scale. The dashed lines indicate the flow curve given by $\tau_{xy} = \eta_0 \dot{\gamma}$ for each system.

shear rates coinciding with shear-banding $\dot{\gamma} \gtrsim \dot{\gamma}_1$, may correspond to spatially averaged quantities across the width of the gap. The flow at shear rates $\dot{\gamma} > 2$ s^{-1} in the TC cell was also prone to foaming and air entrainment leading to further uncertainty in birefringence measurements and therefore optical data at these shear rates have not been included in Figure 5.3.1.

For the CPyCl:NaSal system, $C = -1.1 \times 10^{-7}$ Pa^{-1}, which is very close to the value given by Hu & Lips (2005), listed in Table 2.2.1, for a similar system, but it is a factor of two smaller than the value given in the initial work by Rehage & Hoffmann (1991) for the same system studied here. The magnitude of $C = -3.8 \times 10^{-7}$ Pa^{-1}, for the CTAB:NaSal system is greater by about 20% than the reported value for similar systems given by Shikata *et al.* (1994).

5.4 Experimental Methods for Microfluidic Rheometry

The basic components for each experiment consisted of a microscope, an imaging system, test geometry and fluid, glass syringe (Hamilton Gastight), and a syringe pump, PHD 4000 programmable pump (Harvard Apparatus). Syringes were connected to test geometries using Tygon® microbore tubing (inner diameter 0.508 mm) (Cole Parmer Instrument Co.). In all tests, the length of the tubing was kept to a minimum (10 cm) in order to reduce compliance in the entire system, thereby shortening the duration of experimental transients. Experiments were performed in climate controlled rooms in which the temperature fluctuated between 22-24 °C for the duration of all experiments.

5.4.1 Microchannel Fabrication

For the microfluidic experiments in the present study, it is necessary to construct a high aspect ratio channel, precluding the use of most lithographic techniques. Therefore, the microchannel was manufactured using a technique similar to that described by Guillot *et al.* (2006). Two anodized, 1 mm × 2 cm × 8 cm aluminum strips were used to construct the sidewalls of the channel as shown in Figure 5.4.1. The inside walls of the channel were polished with 2000 grit sandpaper and thoroughly cleaned. A spacer was placed between the two strips to ensure a constant width between the strips, and they were glued together with a two-part epoxy (Devcon). Once the epoxy had set, the spacer was removed and the distance between the strips was checked with an optical microscope in order to ensure that the channel walls were parallel, to within fabrication errors of ± 5 μm. Thin layers of the same epoxy were spread on the top and bottom of the strips and 150 μm thick microscope cover slips were pressed onto the adhesive. Care was taken to ensure that no epoxy seeped into the channel. Luer stub adapter syringe tips were then adhered to the channel at both ends and additional epoxy was added where needed to ensure the channel was sealed. The dimensions of the straight channel used in this study were width $W = 130 \pm 5$ μm, height $H = 1,000 \pm 10$ μm, and length $L = 5$ cm.

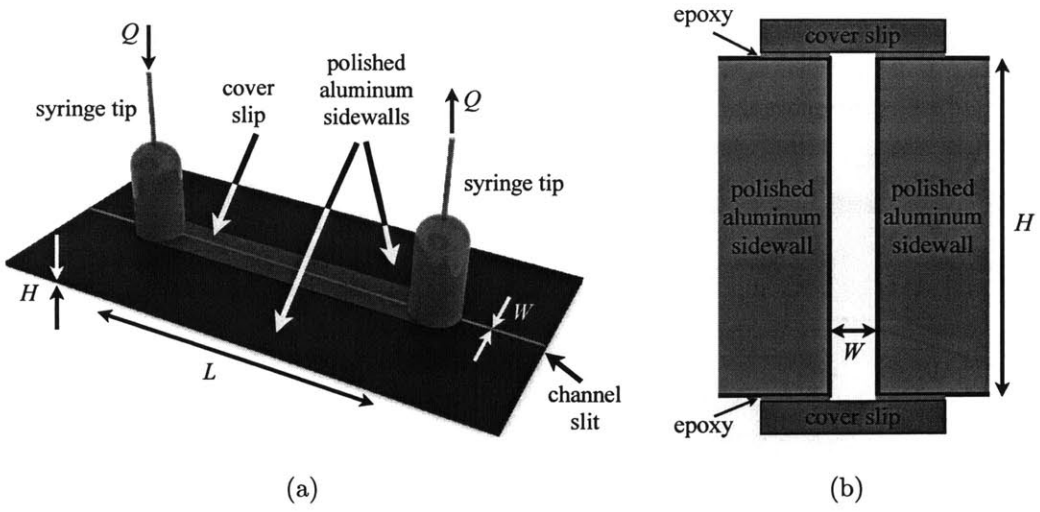

(a) (b)

Figure 5.4.1: (a) Perspective view of straight microchannel. (b) Cross-section of straight channel. Schematic depiction is roughly to scale.

5.4.2 Micro-Particle Image Velocimetry

Micro-particle image velocimetry (μ-PIV) is a correlative technique, in which one images the temporal displacement of micron sized particulate markers, convecting with a flowing fluid in order to infer the local fluid velocity field (Raffel *et al.*, 1998), as shown in Figure 5.4.2. The μ-PIV experiments utilize epifluorescent illumination, whereby the entire volume of a region of flow is illuminated and the spatial resolution of all measurements must be controlled by selecting suitable optical components (Meinhart *et al.*, 2000).

Both test fluids were seeded with 0.02 wt.%, $d_p = 1.1$ μm diameter fluorescent particles (Invitrogen), having excitation and emission wavelengths of 520 and 580 nm, respectively. For neutrally buoyant uncharged particles, the volume fraction of the seed particles is approximately as $\Phi = 2 \times 10^{-4}$, for which the Einstein correction (Larson, 1998), is used to predict a minimal increase in viscosity, $\eta = \eta_0(1 + 2.5\Phi + \mathcal{O}(\Phi^2)) = 1.0005\eta_0$.

The μ-PIV system utilizes epifluorescence microscopy (TE-2000, Nikon, Melville, NY) and is discussed in detail elsewhere (Rodd *et al.*, 2005). This system consisted of a 1.4 megapixel (1376×1024 pixels) CCD camera (PIV-Cam 14-10, TSI Instruments, Shoreview, MN) with spacing between pixels, $e = 6.45$ μm, and a double-pulsed 532 nm Nd:YAG laser (LaVision, Ypsilanti, MI) with pulse width, $\delta t = 5$ ns. A G-

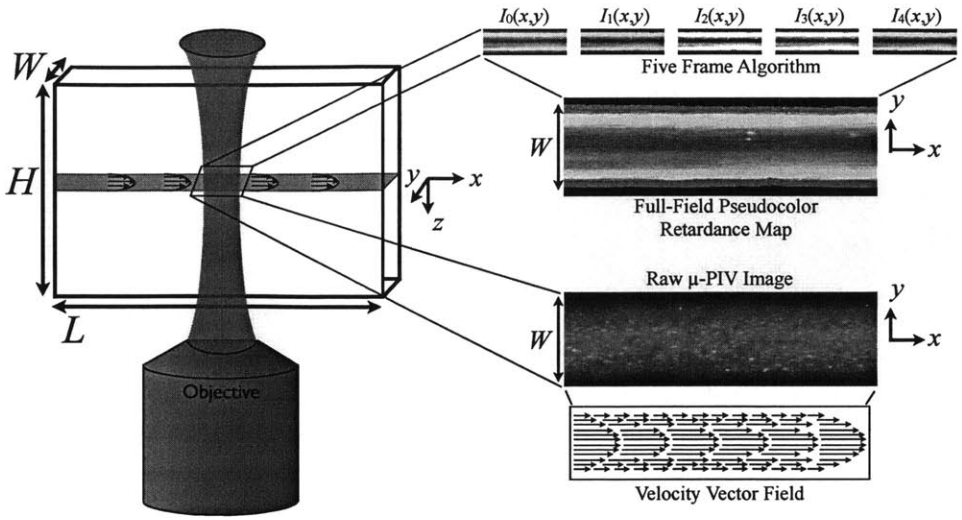

Figure 5.4.2: Schematic depiction of μ-PIV and FIB raw signal measurements on microscope. The xyz-coordinate system is centered along the centroidal axis of the rectangular channel.

2A filter was also used to allow only the emitted light with wavelengths, $\lambda \geq 580$ nm to enter the camera. For a given flow rate, the elapsed time between consecutive image pairs Δt, $(1.2 < \Delta t < 60,000\ \mu\text{s})$, was selected to achieve a particle displacement $(2d_p < \Delta x < 7.5d_p)$ suitable for analysis.

Measurements of velocity profiles in the channel were completed with a $10\times$ 0.25 NA objective. This objective yielded a viewing area encompassing the entire channel width and approximately 1 mm sections along the length (x-axis) of the channel. For the camera and objective used here, the distance over which sample features may be considered in focus is the depth of field, which is $\delta z = 15.8\ \mu$m. The depth of measurement (Meinhart *et al.*, 2000), which is equal to the distance over which additional particles within its vicinity of the focal plane contribute substantially to the overall signal detected by the camera, is $\delta z_m = 47.3\ \mu$m.

At least 35 consecutive image pairs were ensemble-averaged to determine full-field maps of the steady flow velocity profiles using a conventional cross-correlation PIV algorithm (TSI Insight software). Interrogation windows of 16×16 pixels were used in the correlation scheme, hence the uncertainty in the y-positions of a velocity vector are the width of the interrogation window, corresponding to the error bars parallel to

the y-axis shown in velocity profile plots. Each quadrant of an interrogation window was overlapped by the respective quadrant of an adjacent window. Post-processing to remove spurious velocity vectors and any subsequent data analysis of the velocity profiles was completed using MATLAB (Mathworks, Natick, MA) with a script written by the authors.

A series of measurements were taken at focal planes with a spacing of 50 μm across the channel height. The bottom of the channel was identified as the lowest plane for which a stationary fluorescent particle was in focus. The uncertainty in the vertical position of a focal plane was accordingly the depth of field δz. Measurement planes more than 450 μm above the bottom of the channel, were found, in general, to capture an insufficient number of particles to determine velocity fields. This weakened signal was attributed to reduced light intensity at higher image planes caused by reflection and absorption of light at lower imaging planes.

The average x-component of the velocity profile at a particular y-position was determined from the ensemble average of all the measured x-velocities in the viewing area at that particular y-position. The error in the value of the x-velocity, therefore, was taken as the standard deviation of the ensemble average, corresponding to the longitudinal error bars in velocity profile plots. The cross-channel, y-components of the velocity profile were found to be negligibly small in comparison to the x-component at any position in the channel.

5.4.3 Measurement of Birefringence in a Microchannel

The ABRIO^{TM} imaging system (CRi, Inc.) is a commercially available instrument originally designed to measure the birefringence of biological samples. The system can measure retardance to within 0.02 nm and yields much higher spatial resolution (pixel-size Δx, $\Delta y \simeq 1$ μm) than can be obtained with the 1 mm spot size of the ARES OAM system. In the present study, the ABRIO system has been adapted in order to measure the birefringence of flowing complex fluids in microscale geometries. The optical train of this device is shown in Figure 5.4.3. The basic components of the device are the interference filter and circular polarizer, the liquid crystal compensator optic and the

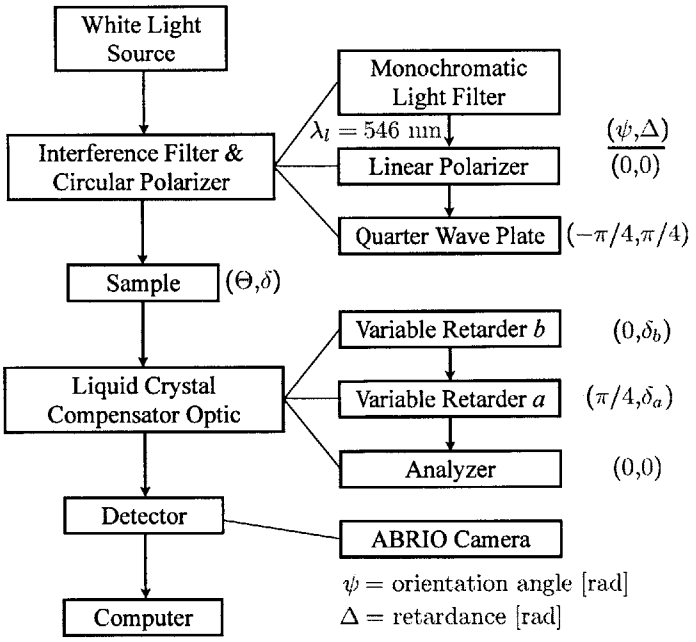

Figure 5.4.3: ABRIO Optical Train.

CCD camera.

The white light source, interference filter and circular polarizer together provide a monochromatic ($\lambda_l = 546$ nm), circularly polarized light wave. The beam then impinges on a birefringent sample and reports both a local retardance $\delta(x, y)$, and an *orientation angle* $\Theta(x, y)$, which by definition, for the ABRIO system corresponds to the angle between the *slow* optical axis of the sample and the optical axis of the analyzer, (which for these experiments coincides with the x-axis as described below). For the WLM systems studied here, the stress-optical coefficient is negative ($C < 0$), and hence the slow optical axis, with angle Θ, is perpendicular to the azimuthal angle χ, corresponding to the direction of stretching of the molecules. Thus for the systems in this study, $\Theta = \chi + \frac{\pi}{2}$, and the azimuthal angle conventionally reported in birefringence studies and orientation angle reported by the ABRIO system are different quantities.

After passing through the sample, the wavefront then passes through a liquid crystal compensator containing two birefringent elements with fixed orientation angles and variable, but known retardances, δ_a and δ_b, and a linear polarizer with a fixed orienta-

tion. The emerging beam then impinges on a CCD array detector, which measures the pixelwise intensity of the beam. Provided there is perfect transmittance and no offset of the intensity signal, the ratio of this measured final intensity, $I(x,y)$, and the initial intensity of the beam, $I_{in}(x,y)$ is obtained from Mueller calculus (Fuller, 1995), and is given by the following relationship:

$$\frac{I}{I_{in}} = \frac{1}{2}\Big\{1+\cos(\delta_a)\sin(2\Theta)\sin(\delta)+\cos(\delta)\cos(\delta_b)\sin(\delta_a)-\cos(2\Theta)\sin(\delta)\sin(\delta_a)\sin(\delta_b)\Big\} \tag{5.4.1}$$

where for compactness, the local spatial variation of each of the quantities δ, Θ and I has not been explicitly indicated.

The operating principles of the ABRIO system are discussed at greater length by Shribak & Oldenbourg (2003). When evaluating a single birefringence image, the ABRIO system records five distinct images, varying the birefringence of the liquid crystal compensator and imposing a swing angle φ, whose value depends on the prevailing specimen retardance, according to the five frame algorithm listed in Table 5.4.1. From these five images, a single full-field map of retardance and orientation angle is generated (see Figure 5.4.2). The five separate measurements are required to apply the background correction, account for any absorbance of light by the sample or an offset of the intensity signal and to ensure equal sensitivity for all sample orientation angles. The exposure time of each frame depends on the sample birefringence, but it is generally 0.02 to 0.1 seconds.

Once the five intensities have been measured at the specified combinations of δ_a and δ_b given in Table 5.4.1, Eq. (5.4.1) can be simplified and the local values of two intensity ratio parameters, $A(x,y)$ and $B(x,y)$, may be calculated from the following relationships

$$\begin{aligned} A &= \frac{I_1 - I_2}{I_1 + I_2 - 2I_0}\tan\left(\frac{\varphi}{2}\right) = \sin(2\Theta)\tan(\delta) \\ B &= \frac{I_4 - I_3}{I_4 + I_3 - 2I_0}\tan\left(\frac{\varphi}{2}\right) = \cos(2\Theta)\tan(\delta) \end{aligned} \tag{5.4.2}$$

where again the spatial variation in the intensities, δ, and Θ have not been explicitly indicated. The local values of the retardance, $\delta(x,y)$, and orientation angle, $\Theta(x,y)$, at each point can then be finally calculated from the expressions

Table 5.4.1: Five frame algorithm for the ABRIO system. For each frame, a unique combination of δ_a and δ_b is used, and the corresponding measured intensity is related to the birefringence of the imaged sample by Eq. (5.4.1). The set of five measured intensities are then used to determine the parameters A and B given by Eq. (5.4.2), which are then used to determine the sample retardance δ, and orientation angle Θ, with Eq. (5.4.3) and Eq. (5.4.4).

Frame Number	δ_a	δ_b	Measured Intensity
0	$\pi/2$	π	I_0
1	$\pi/2-\varphi$	π	I_1
2	$\pi/2+\varphi$	π	I_2
3	$\pi/2$	$\pi-\varphi$	I_3
4	$\pi/2$	$\pi+\varphi$	I_4

$$\delta = \begin{cases} \arctan(\sqrt{A^2+B^2}) & \text{if } I_1+I_2-2I_0 \geq 0 \\ \pi - \arctan(\sqrt{A^2+B^2}) & \text{if } I_1+I_2-2I_0 < 0 \end{cases} \tag{5.4.3}$$

$$\Theta = \begin{cases} \frac{1}{2}\arctan\left(\frac{A}{B}\right) & \text{for } A \geq 0 \;\&\; B \geq 0 \\ \frac{\pi}{2}+\frac{1}{2}\arctan\left(\frac{A}{B}\right) & \text{for } B < 0 \\ \pi+\frac{1}{2}\arctan\left(\frac{A}{B}\right) & \text{for } A < 0 \;\&\; B \geq 0 \end{cases} \tag{5.4.4}$$

The ABRIO system can also apply a separate background correction to account for any residual birefringence of the sample. This feature is especially useful for FIB imaging as the optical anisotropy of the fluid sample at rest should be identically zero. The correction is made by recording a user-specified background image, to calculate the reference values of $A_{bg}(x,y)$ and $B_{bg}(x,y)$ from Eq. (5.4.2) for the image, and then subtracting the values of $A_{bg}(x,y)$ and $B_{bg}(x,y)$, respectively, from the values of $A_{im}(x,y)$ and $B_{im}(x,y)$ from all subsequent images, to obtain the corrected values of $A(x,y)$ and $B(x,y)$. This correction is only applicable in the *small retardation limit* (Li & Burghardt, 1995), when the retardance of the sample and background are small compared to the wavelength of incident light (Shribak & Oldenbourg, 2003).

Measurements of FIB in the microchannel were completed with a 20× 0.5 NA objective with the bottom plane of the channel in focus. In order to minimize possible blurring of the measured birefringence, the half angle of the incident cone of light as set

by the condenser aperture was 2°, which was the minimum collection angle for which the ABRIO system could obtain a strong enough signal to take measurements. Mean birefringence profiles $\delta(y)$ in the fluid across the channel width were calculated from the full field images $\delta(x, y)$ using the same streamwise averaging employed for the velocity profiles. In order to determine if stress-induced birefringence in the channel itself was significant, glycerine, a non-birefringent Newtonian fluid, was pumped through the channel using the syringe pump at a flow rate of $Q = 300$ μL/hr, corresponding to a relatively high calculated wall shear stress of $\tau_w = 30$ Pa ($\dot{\gamma}_w \approx 30$ s^{-1}). At this wall shear stress no appreciable change in the birefringence ($\delta \leq 3 \times 10^{-3}$ rad) of the channel was observed.

5.5 Results and Discussion

5.5.1 Dimensional Analysis

For steady, two-dimensional flow with volumetric flow rate Q, in a channel of width W, and height H, ($W \ll H$) the average velocity is $\langle \mathcal{U} \rangle = Q/WH$. Hence the characteristic deformation rate in the channel is $\dot{\gamma}_c = \langle \mathcal{U} \rangle / W$, and the *Weissenberg* number can be defined as

$$Wi = \frac{\lambda \langle \mathcal{U} \rangle}{W} \tag{5.5.1}$$

The experiments reported here correspond to $10^{-1} \leq Wi \leq 10^3$. For $Wi \sim 1$, deformations occur on timescales roughly equal to the relaxation time of the fluid and the onset of non-Newtonian behavior is to be expected. As the magnitude of the Weissenberg number is increased, strong departures from Newtonian behavior are observed, including shear-thinning and considerable optical anisotropy.

The *Deborah* number is defined as the ratio of the fluid relaxation time to a characteristic timescale for the flow (Dealy, 2010); which here can be considered to be the residence time of the fluid in the channel for a particular observation distance,

$$De = \frac{\lambda \langle \mathcal{U} \rangle}{L_{obs}} \tag{5.5.2}$$

where L_{obs} is the distance downstream of channel entrance, at which the flow is observed. The magnitude of the Deborah number gives an indication for how fully-developed the flow is expected to be at the point of observation. For $De \ll 1$, the residence time is sufficiently long for viscoelastic memory effects to have decayed. In the microchannel experiments, $10^{-3} \leq De \leq 10$.

The relative importance of inertia and viscosity is characterized by the *Reynolds* number

$$Re_0 = \frac{\rho \langle \mathcal{U} \rangle D_h}{\eta_0} \tag{5.5.3}$$

where the hydraulic diameter is $D_h = 2HW/(H+W) \approx 2W = 260$ μm for this channel. For the range of flow rates observed in this study, (10 μL/hr $\leq Q \leq 10^4$ μL/hr), the Reynolds number is $10^{-8} \leq Re_0 \leq 10^{-3}$, indicating that inertial turbulence is never a possibility. If the strong rate dependence of the characteristic viscosity of micellar fluids (*i.e.* $\eta(\dot{\gamma}_c)$) is accounted for, using the flow curves measured with VROC in Figure 5.2.1, then values of $Re(\dot{\gamma}_c)$ are higher, but never exceed unity, which is again far from the critical Reynolds number required for the onset of turbulence ($Re_c \approx 2000$). The values of Re_0 obtained can also be used in an appropriate correlation for determining the entrance length for establishing a fully-developed flow with a Newtonian fluid, $L_e/D_h = [(0.631)^{1.6} + (0.0442 Re_0)^{1.6}]^{1/1.6}$ (Durst *et al.*, 2005). According to this correlation, for $Re_0 \ll 1$, $L_e \approx 0.631 D_h \ll L_{obs}$, thus arguments based on viscous Newtonian fluid mechanics would indicate the flow is kinematically fully-developed. The effect of shear-thinning on the entrance length has also been investigated by Poole & Ridley (2007), who determined that the entrance length increases at most by 40% beyond the Newtonian result in the creeping flow limit. As shown in Section 5.6, however, viscoelasticity complicates this picture because of a convective coupling between evolving velocity and stress profiles.

An additional dimensionless ratio is the elasticity number, which compares the magnitude of elastic stresses to inertial effects in the flow,

$$El_0 = \frac{Wi}{Re_0} = \frac{\lambda \eta_0}{\rho W D_h} = \frac{\Psi_{1,0} \dot{\gamma}_c^2}{\rho \langle \mathcal{U} \rangle^2} \tag{5.5.4}$$

This parameter is independent of the kinematics of the flow, since it depends only on the properties of the fluid and dimensions of the channel. For the present tests the values given in Table 3.3.1 indicate that $El_0^{CPyCl} = 7.0 \times 10^7$ and $El_0^{CTAB} = 2.4 \times 10^6$. Alternatively, one could define a rate dependent elasticity number using the measured first normal difference $El(\dot{\gamma}_c) = N_1(\dot{\gamma}_c)/\rho\langle\mathcal{U}\rangle^2 = \Psi_1/\rho W^2 = 1.6 \times 10^5$ for both the CPyCl:NaSal and CTAB:NaSal systems. These large values of the elasticity number are unique to flows in microchannels, and they indicate that inertial effects are negligible compared to elastic stresses. Microfluidic rheometry thus enables measurements of the rheological behavior of complex fluids at high shear rates in the absence of inertial complications.

5.5.2 Flow Kinematics

Velocity profiles were measured at successive positions, $(-0.5 \leq \frac{z}{H} \leq 0.5)$ across the height of the channel at a fixed observation point downstream ($L_{obs} = 3.5$ cm, $L_{obs}/D_h = 134$). Within statistical uncertainty, flow profiles were observed to be invariant along the z-axis for heights corresponding to $|\frac{z}{H}| \leq 0.4$. Profiles measured between approximately 200 and 300 μm above the bottom of the channel ($0.2 \leq \frac{z}{H} \leq 0.3$) are reported as the characteristic two-dimensional velocity profile for a given Wi, similar to the approach of (Nghe *et al.*, 2008). To verify this assumption of a characteristic velocity profile, the measured velocity profiles were numerically integrated across the channel width to determine the average measured plug velocity $\mathcal{U}_p = \frac{1}{W}\sum_i u_{x,i}\Delta y$ at that value of $\frac{z}{H}$ to be compared against the imposed nominal velocity $\langle\mathcal{U}\rangle$. For all profiles, $1 \leq \mathcal{U}_p/\langle\mathcal{U}\rangle \leq 1.15$, indicating that wall effects due to the finite aspect ratio of the channel effectively reduces the channel cross section by less than 15%, with three-dimensional effects thus confined to $|\frac{z}{H}| \geq 0.4$.

Velocity profiles for the CPyCl:NaSal solution are shown in both dimensional and scaled dimensionless form in Figure 5.5.1 for $1 \leq Wi \leq 45$. The profiles appear to extend beyond the channel width, on account of some variability in the width of the channel (± 5 μm) and the finite spatial error in the velocimetry measurements (5 μm). The most general feature in these profiles is the transition from a mixed Newtonian and shear-banding profile at low $Wi \approx 1$ to a very markedly shear-banding, nearly perfect

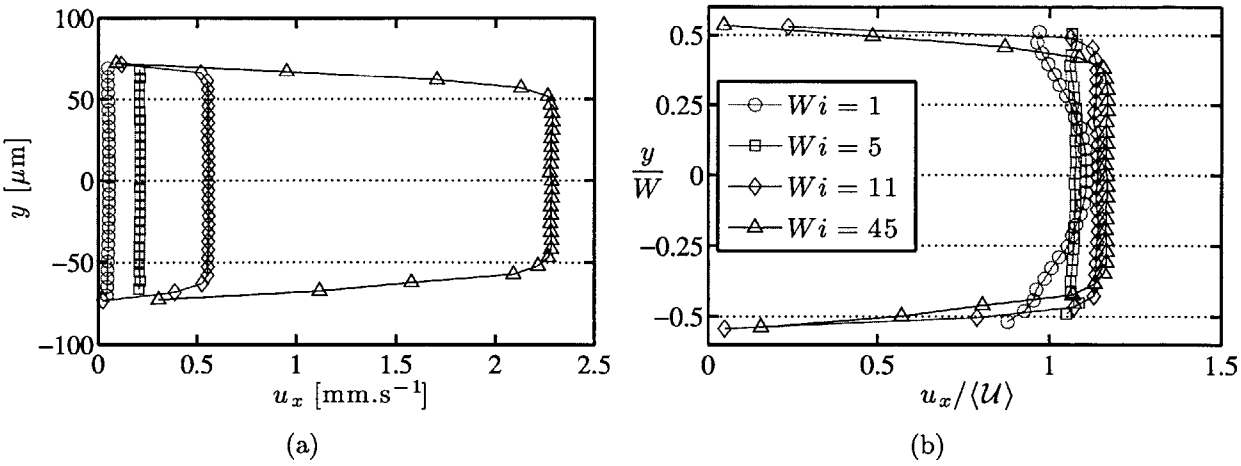

Figure 5.5.1: Representative dimensional (a) and non-dimensionalized (b) velocity profiles for 100:60 mM CPyCl:NaSal at different Weissenberg numbers in the rectangular duct taken at $0.2 \leq \frac{z}{H} \leq 0.3$ above the bottom of the channel at $L_{obs} = 3.5$ cm ($L_{obs}/D_h = 134$).

plug-like profile, with $u_{x,max} = \langle \mathcal{U} \rangle$ at moderate Wi. At higher $Wi > 10$ a departure from perfect plug-like flow is observed, with $u_{x,max} > \langle \mathcal{U} \rangle$, and a progressive increase in the thickness of the shear-banding layer with Wi.

An additional noteworthy feature in the velocity profiles of the CPyCl:NaSal system, especially at low $Wi \leq 5$ is what appears to be evidence of wall slip between the fluid and the channel walls. At the lowest flow rate this apparent slip may be an artifact of very thin shear-banding layers near the walls, which were too thin to be resolved by the μ-PIV system. The expected thickness of the shear-banding layers can be estimated by assuming the previously described, classical picture of a shear-banding fluid, whereby the shear rate within the band is assumed to be $\dot{\gamma}_2 \approx 500$ s^{-1} which lies at the right hand end of the stress plateau for the CPyCl:NaSal system presented in Figure 5.2.1 (a). To first order, this thickness of the shear-banding layer is $l_{SB} \approx \langle \mathcal{U} \rangle / \dot{\gamma}_2$. For $Wi = 1$, the average velocity is $\langle \mathcal{U} \rangle = 47$ μm.s^{-1} and hence $l_{SB} \approx 0.1$ μm. At $Wi = 5$, $\langle \mathcal{U} \rangle = 180$ μm.s^{-1}, the thickness only increases to $l_{SB} \approx 0.4$ μm. For the μ-PIV system used for these experiments, the minimum resolvable feature $e/M = 0.65$ μm and accordingly the shear-banding layer is too thin to be resolved by μ-PIV at low Wi.

Dimensional and dimensionless velocity profiles of the CTAB:NaSal solution are

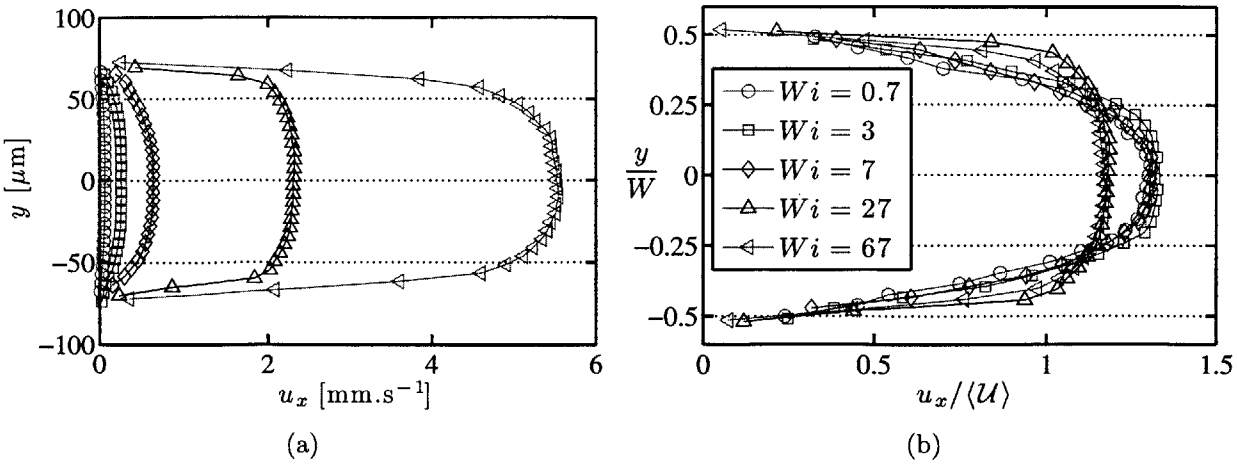

Figure 5.5.2: Representative dimensional (a) and non-dimensionalized (b) velocity profiles for 30:240 mM CTAB:NaSal at different Wi in the rectangular duct taken at $0.2 \leq \frac{z}{H} \leq 0.3$ above the bottom of the channel at $L_{obs} = 3.5$ cm ($L_{obs}/D_h = 134$).

shown in Figure 5.5.2. This solution exhibits a very clear transition from a parabolic-like velocity profile associated with the flow of a Newtonian fluid at low $Wi \leq 1$, to a flatter U-shaped velocity profile characteristic of the flow of a moderately shear-thinning fluid at moderate to high Weissenberg number ($Wi \gg 1$). To within experimental uncertainty (error bars not shown in Figure 5.5.2), measured fluid velocities within 5 μm of the wall are equal to or less than about 15% of the maximum velocity in the channel, $u_w \leq 0.15 u_{max}$. Accordingly, wall slip is not a significant contribution to the flow profile at any flow rate.

5.5.3 Birefringence and Stress

Evolution of the Birefringence Profiles

As the fluids flow down the length of the channel, the local deformation rate and therefore the optical anisotropy varies along both the channel width and length, such that one can expect $\dot{\gamma}(x, y)$, $\delta(x, y)$ and $\Theta(x, y)$. In order to observe the evolution of the optical anisotropy in the channel, full-field pseudocolor retardance maps, for which the imaged channel area was $(\Delta x_{im}, \Delta y_{im}) = (700\ \mu\text{m}, 130\ \mu\text{m})$, were obtained at $L_{obs} = 1.5$, 2, 2.5, 3, 3.5 and 4 cm ($L_{obs}/D_h = 58$, 77, 96, 115, 134, 154) downstream from the inlet of

the channel. Since $\Delta x_{im} \ll L$, and variations in δ are typically small in the x-direction within the field of view Δx_{im}, the local quantity $\delta(x, y)$ can be averaged over the flow direction for each image, to obtain the averaged one-dimensional profiles of $\delta(y)$ shown in Figure 5.5.3. For these measurements, a background image was taken without the channel in view, in order to apply the background correction for the residual birefringence of the optical train only. This approach facilitated observation of the flow-induced birefringence at different positions along the length of the channel without biasing the background correction at all channel positions with that of a single, particular location in the channel. Accordingly, any residual birefringence of the channel, though small compared to the FIB of the flowing fluid, is not accounted for in these images.

For a particular value of Wi, the Deborah number De, is the dimensionless quantity that dictates how fully-developed one can expect the viscoelastic flow and the optical anisotropy to have become (Dealy, 2010). For $Wi \leq 75$, the Deborah numbers corresponding to the different L_{obs} listed above are all less than unity, and the retardance profiles were observed to reach a fully-developed profile within the channel length. The spatially fully-developed nature of the flow is revealed by the superposition of retardance profiles with decreasing De shown in Figure 5.5.3. For $Wi > 75$, the higher velocities result in Deborah numbers (corresponding to the different observation positions L_{obs}) of order unity or greater indicating that within the length of the channel a fully-relaxed stress profile could not be obtained. Thus spatially-developing FIB profiles were observed through the entire length of the channel.

Background Corrected Birefringence Profiles

Measurements of retardance $\delta(x, y)$, and azimuthal angle $\chi(x, y)$, for which the residual birefringence of the channel was corrected, were taken at $L_{obs}/D_h = 134$. Full-field pseudocolor plots of CPyCl:NaSal retardance, are presented in Figure 5.5.4. For fully-developed flow, the quantities $\delta(x, y)$ and $\chi(x, y)$ can be averaged in x, to obtain the steady profiles of $\delta(y)$ and $\chi(y)$ at a selection of Wi, for which $De < 1$, shown in Figures 5.5.5.

At low $Wi < 5$, the retardance profiles increase linearly from the centerline of the

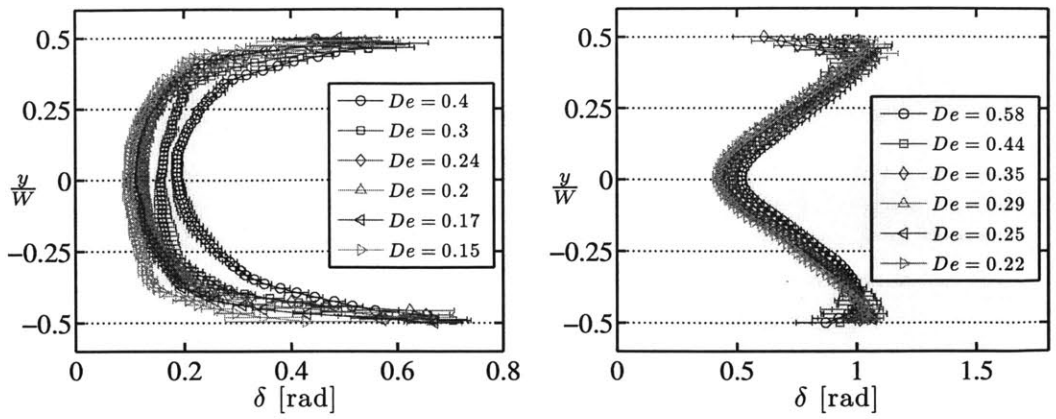

(a) (b)

Figure 5.5.3: Retardance profiles at different Deborah numbers, De, (corresponding to different L_{obs}) in the rectangular duct. Error bars correspond to the standard deviation of the retardance values. (a) 100:60 mM CPyCl:NaSal. $Wi = 45$, $Q = 1000$ μL/hr. (b) 30:240 mM CTAB:NaSal. $Wi = 67$, $Q = 2500$ μL/hr.

channel to the wall, taking on a characteristic V-shaped profile. Since τ_{xy} varies linearly across the channel for rectilinear pressure-driven flow, the linear variation in δ indicates that the shear stress τ_{xy}, is the predominant contribution to $\Delta\sigma$, given by Eq. (5.3.2). The contributions from the normal stress difference N_1, are confined to a thin region near the wall and are negligibly small for low Wi. For increasing $Wi > 10$, regions of high, but localized, retardance develop near the walls yielding a U-shaped profile, indicating the growth in the thickness of high shear rate bands. The change in retardance at the middle of the channel with increasing Wi is much more gradual when compared to the rapid change in the high shear rate regions near the walls. At higher Wi, however, the retardance along the channel centerline is finite indicating non-zero normal stress difference along the center of the channel. The increased contribution of elastic stresses even in regions of low shear rate near the channel centerline can be rationalized by the possibility of diffusion of elastic stresses due to the importance of non-local effects (discussed in Chapter 4) that have been documented in the microfluidic flows of other complex fluids (Masselon *et al.*, 2008), and recently studied numerically (Cromer *et al.*, 2010).

The azimuthal angle profiles exhibit odd symmetry about the centerline of the chan-

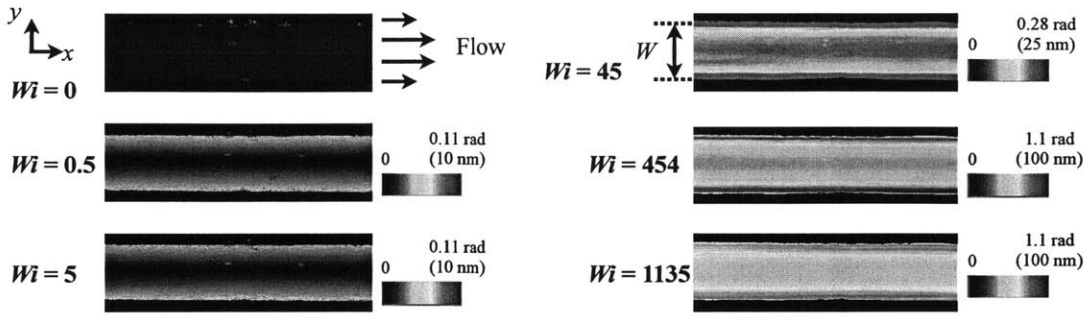

Figure 5.5.4: Pseudocolor plots of retardance maps for the 100:60 mM CPyCl:NaSal solution in the rectangular duct at $L_{obs} = 3.5$ cm ($L_{obs}/D_h = 134$). Color bar indicates linear scaling in retardance for each image. Areas beyond the channel width are shown by the black bands.

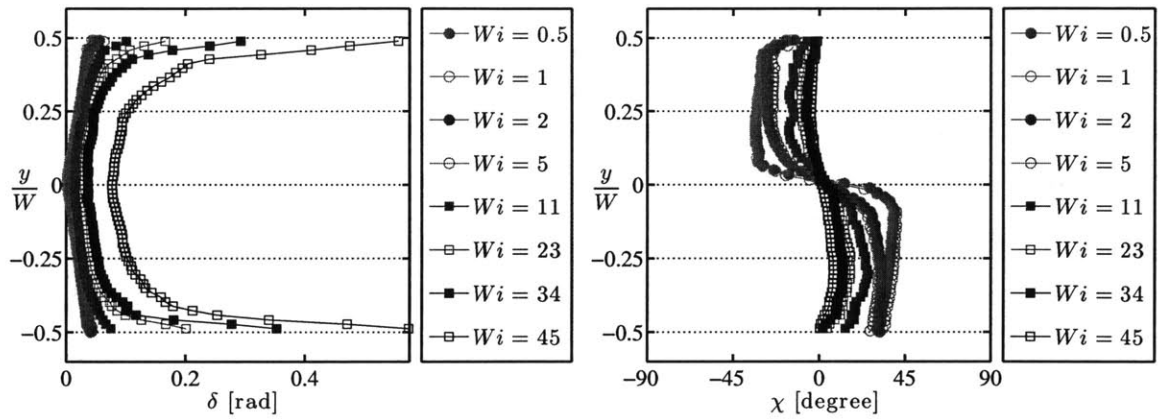

Figure 5.5.5: Experimental retardance and azimuthal angle profiles at increasing Wi for the 100:60 mM CPyCl:NaSal solution in the rectangular duct at $L_{obs} = 3.5$ cm ($L_{obs}/D_h = 134$). (a) Retardance Profiles. (b) Azimuthal Angle Profiles.

nel. At low Wi, the azimuthal angle is $\chi = -45°$ ($\frac{\pi}{4}$) and $\chi = 45°$ ($\frac{3\pi}{4}$) on opposite sides of the channel width. These limiting values for χ predicted by Eq. (5.3.3) also confirm that τ_{xy} is considerably greater than N_1 for this flow rate, with the change from $-45°$ to $45°$ arising from the change in sign of τ_{xy} on opposite sides of the channel. With increasing Wi, the azimuthal angle approaches $0°$ at all points in the channel, further confirming the presence of elastic stresses and high molecular alignment in the direction of flow along the channel centerline.

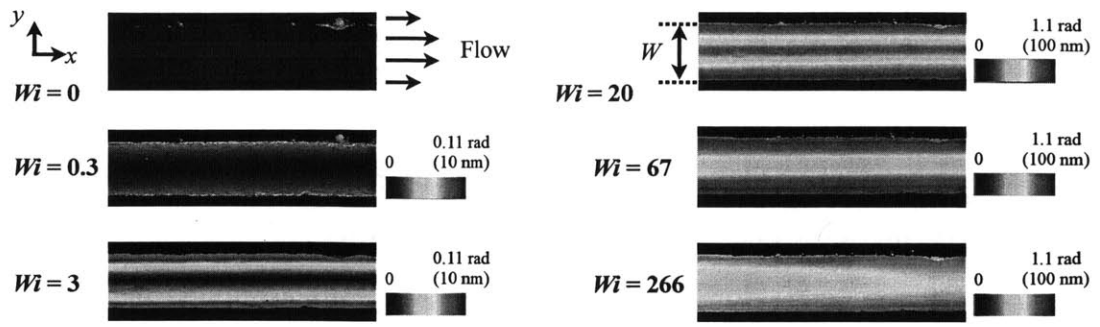

Figure 5.5.6: Pseudocolor plots of retardance maps for the 30:240 mM CTAB:NaSal solution in the rectangular duct at $L_{obs} = 3.5$ cm ($L_{obs}/D_h = 134$). Color bar indicates linear scaling in retardance for each image. Areas beyond the channel width are shown by the black bands.

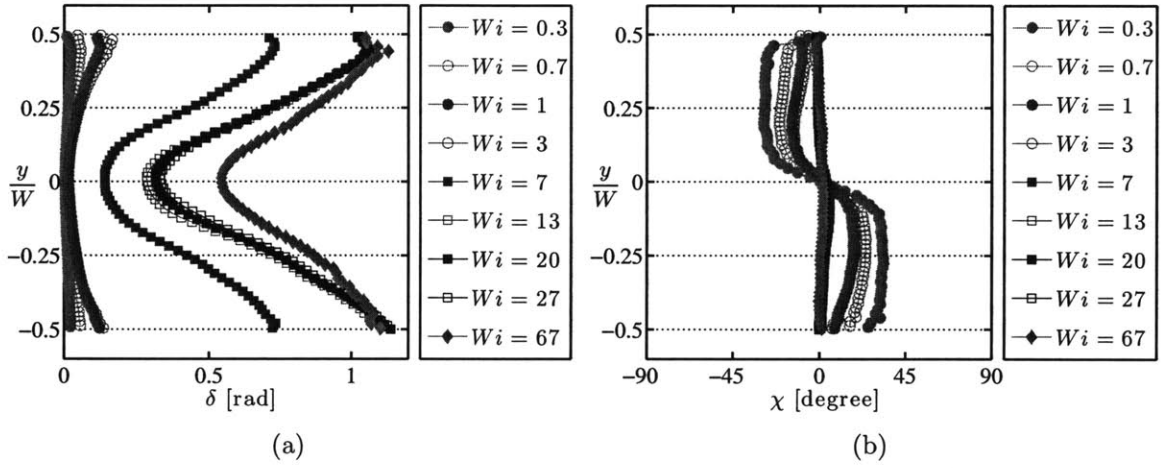

Figure 5.5.7: Experimental retardance and azimuthal angle profiles at increasing Wi for the 30:240 mM CTAB:NaSal solution in the rectangular duct at $L_{obs} = 3.5$ cm ($L_{obs}/D_h = 134$). (a) Retardance Profiles. (b) Azimuthal Angle Profiles.

Background corrected measurements of the birefringence in the CTAB:NaSal system were also taken at $L_{obs}/D_h = 134$. Pseudocolor plots of retardance are shown in Figure 5.5.6 and the resultant spatially-averaged retardance and azimuthal angle profiles are presented in Figures 5.5.7. For all Weissenberg numbers, retardance profiles take on a consistently V-like shape, indicating that there are no banded regions of localized, high shear rate and normal stresses that cause high, localized retardance near the walls. As seen in the CPyCl:NaSal system, at higher flow rates for the CTAB:NaSal system,

the retardance along the channel centerline is finite, and the retardance profiles increase monotonically from the centerline to the wall for all Wi. For the sake of visual clarity, however, error bars have not been shown in Figure 5.5.7. Beyond $Wi \sim 1$, the retardance profile increases substantially and appears to saturate near the wall for $Wi > 30$.

Anti-symmetry in the azimuthal angle profiles about the channel centerline may also be seen for this system. However, even for the lowest Wi examined here seen in Figure 5.5.7 (b), the azimuthal angle did not attain the limiting values of $\chi = \pm 45°$, indicating that the elastic stresses were substantial enough to partially align the molecules in the flow direction at all positions across the width of the channel. For high Wi, the azimuthal angle again approaches 0° across the entire channel, indicating high molecular alignment in the flow direction.

5.5.4 Comparison of Measurements with Theoretical Predictions

In order to validate the birefringence microscopy system for use in optical rheometry, the stress-optical rule is assumed to be valid and the predictions of the Ellis model introduced in Section 3.3.2 for pressure-driven rectilinear flow are compared to the independent measurements of flow kinematics and FIB. Although this model is only a generalized Newtonian fluid model, it has been selected here because it can compactly capture both the zero-shear viscosity and the rate-dependent shear-thinning regime of the fluid and can be used to obtain an analytical result for the velocity profile in the channel (given in Eq. 5.5.7 below). For fully-developed, inertialess flow along the x-axis of the channel with $W \ll H \ll L$ (here $H/W \approx 8$), the governing equation of motion is

$$\frac{\partial P}{\partial x} = \frac{\partial \tau_{xy}}{\partial y} \tag{5.5.5}$$

where τ_{xy} is the shear stress and P is mechanical pressure. This equation may be integrated directly with the boundary condition $y = \pm\frac{W}{2}$, $\tau_{xy} = \mp\tau_w$, to obtain $\tau_{xy}(y) = -\tau_w \frac{2y}{W}$, where $\tau_w = -\frac{W}{2}\frac{\partial P}{\partial x}$. Eq. (3.3.7) may be multiplied by the shear rate, $\dot{\gamma}$, and with rearrangement, one may obtain the following relation between the velocity gradient and shear stress.

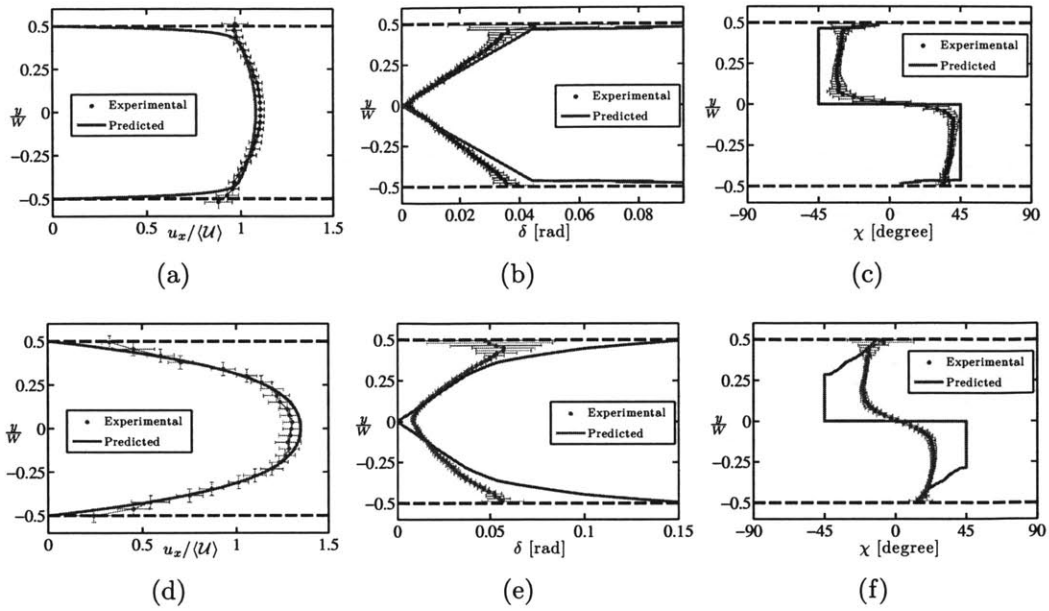

Figure 5.5.8: Representative experimentally-measured and theoretically-predicted velocity, retardance and azimuthal angle profiles at low Wi in the rectangular duct . Data are taken at 200 to 300 μm above the bottom of the channel at $L_{obs}/D_h = 134$. (a)-(c) 100:60 mM CPyCl:NaSal (blue profiles), $Wi = 1$, $Q = 25$ μL/hr. (d)-(f) 30:240 mM CTAB:NaSal (red profiles), $Wi = 0.7$, $Q = 25$ μL/hr.

$$\frac{du_x}{dy} \equiv \dot{\gamma} = \frac{\tau_{xy}}{\eta_0}\left[1 + \left(\frac{\tau_{xy}}{\tau_{1/2}}\right)^{\alpha-1}\right] \tag{5.5.6}$$

Substitution for $\tau_{xy}(y)$ in Eq. (5.5.6), integration and application of the no slip boundary condition $u_x = 0$ at $y = \frac{W}{2}$ yields the resultant velocity profile:

$$u_x = \frac{\tau_w}{4\eta_0}W\left[\left(1 - \frac{4y^2}{W^2}\right) + \frac{2}{\alpha+1}\left(\frac{\tau_w}{\tau_{1/2}}\right)^{\alpha-1}\left(1 - \left|\frac{2y}{W}\right|^{\alpha+1}\right)\right] \tag{5.5.7}$$

The average velocity is

$$\frac{1}{W}\int_{-W/2}^{W/2} u_x dy = \langle\mathcal{U}\rangle \equiv \frac{Q}{WH} = \frac{\tau_w}{6\eta_0}W\left[1 + \frac{3}{\alpha+2}\left(\frac{\tau_w}{\tau_{1/2}}\right)^{\alpha-1}\right] \tag{5.5.8}$$

In the limiting case of $\alpha = 1$, Eq. (5.5.7) and (5.5.8) reduce to the standard result for a Newtonian fluid with viscosity $\mu = \frac{1}{2}\eta_0$, where the factor of $\frac{1}{2}$ results from Eq. (3.3.7). Since the flow rate Q, is prescribed in the present study, the wall shear stress τ_w must be determined implicitly from Eq. (5.5.8) in order to determine the velocity profile for

a given Q. In this manner, the predicted velocity profiles shown in Figures 5.5.8, 5.5.9 and 5.5.10 were obtained for comparison with the experimentally measured results.

For fully-developed viscous flow of any fluid in a high aspect ratio duct, the shear stress varies linearly with position between $-\tau_w \leq \tau_{xy} \leq \tau_w$, and it is therefore necessarily zero at the centerline of the channel. For a given volumetric flow rate Q, the shear stress at all positions across the width of the channel can be determined, once τ_w is calculated from Eq. (5.5.8). In this way, the Ellis model was used to predict the shear rate profile, while the distribution of the first normal stress difference across the channel was predicted by interpolation of rotational rheometer data for $N_1(\dot{\gamma})$, with the local shear rate calculated from the spatial gradient $\dot{\gamma}(y) = \partial u_x/\partial y$ in Eq. (5.5.7). When the imposed flow rate is so high that the resulting calculated shear rate at a particular y-position across the channel is higher than the shear rates for which data from the rotational rheometer could be obtained, no comparative data have been plotted. The calculated values of deviatoric stresses, $\tau_{xy}(y)$ and $N_1(y)$, were then used to calculate the principal stress difference $\Delta\sigma(y)$ from Eq. (5.3.2). This value can then be used to predict the expected optical anisotropy $\Delta n(y)$, from the stress-optical rule in Eq. (5.3.1). Finally, the optical anisotropy can be related to the measured retardance $\delta(y)$, using the assumption that variations in the flow along the height of the channel are negligible so that Δn is invariant along the the z-axis. The anticipated azimuthal angle, which indicates molecular orientation, was calculated from Eq. (5.3.3). For the results presented here, $\chi = 0°$ coincides with the direction of flow (x-axis), with χ increasing counterclockwise, such that $\chi = 90°$ coincides with the y-axis.

At very high flow rates, the flow is not spatially fully-developed and exhibits streamwise variations as can be seen, for example, in the axial variations in retardance for $Wi = 266$ in Figure 5.5.6. Therefore, the quantitative analysis is restricted to $Wi \leq 67$ and $De < 1$ where the flow is fully-developed and steady (see Section 5.6 for additional discussion). A comparison between model predictions and experimental results for $Wi \approx 1$ are shown in Figure 5.5.8. The velocimetry measurements for the CPyCl:NaSal system reveal a Newtonian-like core surrounded by thin shear bands of fluid with high local shear rate. The linear increase in $\delta(y)$ with y in the core region is also quantitatively

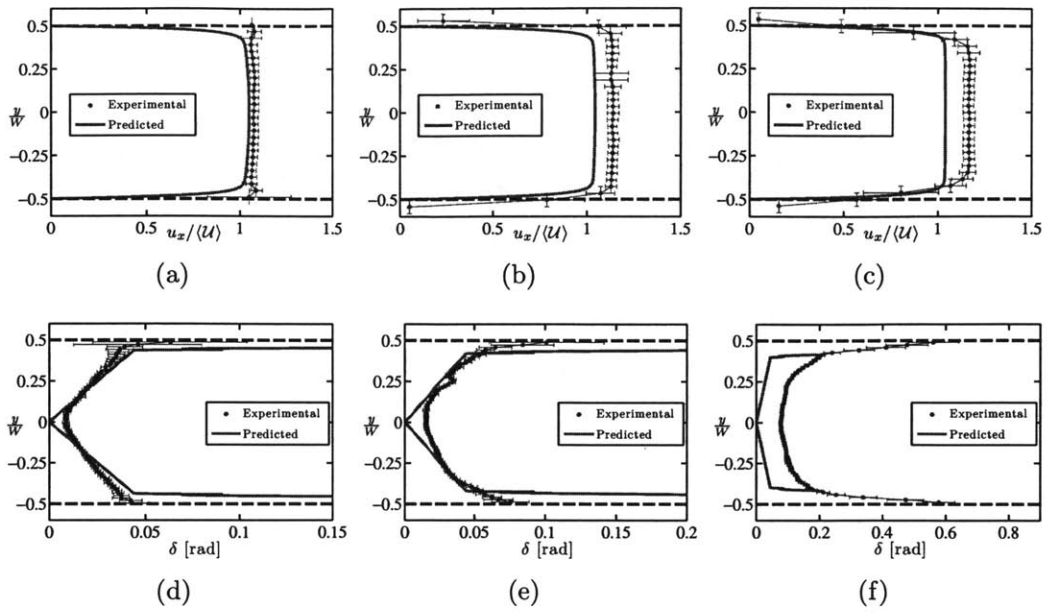

Figure 5.5.9: Representative non-dimensionalized experimental and predicted velocity (a)-(c) and retardance (d)-(f) profiles at different Wi for the 100:60 mM CPyCl:NaSal system in the rectangular duct at $L_{obs}/D_h = 134$. (a) & (d) $Wi = 5$, $Q = 100$ μL/hr. (b) & (e) $Wi = 11$, $Q = 250$ μL/hr. (c) & (f) $Wi = 45$, $Q = 1000$ μL/hr.

described by the Ellis model, confirming the validity of the stress-optical relationship for this micellar system as well as the utility of this model in predicting fully-developed channel flow of viscoelastic micellar liquids at low Wi. Note that the centerline retardance in Figure 5.5.8 (b) is $\delta = 2.5 \times 10^{-3}$ rad ($r = 0.22$ nm, $\Delta n = 2.2 \times 10^{-7}$) which is small enough to be in the experimental noise limit of the ABRIO system, confirming that spatial blurring due to the finite aperture of the incident light is negligible. Similar profiles for the shear-thinning CTAB:NaSal system at $Wi = 0.7$ are shown in Figure 5.5.8. The predicted velocity profile captures the measured results in the core of the flow, and the profiles near the walls agree within experimental uncertainty. The predicted retardance profile also agrees with experimental values in the middle of the channel. The model over-predicts retardance near the walls due to the anticipated presence of normal stress there and the gradual breakdown in the stress-optical rule seen for $\dot{\gamma} > 0.5$ s^{-1} in Figure 5.3.1 (b). The measured azimuthal angle also differs from the predicted values indicating higher than anticipated molecular alignment with the flow even at this low Wi.

Now that the ability of the μ-PIV system and the microfluidic birefringence measurements to probe quantitatively the kinematics and state of stress in a flowing complex liquid at moderate Weissenberg number has been established, these techniques are used to explore strongly viscoelastic channel flows for larger Wi. A series of profiles for the CPyCl:NaSal system at $Wi > 1$, but $De < 1$ are shown in Figure 5.5.9. The Ellis model predictions capture the general form of the experimentally-measured velocity and retardance profiles at $Wi = 5$ to within experimentally resolvable limits. The discrepancy between the model predictions and experimental results increases at high Wi. The systematic underprediction of the velocity in the plug-like core may be due to the confining effects of the upper and lower channel walls. The finite aspect ratio of the channel ($\Lambda = 7.7$) necessitates a higher effective plug velocity than the prediction of the two dimensional model. Velocimetry measurements at $5 < Wi < 100$ also indicate that three dimensional kinematic effects at the bottom of the channel are confined to less than 15% of the channel height, as noted before from the numerical integration of the velocity profiles. This systematic deviation is of the same order as the underprediction shown in Figure 5.5.9 (b) and (c) (see Section 5.6). Additional uncertainty can be attributed to the inability of the simple Ellis model to capture in any quantitative way the underlying shear-banding dynamics associated with the CPyCl:NaSal solution as Wi is increased. Specifically, it cannot describe the evolution in the underlying microstructure that is associated with the stress degeneracy in the shear-banding regime corresponding to $Wi > 1$ and which can be observed in the viscometric measurements, shown in Figure 5.2.1.

With increasing Wi, narrow, localized regions of high retardance emerge near the walls of the channel, whose intensity increases with increasing flow rate, see also Figure 5.5.4. These retardance bands confirm the existence of shear-bands in this fluid and are at least qualitatively captured by the Ellis model. It is noteworthy that the retardance in the unbanded region of the flow near the center of the channel, where shear stress should dominate elastic stress, increases only slightly with increasing Wi, compared to the large increase in retardance in the shear-bands near the wall. This small change is well predicted by the Ellis model and is a result of the *spurt effect*

seen previously for this CPyCl:NaSal system (Mair & Callaghan, 1997; Méndez-Sánchez *et al.*, 2003), whereby a constant wall shear stress is associated with a many fold increase in the average velocity $\langle \mathcal{U} \rangle$ and thus Wi. Quantitative discrepancies between the measured and predicted retardance in the banded region of flow, especially for $Wi = 45$ in Figure 5.5.9 (f), may result from a break down in the stress-optical rule. The validity of the stress-optical rule was not verified for high shear rates in the shear-banding regime, $\dot{\gamma} \sim \mathcal{O}(10^2)$ s^{-1}, by the measurements shown in Figure 5.3.1 (a), so it is unrealistic that extrapolations with this rule well into the stress plateau will yield completely quantitative agreement with experiment.

In nearly all measurements for $Wi > 1$, a finite retardance ($\delta > 5 \times 10^{-3}$ rad) along the centerline ($y = 0$) of the channel is observed, differing from the predictions of the Ellis model for two dimensional flow. Since a near-zero centerline retardance was observed in the CPyCl:NaSal at low Wi, it would seem this finite retardance is not an artifact of the finite aperture of the incident light, and it can be attributed to several different reasons. Firstly, the measured retardance is the result of an integrated signal along the pathlength of the incident lightwave through a truly three-dimensional flow. Secondly, errors may arise from the inability of the model to predict diffusive coupling of elastic stresses from the regions of high to low shear rate shown in Figure 5.5.7 (b). Microstructural stress diffusion can lead to non-local effects (Masselon *et al.*, 2008), that are not captured by the predictions of the simple Ellis model, and more sophisticated models, such as those discussed by (Olmsted *et al.*, 2000; Vasquez *et al.*, 2007; Cromer *et al.*, 2010) are needed to capture non-local effects.

Velocity and retardance profiles for the shear-thinning CTAB:NaSal system at $Wi > 1$ and $De < 1$ are presented in Figure 5.5.10. In contrast to the CPyCl:NaSal system, the velocimetry measurements of the CTAB:NaSal solution do not reveal plug-like flow profiles even up to the maximum flow rate ($Wi = 67$) for which velocimetry measurement were made; the measured and predicted velocity profiles both indicate strong shear-thinning behavior. No regions of localized, high retardance can be identified in the birefringence measurements for the CTAB:NaSal system. The Ellis model is capable of predicting only some of the features observed for the CTAB:NaSal solution at these

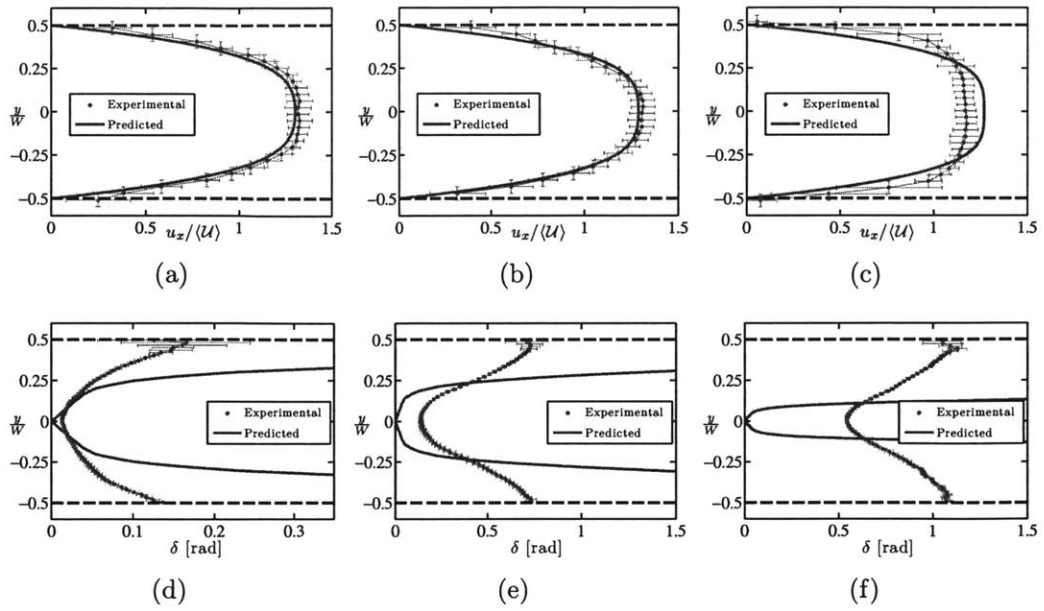

Figure 5.5.10: Representative non-dimensionalized experimental and predicted velocity (a)-(c) and retardance (d)-(f) profiles at different Wi for the 30:240 mM CTAB:NaSal system in the rectangular duct at $L_{obs}/D_h = 134$. (a) & (d) $Wi = 3$, $Q = 100$ μL/hr. (b) & (e) $Wi = 7$, $Q = 250$ μL/hr. (c) & (f) $Wi = 67$, $Q = 2,500$ μL/hr.

Weissenberg numbers. As Wi is increased, the agreement between the experimental and predicted velocity profiles is steadily reduced. In particular, using the model parameters listed in Table 3.3.1 for $Wi = 67$ the measured shear rate near the channel walls is greater than the predicted value by approximately a factor of two. This deviation from predicted behavior indicates a more dramatically reduced viscosity than that predicted by the Ellis model at the corresponding shear rate. Estimates of the shear rate near the wall at this Wi using the Ellis model are on the order of $\dot{\gamma} \sim \mathcal{O}(10^2)$ s^{-1}, which coincides roughly with the apparent stress plateau observed for this fluid in Figure 5.2.1 (b).

Deviations between experimental and predicted results for the CTAB:NaSal system at high deformation rates may be attributed to the same factors given previously for the CPyCl:NaSal system, including a breakdown in the stress-optical rule for $\lambda\dot{\gamma} \geq 1$ seen in Figure 5.3.1 (b). The measured and predicted profiles typically differ by a factor of at least two, which is approximately the extent to which the stress-optical rule fails in Figure 5.3.1. Additionally, a simple generalized Newtonian model like the Ellis model can only be expected to capture some of the gross features of the shear rheology of the

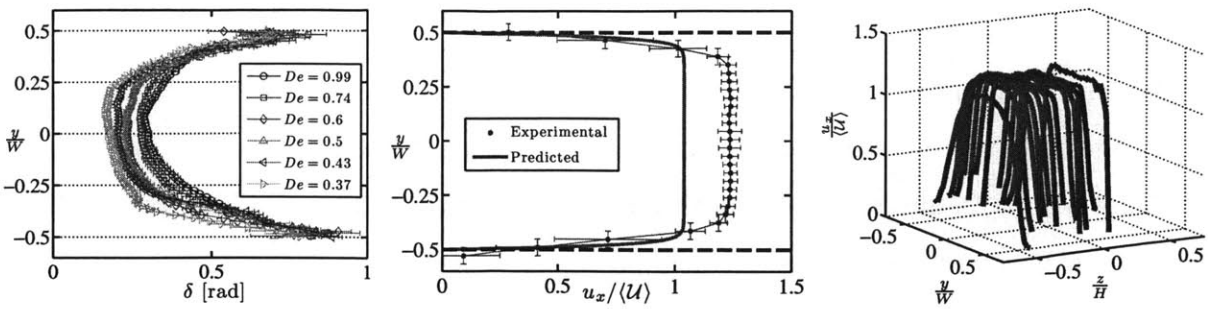

(a) (b) (c)

Figure 5.6.1: 100:60 mM CPyCl:NaSal. $Wi = 113$, $Re_0 = 1.4 \times 10^{-5}$, $Q = 2,500$ μL/hr. (a) Uncorrected retardance profiles at different De (different L_{obs}) in the rectangular duct. (b) Representative experimental and predicted velocity profiles for $De = 0.43$, ($L_{obs} = 3.5$ cm, $z/H = 0.25$). (c) Non-dimensionalized experimental velocity profiles taken at $50 \leq z \leq 900$ μm above the bottom of the channel for $De = 0.43$, ($L_{obs} = 3.5$ cm).

CTAB:NaSal system, since it cannot capture the combined shear-thinning and apparent shear-banding behavior seen in this system for $30 < \dot{\gamma} < 100$ s^{-1} in Figure 5.2.1 (b). Clearly a more sophisticated viscoelastic constitutive model is necessary to predict accurately the stress field and the resulting birefringence in complex micellar fluids for $Wi \gg 10$.

5.6 Three Dimensional and High Weissenberg Number Effects

In the previous sections, comparisons between experimental results and the predictions of the Ellis model were made only for dimensionless shear rates corresponding to spatially fully-developed flow, $De \leq 1$. For these conditions, comparison with the steady state solution of a non-Newtonian constitutive model was appropriate. By contrast, as the flow rate is increased and the residence time in the channel decreases (corresponding to $De > 1$), the flow becomes increasingly unsteady in the Lagrangian frame and the viscoelastic stresses may not be fully-developed at a particular observation point, L_{obs}.

To explore this continuing spatial development in the flow, the birefringence micro-

scope system is used to plot and compare lateral profiles in the retardance at different axial positions along the channel. This spatial development in the flow can be noticed, in particular, in the pseudocolor plot for the flowing CTAB:NaSal solution at $Wi = 266$ in Figure 5.5.6. At any selected y-position, the birefringence intensity increases in the direction of flow even over the short distance $\Delta x_{im} = 700$ μm of channel length that is in view in a single microscope image. Furthermore, the magnitude of the peak retardance across the width of the channel *decreases* with increasing flow rate for $Wi \geq 133$ in the CTAB:NaSal system and $Wi \geq 454$ in the CPyCl:NaSal system. These results suggest that at high flow rates, the residence time for material elements in the channel is insufficient for the local viscoelastic stresses to develop fully.

The evolving retardance profile for the CPyCl:NaSal fluid at $Wi = 113$ is captured by the spatially averaged profiles shown in Figure 5.6.1 (a). With decreasing Deborah number ($De \equiv \lambda\langle\mathcal{U}\rangle/L_{obs}$), corresponding to observation distances further along the channel, the retardance near the middle of the channel ($-0.25 \leq y/W \leq 0.25$) relaxes steadily as the flow approaches the fully-developed limit, $De \rightarrow 0$. For this reason, comparisons between the steady state predictions of Ellis model and the measured birefringence profiles in Section 5.5.4 were restricted to measurements corresponding to $De \leq 0.25$.

The variation in $u_x(y)$ and $u_x(y,z)$ for the CPyCl:NaSal system at $Wi = 113$ are also presented in Figure 5.6.1 (b) and (c), respectively. At this flow rate, the axial velocity of the plug-like core, measured at $z/H = 0.25$, is roughly 20% greater than $\langle\mathcal{U}\rangle$. This core velocity is greater than the axial velocity for the 1D profile predicted by the Ellis model, in part, because the model does not include a finite high shear rate viscosity, so it under predicts the thickness of the high shear rate regions in the velocity profile which give rise to the higher core velocity seen experimentally. The higher core velocity is also caused by the finite aspect ratio of the channel ($\Lambda = 7.7$) giving rise to the vertical variations in the velocity profile shown in Figure 5.6.1 (c). The variations are confined to less than 100 μm above the bottom of the channel. The Reynolds number for this flow rate is sufficiently small ($Re_0 = 1.4 \times 10^{-5}$) that the estimated entrance length for the flow kinematics is much shorter than the observation positions, (*i.e.* $L_e \ll L_{obs}$), as given by the correlation in Section 5.5.1. Therefore, the kinematics remain steady and

close to two dimensional in character, as expected for low Reynolds number flow, and the evolution in the birefringence profiles observed at high Wi and De can be attributed to relaxation in the viscoelastic stress field downstream of the abrupt entrance to the flow channel.

5.7 Summary

The primary goal of the work in this Chapter has been the development and refinement of non-invasive instrumentation for quantifying the rheological response of complex fluids undergoing high rate deformations in microfluidic devices. Unique to this work is the adaptation of a commercially available birefringence microscopy system, originally designed to examine biological systems (Shribak & Oldenbourg, 2003) for optical rheometry. The greatest strengths of the ABRIO^{TM} system in probing the rheo-optical behavior of complex fluids are its ease of use and its ability to achieve highly spatially resolved measurements of the the viscometric flow of a complex fluid as it deforms in a microfluidic device.

The calibration experiments discussed here focused on the canonical case of flow in a rectilinear microchannel. μ-PIV and FIB measurements of two worm-like micellar solutions were compared against the predictions of a relatively simple constitutive model in order to demonstrate that the ABRIO^{TM} system can be reliably used for quantitative optical rheometry. The two test fluids, one a shear-banding 100:60 mM CPyCl:NaSal system, and the other a shear-thinning 30:240 mM CTAB:NaSal system, were first characterized using conventional macroscale as well as microscale rheometric techniques in order to determine the viscometric material functions that can then be used to predict their flow characteristics in more complex microfluidic geometries.

At the low to moderate Weissenberg and Deborah numbers ($Wi < 10$, $De < 1$) for which use of a generalized Newtonian fluid model is anticipated to be most accurate, there is near-quantitative agreement between the predictions of the model and experimental measurements of the flow kinematics as well as the retardance measured with the birefringence microscopy instrument. This agreement validates the use of the ABRIO

system for quantitative optical microfluidic rheometry. At high Weissenberg numbers, the μ-PIV and FIB results indicate that the material response of the fluids is more complex than can be predicted by such a simple generalized Newtonian fluid constitutive model. Clearly, simulations with a more realistic microstructurally-based constitutive model would be necessary for more reliable predictions at high Weissenberg numbers. Now that the ability of this coupled μ-PIV/birefringence microscopy system for studying a simple rectilinear channel flow has been demonstrated, it can confidently be used for making FIB measurements in considerably more complex microfluidic flows with mixed shearing/extensional kinematics, which is the subject of Chapter 6.

Chapter 6

Microfluidic Optical-Rheometry: Extension-Dominated Mixed Flow

6.1 Introduction

Microfluidic devices are ideally suited for the study of complex fluids undergoing large deformation rates in the absence of inertial complications. In the previous Chapter 5, high deformation rate shear flows in a microfluidic device were discussed, and in this Chapter, the same measurement techniques will be applied to study extensionally-dominated flows. In particular, a microfluidic contraction geometry can be utilized to characterize the material response of complex fluids in an extensionally-dominated flow, but the mixed nature of the flow kinematics makes quantitative measurements of material functions such as the true extensional viscosity challenging. In this Chapter, the 'extensional viscometer-rheometer-on-a-chip' (EVROC) is introduced. This device is a hyperbolically-shaped contraction-expansion geometry fabricated using microfluidic technology for characterizing the importance of viscoelastic effects in an extensionally-dominated flow at large extension rates ($\lambda\dot{\varepsilon}_a \gg 1$, where λ is the characteristic relaxation time, or for many industrial processes $\dot{\varepsilon}_a \gg 1\ s^{-1}$). Measurements of flow kinematics, pressure drop across the contraction and spatially-resolved flow-induced birefringence are combined to study model rheological fluids as well as several representative liquid consumer products to assess the utility of EVROC as an extensional viscosity indexer.

6.2 Experimental Methods for Microfluidic Extensional Rheometry

6.2.1 Microchannel Fabrication and the Hyperbolic Geometry

The microfluidic planar hyperbolic contractions were fabricated in Pyrex using standard wet-etching techniques by RheoSense (San Ramon CA, USA) as described elsewhere (Pipe *et al.*, 2008). The pressure measurements were made with a chip constructed by anodically bonding the Pyrex to a silicon wafer with four flush mounted microelectromechanical systems (MEMS) pressure sensors. This fabrication technique, however, produces a chip that must be housed in an opaque container, and therefore it could not be used for flow visualization. Accordingly, a second, transparent contraction of the same dimensions was fabricated from Pyrex and sealed to a 150 μm thick microscope coverslip to enable direct flow visualization experiments. An optical microscopy image and a schematic diagram of the contraction are shown in Figure 6.2.1, with channel dimensions given in the figure caption. The throat of the contraction was positioned at the mid-plane of the entire length of the channel ($\mathcal{L} = 13$ mm), but for convenience the origin of the experimental coordinate system is set to lie along the contraction centerline and at the beginning of the contraction inlet as shown in Figure 6.2.1 (a). The hyperbolic contraction is a unique geometry because it can be used, in principle, to impose a constant, nominal extension rate, owing to the fact that its cross-sectional area varies inversely with axial position. Indeed, if the flow is inviscid, or perfect slip at the wall occurs, for example if the flow is lubricated, then $\dot{\varepsilon}_{xx} = \partial u_x/\partial x = const$ for a given volumetric flow rate. For real fluids, however, the no-slip boundary condition at the wall cannot be circumvented and a more detailed analysis of the kinematics is required.

For the contraction depicted in Figure 6.2.1 having length, l_c, height, h, upstream width, w_u, width at the contraction throat, w_c, the width, $w(x)$, at any x takes the form $w(x) = K/(x_0 + x)$, where $x_0 = l_c w_c/(w_u - w_c)$ and $K = x_0 w_u$. Given a constant volumetric flow rate, Q, through the contraction, the average velocity at any x-position is $u_x = Q/hw(x)$, and so the apparent or nominal extension rate, $\dot{\varepsilon}_a$, neglecting any shearing flow induced by the bounding walls is

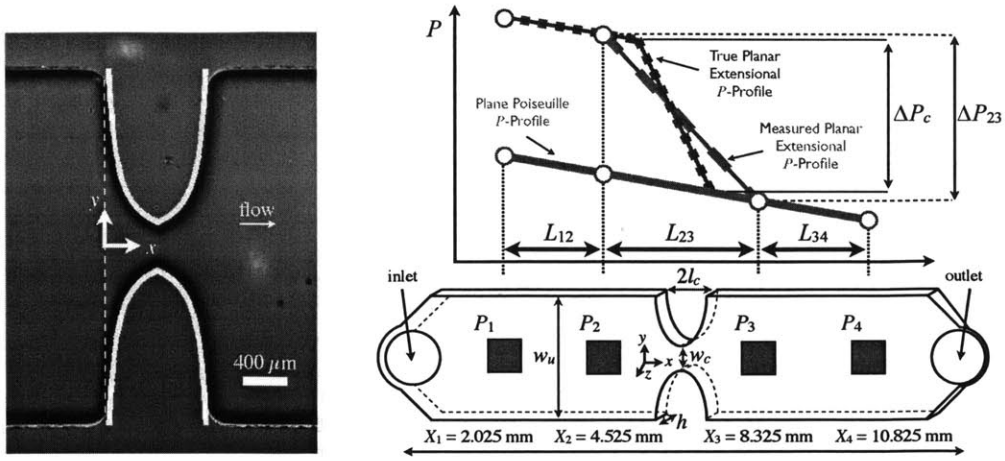

(a) (b)

Figure 6.2.1: (a) Optical transmission microscope image of the planar hyperbolic contraction-expansion geometry. Two curves outlining the contraction walls are superimposed on the image. The origin of the experimental coordinate system lies along the contraction centerline and at the contraction inlet as shown by the dashed white line. (b) Schematic diagram of the hyperbolic planar contraction and representative pressure profile, showing the coordinate system and variables used throughout the text. The contraction dimensions are $h = 200$ μm, $l_c = 400$ μm, $w_c = 400$ μm and $w_u = 2920$ μm. The solid squares indicate the approximate size and location of the flush-mounted MEMS pressure transducers. The schematic depiction is approximately to scale.

$$\dot{\varepsilon}_a = \frac{Q}{l_c h}\left(\frac{1}{w_c} - \frac{1}{w_u}\right) \tag{6.2.1}$$

The Hencky strain experienced by a fluid element, ε_H, flowing into the contraction is given by the equation

$$\varepsilon_H(x) = \int_0^t \dot{\varepsilon}_a dt' = \ln\left(\frac{w_u}{w(x)}\right) \tag{6.2.2}$$

The maximum Hencky strain occurs at the throat of the contraction and is therefore equal to $\varepsilon_H = \ln(w_u/w_c)$. For the specific channel geometry considered here $w_u = 2920$ μm and $w_c = 400$ μm, so the total Hencky strain is $\varepsilon_H = 2$.

Subsequent to the hyperbolic contraction region is a symmetric hyperbolic expansion ($l_c \leq x \leq 2l_c$). This configuration has been designed to generate a kinematically reversible flow for Newtonian fluids at low Reynolds numbers and thus equal energy dissipation in the contraction and expansion sections. There is a major difference between

the contraction and expansion, however, in that the direction of molecular extension is aligned with the flow through the contraction, but perpendicular to the primary flow direction in the expansion.

6.2.2 Pressure and Kinematics Measurement

Pressure drop measurements were made with the EVROC, which was fabricated with four inline, 800×800 μm^2 MEMS-based pressure transducers along the centerline, following the construction methods described in Baek & Magda (2003). The maximum measurable pressure of the device was $P_{max} = 40$ kPa, corresponding to the maximum allowable deflection of the membrane of the MEMS transducer. Measurement precision is approximately 100 Pa (0.2% P_{max}). The temperature of the chip was controlled by a thermal jacket (RheoSense Inc.), and an F12-ED Refrigerated/Heating Circulator (Julabo Inc.). Before each test, the EVROC contraction geometry was washed with ethanol and deionized water and then a sufficiently large amount of the test fluid was flushed through the contraction to ensure that there were no air bubbles remaining in the contraction. The test fluid was then allowed to rest in the microchannel for around 15 minutes, to allow the pressure field to equilibrate, after which the baseline pressure was measured. All tests were completed with a 2.5 mL Hamilton Gastight glass syringe (Reno, NV). For a given test fluid, a set of flow rates was selected so as to yield pressure drops spanning the entire dynamic range of the pressure transducers or to maximize the pump flow rate ($Q_{max} = 5.2$ mL.min^{-1}), whichever occurred first. The sampling period of each flow rate was selected such that the pressure profile attained a steady state value. Typically the lowest flow rates required on the order of minutes to become steady and the highest flow rates required only seconds. Hence, multiple tests were completed for each fluid to determine the necessary duration of each flow rate and to ensure repeatability.

Representative pressure profiles along the microchannel are depicted schematically in Figure 6.2.1 (b). The line labelled 'Plane Poiseuille P-Profile' represents the hypothetical pressure profile that would be measured without a contraction-expansion using an equivalent microfluidic chip designed for shear rheometry. The profile labelled 'Measured

Planar Extensional P-Profile' indicates a typical non-linear profile that is measured using the hyperbolic contraction-expansion geometry. The pressure drop between transducers 2 and 3 is denoted ΔP_{23}. The pressure drop that is of interest for extensional rheology measurements is the pressure drop associated with the contraction alone, ΔP_c, which is somewhat different from ΔP_{23}. This difference arises because the MEMS transducers 2 and 3 are located some distance upstream and downstream of the contraction entrance and exit as a result of fabrication constraints on the minimum relative spacing between each transducer and to ensure that both transducers lie far enough up and downstream of the contraction that they lie in regions of the channel where the rectilinear shear flow provides the dominant contribution to the pressure gradient. To calculate the value of ΔP_c, one can use the average of the pressure gradients for $X_1 < X < X_2$ and $X_3 < X < X_4$ to extrapolate the fully-developed shear flow pressure profile in the upstream and downstream channels to the inlet and outlet of the contraction, similar to the analysis of Wang *et al.* (2010). In making this extrapolation, fully-developed, rectilinear shear flow at low Reynolds number is assumed to dominate between the second transducer and the contraction inlet and between the contraction outlet and the third transducer. Accordingly, under the assumption that any possible inertial contributions to the pressure drop in the contraction region can be neglected, the true pressure drop across the contraction ΔP_c, is related to the measured pressured drop ΔP_{23}, by the relation

$$\Delta P_c = \Delta P_{23}\left\{1 - \frac{1}{2}\left(\frac{1}{\mathcal{P}} - 1\right)\frac{L_{23} - 2l_c}{L}\right\} \tag{6.2.3}$$

where $L_{23} = 3.8$ mm, $L \equiv L_{12} = L_{34} = 2.5$ mm and $l_c = 400$ μm.

A useful dimensionless pressure coefficient is defined in Eq. (6.2.3) as $\mathcal{P} \equiv \Delta P_{23}/\Delta P_{14}$ where ΔP_{14} is the pressure drop between transducers 1 and 4. This coefficient is positive and generally less than unity. It is a measure of the relative importance of the pressure drop in the extension-dominated region of the contraction-expansion geometry compared to the overall pressure drop across the entire microchannel. For low Reynolds number flows, this ratio is a constant independent of flow rate for Newtonian fluids, but it can vary with flow rate for non-Newtonian fluids, reflecting the role of viscoelastic

effects in the extension-dominated flow through the contraction. Therefore, this pressure coefficient serves as a simple metric by which to gauge the relative importance of viscoelastic effects in the contraction, and its use will be explained in more detail below.

These velocimetry measurements were performed in a climate-controlled room in which the temperature was 24 ± 1 °C. The flow rate was controlled with a PHD Ultra syringe pump (Harvard Apparatus). For streakline movies the test fluids were seeded at 0.02 wt.% with fluorescent particles of diameter $d_p = 8$ μm (Invitrogen), having excitation/emission wavelengths of 520/580 nm. Images were recorded with a (640×480 pixels) CCD camera (Blue FOX, Matrix Vision) and a continuous illumination mercury lamp with peak emission at 532 nm. In order to visualize the entire contraction region, the images were recorded with a low magnification 2×, 0.06 NA objective, corresponding to a depth of measurement, $\delta z_m = 938$ μm, using the formulae of Meinhart *et al.* (2000). This depth is greater than the channel thickness, $h = 200$ μm, and accordingly flow across the entire channel height was observed. Higher resolution images are readily possible with a high magnification objective, but it is then not possible to observe the full upstream and downstream flow in a single streak image.

The μ-PIV system used in this study has been described in Section 5.4.2. Velocimetry measurements were taken with a 10× 0.25 NA objective with the PIV-Cam 14-10 (1376×1024 pixels) CCD camera (TSI Instruments,) and a double-pulsed 532 nm Nd:YAG laser. Test fluids were seeded at 0.02 wt.% with monodisperse fluorescent particles of diameter $d_p = 1.1$ μm (Invitrogen). At this magnification, the depth of measurement was $\delta z_m = 47$ μm, and hence roughly one quarter of the contraction thickness was resolved in the velocimetry measurements. Full-field velocity maps were measured at the centerplane of the contraction, and these were ensemble-averaged using a conventional cross-correlation PIV algorithm (TSI Insight software). The x-component of the centerline velocity at a particular x-position was taken as the average of the x-component of the velocity vectors in the middle third of the throat width of the contraction (*i.e.* $-\frac{w_c}{6} = -67 \leq y \leq 67 = \frac{w_c}{6}$ μm). Error bars in the axial velocity profile plot shown in Figure 6.3.2 (a) correspond to the standard deviation of those data points. All post-processing of the velocity vector fields was performed in MATLAB with a script

Table 6.2.1: Newtonian fluid properties at 25 °C measured with a cone-and-plate rotational rheometer.

Fluid	ρ [kg/m^3]	μ [Pa.s]
Deionized H_2O	1000	0.001
44:56 wt% H_2O:Gly	1130	0.0085
34:66 wt% H_2O:Gly	1160	0.0122
S60 oil	877	0.102
N1000 oil	846	2.0

written by the authors.

Measurements of flow-induced birefringence in the hyperbolic contraction geometry were completed using the ABRIO^{TM} microscopy imaging system (CRi, Inc., Woburn, MA) described in Section 5.4.3. This system acquires a sequence of rapidly recorded images with a liquid-crystal-based optical polarizer, to produce spatially-resolved pixelwise measurements of retardance $\delta(x, y)$, of the imaged specimen or flow field. For microfluidic flow of a complex fluid, this retardance is related to the local degree of stretching and orientation of the macromolecules in the fluid, and assuming the validity of the stress-optical rule it can be used to evaluate the principal stress difference in the material.

6.2.3 Test Fluids

Five Newtonian calibration fluids of different dynamic viscosities μ, but similar densities ρ, were first studied. Deionized water was used for flow visualization experiments, and two mixtures of water and glycerol and two silicone-based calibration oils of different viscosities (S60 and N1000, Cannon Inst. Co) were used for pressure calibration measurements in the EVROC device. The rheological properties of these fluids are listed in Table 6.2.1. This selection of Newtonian fluids allowed for pressure measurements over nearly eight decades of Reynolds number ($10^{-5} < Re_0 < 10^3$).

The model non-Newtonian fluids studied were 3000 ppm (2×10^6 g.mol^{-1}) polyethylene oxide (PEO) in 34:66 wt% water:glycerol, and the same shear-banding worm-like micellar solution, consisting of 100 mM cetylpyridinium chloride (CPyCl) (Alfa Aesar) and 60 mM sodium salicylate (NaSal) (Alfa Aesar) in de-ionized water studied in Chap-

Table 6.2.2: Non-Newtonian fluid properties at 25 °C measured with a cone-and-plate rotational rheometer. *Assumed. †Measured using a capillary break-up extensional rheometer (CaBER).

Fluid	ρ [kg/m^3]	η_0 [Pa.s]	G_0 [Pa]	λ [s]	m [Pa.s^n]	n
CPyCl:NaSal	1000	40	26	1.5	15	0.01
PEO	1160*	0.080		0.076†	0.080	0.92
Herbal Essence	1000*	15	240	0.062	86	0.027
DayQuil	1000*	0.06		0.021†	0.1	0.8
Chili Sauce	1000*	–		0.56	0.83	0.57

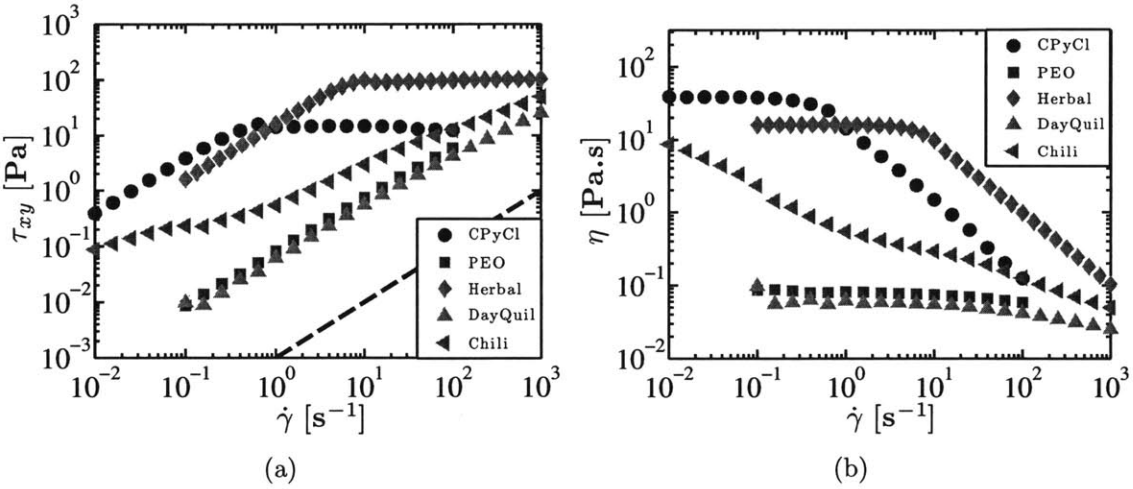

Figure 6.2.2: Steady flow curves of the non-Newtonian test fluids at 25 °C measured with a cone-and-plate rotational rheometer. The dashed line shows the stress/shear rate relationship for a Newtonian fluid with $\mu = 10^{-3}$ Pa.s.

ters 3 and 5. Other commercial fluids that were studied include Herbal Essence shampoo (Procter & Gamble) containing the surfactants sodium dodecyl sulfate (SDS) and sodium laureth sulfate (SLES), DayQuil (Vicks) containing water-borne carboxymethycellulose thickener and, finally, sweet chili sauce (Thai Kitchen) containing xanthan gum. The sweet chili sauce was first filtered to remove food particulates and this filtrate showed features of a critical gel in small amplitude oscillatory shear. The flow curves of these fluids were measured using a cone-and-plate geometry on a DHR3 rheometer (TA Instruments) and are shown in Figure 6.2.2.

All of these fluids exhibited a shear-thinning regime which has been fit with the power-law model (Bird *et al.*, 1987), for which the shear viscosity is given by $\eta = m\dot{\gamma}^{n-1}$,

where m is the consistency index and n is the dimensionless exponent. The rheological properties of the test fluids is given in Table 6.2.2. The linear viscoelastic properties of the CPyCl:NaSal solution and the Herbal Essence fluid were obtained by fitting a single mode Maxwell model to the storage and loss moduli measured in SAOS. The relaxation times of the PEO solution and DayQuil were measured using a capillary break-up extensional rheometer (CaBER) (McKinley & Tripathi, 2000). Because the chili sauce exhibited a yield stress, its relaxation time was not measured with CaBER, but instead was taken to be the inverse of the cross-over frequency in SAOS.

6.3 Results and Discussion

6.3.1 Dimensional Analysis

The relative importance of inertial effects in the device compared to viscous effects is quantified by the Reynolds number

$$Re_0 = \frac{\rho d_h l_c \dot{\varepsilon}_a}{\eta_0} \tag{6.3.1}$$

where ρ is the fluid density and η_0 is the zero-shear-rate viscosity of the test fluid, or equivalently the dynamic viscosity μ, if the fluid is Newtonian. For the flow in the hyperbolic contraction, the characteristic length scale is the hydraulic diameter defined at the throat of the contraction as $d_h = 2hw_c/(h + w_c) = 267$ μm. The hydraulic diameter is also the appropriate length scale because it accounts for the two-dimensionality of the channel cross-section, being calculated from both the height and width of the contraction simultaneously. The characteristic velocity is taken to be $\mathcal{U}_{char} = l_c\dot{\varepsilon}_a$, which is in fact equal only to the change in the average velocity from the inlet to the throat of the contraction. For contractions with a large contraction ratio, however, the magnitude of the change in the velocity through the contraction is of the same order as the average velocity at the throat of the contraction (for the contraction used in this study $Q/hw_c = 1.16 l_c\dot{\varepsilon}_a$), and hence it is an appropriate velocity scale for defining the Reynolds number for the contraction used in this study. The Deborah number is defined as the ratio of the fluid relaxation time to a time scale of observation. For the steady

Table 6.3.1: Range of dimensional and dimensionless parameters explored in this study.

Fluid	$\dot{\varepsilon}_a$ [s^{-1}]	Re_0	De_a	El_0
H_2O	$10^2 - 10^3$	$10^2 - 10^3$	–	–
S60	$1 - 10^2$	$10^{-2} - 1$	–	–
N1000	$0.1 - 10$	$10^{-5} - 10^{-3}$	–	–
CPyCl:NaSal	$0.1 - 10^2$	$10^{-7} - 10^{-4}$	$0.1 - 10^2$	6.5×10^5
PEO	$10 - 10^2$	$10^{-3} - 1$	$0.1 - 10^2$	66
Herbal Ess.	$0.1 - 10^2$	$10^{-6} - 10^{-3}$	$10^{-2} - 10$	1.4×10^4
DayQuil	$10 - 10^3$	$10^{-2} - 1$	$0.1 - 10$	12
Chili Sauce	$10 - 10^3$	–	$1 - 10^2$	–

converging flow in the EVROC, this is taken as the time required for a material element to travel through the contraction, which is proportional to $\dot{\varepsilon}_a^{-1}$, as defined in Eq. (6.2.1). Accordingly, the apparent or nominal Deborah number De_a, based on Eq. (6.2.1) is defined

$$De_a = \lambda \dot{\varepsilon}_a \tag{6.3.2}$$

The elasticity number, which characterizes the relative importance of elastic stresses to inertial stresses is defined as

$$El_0 = \frac{De_a}{Re_0} = \frac{\lambda \eta_0}{\rho l_c d_h} \tag{6.3.3}$$

Here the elasticity number is defined in terms of the zero-shear-rate viscosity.

The range of magnitudes of these dimensionless groups experimentally realized in the study of flow through a hyperbolic contraction are given in Table 6.3.1. For all the fluids, $El_0 \gg 1$, indicating that in the experiments with non-Newtonian fluids discussed below inertial stresses were not of importance.

6.3.2 Flow of Newtonian Fluids

Pressure Measurements

Experimentally measured pressure profiles for the N1000 calibration fluid are shown in Figure 6.3.1 (a) as the flow rate is progressively increased. The flow is viscously domi-

nated and the profiles are self-similar with a pressure drop $\Delta P_{23} \sim \dot{\varepsilon}_a$. For a Newtonian fluid at $Re_0 < 1$, the value of pressure coefficient $\mathcal{P}^N \approx 0.71$, shown in the inset plot of Figure 6.3.1 (a), is independent of the viscosity or flow rate, and only a function of the channel geometry. The pressure drop across the contraction alone ΔP_c is calculated using Eq. (6.2.3). The values of the dimensionless pressure drop $\Delta P_c/\mu\dot{\varepsilon}_a$ measured with all Newtonian test fluids are plotted against Reynolds number in Figure 6.3.1 (b). The onset of inertially-driven secondary flow begins around $Re_0 \approx 10$, coinciding with a non-linear increase in ΔP_c with increasing $\dot{\varepsilon}_a$.

The governing equations for the steady flow of an incompressible Newtonian fluid through the contraction geometry are the continuity equation, $\nabla \cdot \vec{v} = 0$, and the steady Navier-Stokes equation, $\rho\vec{v} \cdot \nabla\vec{v} = -\nabla p + \mu\nabla^2\vec{v}$, with the no-slip boundary condition on the walls. The inertial non-linearity in the momentum equation requires the exact equations to be solved numerically, (Oliveira *et al.*, 2007), but for the case of highly viscous Newtonian flow kinematics in the contraction, the momentum equation can be simplified to obtain an approximate solution using the lubrication approximation, provided $Re_0\frac{w_u}{l_c} \ll 1$. Since $w(x) \geq l_c > h$, the governing momentum equation is approximately given by the equation for two-dimensional Stokes flow which is $\frac{dp}{dx} = \mu\frac{\partial^2 u}{\partial z^2}$. Here p is the pressure, x and z follow the coordinate system given in Figure 6.2.1 (b) and $u = u(x, z)$ is the x-component of the velocity field. Using the lubrication approximation, the relationship between the pressure gradient and the volumetric flow rate appropriate for $h < w(x)$ is given by

$$\frac{dP_c^{2D}}{dx} = -\frac{12\mu Q}{h^3 w(x)} = -\frac{12 l_c}{h^2 w(x)}\left(\frac{w_c w_u}{w_u - w_c}\right)\mu\dot{\varepsilon}_a \tag{6.3.4}$$

Substituting the expression for $w(x)$, therefore the anticipated pressure drop across the contraction-expansion from $x = 0$ to $x = 2l_c$ is

$$\Delta P_c^{2D} = 12\left(\frac{l_c}{h}\right)^2\left(\frac{w_u + w_c}{w_u - w_c}\right)\mu\dot{\varepsilon}_a \tag{6.3.5}$$

The expected pressure drop given by Eq. (6.3.5) for the contraction-expansion used in this study is $\Delta P_c^{2D}/\mu\dot{\varepsilon}_a = 63$, which is indicated by the dashed horizontal line in Figure 6.3.1 (b). For $Re_0 \ll 1$, however, experimental pressure measurements give

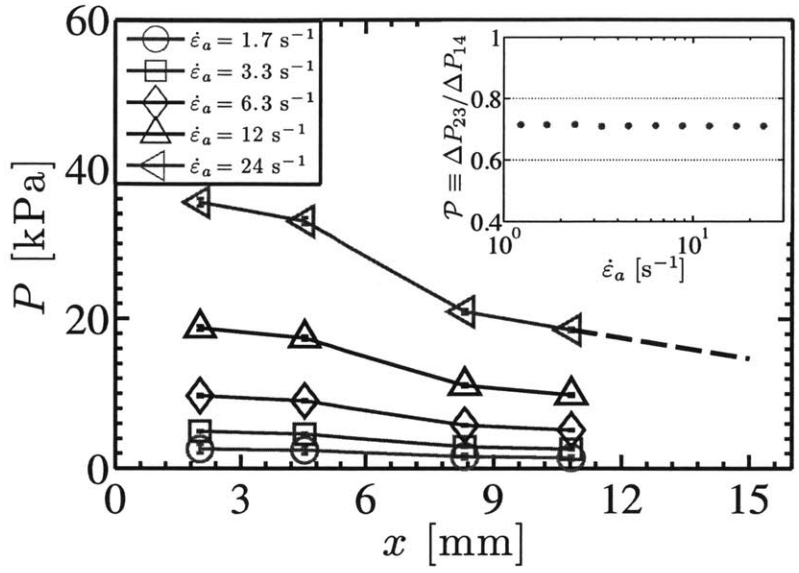

(a)

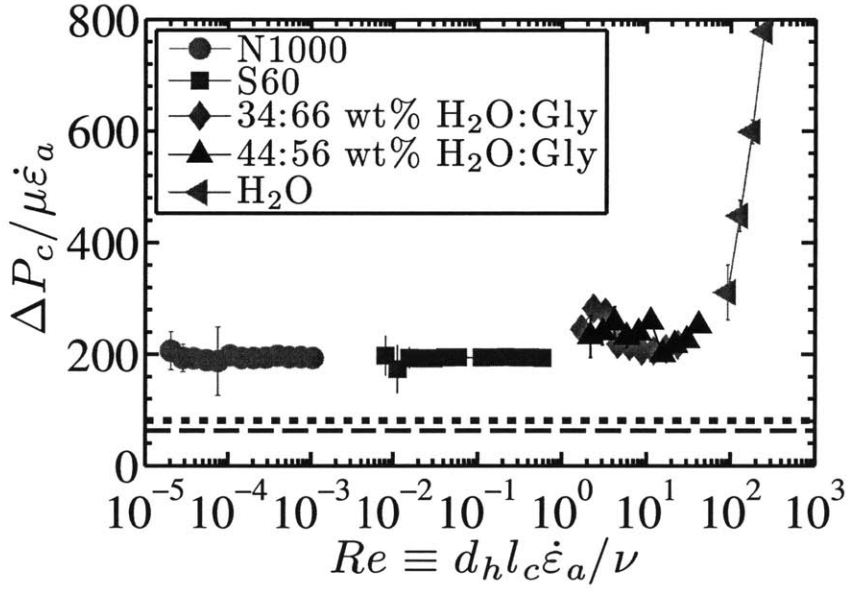

(b)

Figure 6.3.1: (a) Pressure measurements as a function of streamwise distance along the microchannel at different $\dot{\varepsilon}_a$ for the N1000 calibration oil. The dashed line indicates the anticipated pressure gradient in the downstream section of the channel based on Eq. (6.3.16) for a Newtonian fluid ($n = 1$) of the same viscosity as the N1000 calibration oil given in Table 6.2.1 ($m = \mu = 2.0$ Pa.s). The inset plot shows the evolution of the pressure coefficient $\mathcal{P}$, defined for Eq. (6.2.3) in the text above. (b) Measured dimensionless pressure drop for Newtonian fluids at varying Reynolds number. The dashed horizontal line indicates the anticipated dimensionless pressure drop based on the 2D lubrication approximation in Eq. (6.3.5) and the dotted line is based on the 3D lubrication approximation in Eq. (6.3.8).

$\Delta P_c/\mu\dot{\varepsilon}_a \approx 200$, hence the 2D lubrication approximation underpredicts the measured pressure drop by roughly a factor of three.

The accuracy of the prediction can be improved by solving for the lubrication approximation in 3D, in order to correct for the finite aspect ratio of the contraction (*i.e.* variations in the velocity field along y). The governing equation for a Newtonian fluid is $\frac{dp}{dx} = \mu\left(\frac{\partial^2 u}{\partial y^2} + \frac{\partial^2 u}{\partial z^2}\right)$, from which the relationship between the pressure gradient and the volumetric flow rate (White, 2003), appropriate for $h < w(x)$ is

$$\frac{dP_c^{3D}}{dx} = -\frac{12 l_c}{h^2 w(x)}\left[1 - 6\left(\frac{2}{\pi}\right)^5 \frac{h}{w(x)} \sum_{j\ odd}^{\infty} \frac{\tanh(j\pi w(x)/2h)}{j^5}\right]^{-1} \left(\frac{w_u w_c}{w_u - w_c}\right)\mu\dot{\varepsilon}_a \quad (6.3.6)$$

Since $h < w(x)$, the argument of the hyperbolic tangent, $j\pi w(x)/2h > 1$ for all values of j and x, hence the summation is approximately $1 + 1/3^5 + 1/5^5 + ... \approx 1$, so we have

$$\frac{dP_v^{3D}}{dx} \approx -\frac{12 l_c}{h^2 w(x)}\left[1 - 6\left(\frac{2}{\pi}\right)^5 \frac{h}{w(x)}\right]^{-1} \left(\frac{w_u w_c}{w_u - w_c}\right)\mu\dot{\varepsilon}_a \quad (6.3.7)$$

As before, substituting the expression for $w(x)$, and solving for the pressure drop across the contraction-expansion from $x = 0$ to $x = 2l_c$ gives

$$\begin{aligned}\Delta P_v^{3D} &= -2\left\{\frac{\pi^5}{16}\frac{w_c w_u}{h(w_u - w_c)} + \frac{\pi^{10}}{3072}\left(\frac{w_c w_u}{h(w_u - w_c)}\right)^2 \ln\left(\frac{\frac{192h}{\pi^5 w_c} - 1}{\frac{192h}{\pi^5 w_u} - 1}\right)\right\}\left(\frac{l_c}{h}\right)^2 \mu\dot{\varepsilon}_a \\ &= \frac{1}{3}\left(\frac{\pi}{2}\right)^5 \frac{w_c w_u}{h(w_u + w_c)}\left\{\frac{1}{6}\left(\frac{\pi}{2}\right)^5 \frac{w_c w_u}{h(w_u - w_c)} \ln\left(\frac{1 - 6\left(\frac{2}{\pi}\right)^5 \frac{h}{w_u}}{1 - 6\left(\frac{2}{\pi}\right)^5 \frac{h}{w_c}}\right) - 1\right\}\Delta P_v^{2D}\end{aligned} \quad (6.3.8)$$

For the geometry shown in Figure 6.2.1 the predicted pressure drop based on Eq. (6.3.8) is $\Delta P_c^{3D}/\mu\dot{\varepsilon}_a = 81$, and hence even this more accurate 3D lubrication approximation differs from the experimentally measured pressure drop across the contraction by a factor of around two and a half. The cause of this significant difference can be better understood by observing the flow kinematics in the microchannel, which is discussed below.

Flow Kinematics

To understand the discrepancy between the simple two-dimensional calculation of the expected pressure drop across the contraction-expansion given by Eqs. (6.3.5) and (6.3.8) and the experimental measurements, the measured axial velocity profile is compared

against three different characteristic axial velocity profiles. For the hyperbolically shaped planar contraction in this study, the cross-sectional area is $\mathcal{A}(x) = hw(x) \sim x^{-1}$. Therefore, the simplest expected axial velocity profile is the nominal plug-like centerline velocity $u_{cl}^{1D}(x) = Q/\mathcal{A}(x)$, on which the apparent extension rate is based (*i.e.* $\dot{\varepsilon}_a = du_{cl}^{1D}/dx$). Thus in the contraction region ($0 \leq x \leq l_c$), the average axial velocity profile is given by

$$u_{cl}^{1D}(x) = (x_0 + x)\dot{\varepsilon}_a \tag{6.3.9}$$

The anticipated centerline velocity in the contraction region consistent with the two-dimensional lubrication approximation from Eq. (6.3.4) is given by

$$\tilde{u}_{cl}^{2D}(x) = \frac{3}{2}(x_0 + x)\dot{\varepsilon}_a \tag{6.3.10}$$

where the tilde denotes a locally fully developed velocity consistent with the lubrication approximation. Finally, the most accurate centerline velocity is given by the lubrication approximation together with the expression for the velocity field in a rectangular channel of finite aspect ratio, which can be found in White (2003), and for this contraction is

$$\tilde{u}_{cl}^{3D}(x) = K(x)(x_0 + x)\dot{\varepsilon}_a \tag{6.3.11}$$

where $K(x)$ is defined

$$K(x) = \frac{\frac{48}{\pi^3}\sum_{j=odd}^{\infty}\frac{(-1)^{\frac{j-1}{2}}}{j^3}\left[1 - \frac{1}{\cosh\left(\frac{j\pi w(x)}{2h}\right)}\right]}{1 - \frac{192}{\pi^5}\frac{h}{w(x)}\sum_{j=odd}^{\infty}\frac{\tanh\left(\frac{j\pi w(x)}{2h}\right)}{j^5}} \tag{6.3.12}$$

The expected velocity profiles in the expansion region are mirror images of the profiles in the contraction due to the channel symmetry. Upstream of the contraction inlet ($x < 0$), the cross-sectional area is constant, so the approximate velocities to be matched to these profiles are

$$\begin{aligned} u_{cl}^{1D}(x < 0) &= x_0\dot{\varepsilon}_a \\ u_{cl}^{2D}(x < 0) &= \frac{3}{2}x_0\dot{\varepsilon}_a \\ u_{cl}^{3D}(x < 0) &= K_0 x_0\dot{\varepsilon}_a \end{aligned} \tag{6.3.13}$$

where K_0 is defined

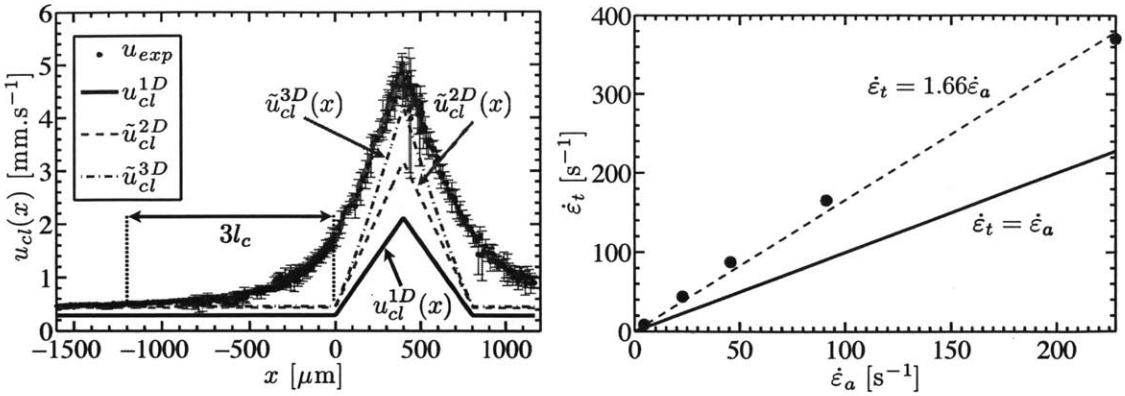

(a) (b)

Figure 6.3.2: (a) Experimentally measured u_{exp} and anticipated velocity profiles along the centerline of the contraction $u_{cl}(x) = u(x, 0, 0)$ in a Newtonian fluid at $Q = 10$ μL/min, $Re_0 \sim 0.5$. The dashed solid line is the linear best-fit to the measured velocity profile in the converging section of the contraction ($0 \leq x \leq l_c$) whose slope equals the experimentally realized extension rate in the contraction, $\dot{\varepsilon}_t$. (b) True extension rate $\dot{\varepsilon}_t$ determined from the slope of the best-fit line to the measured velocity profile as a function of the imposed $\dot{\varepsilon}_a$. The solid line indicates the ideal result of $\dot{\varepsilon}_t = \dot{\varepsilon}_a$, whereas the dashed line indicates the result of a least squares fit to the measured extension rate given by the equation $\dot{\varepsilon}_t = 1.66\dot{\varepsilon}_a$.

$$K_0 = \frac{48}{\pi^3} \frac{\displaystyle\sum_{j=odd}^{\infty} \frac{(-1)^{\frac{j-1}{2}}}{j^3} \left[1 - \frac{1}{\cosh\left(\frac{j\pi w_u}{2h}\right)}\right]}{1 - \frac{192}{\pi^5}\frac{h}{w_u}\displaystyle\sum_{j=odd}^{\infty} \frac{\tanh\left(\frac{j\pi w_u}{2h}\right)}{j^5}} \tag{6.3.14}$$

For the microchannel used in this study, $K_0 = 1.567$.

The expected axial velocity profiles in the contraction-expansion region given by Eq. (6.3.9), (6.3.10) and (6.3.11) are compared with the centerline velocity measured using μ-PIV in Figure 6.3.2 (a). Although the measured profile is qualitatively described by $\tilde{u}_{cl}^{3D}(x)$, it differs from the lubrication solution in two ways. Firstly, the measured centerline velocity profile begins to exceed the anticipated profile starting roughly three contraction lengths upstream of the contraction inlet, as indicated by the horizontal black arrow in Figure 6.3.2 (a). This initial deviation can be attributed to the abruptness of the contraction seen in Figure 6.2.1 (a). The importance of sudden changes in cross-section on the kinematics and pressure field in viscously-dominated flows through microfluidic devices was also previously noted in Oliveira *et al.* (2007). Secondly, the measured

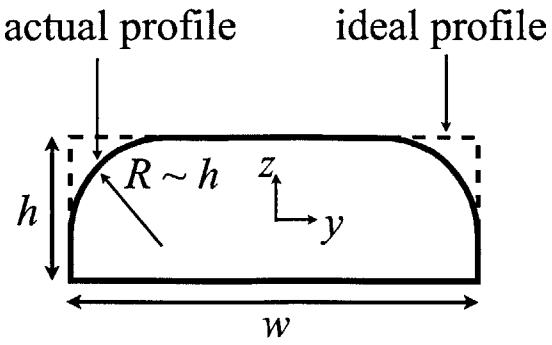

Figure 6.3.3: Schematic illustration of the scalloped profile at the contraction throat.

velocity exceeds $\tilde{u}_{cl}^{3D}(x)$ in the contraction region ($0 \leq x \leq 2l_c$), due to a "scalloping" feature of the wet etching process which causes the idealized sharp corners to in fact be rounded as shown schematically in Figure 6.3.3. To estimate the reduction in the cross-section, one can take the radius of the scalloped sections as being equal to the channel height, for which the cross-sectional area of the channel in the contraction region is reduced by 22% from the anticipated rectangular cross-sectional area. The true extension rate $\dot{\varepsilon}_t$ experimentally realized in the hyperbolic contraction can be calculated from the slope of the best-fit line to the measured velocity profile in the contraction region, and the resulting values are plotted against the nominal extension rate $\dot{\varepsilon}_a$ given by Eq. (6.2.1) in Figure 6.3.2 (b). The true extension rate is roughly 66% greater than the nominal value based on a linear regression to the measured extension rate. These discrepancies between the measured and anticipated kinematics reveal why the lubrication approximation cannot accurately predict the measured pressure drop shown in Figure 6.3.1 (b).

6.3.3 Flow of non-Newtonian Fluids

Pressure Measurements

Measured pressure profiles for one of the non-Newtonian test fluids are shown in Figure 6.3.4 (a). As in the Newtonian case, the dominant contribution to the overall pressure drop in the entire microchannel is ΔP_{23}, and this quantity is plotted as a function of

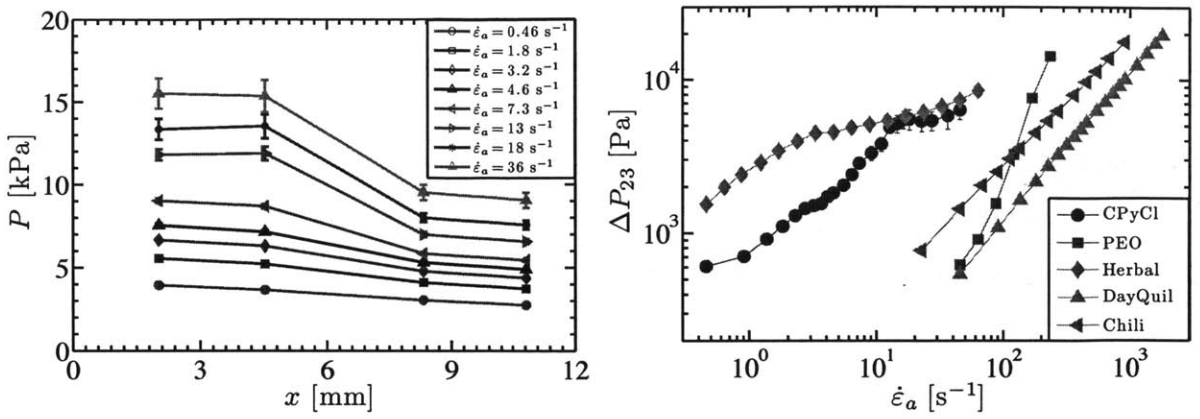

Figure 6.3.4: Pressure measurements in the microfluidic contraction at different nominal extension rates for the 100:60 mM CPyCl:NaSal system. (a) Measured pressure as a function of streamwise distance along the microchannel. (b) Measured pressure drop ΔP_{23} for each fluid as a function of the nominal extension rate.

nominal extension rate for each fluid tested in Figure 6.3.4 (b). This apparent flow curve of pressure drop verses flow rate, however, does not provide an immediately useful metric of the contribution of viscoelastic effects in this mixed flow. One possible metric for quantifying these effects in the contraction is the 'excess pressure drop' (EPD) (Aguayo *et al.*, 2008), which is the ratio of the pressure drop across the contraction for a non-Newtonian fluid to the pressure drop for a Newtonian fluid with the same shear viscosity at a given flow rate. With the exception of Boger fluids (whose shear viscosity is constant), the shear viscosity of most non-Newtonian fluids is rate dependent, and therefore without assuming a constitutive relationship for the shear viscosity of the fluid (*e.g.* a power-law model as utilized in this work) the calculation and interpretation of the EPD for most viscoelastic materials is ambiguous. An alternative metric for gauging the relative importance of non-Newtonian effects is the pressure coefficient $\mathcal{P} \equiv \Delta P_{23}/\Delta P_{14}$, that was introduced previously in Eq. (6.2.3). This quantity is plotted in Figure 6.3.5 (a) and has the advantage that it is based on the uncorrected pressure drop measurements alone and therefore its value can be determined unambiguously. As the fractional contribution of the pressure drop in the contraction to the overall pressure drop in the entire channel increases, the viscoelastic resistance to stretching becomes increasingly important and the pressure coefficient $\mathcal{P}$ approaches unity.

It is important to note that for the non-Newtonian test fluids the value of $\mathcal{P}$ may be lower than the respective value for Newtonian fluids, and also that the value does not necessarily asymptote to a constant value at low flow rates. Therefore, it is helpful to make an estimate of the value of $\mathcal{P}$ at the limiting flow rates for which viscous shear effects would constitute the predominant contribution to the pressure drop. It is common to assume that the overall pressure drop in the device can be decomposed as $\Delta P_c = \Delta P_e + \Delta P_v$, whereby the total pressure drop is the superposition of a viscoelastic component ΔP_e and a viscous component ΔP_v due to shearing at the walls, (Cogswell, 1972). Without complementary numerical simulations, however, it is difficult to ascertain the viscous contribution to the pressure drop with great precision, but for the flow of a shear-thinning non-Newtonian fluid one can estimate the value of ΔP_v using the phenomenological power-law model (Bird *et al.*, 1987) provided the flow is inertialess and the shear stresses in the fluid are independent of net accumulated strain. This approach for calculating ΔP_v is consistent with other recent analyses for planar contraction flows, (Wang *et al.*, 2010). Since the thickness of the hyperbolic contraction flow channel is always less than its width, $h < w_c < w_u$, in the analysis it is assumed that the dominant velocity gradient will be across the channel height (*i.e.* in the z-direction), and therefore in the 2D approximation, velocity gradients across the channel width (*i.e.* in the y-direction) are neglected. For a power law fluid (denoted by the superscript PL), the resulting pressure gradient due to the viscous shearing component of the flow is related to the nominal extension rate $\dot{\varepsilon}_a$ by the equation

$$\frac{dP_v^{PL}}{dx} = -2^{n+1}\left(\frac{2n+1}{n}\right)^n\left(\frac{l_c}{h}\right)^n\left(\frac{w_c w_u}{w_u - w_c}\right)^n \frac{m\dot{\varepsilon}_a^n}{hw(x)^n} \tag{6.3.15}$$

Upstream and downstream of the contraction, $w(x) = w_u$, and thus the pressure gradient in these regions of the channel is constant with value

$$\frac{\Delta P_v^{PL}}{\Delta x} = 2^{n+1}\left(\frac{2n+1}{n}\right)^n\left(\frac{l_c}{h}\right)^n\left(\frac{w_c}{w_u - w_c}\right)^n\left(\frac{1}{h}\right)m\dot{\varepsilon}_a^n \tag{6.3.16}$$

The approximate contribution to the pressure drop across the contraction and expansion from $x = 0$ to $x = 2l_c$ due to viscous shear stresses is found by integration of Eq. (6.3.15) to be

$$\Delta P_{c,v}^{PL} = \frac{2^{n+2}}{n+1}\left(\frac{2n+1}{n}\right)^{n}\left(\frac{l_c}{h}\right)^{n+1} \times \left\{\left(\frac{w_u}{w_u - w_c}\right)^{n+1} - \left(\frac{w_c}{w_u - w_c}\right)^{n+1}\right\} m\dot{\varepsilon}_a^n \tag{6.3.17}$$

In the limiting case of a Newtonian fluid, $m = \mu$ and $n = 1$, and Eq. (6.3.17) reduces to the result for simple 2D plane Poiseuille flow in Eq. (6.3.5). Therefore, the estimated value of $\mathcal{P}$ for a power-law fluid is

$$\mathcal{P}^{PL} = \frac{\frac{\Delta P_v^{PL}}{\Delta x}(L_{23} - 2l_c) + \Delta P_{c,v}^{PL}}{\frac{\Delta P_v^{PL}}{\Delta x}(L_{14} - 2l_c) + \Delta P_{c,v}^{PL}} \tag{6.3.18}$$

where L_{23} and L_{14} are the distances between transducers 2 and 3, and 1 and 4 respectively. The result given in Eq. (6.3.18) is independent of m and $\dot{\varepsilon}_a$, but depends on the value of the power-law index n. This predicted variation in the pressure coefficient for power-law fluids, $\mathcal{P}^{PL}(n)$ is shown as the black curve in Figure 6.3.5 (a) for index values in the range $0 \leq n \leq 1$. The curve represents a lower bound for the pressure ratio, because it does not account for any elastic contribution to the pressure drop and it is based on only a 2D approximation to the flow. Even for a Newtonian fluid, the prediction of Eq. (6.3.18) is $\mathcal{P}^{PL}(n = 1) = 0.56$, which is lower than the typically observed experimental value of $\mathcal{P}^N \approx 0.71$. This remaining difference arises from the three dimensional effects in the flow field. Nevertheless, the utility of the dimensionless pressure coefficient $\mathcal{P}$ lies in the fact that it is a primary measure of the relative importance of viscoelastic contributions to the stresses which can be evaluated independently of the constitutive model of the fluid. Indeed, in assessing the value of $\mathcal{P}$ with increasing $\dot{\varepsilon}_a$, it becomes clear that the pressure profiles for the non-Newtonian fluids differ qualitatively from the Newtonian profiles in Figure 6.3.1 (b), and the contribution of viscoelastic effects generally increases with increasing flow rates for the non-Newtonian test fluids. The two exceptions to this general trend occur for the CPyCl:NaSal system and Herbal Essence shampoo which both exhibit strongly shear-thinning viscosities. For the CPyCl:NaSal system, the slight drop in the pressure coefficient coincides approximately with the onset of a time varying flow, which affects the pressure profile along the entire channel. For the shampoo, the initial decrease in the pressure coefficient results because shear-

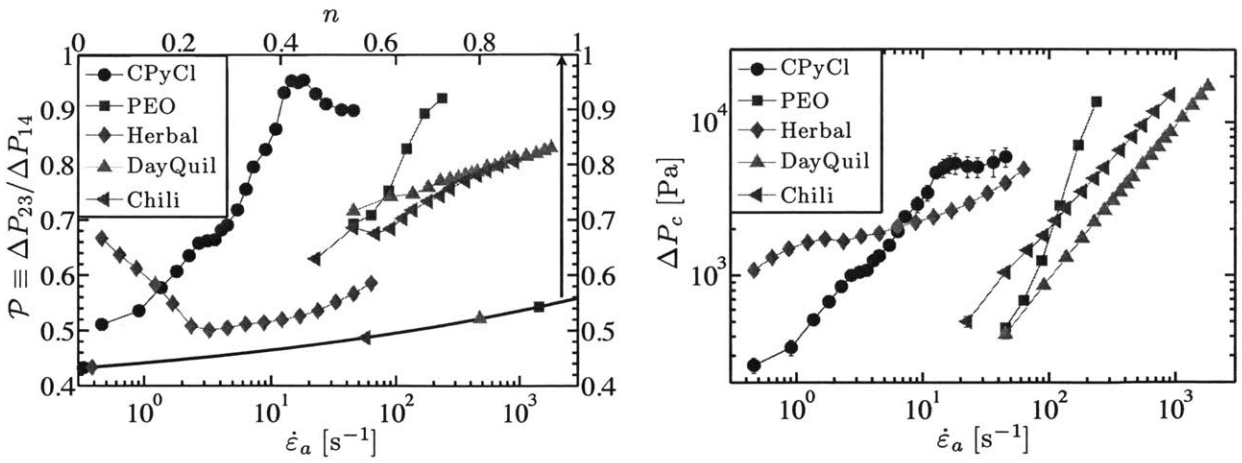

Figure 6.3.5: (a) Pressure coefficient plot for different fluids. The black curve corresponds to the minimum predicted value of the pressure coefficient for a power-law fluid with index $0 \leq n \leq 1$ using Eq. (6.3.18). Each of the five points on the curve indicates the predicted minimum value of $\mathcal{P}$ corresponding to the value of n for each test fluid listed in Table 6.2.2. (b) Corrected pressure drop ΔP_c for each test fluid using Eq. (6.2.3).

thinning becomes more important as the flow rate increases (hence the estimate for the minimum pressure coefficient based on the power-law model becomes more accurate). The eventual increase in the pressure coefficient indicates that viscoelasticity dominates the pressure drop across the contraction with increasing values of $\dot{\varepsilon}_a$.

The apparent extensional viscosity in an elongational flow is

$$\eta_{E,a} \equiv \frac{N_1}{\dot{\varepsilon}_a} \tag{6.3.19}$$

where $N_1 \equiv \tau_{xx} - \tau_{yy}$ is the first normal stress difference. An approximate measure for the value of N_1 can be determined from the elastic contribution to the pressure drop (after subtracting the viscous contribution), $\Delta P_e = \Delta P_c - \Delta P_{c,v}^{PL}$ and then calculated using the following energy argument. For a two-dimensional, incompressible flow, the continuity equation requires that $\dot{\varepsilon}_{xx} = -\dot{\varepsilon}_{yy}$ at each point in the flow. Furthermore, the net rate of work per unit volume associated with a purely extensional deformation is $\dot{\mathcal{W}}''' = \tau_{xx}\dot{\varepsilon}_{xx} + \tau_{yy}\dot{\varepsilon}_{yy}$, or equivalently

$$\frac{D}{Dt}\left(\frac{\partial \mathcal{W}}{\partial \mathcal{V}}\right) = \left(\tau_{xx} - \tau_{yy}\right)\dot{\varepsilon}_{xx} \tag{6.3.20}$$

where $\mathcal{V}$ denotes a unit volume. The incremental work must be equal to the external mechanical work acting on the material, $\partial \mathcal{W} = -P\partial \mathcal{V}$ where P is pressure, or alternatively $\partial \mathcal{W}/\partial \mathcal{V} = -P$. Substituting this result and the definition into Eq. (6.3.20) and equating $\dot{\varepsilon}_{xx} = \dot{\varepsilon}_a$, one obtains $DP/Dt = -N_1\dot{\varepsilon}_a$. Integration of this equation across the length of the contraction under the assumption that N_1 is constant and using the result of Eq. (6.2.2), one obtains $N_1 = \Delta P/\varepsilon_H$, and hence the approximate measure of the apparent extensional viscosity for fully developed extensional flow in the hyperbolic contraction is

$$\eta_{E,a} = \frac{1}{\varepsilon_H}\frac{\Delta P_e}{\dot{\varepsilon}_a} \tag{6.3.21}$$

This result has previously been derived in Collier *et al.* (1998) and it is only valid for an ideal planar elongational flow, provided the value of N_1 is constant for the entire duration of the deformation. Such an assumption does not capture the variation in the normal stresses with net accumulated strain $\varepsilon_H(x)$, and it also neglects experimental transients. Furthermore, this derivation is only appropriate for a flow field in which the maximum achievable value of ε_H is finite, and the net accumulated Hencky strain ε_H is independent of the streamline followed by a material element in the flow, or equivalently for the contraction here $\varepsilon_H(x, y, z) = \varepsilon_H(x)$. Note that the expression for $\eta_{E,a}$ given by Eq. (6.3.21) is specific to the contraction-expansion geometry used here, and that it differs from the expression for extensional viscosity given for the cross-slot geometry studied by Haward *et al.* (2011). This difference arises because the cross-slot flow contains a stagnation point at which the theoretical Hencky strain diverges and the net accumulated strain varies across streamlines. Accordingly, it is not possible to calculate precisely a unique value of N_1 for the entire flow field in the cross-slot, and therefore its value is instead assumed to be approximately equal to the measured excess pressure drop $N_1 \approx \Delta P_{excess}$. Ultimately, however, the two respective expressions for apparent extensional viscosity are consistent, because they are based on the same definition for $\eta_{E,a}$ given by Eq. (6.3.19).

To evaluate $\eta_{E,a}(\dot{\varepsilon}_a)$, the corrected pressure drop ΔP_c must first be determined using Eq. (6.2.3). The values of ΔP_c are plotted against $\dot{\varepsilon}_a$ in Figure 6.3.5 (b) for each

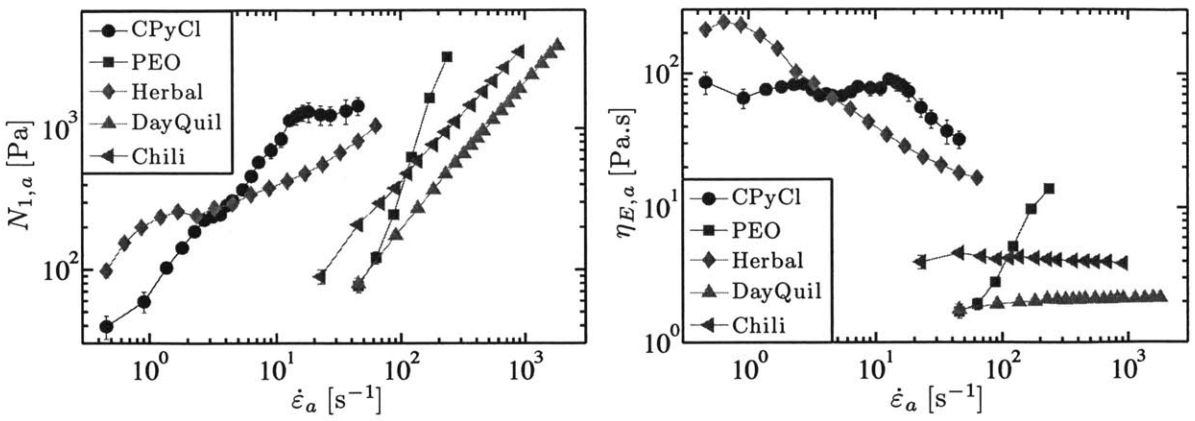

Figure 6.3.6: Calculated values of (a) apparent normal stress difference $N_{1,a} = \Delta P_e/\varepsilon_H$ and (b) apparent extensional viscosity $\eta_{E,a}$ based on Eq. (6.3.21).

fluid. The apparent first normal stress difference and extensional viscosity, calculated from Eq. (6.3.21) (based on the corrected elongational contribution to the pressure drop ΔP_e), are shown in Figure 6.3.6. For all fluids, the apparent first normal stress difference $N_{1,a}$ increases with $\dot{\varepsilon}_a$. When $N_{1,a}$ is normalized by $\dot{\varepsilon}_a$ to calculate the apparent extensional viscosity defined in Eq. (6.3.21), three classes of response emerge. The DayQuil (carboxymethycellulose) and chili sauce (xanthan gum) both exhibit a nearly constant value of $\eta_{E,a}$, whereas the two surfactant systems (CPyCl:NaSal and shampoo) show extensional thinning. Lastly, the PEO system shows extensional-thickening, similar to the behavior of the highest concentration PEO solutions shown in Figure 2.3.3, for which the measured pressure drop increases superlinearly with flow rate.

The Trouton ratio is defined as the ratio of the extensional viscosity to the shear viscosity, and for a planar elongational flow for simple fluids at small extension rates this limiting value is $Tr_{\dot{\varepsilon}\to 0} \equiv \frac{\eta_E}{\eta_0} = 4$. In these experiments, however, with the exception of the CPyCl:NaSal system, the Trouton ratios are notably higher, and their values based on the zero-shear-rate viscosities given in Table 6.2.2 at the smallest values of $\dot{\varepsilon}_a$ for each fluid are (a) CPyCl:NaSal: $Tr \approx 2$, (b) PEO: $Tr \approx 22$, (c) Herbal Essence: $Tr \approx 14$, (d) DayQuil: $Tr = 29$. Such large Trouton ratios have also been reported previously for flow through a hyperbolic contraction, (Wang *et al.*, 2010). It is important to recall that

this simple analysis assumes an ideal fully-developed planar elongational flow, whereas the apparent extensional-thinning/thickening behavior and the experimental values of the Trouton ratio are based on measurements of a transient extension-dominated mixed flow. These metrics are therefore best considered as a relevant measure of viscoelastic resistance to stretching in a mixed flow that is characteristic of what would be encountered in an industrial application (such as flow through a nozzle), but not in an ideal homogeneous extensional flow.

Flow Kinematics

The deviations between the flow kinematics of the non-Newtonian test fluids in the EVROC device and those expected in an ideal homogeneous extensional flow can be investigated with velocimetry measurements. Accordingly, streakline images for all non-Newtonian test fluids are shown together with complementary pseudocolor optical retardance images of the flow-induced birefringence in Figure 6.3.7. The experimental extension rates measured at the contraction mid-plane have been determined from the slope of a linear regression to the centerline axial velocity profiles along the length of the contraction as discussed previously for Newtonian fluids (*cf.* Figure 6.3.2). The true extension rate $\dot{\varepsilon}_t$, realized experimentally is plotted against the nominal extension rate $\dot{\varepsilon}_a$, in Figure 6.3.8.

For most of the test fluids, at least two qualitatively different regimes of behavior are observed with increasing flow rate. At sufficiently small rates, $De_a < \mathcal{O}(1)$, all of the non-Newtonian fluid systems exhibit kinematics that are qualitatively similar to the behavior seen at low Reynolds number in Newtonian fluids. The true extension rate in the contraction is roughly constant and greater than the nominal value as previously noted for the Newtonian case (*cf.* Figure 6.3.2 (b)). Additionally, the streaklines generally follow the contours of the contraction sidewalls as shown in Figure 6.3.7.

At intermediate rates, $De_a \sim \mathcal{O}(10)$, vortices in the upstream corners of the contraction emerge as is evident for the CPyCl:NaSal micellar fluid, PEO solution and DayQuil in Figure 6.3.7. The distortion of the streamlines from those observed in the Newtonian case clearly indicates the influence of fluid elasticity on the flow kinematics even

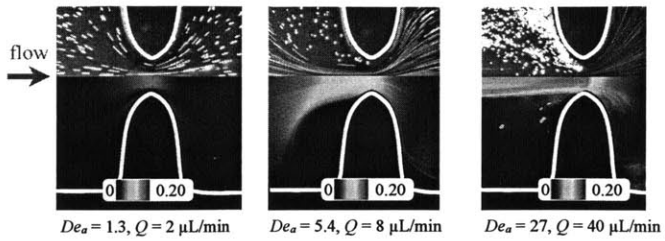

$De_a = 1.3$, $Q = 2$ μL/min $De_a = 5.4$, $Q = 8$ μL/min $De_a = 27$, $Q = 40$ μL/min

(a) 100:60 mM CPyCl:NaSal worm-like micellar fluid.

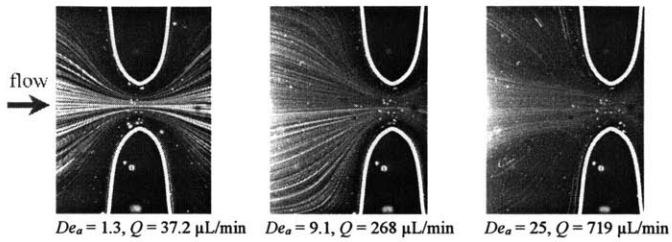

$De_a = 1.3$, $Q = 37.2$ μL/min $De_a = 9.1$, $Q = 268$ μL/min $De_a = 25$, $Q = 719$ μL/min

(b) 3000 ppm PEO in 34:66 wt% water:glycerol semidilute polymer solution.

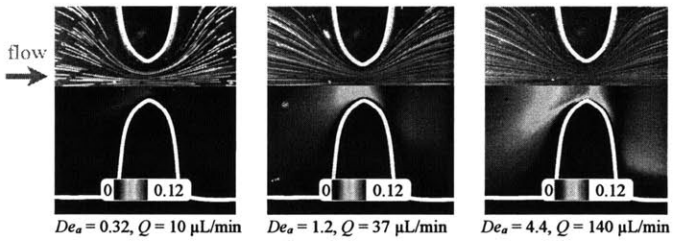

$De_a = 0.32$, $Q = 10$ μL/min $De_a = 1.2$, $Q = 37$ μL/min $De_a = 4.4$, $Q = 140$ μL/min

(c) Herbal Essence (concentrated surfactant system)

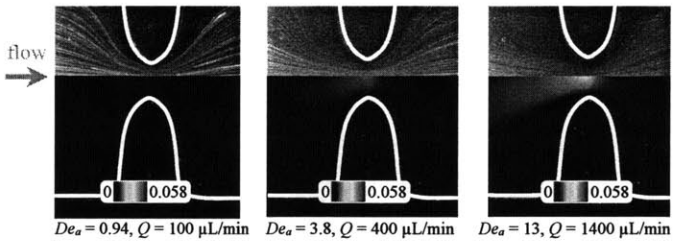

$De_a = 0.94$, $Q = 100$ μL/min $De_a = 3.8$, $Q = 400$ μL/min $De_a = 13$, $Q = 1400$ μL/min

(d) DayQuil (carboxymethycellulose)

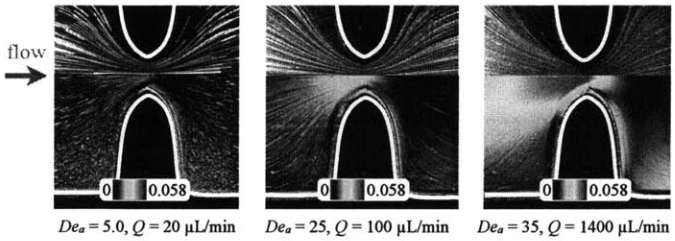

$De_a = 5.0$, $Q = 20$ μL/min $De_a = 25$, $Q = 100$ μL/min $De_a = 35$, $Q = 1400$ μL/min

(e) Sweet Chili Sauce (xanthan gum)

Figure 6.3.7: Streakline images (upper half) and pseudocolor retardance maps (lower half) of flow-induced birefringence for non-Newtonian test fluids flowing through the hyperbolic contraction ($w_c = 400$ μm). In all cases, the kinematics and retardance images are symmetrical about the contraction centerline and flow is from left to right. White curves have been overlaid to indicate the location of the contraction walls. The colorscale is in units of radians. Note that birefringence in the PEO solution was too weak to be observable and therefore no pseudocolor retardance images have been included.

at vanishingly small Re_0. Such vortices are well-known to occur in flows of viscoelastic fluids through contractions (Rodd *et al.*, 2005, 2007). Typically, the presence of vortices also results in the onset of a non-linear dependency of the true extension rate $\dot{\varepsilon}_t$, on the nominal value, $\dot{\varepsilon}_a$ as shown in Figure 6.3.8.

Amongst these fluids, the behavior of the CPyCl:NaSal WLM system is unique. For this fluid, at $De_a > \mathcal{O}(1)$, the images presented in Figure 6.3.7 (a) show that the streamlines in the contraction region become increasing constricted near the throat resulting in a nearly constant value of $\dot{\varepsilon}_t$ across approximately one order of magnitude of apparent strain rate, $1 < \dot{\varepsilon}_a < 10$ s^{-1}. This is also reflected in the weak increase in true extension rate $\dot{\varepsilon}_t$ with increasing flow rate shown in Figure 6.3.8. It is the ability of this fluid to shear band (*i.e.* support localized regions of high shear rate) which causes the value of $\dot{\varepsilon}_t$ to plateau, since the shear bands function effectively as moveable internal slip layers. The narrowing of the streamlines also reduces streamwise curvature, thereby allowing the flow to remain steady up to large values of the apparent Deborah number ($De_a < \mathcal{O}(30)$), before becoming time-varying. In this unsteady regime, measurement of the true extension rate in the contraction was not possible. It is noteworthy that the plateau in the experimentally realized extension rate, $\dot{\varepsilon}_t$ for the CPyCl:NaSal system roughly occurs conjointly with a plateau in the apparent value of $N_{1,a}$ shown in Figure 6.3.6.

The superlinear increase in the apparent normal stress difference $N_{1,a}$ with $\dot{\varepsilon}_a$ for the PEO solution shown in Figure 6.3.6 coincides with the measured rapid increase in the true extension rate $\dot{\varepsilon}_t$ with flow rate. Therefore, it is important to recognize that evidence for extensional thinning or thickening based on pressure measurements with EVROC, may in fact be indicative of the onset of viscoelastic secondary flows such as the upstream vortices seen in Figure 6.3.7 (b). As with virtually every rheometer, it is a challenge with the EVROC to ensure that the flow kinematics remain self-similar and unchanged across all experimentally accessible flow rates $\dot{\varepsilon}_a$. Accordingly this microfluidic device should not be viewed as a true extensional rheometer, *per se*, since the realized flow kinematics can vary with both the test fluid and the flow rate, even in the inertialess flow regime. Instead the EVROC device is best employed as a microfluidic viscosity

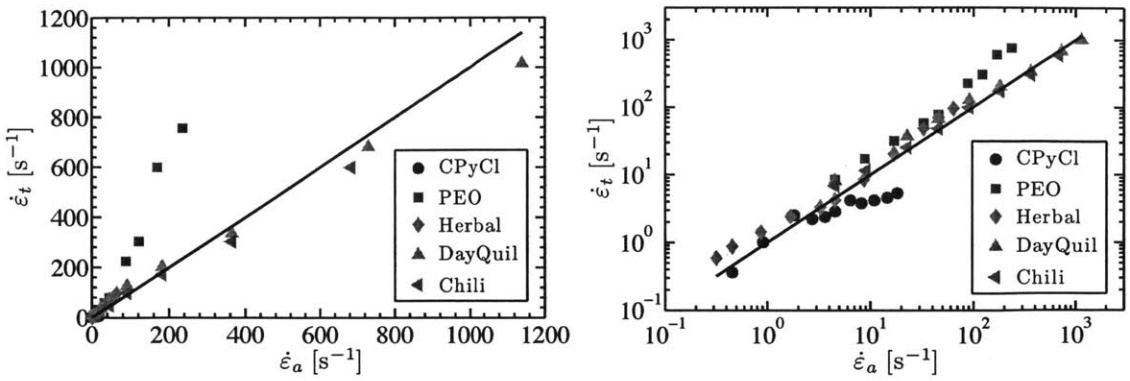

Figure 6.3.8: True extension rate $\dot{\varepsilon}_t$ determined from the slope of the best linear fit $u_x = \dot{\varepsilon}_t x$ line to the measured centerline velocity near the contraction plane as a function of apparent extension rate $\dot{\varepsilon}_a$ given by Eq. (6.2.1). The solid black line indicates the ideal result of $\dot{\varepsilon}_t = \dot{\varepsilon}_a$. Note that the same data are displayed on (a) linear and (b) log scales.

indexer from which a semi-quantitative estimate of the extensional rheology of the test sample can be ascertained in an extension-dominated flow at high deformation rates ($1 \leq \dot{\varepsilon}_a \leq 10^3$ s^{-1}).

Flow-Induced Birefringence and Stress

Spatially resolved FIB measurements complement the streakline images by providing optically non-invasive measurements of local flow-induced molecular anisotropy. Pseudocolor retardance images at different flow rates are shown in the lower halves of each image in Figure 6.3.7. Provided the optical anisotropy Δn, (*i.e.* the difference between the ordinary and extraordinary indices of refraction) in the sample can be assumed constant along the direction of light propagation, then the optical retardance is given by $\delta = 2\pi\Delta n h/\lambda_\ell$, where h is the height of the contraction as before and $\lambda_\ell = 546$ nm is the wavelength of the incident light.

As discussed in Section 5.3, under the appropriate circumstances Δn can be related to the principal stress difference $\Delta\sigma$, in the sample by the stress-optical rule, (Fuller, 1990). This rule is given by the relation $\Delta n = C\Delta\sigma$, where C is the stress-optical coefficient, which is typically determined experimentally (Janeschitz-Kriegl, 1983). In a

purely extensional flow, free from shear stresses, the principal stress difference is equal to the first normal stress difference $\Delta\sigma = N_1$. Under the assumption of a purely two-dimensional, planar elongational deformation, and the applicability of the stress-optical rule, the normal stress difference in the fluid is thus related to the measured optical retardance by the relationship

$$N_1 = \frac{\delta}{2\pi C}\frac{\lambda_\ell}{h} \tag{6.3.22}$$

In reality, the fluid kinematics are not uniform along the direction of light propagation (due to the presence of the bounding end walls), and therefore the retardance images in Figure 6.3.7 are useful primarily for qualitatively assessing the stress field in the geometry. The retardance fields exhibit qualitatively similar trends as those seen in the flow kinematics measurements, especially with regard to the emergence of the upstream vortices which are characterized by slowly moving regions of low stress and low birefringence that appear dark blue in Figure 6.3.7. It is also noteworthy that for flow rates large enough to produce detectable levels of birefringence, (typically $De_a > \mathcal{O}(1)$), the optical retardance does not exhibit fore-aft symmetry about the throat of the contraction (located at $x = l_c$), indicating the importance of tensile viscoelastic stresses as fluid elements are convected and stretched through the converging section of the contraction. Furthermore, for essentially all of the values of $\dot{\varepsilon}_a$ for which the flow is steady in time, the centerline retardance profile in the converging half of the contraction continues to grow monotonically with x-position as fluid elements travel towards the throat of the contraction $x \rightarrow l_c$. This result suggests that the Hencky strain for this channel, $\varepsilon_H = 2$, is not sufficiently large to provide sufficient time for the extensional stress in the fluid element to attain its steady state value. This was a central assumption of the energy analysis presented in Eq. (6.3.20) and (6.3.21) and thus provides an *a posteriori* rationalization for the fact that only an approximate value of the planar extensional viscosity can be measured with a hyperbolic microfluidic device such as EVROC that develops a Hencky strain $\varepsilon_H = 2$.

6.4 Improved Design for the Contraction Geometry

In Section 6.3.2, two issues with the channel construction were identified as the cause of the discrepancy between both the experimentally measured pressure drop and the flow kinematics for Newtonian liquids when compared with predicted values from the lubrication approximation. Firstly, the contraction was so abrupt that its effects on the kinematics propagated as much as three contraction lengths upstream and downstream of the contraction (see Figure 6.3.2 (a)). Secondly, due to a feature of the wet etching process the cross-sectional profile of the contraction was not rectangular, as desired, which further altered the desired kinematics in the contraction region.

In order to improve the contraction design, the basic hyperbolic contraction-expansion profile remains, but new contraction dimensions are considered as well as the introduction of expansion sections immediately upstream and downstream of the contraction. The two basic contraction designs are shown in Figure 6.4.1. The basic design parameters of the contraction are the length l_c, height h, upstream width w_u, width at the contraction throat w_c, and the expansion radius R. Each contraction tested here has the same Hencky strain $\varepsilon_H = \ln(w_u/w_c) = 2$. The introduction of the rounded protrusion sections with radius R is inspired by the simulation work of Alves (2007) and Haward *et al.* (2012b) for optimizing the shape of a flow geometry subject to a fixed constraint on the flow kinematics. Here the design objective is an axial velocity profile that effects a more spatially homogeneous extensional flow along the contraction centerline by more faithfully following the predictions of the three dimensional lubrication profile given by Eq. (6.3.11). The length of the contractions l_c has been increased compared to the value of the original contraction examined in the previous Sections, in order to reduce the abruptness of the contraction. The concave protrusions are aimed at further reducing the influence of the contraction on the kinematics upstream and downstream of the contraction by countering the accelerative effects beyond the contraction entrance due to the converging streamlines. Since no exact function for the shape of the protrusion section was specified in the work of Alves (2007), each profile has been simply constructed from a quarter arc with radius R, followed by one half of a sinusoid with wavelength $4R$. The inclusion of a sigmoidal-like function allows the profile to smoothly transition back

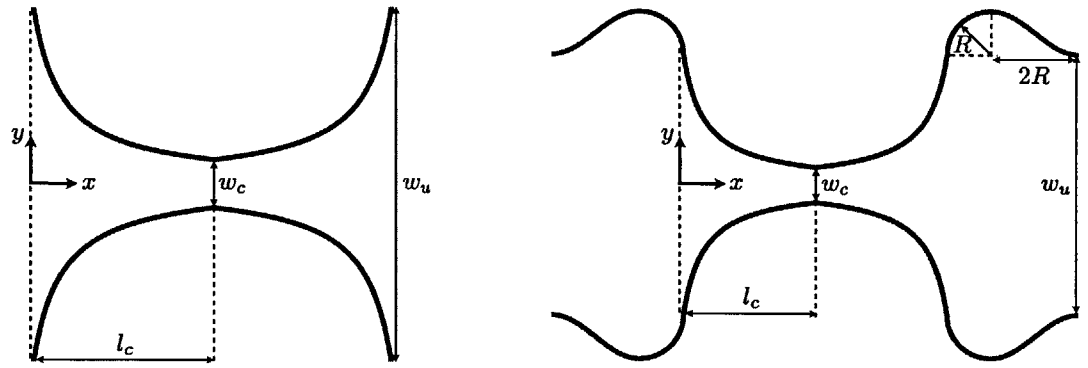

(a) Type I Chip

(b) Type II Chip

Figure 6.4.1: Two potential designs for the contraction profile.

to the inlet width of the contraction w_u.

The profile of the Type I contraction is given by the following piecewise function.

$$w(x) = \begin{cases} w_u & \text{for } x < 0 \\ \dfrac{K}{x_0 + x} & \text{for } 0 \leq x < l_c \\ \dfrac{K}{x_0 + 2l_c - x} & \text{for } l_c \leq x < 2l_c \\ w_u & \text{for } x \geq 2l_c \end{cases} \tag{6.4.1}$$

where $K = l_c w_u w_c/(w_u - w_c)$, $x_0 = l_c w_c/(w_u - w_c)$ and $0 \leq x \leq l_c$. The profile of the Type II contractions is given by the following piecewise function.

Table 6.4.1: Nominal and true dimensions of the redesigned EVROC devices as measured with an optical microscope.

Contraction Designation	Type		l_c [μm]	w_u [μm]	w_c [μm]	h [μm]	R [μm]
W2000-L1000	I	Nominal	1000	2000	267	2000	0
W2000-L1000	I	True	970	1925	255	200	0
W2000-L1000-C333	II	Nominal	1000	2000	267	200	333
W2000-L1000-C333	II	True	965	1936	260	200	323
W3000-L1000	I	Nominal	1000	3000	400	200	0
W3000-L1000	I	True	968	2838	396	210	0
W3000-L1000-C500	II	Nominal	1000	3000	400	200	500
W3000-L1000-C500	II	True	970	2940	475	200	500
W3000-L2000	I	Nominal	2000	3000	400	200	0
W3000-L2000	I	True	1955	2937	445	200	0

$$w(x) = \begin{cases} w_u & \text{for } x < -3R \\ w_u + R\Big(1 + \sin\big(\pi(x+2R)/(2R)\big)\Big) & \text{for } -3R \le x < -R \\ w_u + 2\sqrt{R^2 - (R+x)^2} & \text{for } -R \le x < 0 \\ \dfrac{K}{x_0 + x} & \text{for } 0 \le x < l_c \\ \dfrac{K}{x_0 + 2l_c - x} & \text{for } l_c \le x < 2l_c \\ w_u + 2\sqrt{R^2 - (R + 2l_c - x)^2} & \text{for } l_c \le x < R + 2l_c \\ w_u + R\Big(1 + \sin\big(\pi(2l_c - x + 2R)/(2R)\big)\Big) & \text{for } R + 2l_c \le x < 3R + 2l_c \\ w_u & \text{for } x \ge 3R + 2l_c \end{cases} \tag{6.4.2}$$

The nominal dimensions of the contractions are given in Table 6.4.1.

The microchannels were made with a rapid prototyping fabrication technique described later in Section 8.3.1 that was developed specifically to withstand high pressures ($P > 100$ bar) with minimal bulging. This fabrication method also yielded channels with rectangular cross-sections, thereby eliminating the scalloping effect that would otherwise have occurred if the chip had been made with the wet etching process. During the curing process, the exact dimensions of the channel are liable to change from their nominal values listed in Table 6.4.1. With the exception of the channel height, all dimen-

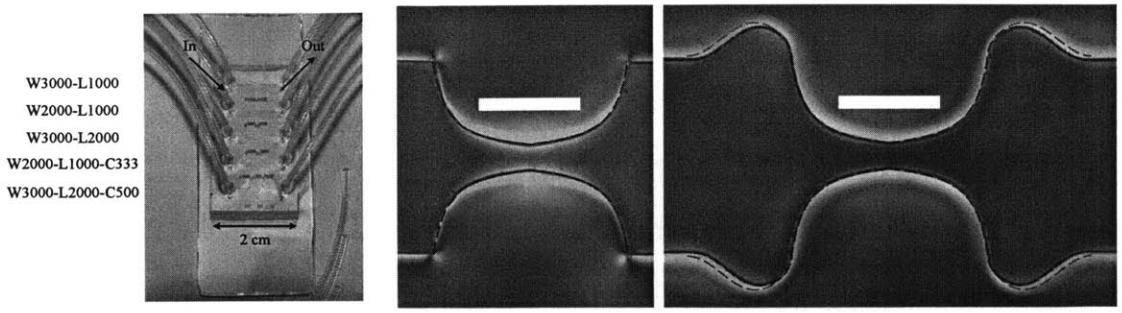

(a) Epoxy Chip

(b) Type I W2000-L1000

(c) Type II W2000-L1000-C333

(d) Type I W3000-L1000

(e) Type II W3000-L1000-C500

(f) Type I W3000-L2000

Figure 6.4.2: New designs for the contraction profile. Scale bar corresponds to 1 mm. The blue dashed curves correspond to the contraction shape based on the nominal dimensions in Table 6.4.1, and the red curves correspond to the profile based on the true dimensions.

sions can accurately be determined from an image captured on an optical microscope. The channel height and its uniformity throughout the channel are more challenging to measure, but appropriate values can be determined by filling the channel with tracer particles and observing the vertical distance between the visualization plane at which particles are in focus at the top and bottom of the channel. The true contraction dimensions were measured under the microscope and they are given in Table 6.4.1. All five contraction-expansion channels were made in one final chip that is shown in Figure 6.4.2 (a) together with the input and output tubing. Images of all five contractions are shown in Figure 6.4.2 (b)–(f).

6.4.1 Velocimetry Measurements

Representative streakline images of the flow through the redesigned contractions are shown in Figure 6.4.3. In all cases, the streaklines display kinematic reversibility which is to be expected for low Reynolds number flows. For viscously dominated flow in narrow gap geometries with $h \ll w_u$, such as the contraction used here, the flow can be described by the Hele-Shaw approximation, whereby the kinematics in the x-y plane are given by a velocity potential (Kundu & Cohen, 2008). For irrotational potential flow, the velocity potential ϕ and the streamfunction ψ constitute Cauchy-Riemann pairs, and hence the flow through the contraction can also be described by a linear combination of a set of basis streamfunctions.

The generic shape of a hyperbolic converging contraction can be obtained from the combination of a free stream and point sources, sinks and vortices as shown in Figure 6.4.4 (a). The streamfunction for a free stream with speed U_0 in the x-direction is $\psi_1 = U_0 y'$. The streamfunction for a point source of strength Λ at $(x', y') = (\pm b, \pm a)$ is $\psi_2 = \Lambda\theta = \Lambda \tan^{-1}\left((y' \mp a)/(x' \mp a)\right)$, and for a point vortex of strength Γ at the same position it is $\psi_3 = \Gamma \ln(r) = \Gamma \ln\left(\sqrt{(x' \mp b)^2 + (y' \mp a)^2}\right)$. Here $x' = r\cos\theta$ and $y' = r\sin\theta$, where r is the radial coordinate emanating from point (b, a) and θ is the angle with respect to the x'-axis. Although the specific number and position of these point sources and sinks within the flow domain is arbitrary, for simplicity the locations of the point sources or sinks and vortices are chosen to be coincident and located at $(x', y') = (\pm b, \pm a)$.

The combined streamfunction is

$$\begin{aligned}\psi(x', y') \;=\; & U_0 y' + \Lambda\left\{ \tan^{-1}\left(\frac{y'+a}{x'+b}\right) + \tan^{-1}\left(\frac{y'-a}{x'+b}\right) - \tan^{-1}\left(\frac{y'+a}{x'-b}\right) - \tan^{-1}\left(\frac{y'-a}{x'-b}\right)\right\} \\ & + \Gamma\left\{ \ln\left(\sqrt{(x'+b)^2 + (y'+a)^2}\right) - \ln\left(\sqrt{(x'+b)^2 + (y'-a)^2}\right)\right. \\ & \left. + \ln\left(\sqrt{(x'-b)^2 + (y'+a)^2}\right) - \ln\left(\sqrt{(x'-b)^2 + (y'-a)^2}\right)\right\}\end{aligned} \tag{6.4.3}$$

where the parameters a and b are the vertical and horizontal distance between the point sources and sinks and the origin, respectively. The streamlines coincide with isocontours

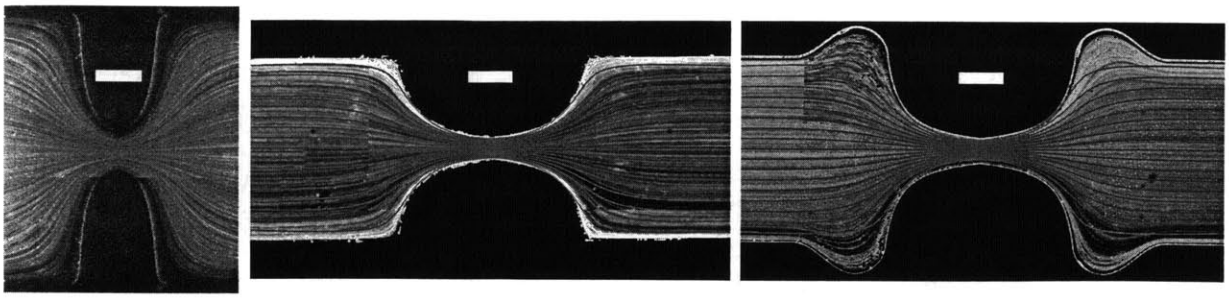

(a) (b) (c)

Figure 6.4.3: Streakline images of the flow of water through the contractions. Scale bar corresponds to 0.5 mm. (a) Original design $Q = 1000$ μL/hr, $Re = 0.80$. (b) W2000-L1000 $Q = 100$ μL/hr, $Re = 0.10$. (c) W2000-L1000-C333 $Q = 100$ μL/hr, $Re = 0.10$. The superposed red curves indicate the predicted streamlines based on the Hele-Shaw approximation in Eq. (6.4.3), where $U_0 = 0.1$ mm.s^{-1}, $a = 960$ μm, $b = 120$ μm, $\Lambda/U_0 b = 66$ and $\Gamma/U_0 b = 5$.

of the streamfunction and are overlaid on the streakline images in Figure 6.4.3 (b) and (c) for $a = 960$ μm, $b = 120$ μm, $U_0 = 0.1$ mm.s^{-1}, $\Lambda/U_0 b = 66$ and $\Gamma/U_0 b = 5$.

The centerline velocity profile is given by the gradient of the streamfunction in y at $y = 0$, and is

$$u_{cl} = U_0 + 2\left(\frac{\Gamma a + \Lambda(x' + b)}{(x' + b)^2 + a^2} + \frac{\Gamma a - \Lambda(x' - b)}{(x' - b)^2 + a^2}\right) \tag{6.4.4}$$

This velocity profile along with the contributions due to the point sources and sinks and the point vortices are shown in Figure 6.4.4 (b). Although this profile is non-linear within the converging and diverging sections of the contraction, in the case of $a \gg b$ for x'-values around $|x'| \simeq b$, the velocity profile is approximately equal to

$$u_{cl} \approx U_0 + 2\left((\Gamma a + \Lambda b)\left(\frac{1}{a^2} + \frac{1}{4b^2 + a^2}\right) + \Lambda x'\left(\frac{1}{a^2} - \frac{1}{4b^2 + a^2}\right)\right) \tag{6.4.5}$$

which is a linear scaling with position along the contraction centerline.

The velocity profiles along the centerline of the contraction were measured in all five contractions using water seeded with 0.02 wt% $d_p = 1.1$ μm fluorescent tracer particles (Invitrogen). The entire length of the contraction was too long to be imaged in a single image with a 10× objective. Therefore, velocimetry measurements were completed at

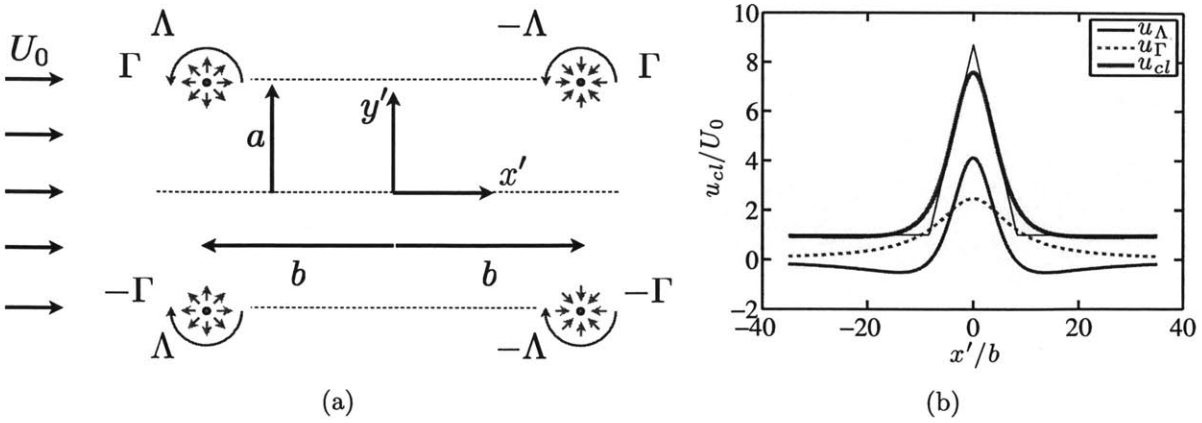

Figure 6.4.4: (a) Distribution of point sources, sink and vortices to describe the Hele-Shaw flow through the contraction. (b) Centerline velocity profile based on Eq. (6.4.4) for $U_0 = 0.1$ mm.s^{-1}, $a = 960$ μm, $b = 120$ μm, $\Lambda/U_0 b = 66$ and $\Gamma/U_0 b = 5$ given by the green curve u_{cl}. The solid blue curve is the contribution from the point sources and sinks u_Λ, the dashed red line is the contribution from the point vortices u_Γ, and the black line is the hypothetical anticipated velocity profile assuming a constant extension rate in the contraction region equal to the maximum extension rate of the overall profile given by the green curve.

evenly spaced intervals along the length of the contraction and each interval was then combined to determine the entire velocity profile along the contraction length. All post-processing of the velocity vector fields was performed in MATLAB. Example velocity profiles are shown in Figure 6.4.5 compared against the velocity profiles expected from the Hele-Shaw approximation in Eq. (6.4.4). This approximation is in good agreement with the experimental measurements near the inlet of the contraction, but it provides an underestimate of the velocity within the contraction region itself. This deviation is to be expected because the Hele-Shaw approximation is not valid near the throat of the contraction since the aspect ratio in that region of the channel approaches unity, which is not sufficiently shallow for the flow kinematics to be described accurately by a velocity potential. Furthermore, the no-slip condition at the walls results in an experimental velocity profile that is higher than the potential flow theory which assumes perfect slip at the walls. Instead, the lubrication approximation provides are more accurate prediction of the velocity profile in the throat of the contraction.

In Figures 6.4.6 (a) and (b) the measured velocity fields and profiles in the 2 mm

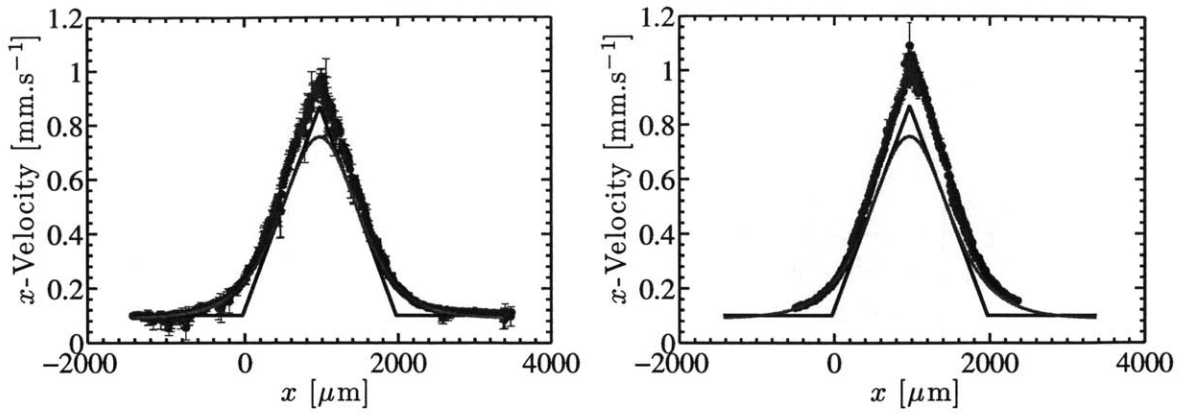

(a) W2000-L1000 $Q = 100$ μL/hr, $Re = 0.1$ (b) W2000-L1000-C333 $Q = 100$ μL/hr, $Re = 0.1$

Figure 6.4.5: Comparison of the experimentally measured velocity profiles (blue) and the expected profile (green) based on the Hele-Shaw approximation of Eq. (6.4.4). Note that in these plots, the x-values from Eq. (6.4.4) have been shifted by $x' = x - l_c$ so that the coordinate systems of both profiles coincide.

wide contractions are shown. The velocity profiles are compared against the predictions of the for 1D, 2D and 3D flow, respectively $u_{cl}^{1D}(x)$, $\tilde{u}_{cl}^{2D}(x)$ and $\tilde{u}_{cl}^{3D}(x)$. Clearly there is good overlap between the measured and predicted 3D profiles in the contraction region, but the velocity profile deviates at the inlet and outlet of the contraction. Furthermore, there does not appear to be a significant difference between the velocity profile in the contraction with the rounded expansion section and the contraction without them. In order to assess quantitatively if the inclusion of the rounded extensions produces a velocity profile that is closer to the 3D lubrication approximation, a dimensionless quantity is defined

$$Error \equiv \frac{1}{2l_c}\int_0^{2l_c} \frac{|u_{exp}(x) - \tilde{u}_{cl}^{3D}(x)|}{\tilde{u}_{cl}^{3D}(x)} dx \tag{6.4.6}$$

This error parameter is a measure of the average fractional difference between the measured profile and that of the 3D lubrication approximation given in Eq. (6.3.11). The values of this error parameter are calculated numerically and are listed in Table 6.4.2. The values of the error parameter for the W2000-L1000 and W2000-L1000-C333 contractions at equivalent flow rates differ by no more than 15%, suggesting that the inclusion of the rounded extensions has a minimal effect on the kinematics along the centerline of

Table 6.4.2: Error parameter for each chip and flow rate.

Contraction Designation	Type	Q [μL/hr]	$Error$ []
Original	I	600	0.7776
Original	I	3000	0.7944
W2000-L1000	I	100	0.1520
W2000-L1000	I	316	0.1462
W2000-L1000	I	1000	0.1622
W2000-L1000-C333	II	100	0.1585
W2000-L1000-C333	II	316	0.1684
W2000-L1000-C333	II	1000	0.1889
W2000-L1000-C333	II	3160	0.1911
W3000-L1000	I	100	0.2144
W3000-L1000	I	316	0.2408
W3000-L1000	I	1000	0.2251
W3000-L1000-C500	II	3000	0.2846
W3000-L2000	I	100	0.1236

the contraction.

Example velocity profiles measured in the 3 mm wide contractions are shown in Figures 6.4.6 (c) and (d). The velocity profiles for the W3000-L1000 and W3000-L1000-C500 contractions also follow the predictions of the 3D lubrication approximation closely. As with the 2 mm wide contractions, however, the error parameter for these two contractions is similar indicating that the rounded corner extensions do not play a significant role in the fluid kinematics along the centerline of the contraction-expansion. The lowest value of the error parameter is for the W3000-L2000 contraction which has the longest contraction length. This result is not surprising since a longer contraction gives kinematics that are more inline with the lubrication approximation. On the other hand, a major potential drawback of the elongated contraction is that for viscoelastic liquids, the viscous contribution to the overall pressure drop across the contraction will be larger (note that $\Delta P \sim l_c^2$ based on Eq. (6.3.5) and (6.3.8)). Therefore despite the improved agreement between the measured velocity field and lubrication approximation as l_c is increased, careful consideration would be required when designing a geometry that would not cause the viscous component of the pressure drop to dominate the overall pressure drop across the contraction.

As shown previously in Figure 6.3.2 (b), the true extension rate $\dot{\varepsilon}_t$ in the contraction

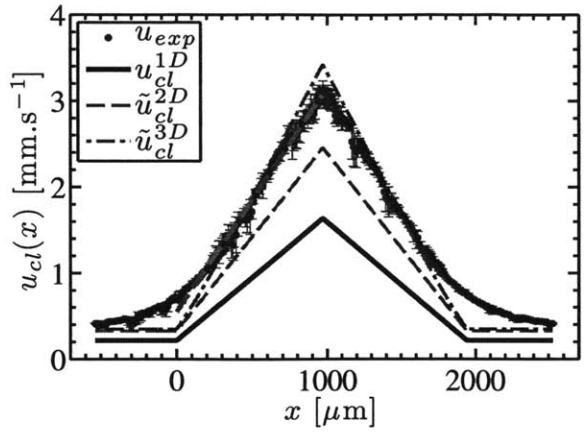

(a) W2000-L1000 $Q = 316$ μL/hr, $Re = 0.32$

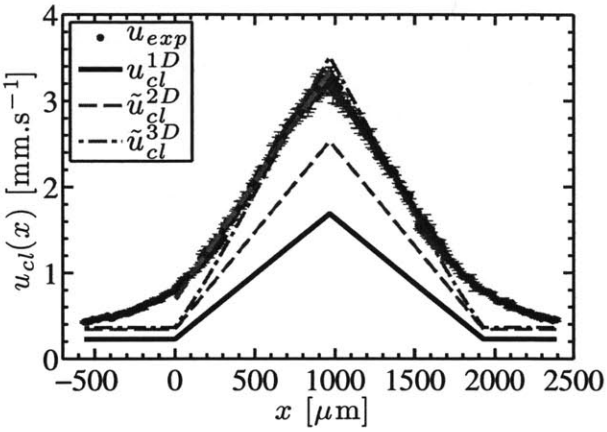

(b) W2000-L1000-C333 $Q = 316$ μL/hr, $Re = 0.32$

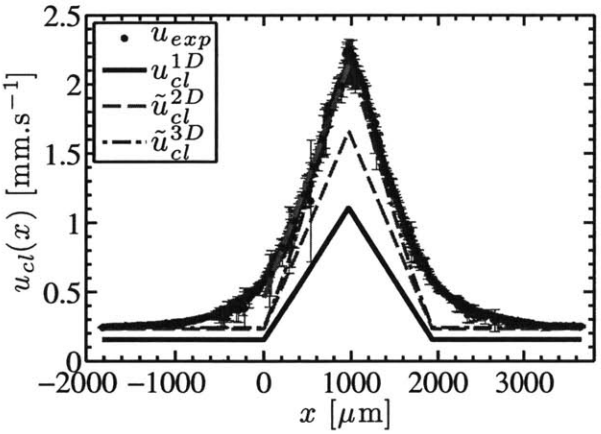

(c) W3000-L1000 $Q = 316$ μL/hr, $Re = 0.25$

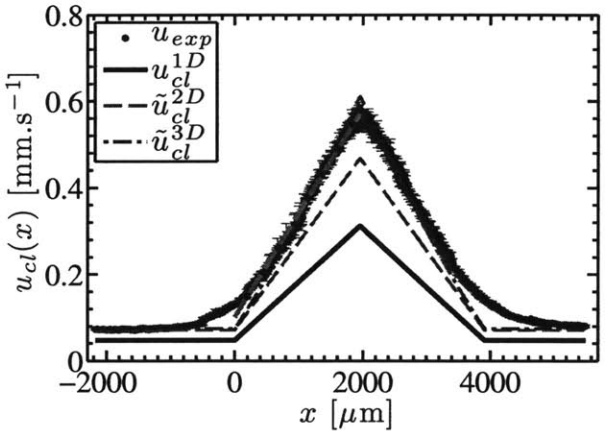

(d) W3000-L2000 $Q = 100$ μL/hr, $Re = 0.08$

Figure 6.4.6: Experimentally measured u_{exp} and anticipated velocity profiles along the centerline of the contraction $u_{cl}(x) = u(x, 0, 0)$ in a Newtonian fluid at low Reynolds number. The profiles are compared against the anticipated profiles from the lubrication approximation given by Eq. (6.3.9) (6.3.10) (6.3.11). The dashed solid line is the linear best-fit to the measured velocity profile in the converging section of the contraction ($0 \leq x \leq l_c$) whose slope $\dot{\varepsilon}_t$ equals the experimentally realized extension rate in the contraction.

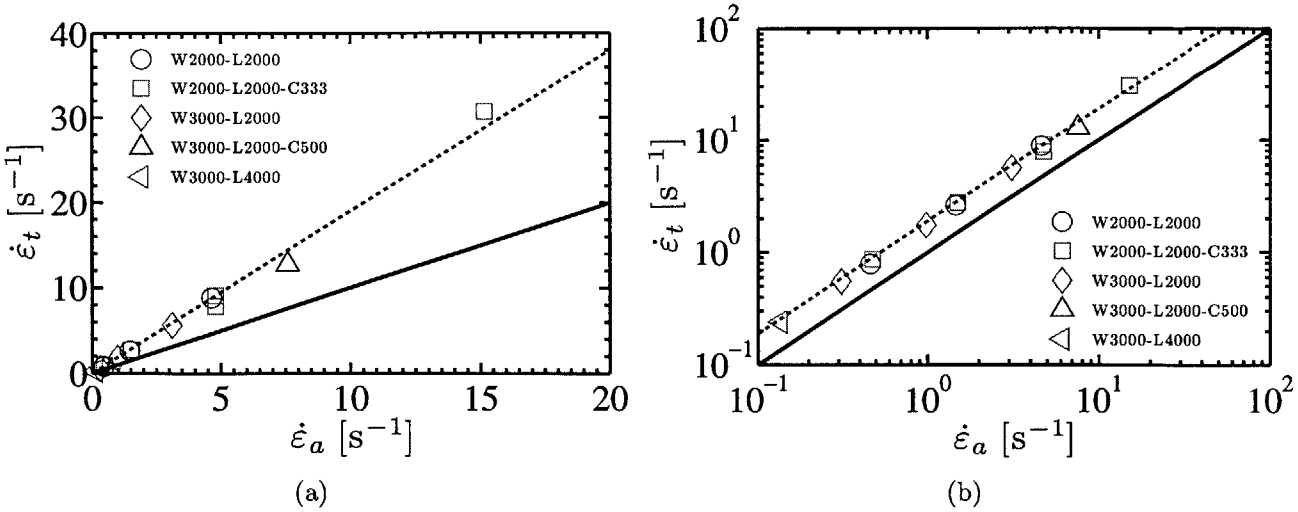

Figure 6.4.7: True extension rate $\dot{\varepsilon}_t$ determined from the slope of the best linear fit $u_x = (x_0 + x)\dot{\varepsilon}_t$ line to the measured centerline velocity near the contraction plane as a function of apparent extension rate $\dot{\varepsilon}_a$ given by Eq. (6.2.1). The solid black line indicates the ideal result of $\dot{\varepsilon}_t = \dot{\varepsilon}_a$, whereas the black dashed line is a fit to the true extension rate $\dot{\varepsilon}_t = 1.9\dot{\varepsilon}_a$. Note that the same data are displayed on (a) linear and (b) log scales.

can be calculated from the slope of the linear regression to the measured velocity profile in the contraction region. These results are shown in Figure 6.4.7. The true extension rate is roughly 90% greater than the nominal value $\dot{\varepsilon}_a$ based on Eq. (6.2.1). This difference between the nominal and true extension rates occurs due to the three dimensionality of the flow described by the full 3D lubrication approximation. The predicted local extension rate can be obtained by differentiating Eq. (6.3.11) with respect to x, which gives

$$\dot{\varepsilon}^{3D} = \frac{d\tilde{u}_{CL}^{3D}}{dx} = \left(\frac{dK}{dx}(x_0 + x) + K(x)\right)\dot{\varepsilon}_a \tag{6.4.7}$$

This value varies along the contraction centerline, but a characteristic value can be ascertained from the average slope of $\tilde{u}_{CL}^{3D}$ in Figure 6.4.6 which is $\dot{\varepsilon}_t \approx 2\dot{\varepsilon}_a$. Accordingly, the measured flow kinematics in the converging-diverging regions of the redesigned contraction geometries are closely described by the 3D lubrication approximation as desired.

6.4.2 Pressure Measurements

A set of pressure measurements were also completed in order to asses how reliably each of the modified contraction designs could be used as a microfluidic extensional viscosity indexer. Since the epoxy devices were not manufactured using the same silicon fabrication methods as those used with the original chip design, the epoxy devices did not contain any MEMS pressure transducers along the length of the channel. Therefore, it was not possible to measure the pressure profile along the length of the channel, but instead the gauge pressure upstream of the channel inlet was measured with a 150 psi UNIK 5000 pressure sensor (GE Druck) using an experimental setup schematically depicted in Figure 6.4.8.

In order to determine the pressure drop across the contraction-expansion section ΔP_c, it was necessary to account for all other contributions to the overall measured pressure drop ΔP. The value of this pressure drop was assumed to be the summation of smaller pressure drops acting in series:

$$\Delta P = \Delta P_T + \Delta P_{Ty} + \Delta P_{in/out} + \Delta P_{rec} + \Delta P_c \tag{6.4.8}$$

where each component is described below.

The first pressure drop ΔP_T is the pressure drop across the needle section of the T-junction, which is connected to the pressure sensor. This pressure drop corresponds the flow through a needle of length $L_T = 12.9$ mm and radius $R_T = 0.35$ mm as well as entrance effects in the T-junction that can be accounted for by a Bagley correction (Macosko, 1994) that is determined empirically. The pressure drop across the needle was thus measured with three Newtonian fluids of different dynamic viscosities (N1000 $\mu = 2.0$ Pa.s, S60 $\mu = 0.102$ Pa.s, 40:60 wt% water:glycerol $\mu = 0.010$ Pa.s) in calibration experiments shown in Figure 6.4.9 (a). The expected pressure drop for Hagen-Poiseuille flow is $\Delta P = 8\mu\mathcal{U}L_T/R_T^2$, where $\mathcal{U} = Q/\pi R_T^2$ is the mean velocity and Q is the volumetric flow rate. Therefore the viscous friction factor is defined $f_v \equiv \Delta P/(\mu\frac{\mathcal{U}}{R}) = 8\frac{L_T}{R_T}$ or equivalently $Re_T \cdot f_v = 8\frac{L_T}{R_T}Re_T$, where $Re_T \equiv 2\mathcal{U}R/\nu$ and ν is the kinematic viscosity. The empirically determined pressure drop across the needle, however, was $f_v = 24\frac{L_T}{R_T}$ or equivalently $Re_T \cdot f_v = 24\frac{L}{R}Re_T$, as shown in Figure 6.4.9 (a). Hence the Bagley correc-

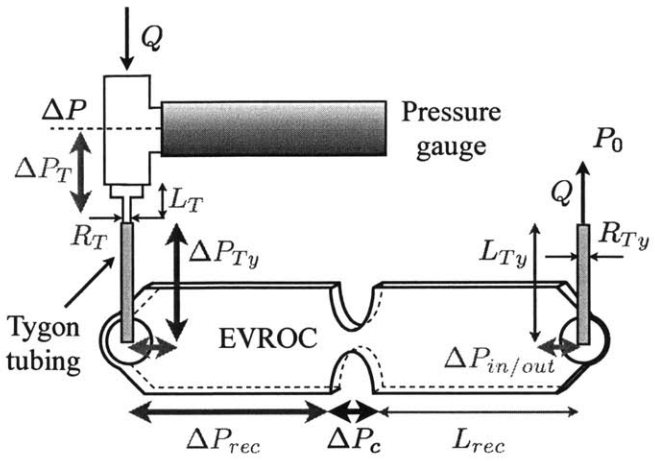

Figure 6.4.8: Schematic diagram of the experimental setup for measuring the pressure drop across the contraction in the epoxy chips.

tion accounts for approximately 66% of the pressure drop across the needle. Substitution of Eq. (6.2.1) into the result for ΔP_T gives

$$\Delta P_T = 24 \frac{L_T}{\pi R_T^4} \frac{w_c w_u}{w_u - w_c} l_c h \mu \dot{\varepsilon}_a \tag{6.4.9}$$

The pressure drop ΔP_{Ty} occurred over the short sections of Tygon tubing (Saint-Gobain) with inner radius $R_{Ty} = 0.26$ mm at the inlet and outlet of the device. The combined length of the tubing was approximately $L_{Ty} = 25$ mm. The pressure drop across the tubing is given by

$$\Delta P_{Ty} = 8 \frac{L_{Ty}}{\pi R_{Ty}^4} \frac{w_c w_u}{w_u - w_c} l_c h \mu \dot{\varepsilon}_a \tag{6.4.10}$$

A third contribution to the overall pressure drop arises from the dissipation in the two rectilinear sections of the channel upstream and downstream of the contraction-expansion, each with length $L_{rec} = (6.5 \text{ mm} - l_c)$, width w_u and height h. The combined pressure drop across both of these sections is

$$\Delta P_{rec} = 24 \frac{w_c l_c L_{rec}}{h^2 (w_u - w_c)} \left(1 - \frac{192}{\pi^5} \frac{h}{w_u} \sum_{j \text{ odd}}^{\infty} \frac{\tanh(j \pi w_u / 2h)}{j^5} \right)^{-1} \mu \dot{\varepsilon}_a \tag{6.4.11}$$

Another contribution to the pressure drop is due to entrance and exit effects at the inlet and outlet of the microfluidic device $\Delta P_{in/out}$. It is not obvious how to account for this pressure drop, since the fabrication method is likely to introduce a degree

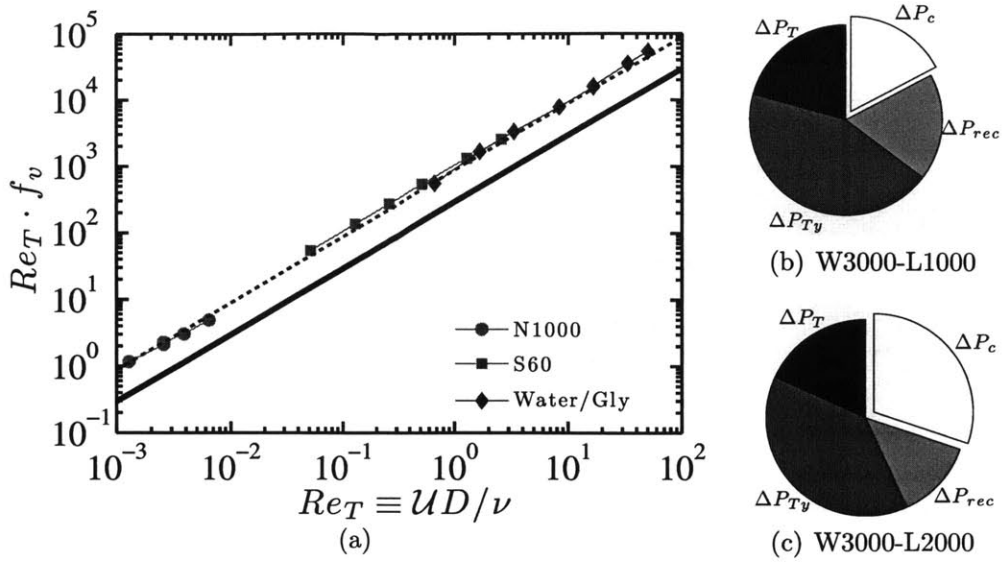

Figure 6.4.9: Pressure calibration tests. (a) Pressure drop across the needle tip connected to the T-junction. The solid line corresponds to the theoretical result of $Re_T \cdot f_v = 8\frac{L_T}{R_T}Re_T$, while the dashed line is a fit to the measured data which include entrance effects on the pressure drop given by $Re_T \cdot f_v = 24\frac{L_T}{R_T}Re_T$. (b) & (c) Fractional contribution to the overall pressure drop predicted using Eqs. (6.3.8), (6.4.9), (6.4.11) and (6.4.10).

of variability between the precise features of the inlet and outlet regions in each microchannel that would make it difficult to measure a Bagley-like correction for this channel. For simplicity, $\Delta P_{in/out}$ is assumed to be negligible (although this assumption is not realistic) and thus the pressure drop across the contraction-expansion is $\Delta P_c \approx \Delta P - \Delta P_T - \Delta P_{Ty} - \Delta P_{rec}$. The relative contributions of each component of the pressure drop to the overall pressure drop predicted based on Eqs. (6.3.8), (6.4.9), (6.4.11) and (6.4.10) are shown for two of the contraction geometries in Figures 6.4.9 (b) and (c). It is clear that the magnitude of ΔP_c is not the major contribution to the overall pressure drop, which poses a challenge for determining its value accurately from experimental measurements.

The pressure drops measured using the 3 mm wide contraction geometries with the 40:60 wt% water:glycerol mixture are shown in Figure 6.4.10 (a). All pressure drops scale linearly with apparent extension rate, indicating that all measurements were completed in the regime of steady laminar flow. The total predicted pressure drops are shown by

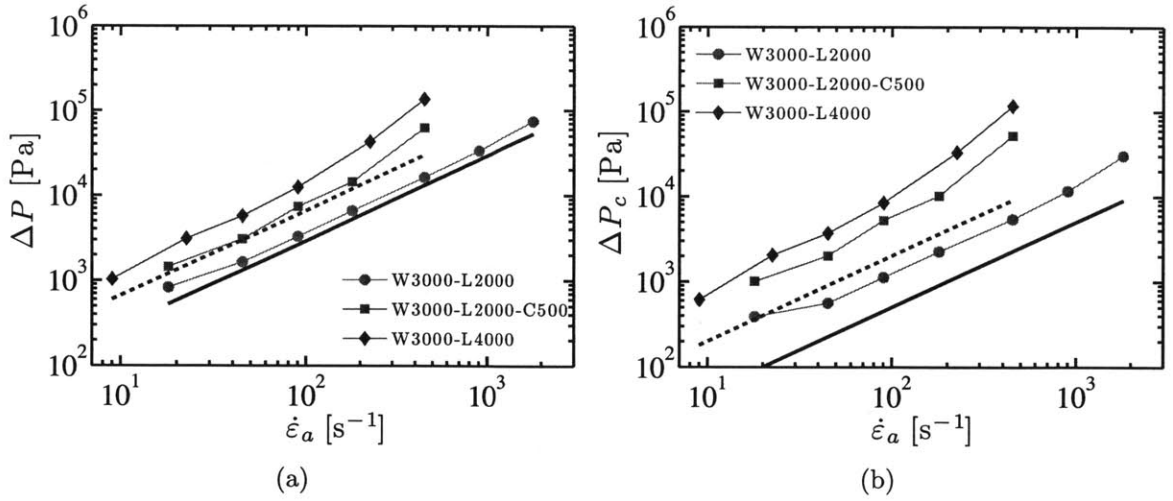

Figure 6.4.10: Pressure measurements with the 40:60 wt% water:glycerol mixture. (a) Total pressure drop measured across three $w_u = 3$ mm wide contraction geometries. (b) Pressure drop across the contraction-expansion region of the geometry. The solid black lines correspond to the predicted value of (a) ΔP and (b) ΔP_c for the W3000-L1000 and W3000-L1000-C500 geometries and the dashed line corresponds to these predicted values for the W3000-L2000 geometry.

the solid and dashed lines in the plot. For W3000-L1000 the actual pressure drop is about 25% larger than the predicted value, for W3000-L1000-C500 it is about 150% larger, and for W3000-L2000 it is about 100% larger. These differences strongly suggest that the pressure losses due to entrance and exit effects $\Delta P_{in/out}$ at the inlet and outlet of the channel are significant although they cannot be easily accounted for. It is therefore unclear if the difference in the measured pressure drop between the W3000-L1000 and W3000-L1000-C500 chips is due to the rounded expansion sections or to differences in the precise features of the inlets and outlets of each channel which lead to appreciably different values of $\Delta P_{in/out}$ at the same flow rate.

The pressure drop across the contraction-expansion section ΔP_c determined after applying the corrections from Eqs. (6.4.9), (6.4.11) and (6.4.10) is shown in Figure 6.4.10 (b). For W3000-L1000 the measured pressure drop ΔP_c is about 150% larger than the predicted value using Eq. (6.3.8), for W3000-L1000-C500 it is about 1000% larger, and for W3000-L2000 it is about 500% larger. Even if the uncertainty in the channel thickness, which is of the order of 10 μm, is considered, the predicted value of ΔP_c and ΔP_{rec} increase only by about 10%, which is clearly not substantial enough to account for the

discrepancy between the predicted and measured values of ΔP_c.

The primary value of these pressure measurements is that they scale linearly with flow rate, which confirms that the flow is laminar and that the epoxy channel does not deform with increasing flow rates. To obtain more accurate measurements of ΔP_c, however, it would be necessary measure the pressure profile within the microfluidic device itself. On the other hand, the flow kinematics are qualitatively and quantitatively in much closer agreement with the predictions of the lubrication approximation in the redesigned chip than in the original design (refer to the error parameter in Table 6.4.2). This agreement suggests that the measured pressure profile along the channel centerline would likewise be more closely predicted by the lubrication approximation provided a microfluidic chip with multiple pressure sensors along the length of the contraction, as is the case in the original microfluidic EVROC device with MEMS transducers, were constructed.

6.5 Summary

In this Chapter, the extensional flows of a range of Newtonian and a non-Newtonian fluids through a microfluidic hyperbolic contraction have been studied using local pressure field measurements, kinematic measurements (using μ-PIV and streakline imaging) and full-field FIB measurements. This device can be used for indexing and comparing the behavior of a wide range of complex fluids in an extension-dominated flow; however, careful measurements of both the pressure field and flow kinematics are important for accurate interpretation of the results.

For the flows of Newtonian liquids at low Reynolds number, $Re_0 < \mathcal{O}(10)$, the measured pressure drop across the contraction, ΔP_{23}, increases linearly with apparent extension rate $\dot{\varepsilon}_a$. Furthermore, provided one accounts for the position of the MEMS transducers, one can estimate the pressure drop across the contraction alone, ΔP_c, which can be predicted using a 2D lubrication approximation for viscous Newtonian flow to within a constant numerical factor of around three. This residual discrepancy can be attributed to the inadequacy of a 2D approximation in capturing a truly 3D flow within this shallow microfludic device, as well as additional complicating effects arising from

the geometric abruptness of the contraction and the non-rectangular cross-section of the contraction region (caused by the wet etching fabrication process).

Flow velocimetry measurements confirm that the hyperbolic contraction imposes an extension rate along the centerline that is approximately uniform spatially, but roughly 66% larger than the nominal value, *i.e.* $\dot{\varepsilon}_t \approx 1.66\dot{\varepsilon}_a$, based on a least squares linear fit to the measured extension rates. These measurements also reveal the onset of initial extensional effects as much as three contraction lengths upstream of the contraction entrance as a result of the abruptness of the hyperbolic contraction. These non-idealities in the extensional flow kinematics are the cause of the larger than anticipated pressure drop based on the lubrication approximation.

Two model viscoelastic liquids and three commercially available complex fluid formulations have been tested in the EVROC. For viscoelastic materials it is assumed that the pressure drop in the contraction ΔP_c, is a superposition of a pressure drop due to viscous shear stresses ΔP_v, and an extra pressure drop due to elastic stresses ΔP_e, hence $\Delta P_c = \Delta P_v + \Delta P_e$. The value of ΔP_v is estimated using a 2D lubrication analysis for a power-law fluid and the remaining elastic contribution to the pressure drop ΔP_e is used to calculate an apparent extensional viscosity $\eta_{E,a}$. Typical Trouton ratios when referenced to the zero-shear-rate viscosity are $\mathcal{O}(10)$, but the values of this ratio should not be interpreted as a true Trouton ratio measured in homogeneous extensional flow, since the flow through this contraction has mixed shear and extensional components.

Flow velocimetry measurements and streakline images demonstrate that typically for $De_a < \mathcal{O}(1)$ the flow field remains largely unchanged from the low Reynolds number flow field expected for a Newtonian fluid in a planar hyperbolic contraction, with the experimentally-realized extension rate along the contraction centerline proportional to the flow rate. For $De_a > \mathcal{O}(1)$, an elastically-driven secondary flow emerges which results in upstream vortex growth and undermines any assumption of a self-similar, Newtonian-like flow. However the experimentally-measured kinematics along the contraction centerline show that the extension rate is still spatially homogeneous for a given flow rate and that useful measurements can still be made in this regime. Above a higher critical Deborah number, $De_a > \mathcal{O}(10)$, the flow becomes time-varying and reliably ex-

tracting $\eta_{E,a}(\dot{\varepsilon})$ from the measured pressure drop is difficult. Full-field measurements of flow-induced birefringence generally confirm the qualitative features seen in the streak-line images, whilst also showing that the local state of tensile stress in the fluid is still evolving as it flows towards the contraction throat.

In order to improve the spatial homogeneity in the flow kinematics of the extension-dominated flow through the contraction section, the contraction length was increased in a set of redesigned contraction geometries to make the velocity profile more in line with the predictions of the lubrication approximation. Additionally, in certain chips a rounded protrusion was included upstream of the hyperbolic contraction aimed at further improving the spatial homogeneity in the extension rate along the contraction centerline. The devices were made from a rigid epoxy and constructed using soft photolithograpy-based fabrication methods. The velocimetry measurements indicate that a longer contraction leads to a velocity profile more in line with the predictions of the lubrication approximation, but that the rounded protrusions do not have an appreciable affect on the centerline velocity profile. Complementary measurements of pressure drop across the entire microfluidic device were completed using a single gauge pressure sensor. The pressure drop increased linearly with flow rate as expected for a laminar flow of a Newtonian fluid, but the exact value of the pressure drop across the contraction-expansion section could not be reliably determined due to uncertainties in the pressure losses in the inlet and outlet regions of the microchannel. These results strongly suggest that an increase in the length of the contraction section would enable the more accurate determination of the viscous contribution to the overall pressure drop with the lubrication approximation and thereby improve the reliability of the EVROC for extracting the extensional viscosity in this extension-dominated flow.

In summary, the microfluidic hyperbolic contraction device described in this Chapter can be used to investigate the extensional viscosity of a complex fluid such as an ink or liquid foodstuff or consumer product up to extension rates $\dot{\varepsilon}_a \sim \mathcal{O}(10^3)$ s^{-1} using the following steps:

(i) A series of steady pressure drop measurements through the device are made as a function of imposed flow rate (*cf.* Figure 6.3.1 and 6.3.4).

(*ii*) The pressure coefficient $\mathcal{P} \equiv \Delta P_{23}/\Delta P_{14}$ can be calculated as a measure of the relative importance of viscoelastic effects to the total pressure drop. This value should approach unity $\mathcal{P} \rightarrow 1$, as viscoelastic effects become increasingly dominant (*cf.* Figure 6.3.5 (a)).

(*iii*) The pressure drop ΔP_c across the contraction is calculated from Eq. (6.2.3) and the apparent extensional rate for each flow rate is calculated from Eq. (6.2.1) (*cf.* Figure 6.3.5 (b)).

(*iv*) The viscoelastic contribution to the pressure drop ΔP_e can be calculated using the equation $\Delta P_e = \Delta P_c - \Delta P_v$, where ΔP_v can be estimated from Eq. (6.3.17). The apparent extensional viscosity $\eta_{E,a}$ can then be determined using Eq. (6.3.21).

(*v*) If desired, a second transparent microfluidic chip can be used to measure the local kinematics and optical retardance with full-field μ-PIV and birefringence measurements as illustrated in Figure 6.3.7. Such measurements can be valuable in ascertaining that the planar elongational flow is stable and the kinematics are homogeneous.

This hyperbolic planar contraction can serve as a complement to the shear viscosity microfluidic viscometer described in Pipe *et al.* (2008) for measuring a nominal extensional viscosity. The combination of measurements obtained with these two devices will be valuable to an applied rheologist for quality control monitoring (*i.e.* indexing variations in the extensional rheology of a specific fluid formulation) as well as for providing a simple and quick evaluation of the performance of a particular viscoelastic fluid in filling and dispensing applications featuring converging nozzles that are characterized by high shear and extension rates.

Chapter 7

Flow-Induced Particle Migration: Inertial Focusing in Diluted and Whole Blood

7.1 Introduction

In the previous Chapters, inertial effects have generally been taken as negligible, since the flows under consideration were highly viscous due to the low speeds and small length scales of the flow geometry. On the other hand, in this Chapter and subsequently in Chapter 8, the fluid velocities are sufficiently large that the role of inertia in the flow cannot be neglected. In this regime the channel Reynolds number $Re_c \equiv \mathcal{U}D/\nu$ is much larger than unity, where $\mathcal{U}$ is the mean velocity in the channel, D is the hydraulic diameter and ν is the kinematic viscosity of the fluid. As discussed previously in the literature review in Section 2.4, when particles of diameter a are seeded in the fluid and are advected in a microchannel, inertial non-linearities can give rise to cross-stream migration and ordering of the particles. The ordering phenomenon in a microfluidic device is commonly called *inertial focusing*, because the particles are driven or *focused* to very specific locations in the channel cross-section. This focusing occurs at moderate to large particle Reynolds numbers $Re_p \equiv Re_c(a/D)^2$, which is a measure of the relative importance of fluid inertia in the immediate vicinity of the particle and is defined in

terms of a characteristic fluid velocity near the particle based on the product of the characteristic shear rate in the channel $\dot{\gamma} \sim \mathcal{U}/D$ and the particle diameter a. Inertial microfluidics has demonstrated the potential to provide a rich range of capabilities to manipulate biological fluids and particles to address various challenges in biomedical science and clinical medicine.

One aspect of inertial focusing that has not been studied is how particles suspended in whole or minimally diluted blood respond to inertial forces in microchannels. The utility of imaging techniques (*i.e.* high-speed bright-field imaging and long exposure fluorescence (streak) imaging) primarily used to observe particle focusing in microchannels is limited in complex fluids such as whole blood due to interference from the large numbers of red blood cells (RBCs). In this Chapter, particle trajectory analysis (PTA) is used to observe the inertial focusing behavior of polystyrene beads, white blood cells, and PC-3 prostate cancer cells in physiological saline and blood. Identification of optically in-focus (fluorescently labeled) particles were achieved at mean particle velocities of up to $\mathcal{U} = 1.85$ m.s^{-1}. Quantitative measurements of optically in-focus particles were used to construct intensity maps of particle frequency in the channel cross-section and scatter plots of particle centroid coordinates against particle diameter. PC-3 cells spiked into whole blood (*i.e.* hematocrit count $HCT = 45\%$) demonstrated a novel focusing mode not observed in physiological saline or diluted blood. PTA can be used as an experimental frame of reference for understanding the physical basis of inertial lift forces in whole blood and discover inertial focusing modes that can be used to enable particle separation in whole blood.

7.2 Materials and Methods

7.2.1 Device Fabrication

A straight rectangular channel ($H = 93$ μm, $W = 45$ μm, $D = 60$ μm, $L = 3.5$ cm) was formed in polydimethylsiloxane (PDMS) using a master mold fabricated via photolithography (Duffy *et al.*, 1998). A 4-inch silicon wafer was spin-coated with a 93 μm thick layer of negative photoresist (SU-8 100, Microchem, Newton, MA), exposed to UV-light

through a Mylar photomask (Fineline Imaging Colorado Springs, CO), and developed (BTS-220, J.T. Baker, Phillipsburg, NJ). A 10:1 mix of PDMS elastomer and curing agent (Sylgard 184, Dow Corning, Midland, MI) was poured onto the master mold and degassed for 60 minutes to remove all trapped bubbles. The master mold was placed in an 80 °C oven for 72 hours to thoroughly cure the PDMS. The cured PDMS replica was peeled away from the master mold before inlet, outlet, and height calibration holes were punched using a coring tool (Harris Uni-Core, Redding, CA) with a hole diameter of 1.5 mm. The hole-punched PDMS replica was irreversibly bonded to a glass coverslip by exposing both PDMS and glass surfaces to oxygen plasma for 30 seconds (Harrick Plasma, Ithaca, NY).

7.2.2 Particle Suspensions

Fluorescently labeled polystyrene beads (FluoSpheres, Invitrogen, Carlsbad, CA) were supplied as stock suspensions in 0.15 M NaCl with 0.05 wt% Tween 20 and 0.02 wt% thimerosal. PC-3 human prostate cancer cells (CRL-1435, ATCC) were grown in F-12 K medium (30–2004, ATCC, Manassas, VA) containing 10% fetal bovine serum (Invitrogen, Carlsbad, CA) and 1% penicillin streptomycin (Invitrogen, Carlsbad, CA) at 37 °C under 5% CO2 conditions. PC-3 cells were fluorescently labeled in physiological saline (Invitrogen, Carlsbad, CA) containing 5 μM calcein red-orange AM (Invitrogen, Carlsbad, CA). Whole blood samples from healthy donors were obtained (Research Blood Components, Boston, MA) in venous blood collection tubes containing EDTA (Vacutainer, BD Biosciences, San Jose, CA). The RBC volume fraction in each sample was determined using a blood analyzer (KX-21, Sysmex, Mundelein, IL). WBCs were recovered from whole blood via RBC lysis buffer (Miltenyi Biotec, Auburn, CA) and fluorescently labeled in physiological saline containing 5 μM calcein red-orange AM. Samples with a specific RBC volume fraction were generated by suspending particles in appropriate amounts of physiological saline and whole blood. The particle concentration was set at 3.0×10^6 particles/mL.

7.2.3 Imaging & Analysis of Fluorescently Labeled Particles

The starting sample containing fluorescently labeled particles was injected into the microchannel using an automated syringe pump (PhD 2000, Harvard Apparatus, Holliston, MA) at flow rates of $Q = 50$, 150, and 450 ml.min^{-1}. These rates correspond to particle velocities of $\mathcal{U} = Q/HW = 0.21$, 0.62, and 1.85 m.s^{-1}. The sample loading system consisted of 5-mL syringe (BD Biosciences, San Jose, CA), 22-gauge blunt needle (Small Parts, Seattle, WA), 0.02-inch inner diameter tubing (Tygon, Small Parts, Seattle, WA), and cyanoacrylate adhesive (Loctite, Henkel, Rocky Hill, CT). Images of particles flowing through the channel were captured using the same epifluorescent inverted microscope, charge-coupled device camera and Nd:YAG laser described in Section 5.4.2. The laser generated $\delta t \sim 10$ ns pulses of light with an excitation wavelength of 532 nm, and the camera detected light from fluorescent particles with an emission wavelength exceeding 565 nm. At a stationary observation distance $L_{obs} = 3.5$ cm downstream from the channel entrance, images were captured at eight different height positions spaced 6 μm apart. Prior to image capture, polystyrene beads with diameter $a = 2$ μm (FluoSpheres, Invitrogen, Carlsbad, CA) were placed in open wells formed when one side of the height calibration holes in the PDMS replica was bonded to a glass coverslip. Optically in-focus polystyrene beads found at the bottom of the well were used to establish the zero height position (*i.e.* floor) of the channel. For each height position, shown schematically in Figure 7.2.1, a set of 400 images was collected at a rate of $F = 5$ frames per second.

The polystyrene beads (mean particle diameter $a = 9.9$ μm) used in this study were monodisperse, while white blood cells ($a = 9.0$ μm, size range of 7-11 μm) and PC-3 cells ($a = 17.8$ μm, size range of 10-35 μm) were polydisperse in nature. Given a 20$\times$ 0.4 NA objective, the depth of field was calculated (Meinhart *et al.*, 2000) to be $\delta y = 5.8$ μm. In order to reliably differentiate between optically in-focus particles found at neighboring vertical positions, the spacing between all vertical positions was set to $\Delta y = 6$ μm, as indicated by the tick marks in Figure 7.2.1. The imaging locations were confined to the bottom half of the channel since particle focusing was expected to be symmetric across the x-z plane at $y = 48$ μm.

ImageJ software (NIH, Bethesda, MD) was used to process raw images and identify

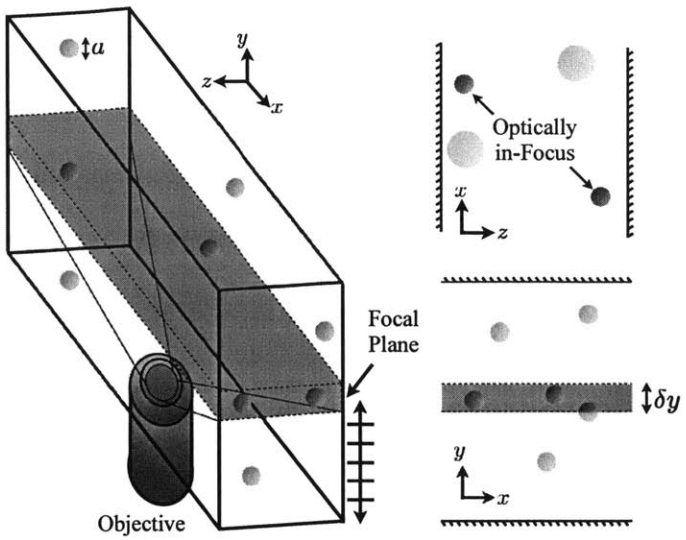

Figure 7.2.1: Imaging of particles in the channel. Particles in the focal plane appear bright with well-defined edges. Particles above and below the imaging plane appear dim and blurry.

optically in-focus particles at each height position. For an optically in-focus particle at a given height location, images were taken at multiple height positions in order to observe corresponding changes in fluorescence signal intensity indicative of an out-of-focus particle. An optically in-focus particle was predominantly found to exhibit both a higher mean 8-bit grayscale value and a steeper edge signal intensity gradient relative to an optically out-of-focus particle. For each set of 400 images at a given height location, an image threshold was automatically set using an iterative procedure based on the isodata algorithm (Ridler & Calvard, 1978). Using a specific cutoff for particle size based on size distribution measurements from a cell analyzer, the image filtering technique automatically generated a table of potential optically in-focus particles. All particles were marked in the set of images and referenced numerically in the table, and each particle was characterized based on a user-defined set of parameters (*e.g.* 2D particle area, mean signal intensity, x-y coordinates, and circularity). The collection of potential optically in-focus particles were examined manually to ensure that optically in-focus particles were identified and measured properly. For a given flow rate and RBC volume fraction, quantitative measurements from the collection of optically in-focus particles were used to construct surface and scatter plots characterizing various aspects of particle focusing behavior using MATLAB.

Image Capture of Optically in-Focus Particles in Diluted Blood

Particle trajectory analysis (PTA) was used to identify polystyrene beads, white blood cells, and PC-3 cells over a range of flow rates Q and RBC volume fractions f_{RBC}, where f_{RBC} is the ratio of RBC volume to the starting sample volume. For example, $HCT = 45\%$ (*i.e.* whole blood in this study) corresponds to $f_{RBC} = 1$, while $HCT = 15\%$ corresponds to $f_{RBC} = 0.33$ (diluted using physiological saline). A straight rectangular channel with a 2:1 (H/W) aspect ratio was used to focus randomly distributed particles to two lateral equilibrium positions centered on the long face of the channel shown in Figure 7.2.3 (a). These equilibrium positions resulted from a balance of a *wall effect* lift that acts to lift particles away from the wall towards the channel centerline and a *particle shear* lift that acts away from the channel centerline towards the wall Figure 7.2.3 (b).

In diluted blood samples where the utility of high-speed bright-field imaging and long-exposure fluorescence is limited, PTA demonstrated the ability to capture images of individual optically in-focus particles moving at ultra-fast velocities as shown in Figure 7.2.3 (d). Image capture of individual optically in-focus particles was achieved at flow rates up to $Q = 450$ μL.min^{-1} in physiological saline initially, which corresponds to a mean flow velocity of $\mathcal{U} = 1.85$ m.s^{-1} and a channel Reynolds number of $Re_c = 158$. The images of the particles showed no sign of blurring at these velocities since the pulse duration of the laser was very short. For the microscope objective and camera used in this work, a single pixel corresponds to $(eM)^2 = 0.323 \times 0.323$ μm^2, thus the flow velocity necessary for a particle to traverse one pixel (and thus show blurring) is $\mathcal{U}_{blur} \sim (eM)\delta t^{-1} = 32$ m.s^{-1}, which is substantially larger than the velocities considered in this Chapter. On the other hand, the flow rates studied in this Chapter are limited to $Q \lesssim 450$ μL.min^{-1} for $f_{RBC} = 1$ since the pressure at the device inlet above this flow rate exceeded the critical delamination pressure of the PDMS-glass interface. At a given vertical position (*e.g.* $y = 48$ μm), optically in-focus particles exhibited peak and uniform fluorescence signal intensity, while out-of-focus particles exhibited suboptimal and radially diffuse fluorescence signal intensity shown in Figure 7.2.3 (c). Using the appropriate image threshold, it was possible to differentiate optically in-focus particles at a given vertical position from optically in-focus particles at neighboring vertical positions.

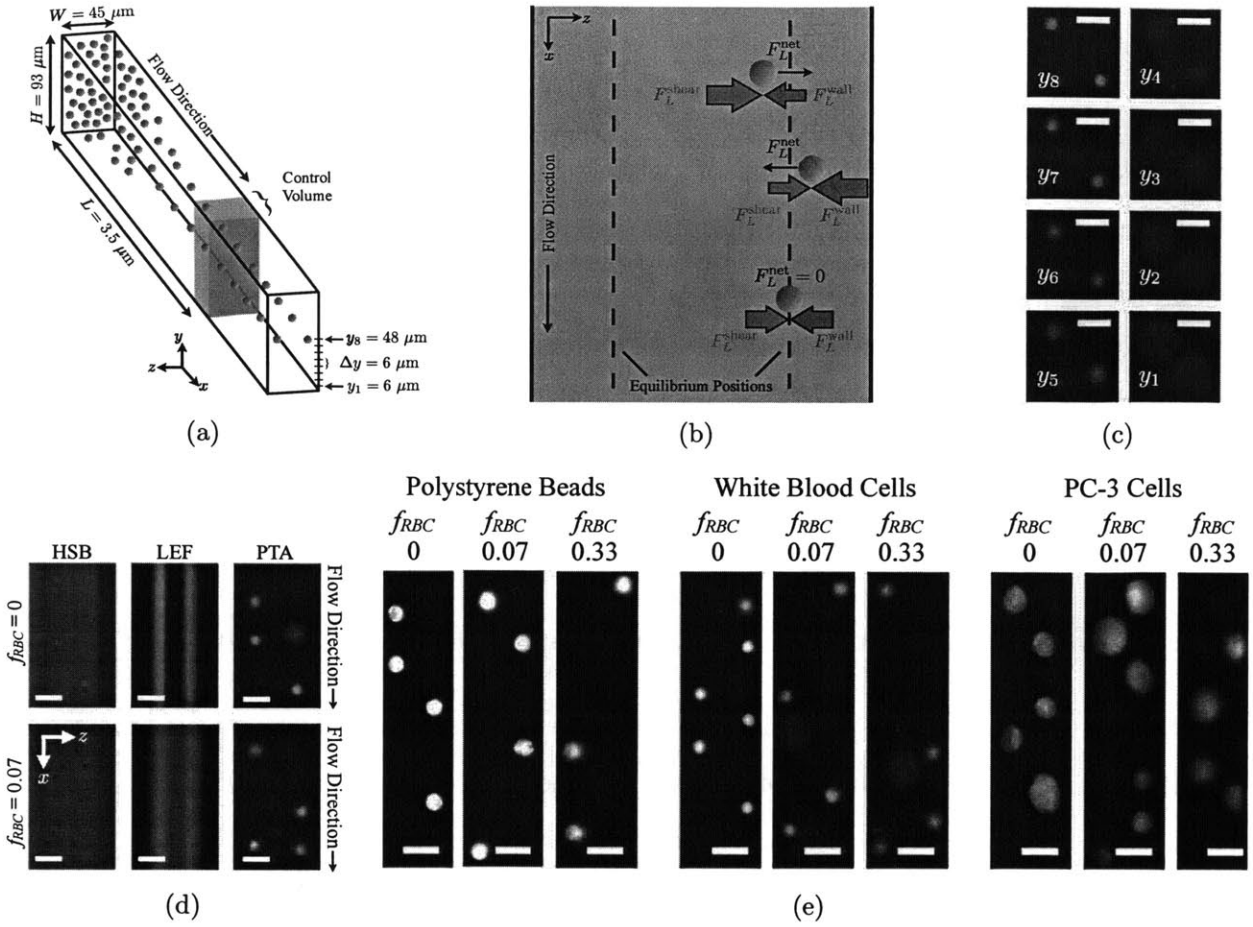

Figure 7.2.2: Using particle trajectory analysis (PTA) to observe particle focusing behavior in diluted blood. (a) Randomly distributed particles predominantly focus to two lateral positions centered on the long face of a straight microchannel with 2:1 aspect ratio. (b) The equilibrium positions result from a balance of a *wall effect* lift that acts away from the wall towards the channel centerline and a *particle shear* lift that acts away from the channel centerline towards the wall. (c) Particle focusing behavior is observed in the x-z plane from eight different vertical positions spanning the bottom half of the channel. Focused particles are shown to be in focus at $y_8 = 48$ μm (scale bar 20 μm). (d) For high-speed bright-field (HSB) microscopy with an exposure time of 2 μs, individual white blood cells can be identified in physiological saline ($f_{RBC} = 0$) but not in diluted blood ($f_{RBC} = 0.07$). For long-exposure fluorescence (LEF) microscopy with an exposure time of 1 s, a bulk white blood cell distribution profile can be identified, but the profile cannot be deconstructed based on height position or particle diameter. For particle trajectory analysis (PTA) with an exposure time of $\delta t = 10$ ns, individual white blood cells resuspended in physiological saline or diluted blood can be identified at multiple vertical positions in the channel (scale bar 20 mm). (e) At a flow rate $Q = 450$ μL.min^{-1}, PTA images of polystyrene beads ($Re_p = 2.91$ for $f_{RBC} = 0$), white blood cells ($Re_p = 2.41$ for $f_{RBC} = 0$), and PC-3 prostate cancer cells ($Re_p = 9.11$ for $f_{RBC} = 0$) suspended in physiological saline and diluted blood demonstrate that individual optically in-focus particles can be identified in starting samples with higher RBC volume fractions (f_{RBC}) without significant degradation in fluorescence signal quality.

As a result, optically in-focus particles found at all vertical positions were used to make quantitative measurements of particle focusing behavior. Once PTA-based identification of optically in-focus particles was demonstrated in physiological saline, these experiments were repeated for polystyrene beads, white blood cells, and PC-3 prostate cancer cells suspended in diluted blood, as shown in Figure 7.2.3 (d). As f_{RBC} increased, optically in-focus particles exhibited a fluorescence signal intensity that was weaker and less uniform. However, it was still possible to distinguish likely optically in-focus particles from undoubtedly out-of-focus particles.

Quantitative Measurements of Particle Focusing Behavior in Diluted Blood

For a given Q and f_{RBC}, optically in-focus particles from all vertical positions were used to make quantitative measurements of particle focusing behavior. The distribution of particles in the channel cross-section (y-z plane) was visualized using an intensity map in which each individual rectangle represented a possible location for the centroid (y_c, z_c) of an optically in-focus particle. The color scale used to represent the particle frequency n_f at a given point in the y-z plane consisted of full color (for $n_f > 10$), grayscale (for $1 < n_f < 10$), and white (for $n_f = 0$). Given the polydisperse nature of white blood cells and PC-3 cells, a scatter plot of lateral centroid coordinate (z_c) versus particle diameter a was constructed. For a straight rectangular channel with a 2:1 (H/W) aspect ratio, particle focusing is predominantly reduced to two lateral equilibrium positions centered on the long face. Particle focusing to lateral equilibrium positions has been shown to occur both at a single vertical position (Di Carlo *et al.*, 2007) and over a wide range of vertical positions (Choi *et al.*, 2011). Applications in flow cytometry would require the former, while applications in rare cell isolation can utilize the latter provided that particle focusing achieves the desired particle separation benchmarks (*e.g.* yield of target cell capture, purity of total cell capture).

Given that particle focusing was observed across multiple vertical locations in these experiments, the inertial focusing quality of particles was evaluated at vertical positions $\sum_{i=5}^{8} y_i$ (*i.e.* near the center of the long channel face). Since no accepted metric exists to define inertial focusing quality, a non-dimensional term *bandwidth efficiency* β_z is

established that is dependent on mean particle diameter a, the mean lateral distance z_m of an optically in-focus particle (as an absolute value) from the channel centerline, and the standard deviation σ_z of optically in-focus particles in the z-direction listed in Table 7.3.1. Bandwidth efficiency was defined as

$$\beta_z = \frac{w_b}{a} = \frac{4\sigma_z + a}{a} \tag{7.2.1}$$

where w_b is the edge-to-edge bandwidth in the z-direction over which 95% of all optically in-focus particles can be found. Note that β_z is normalized by a, which varies depending on the class of particles used. As a result, $\beta_z \geq 1$ in all cases, with $\beta_z \sim 1$ when particle focusing is nearly perfect ($\sigma_z \sim 0$). Based on the current imaging and device setup, scanning resolution in the z-direction was comprehensive and continuous, while scanning resolution in the y-direction was incomplete and segmented. Nonetheless, a second non-dimensional term *focusing utility* Φ_y is established to serve as a crude measure of particle frequency at vertical positions where predicted particle focusing was unlikely to occur. The focusing utility was defined as

$$\Phi_y \equiv \frac{n_f}{N} \tag{7.2.2}$$

where n_f is the number of optically in-focus particles at vertical positions $\sum_{i=5}^{8} y_i$ and N is the number of optically in-focus particles at vertical positions $\sum_{i=0}^{8} y_i$. As a result, $\Phi_y \leq 1$ in all cases, with $\Phi_y \sim 1$ when the particle focusing is nearly perfect ($n_f \sim N$).

7.3 Results

7.3.1 Inertial Focusing of Polystyrene Beads in Blood

Polystyrene beads have been used extensively to study particle focusing behavior in microchannels (Di Carlo *et al.*, 2007, 2009b). As ready-to-use monodisperse particles exhibiting strong and uniform fluorescence intensity, polystyrene beads were an ideal choice for this study. Given the mean particle diameter and channel dimensions, the particle Reynolds numbers of polystyrene beads in physiological saline for flow rates $Q = 50$, 150, and 450 μL.min^{-1} were $Re_p = 0.32$, 0.97, and 2.91. Using flow rates that

	Q [μL.min^{-1}]	f_{RBC} []	Re_p []	z_m [μm]	σ_z [μm]	β_z []	Φ_y []
Polystyrene Beads	50	0	0.32	12.7	0.7	1.27	0.91
		0.07	0.28	13.5	0.9	1.35	0.73
		0.33	0.18	12.5	4.5	2.86	0.81
	150	0	0.97	12.9	0.5	1.08	1
		0.07	0.84	14.1	1.4	1.56	0.96
		0.33	0.26	13.9	2.1	1.82	0.87
	450	0	2.91	13.6	1.1	1.45	0.86
		0.07	2.53	14.2	1.4	1.54	0.91
		0.33	1.68	14.4	2.0	1.79	0.86
White Blood Cells	50	0	0.27	14.4	0.9	1.43	0.79
		0.07	0.23	15.6	2.0	1.56	0.55
		0.33	0.16	11.2	5.3	3.13	0.40
	150	0	0.80	15.5	0.6	1.28	0.72
		0.07	0.70	16.5	1.9	1.82	0.61
		0.33	0.46	15.3	3.3	2.44	0.54
	450	0	2.41	16.1	1.0	1.43	0.75
		0.07	2.10	16.5	1.9	1.82	0.61
		0.33	1.39	16.2	2.9	2.33	0.57
PC-3 Cells	50	0	1.01	8.6	2.1	1.47	1
		0.07	0.88	8.6	2.5	1.56	1
		0.33	0.58	9.9	2.0	1.45	0.92
		1	0.25	1.0	0.9	1.22	0.17
	150	0	3.04	10.1	1.1	1.25	1
		0.07	2.64	10.3	1.4	1.32	1
		0.33	1.76	10.2	1.8	1.41	1
		1	0.76	1.1	1.0	1.22	0
	450	0	9.11	9.9	1.2	1.28	1
		0.07	7.92	11.0	1.3	1.28	1
		0.33	5.27	10.8	1.5	1.35	1
		1	2.28	1.7	1.4	1.32	0

Table 7.3.1: Quantitative measurements of particle focusing behavior as a function of flow rate Q and RBC volume fraction f_{RBC}. For a given Q and f_{RBC}, the particle Reynolds number Re_p, the mean optically in-focus lateral distance z_m from the channel centerline, the bandwidth efficiency β_z, and the focusing utility Φ_y were calculated for polystyrene beads, white blood cells, and PC-3 prostate cancer cells.

correspond to $Re_p < 1$, $Re_p \sim 1$, and $Re_p > 1$, polystyrene beads served as a reference standard for white blood cells and PC-3 cells.

For $Q = 50$ μL.min^{-1} in physiological saline ($f_{RBC} = 0$), bead focusing in both the z-direction ($\beta_z = 1.27$) and the y-direction ($\Phi_y = 0.91$) approached optimal levels as shown in Figure 7.3.1. When $f_{RBC} = 0.07$, bead focusing decreased moderately in the y-direction ($\Phi_y = 0.73$) with minimal decrease in the z-direction ($\beta_z = 1.35$). When $f_{RBC} = 0.33$, bead focusing was poorly organized in both the z-direction ($\beta_z = 2.86$) and y-direction ($\Phi_y = 0.81$).

For $Q = 150$ μL.min^{-1} in physiological saline ($f_{RBC} = 0$), bead focusing in both the z-direction ($\beta_z = 1.08$) and the y-direction ($\Phi_y = 1$) reached optimal levels. When $f_{RBC} = 0.07$, bead focusing decreased moderately in the z-direction ($\beta_z = 1.56$) with minimal decrease in the y-direction ($\Phi_y = 0.96$). For $f_{RBC} = 0.33$, bead focusing decreased further in a similar manner ($\beta_z = 1.82$, $\Phi_y = 0.87$) but remained largely intact.

For $Q = 450$ μL.min^{-1} in physiological saline ($f_{RBC} = 0$), bead focusing became suboptimal in both the z-direction ($\beta_z = 1.45$) and the y-direction ($\Phi_y = 0.86$), as multiple beads occupied a previously unstable equilibrium position despite a non-unity channel aspect ratio. When $f_{RBC} = 0.07$, bead focusing decreased minimally in the z-direction ($\beta_z = 1.54$) but improved minimally in the y-direction ($\Phi_y = 0.91$). When $f_{RBC} = 0.33$, bead focusing remained largely intact despite a moderate decrease in the z-direction ($\beta_z = 1.79$) and a minimal decrease in the y-direction ($\Phi_y = 0.86$).

7.3.2 Inertial Focusing of White Blood Cells in Blood

Inertial focusing may also be a valuable tool for more portable and cost-effective flow cytometry technologies (Hur *et al.*, 2010; Oakey *et al.*, 2010), but the focusing behavior (and separation efficiency) of white blood cells (WBCs) in whole or minimally diluted blood has not been studied. Given the mean particle diameter and channel dimensions, the particle Reynolds numbers of WBCs in physiological saline for flow rates $Q = 50$, 150, and 450 μL.min^{-1} were $Re_p = 0.27$, 0.80, and 2.41. Since WBCs have a size range of 7-11 μm, the lower bound of $Re_p = 0.16$, 0.48, and 1.46, while the upper bound of $Re_p = 0.40$, 1.20, and 3.60.

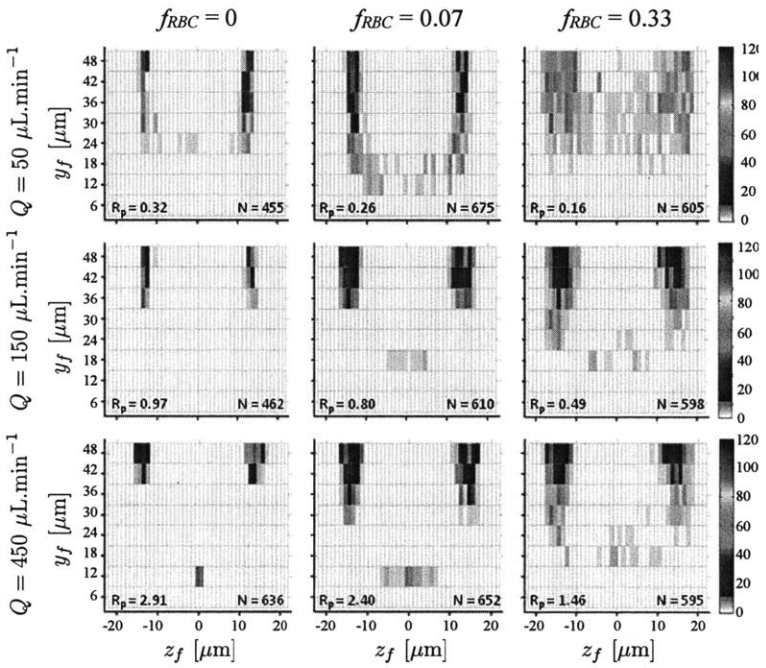

Figure 7.3.1: Polystyrene bead focusing behavior as a function of flow rate Q and RBC volume fraction f_{RBC}. For $f_{RBC} = 0$, values of Q correspond to $Re_p = 0.32$, 0.97, and 2.91. For $f_{RBC} = 0.07$, values of Q correspond to $Re_p = 0.26$, 0.80, and 2.40. For $f_{RBC} = 0.3$, values of Q correspond to $Re_p = 0.16$, 0.49, and 1.46. The optically in-focus vertical position y_f and in-focus lateral distance z_f from the channel centerline for polystyrene beads were used to construct a cross-sectional particle histogram, and calculate the measures β_z and Φ_y given in Table 7.3.1.

For $Q = 50$ μL.min^{-1} in physiological saline ($f_{RBC} = 0$), WBC focusing in both the z-direction ($\beta_z = 1.43$) and the y-direction ($\Phi_y = 0.79$) was weaker relative to polystyrene beads as shown in Figure 7.3.2 (a). In particular, multiple WBCs were found unfocused at vertical positions near the channel floor (*i.e.* $\sum_{i=i}^{4} y_i$). When $f_{RBC} = 0.07$, WBC focusing decreased moderately in both the z-direction ($\beta_z = 1.85$) and y-direction ($\Phi_y = 0.55$). When $f_{RBC} = 0.33$, WBC focusing was poorly organized in both the z-direction ($\beta_z = 3.13$) and y-direction ($\Phi_y = 0.40$).

For $Q = 150$ μL.min^{-1} in physiological saline ($f_{RBC} = 0$), WBC focusing improved in the z-direction ($\beta_z = 1.28$) but deteriorated in the y-direction ($\Phi_y = 0.72$) as more WBCs were found unfocused at vertical positions near the channel floor. When $f_{RBC} = 0.07$, particle focusing deteriorated moderately in both the z-direction ($\beta_z = 1.82$) and the y-direction ($\Phi_y = 0.61$). However, most WBCs were found near a channel wall to the extent that a loose annulus of WBCs appeared to form. When $f_{RBC} = 0.33$, WBC focusing decreased further in both the z-direction ($\beta_z = 2.44$) and the y-direction ($\Phi_y = 0.54$) as the annulus of WBCs became more radially diffuse.

For $Q = 450$ μL.min^{-1} in physiological saline ($f_{RBC} = 0$), WBC focusing decreased moderately in the z-direction ($\beta_z = 1.43$) with minimal improvement in the y-direction ($\Phi_y = 0.75$) as WBCs occupying vertical positions near the channel floor became organized around a previously unstable equilibrium position despite a non-unity aspect ratio. When $f_{RBC} = 0.07$, WBC focusing decreased moderately in the z-direction ($\beta_z = 1.82$) and reversed in the y-direction ($\Phi_y = 0.61$) as an annulus of WBCs appeared to form. When $f_{RBC} = 0.33$, WBC focusing decreased moderately in the z-direction ($\beta_z = 2.33$) and minimally in the y-direction ($\Phi_y = 0.57$) as the annulus of WBCs became more radially diffuse. Since the WBCs used were polydisperse in nature, the relationship between particle diameter a and lateral distance z_f of an optically in-focus WBC (as an absolute value) from the channel centerline was investigated and is shown in Figure 7.3.2 (b). Despite the narrow size range observed, larger WBCs were found to be slightly closer to the channel centerline (*i.e.* smaller z_f).

7.3.3 Inertial Focusing of PC-3 Cells in Blood

There is significant interest to incorporate inertial focusing into cell-friendly and high-throughput rare cell isolation technologies (Hur *et al.*, 2011a; Bhagat *et al.*, 2011), but the focusing behavior (and separation efficiency) of rare cells such as circulating tumor cells (CTCs) in whole or minimally diluted blood has not been studied. A model prostate cancer cell line (PC-3) was used to assess CTC focusing behavior in blood. Given the mean particle diameter and channel dimensions, the particle Reynolds number of PC-3 cells in physiological saline for the given set of flow rates were Re_p = 1.01, 3.04, and 9.11. Since the diameter of the PC-3 cells ranged from 10-35 μm, the lower bound of Re_p = 0.33, 0.99, and 2.97, while the upper bound of Re_p = 3.91, 11.76, and 35.26.

For $Q = 50$ μL.min^{-1} in physiological saline ($f_{RBC} = 0$), PC-3 cell focusing in both the z-direction ($\beta_z = 1.47$) and the y-direction ($\Phi_y = 1$) approached optimal levels as shown in Figure 7.3.3 (a). When $f_{RBC} = 0.07$, PC-3 cell focusing was largely unaffected in both the z-direction ($\beta_z = 1.56$) and y-direction ($\Phi_y = 1$). When $f_{RBC} = 0.33$, PC-3 cell focusing decreased moderately in the y-direction ($\Phi_y = 0.92$) but improved minimally in the z-direction ($\beta_z = 1.45$). Since PC-3 cell focusing remained strong, particularly in the z-direction, this experiment was repeated using whole blood ($HCT = 45\%$). For $f_{RBC} = 1$, PC-3 cell focusing shifted radically ($\beta_z = 1.22$, $\Phi_y = 0.17$) as PC-3 cells were predominantly found along the channel centerline ($z = 0$) around a previously unstable equilibrium position (due to the non-unity channel aspect ratio). No PC-3 cells occupied the previously stable equilibrium positions observed at lower f_{RBC}.

For $Q = 150$ μL.min^{-1} in physiological saline ($f_{RBC} = 0$), PC-3 cell focusing in both the z-direction ($\beta_z = 1.25$) and the y-direction ($\Phi_y = 1$) reached optimal levels. When $f_{RBC} = 0.07$, PC-3 cell focusing was largely unaffected in both the z-direction ($\beta_z = 1.32$) and y-direction ($\Phi_y = 1$). When $f_{RBC} = 0.33$, PC-3 cell focusing decreased moderately in both the z-direction ($\beta_z = 1.41$) and the y-direction ($\Phi_y = 1$). For $f_{RBC} = 1$, PC-3 cell focusing again shifted radically ($\beta_z = 1.22$, $\Phi_y = 0$) as PC-3 cells predominantly occupied an equilibrium position (centered on the short face of the channel) not observed at lower f_{RBC}.

For $Q = 450$ μL.min^{-1} in ($f_{RBC} = 0$), PC-3 cell focusing in both the z-direction

($\beta_z = 1.28$) and the y-direction ($\Phi_y = 1$) remained at optimal levels due to the lack of PC-3 cells found at vertical positions near the channel floor (in contrast to the observations for polystyrene beads and white blood cells). When $f_{RBC} = 0.07$, PC-3 cell focusing was largely unaffected in both the z-direction ($\beta_z = 1.28$) and y-direction ($\Phi_y = 1$). When $f_{RBC} = 0.33$, PC-3 cell focusing decreased moderately in both the z-direction ($\beta_z = 1.35$) and the y-direction ($\Phi_y = 1$). When $f_{RBC} = 1$, PC-3 cell focusing again shifted radically ($\beta_z = 1.32$, $\Phi_y = 0$) as described previously for $Q = 150$ μL.min^{-1}, but PC-3 cell focusing decreased moderately in the z-direction. Since the PC-3 cells used were polydisperse in nature, the relationship between particle diameter a and lateral distance z_f of an optically in-focus PC-3 cell (as an absolute value) from the channel centerline was studied as shown in Figure 7.3.3 (b). When $f_{RBC} = 0$, 0.07, or 0.33, a linear correlation between the two parameters was observed, such that large PC-3 cells were situated closer to the channel centerline ($z = 0$), while small PC-3 cells were situated closer to the channel wall ($z = \pm 22.5$ μm). When $f_{RBC} = 1$, large PC-3 cells formed a tighter distribution around the channel centerline relative to small PC-3 cells.

7.3.4 Rheological Properties of Test Fluids

In an attempt to gain insight into the radical shift in PC-3 cell focusing behavior when f_{RBC} increased from 0.33 to 1, the torsional AR-G2 rheometer was used with a Taylor-Couette cylindrical geometry to measure the effective viscosity of the test fluid at $f_{RBC} = 0$, 0.33, and 1 as a function of shear rate shown in Figure 7.3.4 (a). The governing equations of motion for a non-Newtonian fluid (such as blood) in a rectangular geometry cannot be reduced to simple equations and solved analytically. However, the power-law model is used to describe the test fluid in the x-z plane for the ideal case of $y = 48$ μm (*i.e.* the center of the long channel face) where fluid flow in the x-direction can be approximated using a simple one-dimensional equation. The viscosity η of a power-law fluid (Bird *et al.*, 1987) is defined as $\eta = m|\dot{\gamma}|^{n-1}$ where $\dot{\gamma}$ is an imposed shear rate, m is a positive constant called the consistency index (with dimensions Pa.s^n), and n is a dimensionless positive constant. For a Newtonian fluid $n = 1$, and for a shear-thinning fluid $n < 1$. Using a log-log plot of viscosity against shear rate to

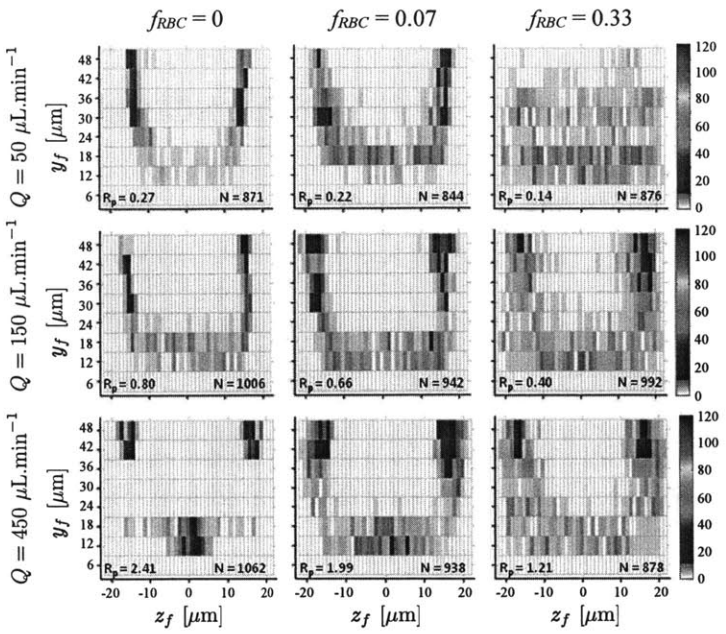

(a)

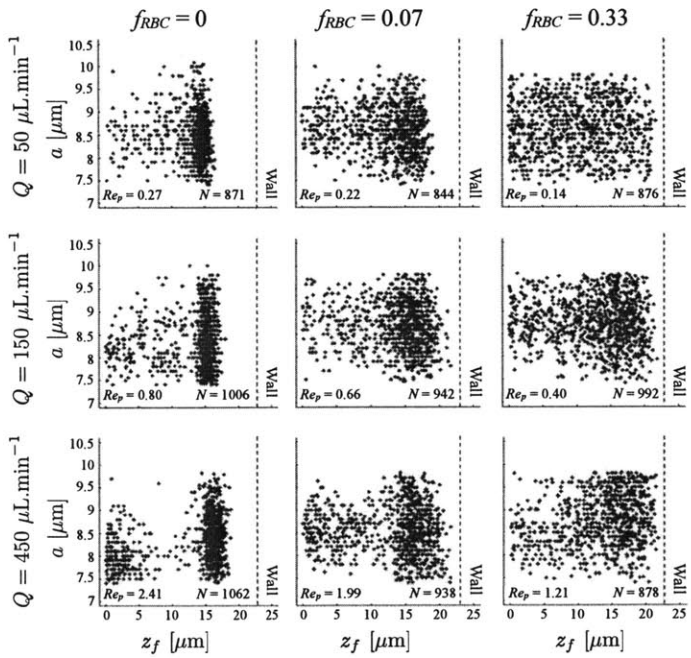

(b)

Figure 7.3.2: White blood cell focusing behavior as a function of flow rate Q and RBC volume fraction f_{RBC}. For $f_{RBC} = 0$, values of Q correspond to $Re_p = 0.27$, 0.80, and 2.41. For $f_{RBC} = 0.07$, values of Q correspond to $Re_p = 0.22$, 0.66, and 1.99. For $f_{RBC} = 0.3$, values of Q correspond to $Re_p = 0.14$, 0.40, and 1.21. (a) The optically in-focus vertical position y_f and in-focus lateral distance z_f from the channel centerline for white blood cells were used to construct a cross-sectional particle histogram. (b) The dependence of particle diameter a on in-focus lateral distance z_f can be illustrated using a particle scatter plot. The dotted line represents the location of the sidewall given a non-deformable microchannel.

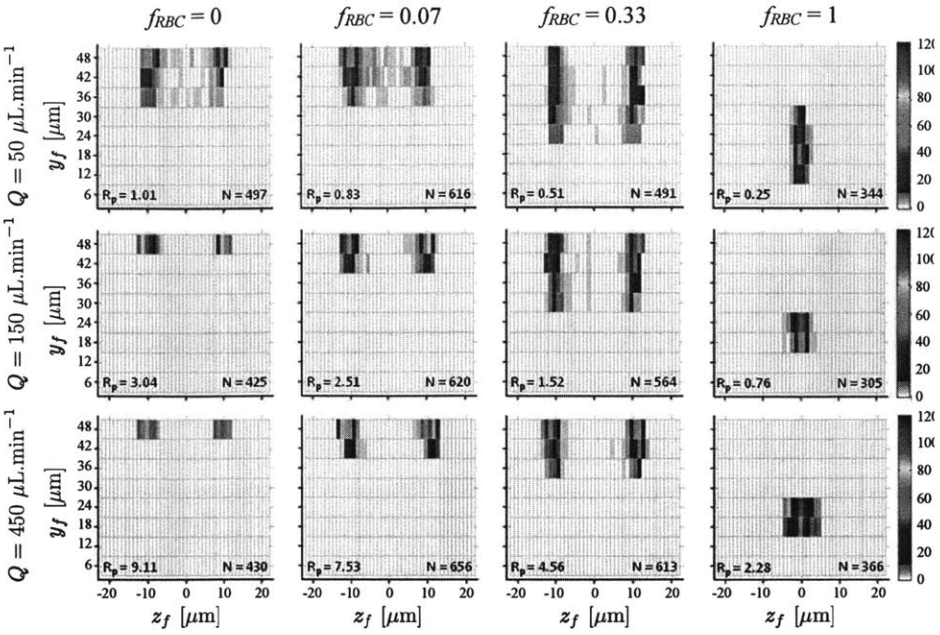

(a)

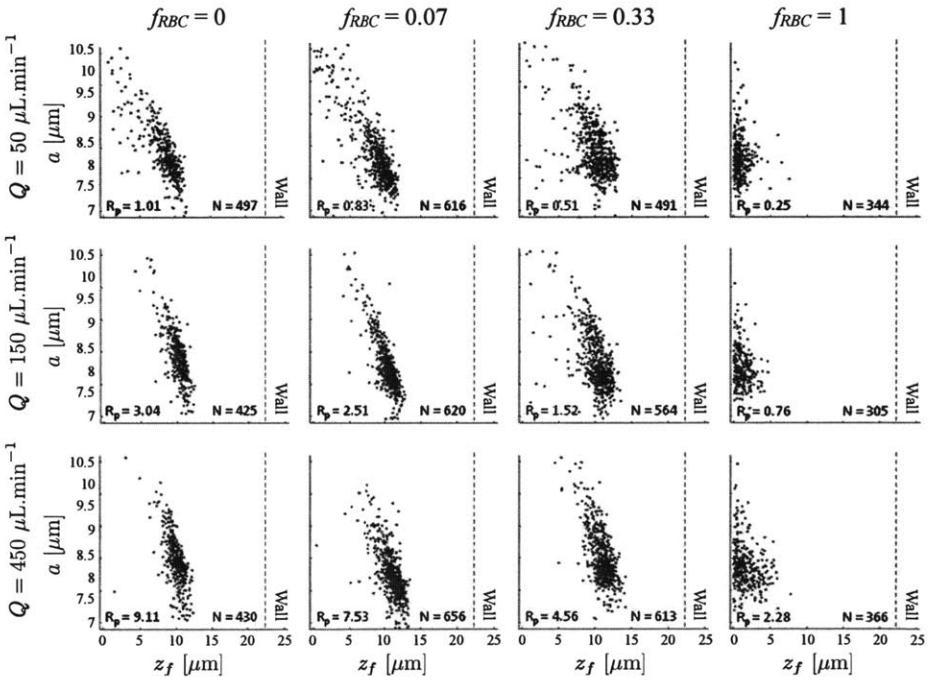

(b)

Figure 7.3.3: PC-3 prostate cancer cell focusing behavior as a function of flow rate Q and RBC volume fraction f_{RBC}. For $f_{RBC} = 0$, values of Q correspond to $Re_p = 0.27$, 0.80, and 2.41. For $f_{RBC} = 0.07$, values of Q correspond to $Re_p = 0.22$, 0.66, and 1.99. For $f_{RBC} = 0.3$, values of Q correspond to $Re_p = 0.14$, 0.40, and 1.21. (a) The optically in-focus vertical position y_f and in-focus lateral distance z_f from the channel centerline for PC-3 cells were used to construct a cross-sectional particle histogram. (b) The dependence of particle diameter a on in-focus lateral distance z_f for PC-3 cells was illustrated using a particle scatter plot. The dotted line represents the location of the sidewall given a non-deformable microchannel.

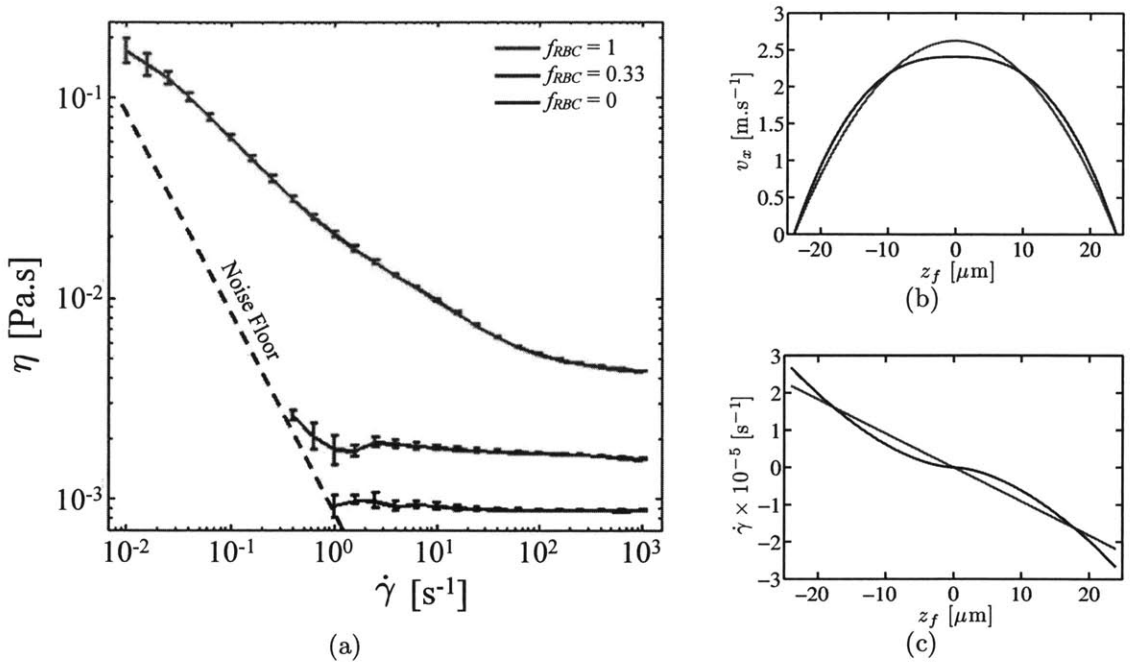

Figure 7.3.4: Rheometer measurements of diluted and whole blood. (a) The effective viscosity η for physiological saline, diluted blood, and whole blood was measured as a function of shear rate $\dot{\gamma}$ using a rheometer with a concentric cylinder geometry. (b) Modeling diluted and whole blood as a power-law fluid, the flow velocity v_x down the microchannel for diluted and whole blood at height $y = 48$ μm was calculated as a function of in-focus lateral distance z_f from the channel centerline. (c) Modeling diluted and whole blood as a power-law fluid, the shear rate $\dot{\gamma}$ for diluted and whole blood at height $y = 48$ μm was calculated as a function of in-focus lateral distance z_f from the channel centerline.

calculate n, the test fluid was found to be Newtonian ($n = 1$) for $f_{RBC} = 0$, very close to Newtonian ($n = 0.98$) for $f_{RBC} = 0.3$, and shear-thinning ($n = 0.60$) for $f_{RBC} = 1$. Assuming well-developed flow at $y = 48$ μm, the equation of motion in the x-direction can be approximated by

$$v_x(z) = \frac{2n+1}{n+1}\mathcal{U}\left(1 - \left|\frac{2z}{W}\right|^{\frac{n+1}{n}}\right), \tag{7.3.1}$$

where $\mathcal{U}$ is the mean flow velocity. The shear rate $\dot{\gamma}(z) = dv_x(z)/dz$ can also be calculated from this equation. A plot of $v_x(z)$ against z (Figure 7.3.4 (b)) and $\dot{\gamma}(z)$ against z (Figure 7.3.4 (c)) was constructed for $f_{RBC} = 0.33$ and $f_{RBC} = 1$. The velocity profile of the test fluid at $f_{RBC} = 0.33$ is expected to be parabolic, while the velocity profile of the test fluid at $f_{RBC} = 1$ is more blunted. This results in a sigmoidal shear rate profile

for the test fluid at $f_{RBC} = 1$ as opposed to a linear shear rate profile for the test fluid at $f_{RBC} = 0.33$. In particular, there exists a region near the channel centerline ($z = 0$) where the predicted shear rate of the test fluid at $f_{RBC} = 1$ is lower than the shear rate of the test fluid at $f_{RBC} = 0.33$.

7.4 Discussion

In this Chapter, particle trajectory analysis (PTA) has been used to identify and characterize individual optically in-focus particles in diluted and whole blood. Direct measurements of these particles were used to generate a two-dimensional (y-z plane) profile of particle focusing behavior and its dependence on particle diameter. These results represents a significant improvement over what has been previously achieved using high-speed bright-field imaging and long-exposure fluorescence imaging. In high-speed bright-field imaging, quantitative measurements of individual cell properties can only be made in very dilute ($f_{RBC} < 0.07$) blood, as the sheer number of RBCs occludes observation of other cell-sized particles in the channel. In long-exposure fluorescence imaging, a quantifiable intensity curve requires an aggregate fluorescence from a population of particles, which means that an ensemble of particles that are polydisperse in nature cannot be differentiated individually according to size or vertical position.

PTA was first used to observe the inertial focusing behavior of polystyrene beads in diluted blood. Polystyrene beads were chosen as an ideal test case (and reference benchmark) given their monodisperse nature and strong, uniform fluorescence intensity. For particle Reynolds numbers $Re_p < 1$, $Re_p = 1$, and $Re_p > 1$ in physiological saline, bead focusing behavior using PTA was largely consistent with previous work in which two microchannels with inverted aspect ratios were used separately to determine the two-dimensional (y-z plane) profile of bead focusing behavior (Hur *et al.*, 2010). PTA has a significant advantage in providing three-dimensional scanning resolution of particle focusing behavior in a single device over a wide range of f_{RBC}, and recent work (Klein & Posner, 2010) suggests that PTA image acquisition using a high-speed spinning (Nipkow) disk confocal μ-PIV system can provide even more comprehensive and accu-

rate three-dimensional scanning resolution. Assuming that particle focusing behavior is well-developed, images of particles in the x-z plane can be taken at kHz frequencies in an automated and continuous manner in the y-direction with exquisite scanning resolution. PTA image analysis can also be optimized by inputting collected images into a supervised machine learning system such as CellProfiler Analyst (Jones *et al.*, 2009) for automated recognition of complicated and subtle phenotypes found in millions of particles.

PTA was then used to observe the inertial focusing behavior of white blood cells (WBCs) in diluted blood. Despite the relative similarity in particle diameter between WBCs ($a = 9.0$ μm) and beads ($a = 9.9$ μm), WBC focusing in both the z-direction and the y-direction was visibly weaker at $f_{RBC} = 0$. PTA demonstrated the ability to deconstruct WBC focusing behavior based on particle diameter and centroid position of individual particles in the channel cross-section (y-z plane). As a result, the decrease in WBC focusing behavior (relative to beads) could be partially attributed to smaller WBCs found unfocused at vertical positions near the channel floor. These results are consistent with the notion that small WBCs experience weaker inertial lift forces relative to large WBCs since $Re_p \sim a^2$ and are thus more likely to remain unfocused at a given Re_p. PTA also captured the formation of a WBC annulus in the channel cross-section (y-z plane) at $f_{RBC} = 0.07$ and 0.33. Leukocyte margination in a straight rectangular channel has been observed at much lower Reynolds numbers but not at the flow rates used in this study (Jain & Munn, 2009; Hou *et al.*, 2010). *In vitro* experiments characterizing the radial distribution of WBCs have shown that leukocyte margination from the center of a blood vessel depends on rheological factors such as hematocrit, blood suspension medium and shear stress (Schmid-Schönbein *et al.*, 1980; Goldsmith & Spain, 1984). Further investigation into leukocyte margination in inertia-dominated flow will be necessary.

Finally, PTA was used to observe the inertial focusing behavior of PC-3 cells in diluted blood and whole blood. A model prostate cancer (PC-3) cell line was used as a surrogate for circulating tumor cells (CTCs). CTC isolation poses an immense technical challenge, as CTCs are present in as few as one cell per 10^9 haematologic cells in the

blood of patients with metastatic cancer (Krivacic *et al.*, 2004; Racila *et al.*, 1998). At $f_{RBC} = 0$, PC-3 cell focusing was strong in both the z-direction and the y-direction, and it remained relatively intact at $f_{RBC} = 0.07$ and $f_{RBC} = 0.33$. Since PC-3 cells are widely polydisperse in nature ($a = 10 - 35$ μm) and can be much larger than the polystyrene beads used here, the inertial lift force on a PC-3 cell is expected to be up to an order of magnitude larger. However, it was unexpected not only to identify in-focus PC-3 cells at $f_{RBC} = 1$, but to observe a radical shift in PC-3 cell focusing behavior as opposed to further decreases in both the z-direction and the y-direction from previously observed equilibrium positions. Despite the increased RBC concentration in the channel at $f_{RBC} = 1$, the preferred equilibrium position found along the channel centerline near the channel floor made it possible to sufficiently resolve in-focus PC-3 cells. Long-exposure fluorescence (streak) imaging of PC-3 cells in straight rectangular channels with inverted aspect ratios ($H/W = 0.5$ and 2) was used to demonstrate that PC-3 cell focusing behavior in whole blood is symmetric across the center of the channel long face in Figure 7.4.1 and is not the result of particle settling or imaging artifacts. However, attempts to sufficiently resolve PC-3 cells in the upper half of the channel were unsuccessful due to light absorption and scattering of RBCs shown in Figure 7.4.1. The concentration of PC-3 cells spiked into the suspending fluid was orders of magnitude higher than previously observed concentrations of CTCs found in cancer patient blood samples. A higher spiking concentration was required to identify and analyze a statistically significant number of PC-3 cells in a manner that was not experimentally or computationally prohibitive. The spiking concentration of PC-3 cells should be varied in future studies to ensure that PC-3 cells can indeed serve as CTC analogs when it comes to particle focusing behavior. However, self-interactions between neighboring PC-3 cells in the channel at the spiking level used here will be negligible in whole blood, as the volume fraction of PC-3 cells (0.89%) is almost two orders of magnitude less than that of RBCs (45%).

In an attempt to provide a physical basis for the radical shift in PC-3 cell focusing behavior at $f_{RBC} = 1$, rheological measurements of the test fluids were made at $f_{RBC} = 0.33$ and 1. The test fluid was found to be very close to Newtonian at

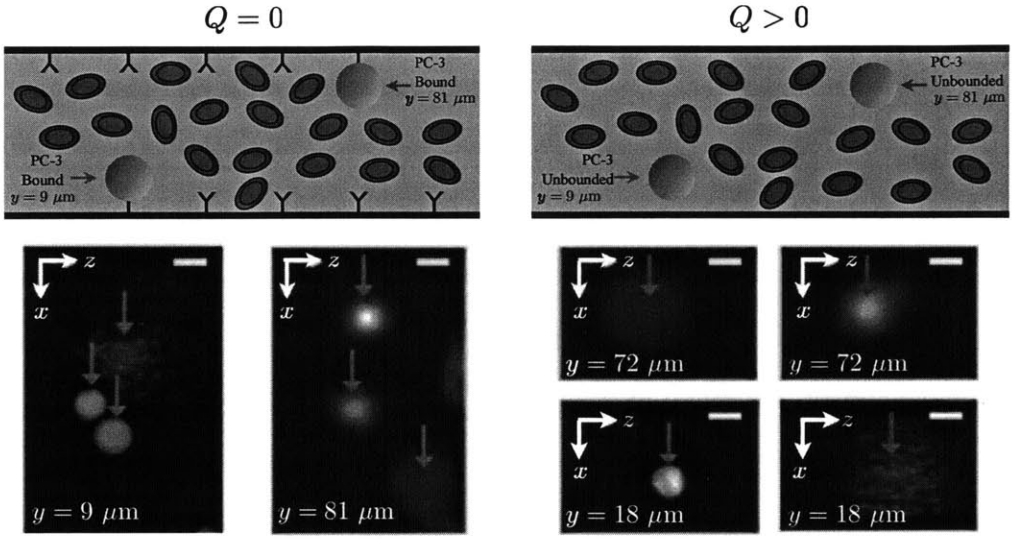

Figure 7.4.1: Identifying PC-3 cells re-suspended in whole blood ($f_{RBC} = 1$, $HCT = 45\%$). (a) A straight rectangular channel with 2:1 aspect ratio was functionalized with anti-EpCAM antibody, which binds to EpCAM surface markers found on PC-3 cells. After PC-3 cells were captured in the channel, images were taken near the channel floor ($y = 9$ μm) to visualize PC-3 cells attached to the channel floor (red arrow) and the channel ceiling (green arrow). Images were also taken near the channel ceiling ($y = 81$ μm) to visualize PC-3 cells attached to the channel floor (red arrow) and the channel ceiling (green arrow). (b) In an unfunctionalized channel, images were taken at $y = 18$ μm to visualize PC-3 cells flowing near the channel floor (red arrow) and the channel ceiling (green arrow). Images were also taken at $y = 72$ μm to visualize PC-3 cells flowing near the channel floor (red arrow) and the channel ceiling (green arrow).

$f_{RBC} = 0.33$ and strongly shear-thinning at $f_{RBC} = 1$. As a result, the flow velocity and shear rate profiles indicated regions of higher viscosity near the channel centerline for the test fluid at $f_{RBC} = 1$ relative to $f_{RBC} = 0.33$. However, the shear-thinning results of dilute and whole blood do not fully explain why PC-3 cell margination differs from that of WBC margination. Particle deformability has also been shown to impact particle position relative to the channel wall, particularly if the cells are either soft or of comparable size to the channel dimensions (Hur *et al.*, 2011a). Given the capacity of PTA to resolve and identify individual particles at the typical flow rates required for inertial focusing, it would be of great interest to characterize the effect of both inertial lift forces and viscoelasticity induced forces of fluorescently labeled particles (*e.g.* CTCs, PDMS elastic particles, and viscous oil droplets) with varying degrees of deformability in dilute and whole blood. Furthermore, blood analogs with shear-thinning behavior similar to that of whole blood, but with substantially different relaxation times have been shown to generate considerably different extensional flow patterns (Sousa *et al.*, 2011). This difference suggests that the elastic properties of the fluid can have a dominant effect on the flow characteristics, which has significant relevance to whole blood given the elastic and deformable RBCs found at high (38-52%) volume fractions.

The flow behavior of RBCs in whole blood under inertial focusing conditions for PC-3 cells (or other target cells) has not yet been previously studied. However, RBCs in highly dilute (0.5% HCT) blood have been shown to focus to two streamlines centered on the long face of a 2:1(H/W) straight rectangular channel (Hur *et al.*, 2010; Mach & Di Carlo, 2010). If RBC-induced margination of PC-3 cells in whole blood is biased due to inertial focusing of RBCs, the larger PC-3 cells may not be able to able to squeeze into near-wall positions along the channel long face that the smaller WBCs can occupy. As a result, the PC-3 cells could be vertically marginated to near-wall positions along the channel short face. Furthermore, channel flows of suspensions are well-known to exhibit weak secondary flows arising from finite normal stress differences (Ramachandran & Leighton, 2008; Zrehen & Ramachandran, 2013). Such secondary flows are also known to occur in flows of polymeric solutions through non-circular ducts and can have a significant impact on the migration behavior of particles seeded in the fluid (Villone *et al.*, 2011a,

2013).

7.5 Summary

Particle tracking analysis (PTA) was used to identify and characterize the inertial focusing behavior of polystyrene beads, white blood cells, and PC-3 cells in diluted and whole blood. Individual optically in-focus particles could be identified (without any visual evidence of fluorescence streak formation) at mean flow velocities up to $\mathcal{U} = 1.85$ m.s^{-1} ($Q = 450$ μL.min^{-1}), in test fluids up to $HCT = 45\%$ ($f_{RBC} = 1$), and at multiple vertical positions across the microchannel. Direct measurements of these particles were used to generate a two-dimensional (y-z plane) profile of particle focusing behavior and its dependence on particle diameter. Of particular interest is the ability of PTA to not only identify in-focus PC-3 cells at $f_{RBC} = 1$, but to observe a radical shift in PC-3 cell focusing behavior as opposed to further decreases in both the z-direction and the y-direction from previously observed equilibrium positions. PTA can be used to provide an experimental frame of reference for understanding the physical basis of inertial lift forces in whole blood via numerical simulations of particle flow in non-Newtonian fluids at high Reynolds number. PTA can also be used to discover inertial focusing modes that enable particle enrichment (and ultimately isolation) directly from whole blood at high throughput for use in global health diagnostics.

In the next Chapter 8, the experimental techniques developed in this Chapter are utilized to study the flow of non-Newtonian liquids at channel Reynolds numbers up to and above the value at the transition to inertially-dominated turbulence. These experiments offer a more complete view on the role of viscoelasticity on particle migration seen in the migration of PC-3 cells in high hematocrit concentrations. The use of model non-Newtonian polymeric solutions instead of physiological fluids such as blood, offers the distinct advantage that they are simpler to prepare and characterize and are generally more amenable to future modeling and theoretical analysis.

Chapter 8

Flow-Induced Particle Migration: Inertia, Elasticity and Transition to Turbulence

8.1 Introduction

As discussed in the literature review in Section 2.4, many important biomedical processes require the isolation of micron-sized particles or cells from a background fluid. Flow induced particle migration in microfluidic devices, often called *inertial focusing* (Di Carlo, 2009a) has been shown to offer great promise for impactful biomedical applications, including disease diagnostics and treatment. In particular, this technology has been proposed as a compact and inexpensive alternative to current high-speed flow cytometers. It has also been identified as a breakthrough technique for high-throughput cell manipulation and the sorting of diseased cells from the bloodstream.

Despite the robustness of particle focusing in Newtonian fluids, its practical implementation for real-world applications has been limited, in part, due to a rudimentary fundamental understanding of the phenomenon and due to the lack of available engineering design guidelines. It has also proven challenging to fabricate microfluidic devices that can withstand the pressures associated with flow rates substantially higher than $Q \sim 1$ mL.min^{-1} in a single microchannel using conventional fabrication methods with

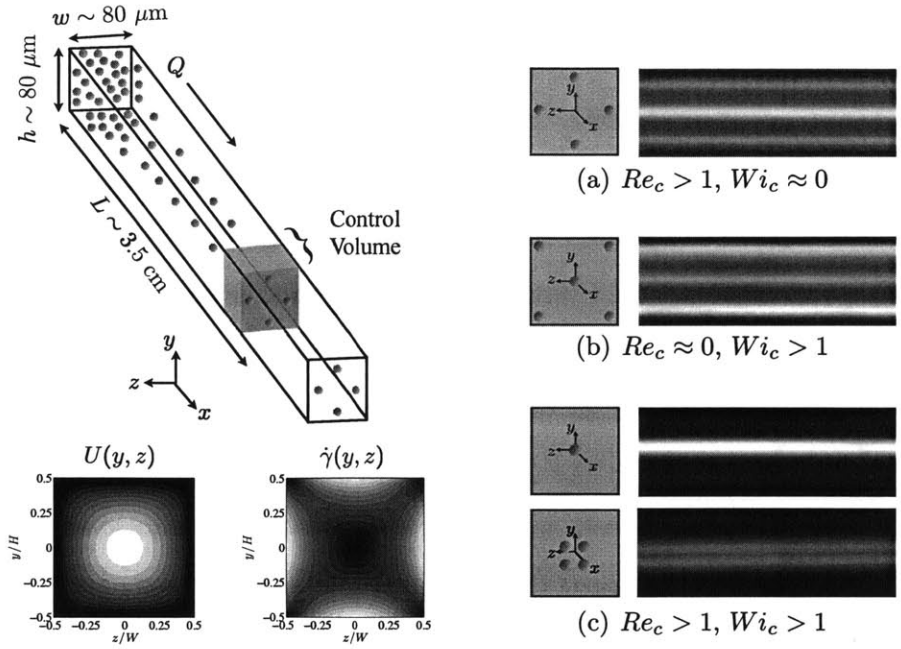

Figure 8.1.1: Schematic diagram of typical particle equilibrium positions in the y-z plane of a straight channel for different ranges of channel Reynolds number Re_c and Weissenberg number Wi_c. The lower figures are contours of the velocity and shear rate in a channel with a square cross-section for a Newtonian fluid. (a)–(c) Equilibrium positions of the particles in different flow regimes in the y-z plane and the corresponding streakline images taken in the x-z plane.

polydimethylsiloxane (PDMS) elastomers. Having more mechanically robust devices would allow larger Reynolds number regimes to be studied and would simplify future implementations of this technology for a real application. Furthermore, in most studies with whole blood and other clinically relevant biofluids, it has been necessary to dilute the samples, as discussed previously in Chapter 7, partly because the undiluted fluids are complex, non-Newtonian suspensions displaying non-linear rheological properties whose role in particle focusing at high-flow rates has not yet been addressed. This dilution step also increases the complexity of any such particle-focusing procedure, thereby mitigating the viability of this otherwise inexpensive biomedical technology. A systematic and fundamental study of flow-induced particle localization in complex fluids is therefore crucial if this technology is ever to be successfully exploited for real-world particle sorting and separation processes.

In addition to fluid rheology, particle size and channel dimensions are also known to affect the particle distribution at steady state (Di Carlo, 2009a). For reasons that

are explained in Section 8.3.1, a channel with a square cross-section has been studied in the work in this Chapter. In order to illustrate the typical particle distributions in a microchannel, the flow of particles in a square channel is shown schematically in Figure 8.1.1. Contour plots of the velocity and shear rate profiles for the flow of a Newtonian fluid in a square duct are shown in the lower left of Figure 8.1.1. Evidently, the shear rates are largest near the mid-faces of the channel edges and smallest in the channel corners and at the centerline.

In the flow of a Newtonian liquid, particles are driven toward regions of high shear rate and take on a diamond-like distribution in the channel with particles located near the middle of each wall of the channel, as shown in Figure 8.1.1 (a). This distribution is analogous to the annular ring of enhanced concentration that forms in the flow through a cylindrical pipe (Segré & Silberberg, 1961). At channel Reynolds number well above $Re_c > \mathcal{O}(100)$, however, other equilibrium positions have been predicted numerically (Chun & Ladd, 2006) including close to the channel corners and centerline. In highly elastic flows of viscoelastic liquids, the equilibrium positions of the particles include the channel corners and centerline forming a *quincunx* pattern as shown in Figure 8.1.1 (b), which correspond to regions of low shear rates and thus low normal stress differences. When inertial and elastic effects are simultaneously important, new particle distributions are also possible such as those shown in Figure 8.1.1 (c). The tendency of particles to be driven toward a single region in the channel (*e.g.* centerline) in this flow regime is extremely attractive for applications in flow cytometry and cell separation and constitutes a prime motivator for the study described in this Chapter.

8.2 Dimensional Analysis

Many of the dimensionless groups that are relevant to the study of particle migration in complex fluids have previously been defined throughout this Thesis, but for the sake of completeness, they are restated here.

For a channel of height H and width W, the characteristic channel dimension is given by the hydraulic diameter defined as $D \equiv 2HW/(H+W)$. Furthermore, for a

given volumetric flow rate Q, the mean velocity in the channel is $\mathcal{U} = Q/HW$. The relative importance of inertial effects to viscous effects is characterized by the channel Reynolds number

$$Re_c = \frac{\rho \mathcal{U} D}{\eta(\dot{\gamma}_c)} \tag{8.2.1}$$

where ρ is the density of the fluid and $\eta(\dot{\gamma}_c)$ is the dynamic viscosity of the fluid defined in terms of a characteristic shear rate $\dot{\gamma}_c$. For a Newtonian liquid the viscosity is constant $\eta(\dot{\gamma}_c) = \mu$, and hence the channel Reynolds number is also given by $Re_c = \mathcal{U}D/\nu$, where ν is the kinematic viscosity of the fluid. For the experiments considered in this Chapter, the channel Reynolds number is in the range $10 \leq Re_c \leq 10^4$.

The measure of fluid inertia in the immediate vicinity of a particle of diameter a advecting in the fluid is given by the particle Reynolds number

$$Re_p = Re_c \left(\frac{a}{D}\right)^2 \tag{8.2.2}$$

The characteristic length in this parameter is the particle diameter and the characteristic velocity is defined relative to the particle based on the product of a characteristic shear rate in the channel $\dot{\gamma}_c \sim \mathcal{U}/D$ and the particle diameter a. This scaling has also been explained in Section 2.4 with reference to Figure 2.4.2. A key feature in inertial microfluidics is that the particle aspect ratio is typically $a/D \sim \mathcal{O}(0.1)$ and hence Re_p can easily be greater than unity, opening up the regime in which particles tend to be precisely focused to well-defined positions in the channel cross-section. In these experiments, the particle Reynolds number is in the range $0.1 \leq Re_p \leq 100$.

An additional dimensionless parameter is the Fanning friction factor f, which is a dimensionless measure of the pressure drop across a channel ΔP of length L, given by

$$f \equiv \frac{\Delta P}{\frac{1}{2}\rho \mathcal{U}^2 (L/D)} \tag{8.2.3}$$

When the flow is laminar, the friction factor scales inversely with Re_c for a Newtonian liquid. Once transition to turbulence occurs, however, the scaling of the friction factor with Re_c changes, providing the experimentalist a simple means of identifying the transition to turbulence.

For the flow of viscoelastic liquids, there are a number of additional relevant dimensionless groups. Firstly a measure of the strength of elasticity in the flow is given by the channel Weissenberg number

$$Wi_c = \frac{\lambda \mathcal{U}}{D} \tag{8.2.4}$$

where λ is the relaxation time of the liquid. This number is equal to the product of the relaxation time and a characteristic shear rate in the flow $\dot{\gamma}_c \sim \mathcal{U}/D$. For a Maxwell fluid, this number is also proportional to the ratio of the first normal stress difference N_1 to the shear stress τ_{xy}, and hence the Weissenberg number can often be interpreted as a ratio of elastic to viscous stresses.

The second parameter is the particle Weissenberg number, defined in terms of the particle diameter and the same characteristic relative velocity used in the particle Reynolds number (*i.e.* $u_{rel} \sim a\dot{\gamma}_c$).

$$Wi_p = \frac{\lambda(a\dot{\gamma}_c)}{a} = \frac{\lambda \mathcal{U}(a/D)}{a} = \frac{\lambda \mathcal{U}}{D} \tag{8.2.5}$$

Evidently, the channel and particle Weissenberg numbers are equivalent. For this study, both Weissenberg numbers are in the range $0.01 \leq Wi_c \leq 10^3$.

The ratio of the Weissenberg and Reynolds numbers is also a dimensionless group called the elasticity number. In principle, this number is independent of the dynamics of the flow since the velocity $\mathcal{U}$ does not explicitly enter in its definition. The value of this number can be taken as a ratio of the timescale over which elastic stresses relax to the timescale over which momentum diffuses. The channel elasticity number is

$$El_{c,0} = \frac{Wi_c}{Re_c} = \frac{\eta_0 \lambda}{\rho D^2} \tag{8.2.6}$$

whereas the particle elasticity number is given by

$$El_{p,0} = \frac{Wi_p}{Re_p} = \frac{\eta_0 \lambda}{\rho a^2} \tag{8.2.7}$$

where η_0 is the zero-shear-rate viscosity. Hence for the particles used in this study, the particle elasticity number is always larger than the channel elasticity number. Again, for a Maxwell fluid, these numbers are also proportional to the ratio of the first normal

stress difference N_1 to the inertial stress in the flow $\rho\mathcal{U}^2$, and hence the elasticity number can often be interpreted as a ratio of elastic to inertial stresses. For this reason, when the elasticity number is less than unity, an inertially-dominated particle migration behavior as that shown schematically in Figure 8.1.1 (a) can be expected. Whereas, when it is greater than unity, an elastically-dominated particle migration behavior such as that shown schematically in Figure 8.1.1 (c) can be expected.

Another dimensionless group that is relevant to channel flows of viscoelastic liquids is the Deborah number. This number is defined as the ratio of the relaxation time of the fluid to the mean residence time in the channel $t_{res} = L/\mathcal{U}$.

$$De = \frac{\lambda}{t_{res}} = \frac{\lambda\mathcal{U}}{L} = Wi_c\frac{D}{L} \tag{8.2.8}$$

This number is generally less than unity for the flow rates considered in this study, indicating that the flow has had sufficient time for the viscoelastic stresses to become fully-developed.

8.3 Experimental Methods

In order to attain high Reynolds numbers in a microfluidic device it is necessary to fabricate a microchannel that can not only withstand large pressures, but also one whose precise dimensions have been carefully selected in light of operating range of the pumping apparatus. Furthermore, the channel must be transparent to allow for flow visualization. The rheology of the test fluids must also be characterized in order to better understand the role of viscoelasticity on the migration behavior of the seeded particles. In this Section, the fabrication methods, imaging techniques and rheological characterization of the test fluids are described.

8.3.1 High Pressure Microfluidics

The small length scales in microfluidic devices give rise to large pressure drops, which can be challenging for channels made with conventional soft photolithographic fabrication techniques using polydimethylsiloxane (PDMS) to withstand. Furthermore, the require-

Chip	ΔP_{max} [psi]	Failure Mode
PDMS on glass	36-67	Delamination
TPE	150	Sensor limit
PUMA	105-120	Delamination/connection leakage
NOA	74-79	Delamination
EpoxAcast	2500-4500	Delamination

Table 8.3.1: Maximum pressure ΔP_{max} before failure of a microfluidic device made using polydimethylsiloxane (PDMS), thermoset polyester (TPE), polyurethane methacrylate (PUMA), Norland Adhesive 81 (NOA), and EpoxAcast 650. Table adapted from Sollier *et al.* (2011).

ment that the material be transparent to enable flow visualization places additional constraints on the type of available materials that can be used to construct channels for high pressure experiments. Three major failure mechanisms of a microfluidic device are bulging, delamination and leakage between the tubing and the channel at the connection point (Sollier *et al.*, 2011). Some materials that have been used to achieve high pressure drops include Pyrex (Pipe *et al.*, 2008), metal oxide semiconductors (Ciftlik *et al.*, 2013), as well as thermoset polymers and adhesives (Sollier *et al.*, 2011). A list of some of these materials and their failure mechanisms is given in Table 8.3.1.

In this Chapter, EpoxAcast 690 (Smooth-On, Easton, PA), which is a two-part epoxy, has been used to fabricate all of the test channels. This material was selected because of its high rigidity (tensile modulus 3.9 GPa) and its adhesive strength enabling delamination pressures as large as 31 MPa (4500 psi). In order to withstand such high pressures, polyetheretherketone (PEEK) tubing (Supelco, ID 0.75 mm, OD 1.55 mm) was used and directly bonded to the channel according to the fabrication methods described in Section 8.3.1. Although only straight channels have been studied in this Chapter, this material and the manufacturing protocol is amenable to fabrication of more complex geometries including the contractions described in Section 6.4.

Careful consideration has been given to the precise channel dimensions in order to ensure that the experimental setup could be used to accomplish one of the primary objectives of the research in this Chapter, namely channel Reynolds numbers that are large enough to observe the transition to inertial turbulence in the flow of water. Since the experiments were completed with a volumetric flow rate controlled pump, the height H

and width W of the channel cross-section were chosen to maximize the Reynolds number for a given volumetric flow rate Q and hydraulic diameter D of the channel. The channel Reynolds number is equal to

$$Re_c = \frac{QD}{HW\nu} = \frac{4Q}{D\nu}\frac{\alpha}{(1+\alpha)^2} \tag{8.3.1}$$

where ν is the kinematic viscosity of the fluid and the aspect ratio of the channel is defined as $\alpha \equiv W/H$ with the constraint that $0 \leq \alpha \leq 1$. A plot of Re_c against α is shown in Figure 8.3.1 (a). Evidently, for a constant ratio of Q/D, the value of Re_c is maximized when $\alpha = 1$, and hence the preferred channel height and width of the channel are equal.

The dimensionless pressure drop across the channel length is given by

$$\frac{\Delta P}{\frac{\mu\nu}{D^2}(L/D)} = \frac{48}{(1+\alpha)^2}\left[1 - \frac{192}{\pi^5}\alpha\sum_{j=odd}^{\infty}\frac{\tanh(j\pi/2\alpha)}{j^5}\right]^{-1} Re_c \tag{8.3.2}$$

The dimensionless pressure drop normalized by the channel Reynolds number is also plotted in Figure 8.3.1 (a). Clearly, ΔP is also minimized for $\alpha = 1$ given a constant value of Re_c. Although the pressure drop is not a design parameter, *per se*, it is important to minimize the pressures in the channel if possible to ensure the durability of the channel. For these two reasons, a channel with a square cross-section was selected for the experiments in this Chapter.

The channel length L must also be selected to ensure that the flow is hydrodynamically fully-developed within the channel for all channel Reynolds numbers for which the flow is laminar. For the flow of a Newtonian fluid in a rectilinear duct, the hydrodynamic entrance length L_e is given by a correlation determined by Durst *et al.* (2005):

$$\frac{L_e}{D} = \left[0.619^{1.6} + \left(0.0567Re_c\right)^{1.6}\right]^{\frac{1}{1.6}} \tag{8.3.3}$$

This correlation is plotted in Figure 8.3.1 (b). Since the transition to inertially-dominated turbulence is expected to occur at $Re_c \gtrsim 2000$, the channel length must be at least as long as the expected value of L_e at this Reynolds number. As shown clearly in the plot, the entrance length at this Reynolds number is $L_e = 113D$, and therefore the selected hydraulic diameter of the channel must be small enough that the total length of the

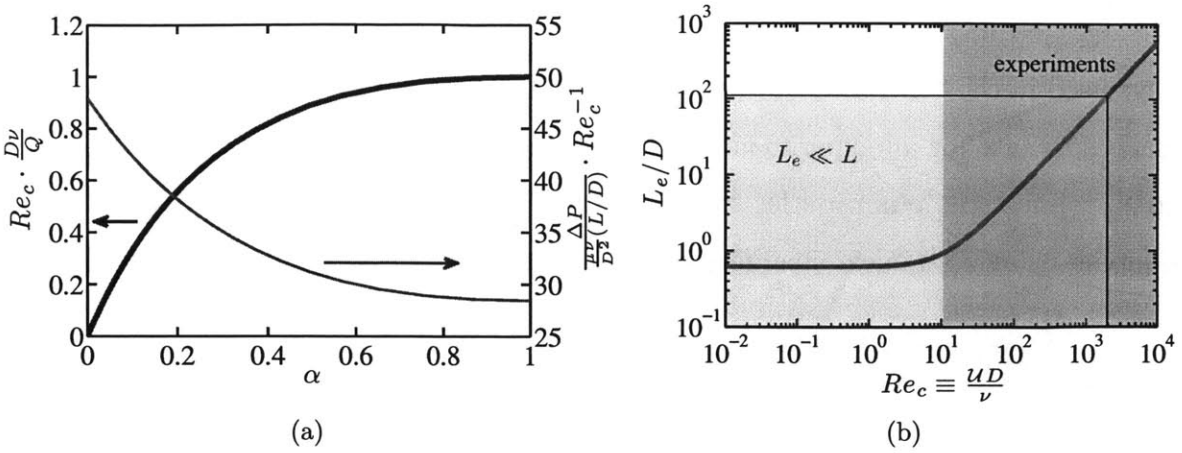

Figure 8.3.1: Design parameters for the microchannel. (a) Plot of the channel Reynolds number for a constant ratio of Q/D, and of the friction factor for a constant value of Re_c against channel aspect ratio $\alpha \equiv W/H$. (b) Hydrodynamic entrance length as a function of channel Reynolds number.

channel can be both larger than $L > 113D$ and short enough to fit on the 75 mm glass slides used as the base of the microfluidic device.

Furthermore, both the channel aspect ratio and the ratio of the particle diameter to the hydrodynamic diameter of the channel play a role in the equilibrium focusing behavior of particles (Di Carlo, 2009a). Since the channel aspect ratio has been fixed for reasons described above, the hydraulic diameter of the square channel used in this Chapter was chosen to be $D = W = H = 80$ μm. This size was chosen because the particle diameters were typically in the range $8 \leq a \leq 10$ μm, and hence the particle aspect ratio was around $a/D \approx 0.1$ ensuring particle Reynolds numbers of at least $Re_p \gtrsim \mathcal{O}(1)$. This value of D was also easy to achieve with the photolithographic fabrication process and ensured that the typical channel length $L = 35$ mm was sufficiently larger than the minimum length required for hydrodynamically fully-developed flow $113D \approx 16$ mm. Finally, for this combination of D and L, the typical pressures in the microchannel seldom exceeded $P \sim 2 \times 10^7$ Pa (2900 psi), which was safely within the operating capacity of the device.

In order to attain the high pressures and flow rates required in this study, a 100DX pump (Teledyne ISCO, Lincoln, NE) was used for all experiments. This maximum capacity of the pump is 103 mL, and it can provide volumetric flow rates in the range

$0.01 \leq Q \leq 50$ mL.min^{-1} and pressures up to 690 bar (10,000 psi). The pump was always used in the controlled flow rate mode, and the in-cylinder pressure was recorded at each flow rate for all experiments. Stainless steel piping (Swagelok, Solon, OH) was used to connect the pump outlet to the PEEK tubing, which was rigidly connected to the piping using a stainless steel ferrule adapter (Swagelok).

Fabrication Methods

In order to manufacture rigid microfluidic chips using the EpoxAcast 650, a more elaborate fabrication protocol than is typically followed in the manufacture of PDMS microfluidic devices (see Section 7.2.1) was necessary. The fabrication protocol used in making the chips used in this Chapter is shown schematically in Figure 8.3.2.

The initial procedure is similar to that used in the manufacture of PDMS chips. The first step is to spin-coat a 4-inch silicon wafer with an 80 μm thick layer of negative photoresist (SU-8 100, Microchem, Newton, MA), which is then exposed to UV-light through a Mylar photomask (Fineline Imaging, Colorado Springs, CO), and developed with an edge bead remover (BTS-220, J.T. Baker, Phillipsburg, NJ). Next, a 10:1 mixture of PDMS elastomer and curing agent (Sylgard 184, Dow Corning, Midland, MI) are poured onto the master mold and degassed for 60 minutes to remove all trapped bubbles. The master mold is then placed in an oven at 90 °C for 24 hours to cure the PDMS. Afterward, the cured PDMS is peeled away from the SU-8 male master mold. This PDMS replicate then becomes the first female master mold, which is coated with a silane derivative (Gelest, Inc. Morrisville, PA). A second batch of PDMS is then prepared and poured over the female master mold and cured for 24 hours at 90 °C to obtain the *s*-PDMS replicate, which is then peeled away from the first mold. This *s*-PDMS replicate then becomes the second male master mold from which the final chip will be molded.

In order to withstand the large pressures in the channel, it is necessary to bond the PEEK tubing directly into the epoxy replicate. Two major challenges in accomplishing this task, however, are the exact placement of the tubing and the prevention of epoxy from seeping into the tubing during the curing process and thereby clogging the channel

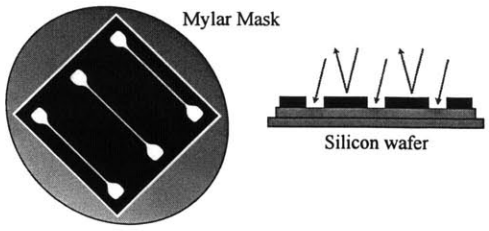

(a) Step 1: UV exposure

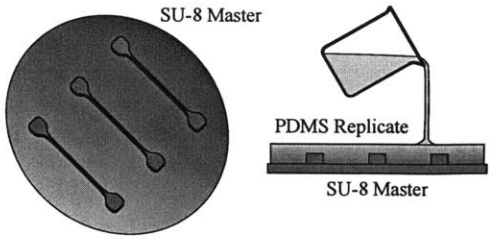

(b) Step 2: Female PDMS master mold

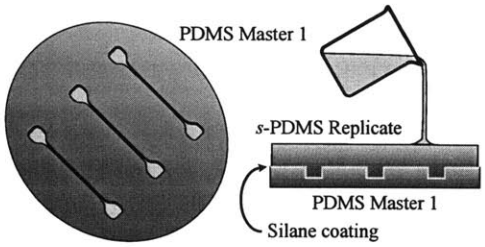

(c) Step 3: Male PDMS master mold

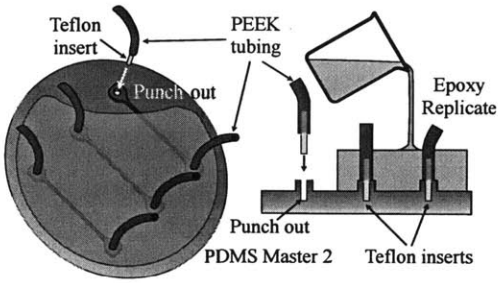

(d) Step 4: Epoxy replicate

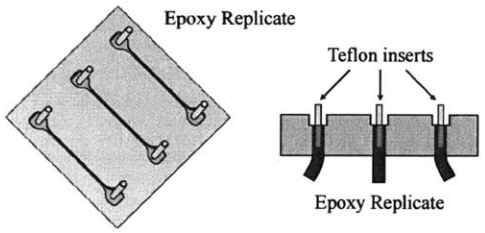

(e) Step 5: Teflon insert removal

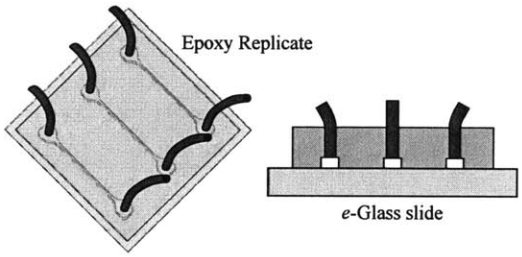

(f) Step 6: Bonding to glass slide

Figure 8.3.2: Fabrication protocol for the high pressure epoxy microfluidic devices used in this study.

inlet or outlet. Both of these potential difficulties are overcome by punching small holes (0.75 mm diameter) into the second male PDMS master mold at the inlet and outlet sections of the channel using a coring tool (Harris Uni-Core, Redding, CA). Small cylindrical Teflon inserts are then inserted into the punch outs, functioning as dowel pins by connecting the PEEK tubing to the PDMS male mold. These inserts not only serve to locate the tubing at well-defined positions in the inlet and outlet sections of the channel, but they fill the entire inner cross-section of the tubing thereby preventing any epoxy from seeping into the tubing during the curing process. The outer walls of the PEEK tubing are first sanded to increase adhesion with the epoxy.

After all the tubing has been connected to the mold in this manner, the EpoxAcast is poured onto the mold. A thin layer (200 ± 50 μm) of the EpoxAcast is also coated onto a $75 \times 25 \times 1$ mm glass slide. The epoxy replicate and *c*-glass slide are concurrently allowed to cure for 32 hours at 20 °C. After this time, the PDMS male mold is peeled away from the epoxy replicate and the Telfon inserts (McMaster-Carr) are carefully removed with a pair of tweezers. The epoxy replicate is then bonded to the *c*-glass slide for 5 minutes at 60 °C and subsequently allowed to cure at room temperature overnight. The channels are then inspected under an optical microscope prior to their use in experiments.

8.3.2 Imaging Techniques

Long exposure fluorescence (LEF) imaging was used to acquire streakline images with a 20× 0.45 NA objective on a Nikon TiE inverted microscope and a Retiga 2000R monochromatic camera. Both bright field and fluorescence images (Cy3 filter) were acquired at 5 mm intervals along the channel length using Nikon NIS-Elements AR 3.10 software and a motorized translation stage. Exposure times were adjusted for the prevailing image intensity ranging from 100 ms to 1 second. The bright field images were used to identify the location of the channel walls, whereas the fluorescence images were used to observe the particle distribution in the channel. In the streakline images shown in Section 8.4.2, the bright field and LEF images have been superposed for visual clarity.

As in the experiments discussed in Chapter 7, the images of individual particles flowing through the channel were captured using a 20× 0.5 NA objective and the same epifluorescent Nikon TE-2000 inverted microscope, camera and Nd:YAG laser described in Section 5.4.2. These short exposure images were acquired at a stationary observation distance $L_{obs} = 3.5$ cm downstream from the channel entrance near the exit of the channel allowing for the most time for the flow to attain steady state. The laser generated 532 nm light pulses with a duration of $\delta t \sim 10$ ns, however given the large fluid velocities in the channel some amount of blurring can be expected despite the extremely short exposure time. For the microscope objective and camera used in this work, a single pixel corresponds to $(eM)^2 = 0.323 \times 0.323$ μm^2, hence the flow velocity necessary for a

particle to traverse one pixel (and thus show blurring) is $\mathcal{U}_{blur} \sim (eM)\delta t^{-1} = 32$ m.s^{-1} which corresponds to $Q \approx 12$ mL.min^{-1}. A typical 10 μm particle used in this study has a diameter of around 31 pixels in an image, hence even at the highest velocities considered in this Chapter around $\mathcal{U} = 52$ m.s^{-1} ($Q = 20$ mL.min^{-1}), the expected blurring will be less than 2 pixels or approximately only 5% of the particle size.

8.3.3 Test Fluid Rheology

Two different polymers were used in this study. The first was polyethylene oxide (PEO), which is a covalently-bonded linear polymer that is commonly used as a model rheological fluid (Rodd *et al.*, 2005, 2007; Tirtaatmadja *et al.*, 2006) and also as a turbulent drag reducing agent (Graham, 2004). The second polymer was hyaluronic acid (HA) which is a linear polysaccharide that is found in many physiologcal fluids and tissues (Kogan *et al.*, 2007; Haward *et al.*, 2012d). The molecular mass of HA can be as large as 10^7 Da giving HA solutions a marked viscoelasticity, and its compatibility with other biological media make it a very attractive viscoelastic material for various biomedical applications, such as drag reducing agents for the prevention of hemorrhagic shock (Kameneva *et al.*, 2004; Kameneva, 2012), or for cell separation processes as considered in this Chapter.

The PEO (Sigma Aldrich) used in this study had a mean molecular weight of $M_w = 3 \times 10^5$ Da, and was dissolved in either deionized water when studied with fluorescent polystyrene beads. The polymer concentrations were varied between 10 ppm to 10^4 ppm, spanning the dilute and semi-dilute concentration regimes. The critical overlap concentration c^* is the concentration marking the transition from the dilute to the semi-dilute regime. It is approximately the concentration at which the polymer coils overlap or impinge on each other and the point at which the viscoelastic properties of a solution are no longer governed by the behavior of a single polymer molecule (Larson, 1998). The overlap concentration can be calculated from the relationship proposed by Graessley (1982)

$$c^* = \frac{0.77}{[\eta]} \tag{8.3.4}$$

where $[\eta]$ is the intrinsic viscosity of the solutions, which is given by the Mark-Houwink-

Sakurada equation for PEO

$$[\eta] = 0.072 M_w^{0.65} \tag{8.3.5}$$

where $[\eta]$ is in units of $\text{cm}^3.\text{g}^{-1}$. For the molecular weight used in this study, the overlap concentration is $c^* = 2.9 \times 10^{-3}$ g.cm^{-3} (2900 ppm).

The Zimm time is the appropriate timescale over which a polymer molecule relaxes in the limit of an infinitely dilute solution. The Zimm model treats the pervaded volume of a polymer as an impermeable sphere that moves through the surrounding medium. The Zimm relaxation time λ_Z is therefore proportional to the time required for the polymer chain to diffuse a distance equal to its own size (Rubinstein & Colby, 2003). For PEO, the Zimm relaxation time is given by

$$\lambda_Z = 0.463 \frac{[\eta] M_w \eta_s}{RT} \tag{8.3.6}$$

where η_s is the solvent viscosity, R is the ideal gas constant and T is the absolute temperature. Therefore, the Zimm relaxation time of the 300 kDa PEO solutions used in this study is $\lambda_Z = 14.5$ μs.

For finite polymer concentrations, however, the effect of hydrodynamic interactions between the polymer coils becomes significant and the Zimm time is no longer the characteristic relaxation timescale of the solution. Instead, the effective relaxation time is determined from an empirical correlation developed by Tirtaatmadja *et al.* (2006):

$$\frac{\lambda_{eff}}{\lambda_Z} = 18.1 \left(\frac{c}{c^*} \right)^{0.65} \text{ for } 0.01 \leq c/c^* \leq 1 \tag{8.3.7}$$

This correlation is only valid in the dilute regime (*i.e.* $c < c^*$), and hence the relaxation times of the solutions in the semi-dilute regime must be determined experimentally using jet break up experiments described below. The effective relaxation times of the PEO solutions are listed in Table 8.3.2.

It has been documented in the literature that the purification process of HA introduces a polydispersity in the molecular weight of the sample (Laurent *et al.*, 1960; Swann *et al.*, 1974; Shimada & Matsumura, 1975), making the calculation of the lin-

[0] $R = 8.314$ J/mol.K

Fluid	c [ppm]	M_w [kDa]	λ [ms]	η_∞ [mPa.s]	η_0 [mPa.s]	$\dot{\gamma}^*$ [s^{-1}]	n	b	c/c^*
Water	–	–	–	9	–	–	–	–	–
PEO	10	300	†0.015	9	1.1	6.7×10^4	0.5	1.0	3×10^{-3}
PEO	100	300	†0.027	9	1.2	3.7×10^4	0.2	1.0	0.03
PEO	1000	300	†0.12	9	1.5	8.3×10^3	0.75	1.0	0.3
PEO	10000	300	‡1.19	9	7.2	4.0×10^3	0.75	1.0	3
HA (unused)	1000	★1650	‡0.87	9	230	4.0	0.45	1.0	10
HA (used)	1000	★1650	–	9	230	33	0.45	1.0	10

Table 8.3.2: Rheological properties of the test solutions measured at 22 °C. ★Molecular weight ranges between $1500 \leq M_w \leq 1800$ kDa. †Values based on the correlation in Eq. (8.3.7). ‡Value determined from capillary thinning measurements using Eq. (8.3.8).

ear viscoelastic properties of HA solutions based on the intrinsic viscosity from the Mark-Houwink-Sakurada equation less straightforward than it is for the PEO solutions. Indeed, the molecular weight of the HA (Sigma Aldrich) sample used in this study ranged between $1.5 \times 10^6 \leq M_w \leq 1.8 \times 10^6$ Da. Therefore the rheological properties of the 1000 ppm HA solution were determined directly from experimental measurements. Based on light scattering experiments (Meyer *et al.*, 2009), the overlap concentration for HA solution is $c^* \approx 100$ ppm in PBS solution, indicating that the 1000 ppm solution used in this Chapter was in the concentrated regime.

Since the 10000 ppm PEO and 1000 ppm HA solutions were both above the overlap concentration, their relaxation times could not be estimated based on the Zimm relaxation time. Their relaxation times were also too short to be determined using oscillatory measurements, so instead they were determined from measurements of the thinning dynamics of the solution in jetting experiments (Ardekani *et al.*, 2010) as shown in Figure 8.3.3 (a). As a viscoelastic liquid bridge thins, the diameter of the filament D will decay according to the relation (McKinley & Tripathi, 2000):

$$\frac{D}{D_0} \sim \exp\left(-\frac{t}{3\lambda}\right) \tag{8.3.8}$$

where D_0 is the initial diameter of the filament. When plotted on a semilogarithmic axes, the slope of the evolution of the diameter is therefore equal to $-1/3\lambda$. The thinning profiles of both solutions are shown in Figure 8.3.3 (b) and (c), and the relaxation times are listed in Table 8.3.2.

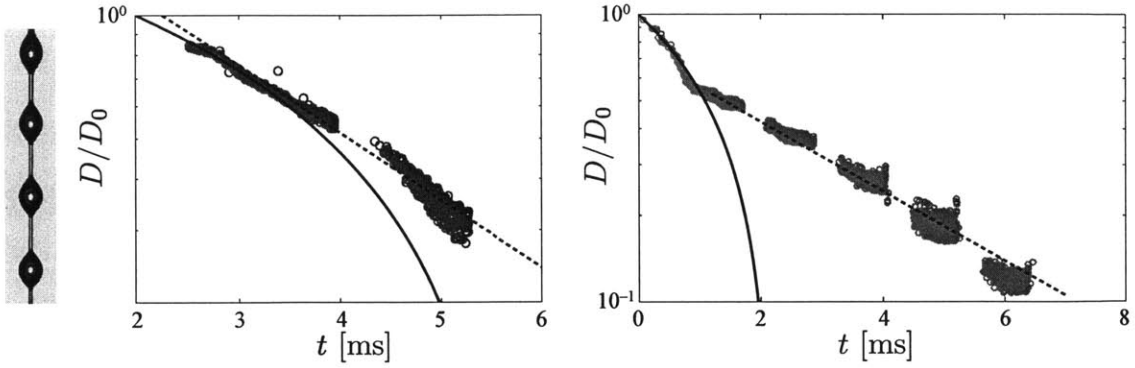

(a) (b) (c)

Figure 8.3.3: (a) Image of the jet break up. Jet break up profile of the (b) HA solution, and (c) PEO solution. The dashed line in each figure indicates the fit of Eq. (8.3.8) to the profile to extract the effective relaxation time of each fluid. The solid line indicates the visco-capillary break up profile (see Papageorgiou (1995)). (Analysis courtesy of Bavand Keshavarz.)

The viscosity of each solution was measured using a double gap Taylor-Couette geometry on the DHR3 torque-controlled rheometer (TA Instruments) for shear rates less than $\dot{\gamma} < 3000$ s^{-1} and with the microfluidic Viscometer/Rheometer-on-a-Chip (VROC, RheoSense Inc.) for shear rates between $5000 \leq \dot{\gamma} \leq 3.3 \times 10^6$ s^{-1}. The flow curves of the PEO solutions are shown in Figure 8.3.4 (a) and (b) and for the HA solution in Figure 8.3.4 (c) and (d). All measured flow curves were fit with the Carreau-Yasuda model (Bird *et al.*, 1987), which is a generalized fluid model that can predict a zero-shear-rate viscosity η_0 and an infinite-shear-rate viscosity η_∞ as well as a rate dependent regime. The Carreau-Yasuda model is given by the equation

$$\frac{\eta - \eta_\infty}{\eta_0 - \eta_\infty} = \left(1 + (\dot{\gamma}/\dot{\gamma}^*)^b\right)^{(n-1)/b} \tag{8.3.9}$$

where η is the viscosity, $\dot{\gamma}^*$ is the characteristic shear rate for the onset of shear-thinning, n is a "power-law exponent" and b is a dimensionless fitting parameter that influences the sharpness of the transition from constant shear viscosity to the power-law region. Since all of the fluids exhibited shear-thinning, the Carreau-Yasuda model was used to estimate the characteristic viscosity in the Reynolds number given by Eq. (8.2.1), based

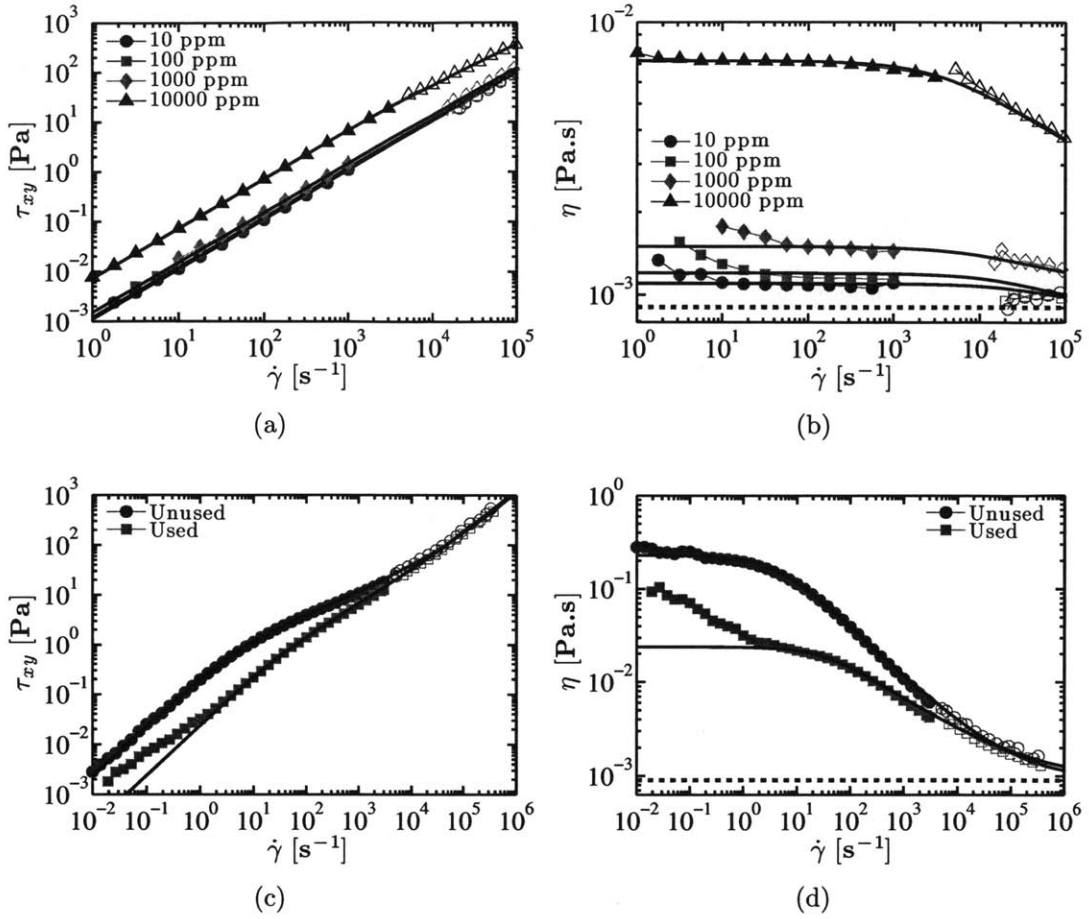

Figure 8.3.4: Flow curves of the non-Newtonian test liquids at 22 °C with respective Carreau-Yasuda model fits shown by the black solid lines. The dashed blue line indicates the viscosity of water. (a) & (b) Polyethylene oxide (PEO) solutions of molecular weight $M_w = 300$ kDa. (c) & (d) Solution of 1650 kDa 1000 ppm hyaluronic acid in water. The data labeled 'unused' correspond to measurements of the fluid prior to being pumped through the microchannel, whereas the data labeled 'used' indicate measurements of the solution after having been pumped through the microchannel at shear rates up to $\dot{\gamma} \sim \mathcal{O}(10^7)$ s^{-1}.

on the characteristic wall shear rate $\dot{\gamma}_{w,3D}$ determined from Eq. (8.4.3).

Measurements of the flow curves were taken of all fluids before and after the solutions had been pumped through the channel in order to determine the role of flow-induced polymer degradation. The measurements of the PEO solutions indicated that polymer degradation was not significant for these fluids and thus only the flow curves of the unused material are shown in Figures 8.3.4 (a) and (b). Conversely, the HA solution exhibited a marked degradation in the viscosity at shear rates below $\dot{\gamma} < \mathcal{O}(10^3)$ s^{-1}, as shown clearly in Figures 8.3.4 (c) and (d). Typical wall shear rates in the microchannel

were at higher shear rates in the range of $10^4 \leq \dot{\gamma}_{w,3D} \leq 10^7$ s^{-1}, however, where the viscosity was nearly the same for the used and unused samples suggesting that polymer degradation did not play a major role in the particle migration behavior. Therefore, the fit of the Carreau-Yasuda model to the viscosity of the unused HA sample has been used for calculating the characteristic viscosity in the Reynolds number.

8.4 Results and Discussion

8.4.1 Pressure Measurements

Measurements of the pressure drop across the channel were obtained using the readings from the pressure sensor in the pump cylinder. Although this reading strictly corresponded to the combined pressure drop across the channel as well as the pump fittings and tubing, separate calibration measurements demonstrated that the hydrodynamic resistance of the piping constituted approximately only 1-2% of the overall pressure drop. Accordingly, the vast majority of the measured pressure was attributable to the hydrodynamic resistance of the microchannel, and thus the pressure in the cylinder was taken as essentially equal to the pressure drop across the microfluidic device. The measured pressure drop is plotted ΔP against volumetric flow rate Q for the PEO solutions in Figure 8.4.1 (a) and for the HA solutions in Figure 8.4.2 (a).

The Fanning friction factor for the laminar flow of a Newtonian fluid through a duct with a square cross-section ($\alpha = 1$) is

$$f \equiv \frac{\Delta P}{\frac{1}{2}\rho \mathcal{U}^2 (L/D)} = \frac{96}{(1+\alpha)^2}\left[1 - \frac{192}{\pi^5}\alpha \sum_{j=odd}^{\infty} \frac{\tanh(j\pi/2\alpha)}{j^5}\right]^{-1} \frac{1}{Re_c} = \frac{56.9}{Re_c} \qquad (8.4.1)$$

where, as defined previously in Section 8.3.1, $\mathcal{U}$ is the mean velocity in the channel, L and D are the length and hydraulic diameter of the channel respectively and α is the aspect ratio of the channel. In this regime, the pressure drop increases linearly with flow rate, however, the friction factor scales inversely with Reynolds number. At channel Reynolds numbers above $Re_c \gtrsim 2000$, channel flow is expected to become turbulent and the friction factor for turbulent flow in a channel is given by White (2003)

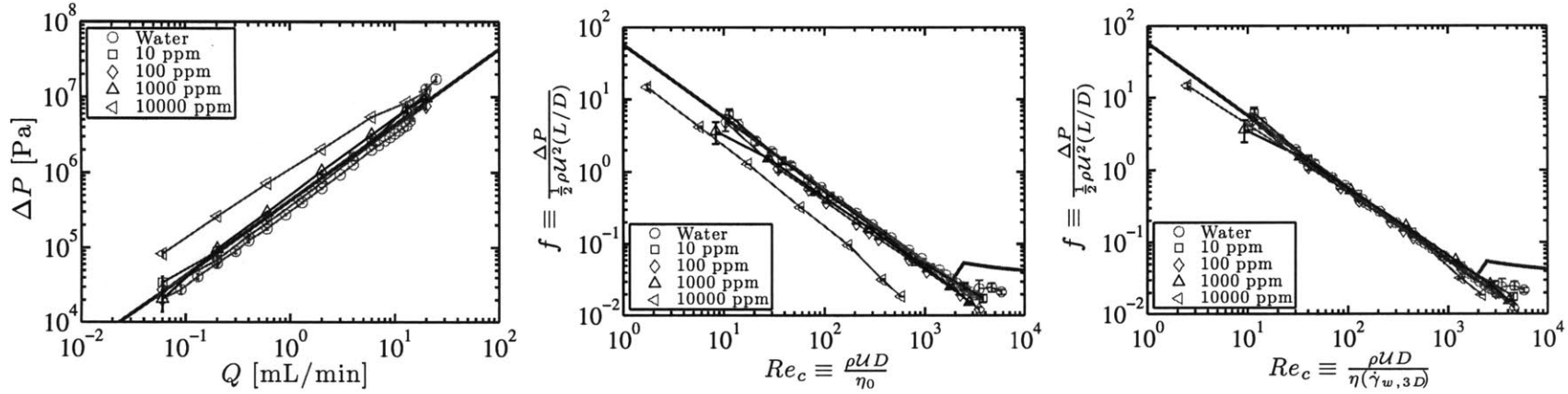

Figure 8.4.1: Pressure measurements with PEO solutions in the 80 μm $\times$ 80 μm $\times$ 37 mm channel. (a) Pressure drop ΔP against volumetric flow rate Q. Fanning friction factor against channel Reynolds number based on (b) a constant and (c) a rate dependent viscosity. The gray line indicates the theoretical friction factor for a Newtonian fluid given by Eq. (8.4.1) and (8.4.2).

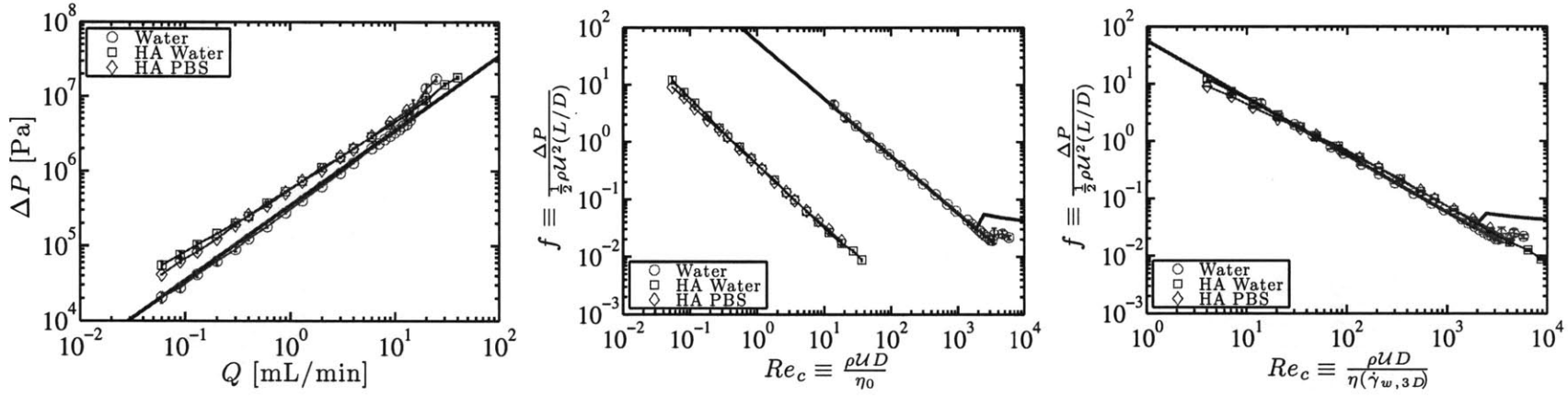

Figure 8.4.2: Pressure measurements with HA solutions in the 80 μm $\times$ 80 μm $\times$ 30 mm channel. (a) Pressure drop ΔP against volumetric flow rate Q. Fanning friction factor against channel Reynolds number based on (b) a constant and (c) a rate dependent viscosity. The gray line indicates the theoretical friction factor for a Newtonian fluid given by Eq. (8.4.1) and (8.4.2).

$$f = \left[-1.8 \ln \left(\frac{6.9}{Re_c} \right) + \left(\frac{\epsilon}{3.7} \right)^{1.11} \right]^{-2} \tag{8.4.2}$$

where $\epsilon \equiv k/D$ is the ratio of the average size of the asperities on the channel wall k to the hydraulic diameter of the channel. The typical roughness scale of the channel inherent to the fabrication processes is a few microns, hence $\epsilon \simeq 0.01$ is assumed in the plots of the friction factor shown in Figures 8.4.1 (b) and 8.4.2 (b).

The Carreau-Yasuda model was used to calculate the characteristic viscosity in the channel as a function wall shear rate for the flow of a Newtonian liquid in the square microchannel. This wall shear rate $\dot{\gamma}_{w,3D}$ was calculated from the well-known analytical solution for flow in a duct of finite aspect ratio (White, 2003), and it is given by

$$\dot{\gamma}_{w,3D} = \frac{\mathcal{U}}{D} \frac{96}{\pi^2(1+\alpha)} \left[\sum_{j=odd}^{\infty} \frac{1 - \frac{1}{\cosh(j\pi/2\alpha)}}{j^2} \right] \cdot \left[1 - \frac{192}{\pi^5} \alpha \sum_{j=odd}^{\infty} \frac{\tanh(j\pi/2\alpha)}{j^5} \right]^{-1} = 9.4 \frac{\mathcal{U}}{D} \tag{8.4.3}$$

The friction factors of the PEO solutions collapse onto the expected curve for a Newtonian fluid when this rate-dependent viscosity is used to calculate the Reynolds number as shown in Figure 8.4.1 (c). This collapse also occurs for the HA solutions shown in Figure 8.4.2 (c).

It is noteworthy that the pressure measurements with water at high flow rates exhibited a jump that is suggestive of a transition to turbulent flow at a critical channel Reynolds number of approximately $Re_c^* \approx 3500$, instead of the generally expected value of $Re_c^* \approx 2000$. This discrepancy is not unprecedented for flows in microchannels, however, although generally it has been observed that transition to turbulence occurs at Reynolds numbers less than $Re_c^* < 2000$ (Li *et al.*, 2005; Li & Olsen, 2006). Possible explanations for the discrepancy that have been proposed include relative surface roughness in microchannels that are larger than typical roughnesses in macroscale pipes as well as viscous heating effects (Zeighami *et al.*, 2000; Ghajar *et al.*, 2010; Natrajan & Christensen, 1992). The rate of energy dissipation in the channel is the pumping power $\dot{W} \sim Q\Delta P$, from which an upper bound of the temperature change of the fluid can be estimated if it is assumed that all energy dissipated goes to heat the fluid so that $\dot{W} \sim \rho Q C_p \Delta T$, where ρ is the fluid density ($\rho \approx 1000$ kg.m^{-3}), C_p is the heat capacity

of the liquid (assumed for water $C_p = 4186$ J.kg^{-1}K^{-1}) and ΔT is the change in temperature. For typical pressure drops in the range $10^4 \leq \Delta P \leq 10^7$ Pa, the expected change in temperature of the fluid is in the range $2.3 \times 10^{-3} \leq \Delta T \leq 2.4$ °C. A rise in the temperature of the fluid would reduce the dynamic viscosity which would led to a transition to turbulence that occurred at a lower apparent channel Reynolds number, which is not the case in these measurements. An alternative explanation for the higher than expected transitional Reynolds number is that the channel may bulge slightly at the high pressures, thereby increasing the true hydraulic diameter of the channel which simultaneously reduces the true channel Reynolds number (since for a given volumetric flow rate Q, the Reynolds number scales with D^{-1}), leading to a higher than expected critical Reynolds number. Additionally, for the Reynolds numbers in the range $2000 \leq Re_c \leq 3500$ the laminar hydrodynamic entrance length predicted from Eq. (8.3.3) and shown in Figure 8.3.1 (b) is of the order of the channel length ($L_e \simeq L$). It is therefore possible that the channel is insufficiently long for a turbulent flow to become fully developed, in which case the marked increase in the pressure drop would be shifted to higher Reynolds number than would ordinarily be expected for a channel flow (*i.e.* $Re_c^* \approx 2000$).

From a practical standpoint, it is also noteworthy that for both the PEO and HA solutions the pressure drop for a given flow rate above $Q \gtrsim 10$ mL.min^{-1} is lower than that for the water as shown in Figures 8.4.1 (a) and 8.4.2 (a). This fact is also reflected by friction factors for the polymer solutions that are lower than that of the water, when the Reynolds number is defined with the rate-dependent viscosity as shown in Figure 8.4.1 (c) and 8.4.2 (c). Evidently, the Reynolds number of the HA solutions reached $Re_c \approx 10^4$ without any accompanying non-linear increase in the pressure drop with flow rate suggesting that the presence of the polymer increased the value of the transitional Reynolds number Re_c^*. The role of polymers on the value of the transitional Reynolds number Re_c^*, however, is an area of some controversy. In one of the earliest studies by Dodge & Metzner (1959), it was found that more strongly shear thinning liquids (*i.e.* those with lower values of the power-law index n when viscosity is fit with a power-law model $\eta = m\dot{\gamma}^{n-1}$) had larger critical transitional Reynolds numbers. Previous experiments have also shown polymers such as xanthan gum (Rochefort & Middleman, 1986;

Bewersdorff & Singh, 1988) or sodium carboxymethyl cellulose (Pinho & Whitelaw, 1990) delay the transition to turbulence (Graham, 2004), with the extent of the delay having been attributed to the increase in the extensional viscosity of the liquid (Escudier *et al.*, 1999). Conversely, it has also been found that the transitional Reynolds number was lower than the typical value for Newtonian liquids in experiments with PEO and polyacrylamide solutions (Forame *et al.*, 1972; Li & McCarthy, 1995). In careful experiments by Draad *et al.* (1998) with a pipe that was isolated from external disturbances, the transition to turbulence in water occurred at Reynolds numbers $Re_c^* \approx 6 \times 10^4$, but when a minute amount of partially hydrolyzed polyacrylamide was added to the water the transition occurred far sooner at Reynolds numbers as low as $Re_c^* \approx 8000$. The authors suggested that viscoelasticity destabilized the flow by altering the development of the boundary layer in the entrance region of the channel. Unfortunately, however, it was not possible to reach flow rates in the experiments discussed in this Chapter that were high enough to observe a transition to turbulence in the polymer solutions without rupturing the channel due to the large pressure drop.

8.4.2 Streakline Measurements

Long exposure fluorescence images were acquired at evenly spaced positions along the length of the channel using a 20× 0.45 NA objective for each fluid seeded with $a = 9.9\ \mu$m highly monodisperse fluorescent polystyrene particles (FluoSpheres, Invitrogen), hence $Re_p \approx 0.01 Re_c$. The exposure time was adjusted to ensure adequate brightness without over saturating the camera sensor. These images serve as a two-dimensional projection of the evolution of the particle distributions along the channel length, with the local intensity peaks corresponding to equilibrium focusing positions.

The streakline images for water over a range of flow rates (rows) and positions along the channel length (columns) are shown in Figure 8.4.3. There are roughly four regimes of migration behavior evident once the flow is fully developed near the end of the channel (*i.e.* rightmost column). At low channel Reynolds number ($Re_c \lesssim 10$), the particle focusing is weak and the fluorescence intensity is correspondingly diffuse across the width of the channel. Within the range of channel Reynolds numbers $10 \lesssim Re_c \lesssim 200$ a clear

three-streak pattern emerges across the channel width indicative of a diamond-like particle distribution in the channel cross-section as shown schematically in Figure 8.1.1 (a). The central streakline is more intense than the two outer streaks adjacent to the wall because of the combined projections of the particles equilibrated on the upper and lower face of the channel. This distribution is in agreement with the diamond-like distributions observed previously in Newtonian liquids (Di Carlo, 2009a,a) at particle Reynolds numbers $Re_p \sim \mathcal{O}(1)$.

As the flow rate is further increased, a new intensity pattern becomes clear. In the range of channel Reynolds numbers $200 \lesssim Re_c \lesssim 1000$, a three-streak pattern still persists, but the intensity of the outer streaklines is now greater than that of the inner streak. This shift in the intensity profiles suggests that the particles are distributed in a quincunx pattern similar to that shown in Figure 8.1.1 (b). A similar pattern was observed in numerical simulations performed by Chun & Ladd (2006) of particle migration in a Newtonian fluid at channel and particle Reynolds numbers in the same range as those in these experiments. The only other study of particle migration in a microchannel in this range of channel Reynolds numbers was performed by Ciftlik *et al.* (2013) in a channel with a rectangular cross-section, for which there was no evidence of particle migration to the corners of the channel. Accordingly, the precise particle migration behavior in Newtonian fluids may be sensitively dependent on the aspect ratio of the channel. In this regime, channel flow lengths that are typically on the order of 100 channel diameters (1 cm) are necessary for a clear particle distribution pattern to emerge. However, the particles continue to be driven even more tightly toward the equilibrium positions as they travel down the channel, as is evident in the growth in the peaks and valleys of the intensity profile along the entire channel as shown in Figure 8.4.4 (a) for $Q = 2$ mL.min^{-1}.

For higher flow rates below those at which turbulences sets in ($1000 \lesssim Re_c \lesssim 3000$), a fourth characteristic particle migration distribution becomes prevalent. In this regime, the particles are driven towards the channel centerline, but they are never fully driven into a single streamline, suggesting the formation of an inner annulus similar to that observed by Matas *et al.* (2004b) in macroscale pipe flows. Based on their subsequent

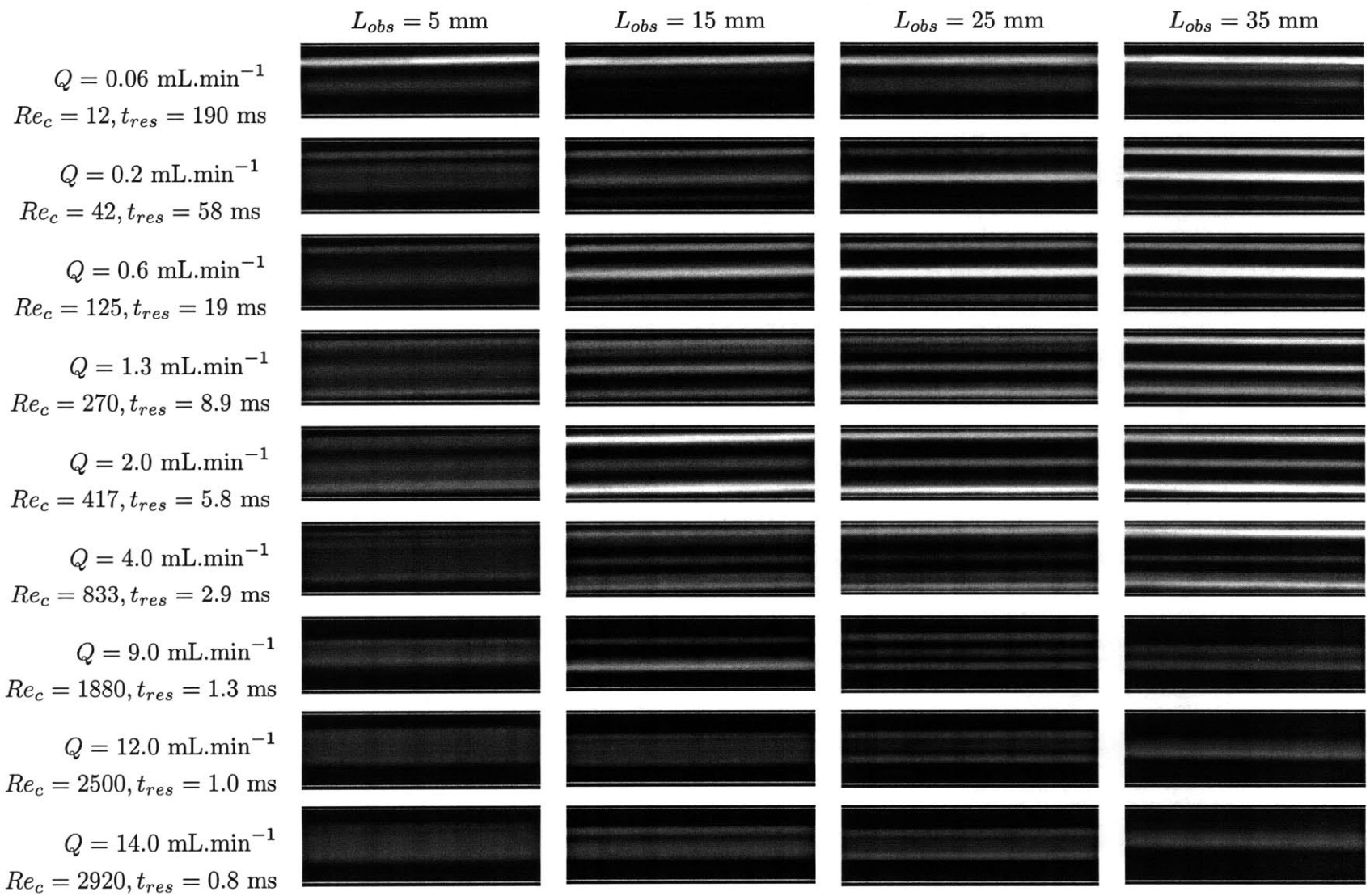

Figure 8.4.3: Streakline images of 8 μm particles in water at different positions along the microchannel. Flow is left to right. Observation positions from left to right are $L_{obs} = 5$, 15, 25, 35 mm downstream from the channel entrance. The bright green lines indicate the approximate position of the channel walls. Here $Re_p \approx 0.01 Re_c$.

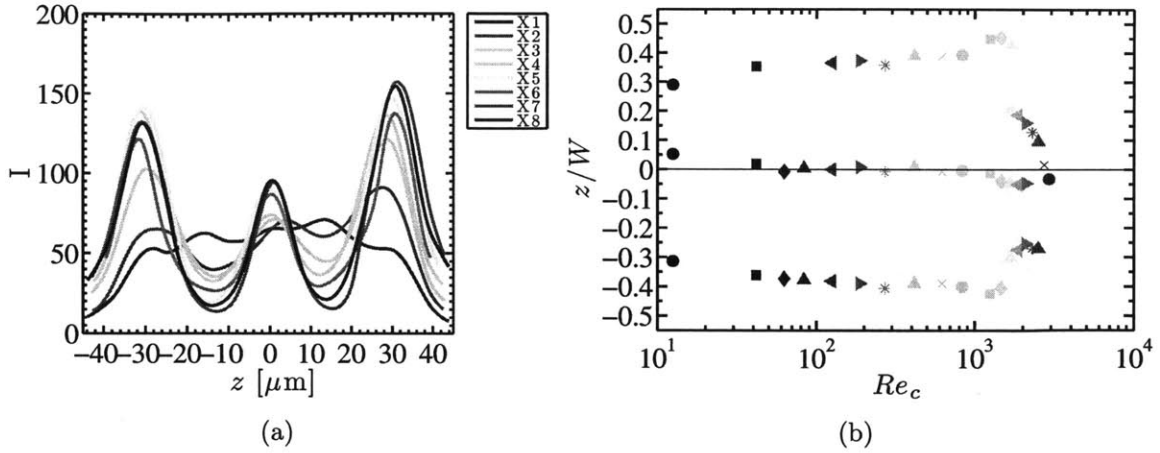

(a) (b)

Figure 8.4.4: (a) Evolution of the intensity profile along the channel length in water at $Q = 2$ mL.min^{-1}, spaced at 5 mm intervals from X1 = 0 mm to X8 = 35 mm. (b) Particle equilibrium positions based on the locations of the local maxima in the intensity profiles from the streakline images of water.

analysis, the authors strongly believed that this inner annulus was not a transient effect caused by a channel that was too short for the particle distribution to fully develop, but instead that the inner annulus was indeed the preferred equilibrium configuration of the particles in that range of channel Reynolds numbers. Likewise, in the microchannel experiments discussed in this Chapter, a narrow annulus around the channel centerline seems to correspond to the fully developed state. Yet, given the continued evolution of the streakline pattern downstream of the channel entrance seen in Figure 8.4.3, the channel length may not have been sufficient to attain the steady state result in these measurements.

The equilibrium positions determined from the local peaks in the intensity profiles are plotted against the channel Reynolds number in Figure 8.4.4 (b). Over the range $10 \lesssim Re_c \lesssim 1000$ the equilibrium position is driven closer to the wall with increasing flow rate. The center streakline does not move since it is the projection of the particles which only move perpendicular to the imaging plane as they are driven closer to the upper or lower wall of the channel. This trend is consistent with experimental studies of particle migration in macroscale pipes (Matas *et al.*, 2004b) as well as analytical modeling (Hogg, 1994; Asmolov, 1999) and numerical simulations (Chun & Ladd, 2006). For higher channel Reynolds numbers the particles are instead driven toward the channel

center, forming a tightly packed inner annulus as shown numerically by Chun & Ladd (2006). At a critical Reynolds number $Re_c^* \approx 3500$ the flow becomes turbulent and the entire channel becomes uniformly illuminated since no clear equilibrium position can exist due to the breakdown in particle focusing.

The streakline images acquired with the different PEO solutions are shown in Figure 8.4.5. Each column corresponds to a particular concentration of PEO and each row corresponds to a constant flow rate. For all four solutions, the channel elasticity numbers El_c defined by the zero-shear-rate viscosity in Eq. (8.2.6) are much smaller than unity and are listed in the subcaptions of Figure 8.4.6. They would be even smaller if this number were to be defined by a rate-dependent viscosity similar to the way in which the channel Reynolds number was defined in the results shown in Figures 8.4.1 (c) and 8.4.2 (c). These low value of El_c would suggest that the observed particle migration behavior in these flows should be highly similar to the behavior in purely Newtonian liquids. On the other hand, the particle elasticity number defined in Eq. (8.2.7) is on the order of one or larger for these measurements and therefore elastic contributions to the force balance on a particle can nevertheless play a dominant role in the migration behavior of the particles.

For the 10 ppm solution, at channel Weissenberg numbers below $Wi_c \lesssim 0.1$ a triple streakline pattern similar to that observed in water is evident. As the Weissenberg number approaches unity, the particles are driven toward the center of the channel as seen in the movements of the intensity peaks shown in Figure 8.4.6 (a), until at $Wi_c \gtrsim 3$ the channel Reynolds number exceeds $Re_c \gtrsim 2500$, the fluorescence intensity pattern becomes more diffuse indicating the onset of turbulence.

For the 100 ppm solution, the observed streakline pattern transitions from three streaks associated with inertially-driven focusing to two streaks near the channel centerline at a channel Weissenberg number $Wi_c \approx 1$ as shown in Figure 8.4.6 (b). The two streaks suggest the formation of a square distribution around the channel centerline as shown in Figure 8.1.1 (c). Evidently, this behavior is driven by elasticity and not inertia since particles are driven to the channel center in this PEO solution at much lower channel Reynolds number (*i.e.* $Re_c \approx 100$) than they are in a Newtonian liquid

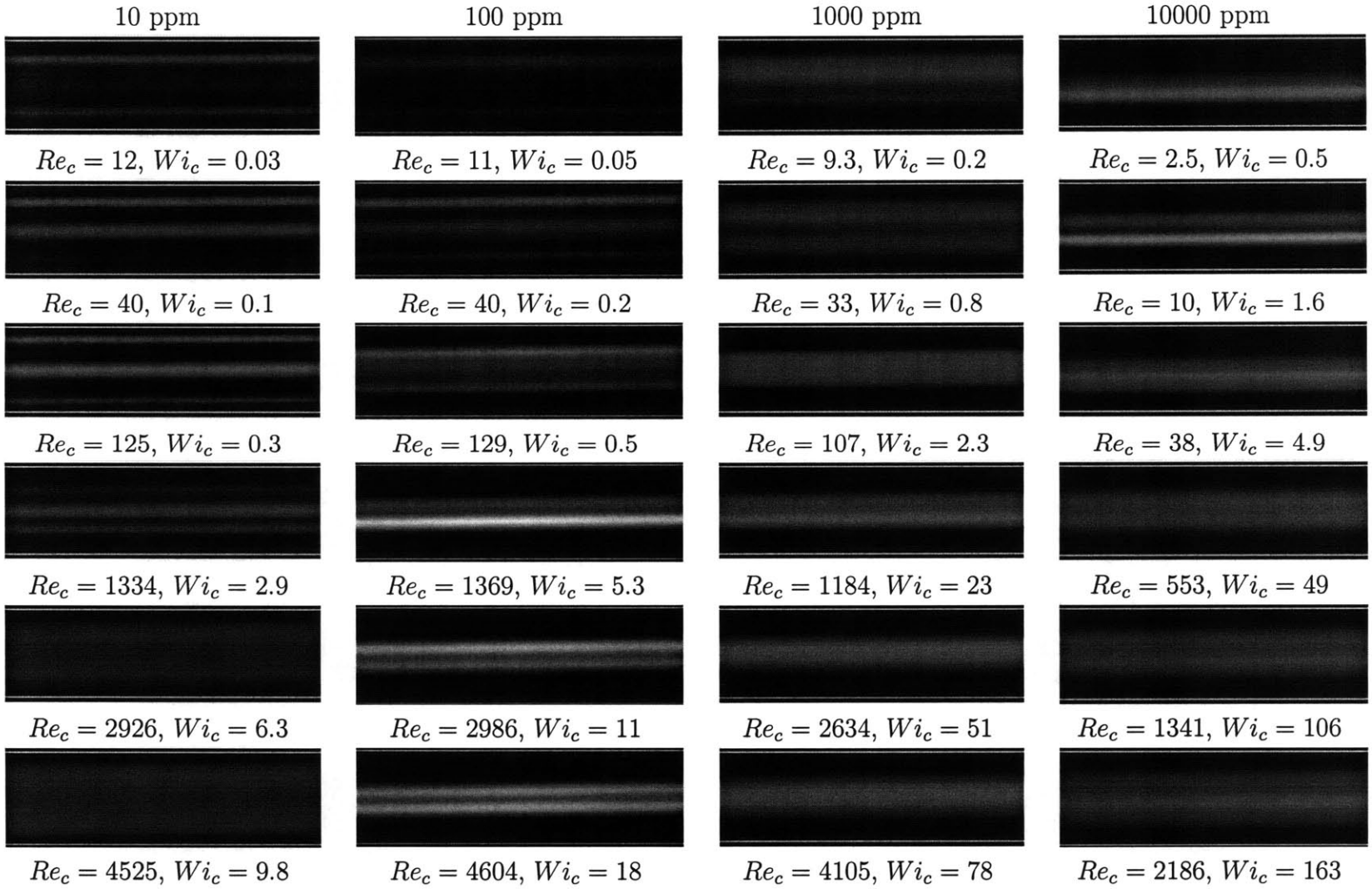

Figure 8.4.5: Streakline images of 8 μm particles in PEO solutions of different polymer concentrations (columns) at different flow rates (rows) near the end of the microchannel $L_{obs} = 35$ μm. Flow is left to right. From top to bottom, each row corresponds to $Q = 0.06$, 0.2, 0.6, 6, 13, 20 mL.min^{-1}. The bright green lines indicate the approximate position of the channel walls. Note that the channel Reynolds number is defined in terms of the rate dependent viscosity $\eta(\dot{\gamma}_{W,3D})$.

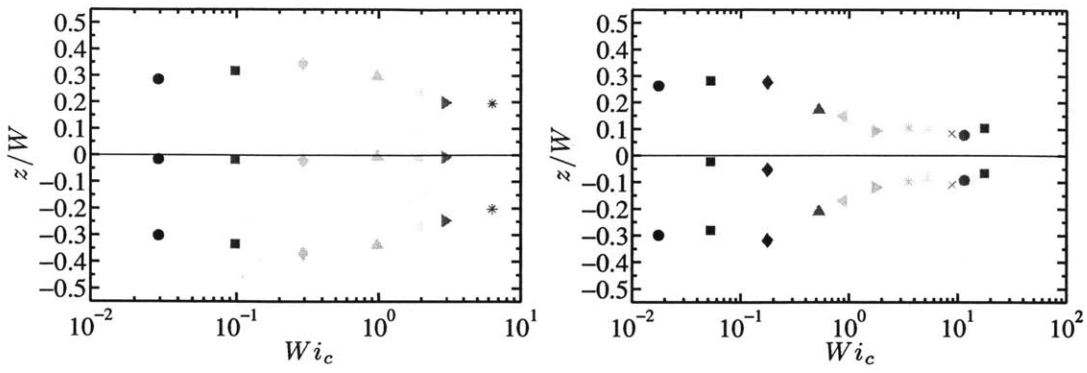

(a) 10 ppm, $El_c = 2.1 \times 10^{-3}$, $El_p = 0.21$ (b) 100 ppm, $El_c = 3.8 \times 10^{-3}$, $El_p = 0.38$

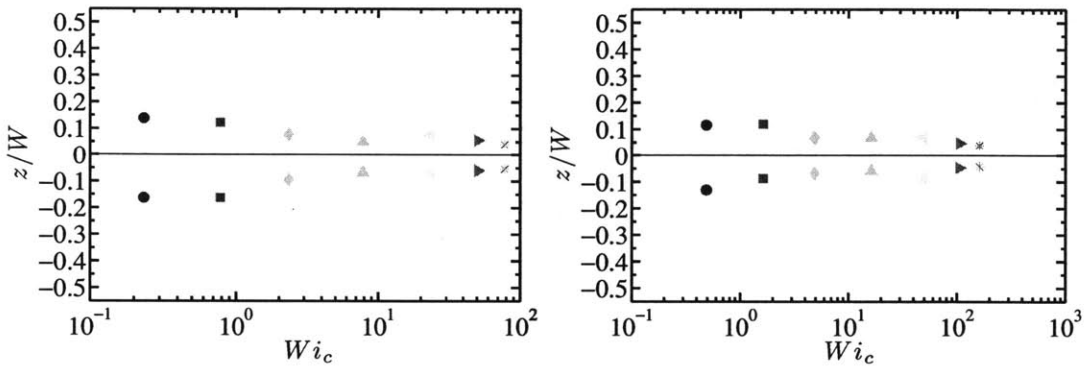

(c) 1000 ppm, $El_c = 1.7 \times 10^{-2}$, $El_p = 1.7$ (d) 10000 ppm, $El_c = 3.5 \times 10^{-2}$, $El_p = 3.5$

Figure 8.4.6: Particle equilibrium positions based on the locations of the local maxima in the intensity profiles from the streakline images of PEO near the end of the channel $L_{obs} = 35$ mm.

(*i.e.* $Re_c \gtrsim 1000$).

The migration behavior in both the 1000 ppm and the 10000 ppm solutions is similar as seen by the proximity of the intensity peaks to the channel centerline in Figures 8.4.6 (c) and (d). Over the entire range of channel Weissenberg numbers observed, there are two peaks in the intensity profiles that are driven more tightly toward the channel centerline with increasing values of Wi_c. An example of the evolution of the fluorescence intensity along the length of the channel for the 10000 ppm solution is shown in Figure 8.4.7. Evidently, two distinct peaks persist to the exit of the channel.

The streakline images of the flow of the HA solutions are shown in Figure 8.4.8. In this figure, each row corresponds to a constant flow rate and each column to a given observation position along the length of the channel. The over arching trend for the HA

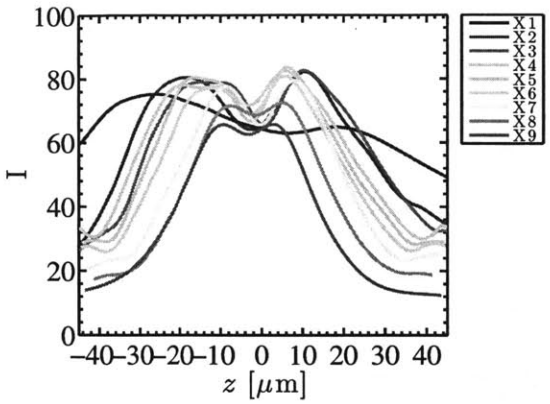

Figure 8.4.7: Evolution of the intensity profile along the channel length in 10000 ppm PEO solution at $Q = 6$ mL.min^{-1} ($Re_c = 553$, $Wi_c = 49$), spaced at 5 mm intervals from X1 = 0 mm to X8 = 35 mm.

is quite obvious. With increasing flow rates and farther downstream from the channel entrance the average particle position becomes more tightly localized near the channel centerline. This migration of the particles to the channel center is also clearly seen from the central position of the single peak in the streakline across all channel Weissenberg number as shown in Figure 8.4.9 (a). It is also noteworthy that this migration toward the channel centerline persists to flow rates up to at least $Q \geq 50$ mL.min^{-1}, which is the maximum flow rate achievable with the pump.

The relative similarity in the streak widths at the two most downstream observation positions ($L_{obs} = 25$ and 35 mm) for each flow rate shown in Figure 8.4.8, also suggests that the particles reach their equilibrium positions within the channel length even for Deborah numbers larger than one. This rapid evolution toward the steady fully developed particle distribution is also evident from the evolution of the fluorescence intensity along the channel length is shown in Figure 8.4.9 (b).

The observed particle migration behavior in both the PEO and HA solutions clearly demonstrates the importance of viscoelasticity even at large channel Reynolds numbers, but the difference between the behavior in the two polymer systems is equally remarkable. The tendency of particles to be driven to the channel center in flows of viscoelastic liquids in microchannels has been well-documented experimentally when the Reynolds number is vanishingly small (Leshansky *et al.*, 2007; Yang *et al.*, 2011) and has been at-

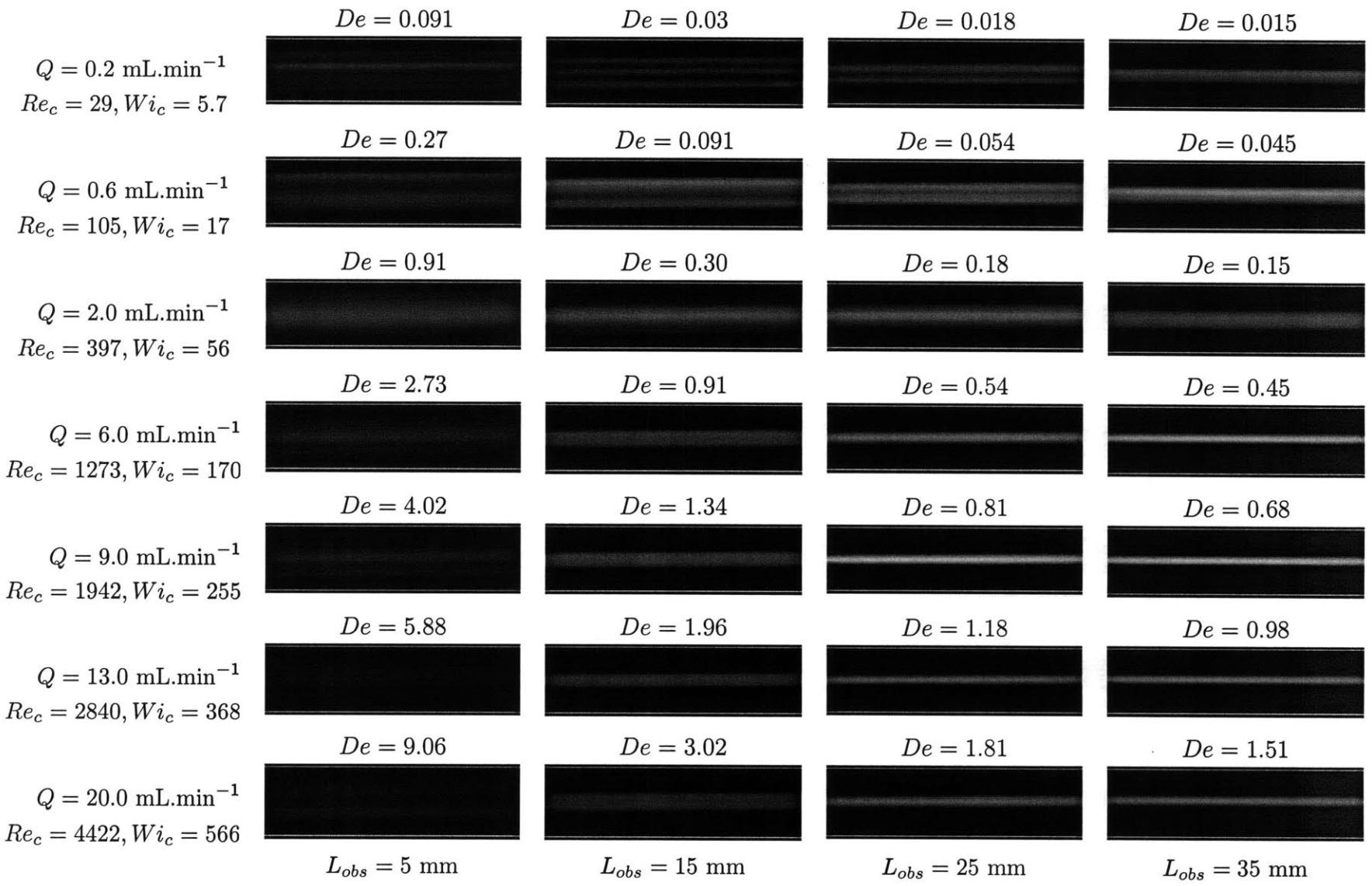

Figure 8.4.8: Streakline images of 8 μm particles in HA at different positions along the microchannel. Flow is left to right. Observation positions from left to right are $L_{obs} = 5$, 15, 25, 35 μm downstream from the channel entrance. The bright green lines indicate the approximate position of the channel walls.

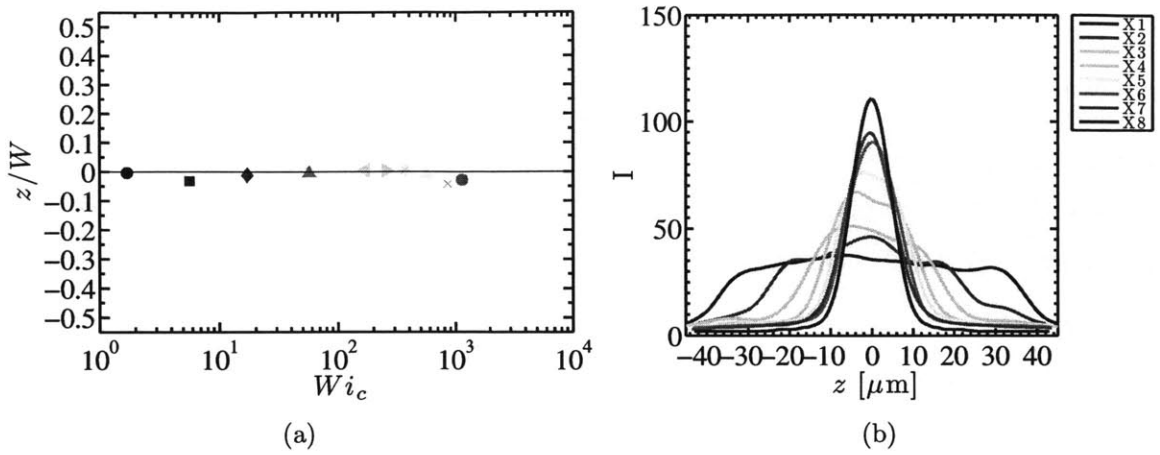

Figure 8.4.9: (a) Particle equilibrium positions based on the locations of the local maxima in the intensity profiles from the streakline images of 1000 ppm HA near the end of the channel $L_{obs} = 35$ mm. (b) Evolution of the intensity profile along the channel length in 1000 ppm HA at $Q = 6$ mL.min^{-1}, spaced at 5 mm intervals from X1 = 0 mm to X8 = 35 mm.

tributed analytically to gradients in the normal stress differences that drive the particles to regions where the stress differences are lowest (Ho & Leal, 1976). Generally, the shear rates are lowest near the channel center and four corners, which explains the quincunx distribution pattern commonly seen in particle migration in viscoelastic liquids. It has also been shown that shear-thinning in inertialess flows can drive particles toward the wall as well (Villone *et al.*, 2011a; D'Avino *et al.*, 2012). Much of the simulation work for this regime of particle migration has focused on long-term trajectories of individual particles depending on their initial position at the channel inlet, with particles starting near the wall tending to be driven toward it and particles near the centerline being driven toward the channel center.

The experimental results in this Chapter, however, constitute some of the first observations of migration at simultaneously large channel Reynolds number ($Re_c \gg 1$) and channel Weissenberg number ($Wi_c \gg 1$). In this regime, many physical phenomena, such as inertia, viscoelasticity, shear-thinning and secondary flows (which all scale nonlinearly with flow rate), can all synergistcally play a role in the observed particle migration behavior. In order to better understand the physical mechanism and the robustness behind the migration behavior in this regime, it is valuable to incorporate measurements

of the flow kinematics in the channel as well as individual particle statistics, which are addressed in the subsequent Sections of this Chapter.

Furthermore, in comparison to the migration behavior observed in water and the PEO solutions, the migration behavior in the HA solutions is remarkably robust and similar across all the flow rates tested. The tendency of the HA solution to consistently drive particles to the channel centerline makes it a more viable system compared to the PEO solutions studied thus far for practical engineering applications that are commonly proposed for inertial focusing technologies. For this reason, in the remaining portion of the Chapter, particle migration will be studied in only water and the 1000 ppm HA solution.

8.4.3 Particle Distributions

In order to determine the overall particle distribution in the channel from individual particle statistics, it is necessary to acquire still images of the particles in the channel by exploiting the short exposure times of the laser imaging system discussed in Section 8.3.2. Through careful selection of the objective magnification, it is possible to determine the spatial distribution of the particles across both the width and height of the channel.

One-Dimensional Distributions

The one-dimensional distributions of highly monodisperse $a = 9.9$ μm particles across the channel width (*i.e.* z-axis) were determined from 500 images that were acquired near the exit of the channel at each flow rate. Within this set of images there were typically between 250 to 750 particles in total, whose position across the width of the channel was identified using an image analysis script written in MATLAB. These data were then used to determine the particle probability density functions (PDF) for each flow rate.

The total particle count and the PDF for water are shown in Figure 8.4.10 (a) and (b) respectively. For all flow rates for which the flow is laminar, there were multiple equilibrium positions within the channel cross-section, confirming results obtained from the long exposure fluorescence images. Additionally, at $Q = 15$ mL.min^{-1} ($Re_c = 3130$) the particles were driven to a region approximately 20 μm from the channel centerline in

agreement with the streakline images for $Q = 12$ and 14 mL.min^{-1} in Figure 8.4.3. At higher flow rates, the flow was turbulent and any semblance of particle focusing broke down and hence the particles were distributed uniformly across the channel width.

The measured particle distributions in the HA solutions are shown in Figure 8.4.10 (c) and (d). Evidently, the particles were driven to the center of the channel with the center of nearly every particle lying within one particle diameter from the channel centerline (*i.e.* more than 95% within $z = \pm 10$ μm) over the entire range of flow rates measured.

Example plots of the one-dimensional histogram and the intensity profile obtained from the long exposure fluorescence images are shown in Figure 8.4.11. The agreement between the histogram and streakline images confirms the consistency between the two measurement techniques as well as the repeatability of the migration behavior in these liquids, since each type of measurement was taken in separate experiments with different imaging systems.

Two-Dimensional Distributions

Two-dimensional particle distributions across the height and width of the channel (*i.e.* in the y-z plane) are shown in Figure 8.4.12 using the particle tracking analysis (PTA) technique described in Section 7.2.3. Sets of 300 images were acquired with a 20× 0.5 NA objective at vertical spacing 6 μm apart from the bottom of the channel to the mid-plane. These images were acquired only in the lower half of the channel to reduce the total amount of necessary data processing on the assumption that the particle distributions are symmetrical about the mid-plane of the channel. For these measurements, the epoxy channel was bonded to a 300 μm thick glass coverslip (instead of the 1 mm coverslip) to reduce the effects of light absorption and limitations of focal depth in the glass on the intensity of the particles.

All particles in each image were examined using image analysis tools in MATLAB in order to determine those that were optically in-focus based on cutoff criteria on the maximum intensity of each particle and the spatial gradients in intensity to determine the optical sharpness of the particle. The position of each optically in-focus particle was then tabulated in order to construct the particle distributions in Figure 8.4.12. Note

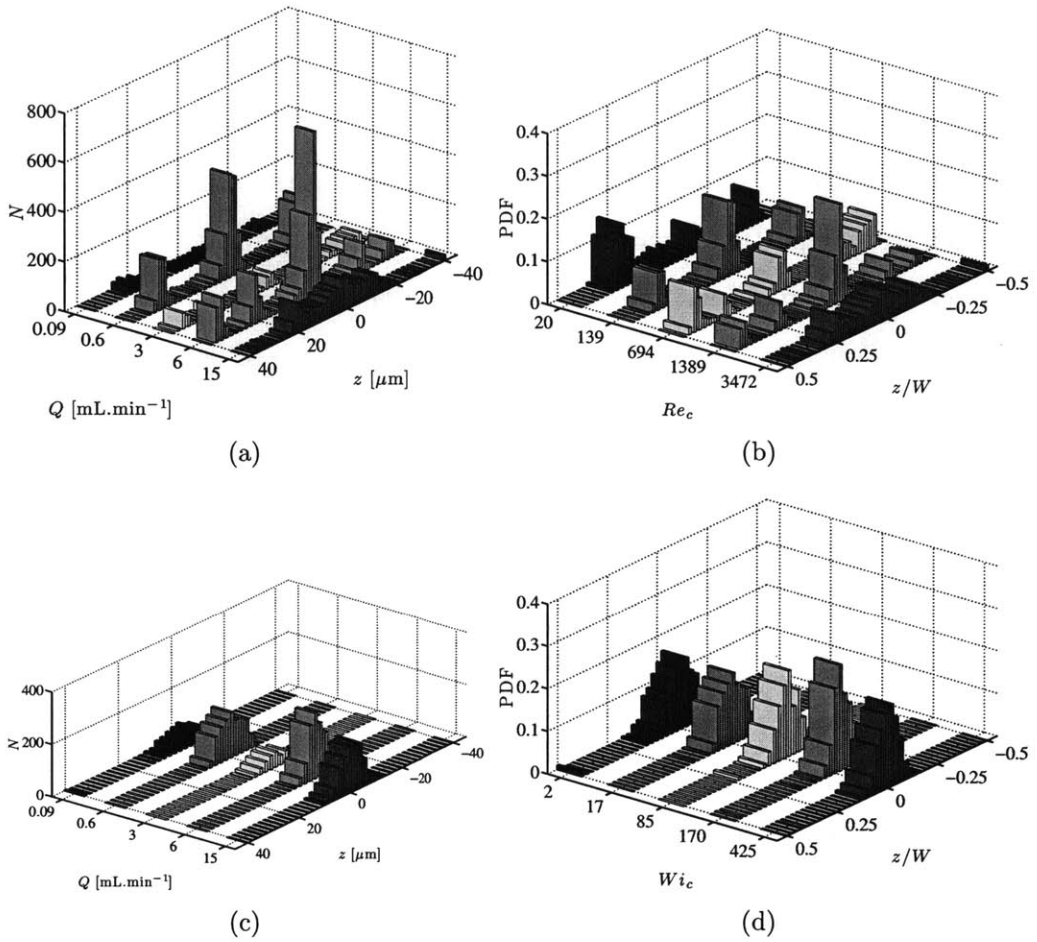

Figure 8.4.10: One-dimensional particle distributions for (a) & (b) water and (c) & (d) 1000 ppm HA solution across the channel width at $L_{obs} = 3.5$ mm for a range of flow rates. The PDFs were determined at flow rates $Q = 0.09$, 0.6, 3 6 and 15 mL.min^{-1}.

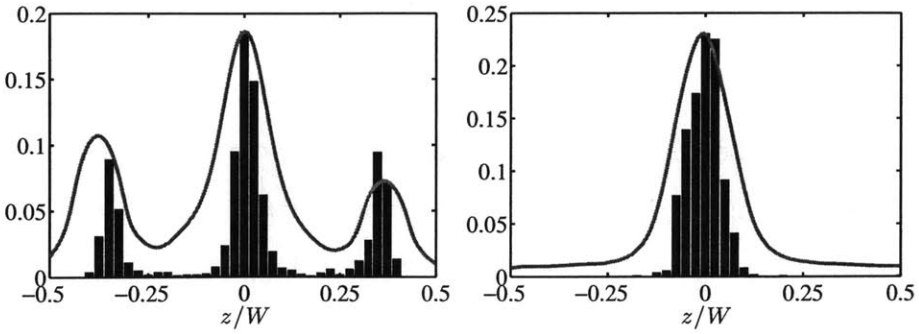

(a) Water $Q = 0.6$ mL.min^{-1}, $Re_c = 125$ (b) 1000 ppm HA $Q = 6.0$ mL.min^{-1}, $Re_c = 1273$, $Wi_c = 170$

Figure 8.4.11: One-dimensional particle histograms and long exposure fluorescence intensity profiles for (a) water and (b) HA. The red line is the intensity profile and the blue bars are the particle histograms.

that while the location of the center of a particle can be precisely located along the width of the channel (*i.e.* z-axis) to within one pixel (*i.e.* 0.323 μm), the location of the particle along the channel height (*i.e.* y-axis) is subject to errors on the order of the depth of field of the imaging system (*i.e.* 3.94 μm). Thus while the z-positions of each particle in the distribution maps are highly precise, the y-position of each particle is correct to within one row.

At $Q = 0.6$ mL.min^{-1} ($Re_c = 125$) in water, the particles were clearly distributed in a diamond pattern with equilibrium positions located at the middle of each wall as shown in Figure 8.4.12 (a). This distribution for the channel Reynolds number ($Re_c = 125$) was in agreement with the triple streak pattern seen in Figure 8.4.3 as well as the distribution illustrated schematically in Figure 8.1.1 (a). For the HA solution shown in Figure 8.4.12 (b), the particles were located near the centerline of the channel in a region whose diameter was approximately four times that of the particle (*i.e.* $4a \approx 40$ μm).

At $Q = 6.0$ mL.min^{-1} ($Re_c = 1250$ for water), a large fraction of the particles were located within 20 μm of the channel centerline, but additional equilibrium positions emerged in the corners of the channel at this flow rate in Figure 8.4.12 (c). These equilibrium positions have not been previously observed experimentally for the flow of a Newtonian fluid in a square microchannel, however they have been predicted in numerical simulations of Chun & Ladd (2006) for channel Reynolds numbers at $Re_c \sim 1000$ and for a similar ratio of particle diameter to channel size ($a/D \sim 0.1$) as in this study. The migration of particles toward the corners of the channel was also in agreement with the quincunx pattern of the form shown in Figure 8.1.1 (b) and suggested by the intensification of the streaks near the channel edges shown in the streakline images presented in Figure 8.4.3 for this flow rate. For the HA solution, the particles migrated toward the channel centerline as shown in Figure 8.4.12 (d) confirming the centralized streakline in the long exposure fluorescence image at this flow rate in Figure 8.4.8.

At $Q = 15.0$ mL.min^{-1}, the channel Reynolds number for water is $Re_c = 3130$, which was very near the transition to inertially-driven turbulence. In this regime, the streakline images in Figure 8.4.3 indicated that the particles were driven toward the center which is confirmed in Figure 8.4.12 (e). Evidently, the qualitative features of the particle

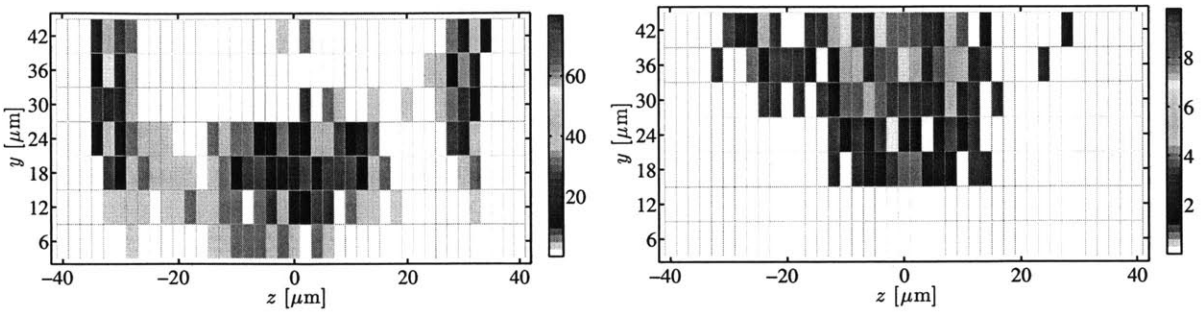

(a) Water $Q = 0.6$ mL.min^{-1}

(b) HA $Q = 0.6$ mL.min^{-1}

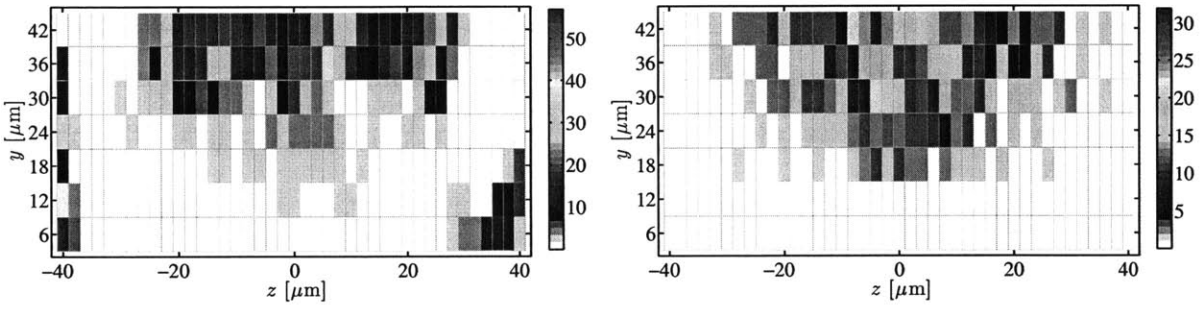

(c) Water $Q = 6.0$ mL.min^{-1}

(d) HA $Q = 6.0$ mL.min^{-1}

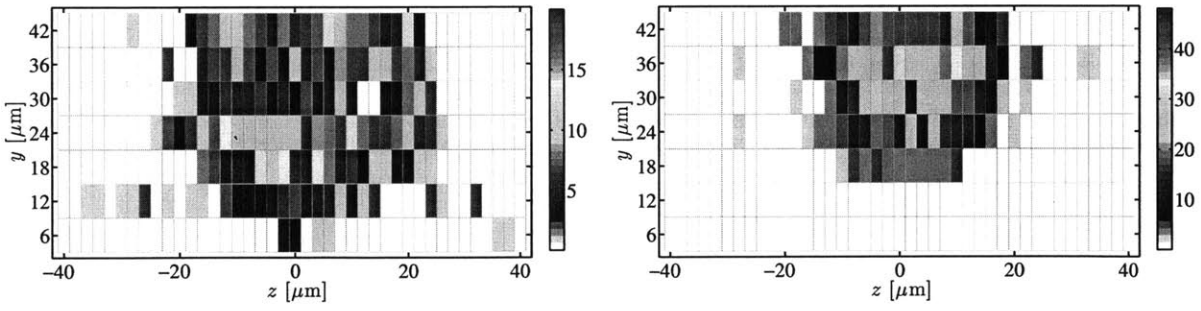

(e) Water $Q = 15.0$ mL.min^{-1}

(f) HA $Q = 15.0$ mL.min^{-1}

Figure 8.4.12: Two-dimensional particle distributions for (a), (c) & (e) water and (b), (d) & (f) 1000 ppm HA solution across the channel height and width near the exit of the channel $L_{obs} = 3.5$ mm for a range of flow rates. The vertical color bars indicate the total number of particles identified at each position. The PDFs were determined at flow rates (a) & (b) $Q = 0.6$, (c) & (d) $Q = 6.0$ and (e) & (f) $Q = 15.0$ mL.min^{-1}.

distribution in water were very sensitive to the channel Reynolds number, which would pose great challenges for any applications of inertial focusing in water for high throughput technologies. On the other hand, in the HA solution at the higher flow rate shown in Figure 8.4.12 (f), the particles were most tightly driven to the a region within around 15 μm from the channel centerline. Thus the streakline images, and the one and two-dimensional particle distributions based on the snapshot images of individual particles revealed quite clearly the robustness of the elastically-driven particle migration toward the channel center in the HA solutions, which was robust over nearly three orders of magnitude of flow rates ($\mathcal{O}(1) \leq Wi_c \leq \mathcal{O}(10^3)$).

8.4.4 Velocimetry Measurements

Velocimetry measurements constitute a valuable complement to the long exposure images and particle snapshots by providing quantitative details about the kinematics of the flow. These measurements can be used to determine the relative velocities of the particles with respect to the local fluid velocity and also give insight into possible effects of wall slip and shear-thinning in the flow.

The velocity of each of the large particles was determined using particle tracking velocimetry (PTV). A set of image pairs was acquired using a 20$\times$ 0.45 NA objective and the velocity of each particle was analyzed using MATLAB, based on the displacement of a single particle measured on the same streamline (*i.e.* line of constant x) between the two images. An example PTV measurement is shown in Figure 8.4.13. Note that these particles were large enough that even the fluorescent intensity of those lying outside the depth of measurement was sufficiently intense to be identified by the PTV algorithm. Therefore, unlike the PTA measurements in Figure 8.4.12, the precise y-position of each particle indicated by the black circles in Figure 8.4.14 was not determined.

The fluid velocity was measured using particle imaging velocimetry (PIV) with 1 μm particles. These smaller particles were suited to velocimetry measurements because they were not subject to the migration effects seen in the larger particles as shown in Section 8.4.5, and therefore they more faithfully followed the local fluid velocity field, which was necessary for accurate velocimetry measurements. These velocity measure-

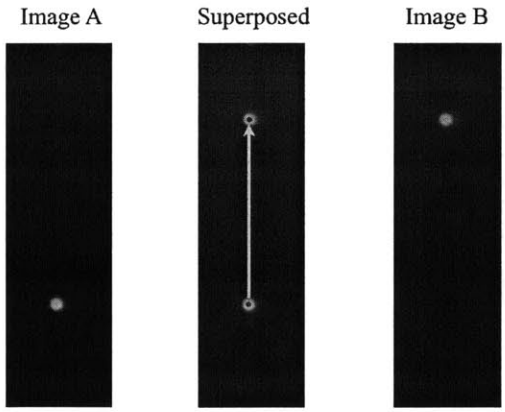

Figure 8.4.13: Example particle tracking velocimetry image pair for determining the velocity of individual 8 μm particles in the channel.

ments were completed without any of the larger 8 μm particles in the fluid, because the presence of the larger particles in the images would otherwise have reduced the spatial resolution of the auto and cross-correlations on the image pairs. Images were acquired near the end of the channel ($L_{obs} = 35$ mm) using a 20× 0.45 NA objective (depth of measurement 14 μm) that was focused at approximately the mid-plane of the channel (*i.e.* $y = 0$ μm).

The fluid velocity profiles are shown in Figure 8.4.14 for both the water and the HA solution. For comparison, the expected velocity profile for the flow of a Newtonian fluid at the mid-plane of the channel is shown by the green curve in each plot. The anticipated velocity profile across the channel width at the mid-plane of the channel (*i.e.* $y = 0$ μm) for a Newtonian fluid is given by (White, 2003)

$$\frac{u_x(z)}{\mathcal{U}} = \frac{48}{\pi^3}\left[\sum_{j\ odd}^{\infty}(-1)^{\frac{j-1}{2}}\left(1-\frac{1}{\cosh(j\pi/2\alpha)}\right)\frac{\cos(j\pi z/W)}{j^3}\right]\cdot\left[1-\frac{192}{\pi^5}\alpha\sum_{j\ odd}^{\infty}\frac{\tanh(j\pi/2\alpha)}{j^5}\right]^{-1} \tag{8.4.4}$$

The precise dimensions of the channel cross-section at the downstream position where the velocity profile was observed were measured using a laser confocal displacement meter (LT Series, Keyence), for which the channel height was measured to be $H = 85 \pm 5$ μm as expected. The channel width was determined from a brightfield image focused at the bottom of channel and was $W = 90$ μm. This measured width is 10 μm larger than the design value, but it is within the manufacturing tolerances of a soft photolithography-

based fabrication technique.

The measured profiles were determined using a correlative algorithm to track the displacement of a group of neighboring particles over a short period of time. For the imaging acquisition system used in this thesis and described in Section 8.3.2, the shortest time step between laser pulses that would allow each pulse to be captured on separate images, and therefore be amenable to cross-correlative analysis with the Insight6 software (TSI), was $\delta t = 2.4$ μs. For larger fluid velocities, shorter time steps (down to the lower limit of the pulsed laser synchronizer $\delta t_{min} = 0.2$ μs) were necessary to ensure the tracer particles translated only approximately four pixels between laser pulses. These shorter time steps would result in a single double-exposed image, which had to be analyzed using an auto-correlative algorithm (LaVision, courtesy Douglas Neal).

At $Q = 0.09$ mL.min^{-1}, the particle velocities were sufficiently small that the standard cross-correlative algorithm could be used. These velocity profiles are shown in Figure 8.4.14 (a) and (c). The measured velocity profiles extend fully to the wall where the velocity approaches zero indicating that wall slip does not play a significant role in the flow kinematics. On the other hand, the measured profiles do not overlap with the anticipated profile, and instead the maximum velocity of each measured profile is approximately 10% lower than the maximum velocity profile predicted from Eq. (8.4.4). This deviation may be a result of the uncertainty in the precise channel dimensions or some error in locating the channel mid-plane to within the depth of measurement of the objective and camera. Nevertheless, the imaging plane was the same for both the velocimetry measurements in the water and HA solution and therefore these results can be directly compared in Figure 8.4.14 (e). Evidently, the velocity of the water near the channel center (*i.e.* $z = 0$ μm) is about 5% larger than the respective profile for the HA solution. At this flow rate, the typical wall shear rates are $\dot{\gamma} \simeq \mathcal{O}(10^3)$ s^{-1}, which is in the range of shear rates for which shear thinning in the HA solutions is prevalent as shown in Figure 8.3.4 (d). Therefore, the difference is likely attributable to shear thinning which blunts the velocity profile resulting in a lower centerline velocity than would be found for a Newtonian fluid. This observation is noteworthy, since it is known that, in general, shear thinning effects tend to drive particles toward the wall (D'Avino *et al.*,

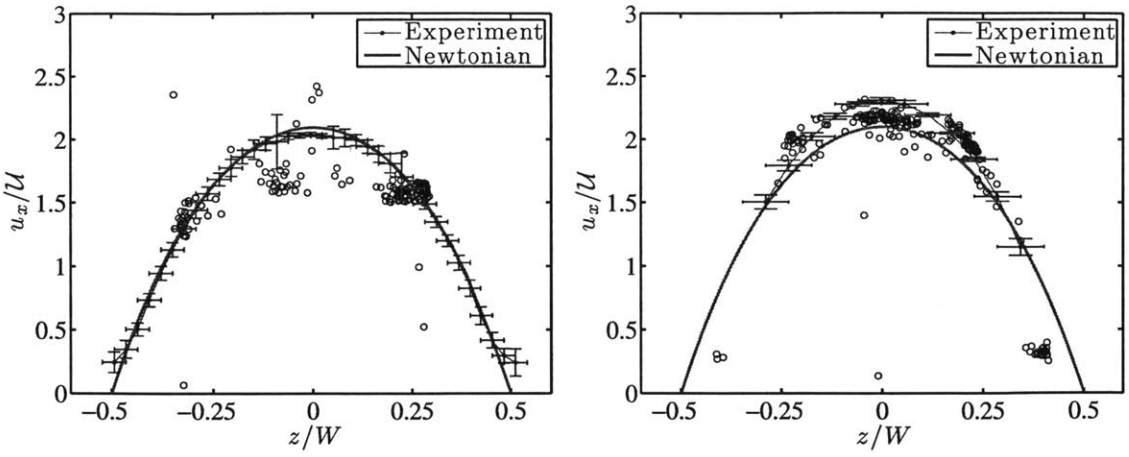

(a) Water $Q = 0.09$ mL.min^{-1}, $\mathcal{U} = 0.20$ m.s^{-1} (b) Water $Q = 6.0$ mL.min^{-1}, $\mathcal{U} = 13.9$ m.s^{-1}

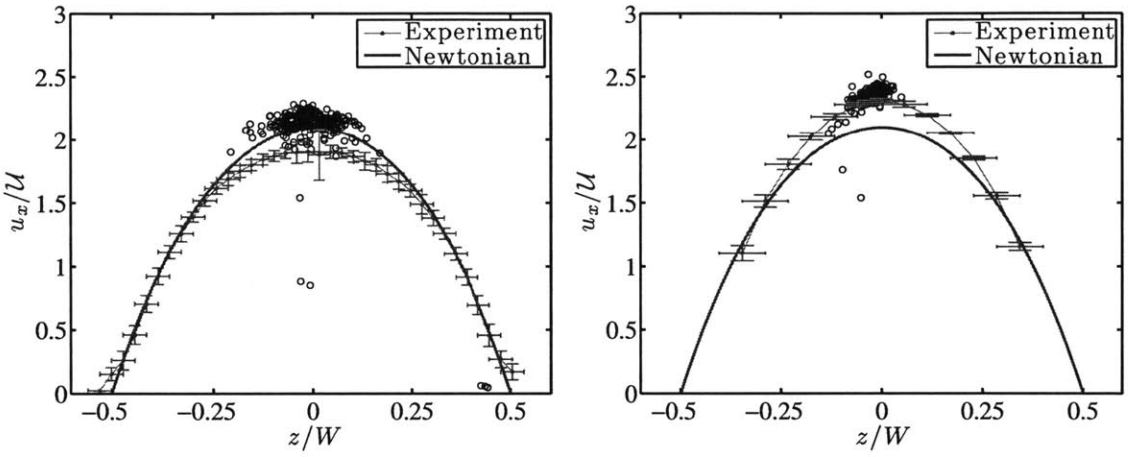

(c) HA $Q = 0.09$ mL.min^{-1}, $\mathcal{U} = 0.20$ m.s^{-1} (d) HA $Q = 6.0$ mL.min^{-1}, $\mathcal{U} = 13.9$ m.s^{-1}

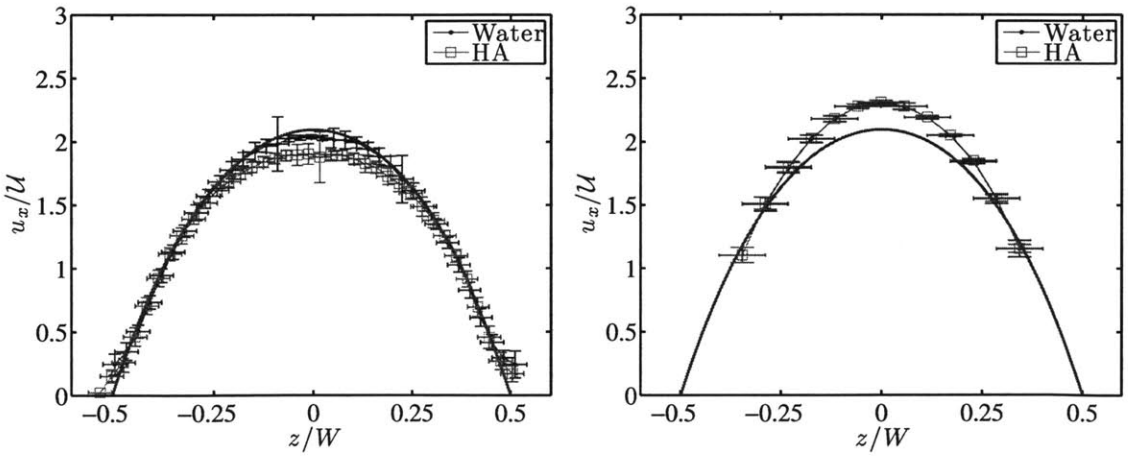

(e) $Q = 0.09$ mL.min^{-1}, $\mathcal{U} = 0.20$ m.s^{-1} (f) $Q = 6.0$ mL.min^{-1}, $\mathcal{U} = 13.9$ m.s^{-1}

Figure 8.4.14: Velocity profiles measured near the channel mid-plane $z = 0$ μm. The velocity profiles of the fluid across the entire channel width were acquired from velocimetry measurements with 1 μm particles. The solid curve indicates the expected analytical solution for the velocity of Poiseuille flow in a duct of finite aspect ration given by Eq. (8.4.4). (a)–(d) The measured velocity of each individual 8 μm bead is shown by the black circles in the plots. (e) & (f) Comparison plots of the water and HA velocities.

2012), however essentially all particles were located near the channel centerline indicating that for the HA solution, shear thinning in the viscosity did not play a dominant role in the particle migration behavior.

The velocities of the larger 8 μm particles, shown by the black circles in the plot for water, were all approximately $u = 0.30$ m.s^{-1}, which is approximately equal to the fluid velocity at $z/W = \pm 0.25$. This uniformity in the particle velocity occurred because essentially all of the particles were distributed in a diamond-like distribution thus positioned in the same relative location in the underlying parabolic velocity profile. For the HA solution, the particles were located near the channel centerline and translated at a speed that was approximately 10% faster than maximum measured velocity of the fluid.

The fluid velocities at $Q = 6.0$ mL.min^{-1} were sufficiently large that it was necessary to use a short time step between subsequent laser pulses and therefore the velocity profile had to be determined using an auto-correlation. The velocity near the walls could not be readily determined with the auto-correlation due to the small particle displacements there. The velocity profiles for each fluid at this flow rate are compared in Figure 8.4.14 (f). At this larger flow rate, the two profiles were nearly identical indicating that shear thinning was not important and therefore did not play a role in the particle migration behavior. It is also noteworthy that the larger particles lagged behind the local fluid velocity in the Newtonian fluid, but led the fluid in the HA solution. This difference suggests that the larger particles in the HA solution were pulled through the fluid or equivalently that the drag force on the particle was lower in the HA solution than it was in the water. It is well-known that inertia and elasticity can have competing effects on the net drag on a particle (Joseph & Liao, 1994), and hence the tendency of the particles to lead the flow may result from a net reduction in the fluid drag on the particle. For particle migration in Newtonian liquids, it has also been experimentally observed that particles leading the local velocity tend to be driven toward the channel walls (Hogg, 1994), however the opposite was true for the migration of particles in the HA solution, indicating clearly that inertia did not provide the dominant force acting on the particles.

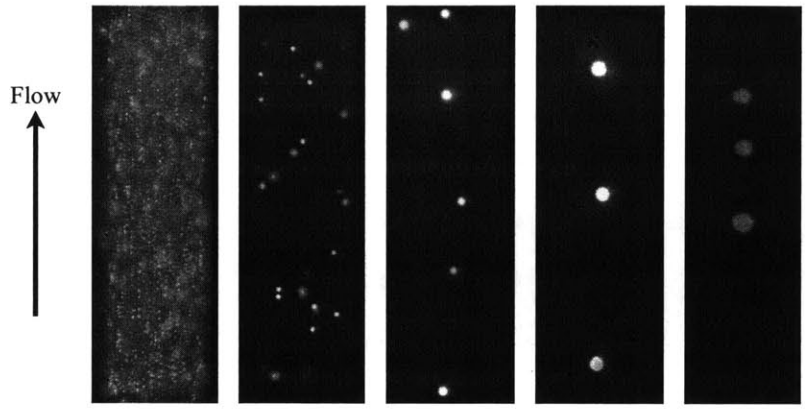

Figure 8.4.15: Snapshots of particles in the channel with flow from bottom to top all at $Q = 6$ mL.min^{-1}, $Re_c = 1273$ and $Wi_c = 170$. Average particle diameters are (a) $a = 1$ μm, (b) $a = 3$ μm, (c) $a = 6$ μm, (d) $a = 10$ μm and (e) $a = 13$ μm.

8.4.5 Effect of Particle Size and Shape and Channel Shape

The role of particle size in confined flows of Newtonian liquids has been previously studied both experimentally and numerically by Di Carlo *et al.* (2009b), who gave scaling relationships for the dependence of the inertial lift forces on fluid velocity, particle size and channel dimensions. Generally, the larger particle Reynolds numbers associated with larger particles result in equilibrium positions that are closer to the channel walls.

Measurements of particle distributions in the HA solution over a range of flow rates were taken using batches of fluid seeded with $a = 1$, 3, 6, 10 or 13 μm fluorescent polystyrene particles (Fluoro-Max, Thermo Scientific). These particle diameters were within the size range of typical cellular material that can be found circulating in blood such as bacteria ($a \approx 1 - 2$ μm), red blood cells ($a \approx 6 - 8$ μm), white blood cells ($a \approx 8 - 10$ μm) and small cancer cells, ($a \gtrsim 13$ μm). Snapshots of the particles across the channel width are shown in Figure 8.4.15. It is quite clear that the larger the particle, the more reliably it could be driven to the channel center. Furthermore, for this channel, there was a clear difference between the migration behavior of the 1 and 3 μm and the 6, 10 and 13 μm particles, as the smaller particles did not migrate to any single dominant position.

To illustrate this point further, particle histograms for the 3 and 6 μm particles are

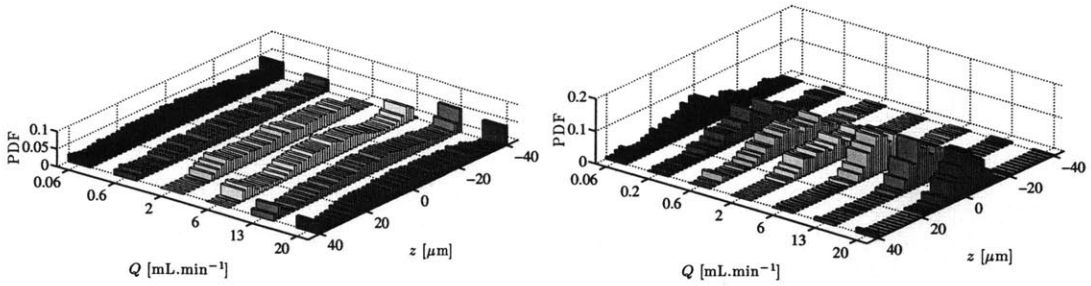

Figure 8.4.16: Histograms of (a) $a = 3$ μm and (b) $a = 6$ μm particles across the channel width over a range of flow rates with the 1000 ppm HA solution.

shown in Figure 8.4.16. For the 3 μm particles, the standard deviations of a normal distribution fit were approximately 20 μm at all flow rates, indicating that the particles were fairly uniformly distributed across the channel width. The slightly larger local concentration of particles near the channel walls at larger flow rates seen in Figure 8.4.16 (a) may have been caused by shear-thinning effects which are known to drive particles toward the wall. For the 6 μm particles shown in Figure 8.4.16 (b), the particles were driven to the channel center (with standard deviations of approximately 8 μm) and the distributions were far more consistent with those of larger particles shown in Figure 8.4.17. In general, higher flow rates and larger particle sizes increased the tendency of particles to be driven to the channel center.

It is also a peculiar fact that while the channel and particle Weissenberg numbers are independent of particle diameter, the particle elasticity number increases as the particle size decreases and yet the apparent effect of viscoelasticity on the migration behavior diminishes as the particle size decreases. For example at $Q = 0.6$ mL.min^{-1} in Figure 8.4.17 (b), while the channel elasticity number was small $El_c = 0.11$, the particle elasticity numbers, based on the rate dependent viscosity, for the 1 μm beads was $El_p = 725$, for the 3 μm beads was $El_p = 81$, for the 6 μm beads was $El_p = 20$, for the 8 μm beads was $El_p = 11$, for the 10 μm beads was $El_p = 7.3$, and for the 13 μm beads was $El_p = 4.2$. This seemingly counterintuitive result can be rationalized by considering the asymptotic analysis of Ho & Leal (1976) for the flow of a second order fluid in the limit of zero Reynolds and Weissenberg numbers. The lateral lift force

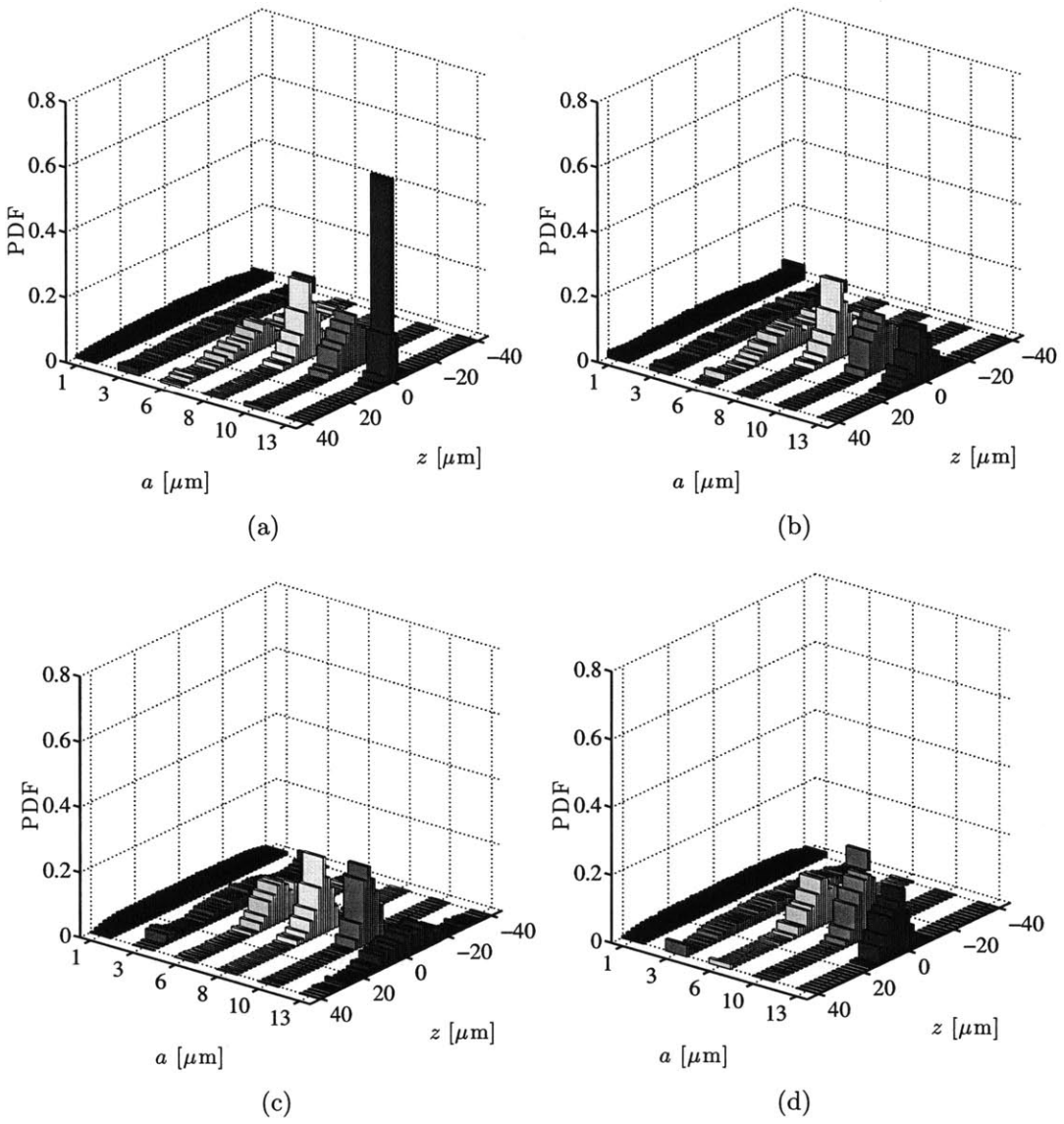

Figure 8.4.17: Particle distributions across the channel width for a range of particle sizes in the 1000 ppm HA solution at (a) $Q = 0.06$ mL.min^{-1}, (b) $Q = 0.6$ mL.min^{-1}, (c) $Q = 6.0$ mL.min^{-1} and (d) $Q = 20.0$ mL.min^{-1}.

on the particle arising from gradients in normal stress differences was found to scale cubically with particle diameter. On the other hand a resistive Stokes drag force on the particle as it travels across streamlines scales only linearly with particle size. Hence, according to this rudimentary analysis (whose validity in the regime of $Re_c \gg 1$ and $Wi_c \gg 1$ is questionable), a smaller particle would require significantly more time to migrate to its equilibrium position, explaining the lack of particle migration observed for the smaller 1 and 3 μm particles. While the magnitude of the particle elasticity number may indicate the relative dominance of elastic or inertial forces acting on the particle, it evidently cannot be used to anticipate the net particle migration behavior observed compared to particles of other sizes. An additional factor to consider is the role of secondary flows on the particle migration, which though caused by normal stress differences, do not necessarily manifest themselves in such a straightforward manner as a unidirectional lateral force balance.

It is known that the presence of viscoelasticity in the flow gives rise to second normal stress differences that drive secondary flows in pressure-driven flow through non-axisymmetric rectilinear channels. Such secondary flows occur in polymer solutions (Xue *et al.*, 1995) as well as suspensions (Ramachandran & Leighton, 2008; Zrehen & Ramachandran, 2013), and their role on particle migration has been recently considered numerically by Villone *et al.* (2013) (see Figure 2.4.4 (a)). In this latter study, it was found that sufficiently small particles could be driven to off-center equilibrium positions generally near the channel corners within the vortex structures of the secondary flow. Typically the secondary flow speeds $\mathcal{U}_{2nd}$ are two to three orders of magnitude smaller than the primary flow speeds, hence a crude estimate of the relevance of secondary flows on particle migration can be ascertained by determining the number of times a material element in a vortex cycles through the channel size within the residence time in the channel. This number is given by $N = L\mathcal{U}_{2nd}/D\mathcal{U}$. Taking the ratio $\mathcal{U}_{2nd}/\mathcal{U} \sim 0.01$, the value of $N \gtrsim 1$, suggesting that secondary flow are not *a priori* negligible for the experiments here.

To investigate the relevance of secondary flows in the particle migration behavior of the HA solution, the particle distributions of 8 μm beads were measured in glass

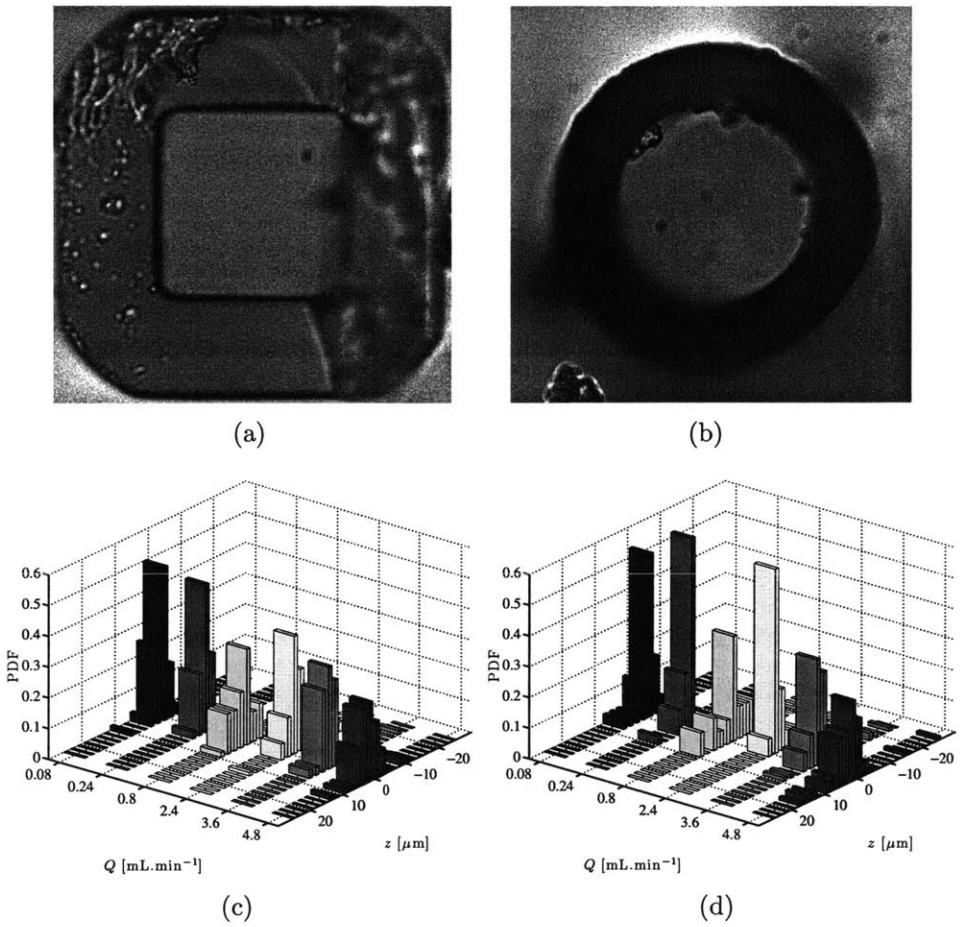

Figure 8.4.18: Bright field images of a (a) 50×50 μm square cross-section glass capillary and (b) 50 μm diameter circular cross-section glass capillary tube. Particle distributions in the HA solution across the channel width over a range of flow rates in a (c) 50×50 μm square glass capillary and a (d) 50 μm diameter cylindrical glass capillary tube. ($15 < Re_c < 1615$ and $9 < Wi_c < 557$.)

capillaries (Vitrocom) with a 50×50 μm square and a 50 μm circular cross-section. The cross sections of each channel are shown in Figure 8.4.18 (a) and (b). Due to the axisymmetry of the cross-section, secondary flows cannot arise in the cylindrical tube but may occur in the square channel (Bird *et al.*, 1987). In the case that the secondary flows dominate the particle migration behavior, the particle distributions in the square channel should be more broadly distributed around the channel centerline.

The particle distributions in both channels over a range of flow rates were acquired at approximately $L_{obs} = 35$ mm ($L_{obs}/D \sim 440$) downstream from the channel inlet and are shown in Figure 8.4.18 (c) and (d). It is clear that the distributions over the range of flow rates in both channels were qualitatively similar, with nearly all particles lying within one particle diameter $\Delta z \pm 8$ μm from the channel centerline. The histograms for each flow rate were also fit with normal distributions, whose standard deviations did not show a systematic difference in the spread of the particles in the square and circular cross-section channels. This result strongly suggests that in the HA solutions studied here, secondary flows did not affect the ultimate equilibrium positions of the 8 μm particles.

The effect of particle shape on the migration in Newtonian fluids has been previously investigated by Hur *et al.* (2011b), who found that for most particles the rotational diameter of a particle was the key parameter that determined its equilibrium position. In Newtonian liquids, for which equilibrium positions are typically near the walls where the shear rates are largest, this finding is sensible for particles of all shapes since the rotation of the particle can play a role in the resultant inertial focusing behavior. For the viscoelastic liquids considered in this Chapter, however, the tendency of particles to be driven toward the channel centerline where the shear rate vanishes suggests that particle rotation may be irrelevant to the final equilibrium migration behavior.

To explore this possibility further, cylindrical cross-linked polyethylene glycol (PEG) particles ($d = 6$ μm, $l = 18$ μm) made with stop-flow lithography (Dendukuri *et al.*, 2007) were seeded in the HA solution. Snapshots of the particles at the end of the channel ($L_{obs} = 35$ mm) over a range of flow rates are shown in Figure 8.4.19. In all cases, the axes of the particles are oriented along the streamlines and near the middle

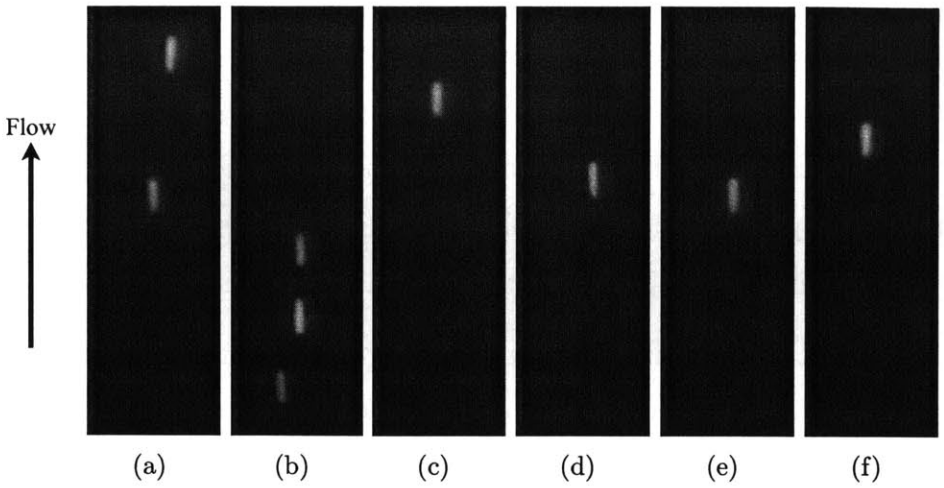

Figure 8.4.19: Snapshots of cross-linked cylindrical polyethylene glycol (PEG) particles ($d = 8$ μm, $l = 30$ μm) flowing in the HA solution at (a) $Q = 0.2$ $(Re_c, Wi_c) = (29, 5.7)$, (b) $Q = 0.6$ $(105, 17)$, (c) $Q = 2.0$ $(397, 56)$, (d) $Q = 13.0$ $(2840, 368)$ and (e) $Q = 20.0$ mL.min^{-1} $(4422, 566)$. The orientation of the particles coincident with the channel centerline is robust across all flow rate and indicates that the particles do not rotate is they travel downstream. (PEG particles courtesy of Ki Wan Bong.)

of the channel, strongly suggesting that they do not rotate as they advect downstream. This alignment of particles with the flow is in agreement with previous observations of the sedimentation of long bodies in viscoelastic liquids (Joseph *et al.*, 1992; Joseph & Liu, 1993). It has been found that when elasticity is the dominant contribution to the stresses on oblong particles they are oriented parallel to the streamlines, whereas in an inertially-dominated flow the axes of the particles are oriented perpendicular to the streamlines. When both effects are important simultaneously, particles can be oriented obliquely with the streamlines. Since the PEG particles shown in Figure 8.4.19 are consistently oriented along the streamlines, it is clear that elasticity plays the dominant role in particle orientation and migration for these oblong particles.

8.5 Summary

In this Chapter, particle migration in water and dilute and semi-dilute solutions of polyethylene oxide and a concentrated solution of hyaluronic acid was studied at simultaneously large Reynolds and Weissenberg numbers. Both rigid spherical polystyrene

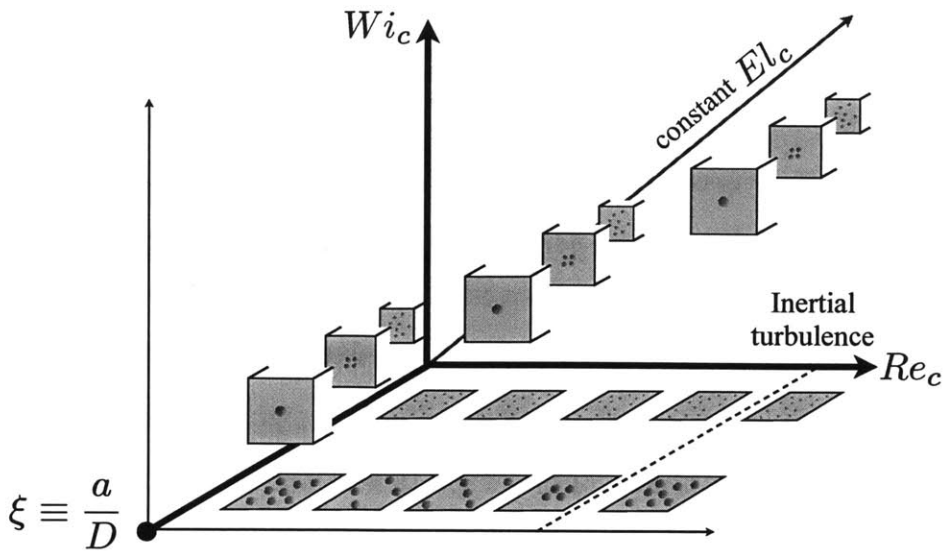

Figure 8.5.1: Schematic illustration of the dependency of particle migration behavior on the channel Reynolds number Re_c, channel Weissenberg number Wi_c and the ratio of the particle diameter to channel hydraulic diameter $\xi \equiv a/D$.

beads with diameter between $1 < a < 13$ μm and oblong polyethylene glycol particles were used. These experiments were performed in a rigid microchannel with a square cross-section made with an epoxy-based fabrication technique enabling pressure drops large enough to observe the onset of turbulent flow in water. The particle migration behavior in the channel was observed with long exposure streakline images, and one and two-dimensional particle distributions were determined from short exposure images captured using a pulsed laser imaging system.

For 8 μm beads in an 80 μm $\times$ 80 μm cross-section channel, four distinct types of particle distributions were observed with increasing channel Reynolds number in water. At low channel Reynolds number ($Re_c \lesssim 10$), no distinct particle migration was observed. For $10 \lesssim Re_c \lesssim 200$, the particles were distributed in a diamond-like pattern, while for $200 \lesssim Re_c \lesssim 1000$ the particles were distributed in a quincunx pattern, and for higher channel Reynolds number up until the transition to turbulence the particles were driven toward the channel center. The velocities of the particles were always equal to or less than the local fluid velocity.

The addition of polymer introduced fluid viscoelasticity, shear thinning and sec-

ondary flows to the overall dynamics of particle migration. In both the polyethylene oxide and hyaluronic acid solution, at channel Weissenberg numbers $Wi_c \gtrsim 1$, the particles were driven toward the channel centerline regardless of the value of the corresponding channel Reynolds number. These trends are illustrated schematically in Figure 8.5.1. Velocimetry measurements of both the water and the HA solution suggested that neither shear thinning nor wall slip played an important role in the migration behavior. Furthermore, elastically-driven secondary flows which depend on the shape of the channel cross-section did not have a significant effect on the equilibrium distribution of the particles. Accordingly, the tendency of the particles to be driven toward the channel centerline was dominated by the viscoelasticity of the liquid. Theoretical analysis shows that this viscoelasticity gives rise to gradients in the normal stress differences and a streamwise tension that acts on rigid particles.

This investigation of flow-induced particle migration in microfluidic devices is the first to comprehensively study the simultaneous roles of fluid inertia and elasticity at large channel Reynolds and Weissenberg numbers using high speed imaging techniques. Thus the combination of streakline images, one and two-dimensional particle distributions as well as velocimetry measurements enables the thorough characterization of particle migration in optically transparent fluids and can be readily adopted for future studies.

Chapter 9

Conclusion

The central aim of this thesis has been on studying the role of viscoelasticity on the flow of complex fluids at large deformation rates. In particular, this work has focused on three topics: firstly, 1) shear banding and other flow inhomogeneities in flows of worm-like micellar fluids, secondly, 2) flow instabilities and extension-dominated flows in microfluidic devices, and finally, 3) inertially and elastically-driven particle migration in microchannels. The utilization of microfluidic devices for rheometry is also a central feature of this study, enabling viscometric measurements at deformation rates as large as $\dot{\gamma} \simeq \mathcal{O}(10^5)$ s^{-1}. With the completion of this study, one can draw the following conclusions:

Firstly, in Chapters 3 and 4, the influence of shear banding on the rheological characterization of worm-like micellar liquids in shear was studied using conventional macroscale rheometric techniques as well as velocimetry measurements. The onset of shear banding occurs for Weissenberg number $Wi \approx 1$. The velocimetry measurements revealed the existence of three shear bands in the cone-and-plate geometry, in contrast to the two-band scenario conventionally assumed, and thus it may have arisen due to the nearly uniform stress field in the gap coupled with the curvature of the flow. The onset of a secondary flow driven by elasticity at $Wi \gtrsim \mathcal{O}(10)$ caused an edge instability and the ejection of the fluid sample from the gap, limiting the range of shear rates over which the cone-and-plate configuration could be used for rheometry. In order to understand the role of shear banding on the onset of the flow instability, an analytical

solution for the velocity and stress field was derived for planar Couette flow using the diffusive Johnson-Segalman model. The inclusion of a non-local diffusive term in the governing equation for the polymeric stress guaranteed the selection of a unique value for the stress plateau and thereby enabled the prediction of a shear banded velocity profile. This analytical result was then utilized to develop a dimensionless stability criterion to anticipate the onset of secondary flows in the base shear-banding flow of worm-like micelles.

Future work on this topic area should study more closely the interplay between normal stress differences and shear banding in a cone-and-plate geometry. The edge instability in steady shear that prevents the rheological characterization at high shear rates is linked to normal stresses in the sample (Skorski & Olmsted, 2011). Furthermore, the break-down in the Lodge-Meissner rule in step strain stress relaxation tests at large strains is likely coupled to the onset of shear banding. A greater understanding of growth of normal stresses in shear-banding liquids would not only improve constitutive models, but it would be valuable for investigating the validity of the proposed linear stability criterion more generally in complex flows. The criterion has been developed assuming a two-banded scenario like that typically seen in the Taylor-Couette geometry, where its validity has been investigated by Fardin & Lerouge (2012). On the other hand, the three-banded scenario in the cone-and-plate configuration may necessitate a reevaluation of this criterion, building on the analysis of Kumar & Larson (2000) for example. The stability criterion has also been developed to predict the onset of a linear instability which requires finite curvature of the streamlines in the underlying base flow. However, it is also expected that viscoelastic liquids in rectilinear base flows are susceptible to subcritical, or non-linear instabilities (Meulenbroek *et al.*, 2004; Morozov & van Saarloos, 2007), which require perturbations of finite amplitude to trigger the secondary flow. For shear-banding worm-like micellar liquids it has been shown experimentally and numerically that the jump in normal stress differences across shear bands in the channel flow drives an interfacial instability that leads to a secondary flow (Nghe *et al.*, 2010). Therefore, more thorough measurements of N_1 and N_2 in shear-banding fluids would greatly improve the accuracy with which the onset of elastically-driven secondary flows can be predicted.

Secondly, in Chapters 5 and 6 the small length scales accessible in microchannels were exploited to achieve high deformation rate flows at low Reynolds number, which is crucial for accurate measurement of viscometric material functions. The behavior of worm-like micellar fluids and other complex fluids was studied in both shear and extension-dominated flows at deformation rates up to $\dot{\gamma} \simeq \mathcal{O}(10^5)$ s^{-1}, which is well above those which could be attained using conventional macroscale rheometric techniques. Pressure measurements and kinematics measurements of the flow in microfluidic devices were enhanced with spatially-resolved measurements of flow-induced birefringence enabling the observation of the evolution of stresses in the channels as well as evidence of non-local effects in steady shear. Furthermore, a framework for the extraction of the effective extensional viscosity from the extension-dominated flow through a microfluidic hyperbolic planar contraction was developed, which can serve as a complement to the shear viscosity microfluidic viscometer described in Pipe *et al.* (2008) for measuring a nominal extensional viscosity.

Microfluidic rheometry now constitutes one of the most effective techniques for extending the range of deformation rates at which the rheological behavior of complex fluids can be characterized to at least $\dot{\gamma} \simeq \mathcal{O}(10^5)$ s^{-1} or beyond. Much of the hardware and fabrication techniques are well established and therefore future development work for this technology should be aimed at the optimization of channel designs to achieve a desired flow type through the incorporation numerical simulations. For example, recent work by Haward *et al.* (2012b) has shown that the extensional kinematics of a cross-slot geometry can be optimized with numerical simulations to achieve a practically homogeneous extensional flow field. The experimental validation of numerical optimization routines using microfluidic devices would also provide constructive feedback for the improvement of viscoelastic constitutive models especially at high Weissenberg numbers.

Finally, in Chapters 7 and 8, the effects of fluid inertia and elasticity on the flow-induced migration of particles in a microchannel was experimentally investigated. The particle tracking analysis (PTA) technique was developed to determine the two-dimensional (y-z plane) distribution of polystyrene beads, white blood cells, and PC-3 cells in diluted and whole blood across both the height and width of the channel. The initial experi-

ments with whole blood at channel Reynolds number up to $Re_c \simeq 200$ in a 93×45 μm^2 channel cross-section demonstrated a dramatic shift in the particle migration behavior compared to the typical behavior in a Newtonian fluid. This radical shift in particle migration behavior arising from the non-Newtonian rheology of whole blood was then more systematically investigated with model non-Newtonian liquids in a square 80×80 μm^2 channel at channel Reynolds numbers up to, and above, the value at the transition to inertially-dominated turbulence. Streakline measurements, ultra-short exposure images, PTA and velocimetry measurements were combined to characterize the migration behavior of a range of particle sizes in viscoelastic liquids at large channel Reynolds number $Re_c \lesssim \mathcal{O}(10^4)$ and Weissenberg number $Wi_c \lesssim 500$. At these flow rates, the particle migration was clearly dominated by the elasticity of the fluid, driving the particles toward a single region in the center of the channel.

One of the major aims of research on particle migration in microfluidic devices is the application of this phenomenon for biomedical devices for isolation of rare cells from the blood stream. Yet, there are many crucial developments that must be made for this technology to become viable. In particular, much of the knowledge of particle migration is empirical, which poses a limitation on the long-term development of this technology that would otherwise benefit from a stronger theoretical understanding. Given the importance of non-linear effects in the migration phenomenon, however, it is unlikely that analytical methods will make much headway particularly for finite channel dimensions and finite particle Reynolds and Weissenberg numbers. Instead, numerical simulations offer the most viable way forward, and while many numerical studies have considered inertial or elastic effects in isolation, no major study of the simultaneous relevance of both effects has yet been undertaken especially with the aim of optimizing a channel shape for a particular separation application. Additional challenges that must be overcome include the design and optimization of separation sections of the microchannel as well as a thorough assessment of the long-term viability of living cells after sustaining the large deformation rates that are endemic to high throughput flows in microfluidic devices. The imaging and velocimetry measurement techniques developed in this thesis, however, constitute a versatile toolset that can be used to study new particle migra-

tion modes in complex physiological fluids, which could enable the isolation of rare cells directly from whole blood at high throughput for use in global health diagnostics.

In short, the overarching focus of this thesis is in the characterization of complex fluids at large deformation rates. One of the major accomplishments of the work is the incorporation of pressure, birefringence and flow kinematics measurements with microfluidic technologies for the rheologcial characterization of complex liquids over a wide range of deformation rates. Microfluidic fabrication methods are now firmly established and can be utilized to create virtually any complex flow geometry desired. This technology enables one to extend the range of deformation rates at which relevant viscometric material functions can be measured well beyond those accessible with conventional macroscale rheometric devices. In time, improved understanding of flows of complex fluids in microfluidic devices stands to make great impact on many fields including materials processing, biomedical devices and separation processes.

Appendix A

Maxwell Model

A.1 Governing Linear Equation

While contemplating the possibility that gases could exhibit viscoelastic behavior, James Clerk Maxwell proposed a constitutive equation for the shear stress, τ, in a linear viscoelastic material having relaxation time, λ and viscosity η (Maxwell, 1867)

$$\tau + \lambda \frac{d\tau}{dt} = \eta\dot{\gamma} \tag{A.1.1}$$

where t is time and $\dot{\gamma}$ is an applied shear strain rate.

A.2 Solving the Linear Maxwell Model

A commonly utilized test in the determination of important rheological properties of a material is small amplitude oscillatory shear (SAOS). In this test, a material sample experiences a sinusoidally varying shear strain in time. The applied shear strain, $\gamma(t)$, obeys the relation $\gamma(t) = \gamma_0 \sin\omega t$, where γ_0 is the shear strain amplitude, ω is the oscillation frequency of the applied strain and t is time. Evidently, the shear strain rate, $\dot{\gamma}$, follows the relation $\dot{\gamma} = \gamma_0\omega\cos\omega t$. If such a deformation is imposed on a material governed by the Maxwell equation, Eq. (A.1.1) becomes

$$\tau + \lambda \frac{d\tau}{dt} = \eta\gamma_0\omega\cos\omega t \tag{A.2.1}$$

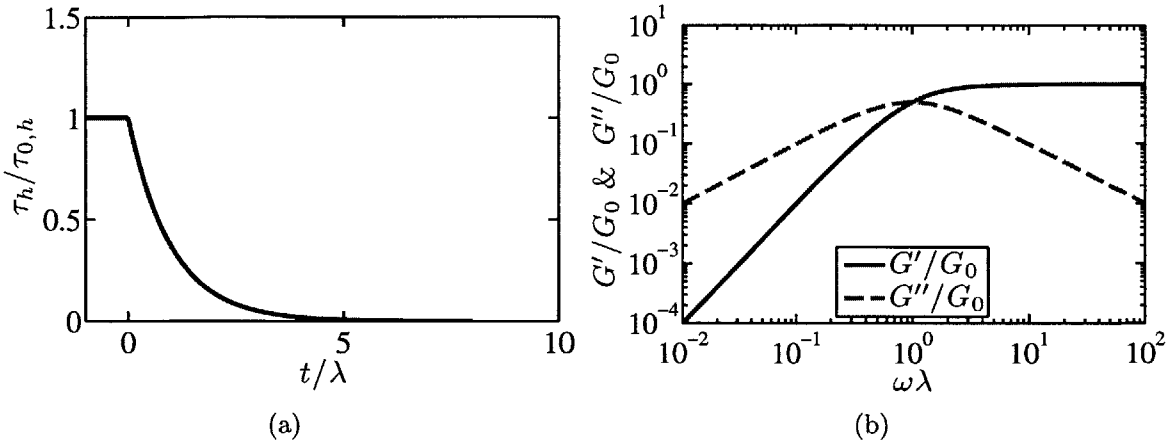

Figure A.2.1: (a) Stress decay for a Maxwell fluid. (b) Normalized moduli for a Maxwell fluid undergoing an oscillatory shear deformation.

The solution to Eq. (A.2.1) consists of a homogenous solution, τ_h, and a particular solution, τ_p, such that $\tau = \tau_h + \tau_p$.

First, we solve for the homogenous solution:

$$\tau_h + \lambda \frac{d\tau_h}{dt} = 0 \tag{A.2.2}$$

Clearly the solution τ_h is given by the relation $\tau_h = \tau_{0,h} e^{-t/\lambda}$, where $\tau_{0,h}$ is the stress applied to the material at $t = 0$, which is then completely removed for all $t > 0$. Eq. (A.2.2) describes the scenario in which a material experiences a constant shear stress of magnitude $\tau_{0,h}$ for all $t < 0$, when at $t = 0$ at the imposed shear deformation is instantly and entirely removed. In this case, for all $t > 0$, the stress in the material decays exponentially with time constant λ as shown in Figure A.2.1 (a).

For the case of small amplitude oscillatory shear, the homogeneous solution is not important since the effect of any non-zero $\tau_{0,h}$ on the material stress, τ, decays exponentially in time, such that in the limit of long times ($t/\lambda \gg 1$) only the particular solution, τ_p will be observed. Consequently $\tau = \tau_p$, and we must solve Eq. (A.2.1).

Since the imposed shear strain rate is sinusoidally varying in time, it is logical to seek a solution for the resultant material stress which takes the form $\tau = A \sin \omega t + B \cos \omega t$, where A and B are coefficients yet to be determined. Since the applied strain obeys $\gamma = \gamma_0 \sin \omega t$, the magnitude of A distinguishes the elastic or *stored* response of the

material, and since the applied shear strain rate obeys $\dot{\gamma} = \gamma_0 \omega \cos \omega t$, the magnitude of B distinguishes the viscous or *lost* response of the material. In this case, Eq. (A.2.1) becomes

$$A \sin \omega t + B \cos \omega t + \lambda\big(A\omega \cos \omega t - B\omega \sin \omega t\big) = \eta \gamma_0 \omega \cos \omega t \tag{A.2.3}$$

When the sine and cosine terms in Eq. (A.2.3) are segregated, we obtain the following two equations which may be used to determine A and B.

$$\begin{aligned} A - \lambda \omega B &= 0 \\ B + \lambda \omega A &= \eta \gamma_0 \omega \end{aligned} \tag{A.2.4}$$

After some algebra we obtain

$$A = G_0 \gamma_0 \left(\frac{(\lambda\omega)^2}{1 + (\lambda\omega)^2} \right) \tag{A.2.5}$$

$$B = G_0 \gamma_0 \left(\frac{(\lambda\omega)}{1 + (\lambda\omega)^2} \right) \tag{A.2.6}$$

where G_0 is called the plateau modulus and is defined $G_0 \equiv \eta/\lambda$. Linearity dictates that A/γ_0 and B/γ_0 are the actual material coefficients of interest in characterizing the linear viscoelastic response of a material to an oscillatory deformation. In this manner the elastic modulus or *storage modulus*, G' is defined as

$$G'(\omega) = G_0 \left(\frac{(\lambda\omega)^2}{1 + (\lambda\omega)^2} \right) \tag{A.2.7}$$

and the viscous modulus or *loss modulus*, G'' is defined as

$$G''(\omega) = G_0 \left(\frac{\lambda\omega}{1 + (\lambda\omega)^2} \right) \tag{A.2.8}$$

These moduli are plotted in Figure A.2.1 (b).

Evidently, the resultant response of a Maxwell fluid to time-dependent, oscillatory deformations obeys the relation

$$\tau = G'(\omega)\gamma_0 \sin \omega t + G''(\omega)\gamma_0 \cos \omega t \tag{A.2.9}$$

or alternatively,

$$\tau = G^* \gamma_0 \sin(\omega t + \phi) \tag{A.2.10}$$

where G^* is called the *complex modulus*, such that $G^* = \sqrt{G'^2 + G''^2}$, and ϕ is the phase angle difference between imposed shear strain and the stress, such that $\phi = \tan^{-1}(G''/G') = 1/\lambda\omega$.

In the limit of $\lambda\omega \to 0$, the storage modulus scales quadratically with ω, but the loss modulus varies linearly with increasing ω. In this regime, the characteristic timescale of the imposed shear strain (*i.e.* ω^{-1}) is very large compared to the relaxation time of the material, and as a consequence the material has ample time to adjust to the imposed strain and as such the work associated with imparting that deformation on the fluid is mostly lost through viscous dissipation. Hence in the limit of $\lambda\omega \to 0$, $G'' \gg G'$ and $\phi \to \pi/2$.

In the opposite limit of $\lambda\omega \to \infty$, the storage modulus is invariant to ω, while the loss modulus decreases linearly with increasing ω. In this regime, the characteristic timescale of the imposed shear strain is very small compared to the relaxation time of the material, and accordingly the material is unable to adjust to the imposed strain and thus the work associated with imparting that deformation on the fluid is mostly stored as elastic energy. Hence in the limit of $\lambda\omega \to \infty$, $G' \gg G''$ and $\phi \to 0$.

The magnitudes of G' and G'' are equal when $\lambda\omega = 1$. At this cross-over frequency, $\omega^{-1} = \lambda$ and $\phi = \pi/4$ and accordingly the characteristic timescale of the imposed deformation is equal to the relaxation time of the material.

A.2.1 Effects of Inertia

At high frequencies, the inertia of the fixture or the fluid can dominate the imposed torque in stress-controlled rheometers. In this analysis, the inertial contribution of only the fixture is accounted for in order to correctly determine the storage and loss moduli of the test sample. For a cone-and-plate fixture with radius R and moment of inertia I, the imposed torque $\mathcal{T}$ is (Macosko, 1994)

$$\begin{aligned} \mathcal{T}(t) &= I\frac{d^2\alpha}{dt^2} + \frac{2}{3}\pi R^3\big(G'(\omega)\gamma(t) + G''(\omega)\dot{\gamma}(t)/\omega\big) \\ &= -I\gamma_0\theta\omega^2\sin(\omega t) + \tfrac{2}{3}\pi R^3\big(G'(\omega)\gamma_0\sin(\omega t) + G''(\omega)\gamma_0\cos(\omega t)\big) \\ &= \big[\tfrac{2}{3}\pi R^3 G'(\omega) - I\theta\omega^2\big]\gamma_0\sin(\omega t) + \tfrac{2}{3}\pi R^3 G''(\omega)\gamma_0\cos(\omega t) \end{aligned} \qquad \text{(A.2.11)}$$

where α is the angular displacement of the fixture relative to its initial angular position

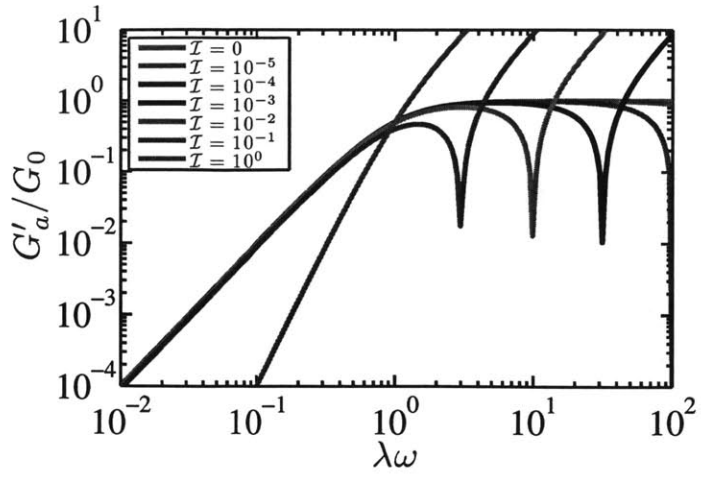

(a)

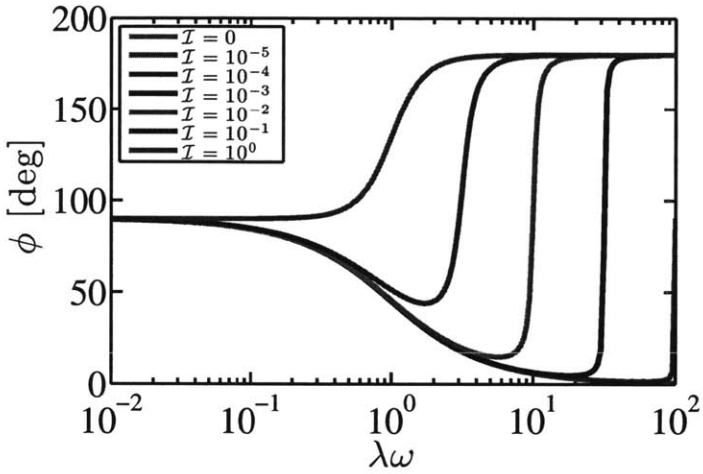

(b)

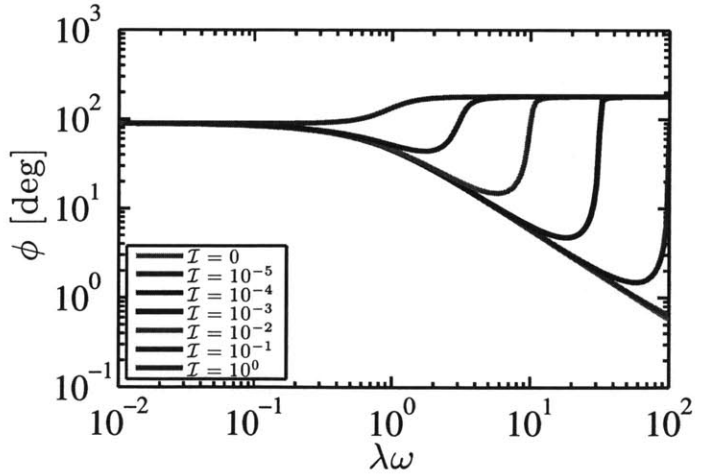

(c)

Figure A.2.2: (a) Apparent storage modulus for a range of moments of inertia. (b) & (c) Phase angle for a range of moments of inertia.

when the test sample is unstrained (*i.e.* $\alpha = 0$ when $\gamma = 0$). Here the angular position of the fixture is $\alpha(t) = \gamma_0\theta\sin(\omega t)$, where θ is the cone angle of a cone-and-plate fixture. Therefore the torque is given by

$$\mathcal{T}(t) = \frac{2}{3}\pi R^3 C\sin(\omega t + \phi) \tag{A.2.12}$$

where

$$C = \sqrt{\left(G'(\omega) - \frac{3I\theta}{2\pi R^3}\omega^2\right)^2 + G''(\omega)^2} \tag{A.2.13}$$

and

$$\phi = \tan^{-1}\left(\frac{G''(\omega)}{G'(\omega) - \frac{3I\theta}{2\pi R^3}\omega^2}\right) \tag{A.2.14}$$

If storage and loss moduli are given by Eq. (A.2.7) and Eq. (A.2.8) then, the apparent storage modulus is

$$\frac{G'_a(\omega)}{G_0} = \left(\frac{(\lambda\omega)^2}{1+(\lambda\omega)^2}\right) - \mathcal{I}(\lambda\omega)^2 \tag{A.2.15}$$

and the phase angle is

$$\phi = \tan^{-1}\left(\frac{1}{\lambda\omega\left[1 - \mathcal{I}(1+(\lambda\omega)^2)\right]}\right) \tag{A.2.16}$$

where $\mathcal{I} \equiv \frac{3I\theta}{2\pi R^3 G_0\lambda^2}$. Plots of the apparent storage modulus and the phase angle are shown in Figure A.2.2.

A.3 A Frame Invariant Viscoelastic Constitutive Model

Despite the versatility of the scalar Maxwell model, it is not frame invariant (Bird *et al.*, 1987). The scalar equation is restricted to 1) small shear rates for which the material viscosity is independent of shear rate, and 2) it cannot predict a normal stress difference, and 3) it cannot predict flows which are themselves moving in some other frame of reference. Some of these deficiencies of the scalar equation can be overcome if one considers the upper convected Maxwell model, given by

$$\mathbf{T} + \lambda \check{\mathbf{T}} = 2\eta \mathbf{D} \tag{A.3.1}$$

where $\mathbf{T}$ is the stress tensor, $\check{\mathbf{T}}$ denotes the upper convected derivative of $\mathbf{T}$ and $2\mathbf{D}$ is the strain rate tensor. The upper convected derivative of $\mathbf{T}$ is defined

$$\check{\mathbf{T}} = \frac{D\mathbf{T}}{Dt} - \left((\nabla \vec{v})^{\dagger} \cdot \mathbf{T} + \mathbf{T} \cdot (\nabla \vec{v}) \right) \tag{A.3.2}$$

where t is time, ∇ is the gradient vector, $\mathbf{V}$ is the velocity vector, and the superscript $\dagger$ denotes the transpose of that vector. The strain rate tensor is defined $\mathbf{D} = \frac{1}{2}(\nabla \vec{v} + (\nabla \vec{v})^{\dagger})$. Eq. (A.3.1) is capable of rectifying deficiencies 2) and 3) of the scalar Maxwell model.

A.3.1 First Normal Stress Coefficient

The first normal stress coefficient for a steady shear flow will now be derived from Eq. (A.3.1).

For an imposed shear strain rate, $\dot{\gamma}_{yx} = \frac{du_x}{dy} = \dot{\gamma}$,

$$\nabla \vec{v} = \dot{\gamma} \begin{bmatrix} 0 & 0 & 0 \\ 1 & 0 & 0 \\ 0 & 0 & 0 \end{bmatrix} \tag{A.3.3}$$

and accordingly

$$\mathbf{D} = \dot{\gamma} \begin{bmatrix} 0 & 1 & 0 \\ 1 & 0 & 0 \\ 0 & 0 & 0 \end{bmatrix} \tag{A.3.4}$$

For a steady deformation, the material derivative of the stress tensor vanishes, and the relevant governing equation is

$$\mathbf{T} - \lambda \Big((\nabla \tilde{\mathbf{v}})^{\dagger} \cdot \mathbf{T} + \mathbf{T} \cdot (\nabla \tilde{\mathbf{v}}) \Big) = \eta \mathbf{D} \tag{A.3.5}$$

When the proper substitutions are made in Eq. (A.3.5), one obtains

$$\begin{bmatrix} \tau_{xx} & \tau_{xy} & \tau_{xz} \\ \tau_{yx} & \tau_{yy} & \tau_{yz} \\ \tau_{zx} & \tau_{zy} & \tau_{zz} \end{bmatrix} - \lambda\dot{\gamma} \begin{bmatrix} 0 & 1 & 0 \\ 0 & 0 & 0 \\ 0 & 0 & 0 \end{bmatrix} \begin{bmatrix} \tau_{xx} & \tau_{xy} & \tau_{xz} \\ \tau_{yx} & \tau_{yy} & \tau_{yz} \\ \tau_{zx} & \tau_{zy} & \tau_{zz} \end{bmatrix} - \lambda\dot{\gamma} \begin{bmatrix} 0 & 0 & 0 \\ 1 & 0 & 0 \\ 0 & 0 & 0 \end{bmatrix} \begin{bmatrix} \tau_{xx} & \tau_{xy} & \tau_{xz} \\ \tau_{yx} & \tau_{yy} & \tau_{yz} \\ \tau_{zx} & \tau_{zy} & \tau_{zz} \end{bmatrix} = \eta\dot{\gamma} \begin{bmatrix} 0 & 1 & 0 \\ 1 & 0 & 0 \\ 0 & 0 & 0 \end{bmatrix} \tag{A.3.6}$$

This result reduces to

$$\begin{bmatrix} \tau_{xx} & \tau_{xy} & \tau_{xz} \\ \tau_{yx} & \tau_{yy} & \tau_{yz} \\ \tau_{zx} & \tau_{zy} & \tau_{zz} \end{bmatrix} - \lambda\dot{\gamma} \begin{bmatrix} \tau_{xy}+\tau_{yx} & \tau_{yy} & \tau_{yz} \\ \tau_{yy} & 0 & 0 \\ \tau_{zy} & 0 & 0 \end{bmatrix} = \eta\dot{\gamma} \begin{bmatrix} 0 & 1 & 0 \\ 1 & 0 & 0 \\ 0 & 0 & 0 \end{bmatrix} \tag{A.3.7}$$

When corresponding stresses are equated, one finds

$$\begin{gathered} \tau_{xx} - \lambda\dot{\gamma}(\tau_{xy}+\tau_{yx}) = 0 \\ \tau_{yx} - \lambda\dot{\gamma}\tau_{yy} = \eta\dot{\gamma} \\ \tau_{zx} - \lambda\dot{\gamma}\tau_{zy} = 0 \\ \tau_{xy} - \lambda\dot{\gamma}\tau_{yy} = \eta\dot{\gamma} \\ \tau_{yy} = 0 \\ \tau_{zy} = 0 \\ \tau_{xz} - \lambda\dot{\gamma}\tau_{yz} = 0 \\ \tau_{yz} = 0 \\ \tau_{zz} = 0 \\ \tau_{yy} - 2\lambda\gamma\tau_{yx} = 0 \end{gathered} \tag{A.3.8}$$

or alternatively,

$$\begin{gathered} \tau_{yx} = \tau_{xy} = \eta\dot{\gamma} \\ \tau_{xx} - \tau_{yy} = 2\lambda\eta\dot{\gamma}^2 = \Psi_1\dot{\gamma}^2 \\ \tau_{yy} = \tau_{zz} = \tau_{yz} = \tau_{yz} = \tau_{xz} = \tau_{zx} = 0 \end{gathered} \tag{A.3.9}$$

Hence, for a Maxwell fluid, the shear stress scales linearly with shear rate and the first normal stress difference scales quadratically with shear rate. The first normal stress coefficient, $\Psi_1 \equiv N_1/\dot{\gamma}^2 = 2\lambda\eta$.

Appendix B

Rheological Measurements with the Offset Cone-and-Plate

B.1 Cone-and-Plate and Plate-Plate

It can be shown (Bird *et al.*, 1987), that the torque $\mathcal{T}_{CP}$ acting on the cone-and-plate (CP) geometry shown in Figure B.1.1 (a) is

$$\frac{3\mathcal{T}_{CP}}{2\pi R^3} = \eta(\dot{\gamma}_R)\dot{\gamma}_R \tag{B.1.1}$$

where R is the radius of the geometry, η is the shear viscosity and $\dot{\gamma}_R$ is the shear rate at the rim which is uniform throughout the sample in the CP geometry. Similarly, the relationship between torque $\mathcal{T}_{PP}$ acting on the plate-plate (PP) geometry shown in Figure B.1.1 (b) and viscosity is (Bird *et al.*, 1987)

$$\frac{\mathcal{T}_{PP}}{2\pi R^3}\left[3 + \frac{d\ln(\mathcal{T}_{PP}/2\pi R^3)}{d\ln(\dot{\gamma}_R)}\right] = \eta(\dot{\gamma}_R)\dot{\gamma}_R \tag{B.1.2}$$

The axial force acting $\mathcal{F}_{CP}$ on the CP geometry is

$$\frac{2\mathcal{F}_{CP}}{\pi R^2} = \Psi_1(\dot{\gamma}_R)\dot{\gamma}_R^2 \tag{B.1.3}$$

where Ψ_1 is the first normal stress coefficient of the test material. The axial force $\mathcal{F}_{PP}$ acting on the PP geometry is

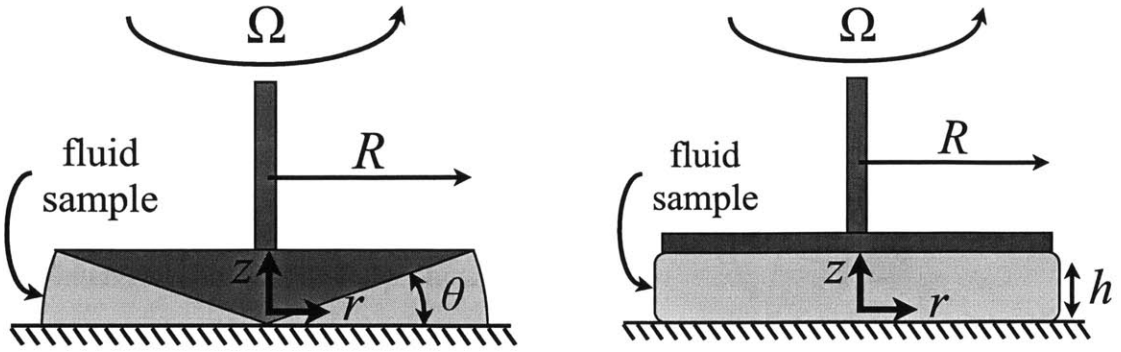

(a) Cone-and-plate.

(b) Parallel plate.

Figure B.1.1: Schematic diagram of the cone-and-plate (CP) and parallel plate (PP) geometries. In the CP geometry the shear rate is spatially uniform and is $\dot{\gamma}(r) = \dot{\gamma}_R = \Omega/\theta$. In the PP geometry the shear rate varies with radial position and is $\dot{\gamma}(r) = r\Omega/h$ so that for the PP $\dot{\gamma}(r = R) = \dot{\gamma}_R = R\Omega/h$.

$$\frac{\mathcal{F}_{PP}}{\pi R^2}\left[2 + \frac{d\ln(\mathcal{F}_{PP}/\pi R^2)}{d\ln(\dot{\gamma}_R)}\right] = \Psi_1(\dot{\gamma}_R)\dot{\gamma}_R^2 - \Psi_2(\dot{\gamma}_R)\dot{\gamma}_R^2 \tag{B.1.4}$$

where Ψ_2 is the second normal stress coefficient of the test material.

B.2 Axial Force for Cone-and-Plate and Plate-Plate

Here we show that for a simple viscoelastic fluid, the axial force measured on a CP geometry will be higher than the axial force measured on a PP geometry of the same radius R and at the same rim shear rate $\dot{\gamma}_R$. Recall that in the CP geometry $\dot{\gamma}_R = \Omega/\theta$, where Ω is the angular rotation speed of the fixture, and θ is the cone angle, whereas in the PP geometry $\dot{\gamma}_R = R\Omega/h$, where h is the gap height.

In the CP geometry the axial force is given by

$$\mathcal{F}_{CP} = \frac{1}{2}N_1\pi R^2 = \frac{1}{2}\Psi_1\dot{\gamma}_R^2\pi R^2 \tag{B.2.1}$$

where N_1 is the first normal stress difference of the specific test fluid.

In the PP geometry, the axial force on the fixture is

$$\mathcal{F}_{PP} = \pi\int_0^R r(N_1 - N_2)dr = \pi\int_0^R r(\Psi_1 - \Psi_2)\dot{\gamma}^2 dr \tag{B.2.2}$$

where N_2 is the second normal stress difference.

If we assume for a simple viscoelastic fluid, Ψ_1 and Ψ_2 are constant, and we assume that $\Psi_2 = -\alpha\Psi_1$ where for most fluids (Larson, 1998) $0 < \alpha < 1$ (but more generally $-1 < \alpha < 1$), the axial force on the PP geometry is

$$\mathcal{F}_{PP} = \pi(1+\alpha)\Psi_1 \int_0^R r\dot{\gamma}^2 dr \tag{B.2.3}$$

For the PP geometry, the shear rate is $\dot{\gamma} = \frac{r}{R}\dot{\gamma}_R$, hence

$$\mathcal{F}_{PP} = \pi(1+\alpha)\Psi_1 \int_0^R \frac{r^3}{R^2}\dot{\gamma}_R^2 dr = (1+\alpha)\Psi_1\dot{\gamma}_R^2\pi R^2 \int_0^1 \mathcal{R}^3 d\mathcal{R} \tag{B.2.4}$$

where $\mathcal{R} \equiv r/R$. So we have

$$\mathcal{F}_{PP} = \frac{1}{4}(1+\alpha)\Psi_1\dot{\gamma}_R^2\pi R^2 \tag{B.2.5}$$

Therefore the ratio of the force measured on the CP and PP geometries for the same values of R and $\dot{\gamma}_R$ is

$$\frac{\mathcal{F}_{CP}}{\mathcal{F}_{PP}} = \frac{\frac{1}{2}\Psi_1\dot{\gamma}_R^2\pi R^2}{\frac{1}{4}(1+\alpha)\Psi_1\dot{\gamma}_R^2\pi R^2} = \frac{2}{1+\alpha} \tag{B.2.6}$$

So for all physically realistic values of α, be they positive *or* negative, we find that the axial force measured by the CP geometry should be larger than the the axial force measured on the PP geometry.

B.3 Offset Cone-and-Plate

In this derivation, we calculate the torque and axial force acting on an offset cone-and-plate (OCP) geometry, first studied by Jackson & Kaye (1966), shown in Figure B.3.1. For a given OCP geometry with radius R, angle θ (where $0 \leq \theta \ll 1$), height h ($h \geq 0$) and angular rotation rate Ω, the shear rate in the absence of secondary flows is given by

$$\dot{\gamma}(r) = \frac{r\Omega}{h + r\theta} \tag{B.3.1}$$

Hence the shear rate at the rim for the OCP is

$$\dot{\gamma}_R = \frac{R\Omega}{h + R\theta} \tag{B.3.2}$$

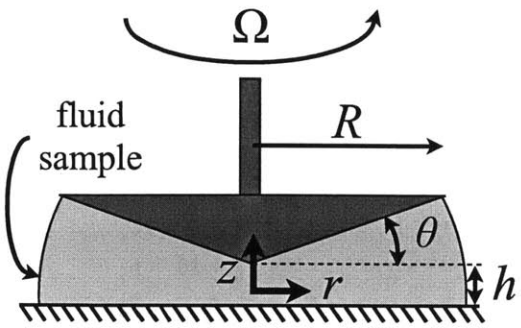

Figure B.3.1: Schematic diagram of the offset cone-and-plate geometry.

We can invert the relationship between r and $\dot{\gamma}$ to obtain

$$r = \frac{h\dot{\gamma}}{\Omega - \theta\dot{\gamma}} \tag{B.3.3}$$

Therefore

$$\frac{dr}{d\dot{\gamma}} = \frac{h\Omega}{\left(\Omega - \theta\dot{\gamma}\right)^2} \tag{B.3.4}$$

If we define the following dimensionless quantities $\mathcal{R} \equiv r/R$, and $\kappa \equiv R\theta/h$ $(0 \leq \kappa \leq \infty)$, then we also have the relationships

$$\frac{\theta}{\Omega} = \frac{\kappa}{\dot{\gamma}_R\left(1+\kappa\right)} \tag{B.3.5}$$

and

$$\frac{h}{\Omega} = \frac{R}{\dot{\gamma}_R\left(1+\kappa\right)} \tag{B.3.6}$$

and

$$\frac{\dot{\gamma}(\mathcal{R})}{\dot{\gamma}_R} = \frac{(1+\kappa)\mathcal{R}}{1+\kappa\mathcal{R}} \tag{B.3.7}$$

B.3.1 Torque

We can derive the expected torque on the offset cone-and-plate (OCP) geometry using the following equation

$$\mathcal{T}_{OCP} = 2\pi \int_0^R \eta(\dot{\gamma})\dot{\gamma} r^2 dr \tag{B.3.8}$$

If we substitute for r in terms of $\dot{\gamma}$ and other parameters, we have

$$\mathcal{T}_{OCP} = 2\pi \int_0^{\dot{\gamma}_R} \eta(\dot{\gamma})\dot{\gamma} r(\dot{\gamma})^2 \frac{dr}{d\dot{\gamma}} d\dot{\gamma} = 2\pi \int_0^{\dot{\gamma}_R} \eta(\dot{\gamma}) \frac{h^3\Omega}{\left(\Omega - \theta\dot{\gamma}\right)^4} \dot{\gamma}^3 d\dot{\gamma} \tag{B.3.9}$$

Further substitution yields

$$\mathcal{T}_{OCP} = 2\pi R^3 \int_0^{\dot{\gamma}_R} \eta(\dot{\gamma}) \frac{1}{(1+\kappa)^3} \frac{1}{\left(1 - \frac{\theta\dot{\gamma}}{\Omega}\right)^4} \left(\frac{\dot{\gamma}}{\dot{\gamma}_R}\right)^3 d\dot{\gamma} = 2\pi R^3 \int_0^{\dot{\gamma}_R} \eta(\dot{\gamma}) \frac{1+\kappa}{\left(1 + \kappa\left(1 - \frac{\dot{\gamma}}{\dot{\gamma}_R}\right)\right)^4} \left(\frac{\dot{\gamma}}{\dot{\gamma}_R}\right)^3 d\dot{\gamma} \tag{B.3.10}$$

This result is also equivalent to

$$\frac{\mathcal{T}_{OCP}\dot{\gamma}_R^3}{2\pi R^3}(1+\kappa)^3 = \int_0^{\dot{\gamma}_R} \eta(\dot{\gamma}) \frac{1}{\left(1 - \frac{\theta\dot{\gamma}}{\Omega}\right)^4} \dot{\gamma}^3 d\dot{\gamma} \tag{B.3.11}$$

And if we replace κ using Eq. (B.3.5), we have

$$\frac{\mathcal{T}_{OCP}}{2\pi R^3} \frac{\dot{\gamma}_R^3}{\left(1 - \frac{\theta\dot{\gamma}_R}{\Omega}\right)^3} = \int_0^{\dot{\gamma}_R} \eta(\dot{\gamma}) \frac{1}{\left(1 - \frac{\theta\dot{\gamma}}{\Omega}\right)^4} \dot{\gamma}^3 d\dot{\gamma} \tag{B.3.12}$$

To determine the relationship between torque and viscosity for an arbitrary $\eta(\dot{\gamma})$, we can proceed in two ways.

Holding Ω/θ Constant

If we perform a set of experiments for which we hold the parameter Ω/θ constant for different gap heights h (*i.e.* varying κ), then we can use the Leibniz theorem on Eq. (B.3.12) to obtain

$$\left.\frac{d}{d\dot{\gamma}_R}\right|_{\Omega/\theta} \left\{ \frac{\mathcal{T}_{OCP}}{2\pi R^3} \frac{\dot{\gamma}_R^3}{\left(1 - \frac{\theta\dot{\gamma}_R}{\Omega}\right)^3} \right\} = \int_0^{\dot{\gamma}_R} \left.\frac{\partial}{\partial\dot{\gamma}_R}\right|_{\Omega/\theta} \left\{ \eta(\dot{\gamma}) \frac{1}{\left(1 - \frac{\theta\dot{\gamma}}{\Omega}\right)^4} \dot{\gamma}^3 d\dot{\gamma} \right\} + \frac{\eta(\dot{\gamma}_R)\dot{\gamma}_R^3}{\left(1 - \frac{\theta\dot{\gamma}_R}{\Omega}\right)^4} \tag{B.3.13}$$

And hence

$$\boxed{\eta(\dot{\gamma}_R)\dot{\gamma}_R = \frac{\mathcal{T}_{OCP}}{2\pi R^3}\left[3 + \frac{1}{1+\kappa} \left.\frac{d\ln\left(\mathcal{T}_{OCP}/2\pi R^3\right)}{d\ln\left(\dot{\gamma}_R\right)}\right|_{\Omega/\theta}\right]} \tag{B.3.14}$$

One can show via the chain rule that this is equivalent to

$$\boxed{\eta(\dot{\gamma}_R)\dot{\gamma}_R = \frac{\mathcal{T}_{OCP}}{2\pi R^3}\left[3 + \left.\frac{d\ln\left(\mathcal{T}_{OCP}/2\pi R^3\right)}{d\ln\left(\kappa\right)}\right|_{\Omega/\theta}\right]} \tag{B.3.15}$$

This result clearly reduces to the CP and PP results in the appropriate limits for κ. In the case of the CP, $\kappa \to \infty$ and we have Eq. (B.1.1), and the condition of holding the ratio Ω/θ constant is not required, since the derivative term is eliminated. In the case of the PP, $\kappa = 0$ and we have Eq. (B.1.2), and the condition of holding the ratio Ω/θ constant is automatically satisfied since $\theta = 0$ in the case of PP.

Varying Ω/θ

If we wish to evaluate the differential term for a single experiment at a given gap value of h (*i.e.* constant κ), then we must consider the derivative in which we allow the ratio Ω/θ to vary. In this case we have

$$\frac{d}{d\dot{\gamma}_R}\left\{\frac{\mathcal{T}_{OCP}\dot{\gamma}_R^3}{2\pi R^3}\right\} = \int_0^{\dot{\gamma}_R}\frac{\partial}{\partial\dot{\gamma}_R}\left\{\eta(\dot{\gamma})\frac{1+\kappa}{\left(1+\kappa\left(1-\frac{\dot{\gamma}}{\dot{\gamma}_R}\right)\right)^4}\dot{\gamma}^3 d\dot{\gamma}\right\} + \eta(\dot{\gamma}_R)\dot{\gamma}_R^3\left(1+\kappa\right) \tag{B.3.16}$$

This gives

$$\frac{d}{d\dot{\gamma}_R}\left\{\frac{\mathcal{T}_{OCP}\dot{\gamma}_R^3}{2\pi R^3}\right\} = -\int_0^{\dot{\gamma}_R}\eta(\dot{\gamma})\frac{4\kappa\left(1+\kappa\right)}{\dot{\gamma}_R^2\left(1+\kappa\left(1-\frac{\dot{\gamma}}{\dot{\gamma}_R}\right)\right)^5}\dot{\gamma}^4 d\dot{\gamma} + \eta(\dot{\gamma}_R)\dot{\gamma}_R^3\left(1+\kappa\right) \tag{B.3.17}$$

Without *a priori* knowledge of the functional form of $\eta(\dot{\gamma})$ it is difficult to proceed using this latter route.

B.3.2 Axial Force

We can derive the expected axial force on the offset cone-and-plate (OCP) geometry using the following equation

$$\mathcal{F}_{OCP} = \pi\int_0^R r(N_1 - N_2)dr + \pi\int_0^R rN_2\left(\frac{r\theta}{h+r\theta}\right)dr = \pi\int_0^R r(\Psi_1 - \Psi_2)\dot{\gamma}^2 dr + \pi\int_0^R r\Psi_2\dot{\gamma}^2\left(\frac{r\theta}{h+r\theta}\right)dr \tag{B.3.18}$$

This result is equivalent to

$$\mathcal{F}_{OCP} = \pi \int_0^R \left\{ (\Psi_1 - \Psi_2) + \Psi_2 \left(\frac{r\theta}{h + r\theta} \right) \right\} \dot{\gamma}^2 r dr = \pi \int_0^R \left\{ (\Psi_1 - \Psi_2) + \Psi_2 \frac{\theta}{\Omega} \left(\frac{r\Omega}{h + r\theta} \right) \right\} \dot{\gamma}^2 r dr \tag{B.3.19}$$

Again, if we substitute for r in terms of $\dot{\gamma}$ and other parameters, we have

$$\mathcal{F}_{OCP} = \pi \int_0^{\dot{\gamma}_R} \left\{ (\Psi_1 - \Psi_2) + \Psi_2 \frac{\theta}{\Omega} \dot{\gamma} \right\} \dot{\gamma}^2 r(\dot{\gamma}) \frac{dr}{d\dot{\gamma}} d\dot{\gamma} = \pi \int_0^{\dot{\gamma}_R} \left\{ (\Psi_1 - \Psi_2) + \Psi_2 \frac{\theta}{\Omega} \dot{\gamma} \right\} \frac{h^2 \Omega}{(\Omega - \theta\dot{\gamma})^3} \dot{\gamma}^3 d\dot{\gamma} \tag{B.3.20}$$

Further substitution yields

$$\begin{aligned} \mathcal{F}_{OCP} &= \pi R^2 \int_0^{\dot{\gamma}_R} \left\{ (\Psi_1 - \Psi_2) + \Psi_2 \frac{\theta}{\Omega} \dot{\gamma} \right\} \frac{1}{(1+\kappa)^2} \frac{1}{\left(1 - \frac{\theta\dot{\gamma}}{\Omega}\right)^3} \frac{\dot{\gamma}^3}{\dot{\gamma}_R^2} d\dot{\gamma} \\ &= \pi R^2 \int_0^{\dot{\gamma}_R} \left\{ (\Psi_1 - \Psi_2) + \Psi_2 \frac{\kappa}{1+\kappa} \frac{\dot{\gamma}}{\dot{\gamma}_R} \right\} \frac{1+\kappa}{\left(1 + \kappa\left(1 - \frac{\dot{\gamma}}{\dot{\gamma}_R}\right)\right)^3} \frac{\dot{\gamma}^3}{\dot{\gamma}_R^2} d\dot{\gamma} \end{aligned} \tag{B.3.21}$$

These results are also equivalent to

$$\begin{aligned} \frac{\mathcal{F}_{OCP} \dot{\gamma}_R^2}{\pi R^2} (1+\kappa)^2 &= \int_0^{\dot{\gamma}_R} \left\{ (\Psi_1 - \Psi_2) + \Psi_2 \frac{\theta}{\Omega} \dot{\gamma} \right\} \frac{1}{\left(1 - \frac{\theta\dot{\gamma}}{\Omega}\right)^3} \dot{\gamma}^3 d\dot{\gamma} \\ &= \int_0^{\dot{\gamma}_R} \left\{ (\Psi_1 - \Psi_2) + \Psi_2 \frac{\kappa}{1+\kappa} \frac{\dot{\gamma}}{\dot{\gamma}_R} \right\} \frac{(1+\kappa)^3}{\left(1 + \kappa\left(1 - \frac{\dot{\gamma}}{\dot{\gamma}_R}\right)\right)^3} \dot{\gamma}^3 d\dot{\gamma} \end{aligned} \tag{B.3.22}$$

Again, if we replace κ using Eq. (B.3.5), we have

$$\frac{\mathcal{F}_{OCP}}{\pi R^2} \frac{\dot{\gamma}_R^2}{\left(1 - \frac{\theta\dot{\gamma}_R}{\Omega}\right)^2} = \int_0^{\dot{\gamma}_R} \left\{ (\Psi_1 - \Psi_2) + \Psi_2 \frac{\theta}{\Omega} \dot{\gamma} \right\} \frac{1}{\left(1 - \frac{\theta\dot{\gamma}}{\Omega}\right)^3} \dot{\gamma}^3 d\dot{\gamma} \tag{B.3.23}$$

As before, to determine the relationship between axial force and normal stress coefficients for arbitrary $\Psi_1(\dot{\gamma})$ and $\Psi_2(\dot{\gamma})$, we can proceed in two ways.

Holding Ω/θ Constant

If we perform a set of experiments for which we hold the parameter Ω/θ constant for different gap heights h (*i.e.* varying κ), then we can use the Leibniz theorem on the upper equation in Eq. (B.3.22) to obtain

$$\left.\frac{d}{d\dot{\gamma}_R}\right|_{\Omega/\theta}\left\{\frac{\mathcal{F}_{OCP}}{\pi R^2}\frac{\dot{\gamma}_R^2}{\left(1-\frac{\theta\dot{\gamma}_R}{\Omega}\right)^2}\right\} = \int_0^{\dot{\gamma}_R}\left.\frac{\partial}{\partial\dot{\gamma}_R}\right|_{\Omega/\theta}\left\{\left\{(\Psi_1-\Psi_2)+\Psi_2\frac{\theta}{\Omega}\dot{\gamma}\right\}\frac{1}{\left(1-\frac{\theta\dot{\gamma}}{\Omega}\right)^3}\dot{\gamma}^3 d\dot{\gamma}\right\}$$
$$+\left\{\left\{(\Psi_1-\Psi_2)+\Psi_2\frac{\theta}{\Omega}\dot{\gamma}_R\right\}\frac{1}{\left(1-\frac{\theta\dot{\gamma}_R}{\Omega}\right)^3}\dot{\gamma}_R^3\right\} \tag{B.3.24}$$

And hence

$$\boxed{\Psi_1\dot{\gamma}_R^2-\frac{1}{1+\kappa}\Psi_2\dot{\gamma}_R^2=\frac{\mathcal{F}_{OCP}}{\pi R^2}\left[2+\frac{1}{1+\kappa}\left.\frac{d\ln\left(\mathcal{F}_{OCP}/\pi R^2\right)}{d\ln\left(\dot{\gamma}_R\right)}\right|_{\Omega/\theta}\right]} \tag{B.3.25}$$

Again, one can show via the chain rule that this is equivalent to

$$\boxed{\Psi_1\dot{\gamma}_R^2-\frac{1}{1+\kappa}\Psi_2\dot{\gamma}_R^2=\frac{\mathcal{F}_{OCP}}{\pi R^2}\left[2+\left.\frac{d\ln\left(\mathcal{F}_{OCP}/\pi R^2\right)}{d\ln\left(\kappa\right)}\right|_{\Omega/\theta}\right]} \tag{B.3.26}$$

Once again, this result reduces to the CP and PP results in the appropriate limits for κ. In the case of the CP, $\kappa\to\infty$ and we have Eq. (B.1.3), and the condition of holding the ratio Ω/θ constant is not required, since the derivative term is eliminated. In the case of the PP, $\kappa=0$ and we have Eq. (B.1.4), and the condition of holding the ratio Ω/θ constant is automatically satisfied since $\theta=0$ in the case of PP.

Varying Ω/θ

If we wish to evaluate the differential term for a single experiment of a given gap value of κ, then we must consider the derivative in which we allow the ratio Ω/θ to vary. In this case we have

$$\frac{d}{d\dot{\gamma}_R}\left\{\frac{\mathcal{F}_{OCP}\dot{\gamma}_R^2}{\pi R^2}\right\} = \int_0^{\dot{\gamma}_R}\frac{\partial}{\partial\dot{\gamma}_R}\left\{\left\{(\Psi_1-\Psi_2)+\Psi_2\frac{\kappa}{1+\kappa}\frac{\dot{\gamma}}{\dot{\gamma}_R}\right\}\frac{1+\kappa}{\left(1+\kappa\left(1-\frac{\dot{\gamma}}{\dot{\gamma}_R}\right)\right)^3}\dot{\gamma}^3 d\dot{\gamma}\right\}$$
$$+\left\{(1+\kappa)\Psi_1-\Psi_2\right\}\dot{\gamma}_R^3 \tag{B.3.27}$$

This gives

$$\frac{d}{d\dot{\gamma}_R}\left\{\frac{\mathcal{F}_{OCP}\dot{\gamma}_R^2}{\pi R^2}\right\} = -\int_0^{\dot{\gamma}_R}\left\{(\Psi_1-\Psi_2)\frac{3(1+\kappa)}{\left(1+\kappa\left(1-\frac{\dot{\gamma}}{\dot{\gamma}_R}\right)\right)^4} + \Psi_2\left(\frac{1}{\left(1+\kappa\left(1-\frac{\dot{\gamma}}{\dot{\gamma}_R}\right)\right)^3}+\frac{3\kappa}{\left(1+\kappa\left(1-\frac{\dot{\gamma}}{\dot{\gamma}_R}\right)\right)^4}\frac{\dot{\gamma}}{\dot{\gamma}_R}\right)\right\}\frac{\kappa\dot{\gamma}^4}{\dot{\gamma}_R^2}d\dot{\gamma} + \left\{(1+\kappa)\Psi_1-\Psi_2\right\}\dot{\gamma}_R^3 \tag{B.3.28}$$

Likewise, without *a priori* knowledge of the functional form of $\Psi_1(\dot{\gamma})$ and $\Psi_2(\dot{\gamma})$ it is difficult to proceed using this latter route.

B.4 Torque and Axial Force for Criminale-Ericksen-Filbey (CEF) Fluid

Following the derivation in Bird *et al.* (1987), we can show that for simple shear, the stress tensor depends only on three kinematics tensors $\gamma_{(1)}$, $\gamma_{(2)}$ and $\{\gamma_{(1)}\cdot\gamma_{(1)}\}$. Accordingly we can describe the stresses in simple shear by

$$\begin{aligned}\tau_{xy} &= \eta(\dot{\gamma})\dot{\gamma}\\ N_1 \equiv \tau_{xx}-\tau_{yy} &= \Psi_1(\dot{\gamma})\dot{\gamma}^2\\ N_2 \equiv \tau_{yy}-\tau_{zz} &= \Psi_2(\dot{\gamma})\dot{\gamma}^2\end{aligned} \tag{B.4.1}$$

where η is the viscosity, N_1 is the first normal stress difference ($N_1 > 0$ and $\Psi_1(\dot{\gamma}) > 0$) and N_2 is the second normal stress difference ($N_2 < 0$ and $\Psi_2(\dot{\gamma}) < 0$ generally).

B.4.1 Torque for a Second Order Fluid

To calculate the torque acting on the upper fixture we have Eq. (B.4.1). If we assume that the viscosity is constant, then the integral expression for the OCP becomes

$$\begin{aligned}\mathcal{T}_{OCP} &= 2\pi\int_0^R \eta\dot{\gamma}r^2dr\\ &= 2\pi\eta\int_0^R\frac{r\Omega}{h+r\theta}r^2dr\\ &= 2\pi\eta\dot{\gamma}_R R^3(1+\kappa)\int_0^1\frac{\mathcal{R}^3}{1+\kappa\mathcal{R}}d\mathcal{R}\\ &= \frac{2}{3}\pi\eta\dot{\gamma}_R R^3\left(1-\frac{1}{2\kappa}+\frac{3}{2\kappa^2}+\frac{3}{\kappa^3}-3\frac{(1+\kappa)}{\kappa^4}\ln(1+\kappa)\right)\end{aligned} \tag{B.4.2}$$

Recall that for the CP geometry, the expression for torque is given by

$$\mathcal{T}_{CP} = \frac{2}{3}\pi\eta\dot{\gamma}_R R^3 \tag{B.4.3}$$

A plot of Eq. (B.4.2) normalized by $\mathcal{T}_{CP}$ for a constant value of $\dot{\gamma}_R$ is shown in Figure B.4.1 (a) and (b). In the CP limit $\kappa \to \infty$, the normalized torque is equal to unity, as expected. In the limit $\kappa \to 0$, the normalized torque approaches the value expected for a constant viscosity fluid in a PP geometry which is given by

$$\mathcal{T}_{PP} = \frac{1}{2}\pi\eta\dot{\gamma}_R R^3 \tag{B.4.4}$$

The ratio between these two values is $\mathcal{T}_{PP}/\mathcal{T}_{CP} = 0.75$, which is the asymptotic limit shown in Figure B.4.1 (a) and (b).

In order to apply the results of Eq. (B.3.14), however, the ratio of Ω/θ must be held constant to evaluate the derivative term. Substituting Eq. (B.3.5) into Eq. (B.4.2) to eliminate $\dot{\gamma}_R$, the new result is

$$\mathcal{T}_{OCP} = \frac{2}{3}\pi\eta\frac{\Omega}{\theta}R^3\frac{\kappa}{(1+\kappa)}\left(1 - \frac{1}{2\kappa} + \frac{3}{2\kappa^2} + \frac{3}{\kappa^3} - 3\frac{(1+\kappa)}{\kappa^4}\ln(1+\kappa)\right) \tag{B.4.5}$$

Plots of Eq. (B.4.5) normalized by $\frac{2}{3}\pi\eta\frac{\Omega}{\theta}R^3$ for a constant value of Ω/θ are shown in Figure B.4.1 (c) and (d).

B.4.2 Axial Force for Simple Fluid

We also assume, as before, that $\Psi_1 = -\alpha\Psi_2$. Substituting these expressions into Eq. (B.3.19), we have

$$\begin{aligned}
\mathcal{F}_{OCP} &= \pi\int_0^R \left\{(\Psi_1 - \Psi_2) + \Psi_2\left(\frac{r\theta}{h + r\theta}\right)\right\}\dot{\gamma}^2 r dr \\
&= \Psi_1\dot{\gamma}_R^2\pi R^2(1+\kappa)^2\int_0^1 \left\{(1+\alpha)\frac{\mathcal{R}^3}{(1+\kappa\mathcal{R})^2} - \alpha\kappa\frac{\mathcal{R}^4}{(1+\kappa\mathcal{R})^3}\right\}d\mathcal{R} \\
&= \frac{1}{2}\Psi_1\dot{\gamma}_R^2\pi R^2\left\{1 - (1-\alpha)\left(\frac{2}{\kappa} + \frac{9}{\kappa^2} + \frac{6}{\kappa^3} - 6\frac{(1+\kappa)^2}{\kappa^4}\ln(1+\kappa)\right)\right\}
\end{aligned} \tag{B.4.6}$$

Plots of this result are shown in Figure B.4.2 (a) and (b).

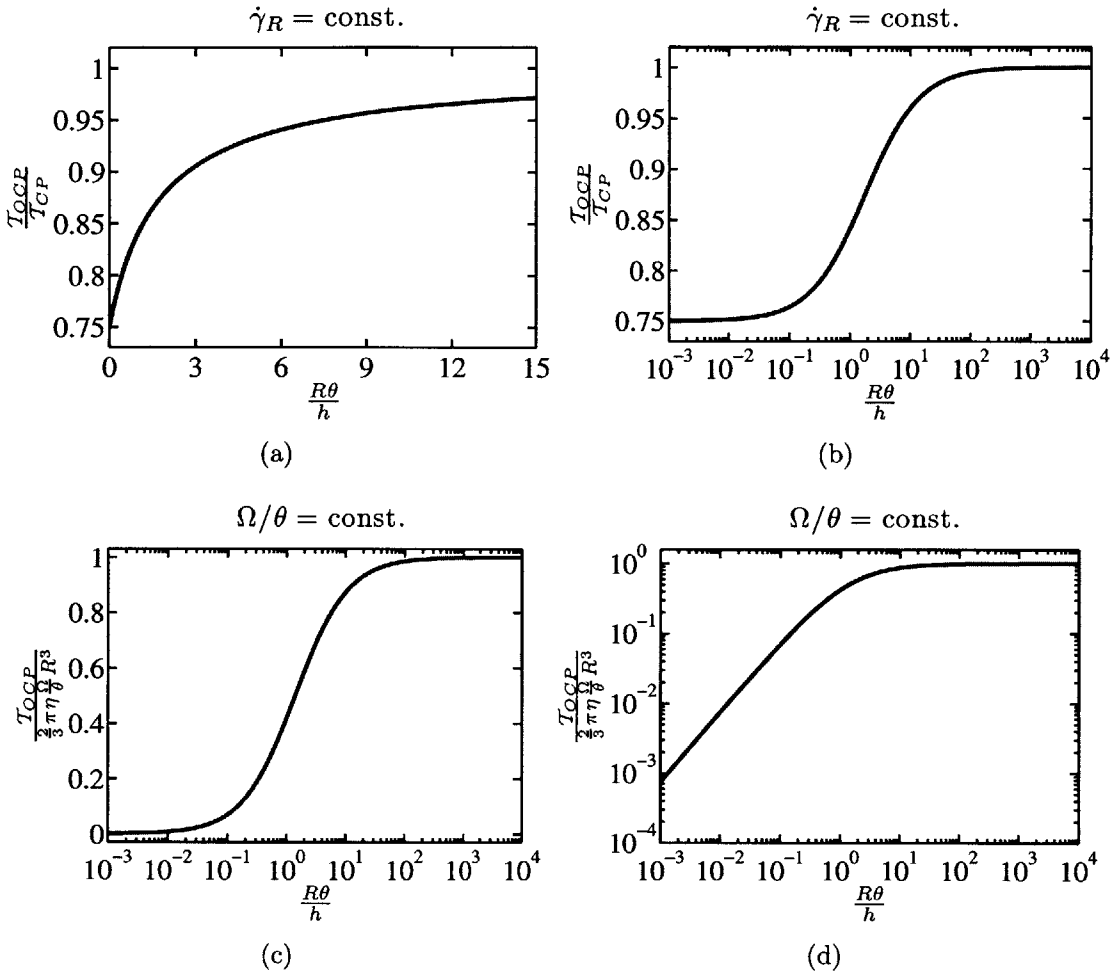

Figure B.4.1: Normalized torque for a second order fluid with constant shear viscosity measured with an offset cone-and-plate geometry. (a) & (b) Torque dependence on $\kappa = \frac{R\theta}{h}$ holding $\dot{\gamma}_R$ constant. (c) & (d) Torque dependence on $\kappa = \frac{R\theta}{h}$ holding Ω/θ constant.

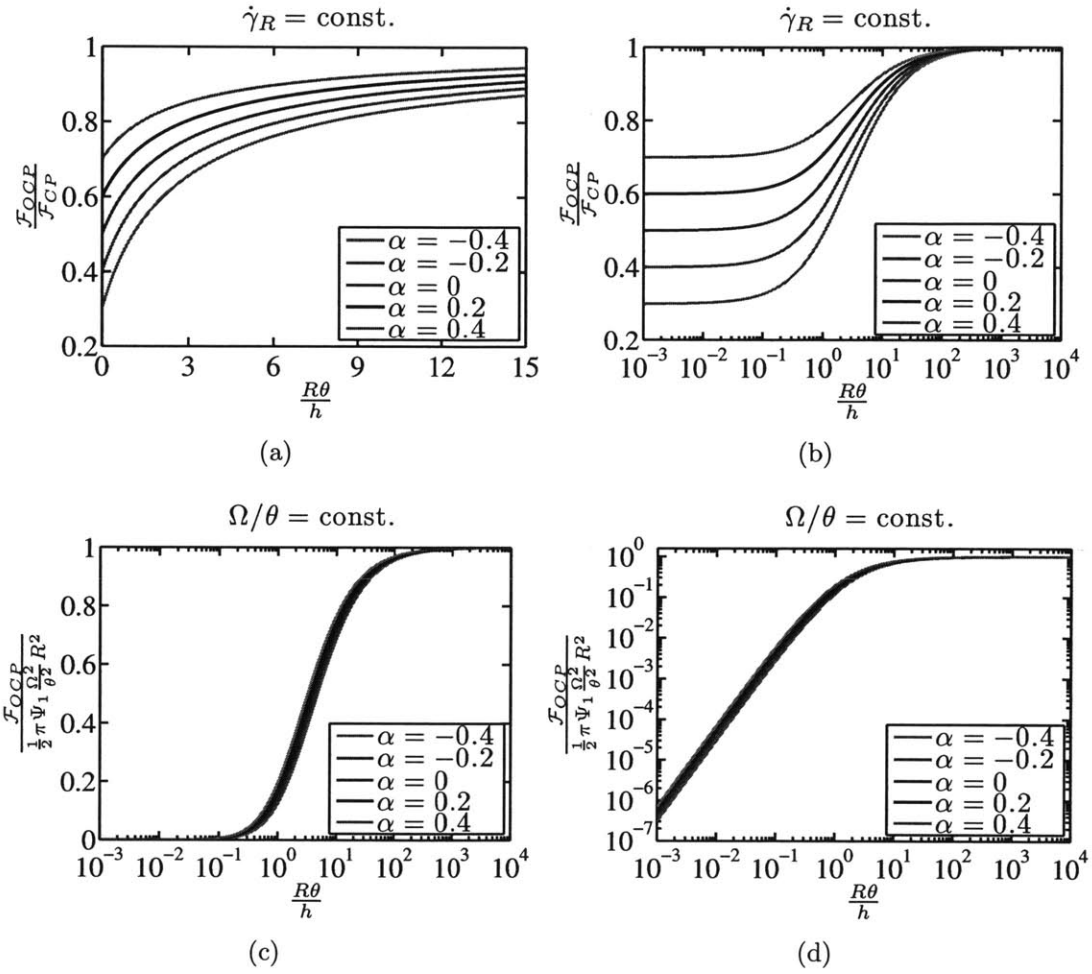

Figure B.4.2: Normalized axial force at different values of α for a second order fluid with constant normal stress coefficients measured with an offset cone-and-plate geometry. (a) & (b) Force dependence on $\kappa = \frac{R\theta}{h}$ holding $\dot{\gamma}_R$ constant. (c) & (d) Force dependence on $\kappa = \frac{R\theta}{h}$ holding Ω/θ constant.

As before, in order to apply the results of Eq. (B.3.25), the ratio Ω/θ must be held constant. Substituting Eq. (B.3.5) into Eq. (B.4.6) to eliminate $\dot{\gamma}_R$, the new result is

$$\mathcal{F}_{OCP} = \frac{1}{2}\Psi_1 \frac{\Omega^2}{\theta^2}\pi R^2 \frac{\kappa^2}{(1+\kappa)^2}\left\{1-(1-\alpha)\left(\frac{2}{\kappa}+\frac{9}{\kappa^2}+\frac{6}{\kappa^3}-6\frac{(1+\kappa)^2}{\kappa^4}\ln(1+\kappa)\right)\right\} \quad \text{(B.4.7)}$$

Plots of this result are shown in Figure B.4.2 (c) and (d).

To recover the expression given in Eq. (B.1.3) for the CP geometry, we must take the limit $\kappa \to \infty$. All terms, except the rightmost term obviously approach zero as $\kappa \to \infty$, and we can determine the limiting expression for the rightmost term by applying L'Hopital's Rule

$$\lim_{\kappa\to\infty} 6\frac{(1+\kappa)^2}{\kappa^4}\ln(1+\kappa) = \frac{\frac{d^3}{d\kappa^3}6(1+\kappa)^2\ln(1+\kappa)}{\frac{d^3}{d\kappa^3}\kappa^4} = \frac{1}{2\kappa(1+\kappa)} = 0 \quad \text{(B.4.8)}$$

So, clearly we recover the expression given in Eq. (B.1.3) for the CP geometry. To recover the expression given in Eq. (B.1.4) for the PP geometry in the limit $\kappa \to 0$, we expand the rightmost term around $\kappa = 0$

$$\lim_{\kappa\to 0} 6\frac{(1+\kappa)^2}{\kappa^4}\ln(1+\kappa) = \frac{2}{\kappa}+\frac{9}{\kappa^2}+\frac{6}{\kappa^3}-\frac{1}{2}+\frac{\kappa}{5}-\frac{\kappa^2}{10}+O(\kappa^3) \quad \text{(B.4.9)}$$

Evidently all the κ terms in Eq. (B.4.6) cancel or go to zero as $\kappa \to 0$, and we recover the expression given in Eq. (B.1.4) for the PP geometry.

We can also calculate the sensitivity of the measurement of $\mathcal{F}_{OCP}$ on the value of κ by taking the derivative of Eq. (B.4.6) with respect to κ.

$$\frac{d\mathcal{F}_{OCP}}{d\kappa} = \frac{1}{2}\Psi_1\dot{\gamma}_R^2\pi R^2\left\{2(1-\alpha)\left(\frac{1}{\kappa^2}+\frac{12}{\kappa^3}+\frac{12}{\kappa^4}-6\left(\frac{1}{\kappa^3}+\frac{3}{\kappa^4}+\frac{2}{\kappa^5}\right)\ln(1+\kappa)\right)\right\} \quad \text{(B.4.10)}$$

The limiting value of this equation as $\kappa \to 0$ is $\frac{1}{10}(1-\alpha)\Psi_1\dot{\gamma}_R^2\pi R^2$.

B.4.3 Axial Force for Rate-Dependent Normal Stress Coefficients

To generalize our results in Eq. (B.4.6) even further, let us consider including rate-dependent normal stress coefficients. Here we consider a CEF fluid in which we let the normal stress coefficients be given by

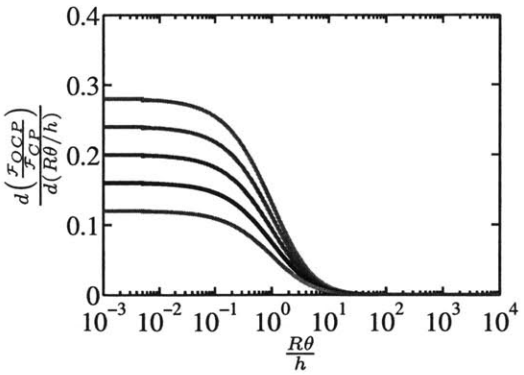

Figure B.4.3: Axial Force Sensitivity Dependence on α and $\kappa = \frac{R\theta}{h}$ for a simple viscoelastic fluid with constant normal stress coefficients.

$$\Psi_1(\dot{\gamma}) = \frac{\Psi_{1,0}}{1+(\lambda_1\dot{\gamma})^2} \quad \& \quad \Psi_2(\dot{\gamma}) = \frac{\Psi_{2,0}}{1+(\lambda_2\dot{\gamma})^2} \tag{B.4.11}$$

where $\Psi_{1,0}$ and $\Psi_{2,0}$ are constants and in general $\Psi_{1,0} > |\Psi_{2,0}| > 0$ and $\Psi_{2,0} < 0$ and λ_1 and λ_2 are constants. As before, we set $\Psi_{1,0} = -\alpha\Psi_{2,0}$. The axial force is now given by the equation

$$\begin{aligned}
\mathcal{F}_{OCP} &= \pi\int_0^R \left\{(\Psi_1-\Psi_2)+\Psi_2\left(\frac{r\theta}{h+r\theta}\right)\right\}\dot{\gamma}^2 r dr = \pi\int_0^R \left\{\Psi_1-\Psi_2\left(\frac{h}{h+r\theta}\right)\right\}\dot{\gamma}^2 r dr \\
&= \pi\int_0^R \left\{\frac{\Psi_{1,0}}{1+(\lambda_1\dot{\gamma})^2}-\frac{\Psi_{2,0}}{1+(\lambda_2\dot{\gamma})^2}\left(\frac{h}{h+r\theta}\right)\right\}\dot{\gamma}^2 r dr \\
&= \pi R^2\dot{\gamma}_R\int_0^R \left\{\frac{\Psi_{1,0}}{1+(\lambda_1\dot{\gamma}_R)^2\left(\frac{(1+\kappa)\mathcal{R}}{1+\kappa\mathcal{R}}\right)^2}-\frac{\Psi_{2,0}}{1+(\lambda_2\dot{\gamma}_R)^2\left(\frac{(1+\kappa)\mathcal{R}}{1+\kappa\mathcal{R}}\right)^2}\left(\frac{1}{1+\kappa\mathcal{R}}\right)\right\}\left(\frac{(1+\kappa)\mathcal{R}}{1+\kappa\mathcal{R}}\right)^2\mathcal{R}d\mathcal{R} \\
&= \Psi_{1,0}\dot{\gamma}_R^2\pi R^2(1+\kappa)^2\int_0^1 \left\{\frac{1}{(1+\kappa\mathcal{R})^2+(\lambda_1\dot{\gamma}_R)^2(1+\kappa)^2\mathcal{R}^2}+\frac{\alpha}{(1+\kappa\mathcal{R})^3+(\lambda_2\dot{\gamma}_R)^2(1+\kappa)^2(1+\kappa\mathcal{R})\mathcal{R}^2}\right\}\mathcal{R}^3 d\mathcal{R}
\end{aligned} \tag{B.4.12}$$

For succinctness, we define $b \equiv (\lambda_1\dot{\gamma}_R)^2$ and $c \equiv (\lambda_2\dot{\gamma}_R)^2$. The solution to this integral equation is

$$
\begin{aligned}
\mathcal{F}_{OCP} \;=\; & \tfrac{1}{2}\Psi_{1,0}\dot{\gamma}_R^2\pi R^2\Bigg\{\tfrac{1+\kappa}{\left(b(1+\kappa)^2+\kappa^2\right)^3}\Bigg[2\kappa\Big(3b(1+\kappa)^2-\kappa^2\Big)\tfrac{\tan^{-1}\left(\sqrt{b}\right)}{\sqrt{b}} \\
& +(1+\kappa)\Bigg(\Big(\kappa^2+b(1+\kappa)^2-4\kappa\Big)\Big(\kappa^2+b(1+\kappa)^2\Big) \\
& -\Big(b(1+\kappa)^2-3\kappa^2\Big)\Big(\ln(1+b)+2\ln(1+\kappa)\Big)\Bigg)\Bigg] \\
& +\alpha\Bigg[\tfrac{1}{\left(c(1+\kappa)^2+\kappa^2\right)^2}\Bigg(4\kappa(1+\kappa)\tfrac{\tan^{-1}\left(\sqrt{c}\right)}{\sqrt{c}} \\
& +\tfrac{2(1+\kappa)^2}{\kappa^2}\Big(\kappa\Big(c(1+\kappa)^2+\kappa^2\Big)-\Big(c(1+\kappa)^2+3\kappa^2\Big)\ln(1+\kappa)\Big) \\
& -\Big(c(1+\kappa)^2-\kappa^2\Big)\tfrac{\ln(1+c)}{c}\Big)\Bigg]\Bigg\}
\end{aligned}
\tag{B.4.13}
$$

For the sake of example, we assume that $\lambda_1 = \lambda_2$ and we set $b = c = Wi^2$, and we plot below the normalized axial force for different values of α and $\kappa = \frac{R\theta}{h}$. Notice that for vanishingly small values of Wi, we recover the result in Eq. (B.4.6), as seen by the similarity between Figure B.4.2 and Figure B.4.4 (a). Note that in Figure B.4.4, we have normalized $\mathcal{F}_{OCP}$ by $\mathcal{F}_{CP}$, where $\mathcal{F}_{CP}$ is in the limit of $Wi \to 0$. This scaling comes naturally from the result in Eq. (B.4.13), but it results in very low values of the normalized axial force at large Wi because of shear thinning.

To rescale this equation with the true force one would measure in the CP geometry, we have

$$
\begin{aligned}
\tfrac{\mathcal{F}_{OCP}}{\frac{1}{2}\Psi_{1,0}\dot{\gamma}_R^2\pi R^2} \;=\; & \left(1+(b\dot{\gamma}_R)^2\right)\Bigg\{\tfrac{1+\kappa}{\left(b(1+\kappa)^2+\kappa^2\right)^3}\Bigg[2\kappa\Big(3b(1+\kappa)^2-\kappa^2\Big)\tfrac{\tan^{-1}\left(\sqrt{b}\right)}{\sqrt{b}} \\
& +(1+\kappa)\Bigg(\Big(\kappa^2+b(1+\kappa)^2-4\kappa\Big)\Big(\kappa^2+b(1+\kappa)^2\Big) \\
& -\Big(b(1+\kappa)^2-3\kappa^2\Big)\Big(\ln(1+b)+2\ln(1+\kappa)\Big)\Bigg)\Bigg] \\
& +\alpha\Bigg[\tfrac{1}{\left(c(1+\kappa)^2+\kappa^2\right)^2}\Bigg(4\kappa(1+\kappa)\tfrac{\tan^{-1}\left(\sqrt{c}\right)}{\sqrt{c}} \\
& +\tfrac{2(1+\kappa)^2}{\kappa^2}\Big(\kappa\Big(c(1+\kappa)^2+\kappa^2\Big)-\Big(c(1+\kappa)^2+3\kappa^2\Big)\ln(1+\kappa)\Big) \\
& -\Big(c*(1+\kappa)^2-\kappa^2\Big)\tfrac{\ln(1+c)}{c}\Big)\Bigg]\Bigg\}
\end{aligned}
\tag{B.4.14}
$$

which is plotted at different Weissenberg numbers in Figure B.4.5.

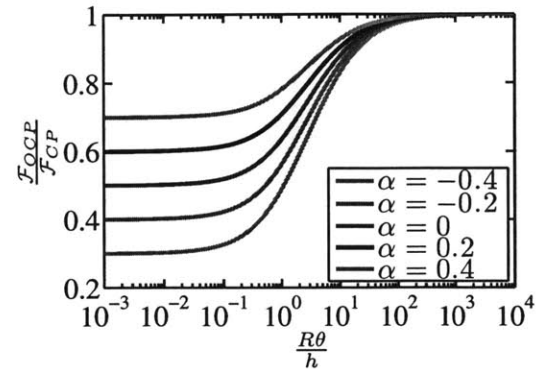

(a) $Wi = 0.01$

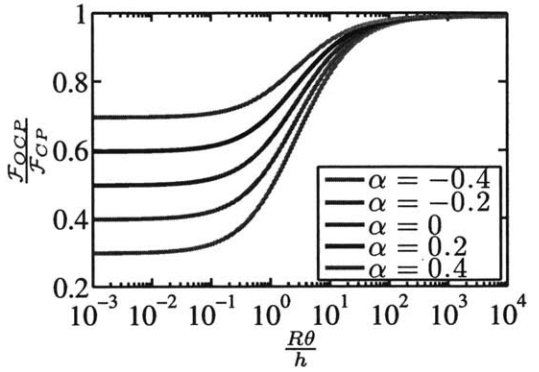

(b) $Wi = 0.1$

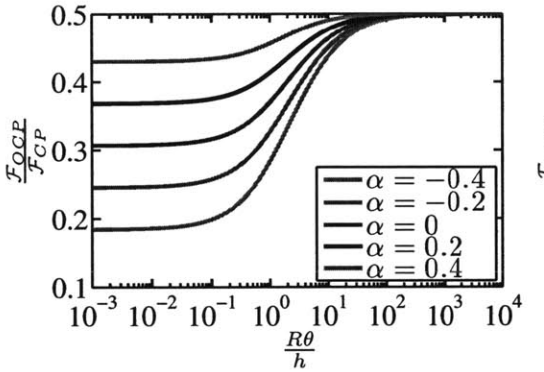

(c) $Wi = 1$

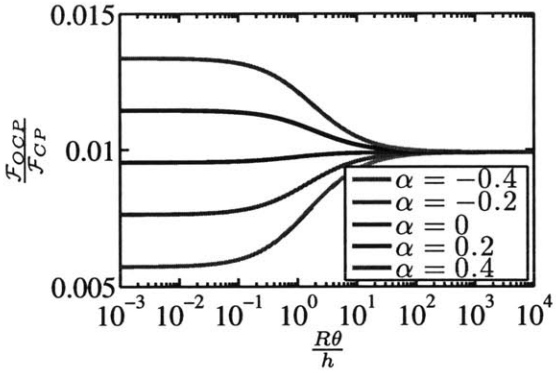

(d) $Wi = 10$

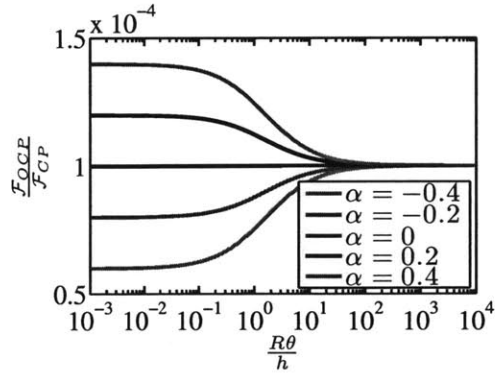

(e) $Wi = 100$

Figure B.4.4: Plots of $\frac{\mathcal{F}_{OCP}}{\mathcal{F}_{CP}} = \frac{\mathcal{F}_{OCP}}{\frac{1}{2}\Psi_{1,0}\dot{\gamma}_R^2\pi R^2}$ for different values of α and Wi as the ratio $\kappa = \frac{R\theta}{h}$ is changed.

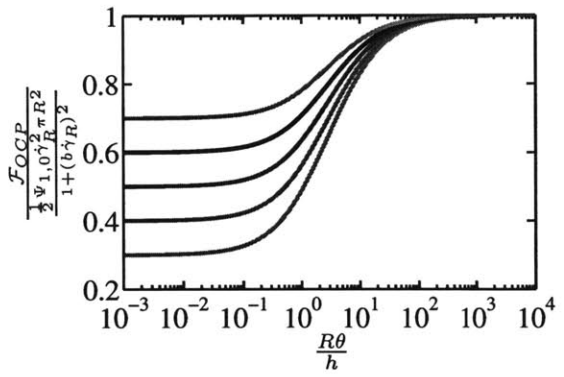

(a) $Wi = 0.01$

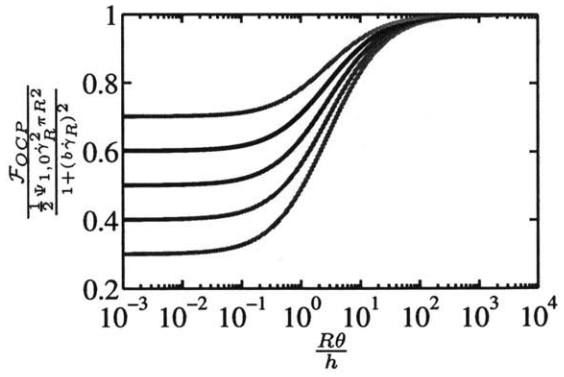

(b) $Wi = 0.1$

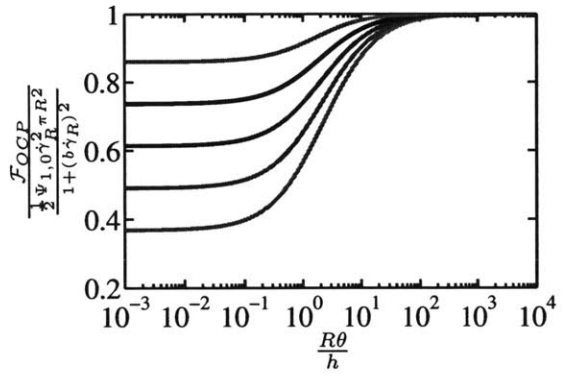

(c) $Wi = 1$

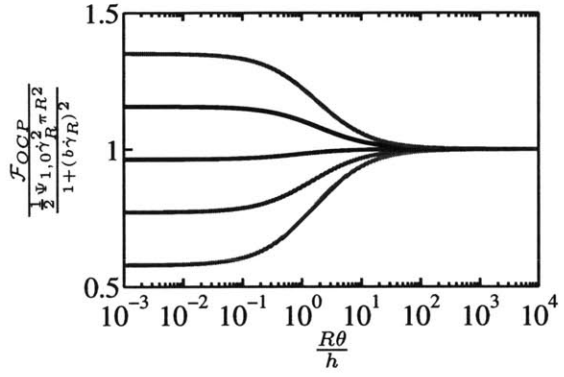

(d) $Wi = 10$

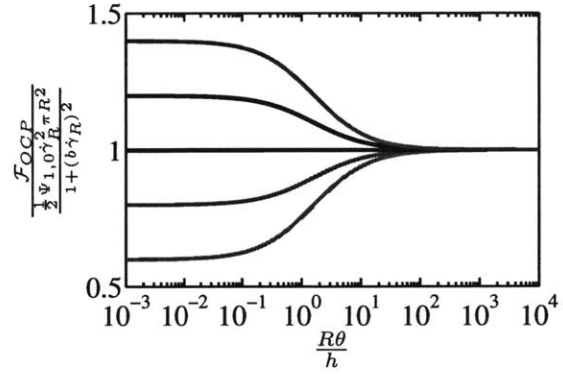

(e) $Wi = 100$

Figure B.4.5: Plots of $\frac{\mathcal{F}_{OCP}}{\mathcal{F}_{CP}} = \frac{\mathcal{F}_{OCP}}{\frac{1}{2}\Psi_{1,0}\dot{\gamma}_R^2\pi R^2}$ for different values of α and $\kappa = \frac{R\theta}{h}$.

Appendix C

Pedagogical Notes on the Johnson-Segalman Model

C.1 Governing Equation

The model proposed by Johnson & Segalman (1977) is a modification to the upper convected Maxwell model introduced in Appendix A in order to allow the model to predict rate-dependent material properties in steady simple shear. This model supposes that network strands in the material can slip with respect to a purely linear deformation. This slipping yields an effective velocity gradient field which is given by

$$\mathbf{L} = \nabla\vec{v} - 2\zeta\mathbf{D} \tag{C.1.1}$$

where ζ is a scalar slip coefficient in the range $0 \leq \zeta \leq 1$, $\nabla\vec{v}$ is the velocity gradient tensor, and $\mathbf{D} = \frac{1}{2}((\nabla\vec{v})^{\dagger} + \nabla\vec{v})$ is the strain rate tensor. The new convected derivative operator is

$$\widehat{(\,)} = \frac{D(\,)}{Dt} - \mathbf{L}^{\dagger}\cdot(\,) - (\,)\cdot\mathbf{L} \tag{C.1.2}$$

where $\frac{D(\,)}{Dt} \equiv \frac{\partial(\,)}{\partial t} + \vec{v}\cdot\nabla(\,)$ is the material derivative. The resulting constitutive equation for the polymeric stress tensor $\mathbf{T}$, is written

$$\mathbf{T} + \lambda\widehat{\mathbf{T}} = 2\eta_p\mathbf{D} \tag{C.1.3}$$

where λ is the polymer relaxation time and η_p is the polymer viscosity.

Although the form of the governing equation for $\mathbf{T}$ given by Eq. (C.1.3) is correct, we wish to rewrite it in the form that is given in Sato *et al.* (2010) which is more conducive to our subsequent analysis. First we expand the operator in Eq. (C.1.2) to obtain

$$\widehat{(\,)} = \frac{D(\,)}{Dt} - (\nabla\vec{v})^{\dagger}\cdot(\,) + 2\zeta\mathbf{D}^{\dagger}\cdot(\,) - (\,)\cdot\nabla\vec{v} + 2\zeta(\,)\cdot\mathbf{D} \tag{C.1.4}$$

or equivalently since $\mathbf{D}^{\dagger} = \mathbf{D}$

$$\widehat{(\,)} = \frac{D(\,)}{Dt} - \Big((\nabla\vec{v})^{\dagger}\cdot(\,) + (\,)\cdot\nabla\vec{v}\Big) + 2\zeta\Big(\mathbf{D}\cdot(\,) + (\,)\cdot\mathbf{D}\Big) \tag{C.1.5}$$

We modify the operator in Eq. (C.1.5) by adding to and subtracting from it the quantity $\frac{1}{2}[(\nabla\vec{v})^{\dagger}\cdot(\,) + \nabla\vec{v}\cdot(\,) + (\,)\cdot(\nabla\vec{v})^{\dagger} + (\,)\cdot\nabla\vec{v}]$, and simplify to obtain

$$\widehat{(\,)} = \frac{D(\,)}{Dt} - \Big(\mathbf{\Omega}\cdot(\,) - (\,)\cdot\mathbf{\Omega}\Big) - (1-2\zeta)\Big(\mathbf{D}\cdot(\,) + (\,)\cdot\mathbf{D}\Big) \tag{C.1.6}$$

where $\mathbf{\Omega} = \frac{1}{2}((\nabla\vec{v})^{\dagger} - \nabla\vec{v})$ is the vorticity tensor.

Hence the Johnson-Segalman model, in the absence of diffusion is now written

$$\mathbf{T} + \lambda\left\{\frac{\partial\mathbf{T}}{\partial t} + \vec{v}\cdot\nabla\mathbf{T} - \Big(\mathbf{\Omega}\cdot\mathbf{T} - \mathbf{T}\cdot\mathbf{\Omega}\Big) - a\Big(\mathbf{D}\cdot\mathbf{T} + \mathbf{T}\cdot\mathbf{D}\Big)\right\} = 2\eta_p\mathbf{D} \tag{C.1.7}$$

where we define $a \equiv 1 - 2\zeta$, where $-1 \leq a \leq 1$. For the case of $a = 1$, we obtain the upper convected Maxwell model, if $a = -1$ we have the lower convected Maxwell model, and if $a = 0$ we have the corotational Maxwell model (Bird *et al.*, 1987).

C.2 Model Predictions in Steady Shear

In a steady simple shearing flow, we have $\vec{v} = [u, 0, 0]$, and gradients in the flow properties exist only in the y-direction. Therefore we have

$$\nabla\vec{v} = \dot{\gamma}\begin{bmatrix} 0 & 0 & 0 \\ 1 & 0 & 0 \\ 0 & 0 & 0 \end{bmatrix} \tag{C.2.1}$$

where $\dot{\gamma} = \frac{\partial u}{\partial y}$, and also we have

$$\mathbf{D} = \frac{1}{2}\dot{\gamma}\begin{bmatrix} 0 & 1 & 0 \\ 1 & 0 & 0 \\ 0 & 0 & 0 \end{bmatrix} \tag{C.2.2}$$

and

$$\mathbf{\Omega} = \frac{1}{2}\dot{\gamma}\begin{bmatrix} 0 & 1 & 0 \\ -1 & 0 & 0 \\ 0 & 0 & 0 \end{bmatrix} \tag{C.2.3}$$

It can be shown that in a simple shearing flow only five components of the deviatoric stress tensor can be non-zero (Bird *et al.*, 1987). So the polymeric stress tensor is given by

$$\mathbf{T} = \begin{bmatrix} \tau_{xx} & \tau_{yx} & 0 \\ \tau_{xy} & \tau_{yy} & 0 \\ 0 & 0 & \tau_{zz} \end{bmatrix} \tag{C.2.4}$$

Furthermore, this stress tensor is necessarily symmetric, and so it should be noted that $\tau_{yx} = \tau_{xy}$. To obtain the resulting set of governing differential equations, we substitute Eq. (C.2.2), (C.2.3) and (C.2.4) into Eq. (C.1.7), and the resultant equations are

$$\tau_{xx} + \lambda\frac{\partial}{\partial t}\tau_{xx} - (1+a)\lambda\dot{\gamma}\tau_{xy} = 0 \tag{C.2.5}$$

$$\tau_{yy} + \lambda\frac{\partial}{\partial t}\tau_{yy} + (1-a)\lambda\dot{\gamma}\tau_{xy} = 0 \tag{C.2.6}$$

$$\tau_{zz} + \lambda\frac{\partial}{\partial t}\tau_{zz} = 0 \tag{C.2.7}$$

$$\tau_{xy} + \lambda\frac{\partial}{\partial t}\tau_{xy} + \frac{1}{2}\lambda\dot{\gamma}\Big[(1-a)\tau_{xx} - (1+a)\tau_{yy}\Big] = \eta_p\dot{\gamma} \tag{C.2.8}$$

We now consider the case of steady simple shear, whereby $\frac{\partial}{\partial t} = 0$. In this case we substitute the expressions for τ_{xx} and τ_{yy} given in Eq. (C.2.5) and (C.2.6) into the governing equation for τ_{xy} given by Eq. (C.2.8), solve for τ_{xy} and we obtain

$$\tau_{xy} = \frac{\eta_p\dot{\gamma}}{1 + (\lambda\dot{\gamma})^2(1-a^2)} \tag{C.2.9}$$

and solving for the normal stresses

$$\tau_{xx} = \frac{\eta_p \dot{\gamma}(\lambda\dot{\gamma})(1+a)}{1+(\lambda\dot{\gamma})^2(1-a^2)} = \frac{G_0(\lambda\dot{\gamma})^2(1+a)}{1+(\lambda\dot{\gamma})^2(1-a^2)} \tag{C.2.10}$$

$$\tau_{yy} = -\frac{\eta_p \dot{\gamma}(\lambda\dot{\gamma})(1-a)}{1+(\lambda\dot{\gamma})^2(1-a^2)} = -\frac{G_0(\lambda\dot{\gamma})^2(1-a)}{1+(\lambda\dot{\gamma})^2(1-a^2)} \tag{C.2.11}$$

$$\tau_{zz} = 0 \tag{C.2.12}$$

where the polymeric modulus is given by $G_0 = \eta_p/\lambda$. Note that this scaling of the normal stresses with shear rate is analogous to the scaling used for the normal stress coefficients in Eq. (B.4.11) for the analysis in the offset cone-and-plate geometry, when $\lambda_1 = \lambda_2$. On inspection of Eq. (C.2.9), we notice that the underlying flow curve for the polymeric shear stress is non-monotonic since for $\lambda\dot{\gamma} \ll 1$, $\tau_{xy} \sim \dot{\gamma}$, but as $\lambda\dot{\gamma} \to \infty$, $\tau_{xy} \sim \dot{\gamma}^{-1}$. In truth, however, the total stress $\boldsymbol{\Sigma}$ is the sum of the polymeric stress and the solvent stress, hence

$$\boldsymbol{\Sigma} = \mathbf{T} + 2\eta_s \mathbf{D} \tag{C.2.13}$$

where η_s is the Newtonian dynamic viscosity of the solvent. Now, for convenience, we define the Weissenberg number $Wi \equiv \lambda\dot{\gamma}$. The total normalized shear stress acting on the fluid as it deforms in steady simple shear is

$$\sigma \equiv \frac{\Sigma_{xy}}{G_0} = \frac{Wi}{1+Wi^2(1-a^2)} + \eta Wi \tag{C.2.14}$$

where $\eta \equiv \frac{\eta_s}{\eta_p}$ is the solvent viscosity ratio. The normalized normal stresses are

$$\frac{\Sigma_{xx}}{G_0} = \frac{Wi^2(1+a)}{1+Wi^2(1-a^2)} \tag{C.2.15}$$

$$\frac{\Sigma_{yy}}{G_0} = -\frac{Wi^2(1-a)}{1+Wi^2(1-a^2)} \tag{C.2.16}$$

$$\frac{\Sigma_{zz}}{G_0} = 0 \tag{C.2.17}$$

The first normal stress difference is therefore

$$\frac{N_1}{G_0} = \frac{\Sigma_{xx}}{G_0} - \frac{\Sigma_{yy}}{G_0} = \frac{2Wi^2}{1 + Wi^2(1-a^2)} \tag{C.2.18}$$

Plots of total shear stress and first normal stress difference for different values of η are shown in Figure C.2.1.

Even if solvent stresses are included, it is still possible to obtain an underlying flow curve of the shear stress that is non-monotonic. To determine the critical value of the solvent viscosity ratio η_c above which the total shear stress is monotonically increasing for all values of Wi, we must determine the value of η for which the total shear stress curve has a local extremum that coincides with an inflection point. That is to say, we require

$$\left.\frac{1}{G_0}\frac{\partial \Sigma_{xy}}{\partial Wi}\right|_{\eta_c} = \left.\frac{1}{G_0}\frac{\partial^2 \Sigma_{xy}}{\partial Wi^2}\right|_{\eta_c} = 0 \tag{C.2.19}$$

We have

$$\frac{1}{G_0}\frac{\partial \Sigma_{xy}}{\partial Wi} = \frac{1 - Wi^2(1-a^2)}{[1 + Wi^2(1-a^2)]^2} + \eta \tag{C.2.20}$$

and

$$\frac{1}{G_0}\frac{\partial^2 \Sigma_{xy}}{\partial Wi^2} = -\frac{2Wi(1-a^2)\Big(1 + Wi^2(1-a^2)\Big)\Big(3 - Wi^2(1-a^2)\Big)}{[1 + Wi^2(1-a^2)]^4} \tag{C.2.21}$$

For finite values of Wi, and $0 \leq a < 1$, the inflection point occurs only when

$$Wi_c^2 = \frac{3}{1-a^2} \tag{C.2.22}$$

Substituting this value of Wi_c into Eq. (C.2.20) and solving for the critical viscosity ratio, we have $\eta_c = \frac{1}{8}$.

Alternatively, this result can be derived by calculating the values of the Weissenberg number at which the flow curve is a local extremum, $Wi_{\pm}$. Setting Eq. (C.2.20) equal to zero, we have

$$Wi_{\pm}^4(1-a^2)\eta + Wi_{\pm}^2(1-a^2)(2\eta - 1) + (1+\eta) = 0 \tag{C.2.23}$$

This result is a quadratic equation for Wi^2, whose roots are given by the quadratic formula

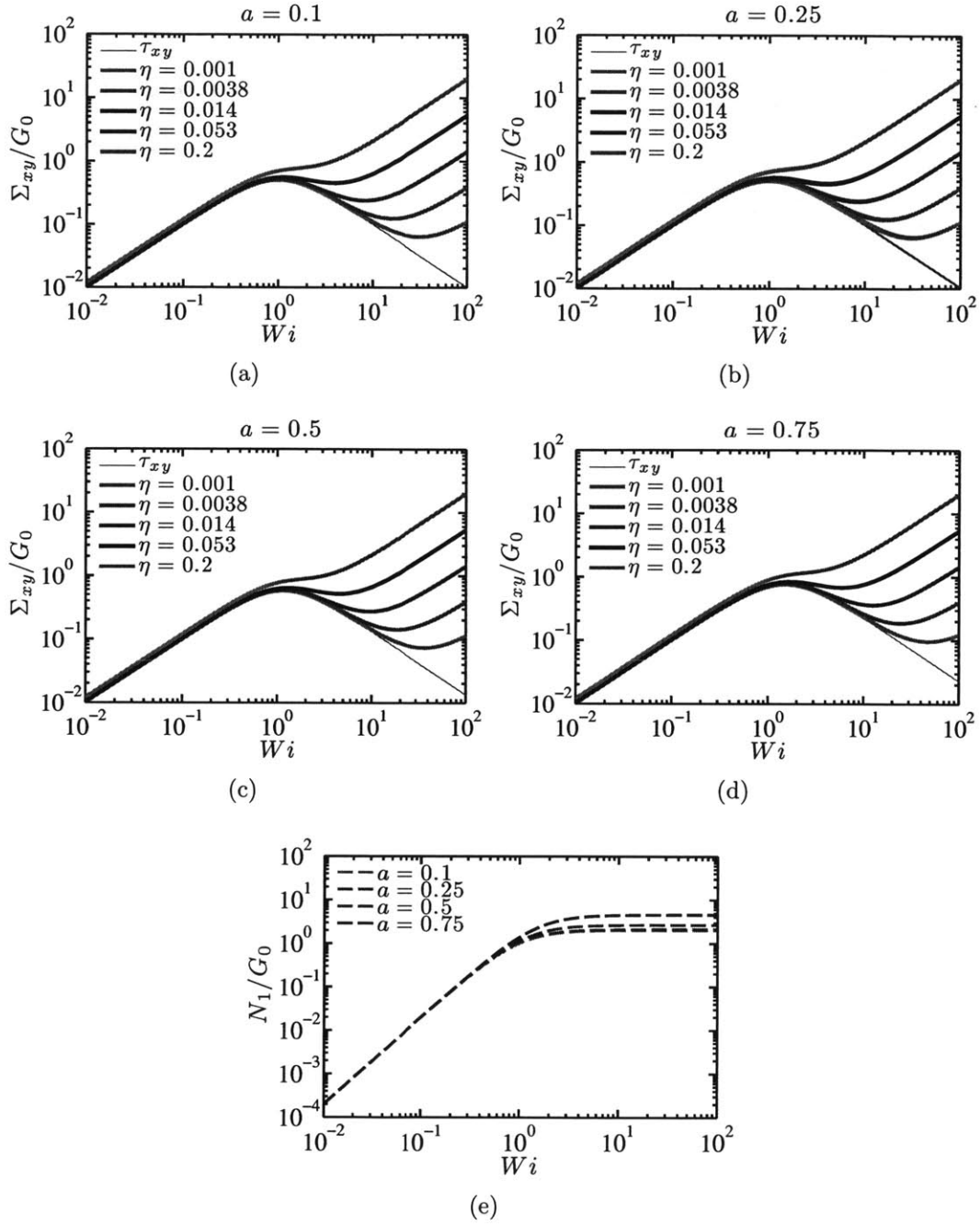

Figure C.2.1: (a)–(d) Normalized homogeneous flow curves for the Johnson-Segalman model for a range of a and η-values. (e) Normalized first normal stress difference.

$$Wi_{\pm}^2 = \frac{(1-2\eta) \pm \sqrt{1-8\eta}}{2(1-a^2)\eta} \tag{C.2.24}$$

Here we see again that for $\eta_c = \frac{1}{8}$, since for this value of the viscosity ratio, $Wi_+ = Wi_-$ and the flow curve contains only one extremum. Furthermore, only for $\eta < \frac{1}{8}$, are the values of $Wi_{\pm}$ real, and hence only for such values is the underlying flow curve non-monotonic. The value of the shear stress at the inflection point is the value of Σ_{xy}/G_0 at Wi_c and η_c, which is

$$\left.\frac{\Sigma_{xy}}{G_0}\right|_{Wi_c,\eta_c} = \frac{3}{8}\sqrt{\frac{3}{1-a^2}} \tag{C.2.25}$$

C.3 Diffusive Johnson-Segalman Model

The underlying flow curve is non-monotonic for values of $\eta < \eta_c$, and the model predicts a hysteretic behavior in the flow (Radulescu *et al.*, 1999). Hence for the range of Weissenberg numbers ($Wi_- \leq Wi \leq Wi_+$) for which the flow curve is negatively sloped the flow curve is unstable and the flow is inhomogeneous. However, the Johnson-Segalman model, given by Eq. (C.1.7), cannot be used to predict a unique value of the shear stress in this range (Spenley *et al.*, 1996). Experimentally, it has often been observed that the selection of the stress plateau is independent of the flow history (Porte *et al.*, 1997; Olmsted, 2008), and consequently the value of the stress plateau, τ_c is unique for a particular system. This observation and the predictions of the Johnson-Segalman can be reconciled by the inclusion of a diffusive term in the governing equation (Radulescu *et al.*, 1999), which can capture the importance of diffusion in the polymeric system on the selection of the stress plateau. The diffusive Johnson-Segalman model is given by

$$\mathbf{T} + \lambda\left\{\frac{\partial \mathbf{T}}{\partial t} + \vec{v}\cdot\nabla\mathbf{T} - \Big(\mathbf{\Omega}\cdot\mathbf{T} - \mathbf{T}\cdot\mathbf{\Omega}\Big) - a\Big(\mathbf{D}\cdot\mathbf{T} + \mathbf{T}\cdot\mathbf{D}\Big)\right\} = 2\eta_p\mathbf{D} - 2\mathcal{D}_0\lambda\nabla^2\mathbf{D} \tag{C.3.1}$$

Evidently, the units of the diffusion coefficient $\mathcal{D}_0$ in SI are [Pa.m^2] or equivalently [kg.m/s^2]. The components of $\nabla^2\mathbf{D}$ are $\Sigma_i \partial^2 D_{jk}/\partial x_i^2$ for i, j, $k = x$, y, z. The governing equations for the normal stresses are unchanged by the inclusion of the diffusion term and they are given by Eq. (C.2.5), (C.2.6) and (C.2.7) as before. The governing equation for the shear stress, however, is now written

$$\tau_{xy} + \lambda \frac{\partial}{\partial t}\tau_{xy} + \frac{1}{2}\lambda\dot{\gamma}\Big[(1-a)\tau_{xx} - (1+a)\tau_{yy}\Big] = \eta_p\dot{\gamma} - \mathcal{D}_0\lambda\frac{\partial^2}{\partial y^2}\dot{\gamma} \tag{C.3.2}$$

The additional governing equations for the flow of an isothermal, incompressible polymeric system the are the continuity equation:

$$\nabla \cdot \vec{v} = 0 \tag{C.3.3}$$

and the Cauchy momentum equation:

$$\rho\left(\frac{\partial}{\partial t} + \vec{v}\cdot\nabla\right)\vec{v} = \nabla\cdot\Big(\mathbf{T} + 2\eta_s\mathbf{D} - p\mathbf{I}\Big) \tag{C.3.4}$$

Using the notation of Sato *et al.* (2010), (although similar scalings were introduced earlier by Radulescu *et al.* (2000)) we also define the following quantities[1]

$$K \equiv \sqrt{1-a^2}\lambda\frac{\partial u}{\partial y} = \sqrt{1-a^2}\lambda\dot{\gamma} \tag{C.3.5a}$$

$$S \equiv \sqrt{1-a^2}\frac{\tau_{xy}}{G_0} \tag{C.3.5b}$$

$$N \equiv (1-a)\frac{\tau_{xx}}{2G_0} - (1+a)\frac{\tau_{yy}}{2G_0} \tag{C.3.5c}$$

Furthermore, we introduce the quantity

$$Z \equiv (1-a)\frac{\tau_{xx}}{2G_0} + (1+a)\frac{\tau_{yy}}{2G_0} \tag{C.3.5d}$$

which can be used to determine the dimensional first normal stress difference N_1 for the inhomogeneous flow case.

Noting that the shear rate, $\dot{\gamma}$ varies with position in the case of inhomogeneous flow, we abstain from writing $\lambda\dot{\gamma}$ as Wi in the definition of K. In what follows we seek to determine the governing differential equations for the quantities K, S and N from Eq. (C.3.1), (C.3.3) and (C.3.4). First, we define the dimensionless quantities, $t^* \equiv t/\lambda$, $y^* \equiv y/L$, where L is the gap height of the flow device, $\rho^* \equiv \rho L^2/\lambda^2 G_0$, and $\mathcal{D}^* \equiv \mathcal{D}_0/G_0L^2$.

[1]Note for clarity: the quantities S, N and Z are defined in terms of only the polymeric stresses, τ_{ij}, not in terms of the total stress Σ_{ij}.

To obtain the first of three governing evolution equations, we take the x-component of the momentum equation,

$$\rho\frac{\partial u}{\partial t} = \frac{\partial \tau_{xy}}{\partial y} + \eta_s\frac{\partial^2 u}{\partial y^2} \tag{C.3.6}$$

differentiate it with respect to y, to obtain

$$\frac{\partial}{\partial y}\left[\rho\frac{\partial u}{\partial t} = \frac{\partial \tau_{xy}}{\partial y} + \eta_s\frac{\partial^2 u}{\partial y^2}\right] \Longrightarrow \rho\frac{\partial}{\partial t}\frac{\partial u}{\partial y} = \frac{\partial^2}{\partial y^2}\left\{\tau_{xy} + \eta_s\frac{\partial u}{\partial y}\right\} \tag{C.3.7}$$

multiply this result by the quantity $\sqrt{1-a^2}\lambda$, and we have

$$\rho\frac{\partial}{\partial t}\left(\sqrt{1-a^2}\lambda\frac{\partial u}{\partial y}\right) = \frac{\partial^2}{\partial y^2}\left\{\left(\sqrt{1-a^2}\lambda\tau_{xy}\right) + \eta_s\left(\sqrt{1-a^2}\lambda\frac{\partial u}{\partial y}\right)\right\} \tag{C.3.8}$$

Substitution of the dimensionless quantities and rearrangement gives

$$\frac{\partial}{\partial t^*}\left(\sqrt{1-a^2}\lambda\frac{\partial u}{\partial y}\right) = \frac{\lambda^2 G_0}{\rho L^2}\frac{\partial^2}{\partial y^{*2}}\left\{\sqrt{1-a^2}\frac{\tau_{xy}}{G_0} + \eta\left(\sqrt{1-a^2}\lambda\frac{\partial u}{\partial y}\right)\right\} \tag{C.3.9}$$

Hence the governing equation for K is

$$\boxed{\frac{\partial}{\partial t^*}K = \frac{1}{\rho^*}\frac{\partial^2}{\partial y^{*2}}\left\{S + \eta K\right\}} \tag{C.3.10}$$

To derive the second governing equation, we multiply Eq. (C.3.2) by $\sqrt{1-a^2}/G_0$ and obtain

$$\begin{aligned}&\sqrt{1-a^2}\frac{\tau_{xy}}{G_0} + \lambda\frac{\partial}{\partial t}\left(\sqrt{1-a^2}\frac{\tau_{xy}}{G_0}\right) + \sqrt{1-a^2}\lambda\dot{\gamma}\left[(1-a)\frac{\tau_{xx}}{2G_0} - (1+a)\frac{\tau_{yy}}{2G_0}\right] \\ &= \sqrt{1-a^2}\lambda\dot{\gamma} - \frac{\mathcal{D}_0}{G_0}\frac{\partial^2}{\partial y^2}\left(\sqrt{1-a^2}\lambda\dot{\gamma}\right)\end{aligned} \tag{C.3.11}$$

Again, substitution of the dimensionless quantities and rearrangement gives

$$\begin{aligned}\frac{\partial}{\partial t^*}\left(\sqrt{1-a^2}\frac{\tau_{xy}}{G_0}\right) &= -\sqrt{1-a^2}\lambda\dot{\gamma}\left[(1-a)\frac{\tau_{xx}}{2G_0} - (1+a)\frac{\tau_{yy}}{2G_0}\right] + \sqrt{1-a^2}\lambda\dot{\gamma} \\ &-\sqrt{1-a^2}\frac{\tau_{xy}}{G_0} - \frac{\mathcal{D}_0}{G_0 L^2}\frac{\partial^2}{\partial y^{*2}}\left(\sqrt{1-a^2}\lambda\dot{\gamma}\right)\end{aligned} \tag{C.3.12}$$

Hence the governing equation for S is

$$\boxed{\frac{\partial}{\partial t^*}S = -KN + K - S - \mathcal{D}^*\frac{\partial^2}{\partial y^{*2}}K} \tag{C.3.13}$$

The third evolution equation is obtained by multiplying Eq. (C.2.5) by $(1-a)/2G_0$ and subtracting from it Eq. (C.2.6) multiplied by $(1+a)/2G_0$. So we have

$$(1-a)\frac{\tau_{xx}}{2G_0} - (1+a)\frac{\tau_{yy}}{2G_0} + \lambda\frac{\partial}{\partial t}\left\{(1-a)\frac{\tau_{xx}}{2G_0} - (1+a)\frac{\tau_{yy}}{2G_0}\right\} - (1-a^2)\lambda\dot{\gamma}\frac{\tau_{xy}}{G_0} = 0 \tag{C.3.14}$$

Substitution of the dimensionless quantities and rearrangement once more gives

$$\begin{aligned}\frac{\partial}{\partial t^*}\left\{(1-a)\frac{\tau_{xx}}{2G_0} - (1+a)\frac{\tau_{yy}}{2G_0}\right\} &= \left(\sqrt{1-a^2}\lambda\dot{\gamma}\right)\left(\sqrt{1-a^2}\frac{\tau_{xy}}{G_0}\right) \\ -\left\{(1-a)\frac{\tau_{xx}}{2G_0} - (1+a)\frac{\tau_{yy}}{2G_0}\right\}&\end{aligned} \tag{C.3.15}$$

Finally, we have the governing equation for N

$$\boxed{\frac{\partial}{\partial t^*}N = KS - N} \tag{C.3.16}$$

The fourth and last evolution equation is obtained by multiplying Eq. (C.2.5) by $(1-a)/2G_0$ and adding to it Eq. (C.2.6) multiplied by $(1+a)/2G_0$. This operation gives

$$(1-a)\frac{\tau_{xx}}{2G_0} + (1+a)\frac{\tau_{yy}}{2G_0} + \lambda\frac{\partial}{\partial t}\left\{(1-a)\frac{\tau_{xx}}{2G_0} + (1+a)\frac{\tau_{yy}}{2G_0}\right\} = 0 \tag{C.3.17}$$

which is equivalently

$$\boxed{\frac{\partial}{\partial t^*}Z = -Z} \tag{C.3.18}$$

The utility of Eq. (C.3.10), (C.3.13), (C.3.16) and (C.3.18) is their independence from the value of the anisotropy parameter a. The boundary conditions for plane Couette flow are (1) $u = 0$ at $y = 0$ and (2) $u = U$ at $y = L$. In terms of the dimensionless variables, these conditions become

$$\bar{K} \equiv \int_0^1 K(y^*, t^*)dy^* = \sqrt{1-a^2}\frac{\lambda U}{L} \tag{C.3.19}$$

Furthermore, there can be no polymer diffusion through walls, and with polymer flux proportional to $\mathcal{D}_0\nabla\dot{\gamma}$, we have $\frac{\partial^2 u}{\partial y^2} = 0$ at (3) $y = 0$ and (4) at $y = L$. These conditions are equivalent to

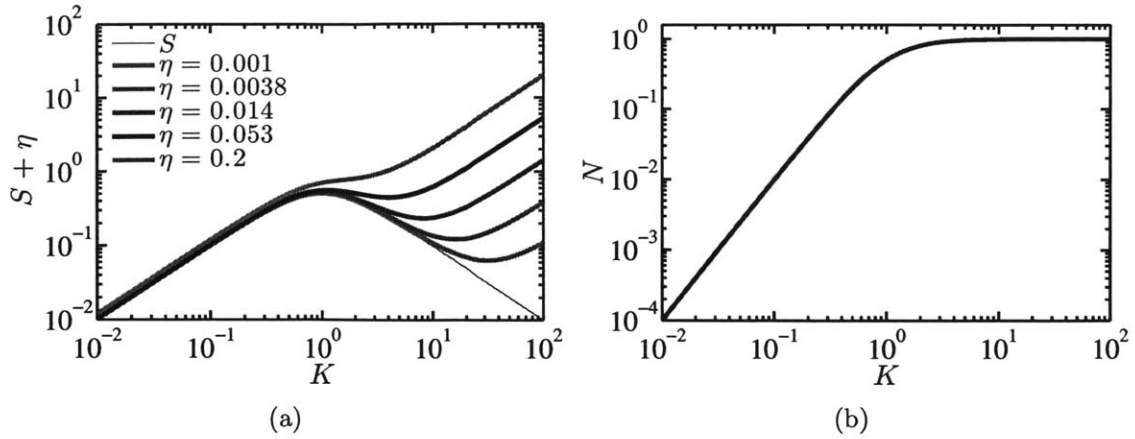

(a) (b)

Figure C.3.1: Homogeneous flow curves based on the rescaled variables defined in Section C.3.1.

$$\left.\frac{\partial S(y^*, t^*)}{\partial y^*}\right|_{y^*=0,1} = \left.\frac{\partial K(y^*, t^*)}{\partial y^*}\right|_{y^*=0,1} = 0 \tag{C.3.20}$$

C.3.1 Homogeneous Flow Solution

In the case of steady homogeneous flow, the dimensionless shear rate K is everywhere uniform and equal to the value $K = \bar{K}$, and the governing equations are

$$\frac{\partial^2}{\partial y^{*2}}\left\{S + \eta\bar{K}\right\} = 0 \tag{C.3.21a}$$

$$-\bar{K}N + \bar{K} - S = 0 \tag{C.3.21b}$$

$$\bar{K}S - N = 0 \tag{C.3.21c}$$

$$Z = 0 \tag{C.3.21d}$$

Combining Eq. (C.3.21b) and (C.3.21c) to eliminate N and solving for S, we have $S = \frac{\bar{K}}{1+\bar{K}^2}$, which is consistent with our result for τ_{xy} in Eq. (C.2.9). The total normalized shear stress is $\sigma \equiv \frac{\bar{K}}{1+\bar{K}^2} + \eta\bar{K}$. Solving for N, we have $N = \frac{\bar{K}^2}{1+\bar{K}^2}$, which is also consistent with our results for normal stresses in Eq. (C.2.10) and (C.2.11) and the definition of N. The homogenous flow curves are plotted in Figure C.3.1.

The dimensionless shear rates corresponding to the local minimum and maximum in the flow curve for the total shear stress σ are given by

$$K_{\pm} = \sqrt{\frac{1}{2\eta} - 1 \pm \frac{\sqrt{1-8\eta}}{2\eta}} \tag{C.3.22}$$

Evidently for values of $0 < \eta \leq \eta_c$, the values of $K_{\pm}$ are always real and finite. Finally, we have the critical point given by $(K_c, \eta_c, \sigma_c) = (\sqrt{3}, 1/8, 3\sqrt{3}/8)$.

C.3.2 Inhomogeneous Flow Solution

In order to solve for the case of steady, inhomogeneous shearing flow, we must include the diffusive term in the governing equation for S. Furthermore, we recognize that at values of $\bar{K}$ corresponding to the stress plateau, the shear stress is given by $\sigma_{sp} \equiv S + \eta K$,[2] where the subscript *sp* denotes *stress plateau.* Combining this definition of σ_{sp} and Eq. (C.3.13) and (C.3.16) we obtain the single governing equation

$$K\big(1 - K(\sigma_{sp} - \eta K)\big) - (\sigma_{sp} - \eta K) - \mathcal{D}^* \frac{\partial^2 K}{\partial y^{*2}} = 0 \tag{C.3.23}$$

This equation can be rearranged to obtain

$$\mathcal{D}^* \frac{\partial^2 K}{\partial y^{*2}} = \eta K^3 - \sigma_{sp} K^2 + (1+\eta)K - \sigma_{sp} \tag{C.3.24}$$

This result is a second-order, nonlinear, ordinary differential equation, for which the value of σ_{sp} is unknown. We may solve it more readily by converting it to a first order equation, recognizing that Eq. (C.3.24) is equivalent to the governing equation for a particle undergoing undamped oscillations in a quartic potential, $V(K)$. Therefore the equation is of the form

$$\mathcal{D}^* \frac{d^2 K}{dy^{*2}} = -\frac{dV}{dK} \tag{C.3.25}$$

By partial fractions, this result is equivalently,

$$\mathcal{D}^* \left(\frac{d^2 K}{dy^{*2}}\right)\left(\frac{dK}{dy^*}\right) dy^* = -dV \tag{C.3.26}$$

[2]Although the value of σ_{sp} is a constant throughout the gap, the values of S and K may vary with position y^* in the shear banding regime.

Integrating this equation, we obtain

$$\frac{1}{2}\mathcal{D}^*\left(\frac{dK}{dy^*}\right)^2 = -V(K) + E \tag{C.3.27}$$

where $V(K) = -\frac{1}{4}\eta K^4 + \frac{1}{3}\sigma_{sp}K^3 - \frac{1}{2}(1+\eta)K^2 + \sigma_{sp}K$ is analogous to a potential energy function, and E is a constant of integration, analogous to the total system energy in the case of a harmonic oscillator. This equation is a first order, non-linear ordinary differential equation, with two unknown constants, namely σ_{sp} and E, which may be determined from the boundary conditions.

First, we note the boundary conditions given by Eq. (C.3.20). These conditions give

$$\frac{1}{2}\mathcal{D}^*\left(\frac{dK}{dy^*}\right)^2_{y^*=0} + V\big(K(y^*=0)\big) = \frac{1}{2}\mathcal{D}^*\left(\frac{dK}{dy^*}\right)^2_{y^*=1} + V\big(K(y^*=1)\big) = E \tag{C.3.28}$$

Therefore

$$\boxed{V\big(K(y^*=0)\big) = V\big(K(y^*=1)\big) = E} \tag{C.3.29}$$

Furthermore, the kinetic energy term is positive definite, and accordingly the values of the potential V are maximized at the values of K for which $dK/dy^* = 0$. We can express this fact mathematically by differentiating Eq. (C.3.27) with respect to K to obtain

$$\mathcal{D}^*\left(\frac{dK}{dy^*}\right)\frac{d}{dK}\left(\frac{dK}{dy^*}\right) = -\frac{dV}{dK} \tag{C.3.30}$$

Evaluating this result at $y^* = 0$ and $y^* = 1$, we have

$$\mathcal{D}^*\left(\frac{dK}{dy^*}\right)_{y^*=0}\left\{\frac{d}{dK}\left(\frac{dK}{dy^*}\right)\right\}_{y^*=0} = -\left.\frac{dV}{dK}\right|_{y^*=0} \tag{C.3.31}$$

and

$$\mathcal{D}^*\left(\frac{dK}{dy^*}\right)_{y^*=1}\left\{\frac{d}{dK}\left(\frac{dK}{dy^*}\right)\right\}_{y^*=1} = -\left.\frac{dV}{dK}\right|_{y^*=1} \tag{C.3.32}$$

and accordingly

$$\boxed{\left.\frac{dV}{dK}\right|_{K(y^*=0)} = \left.\frac{dV}{dK}\right|_{K(y^*=1)} = 0} \tag{C.3.33}$$

Evidently, we see that the potential energy function is a *potential barrier*, as opposed to a *potential well*, since the maximum values of $V(K)$ are finite. By Eq. (C.3.25) this result also requires

$$\left.\frac{d^2K}{dy^{*2}}\right|_{y^*=0} = \left.\frac{d^2K}{dy^{*2}}\right|_{y^*=1} = 0 \tag{C.3.34}$$

Taking the derivative of $V(K)$ with respect to K, we have from Eq. (C.3.24)

$$\frac{dV}{dK} = -\eta K^3 + \sigma_{sp}K^2 - (1+\eta)K + \sigma_{sp} \tag{C.3.35}$$

This is a cubic equation with three unique roots that satisfy $\nabla_K V = 0$. Since $V(K)$ is a continuous function with two maxima at $K_\pm$, we anticipate that the third extremum is a local minimum that lies at a value of K_0 (*i.e.* the third root of dV/dK) such that $K_- < K_0 < K_+$,[3] where K_- and K_+ are the values of K at $y^* = 0$ and $y^* = 1$, respectively. We seek now to determine these roots as well as the value of the stress plateau, σ_{sp}.

It is plain to see by setting Eq. (C.3.35) equal to zero, that all three roots must satisfy the following result

$$\sigma_{sp} = \frac{\eta K_-^3 + (1+\eta)K_-}{1+K_-^2} = \frac{\eta K_0^3 + (1+\eta)K_0}{1+K_0^2} = \frac{\eta K_+^3 + (1+\eta)K_+}{1+K_+^2} \tag{C.3.36}$$

But as of yet, the values of σ_{sp} and the three roots are unknown.

Now as a matter of convenience, we define a new variable $\chi \equiv K - K_-$. We substitute the result of $K = \chi + K_-$ into our equation for $V(K)$, rearrange and simplify to obtain

$$\begin{aligned} V(\chi) = &-\tfrac{1}{4}\eta\chi^4 + \left(\tfrac{\sigma_{sp}}{3} - \eta K_-\right)\chi^3 + \left(-\tfrac{3}{2}\eta K_-^2 + \sigma_{sp}K_- - \tfrac{1}{2}(1+\eta)\right)\chi^2 \\ &+ \left[\sigma_{sp} - \eta K_-^3 + K_-^2\sigma_{sp} - K_-(1+\eta)\right]\chi - \left\{\tfrac{1}{4}\eta K_-^4 + \tfrac{1}{3}\sigma_{sp}K_-^3 - \tfrac{1}{2}(1+\eta)K_-^2 + \sigma_{sp}K_-\right\} \end{aligned} \tag{C.3.37}$$

Furthermore, we define a new function analogous to the kinetic energy in the system by $\phi \equiv E - V(\chi)$. We also note that the term in brackets [ ] in the above equation is equal to zero by Eq. (C.3.36) and that the term in braces { } in the above equation

[3]The values of $K_\pm$ in the inhomogeneous case are not to be confused with the values of $K_\pm$ given in Eq. (C.3.22) for the homogeneous case.

is the potential energy at $K(y^* = 0)$, which is equal to E by Eq. (C.3.28). Hence, the equation for ϕ is given

$$\phi(\chi) = \frac{1}{4}\eta\chi^4 + \left(\eta K_- - \frac{\sigma_{sp}}{3}\right)\chi^3 + \left(\frac{3}{2}\eta K_-^2 - \sigma_{sp}K_- + \frac{1}{2}(1+\eta)\right)\chi^2 \qquad \text{(C.3.38)}$$

We have deliberately defined ϕ such that at $\chi = 0$ (*i.e.* $K = K_-$), $\phi = 0$ and this value lies at a local extremum, which is now a minimum (since $d\phi/d\chi = -dV/dK$). We note also that $\phi = 0$ at a second value of $\chi = \chi_+$ by Eq. (C.3.28), which is also a local minimum by Eq. (C.3.33). Accordingly, we have the two equations

$$\phi(\chi_+) = 0 = \frac{1}{4}\eta\chi_+^4 + \left(\eta K_- - \frac{\sigma_{sp}}{3}\right)\chi_+^3 + \left(\frac{3}{2}\eta K_-^2 - \sigma_{sp}K_- + \frac{1}{2}(1+\eta)\right)\chi_+^2 \qquad \text{(C.3.39)}$$

and

$$\left.\frac{d\phi}{d\chi}\right|_{\chi_+} = 0 = \eta\chi_+^3 + \left(3\eta K_- - \sigma_{sp}\right)\chi_+^2 + \left(3\eta K_+^2 - 2\sigma_{sp}K_- + (1+\eta)\right)\chi_+ \qquad \text{(C.3.40)}$$

First we solve for the roots of Eq. (C.3.39), which we factor to obtain

$$0 = \left[\frac{1}{4}\eta\chi_+^2 + \left(\eta K_- - \frac{\sigma_{sp}}{3}\right)\chi_+ + \left(\frac{3}{2}\eta K_-^2 - \sigma_{sp}K_- + \frac{1}{2}(1+\eta)\right)\right]\chi_+^2 \qquad \text{(C.3.41)}$$

The non-zero roots of this equation are therefore given by

$$\chi_+ = \frac{\frac{\sigma_{sp}}{3} - \eta K_- \pm \sqrt{\frac{\sigma_{sp}^2}{9} + \frac{1}{3}\eta K_-\sigma_{sp} - \frac{1}{2}\eta^2 K_-^2 - \frac{1}{2}\eta^2 - \frac{1}{2}\eta}}{\frac{1}{2}\eta} \qquad \text{(C.3.42)}$$

This result indicates that there are two values of χ_+, however we anticipate that since there are only two values of χ for which $\phi = 0$, namely $\chi_- = 0$ and χ_+, the radical term in the above expression must be zero. We will confirm this assumption below.

Solving for the non-zero roots of Eq. (C.3.40), we obtain two values, the smaller of which coincides with χ_0, which corresponds to K_0. Hence we solve for the larger root to obtain an expression for χ_+. We have

$$\chi_+ = \frac{\sigma_{sp} - 3\eta K_- + \sqrt{\sigma_{sp}^2 + 2\eta K_-\sigma_{sp} - 3\eta^2 K_-^2 - 4\eta^2 - 4\eta}}{2\eta} \qquad \text{(C.3.43)}$$

Equating these two expressions for χ_+, with the assumption that the radical term in the first equation is zero, we have

$$\frac{\frac{\sigma_{sp}}{3} - \eta K_-}{\frac{1}{2}\eta} = \frac{\sigma_{sp} - 3\eta K_- + \sqrt{\sigma_{sp}^2 + 2\eta K_- \sigma_{sp} - 3\eta^2 K_-^2 - 4\eta^2 - 4\eta}}{2\eta} \tag{C.3.44}$$

Canceling terms we have

$$\frac{\sigma_{sp}}{3} - \eta K_- = \sqrt{\sigma_{sp}^2 + 2\eta K_- \sigma_{sp} - 3\eta^2 K_-^2 - 4\eta^2 - 4\eta} \tag{C.3.45}$$

Squaring both sides, and rearranging gives

$$\frac{\sigma_{sp}^2}{9} + \frac{1}{3}\eta K_- \sigma_{sp} - \frac{1}{2}\eta^2 K_-^2 - \frac{1}{2}\eta^2 - \frac{1}{2}\eta = 0 \tag{C.3.46}$$

as expected. Accordingly, Eq. (C.3.42) gives $\chi_+ = \frac{2}{3}\frac{\sigma_{sp}}{\eta} - 2K_-$ or equivalently $K_+ = \frac{2}{3}\frac{\sigma_{sp}}{\eta} - K_-$.

The equations given by Eq. (C.3.36), which is repeated for convenience below, and (C.3.46) constitute two linearly independent equations to solve for two unknowns, σ_{sp} and K_-.

$$\sigma_{sp} = \frac{\eta K_-^3 + (1+\eta)K_-}{1 + K_-^2} \tag{C.3.36}$$

These two equations, respectively, result from the boundary conditions given by Eq. (C.3.28) and (C.3.33). We eliminate K_- from these equations and obtain

$$\eta\sigma_{sp}^2\left[4\sigma_{sp}^4 + (72\eta^2 - 36\eta)\sigma_{sp}^2 + 324\eta^4 - 324\eta^3 + 81\eta^2\right] = 0 \tag{C.3.47}$$

Within the brackets is a quadratic equation for the quantity σ_{sp}^2, hence the roots of this expression are

$$\boxed{\sigma_{sp} = \pm\frac{3\sqrt{\eta - 2\eta^2}}{\sqrt{2}}} \quad \text{or} \quad \boxed{\sigma_{sp} = 0} \tag{C.3.48}$$

The negative and positive values correspond to that fact that the sign of the stress is arbitrary, whereas $\sigma_{sp} = 0$ comes from the singular case corresponding to $\eta = 0$. We keep the positive value of σ_{sp} by convention. Interestingly, the presence of diffusion requires that there be a unique value for the stress plateau, but this value is independent of the magnitude of the diffusion coefficient.

We solve for $K_\pm$ by substituting the positive value of σ_{sp} into Eq. (C.3.46) and solving for the two roots.

$$\boxed{K_{\pm} = \frac{\sqrt{\frac{1}{\eta} - 2} \pm \sqrt{\frac{1}{\eta} - 8}}{\sqrt{2}}} \tag{C.3.49}$$

Finally, χ_0 which yields K_0 is determined from the smaller root of Eq. (C.3.40) given by

$$\chi_+ = \frac{\sigma_{sp} - 3\eta K_- - \sqrt{\sigma_{sp}^2 + 2\eta K_- \sigma_{sp} - 3\eta^2 K_-^2 - 4\eta^2 - 4\eta}}{2\eta} \tag{C.3.50}$$

and so we have

$$K_0 = \frac{1}{2}(K_- + K_+) = \sqrt{\frac{\frac{1}{\eta} - 2}{2}} \tag{C.3.51}$$

The potential energy $V(K)$ is therefore given by

$$V(K) = -\frac{1}{4}\eta K^4 + \frac{\sqrt{\eta - 2\eta^2}}{\sqrt{2}}K^3 - \frac{1}{2}(1+\eta)K^2 + \frac{3\sqrt{\eta - 2\eta^2}}{\sqrt{2}}K \tag{C.3.52}$$

or equivalently by Eq. (C.3.38)

$$\phi(\chi) = \frac{1}{4}\eta\chi^4 - \frac{\eta\sqrt{\frac{1}{\eta} - 8}}{\sqrt{2}}\chi^3 + \frac{1}{2}(1 - 8\eta)\chi^2 \tag{C.3.53}$$

Although these forms are correct, it is most expedient to define another variable $\xi \equiv \chi - \chi_0 = K - K_0$, and replace χ with $\xi + \sqrt{\frac{\frac{1}{\eta}-8}{2}}$ in the equation for ϕ. Accordingly we have

$$\phi(\xi) = \frac{1}{4}\eta\left(\xi^2 - \frac{\frac{1}{\eta} - 8}{2}\right)^2 \tag{C.3.54}$$

and so we see that the potential energy $V(K)$ is in fact symmetric about the value K_0. These various forms of the potential function are plotted in Figure C.3.2.

By $dK = d\xi$ and by Eq. (C.3.27), the new governing equation is

$$\frac{1}{2}\mathcal{D}^*\left(\frac{d\xi}{dy^*}\right)^2 = \phi(\xi) = \frac{1}{4}\eta\left(\xi^2 - \frac{\frac{1}{\eta} - 8}{2}\right)^2 \tag{C.3.55}$$

This gives

$$\frac{d\xi}{dy^*} = \sqrt{\frac{\eta}{2\mathcal{D}^*}}\left(\xi^2 - \frac{\frac{1}{\eta} - 8}{2}\right) \tag{C.3.56}$$

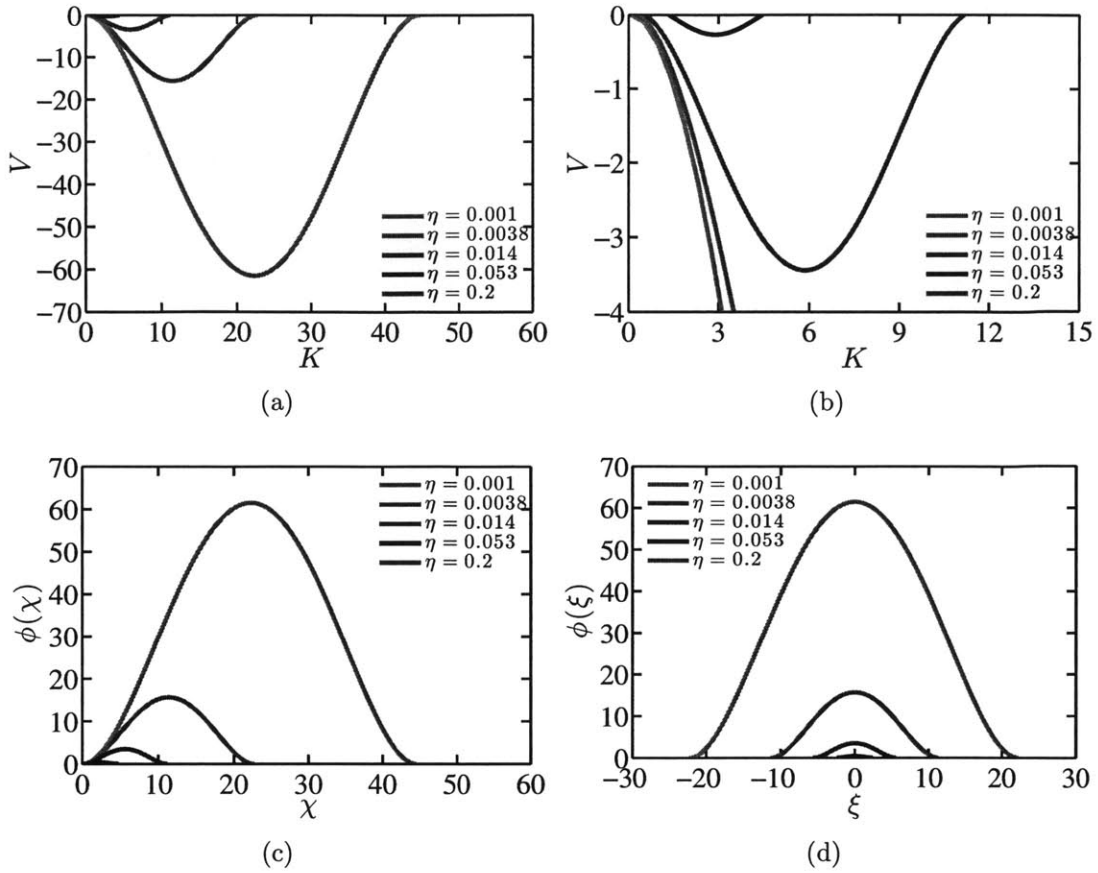

Figure C.3.2: Energy potentials. (a) $V(K)$. (b) Close up of $V(K)$ near origin. (c) $\phi(\chi)$. (d) $\phi(\xi)$.

This gives an integrable result[4]

$$\int \frac{d\xi}{\xi^2 - \left(\frac{\frac{1}{\eta}-8}{2}\right)} = \sqrt{\frac{\eta}{2\mathcal{D}^*}} \int dy^* \tag{C.3.57}$$

whose general solution is (for $\eta < \frac{1}{8}$)

$$\sqrt{\frac{2}{\frac{1}{\eta}-8}} \tanh^{-1}\left(\sqrt{\frac{2}{\frac{1}{\eta}-8}}\xi\right) = \sqrt{\frac{\eta}{2\mathcal{D}^*}} y^* + C \tag{C.3.58}$$

where C is a constant to be determined from the boundary condition for $\bar{K}$ in Eq. (C.3.19). We have

$$\xi = \sqrt{\frac{\frac{1}{\eta}-8}{2}} \tanh\left(\sqrt{\frac{1-8\eta}{4\mathcal{D}^*}} y^* + D\right) \tag{C.3.59}$$

[4]The left hand integral is of the form $\int \frac{dz}{z^2-c^2}$ where c is real. The integral is $\frac{1}{c}\tanh^{-1}(z/c)$.

where $D = \sqrt{\frac{\frac{1}{\eta}-8}{2}}C$ is a constant. Equally, by $\xi = K - K_0$, we have

$$K = \frac{K_+ + K_-}{2} + \frac{K_+ - K_-}{2}\tanh\left(\frac{y^*}{\ell} + D\right) \tag{C.3.60}$$

where we define $\ell \equiv \sqrt{4\mathcal{D}^*/(1-8\eta)}$ as the dimensionless interfacial width between the two shear bands. To solve for the constant D, we have

$$\bar{K} = \int_0^1 K dy^* = \int_0^1 \left\{\frac{K_+ + K_-}{2} + \frac{K_+ - K_-}{2}\tanh\left(\frac{y^*}{\ell} + D\right)\right\} dy^* \tag{C.3.61}$$

which gives

$$\bar{K} = \frac{K_+ + K_-}{2} + \frac{K_+ - K_-}{2}\int_D^{\frac{1}{\ell}+D} \tanh\left(Y\right)\ell dY \tag{C.3.62}$$

and

$$\bar{K} = \frac{K_+ + K_-}{2} + \frac{K_+ - K_-}{2}\ell \ln\Big(\cosh(Y)\Big)_D^{\frac{1}{\ell}+D} \tag{C.3.63}$$

This gives

$$\exp\left(\frac{1}{\ell}\frac{2}{K_+ - K_-}\Big(\bar{K} - \frac{K_+ + K_-}{2}\Big)\right) = \frac{\cosh\left(\frac{1}{\ell} + D\right)}{\cosh(D)} \tag{C.3.64}$$

By a hyperbolic trigonometry identity, we have[5]

$$\exp\left(\sqrt{\frac{\eta}{2\mathcal{D}^*}}\Big(\bar{K} - \frac{K_+ + K_-}{2}\Big)\right) = \cosh\left(\frac{1}{\ell}\right) + \sinh\left(\frac{1}{\ell}\right)\tanh(D) \tag{C.3.65}$$

Thus we obtain

$$D = \tanh^{-1}\left[\frac{\exp\left(\sqrt{\frac{\eta}{2\mathcal{D}^*}}\left(\bar{K} - \frac{K_+ + K_-}{2}\right)\right) - \cosh\left(\frac{1}{\ell}\right)}{\sinh\left(\frac{1}{\ell}\right)}\right] \tag{C.3.66}$$

Expressing the inverse hyperbolic tangent function in logarithmic form[6], we have

$$D = \frac{1}{2}\ln\left[\frac{\sinh\left(\frac{1}{\ell}\right) + \exp\left(\sqrt{\frac{\eta}{2\mathcal{D}^*}}\left(\bar{K} - \frac{K_+ + K_-}{2}\right)\right) - \cosh\left(\frac{1}{\ell}\right)}{\sinh\left(\frac{1}{\ell}\right) - \exp\left(\sqrt{\frac{\eta}{2\mathcal{D}^*}}\left(\bar{K} - \frac{K_+ + K_-}{2}\right)\right) + \cosh\left(\frac{1}{\ell}\right)}\right] \tag{C.3.67}$$

Equally, this result is

[5]Here we use the identity $\cosh(A+B) = \cosh(A)\cosh(B) + \sinh(A)\sinh(B)$.

[6]Here we use the identity $\tanh^{-1}(z) = \frac{1}{2}\ln\left(\frac{1+z}{1-z}\right)$ for $|z| < 1$.

$$D = \frac{1}{2}\ln\left[\frac{-\exp\left(-\frac{1}{\ell}\right)+\exp\left(\sqrt{\frac{\eta}{2\mathcal{D}^*}}(\bar{K}-\frac{K_+ + K_-}{2})\right)}{\exp\left(\frac{1}{\ell}\right)-\exp\left(\sqrt{\frac{\eta}{2\mathcal{D}^*}}(\bar{K}-\frac{K_+ + K_-}{2})\right)}\right] \tag{C.3.68}$$

In the limit of very large gap size, $\ell \to 0$, this constant becomes

$$D \approx \frac{1}{2}\ln\left[\frac{\exp\left(\sqrt{\frac{\eta}{2\mathcal{D}^*}}(\bar{K}-\frac{K_+ + K_-}{2})\right)}{\exp\left(\frac{1}{\ell}\right)}\right] = \frac{1}{2}\left(\sqrt{\frac{\eta}{2\mathcal{D}^*}}(\bar{K}-\frac{K_+ + K_-}{2})-\frac{1}{\ell}\right) = \frac{1}{\ell}\frac{\bar{K}-K_+}{K_+ - K_-} \tag{C.3.69}$$

Comparing the results of Eq. (C.3.60) and (C.3.68) to the result of Sato *et al.* (2010) who have

$$K = \frac{K_+ + K_-}{2} + \frac{K_+ - K_-}{2}\tanh\left(\frac{y^* - \frac{K_+ - \bar{K}}{K_+ - K_-}}{\ell}\right) \tag{C.3.70}$$

we note that their solution is only valid for $\ell \to 0$ in the limit of large gap size compared to the shear banding interface width. The velocity profile given by the result of Sato *et al.* (2010) in Eq. (C.3.70) is

$$\mathcal{U} = \frac{K_+ + K_-}{2}y^* + \frac{K_+ - K_-}{2}\ell\ln\left[\cosh\left(\frac{y^* - \frac{K_+ - \bar{K}}{K_+ - K_-}}{\ell}\right)\Big/\cosh\left(\frac{\frac{K_+ - \bar{K}}{K_+ - K_-}}{\ell}\right)\right] \tag{C.3.71}$$

whereas the velocity profile based on the analysis here is

$$\mathcal{U} = \frac{K_+ + K_-}{2}y^* + \frac{K_+ - K_-}{2}\ell\ln\left[\cosh\left(\frac{y^*}{\ell}+D\right)\Big/\cosh\left(D\right)\right] \tag{C.3.72}$$

For succinctness, we define the following quantities.

$$\Delta \equiv K_+ - K_- \qquad \& \qquad y_0 \equiv -\frac{D}{\ell} \tag{C.3.73}$$

where Δ is difference between the upper and lower shear rates of the plateau and y_0 is the position in the gap of the shear banding interface. The reader is reminded $K_0 = (K_+ + K_-)/2$. So the shear rate is

$$\boxed{K = K_0 + \frac{\Delta}{2}\tanh\left(\frac{y^* - y_0}{\ell}\right)} \tag{C.3.74}$$

and the velocity profile is

$$\boxed{\mathcal{U} = K_0 y^* + \frac{\Delta}{2}\ell \ln\left[\cosh\left(\frac{y^* - y_0}{\ell}\right) \Big/ \cosh\left(\frac{y_0}{\ell}\right)\right]} \tag{C.3.75}$$

Plots of the velocity profile for different values of η and $\mathcal{D}$ are shown in Figure C.3.3.

C.3.3 Normal Stress Differences

The normal stress differences are given by the equations

$$N_1 \equiv \tau_{xx} - \tau_{yy} = \frac{2G_0}{1-a^2}(N + aZ) = \frac{2G_0}{1-a^2}N \tag{C.3.76}$$

and

$$N_2 \equiv \tau_{yy} - \tau_{zz} = \frac{G_0}{1+a}(Z - N) - \tau_{zz} = -\frac{G_0}{1+a}N \tag{C.3.77}$$

Combining Eq. (C.3.16) with the definition of σ_{sp} we have

$$N = KS = K(\sigma_{sp} - \eta K) \tag{C.3.78}$$

$$\boxed{N = (\sigma_{sp} - \eta K_0)\left(K_0 + \frac{\Delta}{2}\tanh\left(\frac{y^* - y_0}{\ell}\right)\right) - \eta\frac{\Delta}{2}\tanh\left(\frac{y^* - y_0}{\ell}\right)\left(K_0 + \frac{\Delta}{2}\tanh\left(\frac{y^* - y_0}{\ell}\right)\right)} \tag{C.3.79}$$

Plots of the dimensionless normal stress N-profile for different values of η and $\mathcal{D}$ are shown in Figure C.3.4.

The gradient in normal stress difference is

$$\frac{dN}{dy^*} = \left[(\sigma_{sp} - \eta K_0) - \eta\left(K_0 + \frac{\Delta}{2}\tanh\left(\frac{y^* - y_0}{\ell}\right)\right)\right]\frac{\Delta}{2\ell}\mathrm{sech}^2\left(\frac{y^* - y_0}{\ell}\right) \tag{C.3.80}$$

Hence there is an extremum in the magnitude of the normal stress difference provided

$$\frac{dN}{dy^*} = 0 = (\sigma_{sp} - \eta K_0) - \eta\left(K_0 + \frac{\Delta}{2}\tanh\left(\frac{y^*_{N_{max}} - y_0}{\ell}\right)\right) \tag{C.3.81}$$

Substitution and rearrangement gives

$$0 = \sqrt{\frac{1}{\eta} - 2} - 2\sqrt{\frac{1}{\eta} - 8}\tanh\left(\frac{y^*_{N_{max}} - y_0}{\ell}\right) \tag{C.3.82}$$

so

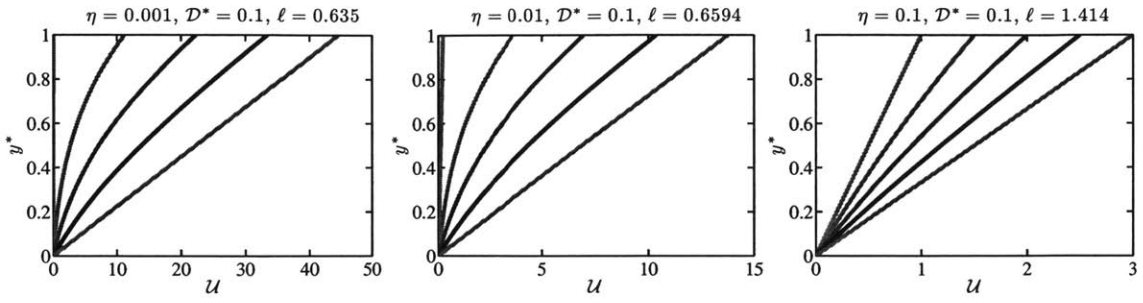

(a)

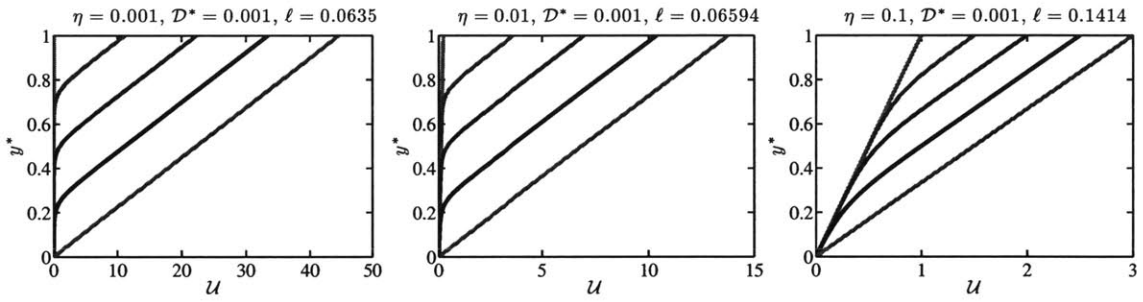

(b)

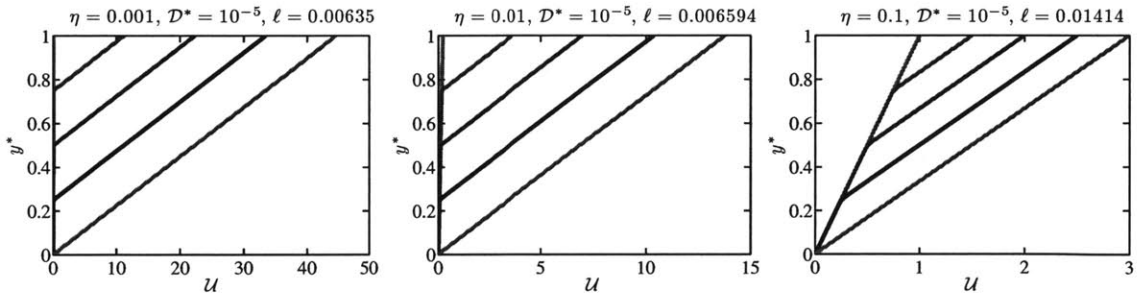

(c)

Figure C.3.3: Velocity profiles as given by Eq. (C.3.72). Each plot contains velocity profiles corresponding to five evenly spaced values of $\bar{K}$ spanning the domain $K_- \leq \bar{K} \leq K_+$.

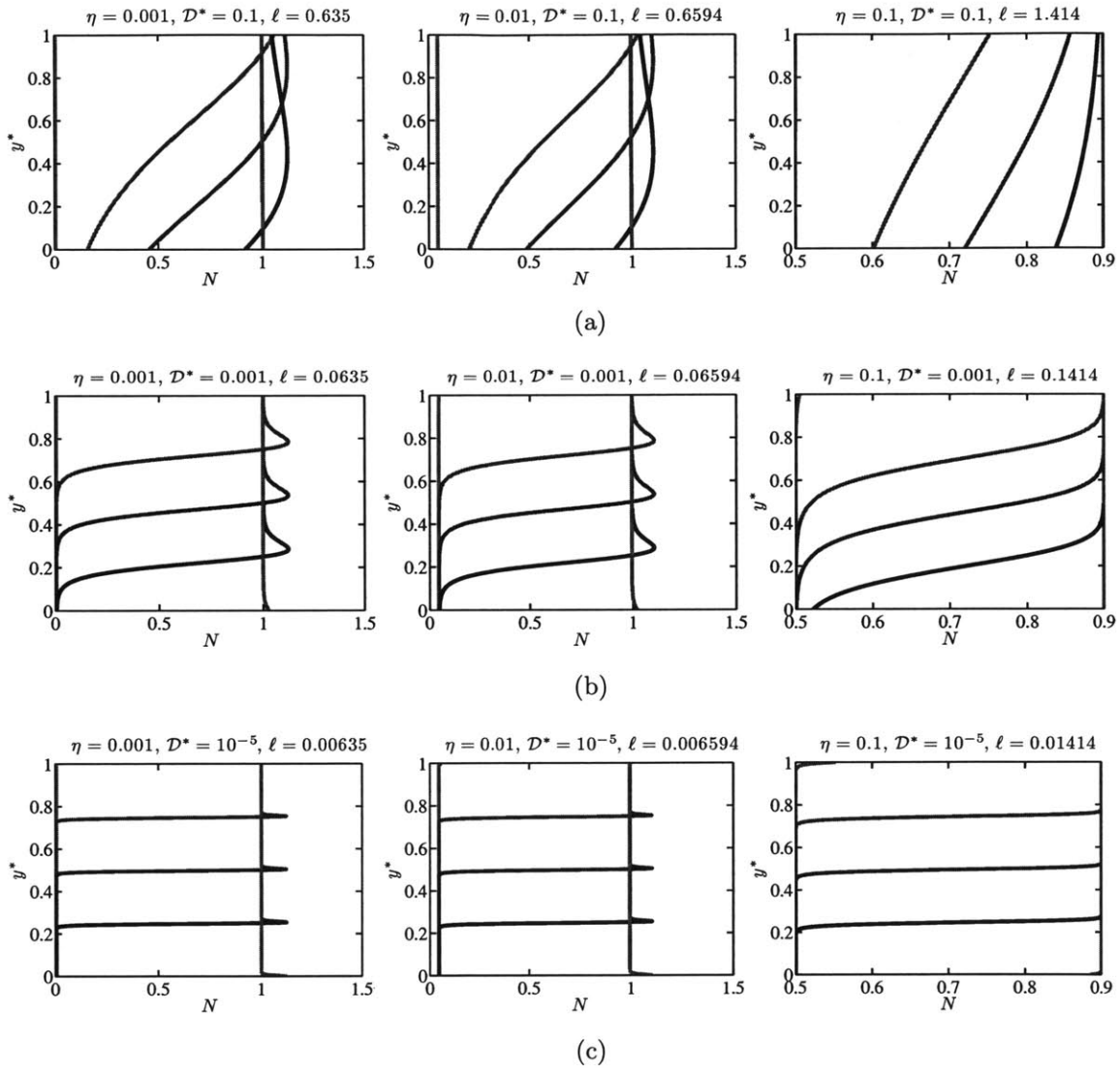

Figure C.3.4: Normal stress profiles as given by Eq. (C.3.79). Each plot contains velocity profiles corresponding to five evenly spaced values of $\bar{K}$ spanning the domain $K_- \leq \bar{K} \leq K_+$.

$$\frac{1}{2}\sqrt{\frac{\frac{1}{\eta}-2}{\frac{1}{\eta}-8}} = \tanh\left(\frac{y^*_{N_{max}} - y_0}{\ell}\right) \tag{C.3.83}$$

$$y^*_{N_{max}} = y_0 + \ell \tanh^{-1}\left(\frac{1}{2}\sqrt{\frac{\frac{1}{\eta}-2}{\frac{1}{\eta}-8}}\right) \tag{C.3.84}$$

If the argument of the inverse hyperbolic tangent function is greater than unity, then there can be no overshoot in normal stress difference. So the critical value of the viscosity ratio $\eta_{c,N}$ for which the value of N varies monotonically across the gap is

$$\frac{1}{2}\sqrt{\frac{\frac{1}{\eta_{c,N}}-2}{\frac{1}{\eta_{c,N}}-8}} \geq 1 \tag{C.3.85}$$

$$\eta_{c,N} \geq \frac{1}{10} \tag{C.3.86}$$

This criterion is not a hard limit, however, since it may be possible to have no normal stress difference overshoots in the gap ($0 \leq y^* \leq 1$) depending on the values of y_0 and ℓ.

C.3.4 Plane Poiseuille Flow

For the case of pressure-driven, rectilinear Poiseuille flow, the governing momentum equation must include a constant pressure gradient term, whereby it becomes

$$\rho\frac{\partial u}{\partial t} = \frac{\partial \tau_{xy}}{\partial y} + \eta_s\frac{\partial^2 u}{\partial y^2} - \frac{dP}{dx} \tag{C.3.87}$$

We can differentiate this equation with respect to y and manipulate it to obtain the same governing equation for S given by Eq. (C.3.10). The other governing equations are as before, and so in fact the four dimensionless governing equations for K, S, N and Z are unchanged by the addition of a constant pressure gradient.

In the case of steady flow, Eq. (C.3.87) can be integrated in y to obtain

$$\Sigma_{xy} = \tau_{xy} + \eta_s\frac{du}{dy} = \frac{dP}{dx}y \tag{C.3.88}$$

where $y = 0$ coincides with the centerline of the channel, with the boundary condition $\Sigma_{xy} = 0$ at $y = 0$.

We convert this result into dimensionless form, by multiplying it by $\sqrt{1-a^2}/G_0$,

and we have

$$\sqrt{1-a^2}\frac{\tau_{xy}}{G_0}+\eta\sqrt{1-a^2}\lambda\frac{du}{dy}=\sqrt{1-a^2}\frac{dP}{dx}\frac{L}{G_0}\frac{y}{L} \tag{C.3.89}$$

which is equivalently

$$S+\eta K=-\mathcal{P}y^* \tag{C.3.90}$$

where $\mathcal{P}\equiv-\sqrt{1-a^2}\frac{dP}{dx}\frac{L}{G_0}$ is the dimensionless pressure gradient. We have defined $\mathcal{P}$, such that it is positive if pressure decreases in the positive x-direction. Let us recast this result as $S=-\mathcal{P}y^*-\eta K$ and, as before, combining it with and Eq. (C.3.16), replace these quantities into Eq. (C.3.10) to obtain

$$K\big(1-K(-\mathcal{P}y^*-\eta K)\big)-(-\mathcal{P}y^*-\eta K)-\mathcal{D}^*\frac{\partial^2 K}{\partial y^{*2}}=0 \tag{C.3.91}$$

which becomes

$$\mathcal{D}^*\frac{\partial^2 K}{\partial y^{*2}}=\eta K^3+(1+K^2)\mathcal{P}y^*+(1+\eta)K \tag{C.3.92}$$

The boundary conditions for this flow are obtained by recognizing that, as in the case of plane Couette flow, there can be no net polymer diffusion at the wall, which is equivalently $dS/dy^*=0$ at $y^*=\pm\frac{1}{2}$. This condition also gives $dK/dy^*=-\mathcal{P}/\eta$ at $y^*=\pm\frac{1}{2}$ by Eq. (C.3.90). We also note that at $y^*=0$, $K=0$ by symmetry, but dK/dy^* may be non-zero.

Equivalently, we have

$$\mathcal{D}^*\frac{\partial^2 K}{\partial y^{*2}}\left(\frac{dK}{dy^*}\right)dy^*=\big(\eta K^3+(1+K^2)\mathcal{P}y^*+(1+\eta)K\big)dK \tag{C.3.93}$$

which, upon integration, gives

$$\frac{1}{2}\mathcal{D}^*\left(\frac{dK}{dy^*}\right)^2=\frac{1}{4}\eta K^4+\left(1+\frac{1}{3}K^2\right)K\mathcal{P}y^*+\frac{1}{2}(1+\eta)K^2+f(y^*) \tag{C.3.94}$$

where $f(y^*)$ is yet to be determined. The governing equation for $f(y^*)$ is obtained by differentiating Eq. (C.3.94) with respect to y^*. We have

$$\mathcal{D}^* \frac{\partial^2 K}{\partial y^{*2}} \left(\frac{dK}{dy^*} \right) = \left(\eta K^3 + (1+K^2)\mathcal{P} y^* + (1+\eta) K \right) \left(\frac{dK}{dy^*} \right) + \left\{ \left(1 + \frac{1}{3} K^2 \right) K\mathcal{P} + \frac{df}{dy^*} \right\} \tag{C.3.95}$$

This result is equivalent to Eq. (C.3.92) if and only if the portion in braces is identically zero. Hence

$$0 = \left(1 + \frac{1}{3} K^2 \right) K\mathcal{P} + \frac{df}{dy^*} \tag{C.3.96}$$

It follows that governing equations for the diffusive Johnson-Segalman model in plane Poiseuille are analogous the governing equations for the motion of a particle in a time-varying potential well since there is an explicit dependence on y^* (the variable analogous to time) on the right hand side of Eq. (C.3.95).

Appendix D

Flow in a Hyperbolic Contraction

The hyperbolic contraction is a unique geometry because it can be used, in principle, to impose a constant, nominal extension rate, owing to the fact that its cross-sectional area varies inversely with axial position. For the hyperbolic contraction depicted in Figure D.1.1 (a) having length, l_c, height, h_c, upstream width, w_u, width at the contraction exit, w_c, the width, w, at any x takes the form

$$w(x) = \frac{K}{x + x_0} \tag{D.0.1}$$

where $K = l_c w_u w_c/(w_u - w_c)$, $x_0 = l_c w_c/(w_u - w_c)$ and $0 \leq x \leq l_c$.

Given a constant volumetric flow rate, Q, through the contraction, the apparent extension rate, $\dot{\varepsilon}_a$, neglecting any shearing flow induced by the bounding walls is

$$\dot{\varepsilon}_a = \frac{Q}{l_c h}\left(\frac{1}{w_c} - \frac{1}{w_u}\right) \tag{D.0.2}$$

and the extensional viscosity is

$$\eta_E = \frac{1}{\varepsilon_H}\frac{\Delta P_e}{\dot{\varepsilon}_a} \tag{D.0.3}$$

where $\varepsilon_H = \ln(w_u/w_c)$. The normal stress difference is

$$N_1 = \eta_E \dot{\varepsilon}_a = \frac{1}{\varepsilon_H}\Delta P_e \tag{D.0.4}$$

D.1 Viscous Shear Stress Contribution

To account for the viscous contribution to the total pressure drop in the contraction, we apply the lubrication approximation for a Newtonian fluid which is valid provided $Re\frac{w_u}{l_c} \ll 1$. Since the thickness of the contraction is always less than its width, $h < w_c < w_u$, we suppose that the dominant velocity gradient will be in z, and that in the 2D approximation, velocity gradients in y are negligible. The pressure gradient is given by

$$\frac{dP_v^{2D}}{dx} = -\frac{12\mu Q}{h^3 w(x)} = -\frac{12 l_c}{h^2 w(x)}\left(\frac{w_c w_u}{w_u - w_c}\right)\mu\dot{\varepsilon}_a \tag{D.1.1}$$

Integrating along x from $x = 0$ to $x = 2l_c$, we obtain the viscous contribution to ΔP_c:

$$\Delta P_v^{2D} = 12\left(\frac{l_c}{h}\right)^2\left(\frac{w_u + w_c}{w_u - w_c}\right)\mu\dot{\varepsilon}_a \tag{D.1.2}$$

For $P = 0$ at $x = l_c$, the pressure profile between $0 \leq x \leq l_c$ is given by

$$P^{2D}(x) = \Delta P_v^{2D} - 6\left(\frac{l_c}{h}\right)^2\left(\frac{w_u w_c}{w_u - w_c}\right)^2\left(\frac{1}{w(x)^2} - \frac{1}{w_u^2}\right)\mu\dot{\varepsilon}_a \tag{D.1.3}$$

The pressure gradient in the lubrication approximation for a power-law fluid is

$$\frac{dP_v^{PL}}{dx} = -\left(\frac{2n+1}{n}\right)^n\left(\frac{2}{h}\right)^{n+1} m\left(\frac{Q}{hw}\right)^n = -\left(\frac{2n+1}{n}\right)^n\left(\frac{2}{h}\right)^{n+1}\left(\frac{l_c w_c w_u}{w_u - w_c}\right)^n \frac{m\dot{\varepsilon}_a^n}{w^n} \tag{D.1.4}$$

Integrating this result, one obtains

$$\Delta P_v^{PL} = \frac{2^{n+2}}{n+1}\left(\frac{2n+1}{n}\right)^n\left(\frac{l_c}{h}\right)^{n+1}\left\{\left(\frac{w_u}{w_u - w_c}\right)^{n+1} - \left(\frac{w_c}{w_u - w_c}\right)^{n+1}\right\} m\dot{\varepsilon}_a^n \tag{D.1.5}$$

For $P = 0$ at $x = l_c$, the pressure profile between $0 \leq x \leq l_c$ is given by

$$P^{PL}(x) = \frac{2^{n+1}}{n+1}\left(\frac{2n+1}{n}\right)^n\left(\frac{l_c}{h}\right)^{n+1}\left(\frac{w_c w_u}{w_u - w_c}\right)^{n+1}\left(\frac{1}{w(x)^{n+1}} - \frac{1}{w_u^{n+1}}\right) m\dot{\varepsilon}_a^n \tag{D.1.6}$$

To correct for the finite aspect ratio of the contraction (*i.e.* variations in the velocity field along y), we apply the lubrication approximation for a Newtonian fluid using the 3D expression for the relationship between the pressure gradient and the volumetric flow rate (White, 2003), appropriate for $h < w(x)$ as written

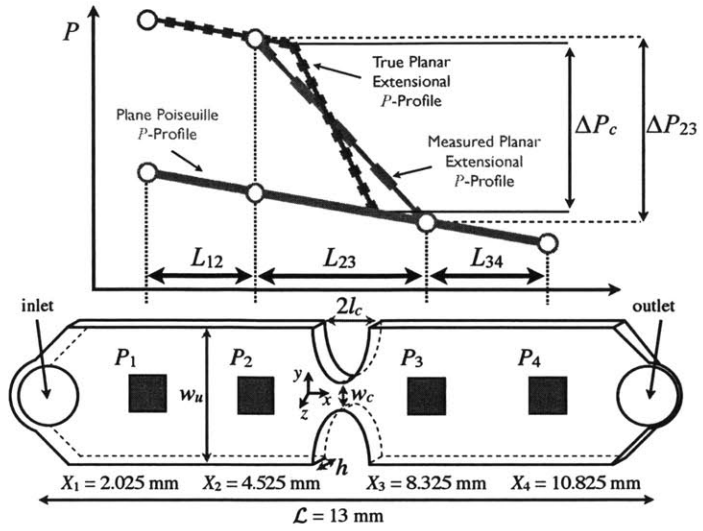

(a)

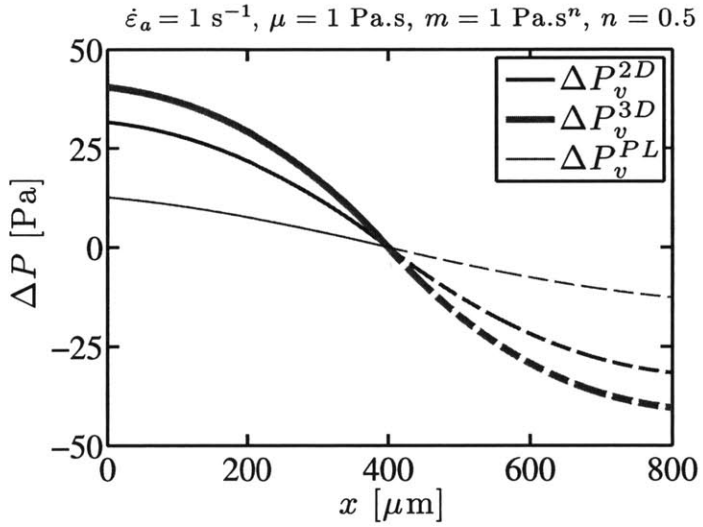

(b)

Figure D.1.1: (a) Qualitative pressure profiles in the contraction geometry. RED: Hypothetical linear pressure profile, if the chip had no contraction (VROC). GREEN: Measured pressure profile, accounting for the fact that the MEMS pressure transducers are located some distance upstream and downstream of the contraction section. BLUE: Anticipated true pressure profile in the channel. Schematic diagram of the hyperbolic planar contraction and representative pressure profile, showing the coordinate system and variables used throughout the text. The contraction dimensions are $h = 200$ μm, $l_c = 400$ μm, $w_c = 400$ μm and $w_u = 2920$ μm. The solid squares indicate the approximate size and location of the flush-mounted MEMS pressure transducers. The schematic depiction is approximately to scale. (b) Pressure profiles across the contraction according to lubrication approximation, as calculated by the 2D Newtonian approximation given by Eq. (D.1.2), 3D Newtonian approximation given by Eq. (D.1.11) and the 2D Power-Law approximation given by Eq. (D.1.5).

$$\begin{aligned}\frac{dP_v^{3D}}{dx} &= \left[1-6\left(\frac{2}{\pi}\right)^5\frac{h}{w(x)}\sum_{j\ odd}^{\infty}\frac{\tanh(j\pi w(x)/2h)}{j^5}\right]^{-1}\frac{dP_v^{2D}}{dx}\\ &= -\frac{12\mu Q}{h^3 w(x)}\left[1-6\left(\frac{2}{\pi}\right)^5\frac{h}{w(x)}\sum_{j\ odd}^{\infty}\frac{\tanh(j\pi w(x)/2h)}{j^5}\right]^{-1}\\ &= -\frac{12 l_c}{h^2 w(x)}\left[1-6\left(\frac{2}{\pi}\right)^5\frac{h}{w(x)}\sum_{j\ odd}^{\infty}\frac{\tanh(j\pi w(x)/2h)}{j^5}\right]^{-1}\left(\frac{w_u w_c}{w_u-w_c}\right)\mu\dot{\varepsilon}_a\end{aligned} \tag{D.1.7}$$

Since $h < w(x)$, the argument of the hyperbolic tangent, $j\pi w(x)/2h > 1$ for all values of j and x, hence the summation is approximately $1 + 1/3^5 + 1/5^5 + ... \approx 1$, so we have

$$\frac{dP_v^{3D}}{dx} \approx -\frac{12\mu Q}{h^3 w(x)}\left[1-6\left(\frac{2}{\pi}\right)^5\frac{h}{w(x)}\right]^{-1} = -\frac{12 l_c}{h^2 w(x)}\left[1-6\left(\frac{2}{\pi}\right)^5\frac{h}{w(x)}\right]^{-1}\left(\frac{w_u w_c}{w_u-w_c}\right)\mu\dot{\varepsilon}_a \tag{D.1.8}$$

this result gives

$$-dP_v^{3D} = \frac{12\mu Q}{h^3}\frac{x+x_0}{K}\left[1-6\left(\frac{2}{\pi}\right)^5\frac{h(x+x_0)}{K}\right]^{-1}dx \tag{D.1.9}$$

$$\Delta P_v^{3D} = -2\left\{\frac{\pi^5}{16}\frac{w_c w_u}{h(w_u-w_c)} + \frac{\pi^{10}}{3072}\left(\frac{w_c w_u}{h(w_u-w_c)}\right)^2\ln\left(\frac{\frac{192h}{\pi^5 w_c}-1}{\frac{192h}{\pi^5 w_u}-1}\right)\right\}\left(\frac{l_c}{h}\right)^2\mu\dot{\varepsilon}_a \tag{D.1.10}$$

Or equivalently,

$$\Delta P_v^{3D} = \frac{1}{3}\left(\frac{\pi}{2}\right)^5\frac{w_c w_u}{h(w_u+w_c)}\left\{\frac{1}{6}\left(\frac{\pi}{2}\right)^5\frac{w_c w_u}{h(w_u-w_c)}\ln\left(\frac{1-6\left(\frac{2}{\pi}\right)^5\frac{h}{w_u}}{1-6\left(\frac{2}{\pi}\right)^5\frac{h}{w_c}}\right)-1\right\}\Delta P_v^{2D} \tag{D.1.11}$$

For $P = 0$ at $x = l_c$, the pressure profile between $0 \le x \le l_c$ in the 3D case is given by

$$P^{3D}(x) = \Delta P_v^{3D} - \frac{1}{3}\left(\frac{\pi}{2}\right)^5\frac{w_c^2 w_u^2}{h^2(w_u^2-w_c^2)}\left\{\frac{1}{6}\left(\frac{\pi}{2}\right)^5\ln\left(\frac{1-6\left(\frac{2}{\pi}\right)^5\frac{h}{w_u}}{1-6\left(\frac{2}{\pi}\right)^5\frac{h}{w(x)}}\right)+h\left(\frac{1}{w_u}-\frac{1}{w(x)}\right)\right\}\Delta P_v^{2D} \tag{D.1.12}$$

In reality, the measured pressure drop between the MEMS transducers 2 and 3, ΔP_{23}, is different from the pressure drop across the contraction, ΔP_c. This difference results from the fact that the MEMS transducers are placed some distance upstream and downstream of the contraction entrance and exit, so we have to account for the

viscous contribution to the measured pressure drop in the upstream and downstream regions from the contraction. This idea is illustrated in Figure D.1.1, and follows from the pressure correction procedure used elsewhere (Wang *et al.*, 2010).

The throat of the contraction is located at the center of the entire microchannel, whereas the origin of the capital x-coordinate system is at the inlet of the entire channel as indicated in Figure D.1.1. We use the average of the pressure gradients for $x_1 < x < x_2$ and $x_3 < x < x_4$ to extrapolate the pressure profile to the point immediately upstream and downstream of the contraction entrance and exit. The assumption underlying this correction is that the flow is a fully-developed steady shear flow between the second transducer and the contraction inlet as well as between the contraction outlet and the third transducer. This simplifying approximation can be justified since the flow is in the low-Re Stokesian regime, but it should be noted that it necessarily results in an underestimate of the overall pressure drop since it neglects any inertial contribution to the pressure drop as well as any viscous dissipation due to the extensional component of the flow.

$$\Delta P_c = \Delta P_{23}\left\{1 - \frac{1}{2}\left(\frac{\Delta P_{14}}{\Delta P_{23}} - 1\right)\frac{l_s - 2l_c}{L}\right\} \tag{D.1.13}$$

The positions of the MEMS transducers are $x_1 = 2.025$ mm, $x_2 = 4.525$ mm, $x_3 = 8.325$ mm, $x_4 = 10.825$ mm. $L = x_2 - x_1 = x_4 - x_3 = 2.5$ mm.

D.2 Operating Bounds of EVROC

The extensional-viscometer-rheometer-on-a-chip (EVROC, Rheosense, Inc.) is a microfluidic hyperbolically-shaped contraction-expansion geometry for characterizing the importance of viscoelastic effects in an extensionally-dominated flow at large extension rates ($\dot{\varepsilon}_a \gg 1\ \mathrm{s}^{-1}$). On account of the mixed shear and extensional flow kinematics in the device, the extraction of a homogeneous extensional viscosity is difficult and restricted to a specific range of viscosities and extension rates that, like any rheometer, is set by the operating limits of the EVROC. Unlike the operating limits of a rotational or capillary rheometer, however, the operating limits of the EVROC cannot be derived from first

principles, and they are therefore approximate. In the following analysis, the approximate operating limits will be formulated for Newtonian fluids and then for viscoelastic fluids by making only a handful of assumptions.

Four inline, 800×800 μm^2 MEMS-based pressure transducers are embedded along the centerline of the microchannel. The maximum measurable pressure of the device is $P_{max} = 44$ kPa, corresponding to the maximum allowable deflection of the membrane of the specific MEMS transducer. The minimum reliably measurable pressure drop across the contraction is $\Delta P_{23,min} = 0.5$ kPa, where ΔP_{23} is the pressure drop between the second and third MEMS transducers. Using a 2.5 mL Hamilton Gastight glass syringe (Reno, NV) the minimum volumetric flow rate is $Q_{min} = 1.0\ \mu$L.min^{-1} and the maximum flow rate is $Q_{max} = 5.2$ mL.min^{-1}. Therefore the attainable range of extension rates from Eq. (D.0.2) is $0.45 \leq \dot{\varepsilon}_a \leq 2.3 \times 10^3$ s^{-1}.

D.2.1 Operating Bounds for Newtonian Fluids

Prior to establishing the operating limits of the EVROC, two quantities must be determined experimentally for a given contraction geometry using a viscous Newtonian fluid flowing through the contraction at low Reynolds number, defined as

$$Re \equiv \frac{\rho d_h l_c \dot{\varepsilon}_a}{\mu} \tag{D.2.1}$$

where ρ is the fluid density and μ is the shear viscosity of the test fluid. The hydraulic diameter defined at the throat of the contraction is $d_h = 2hw_c/(h + w_c) = 267\ \mu$m. For the flow in the hyperbolic contraction, a low Reynolds number requires $Re < Re^* = 10$. At higher Reynolds numbers, the flow kinematics are no longer symmetrical about the contraction-expansion as shown in Figure D.2.1 and the pressure drop begins to be dominated by inertial effects.

The first quantity to be measured is a viscous friction factor

$$f_{23} = \frac{\Delta P_{23}}{\mu \dot{\varepsilon}_a} \tag{D.2.2}$$

At low Reynolds number the value of f_{23} is independent of the viscosity and only depends on the contraction geometry. For the geometry shown in Figure D.1.1, experimental

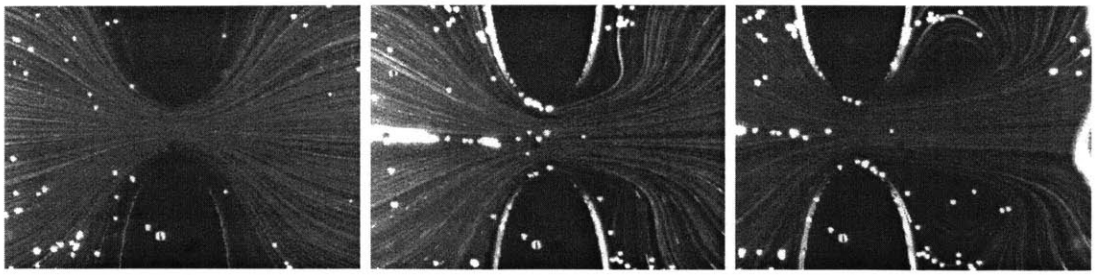

(a) $Re = 5$ (b) $Re = 48$ (c) $Re = 86$

Figure D.2.1: Streaklines of Newtonian flow through the contraction. Flow is left to right.

measurements at low Reynolds number yield a value of $f_{23} \approx 250$.

The second quantity is the pressure coefficient $\mathcal{P} \equiv \Delta P_{23}/\Delta P_{14}$, where ΔP_{14} is the pressure drop between the first and fourth MEMS transducers. At low Reynolds number the value of $\mathcal{P}$ also only depends on the contraction geometry. For the geometry shown in Figure D.1.1, $\mathcal{P} = 0.71$. Therefore, the maximum pressure drop that can hypothetically be measured between the second and third MEMS transducers for a Newtonian fluid is $\Delta P^N_{23,max} = \mathcal{P} P_{max} = 31.24$ kPa.

The final boundary on the measurable pressure drops is set by the onset of inertially driven secondary flows, which is determined by combining Eq. (D.2.1) and D.2.2 to obtain $\Delta P^*_{23} = \frac{f_{23}}{Re^*} \rho d_h l_c \dot{\varepsilon}_a^2$. Note that this inertial limit scales quadratically with nominal extension rate. The operating limits in terms of pressure drop are shown in Figure D.2.2 (a).

The operating limits can also be constructed in terms of the shear viscosity of the fluid and extension rates imposed by the syringe pump. The line of minimum measurable shear viscosity is $\mu_{min} = \Delta P_{23,min}/f_{23}\dot{\varepsilon}_a$, and the maximum measurable viscosity is $\mu_{max} = \Delta P_{23,max}/f_{23}\dot{\varepsilon}_a$. The boundary marking the onset of inertially-driven secondary flows is $\mu^* = \rho d_h l_c \dot{\varepsilon}_a / Re^*$. The operating limits in terms of measurable shear viscosity are shown in Figure D.2.2 (b). It is noteworthy that this inertial upper limit for measurable viscosity scales only linearly with extension rate. To illustrate this point, if the viscosity of test fluid A is twice that of fluid B, fluid A will exhibit secondary flows at twice the extension rate as fluid B, but the corresponding pressure drop at this transitional

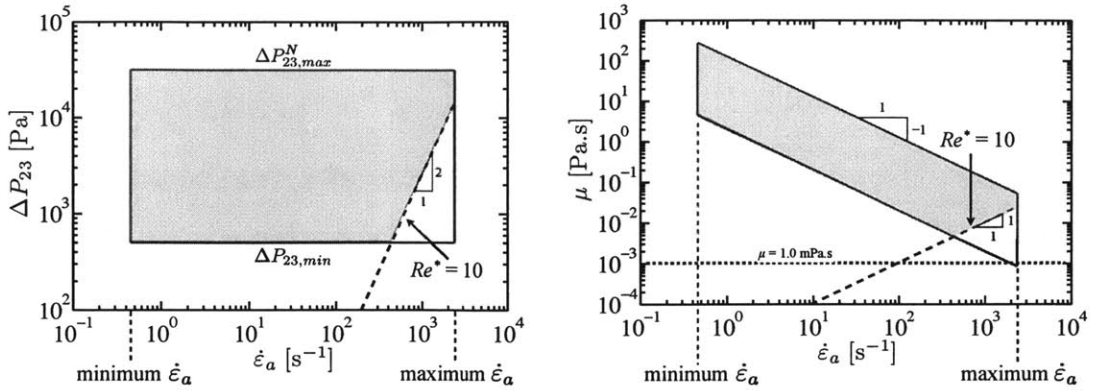

Figure D.2.2: Operating limits for the EVROC device with a Newtonian fluid. Region of reliable measurements lie within the shaded region. (a) Pressure, (b) shear viscosity, the dashed horizontal blue line indicates the viscosity of water.

extension rate for fluid A will be *four* times that of fluid B.

Furthermore, it should be emphasized that for this contraction geometry, the viscosity of water (indicated by the dashed horizontal blue line in Figure D.2.2 (b)) is too low to be measured in the low Reynolds number regime at any extension rate. It is of course possible to perform experiments with low viscosity, water-based liquids at flow rates that yield a measurable pressure drop, but it is evidently most likely that these flow rates will be far too high to ensure low Reynolds number flow. Accordingly, it is especially important to calculate the Reynolds number for low viscosity liquids in order to correctly interpret the measured data from EVROC.

In principle, the EVROC device could be redesigned to realize a range of extension rates at which the viscosity of water could be measured at low Reynolds number, by either reducing the minimum measurable pressure drop $\Delta P_{23,min}$ or reducing the Reynolds number for a given extension rate by reducing the value of l_c or d_h. Such a redesign, however, would not be entirely straight forward since geometric features of the MEMS transducers may set a practical lower limit to the minimum value of $\Delta P_{23,min}$, and the value of f_{23}, which also affects the inertial operating limit, is intimately dependent on the contraction dimensions.

D.2.2 Operating Bounds for Viscoelastic Fluids

In order to calculate the range of measurable apparent extensional viscosities $\eta_{E,a}$ and first normal stress differences $N_{1,a}$, one must consider the following corrections to the measured pressure profiles in the channel.

Firstly, the pressure drop that is of interest for extensional rheology measurements is the pressure drop associated with the contraction alone, ΔP_c, which is somewhat different from ΔP_{23}, because the MEMS transducers 2 and 3 are located some distance upstream and downstream of the contraction entrance and exit. To calculate the value of ΔP_c, one can use the average of the pressure gradients for $X_1 < X < X_2$ and $X_3 < X < X_4$ to extrapolate the fully-developed shear flow pressure profile in the upstream and downstream channels to the inlet and outlet of the contraction. Accordingly, the true pressure drop across the contraction, ΔP_c, is related to the measured pressured drop, ΔP_{23}, by the relation

$$\Delta P_c = \Delta P_{23}\left\{1 - \frac{1}{2}\left(\frac{1}{\mathcal{P}} - 1\right)\frac{L_{23} - 2l_c}{L}\right\} \tag{D.2.3}$$

where $L_{23} = 3.8$ mm, $L \equiv L_{12} = L_{34} = 2.5$ mm. For a viscoelastic fluid, the pressure coefficient $\mathcal{P} \equiv \Delta P_{23}/\Delta P_{14}$ is not necessarily constant with flow rate, but is generally in the range $0 < \mathcal{P} \leq 1$.

The value of the total pressure drop across the contraction ΔP_c can be used to determine the extensional viscosity by assuming that it can be decomposed as $\Delta P_c = \Delta P_e + \Delta P_v$, whereby the total pressure drop is the superposition of a viscoelastic component ΔP_e and a viscous component ΔP_v due to shearing at the walls. The extensional viscosity is calculated based on the viscoelastic contribution to the pressure drop and is given by

$$\eta_E = \frac{1}{\varepsilon_H}\frac{\Delta P_e}{\dot{\varepsilon}_a} \tag{D.2.4}$$

where $\varepsilon_H = \ln(w_u/w_c)$. The first normal stress difference is therefore equal to

$$N_1 = \eta_E \dot{\varepsilon}_a = \frac{1}{\varepsilon_H}\Delta P_e \tag{D.2.5}$$

It is therefore necessary to determine the value of ΔP_v in order to calculate the exten-

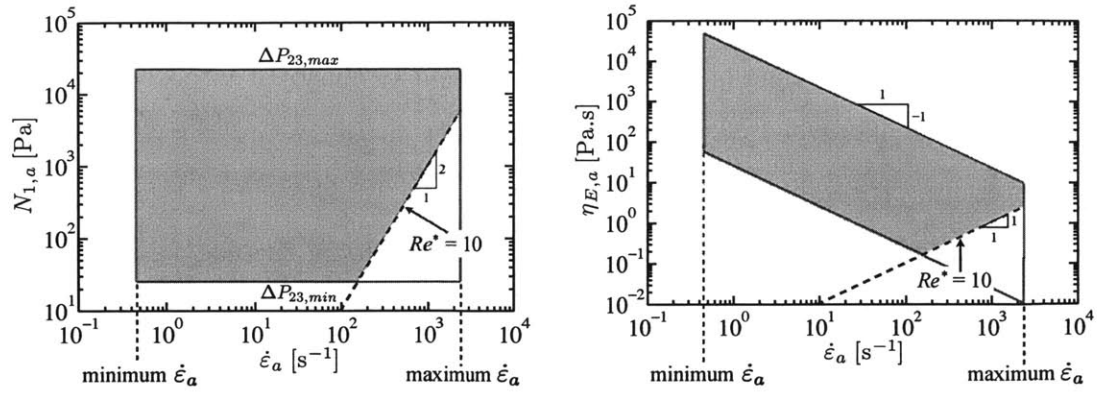

(a) (b)

Figure D.2.3: Operating limits for the EVROC device with a viscoelastic fluid. Largest region of measurable data lie within the shaded region. (a) Apparent first normal stress difference, (b) apparent extensional viscosity.

sional viscosity. The evaluation of ΔP_v is commonly achieved by invoking a lubrication approximation for either a Newtonian fluid or a power-law fluid.

In the interest of determining the largest hypothetical operating range for the EVROC device, we will assume that $\Delta P_v \ll \Delta P_e$, and therefore $\Delta P_c \approx \Delta P_e$. Admittedly, this approximation is unrealistic since it requires a highly viscoelastic fluid with a very low shear viscosity, but it will enable us to determine the most extreme operating limits. Furthermore, for the sake of simplicity, we will assume that $\mathcal{P} \ll 1$ and therefore $\Delta P_c \approx \Delta P_{23}$. Under these assumptions, the maximum pressure drop is $\Delta P_{e,max} = P_{max} = 44$ kPa and the minimum is $\Delta P_{e,min} = \Delta P_{min} = 0.5$ kPa. The operating limits under these assumptions are shown in Figure D.2.3. Unfortunately, it is no longer obvious how to determine when the onset of inertially-driven secondary flows will occur under these assumptions, since it is not clear what the appropriate value of the shear viscosity should be for calculating the Reynolds number. However, to provide an approximate boundary, the limits appropriate to a fluid with a constant viscosity (*e.g.* a second order fluid) have been added to the diagrams.

Bibliography

Adams, E. B., Whitehead, J. C. & Bogue, D. C. (1965). "Stresses in a viscoelastic fluid in converging and diverging flow." *A.I.Ch.E Journal*, **11**(6):1026–1032.

Adams, J. M., Fielding, S. M. & Olmsted, P. D. (2008). "The interplay between boundary conditions and flow geometries in shear banding: Hysteresis, band configurations, and surface transitions." *Journal of Non-Newtonian Fluid Mechanics*, **151**(1–3):101–118.

Adams, J. M. & Olmsted, P. D. (2009a). "Nonmonotonic models are not necessary to obtain shear banding phenomena in entangled polymer solutions." *Physical Review Letters*, **102**(6):067801.

Adams, J. M. & Olmsted, P. D. (2009b). "Comment on "Nonmonotonic models are not necessary to obtain shear banding phenomena in entangled polymer solutions" Reply." *Physical Review Letters*, **103**(21):219802.

Adrian, R. J. (1991). "Particle-imaging techniques for experimental fluid-mechanics." *Annual Review of Fluid Mechanics*, **23**:261–304.

Adrian, R. J. (2005). "Twenty years of particle image velocimetry." *Experiments in Fluids*, **39**(2):159–169.

Adrian, R. J. & Westerweel, J. (2011). *Particle Image Velocimetry.* New York, NY: Cambridge University Press.

Afonso, A. M., Oliveira, P. J., Pinho, F. T. & Alves, M. A. (2011). "Dynamics of

high-Deborah-number entry flows: a numerical study." *Journal of Fluid Mechanics*, **677**:272–304.

Aguayo, J. P., Tamaddon-Jahromi, H. R. & Webster, M. F. (2008). "Excess pressure-drop estimation in contraction and expansion flows for constant shear-viscosity, extension strain-hardening fluids." *Journal of Non-Newtonian Fluid Mechanics*, **153**(2–3):157–176.

Alves, M. A. Optimal shape design for viscoelastic fluid flow. *INNFM Conference on "Whither Rheology"*, April 2–4, 2007 Lake Vyrnwy, Wales.

Anderson, V.J., Pearson, J.R.A. & Boek, E. S. (2006). "The rheology of worm-like micellar fluids." *Rheology Reviews, The British Society of Rheology*, 217–254. D.M. Binding & K. Walters (Eds).

Ardekani, A. M., Sharma, V. & McKinley, G. H. (2010). "Dynamics of bead formation, filament thinning and breakup in weakly viscoelastic jets." *Journal of Fluid Mechanics*, **665**:46–56.

Asmolov, E. S. (1999). "The inertial lift on a spherical particle in a plane Poiseuille flow at large channel Reynolds number." *Journal of Fluid Mechanics*, **381**:63–87.

Atalik, K. & Keunings, R. (2004). "On the occurrence of even harmonics in the shear stress response of viscoelastic fluids in large amplitude oscillatory shear." *Journal of Non-Newtonian Fluid Mechanics*, **122**(1–3):107–116.

Baek, S. G. & Magda, J. J. (2003). "Monolithic rheometer plate fabricated using silicon micromachining technology and containing miniature pressure sensors for N_1 and N_2 measurements." *Journal of Rheology*, **47**(5):1249–1260.

Ballesta, P., Lettinga, M. P. & Sebastien Manneville. (2007). "Superposition rheology of shear-banding wormlike micelles." *Journal of Rheology*, **51**(7):1047–1072.

Bandalusena, H. C. H., Zimmerman, W. B. & Rees, J. M. (2009). "Microfluidic rheometry of a polymer solution by micron resolution particle image velocimetry: a model validation study." *Measurement Science & Technology*, **20**(11):115404.

Bandalusena, H. C. H., Zimmerman, W. B. & Rees, J. M. (2010). "Creeping flow analysis of an integrated microfluidic device for rheometry." *Journal of Non-Newtonian Fluid Mechanics*, **165**(19–20):1302–1308.

Bautista, F., Soltero, J. F. A., Macias, E. R., Puig, J. E. & Manero, O. (2002). "Irreversible thermodynamics approach and modeling of shear-banding flow of wormlike micelles." *Journal of Physical Chemistry*, **106**:13018–13026.

Bécu, L., Manneville, S. & Colin, A. (2006). "Yielding and flow in adhesive and nonadhesive concentrated emulsions." *Physical Review Letters*, **96**(13):138302.

Bejarano, J. D. & Sanchez, A. M. (1989). "Generalized Fourier series for non-linear systems." *Journal of Sound and Vibration*, **134**(2):333–341.

Berret, J.-F., Roux, D. C. & Porte, G. (1994). "Isotropic-to-nematic transition in wormlike micelles under shear." *Journal De Physique II*, 4(8):1261–1279.

Berret, J.-F., Porte, G. & Decruppe, J. P. (1997). "Inhomogeneous shear flows of wormlike micelles: A master dynamic phase diagram." *Physical Review E*, **55**(2):1668–1676.

Berret, J.-F., Lerouge, S. & Decruppe, J. P. (2002). "Kinetics of the shear-thickening transition observed in dilute surfactant solutions and investigated by flow birefringence." *Langmuir*, **18**(20):7279–7286.

Berret, J.-F. (2006). *Rheology of Wormlike Micelles: Equilibrium Properties and Shear Banding Transitions. Molecular Gels*, Springer Netherlands, 667–720.

Bhagat, A. A. S., Kuntaegowdanahalli, S. S. & Papautsky, I. (2008) "Enhanced particle filtration in straight microchannels using shear-modulated inertial migration." *Physics of Fluids*, **20**(10):101702.

Bhagat, A. A. S., Hou, H. W., Li, L. D., Lim, C. T. & Han, J. Y. (2011). "Pinched flow coupled shear-modulated inertial microfluidics for high-throughput rare blood cell separation." *Lab on a Chip*, 11(11):1870–1878.

Binding, D. M. & Walters, K. (1988). "On the use of flow through a contraction in estimating the extensional viscosity of mobile polymer solutions." *Journal of Non-Newtonian Fluid Mechanics*, **30**(2–3):233–250.

Bird, R. B., Armstrong, R. C. & Hassager, O. (1987). *Dynamics of Polymeric Liquids*, 2^{nd} edn. Vol. 1. New York, NY: John Wiley & Sons, Inc.

Bird, J. C., Stewart, W. E. & Lightfoot, E. N. (2002). *Transport Phenomena*, 2^{nd} edn. New York, NY: John Wiley & Sons, Inc.

Bocquet, L., Colin, A. & Ajdari, A. (2009). "Kinetic theory of plastic flow in soft glassy materials." *Physical Review Letters*, **103**(3):036001.

Boek, E. S., Coveney, P. V., Lekkerkerker, H. N. W. & Van der Schoot, P. (1997). "Simulating the rheology of dense colloidal suspensions using dissipative particle dynamics." *Physical Review E*, **55**(3):3124–3133.

Boukany, P. E. & Wang, S. Q. (2008). "Use of particle-tracking velocimetry and flow birefringence to study nonlinear flow behavior of entangled wormlike micellar solution: From wall slip, bulk disentanglement to chain scission." *Macromolecules*, **41**(4):1455–1464.

Bewersdorff, H. W. & Singh, R. P. (1988). "Rheological and drag reduction characteristics of xanthan gum solutions." *Rheologica Acta*, **27**(6):617–627.

Britton, M. M. & Callaghan, P. T. (1997). "Two-phase shear band structures at uniform stress." *Physical Review Letters*, **78**(26):4930–4933.

Britton, M. M. & Callaghan, P. T. (1999). "Shear banding instability in wormlike micellar solutions." *The European Physical Journal B - Condensed Matter and Complex Systems*, **7**(2):1434–6028.

Brown, E. F., Burghardt, W. R. & Venerus, D. C. (1997). "Tests of the Lodge-Meissner relation in anomalous nonlinear step strain of an entangled wormlike micelle solution." *Langmuir*, **13**:3902–3904.

Callaghan, P. T. (2008). "Rheo NMR and shear banding." *Rheologica Acta*, **47**(3):243–255.

Cappelaere, E. & Cressely, R. (1997). "Shear banding structure in viscoelastic micellar solutions." *Colloid and Polymer Science*, **275**(5):407–418.

Cates, M. E. (1987). "Reptation of living polymers - Dynamics of entangled polymers in the presence of reversible chain-scission reactions." *Macromolecules*, **20**(9):2289–2296.

Cates, M. E. (1990). "Nonlinear viscoelasticity of wormlike micelles (and other reversibly breakable polymers)." *Journal of Physical Chemistry*, **94**(1):371–375.

Cates, M. E. & Candau, S. J. (1990). "Statics and dynamics of worm-like surfactant micelles." *Journal of Physics-Condensed Matter*, **2**(33):6869–6892.

Cates, M. E. & Fielding, S. M. (2006). "Rheology of giant micelles." *Advances in Physics*, **55**(7–8):799–879.

Chandrasekhar S. (1981). *Hydrodynamic and Hydromagnetic Stability.* New York, NY: Dover.

Chin, C. D., Linder, V. & Sia, S. K. (2012). "Commercialization of microfluidic point-of-care diagnostic devices." *Lab on a Chip*, **12**:2118–2134.

Cho, K. S., Hyun, K., Ahn, K. H. & Lee, S. J. (2005). "A geometrical interpretation of large amplitude oscillatory shear response." *Journal of Rheology*, **49**(3):747–758.

Choi, Y. S., Seo, K. W. & Lee, S. J. (2011). "Lateral and cross-lateral focusing of spherical particles in a square microchannel." *Lab on a Chip*, **11**:460–465.

Chun, B. & Ladd, A. J. C. (2006). "Inertial migration of neutrally buoyant particles in a square duct: An investigation of multiple equilibrium positions." *Physics of Fluids*, **18**(3):031704.

Chung, A. J., Gossett, D. R. & Di Carlo, D. (2012). "Three dimensional, sheathless, and high-throughput microparticle inertial focusing through geometry-induced secondary flows." *Small*, **9**(5):685–690.

Ciftlik, A. T., Ettori, M. & Gijs, M. A. M. (2013). "High throughput-per-footprint inertial focusing." *Small*, **10**:1–10.

Cogswell, F. N. (1972). "Converging flow of polymer melts in extrusion dies." *Polymer Engineering & Science*, **12**(1):64–73.

Cogswell, F. N. (1978). "Converging flow and stretching flow: a compilation." *Journal of Non-Newtonian Fluid Mechanics*, 4(1–2):23–38.

Cokelet, G. R. & Goldsmith, H. L. (1991). "Decreased hydrodynamic resistance in the 2-phase flow of blood through small vertical tubes at low flow-rates." *Circulation Research*, **68**(1):1–17.

Collier, J. R., Romanoschi, O. & Petrovan, S. (1998). "Elongational rheology of polymer melts and solutions." *Journal of Applied Polymer Science*, **69**:2357–2367.

Coussot, P., Raynaud, J. S., Bertrand, F., Moucheront, P., Guilbaud, J. P., Huynh, H. T., Jarny, S. & Lesueur, D. (2002). "Coexistence of liquid and solid phases in flowing soft-glassy materials." *Physical Review Letters*, **88**(21):218301.

Coussot, P. & Ovarlez, G. (2010). "Physical origin of shear-banding in jammed systems." *European Physical Journal E*, **33**(3):183–188.

Cromer, M., Cook, L. P. & McKinley, G.H. 2010. "Pressure-driven flow of wormlike micellar solutions in rectilinear microchannels." *Journal of Non-Newtonian Fluid Mechanics*. **166**:180–193.

Crumeyrolle, O., Mutabazi, I. & Grisel, M. (2002). "Experimental study of inertioelastic Couette-Taylor instability modes in dilute and semidilute polymer solutions." *Physics of Fluids*, **14**(5):1681–1688.

Davies, C. J., Sederman, A. J., Pipe, C. J., McKinley, G. H. Gladden, L. F. & Johns, M. J. (2010). "Rapid measurement of transient velocity evolution using GERVAIS." *Journal of Magnetic Resonance*, **202**(1):93–101.

D'Avino, G., Romeo, G., Villone, M. M., Greco, F., Netti, P. A. & Maffettone, P. L. (2012). "Single line particle focusing induced by viscoelasticity of the suspending liquid: theory, experiments and simulations to design a micropipe flow-focuser." *Lab on a Chip*, **12**:1638–1645.

Dealy, J. M. & Wissbrun, K. F. (1990). *Melt Rheology and Its Role in Plastics Processing: Theory and Applications.* Van Nostrand Reinhold.

Dealy, J. M. (2010). "Weissenberg and Deborah Numbers – Their definition and use" *Rheology Bulletin (Society of Rheology)*, **79**(2):14–18.

Decruppe, J. P., Cappelaere, E. & Cressely, R. (1997). "Optical and rheological properties of a semi-diluted equimolar solution of cetyltrimethylammonium bromide and potassium bromide." *Journal De Physique II*, **7**(2):257–270.

Decruppe, J. P. & Ponton, A. (2003). "Flow birefringence, stress optical rule and rheology of four micellar solutions with the same low shear viscosity." *European Physical Journal E*, **10**(3):201–207.

Degré, G., Joseph, P., Tabeling, P., Lerouge, S., Cloitre, M. & Ajdari, A. (2006). "Rheology of complex fluids by particle image velocimetry in microchannels." *Applied Physics Letters*, **89**(2):024104.

Dendukuri, D., Gu, S. S., Pregibon, D. C., Hatton, T. A. & Doyle, P. S. (2007). "Stop-flow lithography in a microfluidic device." *Lab on a Chip*, **7**(7):818–828.

Dhont, J. K. G. (1999). "A constitutive relation describing the shear-banding transition." *Physical Review E*, **60**(4):4534–4544.

Di Carlo, D., Irimia, D., Tompkins, R. G. & Toner, M. (2007). "Continuous inertial focusing, ordering, and separation of particles in microchannels." *Proceedings of the National Academy of Sciences of the United States of America*, **104**(48):18892–18897.

Di Carlo, D. (2009a). "Inertial microfluidics." *Lab on a Chip*, **9**:3038–3046.

Di Carlo, D., Edd, J. F., Humphry, K. J., Stone, H. A. & Toner, M. (2009b). "Particle segregation and dynamics in confined flows." *Physical Review Letters*, **102**(9):094503.

Dimitriou, C. J., McKinley, G. H. & Venkatesan, R. (2011). "Rheo-PIV analysis of the yielding and flow of model waxy crude oils." *Energy & Fuels*, **25**(7):3040–3052.

Divoux, T., Tamarii, D., Barentin, C. & Manneville, S. (2010). "Transient shear banding in a simple yield stress fluid." *Physical Review Letters*, **104**:208301.

Divoux, T., Barentin, C. & Manneville, S. (2011). "From stress-induced fluidization processes to Herschel-Bulkley behaviour in simple yield stress fluids." *Soft Matter*, **7**(18):8409–8418.

Dodge, D. W. & Metzner, A. B. (1959). "Turbulent flow of non-Newtonian systems." *A.I.Ch.E Journal*, **5**(2):189–204.

Doi, M. & Edwards, S. F. (1986). *The Theory of Polymer Dynamics.* New York, NY: Oxford University Press.

Draad, A. A., Kuiken, G. D. C. & Nieuwstadt, F. T. M. (1998). "Laminar-turbulent transition in pipe flow for Newtonian and non-Newtonian fluids." *Journal of Fluid Mechanics*, **377**:267–312.

Dubash, N., Cheung, P. & Shen, A. Q. (2012). "Elastic instabilities in a microfluidic cross-slot flow of wormlike micellar solutions." *Soft Matter*, **8**:5847–5856.

Duffy, D. C., McDonald, J. C., Schueller, O. J. A. & Whitesides, G. M. (1998). "Rapid prototyping of microfluidic systems in poly(dimethylsiloxane)." *Analytical Chemistry*, **70**(23):4974–4984.

Durst, F., Ray, S., Unsal, B. & Bayoumi, O. A. (2005). "The development lengths of laminar pipe and channel flows." *Journal of Fluids Engineering*, **127**(6):1154–1160.

El-Kareh, A. W. & Leal, L. G. (1989). "Existence of solutions for all Deborah numbers for a non-Newtonian model modified to include diffusion." *Journal of Non-Newtonian Fluid Mechanics*, **33**(3):257–287.

Escudier, M. P., Presti, F. & Smith, S. (1999). "Drag reduction in the turbulent pipe flow of polymers." *Journal of Non-Newtonian Fluid Mechanics*, **81**:197–213.

Espanol, P., Yuan, X. F. & Ball, R. C. (1996). "Shear banding flow in the Johnson-Segalman fluid." *Journal of Non-Newtonian Fluid Mechanics*, **65**(1):93–109.

Everage, A. E. & Ballman, R. L. (1978). "Extensional flow capillary as a new method for extensional viscosity measurement." *Nature*, **273**(5669):213–215.

Ewoldt, R. H., Hosoi, A. E. & McKinley, G. H. (2008). "New measures for characterizing nonlinear viscoelasticity in large amplitude oscillatory shear." *Journal of Rheology*, **52**(6):1427–1458.

Ewoldt, R. H., Winter, P., Maxey, J. & McKinley, G. H. (2010). "Large amplitude oscillatory shear of pseudoplastic and elastoviscoplastic materials." *Rheological Acta*, **49**(2):191–212.

Fåhræus, R. & Lindqvist, T. (1931). "The viscosity of the blood in narrow capillary tubes." *American Journal of Physiology*, **96**(3):562–568.

Fardin, M. A., Lasne, B., Cardoso, O., Grégoire, G., Argentina, M., Decruppe, J. P. & Lerouge, S. (2009). "Taylor-like vortices in shear-banding flow of giant micelles." *Physical Review Letters*, **103**(2): 028302.

Fardin, M. A., Lopez, D., Croso, J., Grégoire, G., Cardoso, O., McKinley, G. H. & Lerouge, S. (2010). "Elastic turbulence in shear banding wormlike micelles." *Physical Review Letters*, **104**:178303.

Fardin, M. A., Ober, T. J., Gay, C., Grégoire, G., McKinley, G. H. & Lerouge, S. (2011). "Criterion for purely elastic Taylor-Couette instability in the flows of shear-banding fluids." *European Physical Letters*, **96**(4):44004.

Fardin, M. A., Divoux, T., Guedeau-Boudeville, M. A., Buchet-Maulien, I., Browaeys, J., McKinley, G. H., Manneville, S. & Lerouge, S. (2012a). "Shear-banding in surfactant wormlike micelles: elastic instabilities and wall slip." *Soft Matter*, **8**:2535–2553.

Fardin, M. A., Ober, T. J., Gay, C., Grégoire, G., McKinley, G. H. & Lerouge, S. (2012b). "Potential 'ways of thinking' about the shear-banding phenomenon." *Soft Matter*, **8**(4):910–922.

Fardin, M. A. & Lerouge, S. (2012). "Instabilities in wormlike micelle systems: From shear-banding to elastic turbulence." *European Physics Journal E*, **35**(91).

Fedosov, D. A., Pan, W. X., Caswell, B., Gompper, G. & Karniadakis, G. E. (2011). "Predicting human blood viscosity in silico." *Proceedings of the National Academy of Sciences of the United States of America*, **108**(29):11772–11777.

Feigl, K., Tanner, F. X., Edwards, B. J. & Collier, J. R. (2003). "A numerical study of the measurement of elongational viscosity of polymeric fluids in a semihyperbolically converging die." *Journal of Non-Newtonian Fluid Mechanics*, **115**:191–215.

Feindel, K. W. & Callaghan, P. T. (2010). "Anomalous shear banding: multidimensional dynamics under fluctuating slip conditions." *Rheologica Acta*, **49**(10):1003–1013.

Ferer, M., Anna, S. L., Tortora, P., Kadambi, J. R., Oliver, M., Bromhal, G. S. & Smith, D. H. (2011). "Two-phase flow in porous media: Predicting its dependence on capillary number and viscosity ratio." *Transport in Porous Media*, **86**(1):273–289.

Fielding, S. M. & Olmsted, P. D. (2003). "Kinetics of the shear banding instability in startup flows." *Physical Review E*, **68**(3):036313.

Fielding, S. M. (2005). "Linear instability of planar shear banded flow." *Physical Review Letters*, **95**(13):134501.

Fielding, S. M. (2007). "Complex dynamics of shear banded flows." *Soft Matter*, **3**(10):1262–1279.

Fielding, S. M. (2010). "Viscoelastic Taylor-Couette instability of shear banded flow." *Physical Review Letters*, **104**:198303.

Fischer, E. & Callaghan, P. T. (2000). "Is a birefringence band a shear band?" *Europhysics Letters*, **50**(6):803–809.

Fischer, E. & Callaghan, P. T. (2001). "Shear banding and the isotropic-to-nematic transition in wormlike micelles." *Physical Review E*, **64**(1):011501.

Forame, P. C., Hansen, R. J. & Little, R. C. (1972). "Observations of early turbulence in pipe-flow of drag reducing polymer-solutions." *AIChE Journal*, **18**(1):213–217.

Fuller, G. G., Cathey, C. A., Hubbard, B. & Zebrowski, B. E. (1987). "Extensional viscosity measurements for low-viscosity fluids." *Journal of Rheology*, **31**(3):235–249.

Fuller, G. G. (1990). "Optical rheometry." *Annual Review of Fluid Mechanics*, **22**:387–417.

Fuller, G. G. (1995). *Optical Rheometry of Complex Fluids.* Oxford University Press.

Galindo-Rosales, F. J., Alves, M. A. & Oliveira, M. S. N. (2013). "Microdevices for extensional rheometry of low viscosity elastic liquids: A review." *Microfluidics and Nanofluidics*, **14**(1–2):1–19.

Garcia-Margallo, J., Bejarano, J. D. & Yuste, S. B.(1998). "Generalized Fourier series for the study of limit cycles." *Journal of Sound and Vibration*, **125**(1):13–21.

Gauthier, F., Goldsmith, H. L. & Mason, S. G. (1971). "Particle motions in non-Newtonian media II: Poiseuille flow." *Journal of Rheology*, **15**(2):297–330.

de Gennes, P.-G. (1979). *Scaling Concepts in Polymer Physics.* Ithaca, NY: Cornell University Press.

Ghajar, A. J., Tang, C. C. & Cook, W. L. (2010). "Experimental investigation of friction factor in the transition region for water flow in minitubes and microtubes." *Heat Transfer Engineering*, **31**(8):646–657.

Gibaud, T., Barentin, C. & Manneville, S. (2008). "Influence of boundary conditions on yielding in a soft glassy material." *Physical Review Letters*, **101**(25):258302.

Gilbreth, C., Sullivan, S. & Dennin, M. (2006). "Flow transitions in two-dimensional foams." *Physical Review E*, **74**(5):051406.

Goldsmith, H. L. & Skalak, R. (1975). "Hemodynamics." *Annual Review of Fluid Mechanics*, **7**:213–247.

Goldsmith, H. L. & Marlow, J. C. (1979). "Flow behavior of erythrocytes. 2. Particle motions in concentrated suspensions of ghost cells." *Journal of Colloid and Interface Science*, **71**(2):383–407.

Goldsmith, H. L. & Spain, S. (1984). "Margination of leukocytes in blood-flow through small tubes." *Microvascular Research*, **27**(2):204–222.

Gossett, D. R. & Di Carlo, D. (2009). "Particle focusing mechanisms in curving confined flows." *Analytical Chemistry*, **81**(20):8459–8465.

Gossett, D. R., Weaver, W. M., Mach, A. J., Hur, S. C., Tse, H. T. K., Lee, W., Amini, H. & Di Carlo, D. (2010). "Label-free cell separation and sorting in microfluidic systems." *Analytical and Bioanalytical Chemistry*, **397**(8):3249–3267.

Graessley, W. W. (1982). "Entangled linear, branched and network polymer systems - Molecular theories." *Advances in Polymer Science*, **47**:67–117.

Graham, M. D. (2004). "Drag reduction in turbulent flow of polymer solutions." *Rheology Reviews, The British Society of Rheology*, 143–170.

Granek, R. & Cates, M. E. (1992). "Stress-relaxation in living polymers - Results from a Poisson renewal model." *Journal of Chemical Physics*, **96**(6):4758–4767.

Groisman, A. & Steinberg, V. (1998). "Elastic versus inertial instability in Couette-Taylor flow of a polymer solution: Review" *Philosophical Magazine Part B*, **78**:253.

Groisman, A. & Steinberg, V. (2000). "Elastic turbulence in a polymer solution flow." *Nature*, **405**(6782):53–55.

Groisman, A. & Steinberg, V. (2001). "Efficient mixing at low Reynolds numbers using polymer additives." *Nature*, **410**(6831):905–908.

Groisman, A. & Quake, S. R. (2004). "A microfluidic rectifier: Anisotropic flow resistance at low Reynolds numbers." *Physical Review Letters*, **92**(9):094501.

Guillot, P., Panizza, P., Salmon, J. B., Joanicot, M., Colin, A., Bruneau, C. H. & Colin, T. (2006). "Viscosimeter on a microfluidic chip." *Langmuir*, **22**(14):6438–6445.

Han, C. D. & Drexler, L. H. (1973a). "Studies of converging flows of viscoelastic polymeric melts. 1. Stress-birefringent measurements in entrance region of a sharp-edged slit die." *Journal of Applied Polymer Science*, **17**(8):2329–2354.

Han, C. D. & Drexler, L. H. (1973b). "Studies of converging flows of viscoelastic polymeric melts. 3. Stress and velocity distributions in entrance region of a tapered slit die." *Journal of Applied Polymer Science*, **17**(8):2369–2393.

Happel J. & Brenner, H. (1983). *Low Reynolds number hydrodynamics: with special applications to particulate media.* Boston, MA: Kluwer Academic Press.

Hashimoto, T., Kido, K., Kaki, S., Yamamoto, T. & Mori, N. (2006). "Effects of surfactant and salt concentrations on capillary flow and its entry flow for wormlike micelle solutions." *Rheologica Acta*, **45**(6):841–852.

Hatzikiriakos, S. G. & Dealy, J. M. (1991). "Wall slip of molten high-density polyethylenes 1. Sliding plate rheometer studies." *Journal of Rheology*, **35**(4):497–523.

Haward, S. J., Odell, J. A., Berry, M. & Hall, T. (2011). "Extensional rheology of human saliva." *Rheologica Acta*, **50**(11–12):869–879.

Haward, S. J., Ober, T. J., Oliveira, M. S. N, Alves, M. A. & McKinley, G. H. (2012a). "Extensional rheology and elastic instabilities of a wormlike micellar solution in a microfluidic cross-slot device." *Soft Matter*, **8**(2):536–555.

Haward, S. J., Oliveira, M. S. N., Alves, M. A. & McKinley, G. H. (2012b). "Optimized cross-slot flow geometry for microfluidic extensional rheometry." *Physical Review Letters*, **109**(12):128301.

Haward, S. J. & McKinley, G. H. (2012). "Stagnation point flow of wormlike micellar solutions in a microfluidic cross-slot device: Effects of surfactant concentration and ionic environment." *Physical Review E*, **85**:031502.

Haward, S. J., Jaishankar, A., Oliveira, M. S. N., Alves, M. A. & McKinley, G. H. (2012d). "Extensional flow of hyaluronic acid solutions in an optimized microfuidic cross-slot device." *European Conference on Microfluidics*, Heidelberg, Germany.

Helgeson, M. E., Reichert, M. D., Hu, Y. T. & Wagner, N. J. (2009a). "Relating shear banding, structure, and phase behavior in wormlike micellar solutions." *Soft Matter*, **5**(20):3858–3869.

Helgeson, M. E., Vasquez, P. A., Kaler, E. W. & Wagner, N. J. (2009b). "Rheology and spatially resolved structure of cetyltrimethylammonium bromide wormlike micelles through the shear banding transition." *Journal of Rheology*, **53**(3):727–756.

Ho, B. P. & Leal, L. G. (1974). "Inertial migration of rigid spheres in 2-dimensional unidirectional flows." *Journal of Fluid Mechanics*, **65**(2):365–400.

Ho, B. P. & Leal, L. G. (1976). "Migration of rigid spheres in a 2-dimensional unidirectional shear-flow of a 2nd-order fluid." *Journal of Fluid Mechanics*, **76**:783–799.

Hodges, W. (1997). *A Shorter Model Theory.* Cambridge University Press.

Hogg, A. J. (1994). "The inertial migration of non-neutrally buoyant spherical-particles in 2-dimensional shear flows." *Journal of Fluid Mechanics*, **272**:285–318.

Hou, H. W., Bhagat, A. A. S., Chong, A. G. L., Mao, P., Tan, K. S. W., Han, J. Y. & Lim, C. T. (2010). "Deformability based cell margination - A simple microfluidic design for malaria-infected erythrocyte separation." *Lab on a Chip*, **10**(19):2605–2613.

Hu, Y. T. & Lips, A. 2005. "Kinetics and mechanism of shear banding in an entangled micellar solution." *Journal of Rheology*, **49**(5):1001–1027.

Hu, Y. T., Palla, C. & Lips, A. 2008. "Comparison between shear banding and shear thinning in entangled micellar solutions." *Journal of Rheology*, **52**(2):379–400.

Hu, Y. T. (2010). "Steady-state shear banding in entangled polymers?" *Journal of Rheology*, **54**(6):1307–1323.

Huang, P. Y., Feng, J., Hu, H. H. & Joseph, D. D. (1997). "Direct simulation of the motion of solid particles in Couette and Poiseuille flows of viscoelastic fluids." *Journal of Fluid Mechanics*, **343**:73–94.

Hudson, S. D., Phelan, F. R. Jr., Handler, M. D., Cabral, J. T., Migler, K. B. & Amis, E. J. (2004). "Microuidic analog of the four-roll mill." *Applied Physics Letters*, **85**(2):335–337.

Humbert, C. & Decruppe, J. P. 1998. "Stress optical coefficient of viscoelastic solutions of cetyltrimethylammonium bromide and potassium bromide." *Colloid and Polymer Science*, **276**(2):160–168.

Hunter, J. K. & Slemrod, M. (1983). "Viscoelastic Fluid-Flow Exhibiting Hysteritic Phase-Changes." *Physics of Fluids*, **26**(9):2345–2351.

Hur, S. C., Tse, H. T. K. & Di Carlo, D. (2010). "Sheathless inertial cell ordering for extreme throughput flow cytometry." *Lab on a Chip*, **10**(3):274–280.

Hur, S. C., Henderson-MacLennan, N. K., McCabe, E. R. B. & Di Carlo, D. (2011a). "Deformability-based cell classification and enrichment using inertial microfluidics." *Lab on a Chip*, **11**(5):912–920.

Hur, S. C., Choi, S. E., Kwon, S. & Di Carlo, D. (2011b). "Inertial focusing of non-spherical microparticles." *Applied Physics Letters*, **99**(4):044101.

Inn, Y. W., Wissbrun, K. F. & Denn, M. M. (2005). "Effect of edge fracture on constant torque rheometry of entangled polymer solutions." *Macromolecules*, **38**(22):9385–9388.

Israelachvili, J. (2007). *Intermolecular & Surface Forces*. 2^{nd} edn. Academic Press.

Jackson, R. & Kaye, A. (1966). "The measurement of the normal stress differences in a liquid undergoing simple shear flow using a cone-and-plate total thrust apparatus only." *British Journal of Applied Physics*, **17**:1355–1360.

Jain, A. & Munn, L. L. (2009). "Determinants of leukocyte margination in rectangular microchannels." *PLoS One*, 4(9).

James, D. F. & Saringer, J. H. (1982). "Flow of dilute polymer solutions through converging channels." *Journal of Non-Newtonian Fluid Mechanics*, **11**:317–339.

James, D. F. (1991). "Flow in a converging channel at moderate Reynolds-numbers." *AIChE Journal*, **37**(1):59–64.

Janeschitz-Kriegl, H (1983). *Polymer melt rheology and flow birefringence.* Springer-Verlag.

Johnson, M. W. & Segalman, D. A. (1977). "A model for viscoelastic fluid behavior that allows non-affine deformation." *Journal of Non-Newtonian Fluid Mechanics*, **2**(3):255–270.

Jones, T. R., Carpenter, A. E., Lamprecht, M. R., Moffat, J., Silver, S. J., Grenier, J. K., Castoreno, A. B., Eggert, U. S., Root, D. E., Golland, P. & Sabatini, D. M. (2009). "Scoring diverse cellular morphologies in image-based screens with iterative feedback and machine learning." *Proceedings of the National Academy of Sciences of the United States of America*, **106**(6):1826–1831.

Joseph, D. D., Nelson, J., Hu, H. H. & Liu, Y. J. (1992). "Competition between inertial pressure and normal stresses in the flow induced anisotropy of solid particles." *Theoretical and Applied Rheology*, XIth International Congress on Rheology, Brussels, Belgium. P. Moldenaers & R. Keunings (Eds.).

Joseph, D. D. & Liu, Y. J. (1993). "Orientation of long bodies falling in a viscoelastic liquid." *Journal of Rheology*, **37**(6):961–983.

Joseph, D. D. & Liao, T. Y. (1994). "Potential flows of viscous and viscoelastic fluids." *Journal of Fluid Mechanics*, **265**:1–23.

Kameneva, M. K., Wu, Z. J., Uraysh, A., Repko, B., Litwak, K. N., Billiar, T. R., Fink, M. P., Simmons, R. L., Griffith, B. P. & Borovetz, H. S. (2004). "Blood soluble

drag-reducing polymers prevent lethality from hemorrhagic shock in acute animal experiments." *Biorheology*, **41**:53–64.

Kameneva, M. K. (2012). "Microrheological effects of drag-reducing polymers in vitro and in vivo." *International Journal of Engineering Science*, **59**:168–183.

Kang, K., Lee, L. J. & Koelling, K. W. (2005). "High shear microfluidics and its application in rheological measurement." *Experiments in Fluids*, **38**(2):222–232.

Kang, K., Koelling, K. W. & Lee, L. J. (2006). "Microdevice end pressure evaluations with Bagley correction." *Microfluidics and Nanofluidics*, **2**(3):223–235.

Keentok, M., Xue, S. C. (1999). "Edge fracture in cone-plate and parallel plate flows." *Rheologica Acta*, **38**(4):321–348.

Kefi, S., Lee, J., Pope, T. L., Sullivan, P., Nelson, E., *et al.* (2005). "Expanding Applications of Viscoelastic Surfactant Solutions." *Oilfield Review*, **Winter 2004/2005**:10–23.

Khayat, R. E. (1999). "Finite-amplitude Taylor-vortex flow of viscoelastic fluids." *Journal of Fluid Mechanics*, **400**:33–58.

Kim, Y. W. & Yoo, J. Y. (2008). "The lateral migration of neutrally-buoyant spheres transported through square microchannels." *Journal of Micromechanics and Microengineering*, **18**(6):065015.

Klein, S. A. & Posner, J. D. (2010). "Improvement in two-frame correlations by confocal microscopy for temporally resolved micro particle imaging velocimetry." *Measurement Science & Technology*, **21**(10):105409.

Kogan, G., Soltes, L., Stern, R. & Gemeiner, P. (2007). "Hyaluronic acid: a natural biopolymer with a broad range of biomedical and industrial applications." *Biotechnology Letters*, **29**:17–25.

Kolkka, R. W., Malkus, D. S., Hansen, M. G., Ierley, G. R. & Worthing, R. A. (1988). "Spurt phenomena of the Johnson Segalman fluid and related models." *Journal of Non-Newtonian Fluid Mechanics*, **29**(1–3):303–335.

Krivacic, R. T., Ladanyi, A., Curry, D. N., Hsieh, H. B., Kuhn, P., Bergsrud, D. E., Kepros, J. F., Barbera, T., Ho, M. Y., Chen, L. B., Lerner, R. A. & Bruce, R. H. "A rare-cell detector for cancer." *Proceedings of the National Academy of Sciences of the United States of America*, **101**(29):10501–10504.

Kumar, S. & Larson, R. G. (2000). "Shear banding and secondary flow in viscoelastic fluids between a cone and plate." *Journal of Non-Newtonian Fluid Mechanics*, **95**(2–3):295–314.

Kundu, P. K. & Cohen, I. M. (2008). *Fluid Mechanics.* 4^{th} edn. New York, NY: Elsevier.

Landau, L. D. & Lifshitz, E. M. (1976). *Mechanics (Course of theoretical physics).* 3^{rd} edn. Oxford: Butterworth-Heinemann.

Larson, R. G. (1988). *Constitutive Equations for Polymer Melts and Solutions.* Boston, MA: Butterworths.

Larson, R. G., Shaqfeh, E. S. G. & Muller, S. J. (1990). "A purely elastic instability in Taylor-Couette flow." *Journal of Fluid Mechanics*, **218**:573–600.

Larson, R. G. (1992). "Instabilities in Viscoelastic Flows." *Rheologica Acta*, **31**(3):213–263.

Larson, R. G., Muller, S. J. & Shaqfeh, E. S. G. (1994). "The effect of fluid rheology on the elastic Taylor-Couette instability." *Journal of Non-Newtonian Fluid Mechanics*, **51**(2):195–225.

Larson, R. G. (1998). *The Structure and Rheology of Complex Fluids.* New York, NY: Oxford University Press.

Laurent, T. C., Ryan, M. & Pietruszkiewicz, A. (1960). "Fractionation of hyaluronic acid - the polydispersity of hyaluronic acid from the bovine vitreous body." *Biochimica et Biophysica Acta*, **42**(3):476–485.

Lee, C. S., Tripp, B. C. & Magda, J. J. (1992). "Does N_1 or N_2 control the onset of edge fracture." *Rheologica Acta*, **31**(3):306–308.

Lee, J. Y., Fuller, G. G., Hudson, N. E. & Yuan, X. F. (2005). "Investigation of shear-banding structure in wormlike micellar solution by point-wise flow-induced birefringence measurements." *Journal of Rheology*, **49**(2):537–550.

Lee, J. S., Dylla-Spears, R., Teclemariam, N. P. & Muller, S. J. (2007). "Microfluidic four-roll mill for all flow types." *Applied Physics Letters*, **90**(7):074103.

Lee, W., Amini, H., Stone, H. A. & Di Carlo, D. (2010). "Dynamic self-assembly and control of microfluidic particle crystals." *Proceedings of the National Academy of Sciences of the United States of America*, **107**(52):22413–22418.

Lerouge, S., Decruppe, J. P. & Berret, J.-F. (2000). "Correlations between rheological and optical properties of a micellar solution under shear banding flow." *Langmuir*, **16**(16):6464–6474.

Lerouge, S., Decruppe, J. P. & Olmsted, P. D. (2004). "Birefringence banding in a micellar solution or the complexity of heterogeneous flows." *Langmuir*, **20**(26):11355–11365.

Lerouge, S., Argentina, M. & Decruppe, J. P. (2006). "Interface instability in shear-banding flow." *Physical Review Letters*, **96**(8):088301.

Lerouge, S., Fardin, M. A., Argentina, M., Grégoire, G. & Cardoso, O. (2008). "Interface dynamics in shear-banding flow of giant micelles." *Soft Matter*, 4(9):1808–1819.

Lerouge, S. & Berret, J.-F. (2010). "Shear-induced transitions and instabilities in surfactant wormlike micelles." *Advances in Polymer Science*, **230**.

Leshansky, A. M., Bransky, A., Korin, N. & Dinnar, U. (2007). "Tunable nonlinear viscoelastic focusing in a microfluidic device." *Physical Review Letters*, **98**(23): 234501.

Lettinga, M. P. & Manneville, S. (2009). "Competition between shear banding and wall slip in wormlike micelles." *Physical Review Letters*, **103**(24):248302.

Li, J. M. & Burghardt, W. R. (1995). "Flow birefringence in axisymmetrical geometries." *Journal of Rheology*, **39**(4):743–766.

Li, T. Q. & McCarthy, K. L. (1995). "Pipe-flow of aqueous polyacrylamide solutions studied by means of nuclear-magnetic-resonance imaging." *Journal of Non-Newtonian Fluid Mechanics*, **57**(2–3):155–175.

Li, H., Ewoldt, R. H. & Olsen, M. G. (2005). "Turbulent and transitional velocity measurements in a rectangular microchannel using microscopic particle image velocimetry." *Experimental Thermal and Fluid Science*, **29**(4):435–446.

Li, H. & Olsen, M. G. (2006). "MicroPIV measurements of turbulent flow in square microchannels with hydraulic diameters from 200 μm to 640 μm." *International Journal of Heat and Fluid Flow*, **27**(1):123–134.

Lim, E. J., Ober, T. J., Edd, J. F., McKinley, G. H. & Toner, M. (2012). "Visualization of microscale particle focusing in diluted and whole blood using particle trajectory analysis." *Lab on a Chip*, **12**:2199–2210.

Lima, R., Ishikawa, T., Imai, Y., Takeda, M., Wada, S. & Yamaguchi, T. (2008). "Radial dispersion of red blood cells in blood flowing through glass capillaries: The role of hematocrit and geometry." *Journal of Biomechanics*, **41**(10):2188–2196.

Long, D. S., Smith, M. L., Pries, A. R., Ley, K. & Damiano, E. R. (2004). "Microviscometry reveals reduced blood viscosity and altered shear rate and shear stress profiles in microvessels after hemodilution." *Proceedings of the National Academy of Sciences of the United States of America*, **101**(27):10060–10065.

Lopez-Gonzalez, M. R., Holmes, W. M. & Callaghan, P. T. (2006). "Rheo-NMR phenomena of wormlike micelles." *Soft Matter*, **2**(10):855–869.

Losert, W., Bocquet, L., Lubensky, T. C. & Gollub, J. P. (2000). "Particle dynamics in sheared granular matter." *Physical Review Letters*, **85**(7):1428–1431.

Lu, C.-Y. D., Olmsted, P. D. & Ball, R. C. (2000). "Effects of nonlocal stress on the determination of shear banding flow." *Physical Review Letters*, **84**(4):642–645.

Mach, A. J. & Di Carlo, D. (2010). "Continuous scalable blood filtration device using inertial microuidics." *Biotechnology and Bioengineering*, **107**(2):302–311.

Macosko, C. W. (1994). *Rheology: Principles, Measurements and Applications.* New York, NY: Wiley-VCH, Inc.

Mair, R. W. & Callaghan, P. T. (1997). "Shear flow of wormlike micelles in pipe and cylindrical Couette geometries as studied by nuclear magnetic resonance microscopy." *Journal of Rheology*, **41**(4):901–924.

Malik, N. A., Dracos, T. & Papantoniou, D. A. (1993). "Particle tracking velocimetry in 3-dimensional flows. 2. Particle tracking." *Experiments in Fluids*, **15**(4–5):279–294.

Manneville, S., Salmon, J.-B. & Colin, A. (2004a). "A spatio-temporal study of rheo-oscillations in a sheared lamellar phase using ultrasound." *The European Physical Journal E: Soft Matter and Biological Physics*, **13**(2):197–212.

Manneville, S., Salmon, J.-B., Bécu, L., Colin, A. & Molino, F. (2004b). "Inhomogeneous flows in sheared complex fluids." *Rheologica Acta*, **43**(5):408–416.

Manneville, S., Bécu, L., Grondin, P. & Colin, A. (2004a). "High-frequency ultrasonic imaging: A spatio-temporal approach of rheology." *Colloids and Surfaces A: Physicochemical and Engineering Aspects*, **270–271**:195–204.

Manneville, S., Colin, A., Waton, G. & Schosseler, F. (2007). "Wall slip, shear banding, and instability in the flow of a triblock copolymer micellar solution." *Physical Review E*, **75**(6):061502.

Manneville, S. (2008). "Recent experimental probes of shear banding." *Rheologica Acta*, **47**(3):301–318.

Mao, W. B. & Alexeev, A. (2011). "Hydrodynamic sorting of microparticles by size in ridged microchannels." *Physics of Fluids*, **23**(5):051704.

Marín-Santibáñez, B. M., Pérez-González, J., de Vargas, L., Rodríguez-González, F. & Huelsz, G. (2006)., "Rheometry-PIV of Shear-Thickening Wormlike Micelles." *Langmuir*, **22**(9):4015–4026.

Marín-Santibáñez, B. M., Pérez-González, J., de Vargas, L., Decruppe, J. P. & Huelsz, G. (2009). "Visualization of shear banding and entry Poiseuille flow oscillations in a micellar aqueous solution." *Journal of Non-Newtonian Fluid Mechanics*, **157**(1–2):117–125.

Martel, J. M. & Toner, M. (2012). "Inertial focusing dynamics in spiral microchannels." *Physics of Fluids*, **24**:032001.

Masselon, C., Salmon, J. B. & Colin, A. (2008). "Nonlocal effects in flows of wormlike micellar solutions." *Physical Review Letters*, **100**(3):038301.

Masselon, C., Colin, A. & Olmsted, P. D. (2010). "Influence of boundary conditions and confinement on nonlocal effects in flows of wormlike micellar systems." *Physical Review E*, **81**(2):021502.

Matas, J. P., Morris, J. F. & Guazzelli, E. (2004). "Lateral forces on a sphere." *Oil & Gas Science and Technology-Revue D IFP Energies Nouvelles*, **59**(1):59–70.

Matas, J. P., Morris, J. F. & Guazzelli, E. (2004). "Inertial migration of rigid spherical particles in Poiseuille flow." *Journal of Fluid Mechanics*, **515**:171–195.

Maxey, M. R. & Riley, J. J. (1983). "Equation of motion for a small rigid sphere in a nonuniform flow." *Physics of Fluids*, **26**(4):883–889.

Maxey, M. R. (1987). "The gravitational settling of aerosol-particles in homogeneous turbulence and random flow-fields." *Journal of Fluid Mechanics*, **174**:441–465.

Maxwell, J. C. (1867). "On the dynamical theory of gases." *Philosophical Transactions of the Royal Society of London.* **157**:49–88.

McDonald, J. C. & Whitesides, G. M. (2002). "Poly(dimethylsiloxane) as a material for fabricating microfluidic devices." *Accounts of Chemical Research*, **35**(7):491–499.

McKinley, G. H., Oztekin, A., Byars, J. A. & Brown, R. A. (1995). "Self-similar spiral instabilities in elastic flows between a cone and a plate." *Journal of Fluid Mechanics*, **285**:123–164.

McKinley, G. H., Pakdel, P. & Öztekin, A. (1996). "Rheological and geometric scaling of purely elastic flow instabilities." *Journal of Non-Newtonian Fluid Mechanics*, **67**:19–47.

McKinley, G. H. & Tripathi, A. (2000). "How to extract the Newtonian viscosity from capillary breakup measurements in a filament rheometer." *Journal of Rheology*, **44**(3):653–670.

McLeish, T. C. B. & Ball, R. C. (1986). "A molecular approach to the spurt effect in polymer melt flow." *Journal of Polymer Science Part B-Polymer Physics*, **24**(8):1735–1745.

Meeker, S. P., Bonnecaze, R. T. & Cloitre, M. (2004a). "Slip and flow in pastes of soft particles: Direct observation and rheology." *Journal of Rheology*, **48**(6):1295–1320.

Meeker, S. P., Bonnecaze, R. T. & Cloitre, M. (2004b). "Slip and flow in pastes of soft particles: Direct observation and rheology." *Journal of Rheology*, **48**(6):1295–1320.

Meinhart, C. D., Wereley, S. T. & Gray, M. H. B. (2000). "Volume illumination for two-dimensional particle image velocimetry." *Measurement Science & Technology*, **11**(6):809–814.

Méndez-Sánchez, A.F., Pérez-González, J., de Vargas, L., Castrejón-Pita, J.R., Castrejón-Pita, A.A. & Huelsz, G. (2003). "Particle image velocimetry of the unstable capillary flow of a micellar solution." *Journal of Rheology*, **47**(6):1455–1466.

Meulenbroek, B., Storm, C., Morozov, A. N. & van Saarloos, W. (2004). "Weakly nonlinear subcritical instability of visco-elastic Poiseuille flow." *Journal of Non-Newtonian Fluid Mechanics*, **116**(2–3):235–268.

Meyer, F., Lohmann, D. & Kulicke, W. M. (2009). "Determination of the viscoelastic behavior of sodium hyaluronate in phosphate buffered saline with rheo-mechanical and rheo-optical methods." *Journal of Rheology*, **53**(4):799–818.

Miller, E. & Rothstein, J. P. (2007). "Transient evolution of shear-banding wormlike micellar solutions." *Journal of Non-Newtonian Fluid Mechanics*, **143**(1):22–37.

Moller, P. C. F., Rodts, S., Michels, M. A. J. & Bonn, D. (2008). "Shear banding and yield stress in soft glassy materials." *Physical review E*, **77**(4):041507.

Morozov, A. N. & van Saarloos, W. (2007). "An introductory essay on subcritical instabilities and the transition to turbulence in visco-elastic parallel shear flows." *Physics Reports-Review Section of Physics Letters*, **447**(3–6):112–143.

Morris, J. M. & Xie, H. (1994). "Fast algorithms for generalized discrete Gabor expansion." *Signal Processing*, **39**(3):317–331.

Moss, G. R. & Rothstein, J. P. (2010). "Flow of wormlike micelle solutions past a confined circular cylinder." *Journal of Non-Newtonian Fluid Mechanics*, **165**:1505–1515.

Natrajan, V. K. & Christensen, K. T. (2010). "The impact of surface roughness on flow through a rectangular microchannel from the laminar to turbulent regimes." *Microfluidics and Nanofluidics*, **9**(1):95–121.

Nghe, P., Degré, G., Tabeling, P. & Ajdari, A. (2008). "High shear rheology of shear banding fluids in microchannels." *Applied Physics Letters*, **93**(20):204102.

Nghe, P., Fielding, S. M., Tabeling, P. & Ajdari, A. (2010). "Interfacially driven instability in the microchannel flow of a shear-banding fluid." *Physical Review Letters*, **104**(24):248303.

Nyström, M., Tamaddon-Jahromi, H. R., Stading, M. & Webster, M. F. (2012). "Numerical simulations of Boger fluids through different contraction configurations for the development of a measuring system for extensional viscosity." *Rheologica Acta*, **51**:713–727.

Oakey, J., Applegate, R. W., Arellano, E., Di Carlo, D., Graves, S. W. & Toner, M. (2010). "Particle focusing in staged inertial microfluidic devices for flow cytometry." *Analytical Chemistry*, **82**(9):3862–3867.

Ohl, N. & Gleissle, W. (1992). "The second normal stress difference for pure and highly filled viscoelastic fluids." *Rheologica Acta*, **31**:294–305.

Oliveira, M. S. N., Alves, M. A., Pinho, F. T. & McKinley, G. H. (2007). "Viscous flow through microfabricated hyperbolic contractions." *Experiments in Fluids*, **43**(2–3):437–451.

Oliveira, M. S. N., Rodd, L. E., McKinley, G. H. & Alves, M. A. (2008). "Simulations of extensional flow in microrheometric devices." *Microfluidics and Nanofluidics*, **5**(6):809–826.

Olmsted, P. D., Radulescu, O. & Lu, C. Y. D. (2000). "Johnson-Segalman model with a diffusion term in cylindrical Couette flow." *Journal of Rheology*, **44**(2):257–275.

Olmsted, P. D. (2008). "Perspectives on shear banding in complex fluids." *Rheologica Acta*, **47**:283–300.

Owens, R. G. (2006). "A new microstructure-based constitutive model for human blood." *Journal of Non-Newtonian Fluid Mechanics*, **140**(1–3):57–70.

Pakdel, P. & McKinley, G. H. (1996). "Elastic instability and curved streamlines." *Physical Review Letters*, **77**(12):2459–2462.

Pandey, A. & Lele, A. (2007). "Exploring the utility of an axisymmetric semi-hyperbolic die for determining the transient uniaxial elongation viscosity of polymer melts." *Journal of Non-Newtonian Fluid Mechanics*, **144**:170–177.

Papageorgiou, D. T. (1995). "On the breakup of viscous-liquid threads." *Physics of Fluids*, **7**(7):1529–1544.

Pathak, J. A. & Hudson, S. D. (2006). "Rheo-optics of equilibrium polymer solutions: Wormlike micelles in elongational flow in a microfluidic cross-slot." *Macromolecules*, **39**(25):8782–8792.

Patton, T. C. (1979). *Paint Flow and Pigment Dispersion: A Rheological Approach to Coating and Ink Technology.* 2^{nd} edn. New York, NY: Wiley-Interscience.

Patrick, M. J., Chen, C. Y., Frakes, D. H., Dur, O. & Pekkan, K. (2011). "Cellular-level near-wall unsteadiness of high-hematocrit erythrocyte flow using confocal mu PIV." *Experiments in Fluids*, **50**(4):887–904.

Pinho, F. T. & Whitelaw, J. H. (1990). "Flow of non-Newtonian fluids in a pipe." *Journal of Non-Newtonian Fluid Mechanics*, **34**:129–144.

Pipe, C. J., Majmudar, T. S. & McKinley, G. H. (2008). "High shear rate viscometry." *Rheologica Acta*, **47**(5-6):621–642.

Pipe, C. J. & McKinley, G. H. (2009). "Microfluidic rheometry." *Mechanics Research Communications*, **36**(1):110–120.

Pipe, C. J., Kim, N. J., Vasquez, P. A., Cook, L. P. and McKinley, G. H. (2010). "Wormlike micellar solutions: II. Comparison between experimental data and scission model predictions." *Journal of Rheology*, **54**(4):881–913.

Pomeau, Y. (1986). "Front motion, metastability and subcritical bifurcations in hydrodynamics." *Physica D*, **23**(1–3):3–11.

Poole, R. J. & Ridley, B. S. (2007). "Development-length requirements for fully developed Laminar pipe flow of inelastic non-Newtonian liquids." *Journal of Fluids Engineering*, **129**(10):1281–1287.

Porte, G., Berret, J.-F. & Harden, J. L. (1997). "Inhomogeneous flows of complex fluids: Mechanical instability versus non-equilibrium phase transition." *Journal De Physique II*, **7**(3):459–472.

Pranay, P., Henrquez-Rivera, R. G. & Graham, M. D. (2012). "Depletion layer formation in suspensions of elastic capsules in Newtonian and viscoelastic fluids." *Physics of Fluids*, **24**:061902.

Qian, S., Chen, K. & Li, S. (1992). "Optimal biorthogonal functions for finite discrete-time Gabor expansion." *Signal Processing*, **27**(2):177–185.

Racila, E., Euhus, D., Weiss, A. J., Rao, C., McConnell, J., Terstappen, L. W. M. M. & Uhr, J. W. (1998). "Detection and characterization of carcinoma cells in the blood." *Proceedings of the National Academy of Sciences of the United States of America*, **95**(8):4589–4594.

Radulescu, O., Olmsted, P. D. & Lu, C. Y. D. (1999). "Shear banding in reaction-diffusion models." *Rheologica Acta*, **38**:606–613.

Radulescu, O. & Olmsted, P. D. (2000). "Matched asymptotic solutions for the steady banded flow of the diffusive Johnson-Segalman model in various geometries." *Journal of Non-Newtonian Fluid Mechanics*, **91**(2–3):143–164.

Radulescu, O., Olmsted, P. D., Decruppe, J. P., Lerouge, S., Berret, J.-F. & Porte, G. (2003). "Time scales in shear banding of wormlike micelles." *Europhysics Letters*, **62**(2):230–236.

Raffel, M., Willert, C. & Kompenhans, J. (1998). *Particle Image Velocimetry.* Springer-Verlag.

Rajagopalan, D. (2000). "Computational analysis of techniques to determine extensional viscosity from entrance flows." *Rheologica Acta*, **39**:138–151.

Ramachandran, A. & Leighton, D. T. (2008). "The influence of secondary flows induced by normal stress differences on the shear-induced migration of particles in concentrated suspensions." *Journal of Fluid Mechanics*, **603**:207–243.

Raudsepp, A. & Callaghan, P. T. (2008). "A rheo-optical study of shear rate and optical anisotropy in wormlike micelles solutions." *Soft Matter*, **4**(4):784–796.

Rehage, H. & Hoffmann, H. (1991). "Viscoelastic surfactant solutions - model systems for rheological research." *Molecular Physics*, **74**(5):933–973.

Reif, F. (1965). *Berkeley physics course, Volume 5, Statistical physics.* York, NY: McGraw-Hill.

Renardy, M., Hrusa, W. & Nohel, J. (1987). *Mathematical Problems in Viscoelasticity* Essex, England: Longman Sci. & Tech.

Renardy, Y. Y. (1995). "Spurt and instability in a two-layer Johnson-Segalman liquid." *Theoretical and Computational Fluid Dynamics*, **7**(6):463–475.

Ridler, T. W. & Calvard, S. (1978). "Picture thresholding using an iterative selection method." *IEEE Transactions on Systems, Man and Cybernetics*, **8**(8):630–632.

Rochefort, S. & Middleman, S. (1986). "Effect of molecular configuration of xanthan gum drag reduction." *AIP Conference Proceedings*, **137**:117–127.

Rodd, L. E., Scott, T. P., Boger, D. V., Cooper-White, J. J. & McKinley, G. H. (2005). "The inertio-elastic planar entry flow of low-viscosity elastic fluids in micro-fabricated geometries." *Journal of Non-Newtonian Fluid Mechanics*, **129**(1):1–22.

Rodd, L. E., Cooper-White, J. J., Boger, D. V. & McKinley, G. H. (2007). "Role of the elasticity number in the entry flow of dilute polymer solutions in micro-fabricated contraction geometries." *Journal of Non-Newtonian Fluid Mechanics*, **143**:170–191.

Rossi, L. F., McKinley, G. H. & Cook, L. P. (2006). "Slippage and migration in Taylor-Couette flow of a model for dilute wormlike micellar solutions." *Journal of Non-Newtonian Fluid Mechanics*, **136**(2–3):79–92.

Rothstein, J. P. (2008). "Strong flows of viscoelastic wormlike micelle solutions." *Rheology Reviews, The British Soceity of Rheology*, 1–43. D. M. Binding & K. Walters (Eds.).

Rubinstein, M. & Colby, R. H. (2003). *Polymer Physics.* New York, NY: Oxford University Press.

Russel, W. B. & Grant, M. C. (2000). "Distinguishing between dynamic yielding and wall slip in a weakly flocculated colloidal dispersion." *Colloids and Surfaces A: Physicochemical and Engineering Aspects*, **161**(2):271–282.

Salmon, J. B., Colin, A. & Manneville, S. (2003). "Velocity profiles in shear-banding wormlike micelles." *Physical Review Letters*, **90**(22):228303.

Sato, K., Yuan, X. F. & Kawakatsu, T. (2010). "Why does shear banding behave like first-order phase transitions? Derivation of a potential from a mechanical constitutive model." *European Physical Journal E*, **31**:135–144.

Sanchez, A. M., Bejarano, J. D. & Marzal, D. C. (1993). "Solution of the anharmonic quartic potential oscillator problem." *Journal of Sound and Vibration*, **161**(1):19–31.

Schmitt, V., Lequeux, F., Pousse, A. & Roux, D. (1994). "Flow behavior and shear induced transition near an isotropic/nematic transition in equilibrium polymers." *Langmuir*, **3**(10):955–961.

Schmitt, V., Marques, C. M. & Lequeux, F. (1995). "Shear-induced phase-separation of complex fluids - the role of flow-concentration coupling." *Physical Review E*, **52**(4):4009–4015.

Schmid-Schönbein, G. W., Usami, S., Skalak, R. & Chein, S. (1980). "The interaction of leukocytes and erythrocytes in capillary and postcapillary vessels." *Microvascular Research*, **19**:45–70.

Schonberg, J. A. & Hinch, E. J. (1989). "Inertial migration of a sphere in Poiseuille flow." *Journal of Fluid Mechanics*, **203**:517–524.

Schuberth, S. & Münstedt, H. (2008). "Transient elongational viscosities of aqueous polyacrylamide solutions measured with an optical rheometer." *Rheologica Acta*, **47**(2):139–147.

Segré, G. & Silberberg, A. (1961). "Radial particle displacements in Poiseuille flow of suspensions." *Nature*, **189**(476):209–210.

Segré, G. & Silberberg, A. (1962a). "Behaviour of macroscopic rigid spheres in Poiseuille flow. 1. Determination of local concentration by statistical analysis of particle passages through crossed light beams." *Journal of Fluid Mechanics*, **14**(1):115–135.

Segré, G. & Silberberg, A. (1962b). "Behaviour of macroscopic rigid spheres in Poiseuille flow. 2. Experimental results and interpretation." *Journal of Fluid Mechanics*, **14**(1):136–157.

Sentmanat, M. L. (2004). "Miniature universal testing platform: from extensional melt rheology to solid-state deformation behavior." *Rheologica Acta*, **43**(6):657–669.

Shikata, T., Hirata, H. & Kotaka, T. (1987). "Micelle formation of detergent molecules in aqueous-media - Viscoelastic properties of aqueous cetyltrimethylammonium bromide solutions." *Langmuir*, **8**(6):1081–1086.

Shikata, T., Hirata, H., Takatori, E. & Osaki, K. (1988). "Nonlinear viscoelastic behavior of aqueous detergent solutions." *Journal of Non-Newtonian Fluid Mechanics*, **28**(2):171–182.

Shikata, T., Dahman, S. J. & Pearson, D. S. (1994). "Rheooptical behavior of wormlike micelles." *Langmuir*, **10**(10):3470–3476.

Shimada, E. & Matsumura, G. (2003). "Viscosity and molecular weight of hyaluronic acids." *Journal of Biochemistry*, **78**(3):513–517.

Shribak, M. & Oldenbourg, R. (2003). "Techniques for fast and sensitive measurements of two-dimensional birefringence distributions." *Applied Optics*, **42**(16):3009–3017.

Skorski, S. & Olmsted, P. D. (2011). "Loss of solutions in shear banding fluids driven by second normal stress differences." *Journal of Rheology*, **55**(6):1219–1246.

Smits, A. J. & Lim, T. T. (2012). *Flow Visualization: Techniques and Examples*, 2^{nd} edn. London: Imperial College Press.

Snyder, W. H. & Lumley, J. L. (1987). "Some measurements of particle velocity autocorrelation functions in a turbulent flow." *Journal of Fluid Mechanics*, **48**:41–71.

Sollier, E., Murray, C., Maoddi, P. & Di Carlo, D. (2011) "Rapid prototyping polymers for microfluidic devices and high pressure injections." *Lab on a Chip*, **11**(22):3752–3765.

Soulages, J., Oliveira, M. S. N., Sousa, P. C., Alves, M. A. & McKinley, G. H. (2009). "Investigating the stability of viscoelastic stagnation flows in T-shaped microchannels." *Journal of Non-Newtonian Fluid Mechanics*, **163**(1–3):9–24.

Sousa, P. C., Pinho, F. T., Oliveira, M. S. N. & Alves, M. A. (2011). "Extensional flow of blood analog solutions in microfluidic devices." *Biomicrofluidics*, **5**:014108.

Sousa, P. C., Pinho, F. T., Oliveira, M. S. N. & Alves, M. A. (2012). "High performance microfluidic rectifiers for viscoelastic fluid flow." *RSC Advances*, **2**(3):920–929.

Sprakel, J., Spruijt, E., Stuart, M. A. C., Besseling, N. A. M., Lettinga, M. P. & van der Gucht, J. (2008). "Shear banding and rheochaos in associative polymer networks." *Soft Matter*, **4**(8):1696–1705.

Spenley, N. A., Yuan, X. F. & Cates, M. E. (1996). "Nonmonotonic constitutive laws and the formation of shear-banded flows." *Journal De Physique II*, **6**(4):551–571.

Stone, P. A., Hudson, S. D., Dalhaimer, P., Discher, D. E., Amis, E. J. & Migler, K. B. (2006). "Dynamics of wormlike micelles in elongational flows." *Macromolecules*, **39**(20):7144–7148.

Sui, C. & McKenna, G. B. (2007). "Instability of entangled polymers in cone and plate rheometry." *Rheologica Acta*, **46**(6):877–888.

Swann, D. A., Radin, E. L., Nazimiec, M., Weisser, P. A., Curran, N. & Lewinnek, G. (1974). "Role of hyaluronic-acid in joint lubrication." *Annals of the Rheumatic Diseases*, **33**(4):318–326.

Takahashi, T., Shirakashi, M., Miyamoto, K. & Fuller, G. G. (2002). "Development of a double-beam rheo-optical analyzer for full tensor measurement of optical anisotropy in complex fluid flow." *Rheologica Acta*, **41**(5):448–455.

Tamaddon-Jahromi, H. R., Webster, M. F., Aguayo, J. P. & Manero, O. (2011). "Numerical investigation of transient contraction flows for worm-like micellar systems using Bautista-Manero models." *Journal of Non-Newtonian Fluid Mechanics*, **166**(1–2):102–117.

Tanner, R. I. & Keentok, M. (1983). "Shear fracture in cone–plate rheometry." *Journal of Rheology*, **27**(1):47–57.

Tapadia, P. & Wang, S. Q. (2004). "Nonlinear flow behavior of entangled polymer solutions: Yieldlike entanglement-disentanglement transition." *Macromolecules*, **37**(24):9083–9095.

Tapadia, P., Ravindranath, S. & Wang, S. Q. (2006). "Banding in entangled polymer fluids under oscillatory shearing." *Physical Review Letters*, **96**(19):196001.

Taylor, G. I. (1923). "Stability of a viscous liquid contained between two rotating cylinders." *Philosophical Transactions of the Royal Society of London Series A-Mathematical Physical and Engineering Sciences*, **223**:289–343.

Tehrani, M. A. (1996). "An experimental study of particle migration in pipe flow of viscoelastic fluids." *Journal of Rheology*, **40**(6):1057–1077.

Tennekes, H. & Lumley, J. L. (1972). *A First Course in Turbulence*. Cambridge, MA: MIT Press.

Tirtaatmadja, V., McKinley, G. H. & Cooper-White, J. J. (2006). "Drop formation and breakup of low viscosity elastic fluids: Effects of molecular weight and concentration." *Physics of Fluids*, **18**(4):043101.

Turner, M. S. & Cates, M. E. (1991). "Linear viscoelasticity of living polymers - a quantitative probe of chemical relaxation-times." *Langmuir*, **7**(8):1590–1594.

Turner, M. S. & Cates, M. E. (1992). "Linear viscoelasticity of wormlike micelles - a comparison of micellar reaction-ninetics." *Journal De Physique II*, **2**(3):503–519.

Turner, M. S., Marques, C. & Cates, M. E. (1993). "Dynamics of wormlike micelles - the bond-interchange reaction scheme." *Langmuir*, **9**(3):695–701.

Van Dyke, M. (1982). *An Album of Fluid Motion*, 12^{th} edn. Stanford, CA: Parabolic Press, Inc.

Vasquez, P. A., McKinley, G. H. & Cook, L. P. (2007). "A network scission model for wormlike micellar solutions - I. Model formulation and viscometric flow predictions." *Journal of Non-Newtonian Fluid Mechanics*, **144**(2-3):122–139.

Villone, M. M., D'Avino, G., Hulsen, M. A., Greco, F. & Maffettone, P. L. (2011a). "Simulations of viscoelasticity-induced focusing of particles in pressure-driven micro-slit flow." *Journal of Non-Newtonian Fluid Mechanics*, **166**(23–24):1396–1405.

Villone, M. M., D'Avino, G., Hulsen, M. A., Greco, F. & Maffettone, P. L. (2011b). "Numerical simulations of particle migration in a viscoelastic fluid subjected to Poiseuille flow." *Computers & Fluids*, **42**(1):82–91.

Villone, M. M., D'Avino, G., Hulsen, M. A., Greco, F. & Maffettone, P. L. (2013). "Particle motion in square channel flow of a viscoelastic liquid: Migration vs. secondary flows." *Journal of Non-Newtonian Fluid Mechanics*, **195**:1–8.

Wang, S. Q. (2009). "Comment on "Nonmonotonic Mmodels are not necessary to obtain shear banding phenomena in entangled polymer solutions". " *Physical Review Letters*, **103**(21):219801.

Wang, J. James, D. F. & Park, C. B. (2010). "Planar extensional flow resistance of a foaming plastic." *Journal of Rheology*, **54**(1):95–116.

Wang, J. & James, D. F. (2011). "Lubricated extensional flow of viscoelastic fluids in a convergent microchannel." *Journal of Rheology*, **55**(5):1103–1126.

Wheeler, E. K., Fischer, P. & Fuller, G. G. (1998). "Time-periodic flow induced structures and instabilities in a viscoelastic surfactant solution." *Journal of Non-Newtonian Fluid Mechanics*, **75**(2-3):193–208.

White, F. M. (2006). *Viscous Fluid Flow.* 2^{nd} edn. New York, NY: McGraw-Hill.

White, C. M. & Mungal, M. G. (2008). "Mechanics and prediction of turbulent drag reduction with polymer additives." *Annual Review of Fluid Mechanics*, **40**:235-256.

Whitesides, G. M. (2006). "The origins and the future of microfluidics." *Nature*, **442**(7101):368–373.

Wilhelm, M., Maring, D. & Spiess, H.-W. (1998). "Fourier-transform rheology." *Rheologica Acta*, **37**(4):399–405.

Wu, Z. G., Willing, B., Bjerketorp, J., Jansson, J. K. & Hjort, K. (2009). "Soft inertial microfluidics for high throughput separation of bacteria from human blood cells." *Lab on a Chip*, **9**(9):1193–1199.

Wunderlich, I., Hoffmann, H. & Rehage, H. (1987). "Flow birefringence and rheological measurements on shear induced micellar structures." *Rheologica Acta*, **26**(6):532–542.

Wyss, H. M., Miyazaki, K., Mattsson, J., Hu, Z. and Reichman, D. R. & Weitz, D. A. (2007) "Strain-rate frequency superposition: A rheological probe of structural relaxation in soft materials." *Physical Review Letters*, **98**(23):238303.

Xue, S.-C., Phan-Thein, N. & Tanner, R. I. (1995). "Numerical study of secondary flows of viscoelastic fluid in straight pipes by an implicit finite volume method." *Journal of Non-Newtonian Fluid Mechanics*, **59**:191–213.

Yager, P., Domingo, G. J. & Gerdes, J. (2008). "Point-of-care diagnostics for global health." *Annual Review of Biomedical Engineering*, **10**:107–144.

Yamamoto, T., Hashimoto, T. & Yamashita, A. (2008). "Flow analysis for wormlike micellar solutions in an axisymmetric capillary channel." *Rheologica Acta*, **47**(9):963–974.

Yang, S., Kim, J. Y., Lee, S. J., Lee, S. S. & Kim, J. M. (2011). "Sheathless elasto-inertial particle focusing and continuous separation in a straight rectangular microchannel." *Lab on a Chip*, **11**(2):266–273.

Yesilata, B., Clasen, C. & McKinley, G. H. (2006). "Nonlinear shear and extensional ow dynamics of wormlike surfactant solutions." *Journal of Non-Newtonian Fluid Mechanics*, **133**:73–90.

Zeighami, R., Laser, D., Zhou, P., Asheghi, M., Devasenathipathy, S., Kenny, T., Santiago, J. & Goodson, K. (2000). "Experimental investigation of flow transition in microchannels using micron-resolution particle image velocimetry." *Itherm 2000: Seventh Intersociety Conference on Thermal and Thermomechanical Phenomena in Electronic Systems, Vol 2, Proceedings*, 148–153.

Zhou, L., Vasquez, P. A., Cook, L. P. & McKinley, G. H. (2008). "Modeling the inhomogeneous response and formation of shear bands in steady and transient flows of entangled liquids." *Journal of Rheology*, **52**(2):591–623.

Zhou, L., Cook, L. P. & McKinley, G. H. (2010). "Probing shear-banding transitions of the VCM model for entangled wormlike micellar solutions using large amplitude oscillatory shear (LAOS) deformations." *Journal of Non-Newtonian Fluid Mechanics*, **65**(21–22):1462–1472.

Zrehen, A. & Ramachandran, A. (2013). "Demonstration of secondary currents in the pressure-driven flow of a concentrated suspension through a square conduit." *Physical Review Letters*, **110**:018306.